

Monolithically Integrated Phase Change Material GeTe-Based RF Components for Millimeter Wave Applications

by

Tejinder Singh

A thesis
presented to the University of Waterloo
in fulfillment of the
thesis requirement for the degree of
Doctor of Philosophy
in
Electrical and Computer Engineering

Waterloo, Ontario, Canada, 2020

© Tejinder Singh 2020

Examining Committee Membership

The following served on the Examining Committee for this thesis. The decision of the Examining Committee is by majority vote.

- External Examiner: **Mina Rais-Zadeh**
Group Supervisor and Adj. Associate Professor
Advanced Optical and Electromechanical Microsystems
NASA Jet Propulsion Laboratory (JPL)
California Institute of Technology, Pasadena, CA 91109, USA
also with Electrical Engineering and Computer Science
University of Michigan, Ann Arbor, MI 48109, USA
mina.rais-zadeh@jpl.nasa.gov
- Supervisor: **Raafat R. Mansour**
Professor
Department of Electrical and Computer Engineering
University of Waterloo, Waterloo, ON N2L 3G1, Canada
rrmansour@uwaterloo.ca
- Internal Member(s): **Omar M. Ramahi**
Professor
Department of Electrical and Computer Engineering
University of Waterloo, Waterloo, ON N2L 3G1, Canada
oramahi@uwaterloo.ca
- Bo Cui**
Professor
Department of Electrical and Computer Engineering
University of Waterloo, Waterloo, ON N2L 3G1, Canada
bcui@uwaterloo.ca
- Internal-External Member: **Eihab Abdel-Rahman**
Professor
Department of System Design Engineering
University of Waterloo, Waterloo, ON N2L 3G1, Canada
eihab@uwaterloo.ca

Author's Declaration

I hereby declare that I am the sole author of this thesis. This is a true copy of the thesis, including any required final revisions, as accepted by my examiners.

I understand that my thesis may be made electronically available to the public.

Abstract

RF switches are the fundamental building blocks for realizing reconfigurable front-ends in communication devices. Currently available RF switches are dominated by semiconductor technology which, while performing adequately up to a few GHz, suffer from signal leakage issues at millimeter-wave (mmWave) frequencies. On the other hand, mechanical RF components provide exceptional RF performance and reliability, but are bulky and expensive, whereas switches based on microelectromechanical systems (MEMS) have reliability issues and require high actuation voltage. Therefore, there is a clear need to develop reliable miniature components in order to deliver cost-effective and superior RF performance for various applications at mmWave frequencies.

Chalcogenide phase change materials (PCMs) have been widely used in optical storage media and non-volatile memories. PCM especially germanium telluride (GeTe) exhibits more than five-orders of resistance change with the application of short nanosecond thermal pulses. PCM's property of resistance change is exploited to develop highly miniaturized and latching (non-volatile) RF switches with negligible DC power consumption. RF PCM technology carries a potential to highly miniaturize and monolithically integrate complex reconfigurable microwave components.

This thesis reports the development of miniaturized and reliable PCM GeTe-based RF switch as a fundamental unit-cell for reconfigurable mmWave devices. RF switches that exhibit exceptional RF performance from DC to 67 GHz are developed using an optimized in-house eight layer microfabrication process. Design parameters of the switches and their impact on RF performance is investigated along with material characterization and optimization of GeTe thin films. High power handling and linearity of the switches has been experimentally investigated. The developed GeTe-based RF switches are cycled for more than 1 million times demonstrating high reliability. The non-volatility of the PCM switches has been validated by studying the variation in ON-state and OFF-state resistance over time.

Miniaturization of reconfigurable RF components requires dense integration of RF switches. PCM GeTe-based switch matrices utilizing RF switches as a unit-cell have been

demonstrated for the first time. Compact single-port multiple-throw (SPNT) switches are developed in SP2T, SP3T, SP8T, and SP16T configurations. A monolithically integrated scalable four-port RF switch unit-cell is demonstrated with two operational states. A reconfigurable band rejection module is realized utilizing a scalable switch matrix. A broadband mmWave T-type RF switch with three operational states is demonstrated from DC to 67 GHz. An approach to monolithically cascade T-type switches for redundancy applications is used for the development of a 4×6 redundancy switch matrix. Multiple compact PCM GeTe-based scalable crossbar switch matrices are developed for mmWave applications. Crossbar switch matrices up to 16×16 are also developed for non-volatile low frequency signal routing applications.

This thesis reports first demonstration of various PCM-based reconfigurable RF components. Utilizing multi-port switches and switch matrices, RF components such as switched capacitor banks, reconfigurable switched variable attenuators, true-time-delay switched phase shifters and reflective type phase shifters are developed for mmWave applications. Broadband on-chip integrated resistors and matched terminations are developed. A technique to improve the self-resonance frequency of on-chip capacitors by design optimization has been discussed.

PCM-based switches allow extremely tight integration in reconfigurable RF circuits despite their requirement of higher than 725°C for melt-quench switching action. Heat distribution and thermal cross-coupling (actuation crosstalk) in GeTe-based switches has been experimentally studied for the first time using transient thermal imaging. Intermediate non-volatile resistance states in GeTe are observed at cryogenic and room temperatures. This can be seen as an opportunity to improve the reliability of PCM GeTe-based devices at superconducting temperatures. Possibility of monolithic integration and miniaturization capabilities of PCM technology for reconfigurable RF components demonstrated that are in this doctoral research prove the vast potential of this technology for future wireless networks.



Acknowledgements

First and foremost, I wish to express my sincere appreciation and gratitude to my advisor Prof. Raafat R. Mansour who gave me the opportunity to join his research group. As an educator and engineer, Prof. Mansour has been an exceptional role model with his academic insights and his accessibility to students. I am grateful for his guidance, encouragement and inspiration throughout the course of my doctoral research. The enthusiasm he has for research is contagious and kept me motivated. Apart from research, I have learnt a lot of life skills from him, especially the value of patience.

I would also like to thank my committee member Prof. Mina Rais-Zadeh at NASA Jet Propulsion Laboratory, California Institute of Technology (external committee examiner) for her valuable insights on phase change materials and expert opinions on this doctoral research.

Thanks to the internal committee members at the University of Waterloo, Prof. Omar Ramahi, who motivated me to pursue graduate course in electromagnetics, Prof. Eihab Abdel-Rahman for providing valuable expertise on MEMS/NEMS modeling, and Prof. Bo Cui for his expert opinions on micro/nanofabrication. Special thanks to Prof. Slim Boumaiza and Prof. John R. Long for their advice and help on RF and microwave engineering related queries.

I would like to thank our lab manager Dr. Luis Enrique Gutierrez for maintaining the lab equipment and always there to help in providing necessary inventory/supplies. He also provided training to many cleanroom users. Special thanks to our ex-lab manager Bill Jolley, whose professional experience has been a great help at several times in my research projects. He also trained me on many RF testing and measurement equipment at the Centre for Integrated RF Engineering (CIRFE), University of Waterloo.

I also acknowledge current graduate students of the CIRFE research group especially Navjot Khaira, Huayong Jia, Arash Fouladi, Farzad Yazdani, Edward Jin, Gowrish Bassavarajappa, Hassan Kianmehr, Delaram Ghadri, Peng Zhang, Matthew Ou, Armin Smajevic, and past graduate students Dr. Mostafa Azizi at Skyworks Inc., Dr. Oliver

Wong at Huawei Canada, Dr. Ahmed Abdel-Aziz at McGill University, Dr. Neil Sarkar at ICSPi and Adhawk Microsystems, Dr. Desireh Asanjan at Apple Inc., Dr. Scott Chen at Conestoga College, Dr. Frank Jiang at the University of Waterloo, Bahaedinne Jlassi, Nazli Kheirabi, Brian Cho, Geoffery Lee, Yamuna Jayan and Ali Mojdeh who have contributed immensely through the valuable discussions to make my PhD journey a meaningful experience for me.

It is always cheerful to meet past CIRFE graduates at the IEEE MTT-S International Microwave Symposium (IMS) dinner ritual, I feel great to have fruitful discussions with Late Prof. Mojgan Daneshmand from University of Alberta, Prof. Reena Al-Dahleh at State University of New York, Prof. Paul LaForge at University of Regina, Prof. Soren Piek at Technical University of Bremen, Dr. Mohamed Fahmi at Defence Research and Development Canada, and Dr. Lee Zhu at Telesat Canada.

I am indebted to all the staff members of Quantum-Nano Fabrication and Characterization Facility (QNFCF) at the Waterloo Institute for Nanotechnology who not only trained me on several pieces of cleanroom equipment but also provided their valuable suggestions on process engineering. It was always a pleasure to have insightful discussions with QNFCF staff members, Dr. Nathan Nelson-Fitzpatrick, Dr. Greg Holloway, Dr. Sandra Gibson, Dr. Lino Eugene, Matt Scott, Rodello Salandanan, and Brian Godard.

I love and appreciate the support from my father Harjinder Singh, who always pushed me to move forward and taught me to never quit, my mother Gurdeep Kaur who's creative inspirations and learning motivations made me a better human being. She is always there by my side in the ups and downs of my life. My younger sisters Ramandeep Kaur and Ramneet Kaur for bringing all the fun and laughter into my life. I am grateful to my mother-in-law and father-in-law for all their love and encouragement.

I have no words to express my thanks to my best friend, my colleague, my wife Navjot Khaira for her unconditional love, support and unflinching care throughout my journey. Being in the similar research areas, she provides valuable insights on solving engineering problems from theoretical perspective while I always approach the problems from practical viewpoint. She is a passionate learner and a very good listener. Working in

the cleanroom and in the RF lab over the extended hours/weekends that my research demanded, she always happily accompanied me (two people during extended hours) to follow the lab safety policy without ever complaining. She has provided me extensive moral support. She believed in my research from the very beginning even when my fabricated devices did not show promising results in the initial years. She was always the one who run to Prof. Raafat Mansour's office to bring him to the lab whenever I successfully measure fabricated devices. During the testing of RF devices, she was more happy than me to see the PCM switches cycle for more than 1 million times.

I would like to thank the Almighty for providing me the wisdom and strength during all the low times of my life and blessing me with such amazing and loving people in my life. He has given me the intelligence and will-power to learn and explore the wonders that He has created, for nothing is possible without His will.

Last but not the least, I appreciate the financial support from Natural Sciences and Engineering Research Council of Canada (NSERC), Govt. of Canada for selecting me for highly competitive Vanier Canada Graduate Scholarship (CGS) and Postdoctoral Fellowship (PDF). Financial support from the University of Waterloo in the form of President's Graduate Scholarship, Faculty of Engineering Awards, Waterloo Institute for Nanotechnology (WIN) for selecting me twice as a Nanofellowship recipient. Support from CMC Microsystems, Canada is acknowledged for providing some RF test equipment, access to CAD compute cluster and also for selecting this research nationally for Brian L. Barge Microsystems Integration Award. Research appreciation from IEEE Microwave Theory and Techniques Society (MTT-S) and European Microwave Association (EuMA) for selecting this research for Best Paper awards in International Microwave Symposium (IMS) and European Microwave Conference (EuMC) and various MTT-S conferences. Thanks to Compute Canada for providing access to "Graham" one of Canada's large-scale supercomputer with over 1,000 nodes and 33,000 CPU cores. Complex simulations on this big scale computing resource was always a breeze.

Dedication

*To my father, my mother, my wife,
and my sisters, who see me through.*

Table of Contents

Examination Committee Membership	ii
Author’s Declaration	iii
Abstract	iv
Acknowledgements	vi
Dedication	ix
List of Figures	xviii
List of Tables	xxxvi
List of Terminology	xxxviii
List of Acronyms	xlv
List of Symbols	li
1 Introduction	1
1.1 Motivation	1
1.2 Research Objectives	3
1.3 Thesis Outline	5

TABLE OF CONTENTS

2	Background Information	7
2.1	History of Phase Change Materials	7
2.1.1	Further Advancements in Phase Change Memory	8
2.1.2	Early Attempts with Phase Change Memory	8
2.2	Theoretical Background	9
2.2.1	Basic Principle of Phase Change Materials	9
2.2.2	Phase Change Alloys	10
2.3	Phase Change Materials for RF Applications	11
2.3.1	Metal-Insulator Transition Material - Vanadium Oxide	11
2.3.2	Germanium Telluride (GeTe)	12
2.3.3	Switching from Amorphous to Crystalline State	12
2.3.4	Switching from Crystalline to Amorphous State	14
2.4	Microwave Switching	15
2.4.1	Mechanical RF Switches	16
2.4.2	Solid-State (Semiconductor) Switches	17
2.4.3	RF-MEMS Switches	18
2.4.4	Phase Change RF Switches	20
2.4.5	RF Performance Comparison	22
2.5	Multi-Port Switches and Switch Matrices	24
2.5.1	Switch Matrix Configuration	26
2.5.2	C and R-Type Switches	28
2.5.3	T-Type Switch	29
2.5.4	Switch Matrices Scalability	30
3	Characterization of Chalcogenide PCM GeTe for RF Switches	32
3.1	Phase Transition	33
3.2	PCM Thin-Film Characterization	33
3.2.1	Deposition Conditions	34

TABLE OF CONTENTS

3.2.2	Study of Surface Topography	35
3.2.2.1	Effect on Deposition Temperature	37
3.2.2.2	Roughness Estimation Using Grain Mapping	39
3.2.2.3	Effect on Deposition Pressure	40
3.2.2.4	Resistance Mapping Across Wafer	41
3.2.2.5	PCM Resistance Change	42
3.3	Micro-Heaters for Actuation	43
3.3.1	Residual Stresses in Tungsten	43
3.3.2	Electrical Characterization	44
3.4	RF PCM Development Constraints	45
3.4.1	Voids / Cracks Formation in GeTe	45
3.4.2	Melting	46
3.4.3	Optical Lithography	48
4	Development of PCM GeTe-Based RF Switches	49
4.1	Design, Operation and Fabrication	50
4.1.1	Principle of Operation	50
4.1.2	Microfabrication Process (Gen 1)	51
4.1.3	Parametric Study on Design Optimization	52
4.1.4	Microfabrication Process (Gen 2)	56
4.1.5	Improvements in Bias Networks	58
4.1.6	Microfabrication Process (Gen 3)	59
4.1.6.1	Summary of Microfabrication Processes	62
4.2	Parasitic Capacitance	62
4.3	Lumped Model of the RF PCM Switch	64
4.4	RF PCM Switch Measurements	65
4.4.1	Switch Actuation Testing	65
4.4.1.1	Bias Signature	66

TABLE OF CONTENTS

4.4.2	RF Performance Measurements	66
4.4.3	DC Current Carrying Capacity of PCM Switches	70
4.4.4	RF Power Handling and Self Actuation	72
4.4.4.1	RF Power Handling Measurements	74
4.4.4.2	Self-Actuation using RF Power	75
4.4.5	Linearity and Intermodulation Distortion Measurements	75
4.4.5.1	Harmonic Distortion	75
4.4.6	Intermodulation Distortion	76
4.4.7	Switching Speed Analysis	80
4.4.8	Device Lifetime Cycles and Reliability Testing	82
4.4.8.1	Reliability: Device Switching Cycles	86
4.4.8.2	Reliability: State Stability	86
4.5	Comparison with State-of-the-Art	87
5	Investigation on Transient Heat Distribution in PCM Switches	91
5.1	Thermoreflectance Based Transient Thermal Imaging	92
5.1.1	Experimental Setup	92
5.2	High Speed Refractory Micro-Heaters	96
5.3	Transient Thermal Imaging of Micro-Heaters	97
5.4	Transient Thermal 3D Multiphysics Modeling of PCM Switches	100
5.5	Experimental Investigation of Thermal Crosstalk	104
5.6	Post Pulsing Failure Investigation	108
5.6.1	Thermal Balance in PCM Switches	109
6	Multi-Port Switches and Switch Matrices	111
6.1	Multi-Port Switches	112
6.1.1	SP2T and SP3T Switches	112
6.1.1.1	Routing Functionality	113

TABLE OF CONTENTS

6.1.1.2	RF Port Size and Device Core Area	114
6.1.1.3	SP3T Switch v2	114
6.1.2	SP8T and SP16T Switches	116
6.2	RF PCM Switch Matrices	123
6.2.1	2×2 Scalable Switch Matrix	124
6.2.1.1	Design and Operation Principle	125
6.2.1.2	RF Performance Measurement	126
6.2.1.3	RF Device Selector Application	128
6.2.1.4	Scalability to Higher Order Matrices	130
6.2.2	Reconfigurable Band Rejection Utilizing 2×2 Switch Matrix	131
6.2.3	Miniaturized DC–67 GHz T-type Switch Unit-Cell	134
6.2.3.1	Device Design and Operation	134
6.2.3.2	Thermal Crosstalk	137
6.2.3.3	Performance Optimization of CPW Discontinuities	137
6.2.3.4	RF Performance Measurement	138
6.2.4	Monolithically Integrated DC–60 GHz 4×6 Redundancy Switch Matrix	139
6.2.4.1	RF Performance Measurement	144
6.2.5	Ultra Compact RF mmWave 4×4 Crossbar Switch Matrix	146
6.2.5.1	Scalable Crossbar Switch Matrix Architecture	147
6.2.5.2	Crossbar Switch Matrix Unit-Cell	148
6.2.5.3	2×2 Crossbar Switch Matrix	150
6.2.5.4	4×4 Crossbar Switch Matrix	153
6.2.5.5	RF Performance Evaluation of Crossbar Switch Matrices	155
6.2.6	PCM-based Scalable Latching Crossbar Switch Matrices for Low Frequency Applications	159
6.2.6.1	LF 4×12 Crossbar Switch Matrix	159
6.2.6.2	LF 16×16 Crossbar Switch Matrix	162
6.3	Summary of Devices	164

7	Reconfigurable PCM-Based Passive RF Components	165
7.1	Capacitor Bank	166
7.1.1	Reconfigurable Latching 6-Bit Digital Switched Capacitor Bank	166
7.1.1.1	Operation Principle of Switched Capacitor Bank	167
7.1.1.2	Performance Measurements	170
7.1.2	Self Resonance Frequency Improvement	171
7.1.3	Reconfigurable 8-Bit Rotary Switched Capacitor Bank	174
7.1.3.1	Operation Principle of 8-Bit Switched Capacitor Bank	174
7.1.3.2	Simulation and Measurement	176
7.2	mmWave Variable Attenuators	177
7.2.1	Reconfigurable 28 GHz 4-bit Latching Variable Attenuator	177
7.2.1.1	Description and Operation of Variable Attenuator	178
7.2.1.2	Simulation and Measurement Data	181
7.2.1.3	Broadband On-Chip Resistors	182
7.2.2	Scalable PCM-Based Variable Attenuator Using T-type Switch	183
7.2.2.1	RF Performance Simulation and Measurement	185
7.3	mmWave Phase Shifters	188
7.3.1	Loss Compensated Wideband 3-bit Switched 30 GHz True-Time-Delay Phase Shifter	188
7.3.1.1	Operation Principle of TTD Phase Shifter	191
7.3.1.2	RF Performance Measurement	194
7.3.2	Low Loss 3-bit Switched True-Time-Delay 30 GHz Phase Shifter Using PCM SP8T Switches	196
7.3.2.1	RF Performance Measurement	198
7.3.3	Monolithically Integrated 28 GHz PCM-Based Reflective Type Latching Phase Shifter	201
7.3.3.1	Phase Shifter Design and Operation Principle	202
7.3.3.2	Reflective Loads	202

TABLE OF CONTENTS

7.3.3.3	28 GHz Hybrid Coupler	205
7.3.3.4	RF Performance Measurement	206
7.3.3.5	Comparison of mmWave Phase Shifters	208
7.4	Reconfigurable PCM-Based Impedance Matching Network	208
7.4.0.1	Operation Principle of Impedance Tuner	209
7.4.0.2	RF Performance Simulation and Impedance Coverage	210
7.5	Summary of PCM based RF Components	211
8	Study of PCM RF Switches at Cryogenic Temperature	212
8.1	Temperature Dependant Performance Improvement	213
8.1.1	DC Measurements	216
8.1.1.1	IV Characteristics	216
8.1.1.2	Sub-Teraohm Resistance	217
8.1.1.3	High Resistance Ratio	218
8.1.1.4	Device Cycling at 77 K	219
8.1.2	Temperature Dependency of RF Performance	220
8.2	Intermediate Resistance States in PCM GeTe	221
8.2.1	At Cryogenic Temperature	221
8.2.2	At Room Temperature	223
8.2.3	Stability of Intermediate Resistance State	224
9	Conclusions and Future Directions	226
9.1	Contributions	226
9.2	Future Work	229
	Thesis List of Publications/Contributions	232
	References	235
	Appendices	250

TABLE OF CONTENTS

A	Microfabrication Process Steps	251
A.1	Gen 3 Microfabrication Process Flow Sequence	251
B	List of Equipment Used	267
B.1	Microfabrication Equipment	267
B.2	RF/DC Measurement Equipment	269
B.3	Modeling Softwares	271
	Glossary	273
	Index	276

List of Figures

1.1	RF switch matrix in crossbar topology	3
1.2	3×3 crossbar switch matrix junctions	3
2.1	Reversible switching of phase change material using an electrical pulse, in non-volatile memory applications	9
2.2	Ge-Sb-Te ternary phase diagram depicting various phase change alloys along with single phase compositions that reside on the tie-line of GeTe and Sb_2Te_3	11
2.3	Various waveguide mechanical microwave switches [62]	15
2.4	Coaxial mechanical RF and microwave switches [64]	17
2.5	RF MEMS switches: (a) shunt/capacitive switch in up-state (ON state) and (b) shunt/capacitive switch in down-state (OFF state); (c) series/metal contact switch in up-state (OFF state), and (d) series/metal contact switch in down-state (ON state).	19
2.6	SEM images of GeTe based RF Switch [69]	20
2.7	Optical photos of low-loss phase change series RF switch [70].	21
2.8	Optical micrograph of a GeTe based shunt RF switch [71].	21
2.9	Optical micrograph of a PCM GeTe RF SPDT switch [70]	22
2.10	Optical micrograph of SbTe based RF Switch [71]	22
2.11	RF performance comparison between various RF switch technologies [70]	23

2.12 Satellite payload operation block diagram (red highlights switch matrices that can be potentially substituted with MEMS technology). The signal is received from the antenna and directed through the beam forming network (BFN) and input filter assembly (IFA) to the receivers (RCV). The signal is then processed and, after passing through the multiplexer (MUX) and high-power amplifier (HPA), it is transmitted to the next repeater satellite through the antenna. 24

2.13 Switch matrix application in a beam-link system [12]. The system shown receives six different beams from various locations and transfers them to their intended spots. The beam-link system creates sub-channels for each uplink beam and the switch matrix provides the flexibility to independently direct the sub-channels to the desired downlink beam. 25

2.14 Crossbar switch matrix architecture realization using switch cells 26

2.15 SEM image of fabricated 3×3 crossbar RF MEMS switch matrix [30] 26

2.16 Operating Principle of a C-type switch and its two operational states. This four-port device connects Ports 1 and 4 and Ports 2 and 3 in State I and Ports 1 and 2 and Ports 3 and 4 in State II. 27

2.17 Operating principle of an R-type switch and its three different states. In State I, the signal can be routed between Ports 1 to 4 and Ports 2 to 3; in State II, the signal can be routed between Ports 1 to 2 and Ports 3 to 4; and State III connects Ports 1 and 3. 27

2.18 Operating principle of a T-type switch and its three different states. In State I, the signal can be routed between Ports 1 to 4 and Ports 2 to 4; in State II, the signal can be routed between Ports 1 to 2 and Ports 3 to 4; and between Ports 1 to 3 and Ports 2 to 4 in State III. 28

2.19 Redundancy system with five primary channels and two spare channels using C-type switches as building blocks. 29

2.20 Redundancy system using R-type switches as building blocks. 29

2.21 Switch matrices with pairwise connections showing several $N \times N$ matrices connected to form a larger switch matrix 30

3.1 3D surface scan of GeTe film in (a) amorphous state (Sample 'B'), and (b) crystalline state (Sample 'B'). Scan area is $3 \mu\text{m} \times 3 \mu\text{m}$ 35

LIST OF FIGURES

3.2 AFM scan of GeTe thin film deposited on Al₂O₃ substrate. (a) Sample 'A' amorphous, (b) Sample 'A' crystalline, (c) Sample 'B' amorphous, (d) Sample 'B' crystalline, (e) Sample 'D' amorphous, and (f) Sample 'D' annealed with only two orders of resistance change. Streaks are from substrate with average roughness of 25 nm. 36

3.3 Surface line profile of 3 μm GeTe sample including roughness, texture and waviness of the film in crystalline and amorphous state. 37

3.4 AFM scan of GeTe thin film deposited on glass substrate. (a) Sample 'E' amorphous, (b) Sample 'E' crystalline deposited at room temperature, (c) Sample 'F' amorphous, (d) Sample 'F' crystalline deposited at 100 °C, (e) Sample 'G' amorphous, (f) Sample 'G' crystalline deposited at 150 °C, (g) Sample 'H' amorphous, and (h) Sample 'H' crystalline deposited at 200 °C. Change in grain boundaries is prominent in films deposited at room and elevated temperatures. 38

3.5 3D surface scan of GeTe films in crystalline states deposited at (a). 25 °C (Sample E), (b). 100 °C (Sample F), (c). 150 °C (Sample G), and (d). 200 °C (Sample H). Scan area for the samples is 20 μm × 20 μm. 39

3.6 Grain mapping of GeTe film in crystalline state deposited at 200 °C. (a). 3D surface scan of the film with grain mapping mask, (b). Surface scan of GeTe crystalline film with grain mapping mask revealing grains larger than 0.8 μm. (c). Inset showing profile scan of two grains from (b) surface plot cross-section line. Grain height is relative in all cases. 40

3.7 SEM micrographs of the GeTe films deposited at elevated pressure results in change of film roughness. (a) Amorphous state of GeTe deposited at at 3 mTorr, (b) Crystalline state of GeTe deposited at 3 mTorr, (c) GeTe in amorphous state deposited at 10 mTorr), and (d) GeTe in crystalline state deposited at 10 mTorr). 41

3.8 Sheet resistance measurement across wafer using four-point probe method. (a) Sample 'A', (b) Sample 'B', and (c) Sample 'C' shows the resistance distribution in crystalline state of annealed 150 nm GeTe thin-films. 42

3.9 Sheet resistance change in GeTe thin-films from amorphous to crystalline state. Films are deposited using variation in process parameters. State change occurs at 180 °C to 200 °C. Sample D shows only two order of resistance change while other samples exhibit more than five orders of resistance change. 42

LIST OF FIGURES

3.10 Spring coil stresses formation in tungsten thin films deposited at room temperature 44

3.11 PCM switch showing voids and cracks formation in GeTe region. Inset shows the optical micrograph of switch junction after annealing. A close-up view of the GeTe region is shown highlighting the issues with crystalline GeTe films. 45

3.12 GeTe melting after few actuation cycles: (a) PCM switch when voltage is not applied yet, (b) Melting of GeTe after few voltage pulses applied. This switch was fabricated using four-layer process without any passivation layer on top. 46

3.13 Optical micrograph of PCM switch junction highlighting GeTe melting region, and FIB-SEM showing the cross-section of the melted region. Cut-direction A–A'. Crack in GeTe layer is highlighted in FIB-SEM micrograph. 47

3.14 Optical lithography constraints in the development of PCM switches; optical micrograph of PCM SPST switch junction and FIB-SEM showing the cross-section of the switch where the offset in just nanometer scale can lead to non-working switches. 47

4.1 3D view of PCM-based RF SPST series switch with two metal layers for RF signal flow. Inset shows the close-up view of PCM switching unit highlighting PCM GeTe and embedded micro-heater. Passivation layer between two metal layers is not shown. Close-up view of PCM junction geometry highlights various design parameters for parametric study in FEM simulation. 50

4.2 Cross-section of RF-PCM fabrication process flow using four-layers having one metal layer for RF signal routing. 51

4.3 Optical micrograph of RF-PCM SPST switches (Gen 1): (a) Series configuration, (b) Shunt configuration, (c) Close-up view of switching region in series switch, and (d) 4-Port RF-PCM junction. 52

4.4 Parametric RF performance EM simulation of PCM SPST switch with variation of metal thickness and channel width 53

4.5 Parametric RF performance EM simulation of PCM SPST switch with variation of heater width. 54

4.6 Parametric RF performance EM simulation of PCM SPST switch with variation of channel length. 54

LIST OF FIGURES

4.7 Parametric RF performance EM simulation of PCM SPST switch with variation of taper length. 55

4.8 Parametric RF performance EM simulation of PCM SPST switch with variation of barrier thickness. 56

4.9 Cross-section of Gen 2 RF-PCM fabrication process flow using six-layers having two metal layer for RF signal routing. 57

4.10 Fabricated RF PCM SPST switch (Gen 2): (a) Optical micrograph, (b) inset shows close up view of the switch junction, and (c) SEM micrograph of the PCM region. 58

4.11 Cross-section of Gen 3 RF-PCM fabrication process flow using seven-layers having two metal layer for RF signal routing and two metal layers for bias routing. 60

4.12 Fabricated RF PCM SPST switch (Gen 3): (a) Optical micrograph, (b) False coloured SEM micrograph of the PCM channel, and (c) 3D rendered view of the PCM SPST (Gen 3) switch. 61

4.13 Various parasitic capacitances couple through thin-films degrading device performance 63

4.14 Lumped model of the RF PCM SPST switch showing switching element along with various parasitic circuit elements. 64

4.15 On-wafer DC testing of a four-port PCM switch junction. Optical micrographs highlighting DC probe pads and PCM junction. 65

4.16 (Top) Bias signature applied to cycle the RF PCM SPST switches between amorphous and crystalline states. (Bottom) Measured PCM device resistance with change in applied pulse amplitude. 67

4.17 Measured and simulated RF performance of RF-PCM SPST series and shunt switches with $l_h = 35 \mu\text{m}$, $w_h = 2 \mu\text{m}$, $l_s = 2 \mu\text{m}$ and $w_s = 20 \mu\text{m}$. . . 68

4.18 Measured and simulated RF performance of optimized RF-PCM SPST series switch for millimeter-wave applications. 69

4.19 Measured self actuation and current carrying capacity of four different RF PCM SPST switch geometries: (Top left) Measured IV characteristics highlighting self-actuation, (Bottom left) Resistance change with change in DC voltage, (Top right) Maximum current carrying capacity in ON-state, and (Bottom right) Switch failure with change in DC voltage. 71

LIST OF FIGURES

4.20 Block diagram of on-wafer high RF power handling setup for PCM switches. 73

4.21 Photograph of on-wafer high RF power handling measurements testbench. Inset shows various RF components and RF signal flow direction. 74

4.22 RF power handling measurements of two different RF PCM SPST switches in ON-state and OFF-state. 75

4.23 (a) Harmonics of a fundamental tone. (b) Realistic representation of third order intercept point calculation. 76

4.24 Second and third order intermodulation products with two fundamental tones. 77

4.25 Block diagram of on-wafer linearity or intermodulation distortion measurement setup for PCM switches. 78

4.26 Photograph of on-wafer two-tone linearity / intermodulation distortion measurement test-bench. Inset shows CPW GSG probes landed on a DUT. 78

4.27 Intermodulation distortion measurements of RF PCM SPST switches. (Left) Fundamental and third-order intermodulation products measured and extrapolated third-order intercept point, (Right) Output spectrum observed with 10 dBm power of two fundamental tones with third and fifth order products visible. 79

4.28 Experimental setup for measuring the switching speed of an PCM based RF switch. 81

4.29 Measured switching/transition speed of an RF PCM-based SPST switch. Actuation signal applied to the switch is also shown. 82

4.30 Block diagram of reconfigurable switch cycle testing setup and RF measurements setup. Inset shows RF PCM SPST switch and PCM GeTe junction. Top level circuit model model of the SPST switch in ON-state and OFF-state is highlighted. 83

4.31 Photograph of an automated on-wafer DC switch cycle testing setup. Inset shows an in-house assembled modular connection matrix to connect DC probes to any equipment. Zoomed-in view highlights the fabricated RF-PCM Si wafer probed with four DC probes. 84

4.32 Pulse pattern at the DUT input for switch cycles reliability testing. Crystalline and amorphous pulses are scaled for illustration purposes. Crystalline and amorphous pulse patterns are generated from two independent pulses generators and synced to trigger at 4 Hz frequency. 85

LIST OF FIGURES

4.33 RF PCM switch lifetime switching cycles measurement demonstrating 1 million cycles tested with more than four orders of resistance change. . . . 86

4.34 Non-volatility or resistance stability measurements over a course of more than 28 hours in ON-state and OFF-state. 87

4.35 Measured insertion loss and isolation performance of current state-of-the-art technologies. 88

5.1 Thermoreflectance transient thermal imaging of PCM GeTe-based RF switches highlighting the technique to generate thermal images using lock-in averaged pulses. 93

5.2 Timing diagram of time-resolved imaging data acquisition by pulsing the device excitation and LED illumination pulses at a controllable relative time delay. Timing diagram highlights the acquisition of $t = 0$ data point. Temperature data points are acquired by shifting the timing delay. 94

5.3 Photograph of: (a) thermoreflectance based transient thermal imaging experimental setup, (b) close-up view of probe-station and flexure stage, and (c) pulse generator and oscilloscope. 95

5.4 (Left) FEM simulations of micro-heater highlighting actuation terminals and heated region of the heater. (Right) Change in temperature with various heater lengths for different materials and thickness. 96

5.5 Transient thermal imaging of fabricated tungsten micro-heaters on sapphire substrate. (Left) CCD micrograph and DC probes, (Right) Heat distribution in micro-heater at different time intervals with the application of 200 ns pulse width and change in pulse amplitude. 12 V, 200 ns pulse shows sufficient temperature to melt the PCM GeTe, while 15 V, 500 ns pulse damages the heater. 98

5.6 Heat distribution across micro-heater surface: (a) Cross-section profile across the width of the heater using amorphous pulse, (b) Cross-section profile across the length of the heater using amorphous pulse, and (c) Cross-section profile across the length of the heater captured at 250 ns with the stimulus of 15 V, 200 ns pulse. 99

5.7 Transient heat distribution using FEM modeling of RF PCM SPST switch: (a) Photograph of a fabricated RF PCM SPST switch die/chip on tip of a finger, (b) 3D rendered model of the RF PCM SPST switch with two symmetry planes, (c) Quarter symmetrical 3D model for FEM modeling the heat distribution in the PCM junction. (d) Optical micrograph of the RF PCM SPST switch fabricated using Gen 3 microfabrication process, (e) Amorphous pulse shape applied for FEM transient analysis, (f) 2D cross-section of the quarter model showing heat distribution at $t=195$ ns, (g) 3D rendered model highlighting thin-film stacks equivalent of Gen 3 microfabrication process, and (h) Transient heat distribution in 3D FEM model of the PCM switch at different time intervals with the application of a single amorphous pulse. Temperature starts rising after $t=20$ ns delay and reached its maximum value at $t=195$ ns before quenching. 101

5.8 (Top left) Quarter 3D model of the RF PCM SPST switch highlighting the 3D space coordinates, (Top mid) Cross-sections of vertical profiles along z -axis, A–A' is at the centre of the model while B–B' is at $1.2 \mu\text{m}$ apart under the RF electrodes, (Top right) Horizontal cross-sections along x -axis, solid line for PCM GeTe and dashed line for micro-heater. Change in temperature over time on the surface of PCM GeTe and micro-heater is plotted using amorphous pulse and crystalline pulse. Corresponding plots show temperature across z -axis and x -axis of the FEM model cross-sections. z -axis and x -axis cross-sections are plotted at $t=195$ ns with amorphous pulse stimulus, and at $t=1.2 \mu\text{s}$ with crystalline pulse application. Temperature drops significantly at B–B' as a slightly thicker gold metal layer acts as a heat sink. 103

5.9 Transient thermal imaging of RF PCM SPST switch for investigating thermal cross-talk: (a) CCD micrograph showing the region of interest, DC probes and RF ports, (b). Thermal image of the switch captured at $t=200$ ns on the application of a 15 V , $2 \mu\text{s}$ pulse. (c) Thermal images of the switch captured at different time intervals with the stimulus of pulse conditions mentioned above the temperature scale. Melt sequence completes at $t=200$ ns followed by quench and cool-down sequence from at $t=200$ ns onwards. A CCD micrograph merged with temperature at $t=200$ ns is also shown. . 105

LIST OF FIGURES

5.10 Experimental 3D transient thermal imaging measurements of the RF PCM SPST switch at different time intervals showing melt-quench action with the application of a single 12 V, 200 ns pulse. Maximum temperature is recorded at $t=200$ ns, followed by a quick cool-down phase shown at $t=300$ ns. Temperature scale is different for each image. 106

5.11 Heat distribution across $300\ \mu\text{m}$ A–A' cross-section of the RF PCM switch to study thermal crosstalk: (a) A crystalline pulse of amplitude 8 V and $1.2\ \mu\text{s}$ width generates sufficient heat (T_c) to crystalline the PCM switch. (b) An amorphous pulse of amplitude 12 V and 200 ns width generates temperature (T_a) to melt the PCM GeTe. No thermal crosstalk is seen in (a) and (b). (c) A 15 V amplitude and $2\ \mu\text{s}$ wide pulse is supplied to the heater which is beyond its rated actuation limits. Thermal image is captured just before the switch breakdown showing crosstalk across $80\ \mu\text{m}$ width. 107

5.12 Experimental post pulsing failure investigation in RF PCM switches if excessive power is delivered to the via beyond specified pulse characteristics. (a) 3D plot showing heat distribution across PCM junction region with the maximum temperature of greater than $2000\ ^\circ\text{C}$ before damage. (b) Thermal images of PCM switch at different time intervals. Damage starts within few nanoseconds right after applying 15 V, $2\ \mu\text{s}$ wide pulse. . 109

6.1 Device layouts of RF PCM multi-port switches: (a) SP2T switch, (b) SP3T switch. Device geometries highlight core area of the switch, bias routing, and control pads. 112

6.2 Optical micrographs of RF PCM GeTe-based multi-port switches in (a) SP2T configuration, (b) SP3T configuration. 113

6.3 Optical micrograph of PCM GeTe-based RF SP3T switch. Inset shows an optical micrograph of the SP3T core with dimensions. 115

6.4 Measured and simulated RF performance of RF PCM SP3T switch. RF performance of SP2T switch (*not shown*) is identical to SP3T switch due to its identical core design. 115

6.5 Unit-cells for (a) SP8T switch and (b) SP16T switch. 116

6.6 RF PCM SP8T Switch: (a) Arrangement of unit-cells, (b) Chip layout of the switch. 117

LIST OF FIGURES

6.7 (a) Chip layout of the RF PCM SP16T switch, (b) Symmetrical unit-cells arrangement. 118

6.8 Optical micrographs of the fabricated SP8T switches. (a) Compact SP8T with integrated control pads, (b) SP8T switch with control pads outside the chip periphery. 119

6.9 (a) Optical micrograph of the RF PCM SP16T switch, (b) zoomed-in view a section of SP16T switch, and (c) zoomed-in view of the RF PCM switches utilized in SP16T switch. 120

6.10 Chip layout and optical micrograph of the RF PCM GeTe-based SP16T switch. 121

6.11 Measured and simulated RF performance of RF PCM SP8T switch. Due to the symmetrical nature of design, RF performance is shown for two different ports RF2 and RF4 while input is connected at RFC port. 122

6.12 Measured and simulated RF performance of RF PCM SP16T switch. RF performance is shown for two different ports RF2 and RF8 while input is connected at RFC port. 123

6.13 Chip/Die layout of the miniaturized scalable RF PCM-based four-port switch unit-cell highlighting various layers and RF ports. 124

6.14 Two operational states of switch unit-cell with an option to extend the functionality of an additional state. 125

6.15 Optical micrograph of 2×2 switch matrix unit-cell fabricated using Gen 2 microfabrication process. 126

6.16 (a) Simulated RF performance of the cross-junction with RF signal flowing between port RF1 to RF3 and RF2 to RF4, (b) Measured OFF-state isolation between various ports of PCM-based four-port switch unit-cell from DC to 26 GHz in all possible combinations. 127

6.17 Measured ON-state RF performance of PCM GeTe-based four-port switch unit-cell over DC to 26 GHz in all possible combinations. 128

6.18 Number of switches in the four-port switch unit-cell for narrowband and wideband application. 128

6.19 Traditional approach to device selector reconfigurability by using back to back cascaded multi-port switches. Adding an additional bit requires cascading two more SPDT switches. 129

6.20	Switch unit-cell in a switchable band reject filter application to reject either an individual frequency or rejecting both the frequencies offered by band stop filters. The RF signal can be routed without rejecting any frequency band at all.	129
6.21	Scalability to higher order switch matrices utilizing 2×2 unit-cells.	130
6.22	Optical micrograph of a PCM GeTe-based reconfigurable band reject filter utilizing four-port switch unit-cell.	131
6.23	Measured and simulated RF response of fully integrated PCM-based reconfigurable band rejection circuit.	133
6.24	Three different operational states of a T-type RF switch. RF performance of the state I and II is identical due to the design symmetry.	134
6.25	Chip layout of the monolithically integrated compact RF PCM-based T-type switch.	135
6.26	RF PCM-based T-type switch: (a) Optical micrograph of the fabricated T-type switch developed on sapphire substrate, (b) 3D rendered view of a single RF-PCM SPST switch, (c) Optical micrograph of RF-PCM SPST switch (d) SEM micrograph of SPST switch junction highlighting the RF signal flow path, and (e) SEM micrograph of a close-up view of PCM channel highlighting perfect micro-fabrication alignment of the Au contacts over micro-heater.	136
6.27	EM simulations of the return loss, isolation and insertion loss of cross-over junction and the impact of conductive bias lines routed under 90° CPW bends.	138
6.28	Measured and simulated RF performance of RF PCM-based T-type switch over DC to 67 GHz. Multiple isolation measurements represent the RF performance from different states and combinations.	139
6.29	A 4×6 redundancy system utilizing two switch matrices using six receivers with two of these receivers are used as spare. This figure illustrates the signal routing functionality of the switch matrices in case of failure of two receivers 'D3' and 'D5'.	140
6.30	Layout of the miniaturized monolithically integrated PCM GeTe-based 4×6 redundancy switch matrix developed using cascaded T-type switching unit-cells. Schematic representation shows symbols of four T-type switches arranged in order to develop a 10 port switch matrix.	141

6.31 3D rendered view of redundancy switch matrix: (a) 3D rendered view of a four-port RF crossover, (b) Optical micrograph of the RF crossover, (c) 3D rendered view of redundancy matrix highlighting bias split layer, (d) 3D rendered view of 90° bend with two PCM SPST switches, and (e) Optical micrograph of the 90° bend highlighting M2 to M3 vias, two PCM switches at the both ends and two bias lines crossing underneath. Optical micrographs shown are from the microfabrication process based on sapphire substrate. 142

6.32 Optical micrograph of the PCM-based monolithically integrated redundancy switch matrix using cascaded T-type switching unit cells. Insets (a) and (b) highlights the T-type switching unit-cell and 90° bend with 2 bias lines routed underneath. 143

6.33 Measured and simulated RF response of monolithically integrated PCM-based redundancy switch matrix over DC to 60 GHz. 145

6.34 Scalable $m \times n$ crossbar switch matrix architecture utilizing switch unit-cells and SP2T switches arranged in a grid pattern to achieve signal routing. 147

6.35 Crossbar switch unit-cell operation states and a typical unit-cell configuration with three switches. 148

6.36 Switch unit cells: (a) Schematic of a SP2T switch cell, (b) 3D rendered view of the SP2T switch cell with two SPST switches, (c) schematic and (d) 3D view of the crossbar switch unit-cell with four SPST switches used in crossbar architecture. 149

6.37 Crossbar switch unit-cell highlighting four SPST switches and signal paths in ‘thru’ and ‘turn’ states. 150

6.38 Chip layout and optical micrograph of a ‘turn’ state implementation using unit-cell. 150

6.39 Layout of 2×2 crossbar switch matrix. All signal routing combinations are highlighted to demonstrate fully reconfigurable 2-bit operation of the circuit. 151

6.40 Optical micrograph of 2×2 crossbar switch matrix. Insets show SEM micrographs of PCM SPST switch and PCM junction at two different magnification levels. 152

6.41 Signal routing paths of a 4×4 crossbar switch matrix highlighting longest paths, which have maximum number of switches in the signal path. 153

6.42 Optical micrograph of the PCM GeTe-based 4×4 switch matrix. Inset shows magnified optical micrographs of SP2T switch elements, impedance matching and capacitance compensation of bias network, and a unit-cell implemented in switch matrix highlighting turn state. 154

6.43 Measured and simulated RF performance of an unit-cell for crossbar switch matrix implementation. Insertion loss of a PCM GeTe-based SPST switch is shown for comparison. 156

6.44 Measured RF performance of a 2×2 crossbar switch matrix over DC to 40 GHz in all possible routes. Simulation average is shown. 156

6.45 Measured and simulated RF performance of a PCM GeTe-based 4×4 switch matrix over DC to 40 GHz. RF performance is shown for 7 possible routes, with route 7 exhibiting the worst case scenario. 158

6.46 PCM GeTe-based unit-cells for low frequency crossbar switch matrices: (a) Layout of ver1 unit-cell, (b) layout of ver2 unit-cell, (c) optical micrograph of ver1 unit-cell, and (d) optical micrograph of ver2 unit-cell. 160

6.47 Layout of a 4×12 DC crossbar switch matrix. Only one PCM GeTe-based switch is used per unit-cell. 161

6.48 Optical micrograph of a 4×12 DC crossbar switch matrix developed using ver1 switch unit-cells. 161

6.49 Optical micrograph of 16×16 crossbar switch matrix for DC or low frequency applications. 16×16 crossbar matrix use 64 PCM switches in 256 ver2 switch unit-cells. 162

7.1 Schematic of n -bit digital switched capacitor bank utilizing MIM capacitors. 167

7.2 Chip layout of a monolithically integrated PCM GeTe-based 6-bit switched capacitor bank highlighting various layers and control pads. 168

7.3 Simplified lumped model of the PCM-based 6-bit capacitor bank. PCM switches are represented as reversible binary resistive switches for tuning elements. 168

7.4 Optical micrograph of the fabricated 6-bit latching PCM-based digital switched capacitor bank. Inset shows optical micrograph of a MIM capacitor in series with PCM switch. 169

7.5 Measured and simulated results of 6-bit PCM-based switched capacitor bank showing linear variation from 0.14 pF to 8 pF capacitance. 9 different states are shown out of a total of 64 states. Self-resonance is beyond 8 GHz when all the capacitors are switched to ON state (corresponds to state 64). 170

7.6 Measured and simulated Q -factor of capacitor bank in various states. . . . 171

7.7 Optical micrograph of four MIM capacitors. C1 and C3 have similar capacitance overlapping area, and C2 and C4 has similar capacitance area. C3 and C4 capacitors show improvement in SRF and Q -factor. 172

7.8 Measured capacitance and Q -factor for MIM capacitors C1, C2, C3 and C4. 172

7.9 Optical micrograph of the 6-bit latching digital switched capacitor bank with high self resonance frequency: (a). Optical micrograph of a standard MIM capacitor implementation, (b) Optical micrograph of a high self resonance MIM capacitor, (c) SEM micrograph of a PCM SPST switch, and (d) SEM micrograph of the PCM junction. 173

7.10 Schematic of an n -bit hybrid capacitor/inductor bank. High value MIM capacitors act as inductors at high frequency. SPST switches load or unloads the desired elements to the RF signal path. 174

7.11 Optical micrograph of a highly miniaturized PCM-based hybrid capacitor/inductor bank. Inset shows PCM GeTe SPST switch and a high value low frequency MIM capacitor which acts as an inductor at high frequency. 175

7.12 Simulated and measured inductance over 26 GHz to 30 GHz. Response of 14 states are shown out of a total of 256 possible states. 176

7.13 Schematic of a reconfigurable 4-bit attenuator consisting of SPDT switches and four attenuator bits (A–D). 178

7.14 Operation principle of attenuator bit loading and unloading: Actuating two SPST switches in Path 1 deselects the attenuator bit, while actuating two SPST switches in Path 2 selects the attenuator bit. Attenuator bits (A–D) developed using passive bridged-T resistor network topology sections with different values of R_a and R_b 178

7.15 Layout of the PCM-based 4-bit attenuator. PCM SPDT switches are used to select desired attenuation level by loading/unloading a combination of attenuator section(s). 179

LIST OF FIGURES

7.16 Optical micrograph of the monolithically integrated PCM-based 4-bit variable attenuator. Control pads 1–16 are used to tune the attenuation levels. Four passive bridged-T attenuator sections are shown in zoomed-in view. 180

7.17 Measured and simulated insertion loss and return loss of the PCM-based 4-bit variable attenuator over 24–32 GHz band. Response of all 16 states (4-bit) is shown. 181

7.18 Measured broadband on-chip resistors over DC to 40 GHz. 182

7.19 Schematic of a reconfigurable and scalable variable attenuator consisting of T-type unit cells in 2×4 configuration, PCM SP3T switches and resistor networks. 184

7.20 Layout of scalable PCM-based variable attenuator utilizing T-type unit-cells and multi-port RF switches. 184

7.21 Optical micrograph of the monolithically integrated PCM-based variable attenuator. (a). Passive bridged-T resistor network for attenuation level, (b). Zoomed-in view of three-way junction in a T-type unit-cell. 186

7.22 Measured and simulated attenuation and return loss of the PCM-based scalable variable attenuator over 26 GHz to 34 GHz. Response of all 9 states is shown. 187

7.23 Schematic of a loss compensated 3-bit switched TTD phase shifter consisting SP3T switches and delay lines (t_0 to t_4) cascaded in two stages. . . 189

7.24 Loss compensation in t_0 sections using fixed PCM-GeTe element (S_0) in each stage. Both PCM elements S_0 elements are latched in crystalline state and does not require any switching. Addition of S_0 minimize insertion loss variation between phase shifter states. 189

7.25 Chip layout of the loss compensated PCM-based 3-bit switched TTD phase shifter. PCM SP3T switches are used to select desired phase shift level by loading/unloading a combination of delay line section(s) in the RF path. . 190

7.26 Optical micrograph of the monolithically integrated PCM-based 3-bit mmWave switched TTD phase shifter. Inset shows an optical micrograph of the zoomed-in view of a PCM-based SP3T switch. 3D rendered view of PCM SP3T switch core is highlighted. 191

7.27 Measured and simulated RF performance of PCM-based SP3T switches over 8 GHz bandwidth. Due to the design symmetry, RF performance between RFC and three output ports is identical as shown for two states. . 192

LIST OF FIGURES

7.28 Measured and simulated RF performance of the PCM-based 3-bit switched TTD phase shifter over 26–34 GHz band. Response of all 9 states is shown. Insertion loss variation is minimized by choosing optimum delay line widths for higher states. 193

7.29 Measured and simulated phase shift and group delay of the PCM-based 3-bit TTD phase shifter over 26–34 GHz band. Response of all possible states is shown. 194

7.30 Optical micrograph of the monolithically integrated PCM-based 3-bit mmWave switched TTD phase shifter using SP8T switches. (a). Optical micrograph of SP8T switch core, (b). Zoomed-in view of an individual PCM GeTe SPST switch used in SP8T switches. 197

7.31 Measured and simulated RF response of SP8T switch over 26–34 GHz band. RFC is the common input port. Due to the symmetrical design, response of two states RF2 and RF4 is shown in ON-state and the OFF-state response of two different states RF3 and RF5 is shown. 198

7.32 Measured and simulated insertion loss and return loss of the PCM-based 3-bit TTD phase shifter over 26–34 GHz band. Response of all 8 possible states is shown. 199

7.33 Measured and simulated phase shift and group delay of the PCM-based 3-bit TTD phase shifter over 26–34 GHz band. Response of all possible states is shown. 200

7.34 Schematic of the single-ended RTPS consisting of a quadrature hybrid coupler terminated with two identical reflective loads. The desired phase shift in the output RF signal is added by the hybrid coupler and the reflective loads. Γ is the reflection coefficient and X_L is the tunable reactance of each reflective load. 201

7.35 Comparison of the simulated load impedance range and phase shift range for different reflective load topologies (a) single variable capacitive load, (b) single variable inductive load, (c) fixed inductor and variable capacitor connected in series, (d) fixed capacitor and variable inductor connected in series, and (e) switchable variable capacitor and variable inductor connected in parallel as the proposed load configuration. 203

7.36 Measured and simulated S-parameters of the quadrature hybrid coupler from 26 GHz to 30 GHz. 204

7.37	Optical micrograph of the compact PCM-based mmWave reflective type phase shifter highlighting control pads and reflective loads. (a). Optical micrograph of the mmWave hybrid capacitor/inductor bank, (b). Zoomed-in view of PCM SPST switch in series with tunable component. .	205
7.38	Measured and simulated phase shift of the PCM-based reflective type phase shifter over 26–34 GHz band. Response of 9 states out of 256 possible states is shown.	206
7.39	Measured and simulated RF response of reflective type phase shifter over 26 GHz to 30 GHz. RF response of 9 different states are shown out of a total of 256 states.	207
7.40	Schematic of reconfigurable impedance matching network using PCM-based 4-bit switched capacitor banks and 70° sections.	208
7.41	Optical micrograph: (a) Monolithically integrated PCM-based reconfigurable impedance matching network, (b). 4-bit PCM-based capacitor bank, (c). Zoomed-in view of 4-bit capacitor bank.	209
7.42	Simulated S-parameters and impedance coverage of reconfigurable impedance matching network. Impedance coverage is simulated for circuit model with ideal transmission lines and EM model with transmission lines loss considered. RF response is EM simulated for minimum and maximum capacitance case.	210
8.1	Block diagram of reconfigurable switch DC and and RF measurements test setup at cryogenic temperature.	213
8.2	Photograph of an automated cryogenic DC and RF testing setup. Inset shows the inside of cryo sample stage.	215
8.3	Measured IV characteristics of amorphous PCM GeTe over 77 K to 335 K. Device geometry is chosen with high current carrying capacity to allow reasonable current flow.	216
8.4	Measured OFF-state device resistance with change in applied voltage at different temperatures.	217
8.5	Measured and fitted PCM device resistance and ratio over temperature. .	218
8.6	Device resistance change with number of applied pulses at 77 K. Stable high resistance ratio is achieved at cryogenic temperatures.	219

LIST OF FIGURES

8.7	Measured RF performance of PCM GeTe-based RF switch over DC to 40 GHz from 77 K to 300 K.	220
8.8	Measured reversible intermediate resistance states in PCM GeTe at 77 K with the application of crystalline and amorphous pulses of varying amplitude.	222
8.9	Measured reversible intermediate resistance states in PCM GeTe at 293 K with the application of crystalline and amorphous pulses of varying amplitude.	223
8.10	Measured stability of intermediate resistance states at 77 K over a period of 60 mins.	225

List of Tables

2.1	Summary of the measured physical, electrical, and optical constants of amorphous and crystalline GeTe films [51]	13
2.2	Comparison of operating parameters among MEMS and PCM based RF switches [82]	23
3.1	Deposition Parameters for GeTe Thin-Films	34
3.2	Evaluation of embedded micro-heater's resistance for heater length, $l_h = 20 \mu\text{m}$ and voltage applied = 5 V	44
4.1	Summary of microfabrication processes	62
4.2	Measured RF Performance of RF-PCM Switches with Variations in Design Parameters	69
4.3	Third order intercept point measurements of RF PCM switch at varying centre frequency and tone separation.	80
4.4	Comparison with the commercially available state-of-the-art RF switches	89
6.1	Operational states of the RF PCM-based four-port switch unit-cell with relevant switches and control signals	125
6.2	Switches require to reject appropriate frequency band	130
6.3	Truth table of integrated reconfigurable band rejection circuit	132
6.4	Truth table of 2-bit crossbar switch matrix	151
6.5	Path configuration of 4×4 crossbar switch matrix.	157
6.6	Summary of multi-port switches and switch matrices presented	163

LIST OF TABLES

7.1	Resistor values for attenuation bits	179
7.2	Variation in measured resistor values over bandwidth	183
7.3	Comparison of 2^n and n^2 variable attenuators	185
7.4	Comparison of the mmWave PCM GeTe-based phase shifter with state-of-the-art	195
7.5	Summary of various reflective loads for RTPS	203
7.6	Summary of PCM-based RF components	211

List of Terminology

Amplitude is the magnitude of variation in a changing quantity from its zero value. The word required modification - as with adjectives such as peak, maximum, rms, etc. - to designate the specific amplitude in question.

Attenuation is the decrease of a signal with the distance in the direction of propagation. Attenuation may be expressed as the scalar ratio of the input power to the output power, or as the ratio of the input signal voltage to the output signal voltage.

Attenuator is a passive electronic device that reduces the power of a signal without appreciably distorting its waveform. An attenuator is effectively the opposite of an amplifier, though the two work by different methods. While an amplifier provides gain, an attenuator provides loss, or gain less than 1.

Bandwidth (BW) is the range of frequencies for which the RF performance falls within specific limits.

Bias Tee is used to supply DC currents or voltages to bias RF circuits. A Bias tee is a three-port device consisting a capacitor and an inductor. A Bias Tee can be thought of as a diplexer with an ideal capacitor that allows AC through but blocks the DC bias and an ideal inductor that blocks AC but allows DC.

Characteristic Impedance (Z_0) is the characteristic property of a transmission line describing the ratio between electric and magnetic fields.

Circulator is a passive, non-reciprocal three- or four-port device, in which a microwave or radio-frequency signal entering any port is transmitted to the next port in rotation (only).

Coaxial Cable is a type of transmission line consisting of two concentric conductors insulated from each other. In its flexible form it consists of either a solid or stranded center conductor surrounded by a dielectric. A braid is then woven over the dielectric to form an outer conductor. A protective plastic covering is placed on top of the braid.

Cold Switching is operating the switch in a mode such that no voltage differential exists between source and drain when the switch is closed or no current is flowing from source to drain when the switch opens. Switches have longer life when cold switched.

Coplanar Waveguide (CPW) is a type of electrical planar transmission line which can be fabricated using printed circuit board technology, and is used to convey RF and microwave-frequency signals. On a smaller scale, coplanar waveguide transmission lines are also built into monolithic microwave integrated circuits.

Crosstalk is a measure of undesired signals coupled through from one channel to another mainly due to parasitics.

Cut-off Frequency (F_{co}) is a measured to define the figure of merit of an RF switch and defined as $1/(2\pi \cdot R_{on} \cdot C_{off})$. Higher F_{co} is preferred for RF switches.

dBm is unit of level used to indicate that a power ratio (expressed in dB) with reference to one milli-watt (mW). It is a relative measure of signal power where the reference $0 \text{ dBm} = 1 \text{ mW}$

De-Embedding is mathematically removing the measurements affected by the fixture leaving only the behavior of the device under test. This is commonly used when there are non-coaxial connection from the VNA to the DUT, and it is used on circuit board traces, backplane channels, semiconductor packages, connectors or other discrete components.

Decibel (dB) is a relative unit without dimensions calculated as ten times the logarithm to the base 10 of a power ratio or as twenty times the logarithm to the base 10 of a voltage ratio.

Delay Line A cable that delays electrical signals by a specified amount of time.

Dielectric Constant (ϵ_r) is the electrical property of a material that describes its behavior in an electric field. The dielectric constant of the dielectric material is the most

important design parameter for transmission lines and MIM capacitors, and determines dimensions, losses and propagation characteristics.

Dielectric Loss ($\tan \delta$) is a dielectric material's inherent dissipation of electromagnetic energy. It can be parameterized in terms of either the loss angle δ or the corresponding loss tangent ($\tan \delta$). Both refer to the phaser in the complex plane whose real and imaginary parts are the resistive (lossy) component of an electromagnetic field and its reactive (lossless) counterpart.

Directional Coupler are passive devices used to couple a defined amount of electromagnetic power in a transmission line to a port enabling the signal to be used in another circuit. Directional couplers only couple power flowing in one direction. Power entering the output port is coupled to the isolated port but not to the coupled port.

Dissipation is the unusable or lost energy, such as the production of unused heat in an RF circuit.

Distortion is an unwanted change or addition to a signal or waveform when it is amplified. This definition excludes noise which is an extraneous signal super-imposed on the desired signal.

Dummy Load is a dissipative device used at the end of a transmission line or waveguide to convert transmitted energy into heat, so essentially no energy is radiated outward or reflected back to its source.

Dynamic Range in terms of signal analyzer dynamic range is the maximum power ratio (in dB) between a high power signal and low power signal that are present at the input of the signal analyzer – such that both signals can be discerned and measured at the same time or in the same display.

GSG Probe is a type of contact probe with ground-signal-ground (GSG) contact geometry in coplanar waveguide (CPW) configuration with specified pitch (spacing). GSG probes are most commonly used to perform on-wafer/die RF measurements.

Hermetic Sealing is any type of sealing that makes a given object airtight. Applications for hermetic sealing include semiconductor electronics, optical devices, MEMS, and switches. Electrical or electronic parts may be hermetic sealed to secure against water vapor and foreign bodies to maintain proper functioning and reliability.

Hot Switching is operating the switch in a mode where a voltage differential exists between source and drain when the switch is closed and/or current is flowing between RF channels when the switch is opened. Hot switching results in a reduced switch life, depending on the magnitude of the open circuit voltage between the source and the drain.

Impedance Match is a condition in which the impedance of a component or circuit is equal to the internal impedance of a transmission line. This gives maximum transfer of energy from the source to the load, as well as minimum reflection and distortion.

Insertion loss (IL) is the amount of signal attenuation (expressed in dB) between the input and output ports of the RF device when the switch is in the ON-state. Insertion loss should be as low as possible for maximum power transfer.

Intermodulation Distortion (IMD) is a phenomenon that occurs when two or more fundamental frequencies are present in an electronic circuit.

Isolation (ISo) is the amount of signal attenuation (expressed in dB) between the input and output ports of the RF device when the switch is in the OFF-state. Isolation should as high as possible.

Latching Switch is a switch that maintains its state after being activated. A push-to-make, push-to-break switch would therefore be a latching switch - after actuating it, whichever state the switch is left in will persist until the switch is actuated again.

Lifetime Actuation Cycles is the number of consecutive ON and OFF actuation cycles that can complete without the ON-state or OFF-state resistance exceeding a specified limits and no occurrence of failures to ON-state or OFF-state of the switch.

Lumped Model simplifies the description of the behavior of spatially distributed physical systems into a topology consisting of discrete entities that approximate the behavior of the distributed system under certain assumptions.

Matched Load (ML) is a device used to terminate a transmission line or waveguide so that all the energy from the signal source will be absorbed.

Microstrip is a type of transmission line configuration which consists of a conductor over a parallel ground plane, and separately by a dielectric substrate.

OFF Capacitance (C_{off}) is the parasitic OFF-state capacitance of the RF switch and measured between input and output port of the switch. Low C_{off} is preferred for RF switches to achieve high isolation and high figure of merit.

OFF Resistance (R_{off}) is the resistance (Ω) of the RF switch when the switch is in OFF-state and measured between input and output port of the switch. High R_{off} is preferred for RF switches to achieve high isolation.

ON Resistance (R_{on}) is the resistance (Ω) of the RF switch when the switch is in ON-state and measured between input and output port of the switch. Low R_{on} is preferred for RF switches to achieve low insertion loss and high figure of merit.

Power Sensor converts high-frequency power to a DC or low-frequency signal that the power meter can measure and relate to an RF power level. The meter displays the detected signal as a power value in dBm or watts.

Probe Station is used to physically acquire signals from the internal nodes of a semiconductor device. The probe station utilizes manipulators and probe heads which allow precise positioning of fragile probes (DC/RF) on the surface of a DUT. Probe station allows on-wafer testing flexibility, and is often faster and more flexible to test a new electronic device than to wire bond and package.

Propagation Delay (τ) is the time required for an electronic digital device, or transmission network to transfer information from its input to its output.

Pulse is a change in the level, over a relatively short period of time, of a signal whose value is normally constant.

Pulse Width is the length of time that the pulse voltage is at the transient level. For PCM switches, pulse widths are usually in the microsecond (1×10^{-6} sec) and/or nanosecond (1×10^{-9} sec) range.

Real-Time Oscilloscope captures an entire waveform on each trigger event. Put another way, this means that a large number of data points are captured in one continuous record.

Resistance Lifetime Stability is the continuous lifetime measures how long the RF PCM switch is left in a continuously ON or OFF-state without failure.

Return Loss (RL) is the magnitude of the reflection coefficient (expressed in dB), and the amount of reflected signal relative to the incident signal.

RF Power Amplifier is a type of electronic amplifier that converts a low-power radio-frequency signal into a higher power signal.

RF Power Rating is the maximum level of RF power that passes through the RF device without degradation to the switch lifetime when it is in the ON-state.

S-Parameters are used to describe the relationship between different ports, when it becomes especially important to describe a network in terms of amplitude and phase versus frequencies, rather than voltages and currents.

Single-Pole Multi-Throw (SPNT) a switch that has a single input and can connect to N output. Multipoint switches or single pole, multiple throw (SPNT) switches allow a single input to multiple (two or more) output paths.

Single-Pole Single-Throw (SPST) a switch that only has a single input and can connect only to one output. This means it only has one input terminal and only one output terminal and serves in circuits as on-off switches. When the switch is closed, the circuit is on. When the switch is open, the circuit is off.

SMA Connector (SMA A) is typically $50\ \Omega$ - subminiature coaxial connector with screw type coupling mechanism. SMA A connectors work from DC to 18 GHz.

Source Measure Unit (SMU) is an instrument that can precisely source voltage or current and simultaneously measure voltage and/or current. It combines the useful features of a digital multimeter (DMM), power supply, true current source, electronic load and pulse generator, all into a single, tightly synchronized instrument.

Spectrum Analyzer measures the magnitude of an input signal versus frequency within the full frequency range of the instrument. The primary use is to measure the power of the spectrum of known and unknown signals.

Standing Wave is the distribution of current and voltage on a transmission line, resulting from two sets of waves traveling in opposite directions.

Standing Wave Ratio (SWR) is a measure of the mismatch between the load the line. It is equal to 1 when the line impedance is perfectly matched to the load. The perfect match would be a 1 to 1 ratio.

Switching Speed is the speed at which the RF switch can be switched ON and OFF. It is dependent on both settling times and ON to OFF switching times.

Third-Order Intercept (IIP3) is the intersection point of the input power (P_{in}) vs. fundamental output power (P_{out}) extrapolated line and the third-order intermodulation (TOI) products extrapolated line of a two tone test. IIP3 is a figure of merit that characterizes the switch linearity.

Transmission Line is a specialized cable or other structure designed to conduct alternating current of radio frequency, that is, currents with a frequency high enough that their wave nature must be taken into account.

Vector Network Analyzer (VNA) is a device used to measure S-parameters of the circuit of interest for various frequencies. VNA is a test instrument that measures the response of a network as vector: real and imaginary parameters so that its performance can be characterized.

Voltage Standing Wave Ratio (VSWR) is a measure of the reflection, resulting from a ratio of the input signal to the reflected signal. $VSWR = (1+L) / (1-L)$.

Wavelength (λ) is the distance, measured in the direction of propagation, of a repetitive electrical pulse or waveform between two successive points that are characterized by the same phase of vibration.

List of Acronyms

a-GeTe	Amorphous-GeTe
AFM	Atomic Force Microscope
Ag	Silver
Al₂O₃	Aluminum Oxide
AlGaAs	Aluminum Galium Arsenide
AlN	Alumina nitride
Au	Gold
BFN	Beam Forming Network
c-GeTe	Crystalline-GeTe
CCD	Charge Coupled Device
CIRFE	Centre for Integrated RF Engineering
CMOS	Complementary Metal Oxide Semiconductor
CO₂	Carbon Dioxide
CPW	Co-Planar Waveguide
Cr	Chromium

LIST OF ACRONYMS

CVD	Chemical Vapor Deposition
CW	Continuous Wave RF Power
DC	Direct Current
DFT	Density Function Theory
DUT	Device Under Test
E-pHEMT	Enhancement-Mode Pseudomorphic HEMT
EBL	Electron Beam Lithography
FEM	Finite Element Modeling
FET	Field Effect Transistor
FIB	Focussed Ion Beam
FOM	Figure of Merit
GaAs	Gallium Arsenide
GaN	Galium Nitride
Ge	Germanium
Ge_xSb_yTe_z	Germanium-Antimony-Telluride Alloy
GeTe	Germanium Telluride
GSG	Ground-Signal-Ground
GST	Germanium-Antimony-Telluride

LIST OF ACRONYMS

HBT	Heterojunction Bipolar Transistor
HEMT	High Electron Mobility Transistor
HF	Hydrofluoric Acid
HFSS	High Frequency Structural Simulator
HPA	High Power Amplifier
HRSi	High Resistivity Silicon
IFA	Input Filter Assembly
IV	Current vs. Voltage
LED	Light Emitting Diode
LF	Low Frequency
LHe	Liquid Helium
LN	Liquid Nitrogen
LNA	Low Noise Amplifier
LRSi	Low Resistivity Silicon
LTCC	Low-Temperature Co-Fired Ceramic
MEMS	Microelectromechanical Systems
MESFET	Metal Epitaxial Semiconductor Field Effect Transistor
MIM	Metal-Insulator-Metal
MIT	Metal-Insulator Transition
MLA	Mask-less Aligner

LIST OF ACRONYMS

MMIC	Monolithic Microwave Integrated Circuit
mmWave	Millimeter Wave Frequencies
MODFET	Modulation Doped Field Effect Transistor
MOS	Metal Oxide Semiconductor
MOSFET	Metal Oxide Semiconductor Field Effect Transistor
MUX	Multiplexer
NaCl	Sodium Chloride
NiCr	Nickel Chrome
O₂	Oxygen
PA	Power Amplifier
PCM	Phase Change Material
PCMs	Phase Change Materials
PCS	Phase Change Material Based Switch
PECVD	Plasma Enhanced Chemical Vapor Deposition
PG	Pulse Generator
pHEMT	Pseudomorphic High Electron Mobility Transistor
PI	Polyimide
PLD	Pulsed Laser Deposition
PNA	Performance Network Analyzer
PVD	Physical Vapor Deposition

LIST OF ACRONYMS

QNC	Quantum Nano Fabrication and Characterization Facility
RCV	Receivers
RF	Radio Frequency
RF-MEMS	RF Microelectromechanical Systems
RIE	Reactive Ion Etching
Sb_xTe_y	Antimony-Telluride Alloy
SEM	Scanning Electron Microscope
Si	Silicon
SiGe	Silicon Germanium
SiN_x	Silicon Nitride
SiO₂	Silicon Dioxide
SMU	Source Measure Unit
SOI	Silicon-on-Insulator
SPNT	Single-Pole Multi-Throw
SP4T	Single-Pole Four-Throw
SPDT	Single-Pole Double-Throw
SPST	Single-Pole Single-Throw
Te	Telluride
TEM	Transmission Electron Microscope

LIST OF ACRONYMS

TFR	Thin Film Resistor
UVL	Optical UV Lithography
V₂O₃	Vanadium Sesquioxide or Trioxide
V₂O₅	Vanadium Pentoxide
VNA	Vector Network Analyzer
VO₂	Vanadium Oxide
W	Tungsten

List of Symbols

A	Current in ampere
C_{cont}	Parasitic capacitance in between switch contact gap
C_{hm1}	Parasitic capacitance between micro-heater and RF metal layer
C_{mmpad}	Parasitic capacitance between two RF metal layer pads
C_{mm}	Parasitic capacitance between two RF metal layers
C_{off}	Off-state capacitance
C_{pad}	Parasitic contact pad capacitance
C_{pcm}	Capacitance between crystalline GeTe and micro-heater
\vec{E}	Electric field vector
ϵ_r	Dielectric constant
F_0	Centre frequency
F_{co}	Cut-off frequency
F	Capacitance in farad
G	Giga (1×10^9)
\vec{H}	Magnetic field vector
Hz	Frequency in hertz
H	Inductance in henry

LIST OF SYMBOLS

IL	Insertion loss (dB)
ISo	Isolation (dB)
\vec{J}	Current density vector
L_{junc}	RF PCM switch junction inductance
M	Mega (1×10^6)
dBm	Power ratio in dB in reference to 1 mW
P	Power (P) is the product of voltage (V) and current (I)
RL	Return loss (dB)
R_h	Resistance of micro-heater
R_{off}/R_{on}	Ratio between OFF-state and ON-state resistance
R_{off}	OFF-state resistance
R_{on}	ON-state resistance
R_{pad}	Resistance of contact pad
T_{lin}	RF transmission line
T	Tera (1×10^{12})
V	Voltage Potential in volt
W	Power in watt
α	Rhombohedral phase of GeTe at room temperature
β	Cubic rocksalt type phase of GeTe at high temperature
$^{\circ}\text{C}$	Temperature in celsius
dBc	Power ratio of a signal to a carrier signal in dB.
dB	Decibel
$^{\circ}$	Degree

LIST OF SYMBOLS

Δf	Change in frequency
f	femto (1×10^{-15})
γ	Orthorhombic phase of GeTe at room temperature
g/cc	Density in gram per cubic centimeter
hr	Time in hour
K	Temperature in kelvin
k	Kilo (1×10^3)
l_h	Length of micro-heater
l_s	Length of PCM channel
l_{tp}	Length of transition (taper)
min	Time in minute
m	milli (1×10^{-3})
nm	Dimension in nanometer
n	nano (1×10^{-9})
$\Omega \cdot \mathbf{m}$	Bulk resistivity in ohm · meter
Ω/\square	Sheet resistance in ohm per square
Ω	Resistance in ohm
p	pico (1×10^{-12})
S/m	Conductivity in siemens per meter
s	Time in second
$\tan \delta$	Loss tangent
t_{br}	Thickness of barrier layer
t_m	Thickness of RF metal layer

LIST OF SYMBOLS

t_{off}	Device ON to OFF time
t_{on}	Device OFF to ON time
t_{pcm}	Thickness of PCM GeTe layer
$\mu\mathbf{m}$	Dimension in micrometer
μ	micro (1×10^{-6})
w_h	Width of micro-heater
w_s	Width of PCM channel

Chapter 1

Introduction

1.1 Motivation

The telecommunication industry across the globe is an area of strategic international interest. It is enjoying phenomenal growth with no sign of slowing down. The demand for bandwidth has continued to grow over the last few years, largely due to an increased use and number of communication devices. Current generation of wireless technologies are limited in terms of meeting higher network capacity and throughput demands of wireless devices. 5G millimeter wave (mmWave) spectrum ranging from 24 GHz to 95 GHz carries the potential to provide a solution to the growing demands by providing access to high-data-rate wireless connections, wider bandwidth, miniaturization of component sizes, low interference, and low latency.

Radio frequency (RF) components will have a market of \$45 billion by 2025; North America accounted for over 28% of the global revenue in 2019 [1]. RF devices are expected to exhibit rapid growth over the coming years, primarily due to increasing experimentation with switch architectures. For 5G roll-out, affordable RF components are necessary to configure antennas, filters, and multi-band amplifiers in RF modules responsible for transmitting and receiving radio signals. Microwave switching networks [2, 3], the major building blocks in wireless communication systems and satellite payloads, are used for signal routing and provide system redundancy [4–6]. In addition, switch matrices allow signal reconfigurability between various ports and channels [2–7].

RF switches are the fundamental building blocks for realizing reconfigurable front-ends in communication devices. Currently available RF switches are dominated by semiconductor technology, suffer from signal leakage issues at mmWave frequencies. On the

other hand, mechanical RF components provide exceptional RF performance and reliability, but are bulky and expensive [8–10]. Although RF-MEMS outperformed the semiconductor based and mechanical switches in terms of optimal RF performance [10–12], unfortunately, these micro-mechanical switches have reliability issues and need high dc voltage to operate [11, 13–16]. Therefore, there is a clear need to develop reliable miniature components in order to deliver cost-effective and superior RF performance for various applications at mmWave frequencies.

Phase change material (PCM), presently the most promising candidate for building low-cost, low-loss broadband mmWave components, has been widely used in optical storage media [17–19]. More recently, phase-change chalcogenides have been used in digital non-volatile memory devices [19–21], taking advantage of the electrical resistance change to improve memory density and switching speed over flash-memory devices. PCMs, have been known for many years that was originally identified by Ovshinsky [22], in electrical signal switching, in addition to its current applications in non-volatile memory and optical storage. The use of PCM in RF technology has recently been exploited with the first demonstration of a functional chalcogenide RF PCM switch was reported in 2013 [23–27]. PCM technology offers development of highly miniaturized and latching (non-volatile) switches with negligible dc power consumption. PCM’s property of offering more than six orders of resistance change with the application of nanosecond voltage pulses, makes this technology an ideal candidate for high-speed switching at mmWave frequencies.

Recent studies on the behavior of these materials in RF devices, suggest that they can be further used in designing complex communication subsystems such as switch matrices [20, 23, 24, 27]. A typical switch-matrix topology is shown in Fig. 1.1, and a detailed view of the network is shown in Fig. 1.2 [28–30]. The matrix shown has N columns and M rows in a cross bar configuration. The RF switches in the given configuration are placed at the S junctions. Activating $S_{i,j}$ (a unit cell consisting of three switches) connects the signal from RF- R_i to RF- C_j . The challenges are to isolate other switches and improve device performance, since as the number of elements increases, the transmission loss also increases. In addition to the crossbar switch matrices, other architectures for switch-matrices are investigated in this research. To the best of our knowledge, no work has been reported on PCM-based integrated switch matrices till date.

The goal of this doctoral research is to exploit the phase change material technology to develop reliable PCM-GeTe based multi-port RF switches, introduce novel RF switch matrices and develop reconfigurable and miniaturized RF components. An extensive set of RF components including switchable capacitor banks, variable mmWave attenuator, phase shifters and impedance tuner are developed. PCM GeTe-based switches are used

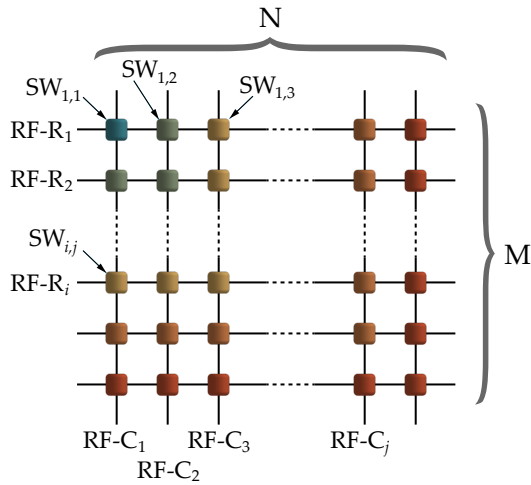


Figure 1.1: RF switch matrix in crossbar topology

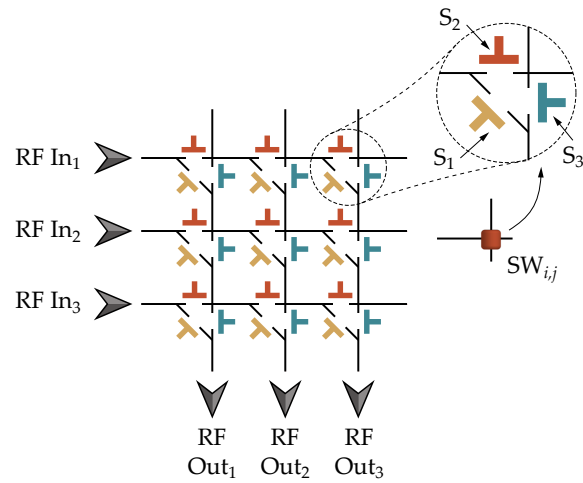


Figure 1.2: 3×3 crossbar switch matrix junctions

as unit-cells to develop switch-matrix architectures and reconfigurable RF components. PCMs offer unique advantages in RF applications: (a) being latching switches, they consume very little dc power [23, 24]; (b) being very small, they allow the realization of highly miniaturized monolithically integrated devices and; (c) having no mechanical actuation components, they offer high reliability [11].

1.2 Research Objectives

Development of Reliable PCM GeTe-based RF switches for mmWave applications

The primary objective of this research is to develop PCM GeTe-based RF switches with RF performance surpassing the current state-of-the-art. Recently reported RF PCM switches have poor RF performance at mmWave frequencies. The objective is to study the PCM GeTe using various characterization tools such as atomic force microscopy, scanning electron microscopy and other material characterization methods. This task involved optimization of PCM GeTe and to incorporate into custom microfabrication processes developed in-house with improvement in RF performance and reliability. The research is focused on RF performance im-

provement by investigating design parameters and developing RF switches with excellent RF performance over DC to 60 GHz. Various performance parameters of the developed switch such as linearity, intermodulation distortion, third order intercept point (IP3), power handling, current carrying capacity need to be studied and compared with current state-of-the-art. This objective is further focused into investigation of any self-actuation or power handling limitations of the RF PCM switches. The ultimate goal is to develop reliable PCM RF switches with stable switching actuations.

Experimental investigation on transient heat distribution and thermal actuation crosstalk in GeTe RF Switches

PCM GeTe-based RF switches require high speed (in nanosecond regime) embedded thin-film micro-heaters to provide actuation pulse signal. GeTe requires more than 725 °C heat for nanosecond duration to achieve melt-quench sequence for reversible phase change operation. Embedded refractory ultra high speed micro-heaters are developed. The objective is to study the heat profile of the micro-heaters using FEM modeling and to experimentally investigate transient thermal performance of the micro-heaters for PCM switches utilizing a highly efficient thermoreflectance based transient thermal imaging technique with nanosecond spatial resolution. The goal is to investigate the heat distribution in refractory thin-film micro-heaters and RF switches to accurately study any thermal crosstalk in PCM RF switches. Study of the transient thermal behavior is required to estimate integration density limits of PCM switches in multi-port switching networks and reconfigurable RF circuits.

Development of multi-port PCM-based RF switches and monolithically integrated miniaturized switch matrices

Multi-port switches are an integral part of any reconfigurable and switchable RF system. Multi-port switch configuration SPNT provides the flexibility to route the RF signal at input port to any available output port. The objective is to utilize PCM SPST switches for the development of various multi-port PCM GeTe-based RF switch configurations such as SP2T, SP3T, SP8T and so on. The task is divided in two sub-tasks. One is to investigate highly miniaturized multi-port device configurations, and second task is focused on utilizing multi-port unit-cells for the development of various switch matrices. The goal is to develop various monolith-

ically integrated RF switch matrix configurations for signal routing applications and redundancy applications for mmWave applications.

Demonstration of reconfigurable monolithically integrated PCM GeTe-based RF components

This objective is focused on incorporating PCM RF SPST and SPNT switches in various RF components. The research goal of this objective revolves around developing reconfigurable passive components such as capacitor banks, variable attenuators and phase shifters. Miniaturized configurations, dense integration and latching operation of PCM switches allow developing a library of passive reconfigurable RF components.

Characterization of PCM GeTe RF switches at cryogenic temperatures

The final objective is to characterize RF PCM switches at cryogenic temperature. The goal is to investigate performance stability and resistance change effect at low temperatures. The focus is to investigate any stable intermediate resistance states in PCM GeTe at cryogenic temperature.

1.3 Thesis Outline

This chapter reviews the introduction, motivation and research objectives followed by chapter 2 that includes the background information about phase change materials and their potential use in RF systems. Current state-of-the-art RF switches and switch matrix topologies are also discussed in chapter 2. Chapter 3 discusses characterization and optimization of PCM GeTe using various material characterization tools. Various thin-films used in PCM microfabrication processes are characterized. Methods to alleviate stresses are also discussed in chapter 3. The PCM GeTe-based RF switches are reported in chapter 4 including three generations of microfabrication processes and parametric design studies. Various measurement test setups are reported in chapter 4 including high RF power testing, linearity, intermodulation distortion measurements, switching speed testing, DC IV characteristics testing and device cycle/reliability testing. Chapter 5 reports transient thermal modeling and measurements of PCM switches to investigate thermal crosstalk and bias limits. Multi-port PCM-based switches including SP2T,

SP3T, SP6T and SP18T are reported in chapter 6 which also includes various switch matrices topologies including, T-type switch, redundancy matrix, device selector and cross-bar matrices for mmWave and also for low-frequency applications. Chapter 7 discusses PCM-based RF components developed including capacitor banks, variable attenuators, switched type phase shifters and reflective type phase shifters. PCM switches are characterized at cryogenic temperatures to room temperatures (77 K to 335 K) and the IV characteristics are recorded over temperature change which is presented in chapter 8. Intermediate resistance states in PCM GeTe switches are observed which is also reported in chapter 8. Conclusions and future work on this research are summarized in chapter 9. An in-depth microfabrication process flow is summarized in Appendices A and the list of equipment/software used in this research is reported in B.

Chapter 2

Background Information

2.1 History of Phase Change Materials

While Ovshinsky is generally credited as the inventor of phase change materials for information storage [22], the discovery of phase changing electrical characteristics dates back to the early 1900s in the little known and seldom cited pioneering work of Alan Tower Waterman. While studying thermionic emission of certain hot salts [31], Waterman noted some peculiarities in the conductivity of MoS₂. This observation led him to further investigation of the conductivity of MoS₂. He observed a large negative coefficient of resistance of the MoS₂ with respect to temperature in as much Ohm's law is not obeyed. This large negative coefficient of resistivity is typical of semiconducting chalcogenide materials. More significantly, he also observed a breakdown characteristic when the device under test was heated by means of the electronic current. He pointed out that MoS₂ may exist in two forms, α of high resistance and β of low resistance. The breakdown phenomenon and progressive conductivity changes are prominent of the phase change behavior in chalcogenide materials. In his study, however, without high speed melt-quench technique, the phase change or conductivity change is either permanent or semi-permanent [32].

Waterman pointed out that the transition from α form to β form was initiated by heat, electric field or light. Without the use of modern physical analysis tools such as transmission electron microscopy and x-ray crystallography, Waterman was not able to observe any physical changes of MoS₂ along with the conductivity changes. He did notice an increase in hardness accompanying increased conductivity [17].

2.1.1 Further Advancements in Phase Change Memory

In 1962, studying the chemical, physical, and electrical properties of some unusual inorganic glasses, A. David Pearson et al. [33] of Bell Laboratories observed the extraordinary current-voltage characteristics when a point contact is set down on a slice of the As-Te-I glass with a broad-area low-resistance contact on the back. There was no attempt made to explain the mechanism which might have caused such extraordinary characteristics.

Since 1960, Ovshinsky has been working with amorphous chalcogenides. He developed both electrically controlled threshold and memory switching devices and first reported his findings in a paper published in Physical Review Letters in 1968 [22] which detailed the operations of reversible switching in memory devices composed of 48 at. % tellurium, 30 at. % arsenic, 12 at. % silicon, and 10 at. % germanium. The most significant contribution of Ovshinsky's work is that the practicality of the switching phenomenon was demonstrated in continuous successful switching operations of multiple devices over periods of many months. Interest in phase change memory was practically initiated by this ground-breaking paper by Ovshinsky which remains the most cited literature in the field of phase change memory [17].

2.1.2 Early Attempts with Phase Change Memory

In the early 1970's, phase change memory drew a lot of interest in the industry and academia with the rapid expansion of applications of computers. The most notable work was the development of a 256-bit array comprised of a 16x16 matrix of phase change memory cells by R. G. Neale and D. L. Nelson of Energy Conversion Devices along with Gordon E. Moore of Intel [34]. Their memory cell consisted of a storage element, coined as the Ovonic amorphous semiconductor switching device, in series with a silicon p-n junction diode. The Ovonic memory element comprised of a thin film of phase change material sandwiched between two molybdenum electrodes was a non-volatile bi-stable resistor. The high-to-low resistance ratio was about 10^3 providing ample data signal. The peculiar switching characteristics of phase change semiconductor devices along with other devices with similar characteristics such as binary metal or semiconductor oxide and solid state electrolytic devices continued to stir up interest in industry and academia. In 1971, while at Purdue University, Leon Chua classified these devices, along with resistor, inductor and capacitor, as the fourth of basic two-terminal elements he called memristor [35]. The fourth element, memristor, is a contraction of memory and resistor. Chua argued that this new element is necessary to complete the symmetric

relationships connecting two of the four fundamental circuit variables: the current, the voltage, the charge and the flux-linkage.

Before the phase change memory device went into hibernation, another attempt to build a phase change memory device was disclosed by Roy R. Shanks and Craig Davis of the Burroughs Corporation. They published their result of a 1024-bit phase change memory in 1978 [17, 36].

2.2 Theoretical Background

2.2.1 Basic Principle of Phase Change Materials

Phase change material (PCM) has the unique property of reversible switching between amorphous and crystalline states upon specific heat treatment by means of electrical pulses. The state where atoms are arranged in a disorderly manner (short range order) is called the amorphous state, whereas the state where atoms are organized in an orderly manner (long range order) is called crystalline state. The disordered amorphous state has a lower mean free path of conduction for electrons that impedes current flow due to electron scattering, thus resulting in a higher resistance when compared to the crystalline state. For non-volatile memory applications, the conventional principle of PCM is illustrated in Fig. 2.1. The large contrast in resistance between the two states is used as a form of non-volatile memory to represent two states of binary [37].

A medium amplitude (typically 1-2 V) and long duration (typically >100 ns) SET electrical pulse is used for crystallization during a transition to the ON state. Energy from

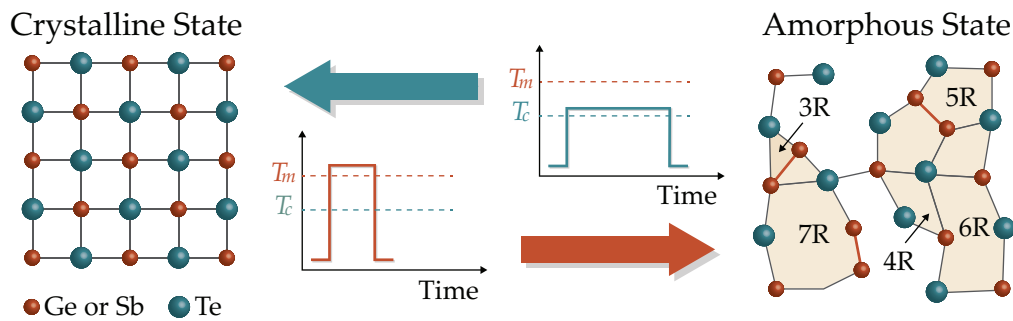


Figure 2.1: Reversible switching of phase change material using an electrical pulse, in non-volatile memory applications

the SET pulse heats the material for sufficient time to crystallize the material and provides adequate time for the atoms to reorganize to an orderly arrangement, thus transforming from an amorphous state to crystalline state. The mechanism for SET operation will be elaborate in section 2.3.3. The SET pulse is illustrated by the blue arrow in Fig. 2.1.

A short duration (typically <40 ns) and high amplitude (typically >2 V) RESET electrical pulse is used for re-amorphization. The RESET pulse provides sufficient energy to melt the material to disorder the atoms follow by rapid quenching to freeze the atoms, thus transforming the material from a crystalline state to an amorphous state. This is elaborated in section 2.3.3. Some recent work suggests that it is possible to carry out re-amorphization during the RESET operation without melting the material, which is also discussed in section 2.3.3. The RESET pulse is illustrated by the red arrow in Fig. 2.1.

The information can be extracted or simply read back by measuring the resistance of the phase change material using a low amplitude (typically 0.2 V) electrical pulse. The read voltage pulse must not only be low enough to prevent unwanted phase transformation, but also it must be lower than the threshold voltage. A higher energy pulse is required for the RESET operation to melt the material as compared to the SET operation to crystallize the material, since the crystallization temperature is lower than the melting temperature of the material. This is the primary factor limiting the reduction of power consumption in these type of devices.

For optical storage applications, the electrical pulse is replaced with a laser pulse to transform the material between the amorphous and crystalline states. The reflectivity is detected using a lower power laser to differentiate between the amorphous state (low reflectivity) and crystalline state (high reflectivity) This operation of the phase change switch is similar to the scheme applied for non-volatile memory.

2.2.2 Phase Change Alloys

Phase change (chalcogenide) material is defined as alloys containing group VI elements such as sulfur (S), selenium (Se) and telluride (Te). Alloys containing germanium (Ge), antimony (Sb) and Te are most common, with germanium-antimony-telluride ($\text{Ge}_2\text{Sb}_2\text{Te}_5$) alloy being the most thoroughly researched material. Fig. 2.2 shows the ternary phase diagram for this system where single phase alloys that lie on the pseudo binary line of germanium telluride (GeTe) and antimony telluride (Sb_2Te_3) are indicated. Allies include $\text{Ge}_1\text{Sb}_2\text{Te}_4$, $\text{Ge}_2\text{Sb}_2\text{Te}_5$, and $\text{Ge}_1\text{Sb}_4\text{Te}_7$. Along the pseudo binary line from GeTe to Sb_2Te_3 , the properties change from high stability and low speed to low

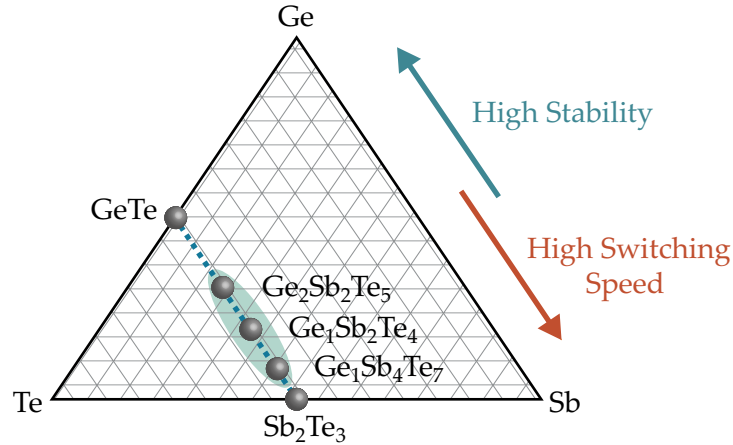


Figure 2.2: Ge-Sb-Te ternary phase diagram depicting various phase change alloys along with single phase compositions that reside on the tie-line of GeTe and Sb₂Te₃

stability and high speed [37, 38]. A material composition selected from the pseudo binary line may typically achieve fast crystallization and reasonable stability. However for a reconfigurable switch in RF applications, low ON state resistance and large dynamic range is very crucial.

2.3 Phase Change Materials for RF Applications

2.3.1 Metal-Insulator Transition Material - Vanadium Oxide

Vanadium (IV) dioxide or simply VO₂ in short is an inorganic compound. It is a dark blue solid. VO₂ is amphoteric, dissolving in non-oxidizing acids to give the blue vanadyl ion, [VO]²⁺ and in alkali to give the brown [V₄O₉]²⁻ ion, or at high pH [VO₄]⁴⁻ [39]. VO₂ has a phase transition very close to room temperature ($\approx 68^\circ\text{C}$). Electrical resistivity, opacity, etc., can change up several orders. At the rutile to monoclinic transition temperature, VO₂ also exhibits a metal to semiconductor transition in its electronic structure: the rutile phase is metallic while the monoclinic phase is semiconducting [40]. The optical band gap of VO₂ in the low-temperature monoclinic phase is about 0.7 eV. Due to these properties, it has been widely used in surface coating [41], sensors [42], and imaging [43]. Potential applications include in modern era witness its use in memory devices [44] and RF systems [45].

As discussed before, GeTe is preferred as a perfect material for RF devices due to the latching nature of the material. Just a short duration of pulse is required to switch the state, while VO₂ requires consistent biasing, thus consumes continuous power. Moreover, deposition of VO₂ is very inconsistent due to the requirement of reactive sputtering. As depositing thin films of VO₂ requires precise amount of oxygen in the sputtering chamber, slight variation of oxygen rate or pressure can produce different undesired oxides like vanadium sesquioxide or trioxide (V₂O₃), vanadium pentoxide (V₂O₅) or other oxides, which does not exhibit metal-insulator transition (MIT) or in simple words, does not show resistance change behavior. Sputtering target gets oxidized fast and needs cleaning after 3-4 depositions. On the other hand, GeTe target can be used for DC sputtering [46]. As there is no any reactive component involved, thus design to development time is short. These advantages of GeTe makes it a an ideal phase change material for the development of RF devices and systems.

2.3.2 Germanium Telluride (GeTe)

GeTe is a chemical compound of germanium and tellurium and is a component of chalcogenide glasses. It shows semi-metallic conduction and ferroelectric behavior [47]. GeTe exists in three major crystalline forms, room-temperature α (rhombohedral) and γ (orthorhombic) structures and high-temperature β (cubic rocksalt-type) phase; α phase being the most phase of pure GeTe below the ferroelectric Curie temperature of approximately 670 K [48, 49]. Doped GeTe is a low temperature superconductor [50]. Table 2.1 summarizes the relevant measured physical, electrical, and optical constants of amorphous and crystalline GeTe films [51]. The ON (crystalline) state resistivity is $2 \times 10^{-4} \Omega \cdot \text{cm}$ and OFF (amorphous) state resistivity is $>10^3 \Omega \cdot \text{cm}$. This results in a dynamic range (OFF state/ON state resistance ratio) of around 5×10^6 times. These results satisfy the requirements for reconfigurable switches in RF applications [23, 24, 37].

2.3.3 Switching from Amorphous to Crystalline State

Phase change (memory) switching and threshold switching are two types of switching effects in the phase change chalcogenide systems. In amorphous state, the current is low till threshold voltage. This type of switching occurs when the programming voltage reaches beyond the threshold voltage. The amorphous material switches from a high resistivity to a low resistivity state, with a rapid concurrent increase in current after the voltage snapback. The material is said to be in “ON” state. In this state the material is still

Table 2.1: Summary of the measured physical, electrical, and optical constants of amorphous and crystalline GeTe films [51]

Material Property	Units	Amorphous ^a	Crystalline
Density	g/cc	5.6 ± 0.5	6.17
Resistivity	$\Omega \cdot \text{cm}$		
<i>at 300 K</i>		$\sim 10^3$	$\sim 2 \times 10^{-4}$
<i>at 77 K</i>		$> 10^{10}$	$\approx 1.5 \times 10^{-4}$
Temperature Coeff. Resistivity		Negative	Positive
Conductivity type (Hall)		<i>p</i>	<i>p</i>
Carrier concentration	cm^{-3}	$\sim 10^{18}$	$10^{20} - 10^{21}$
Mobility	$\text{cm}^2 \text{V}^{-1} \text{sec}^{-1}$		
<i>at 300 K</i>		$< 10^{-2}$	15 – 120
<i>at 77 K</i>		NA ^b	20 – 250
Susceptibility mass	m_s / m_e	NA ^b	0.16 – 0.35
Fermi energy <i>at 300 K</i>	eV	NA ^b	0.3 – 0.5
Optical gap	eV	~ 0.85	$\sim 0.73 - 0.95$
Electrical band gap	eV	~ 0.8 (intrinsic)	$\sim 0.1 - 0.2$

^a Amorphous films are stable below 145 °C

^b NA: Data not available

amorphous but in a highly conductive state. Increasing the applied voltage beyond the threshold voltage, the resistivity can be further reduced and that allow an even higher \vec{J} through the material. This eventually causes the material to switch to the crystalline state as a result of joule heating effect and this is experimentally observed [37]. The threshold voltage is essential in getting enough power to the amorphous state of material such that it can switch to crystalline state at reasonable voltages. Since the resistance of amorphous state of phase change device is typically in the order of $\sim 10^6 \Omega$, the voltage has to be large enough to provide sufficient power to change the state of the device. The threshold switching effect enables the switching of amorphous to crystalline state at reasonable voltages.

There have been many models proposed to explain threshold switching in depth. Impact ionization and recombination based electronic model [52, 53] proposes that the transition occurs when a critical \vec{E} field is reached that cause field induced carrier generation that neutralize the charged traps. When all the traps are filled, carriers can traverse the device with increased mobility and the generation rate required to keep the traps

filled is reduced from its threshold value. This effect is mainly due to the lone-pair valence electrons that create valence alternation pairs like defects that exist in chalcogenide phase change materials [52]. This enables the excitation of a large concentration of free carriers without breaking the bonds or phase transformation, while leading to a large density of valence alternation pairs at the same time. Poole-Frenkel conduction [54] is another electronic model that proposes the \vec{E} increases the probability of a carrier that hops from one trap to a nearby trap. This requires extended states, at low fields, while at the threshold field, direct tunneling becomes possible which leads to an increase in conductivity.

Polaron instability [55] model proposes that at high fields, the density of small polarons increases. Due to their proximity, lattice deformation becomes difficult once the threshold field is reached. Thus, carriers may not localize and the material becomes conductive. An alternative to electronic models of threshold switching is Field induced nucleation [56] (crystallization model). This model proposes that a crystalline filament forms in the amorphous background at the threshold field. This effect is due to a field-dependence of the free energy of the system. The filament is either stable or collapses upon removing the electric field depending on the size of the filament [37].

In a nutshell, most authors presume that the threshold switching is an electronic effect rather than thermal or structural effect, although the exact mechanism is still uncertain. In contrast, phase change (memory) switching is more clear. It involves a structural rearrangement that causes long range order to improve. Phase change switching at reasonable voltages is, though, enabled by threshold switching, as mentioned above. In this work, phase change switching will be used since a bias is not required to maintain the ON and OFF state [37].

2.3.4 Switching from Crystalline to Amorphous State

The switching from the crystalline to amorphous phase of chalcogenide phase change material is accomplished through the melting and quenching (typical cooling rate of 109 - 1011 °C/s [22, 34, 37, 57, 57–59]). The transformation from the crystalline to the amorphous state is purely by joule heating. This sets the power consumption for the device, since the melting temperature is higher than crystallization temperature. Thus the RESET operation should be the focus of attempts to reduce cell power consumption.

One recent work [60] demonstrated that to reset from the crystalline to amorphous state, appropriate distortions in crystals that have a bonding energy hierarchy can trigger destruction of a subsystem of weaker (resonant) bonds and result in a collapse of the

long range order. In this way, the re-amorphization process is achieved without melting the material. That work also proposed a way to reduce the energy consumption through using shorter pulses. This is in contrast to previous work done using density functional theory (DFT), whereby the amorphous state was understood to occur by the melting of the material, followed by fast quenching. Previous work [61] shows that Ge umbrella flipping causes re-amorphization without having a molten state as the strong covalent bond remain intact even at melting temperature. However, careful analysis of the atomic trajectories reveals that the tetrahedral coordinated Ge atoms in amorphous state do not acquire this bonding geometry through the umbrella flip process proposed earlier. While these mechanisms offer the possibility of melt-free transformation to the amorphous state, the standard method of melting and quenching is certainly still the main explanation in many systems [37].

2.4 Microwave Switching

Telecommunication usually involves a broad range of frequencies from below HF up to millimeter waves. Along with varying operating frequency requirements, the switch specifications can also differ. RF devices including switching networks to amplifiers and other passive or active networks are the functional parts of any telecommunication network. With the advancements in communication protocols and standards, there is a need of new state of the art RF devices. As electronics switches like field effect transis-



Figure 2.3: Various waveguide mechanical microwave switches [62]

tor (FET) or transistors serve as a fundamental block of any digital integrated circuit, RF switches are extremely important elements in RF systems. There are many factors that must be considered in evaluating RF switches including insertion loss and isolation. These two critical parameters directly affect the overall RF performance of the system. Also, the DC power consumption of the switches is a key factor in system considerations particularly in space applications where the DC power requirement is one of the main design drivers. Advanced latching switches can be designed with no DC power consumption. Switch cost may not be the driving factor in satellite applications but it becomes the most important factor in other applications such as cellular phones or Bluetooth devices. Another important design consideration is the RF power handling capability in both the ON and OFF states [63]. In the following sections, conventional mechanical and semiconductor switches are reviewed and their limitations in view of the above design considerations are deliberated.

2.4.1 Mechanical RF Switches

Mechanical switching is achieved through a discontinuity in the signal line or electrical path by a control signal activating an electromagnetic relay. These moving parts provide the ON and OFF states.

Fig. 2.3 depicts waveguide mechanical switches from Sivers Lab Switches [62]. By the rotation of the waveguide, the switch moves from its normal position and shifts the connection between the ports. These switches offer the benefits of a low insertion loss of typically 0.05 dB, a large OFF state isolation around 60-70 dB and capability of handling high power up to 3.5 KW average power at about 10 GHz [63].

A coaxial switch is also shown in Fig. 2.4 from Dow-Key Microwave Corp. [64]. The switch employs an electromagnet for the actuation to move the arm, and a spring to pull it back to the initial position. Such a switch is consistently in the normal position until the application of the current to the coil actuates it. When the power is removed from the coil, the switch returns to the normal position. Typically, these switches have good RF characteristics: i.e., around 60 dB isolation, and typically 0.5 dB insertion loss at 10 GHz [64]. Due to this fact, they have been used in applications with large number of elements such as matrix configurations as discussed further [63].

Although mechanical switches exhibit excellent RF characteristics, they have a very slow switching speed, typically 2 to 50 ms [11, 63]. The switches are also heavy and bulky thus require some different solution especially in satellite communications for reduction in mass as cost to carry mass in space is extremely costly.

2.4.2 Solid-State (Semiconductor) Switches

Generally, p-i-n diode and FET semiconductor switches are suitable for high-speed (in ns) switching applications. Semiconductor switches have a much faster switching speed (even in ns) and are smaller in size and weight than their mechanical counterparts, but are inferior in terms of RF performance including insertion loss, DC power consumption, isolation and power handling capabilities. Moreover, semiconductor switches are not suitable for millimeter wave frequencies due to leakage concerns [65].

Solid-state semiconductor switches can be easily implemented with respect to the transmission direction and configured as switches. The circuit can be also embedded in microstrip lines. The signal passes through the line if the p-i-n is forward biased. It leads to low impedance (ON) and such that the signal flows from the input to the output. When the it is reverse biased (OFF), it goes to a high impedance state, causing the input signal to be reflected. The FET switch on the other hand is a three-terminal device with the switching control is the gate voltage. The low and high impedance states required for switching applications are obtained by making the gate voltage equal to zero and greater than the pinch off voltage, respectively and it is determined by the type of FET selected.

Semiconductor circuits can be fabricated in a hybrid integrated circuit configuration or monolithically in Monolithic microwave integrated circuit (MMIC) circuits. In hybrid



Figure 2.4: Coaxial mechanical RF and microwave switches [64]

microwave integrated circuits, the active and lumped components are connected to distributed circuits by wire bonding or soldering which also adds some loss to the switch. However in MMICs, both active and passive components are fabricated simultaneously on a semiconductor substrate such as Gallium Arsenide (GaAs). Manufacturing at large scale is one of the major advantage of MMICs, hence MMIC switches have been widely used in large number applications such as switch matrices and other complex RF and microwave systems [63].

Solid-state switches have a much larger insertion loss in the ON state (typically 1 to 2 dB), and a poor isolation in the OFF state (~ 20 dB) if the operating frequency is greater than 1-2 GHz [65]. The limitations of mechanical switches and solid state technology motivated the development of RF-Microelectromechanical Systems (MEMS) switches [11]. MEMS technology provides the possibility of replacing many of the microwave switches in today's mobile, communication, and satellite systems.

2.4.3 RF-MEMS Switches

MEMS switches are promising to combine the advantageous properties of both mechanical and semiconductor switches [11]. MEMS switches offer high RF performance and low DC power consumption of mechanical switches with the small size, low weight and inexpensive cost features of semiconductor switches. Fig. 2.5 shows a typical MEMS switch in co-planar waveguide (CPW) configuration. Most MEMS switches are actuated by electrostatic forces leading to near zero power consumption, since there is no current flow. In addition, MEMS switches use air gaps for the OFF state resulting in excellent isolation and have very low insertion loss. Based on the RF characteristics of these switches, figure of merit (FOM) is introduced as "ON state resistance \times OFF state capacitance," demonstrating the superior performance of MEMS over that of semiconductor switches [63]. Moreover, they are very linear devices that result in very low intermodulation products.

Majority of the MEMS switches are fabricated using surface micromachining technology and consist of sputtered or evaporated thin metal films and silicon nitride or dioxide to create cantilever and membrane configurations. These switches can be built on quartz, Pyrex, low temperature co-fired ceramic (LTCC), mechanical-grade high resistivity silicon or GaAs substrates [66].

However, RF-MEMS switches do have their problems. These switches have relatively low switching speed of approximately 2 to 40 μ s. For most of the application these switching speeds are suitable but certain communication systems require much faster

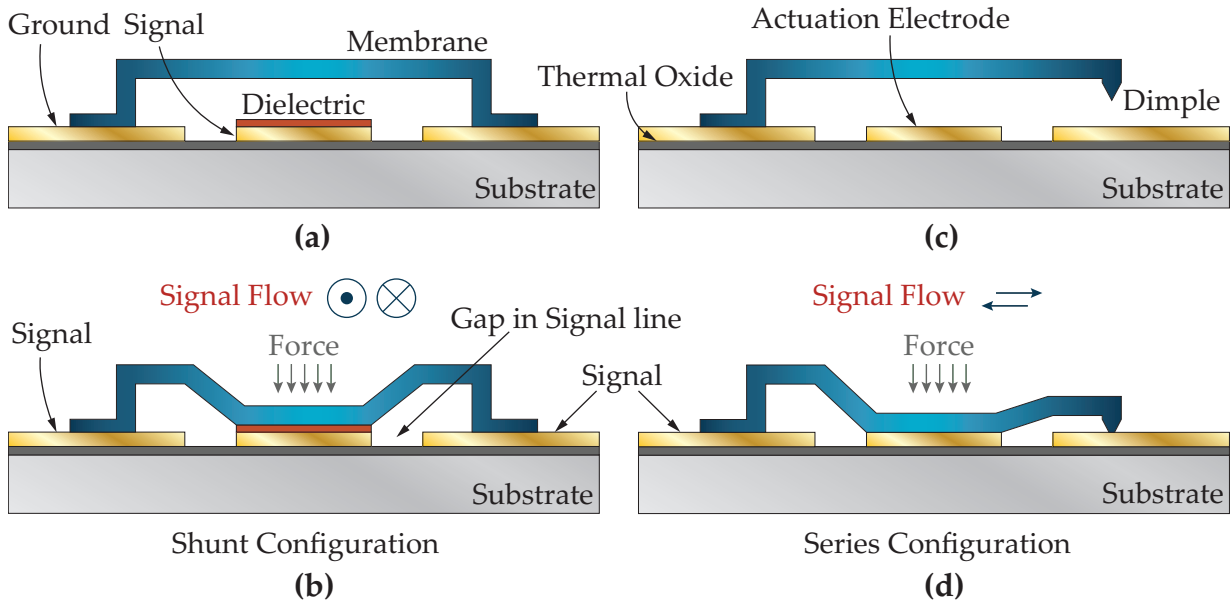


Figure 2.5: RF MEMS switches: (a) shunt/capacitive switch in up-state (ON state) and (b) shunt/capacitive switch in down-state (OFF state); (c) series/metal contact switch in up-state (OFF state), and (d) series/metal contact switch in down-state (ON state).

switching speeds. Since most of the MEMS switches can only handle mW of power, but recently GE have developed switches that can handle much higher power [67]. Researchers are still struggling for an ideal and reliable MEMS switch [68]. The electrostatic movement of the mechanical parts also requires high voltage of approximately 20 to 200 Volts for consistent operation which is well above the required voltage of other solid state technologies [63]. In addition to that, these devices need to be vacuum packaged (hermetic sealing) that simply increase the cost of the switches.

Reliability is the top most concern for these switches. Due to the micro-scale mechanical movable membrane, there is a high change of stiction of membrane or failure due to stresses. But from the RF performance aspect, these switches offer excellent performance. Recently, various kinds of MEMS switches have been extensively studied in series and shunt structures [5, 11, 12, 28] for different RF frequencies. Although, MEMS switches were introduced to get the benefits of mechanical and semiconductor switches, but in practice due to reliability and packaging concerns going back to square one, there is a requirement for some new type of devices that should be the quintessential RF switch.

2.4.4 Phase Change RF Switches

Phase change RF switch is presented very recently and shows promising results to become a candidate for RF applications. Phase change material based switch as described before rely on the change of the material's resistance when heated (phase change). GeTe and VO₂ materials offers change in resistance when heated and are potential candidates for phase change material based switches. GeTe require just ns pulse of voltage to generate enough heat (depending on the topology of micro-heater) that can change the material from crystalline to amorphous state, resulting in change in resistance. This action corresponds directly to the ON and OFF state of RF switch. PCM based switches offer the advantages including great RF performance, linearity and high switching speeds, but these devices are in very early stage, hence many areas are still unexplored. These switches have poor power handling capability and their use for millimeter wave frequencies is not yet explored properly. These challenges can be tackled with sophisticated designs and tailored fabrication process. Initial PCM based switches show great RF performance and the advantages can be explored further while tackling issues simultaneously.

A chalcogenide phase change material GeTe based reconfigurable switch was first presented by E. Chua in 2010 [72]. The switch presented has low ON state resistance of 180 Ω and large dynamic range of (7×10^3) that was achieved through low resistance electrode design and high current. This paper also reported a partial crystallization and partial re-amorphization model to explain the differences between the measured and calculated device in OFF and ON state resistances, respectively. Although this paper reports the switching properties of phase change material by using a phase change via,

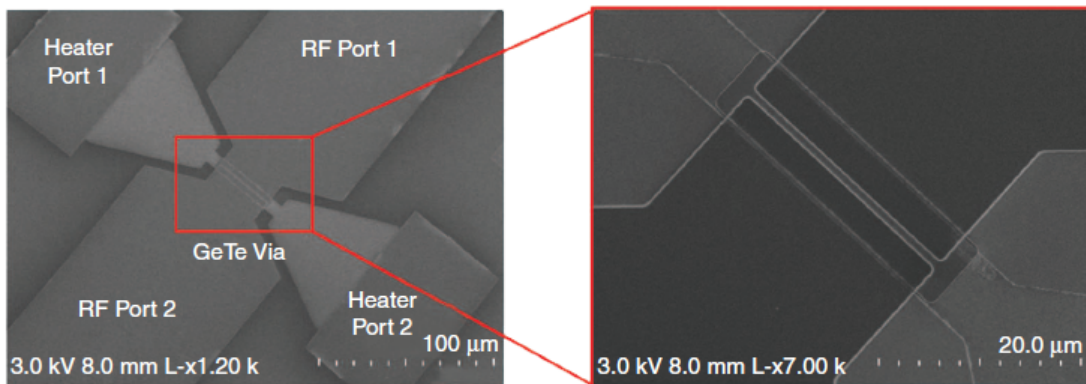


Figure 2.6: SEM images of GeTe based RF Switch [69]

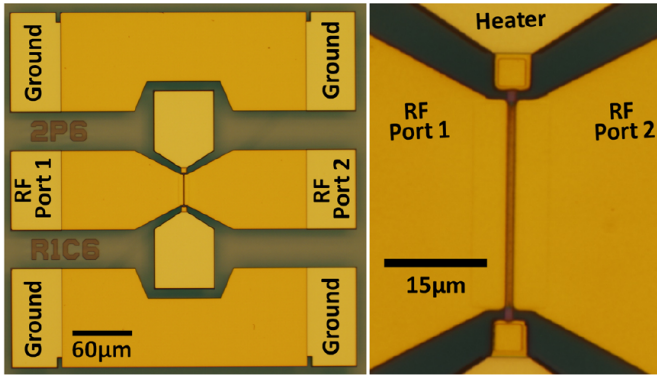


Figure 2.7: Optical photos of low-loss phase change series RF switch [70].

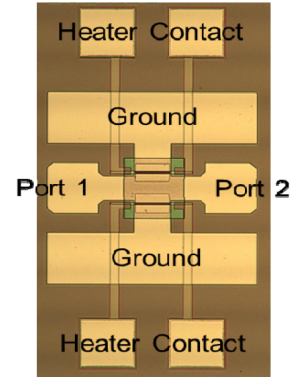


Figure 2.8: Optical micrograph of a GeTe based shunt RF switch [71].

but no RF parameters are reported. The primary focus is on resistance change and its application for RF industry.

A thermally driven RF switch using the properties of metal insulator transition in VO_2 was reported by Teledyne in 2015 [73]. The switch reported shows promising results for millimeter wave frequencies till 50 GHz with cut-off frequency of 45 THz. The heating mechanism is implemented using integrated chip heaters to provide local thermal control. The switch reported 0.13 dB of insertion loss and 20 dB isolation till 50 GHz. Dynamic range for this switch is (4.4×10^4) with low resistance of 3.3Ω at 68°C .

Recently, directly and indirectly heated GeTe based switches are reported by M. Wang from University of Michigan [24, 74, 75], N. El-Hinnawy from Northrop Corp. [23, 70, 76] and J. Moon from HRL Laboratories [71, 77–79] as shown in as shown in Fig. 2.6, Fig. 2.7 and in Fig. 2.8 respectively. Most of these switches have a cut-off frequency of 10 - 12 THz with acceptable RF performance. As these switches reported are in very early stage, work has to be done for the improvement of many different factors like power handling capability of these switches, linearity and extending the operating range to millimeter wave frequency with better RF performance than currently available RF switches including semiconductor switches. Apart from PCM based RF single-pole single-throw (SPST) switches, recently Northrop Grumman Corp. reported a PCM GeTe-based SPDT switch for mmWave applications [80]. The optical micrograph of the SPDT switch is shown in Fig. 2.9 with three RF ports.

Another interesting chalcogenide phase change material SbTe-based RF SPST switch is reported by HRL Laboratories [81]. Optical micrograph of the SbTe based RF switch is shown in Fig. 2.10. The switch design topology and fabrication process is similar to the

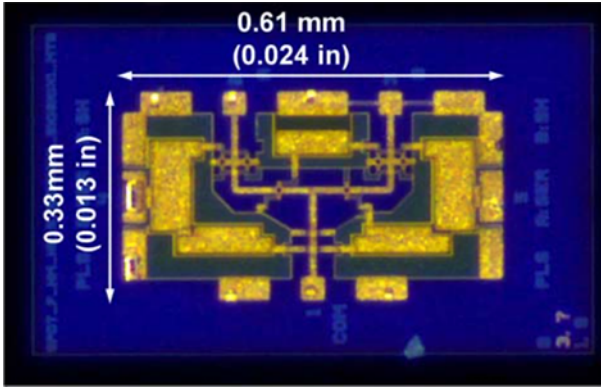


Figure 2.9: Optical micrograph of a PCM GeTe RF SPDT switch [70]

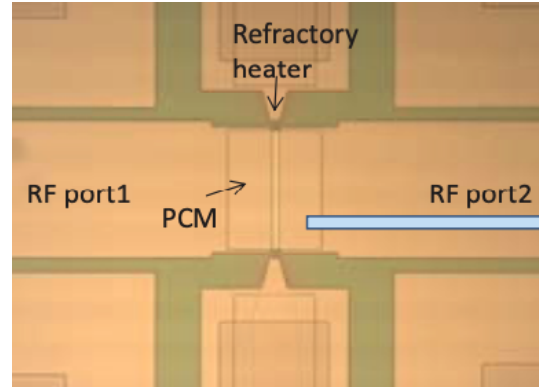


Figure 2.10: Optical micrograph of SbTe based RF Switch [71]

previously reported RF switches except from the phase change material. SbTe does not offer RF performance as comparable to that of GeTe based switches due to the higher ON state resistance and lower OFF state resistance compared to GeTe-based RF switches. The advantage of SbTe material is the lower temperature required for melt-quench operation. The melting temperature of SbTe material depends on the material ratio. Generally, SbTe melts at $635^{\circ}C$, which is approximately $100^{\circ}C$ lower than GeTe melting temperature. The SbTe based switch reported in [81] claims 10 million switching cycles endurance. PCM SbTe is primarily used for memory applications, but characterization and optimization of SbTe alloy ratio might allow getting the optimal resistivity for improved RF switches in near future.

2.4.5 RF Performance Comparison

RF performance comparison including insertion loss and isolation till 20 GHz between phase change material based switches, MEMS, AlGaAs diode, GaN, HEMT, CMOS, GaAs and pHEMT is shown in Fig. 2.11. It is clear from the figure that phase change switches outperformed MEMS and solid-state semiconductor based switches with lowest insertion loss of better than 0.23 dB till 20 GHz followed by MEMS and AlGaAs diode with insertion loss of 0.35 dB and 0.4 dB respectively. Semiconductor switches have high losses as the frequency increases. Similarly, phase change switch has second best OFF state performance with better than 35 dB isolation till 20 GHz.

From this comparison, phase change switches even being in early stage of research demonstrated great RF performance and even outperformed many current generation

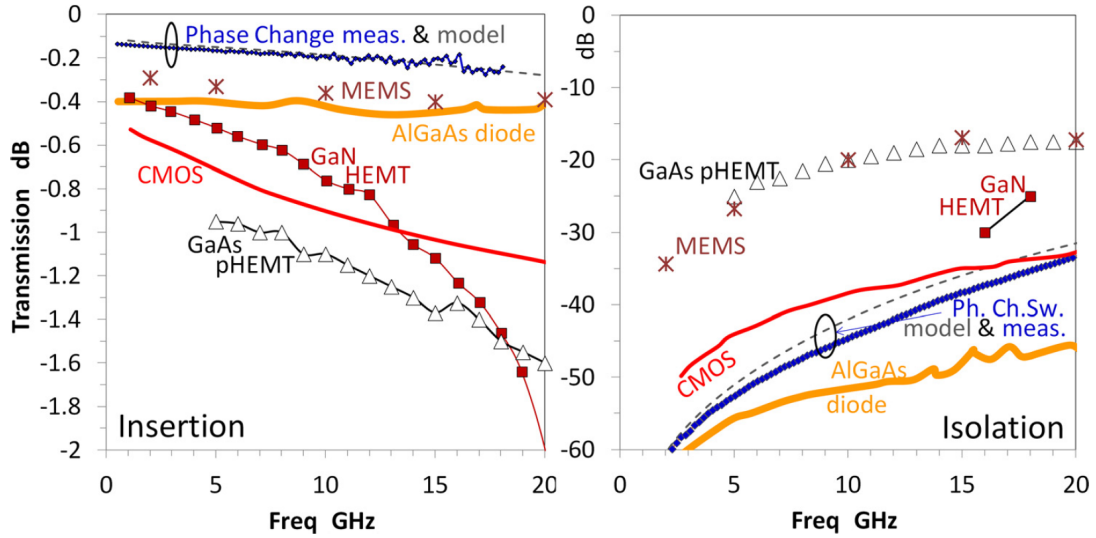


Figure 2.11: RF performance comparison between various RF switch technologies [70]

of devices. Phase change materials have a lot of potential in RF industry and will be explored further. Highly complex switch matrices (network of switches that routes the signals) as described in detail in the following section, are one of the potential application in which PCM based RF switches can be integrated.

PCM based RF switches have comparable performance to MEMS based RF switches without reliability concerns. Table 2.2 shows the comparison of various operating parameters among MEMS and PCM based RF switches.

Table 2.2: Comparison of operating parameters among MEMS and PCM based RF switches [82]

Parameter	MEMS	VO ₂	GeTe
Return Loss	Good	Good	Good
Insertion Loss	Low	Low	Low
Switching Speed	in μ s	in μ s	in μ s
Reliability	Poor	Good	Good
Power Handling	High	Relatively Low	High
Power Consumption ^a	Series SW (~ 1 mW) Shunt SW (0 mW)	DC SW (<1 mW) Thermal SW (10-100 mW)	0 mW

^a Steady-state power consumption

2.5 Multi-Port Switches and Switch Matrices

Spacecraft applications and wireless communication devices are the two major applications that reflect opposite extremes of the RF switch market. While there is a requirement for highest switching performance in the area of volume and mass reduction and communication devices need low-cost devices. Low insertion loss, near zero DC power consumption can potentially be achieved with PCM technology while fulfilling the requirements. RF Switches being the fundamental building block of many RF systems, one of the most highly sought-after application is multi-port switches and switch matrices. Microwave switch matrices are essential components in satellite payloads that enhance the satellite capacity by providing full and flexible interconnectivity between the received and transmitted signals and facilitate optimum utilization of system bandwidth.

Waveguide and semiconductor technology are two prominent candidates for realizing such types of switch matrices. Waveguide switches are dominant in high frequency

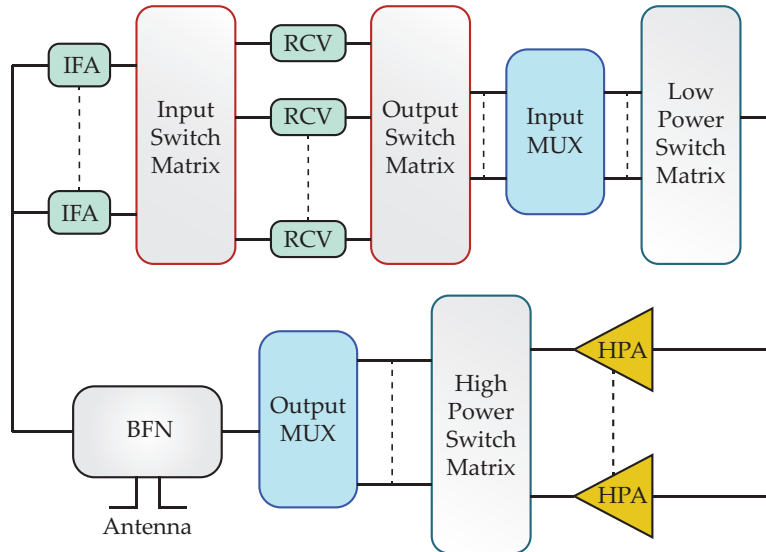


Figure 2.12: Satellite payload operation block diagram (red highlights switch matrices that can be potentially substituted with MEMS technology). The signal is received from the antenna and directed through the beam forming network (BFN) and input filter assembly (IFA) to the receivers (RCV). The signal is then processed and, after passing through the multiplexer (MUX) and high-power amplifier (HPA), it is transmitted to the next repeater satellite through the antenna.

applications (100 - 200 GHz) and in high power satellite communication. However, their heavy and bulky profile reinforces the need for a replacement. While, semiconductor switches are miniature alternatives to mechanical waveguide switches, they exhibit poor RF performance and low power handling [63]. Recently, RF-MEMS based switch matrices were developed by M. Daneshmand [5] that exhibit great RF performance and compact size. But, the only limitation as discussed before is reliability. Phase change materials based switches can take the replacement and can provide same level of RF performance. PCM-MEMS based switch matrices can also be developed monolithically.

Switch matrices are most commonly used in satellite payloads to provide system redundancy. Fig. 2.12 shows a block diagram of a repeater-satellite payload. The signal passes through four sets of switch matrices during the signal processing, in which three of them operate at low power and can be potentially substituted by PCM technology.

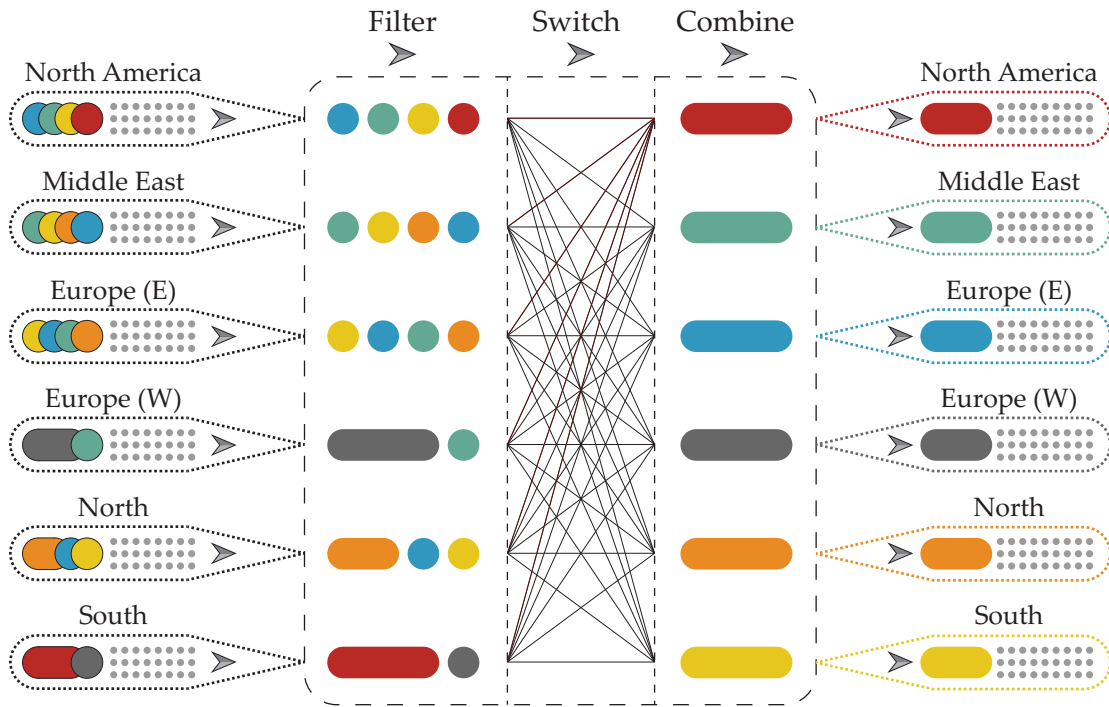


Figure 2.13: Switch matrix application in a beam-link system [12]. The system shown receives six different beams from various locations and transfers them to their intended spots. The beam-link system creates sub-channels for each uplink beam and the switch matrix provides the flexibility to independently direct the sub-channels to the desired downlink beam.

The switch matrices shown provide system redundancy for the satellite payload against receiver or high-power amplifier failures. The switch matrices reroute the signal to the spare component located in the system and maintain the full functionality of system in case of any failure. Satellite communication systems also rely on switch matrices to provide system redundancy and to enhance the satellite capacity by providing full and flexible interconnectivity between the received and transmitted signals. Fig. 2.13 is an example of a satellite payload employing switch matrices for beam linking [12]. The switch matrix provides the flexibility to independently direct the sub-channels to the desired downlink beam.

2.5.1 Switch Matrix Configuration

Crossbar switch matrices are one of the most common configurations used for signal routing in communication systems. This topology offers flexible connectivity between any of the multiple inputs to any of the multiple outputs and can be easily expanded to large size matrices. Fig. 2.14 shows a configuration with the topology of a 4×4 crossbar switch matrix and Fig. 2.15 shows the SEM image of fabricated 3×3 crossbar switch matrix using RF-MEMS switches at Centre for Integrated RF Engineering (CIRFE) [12].

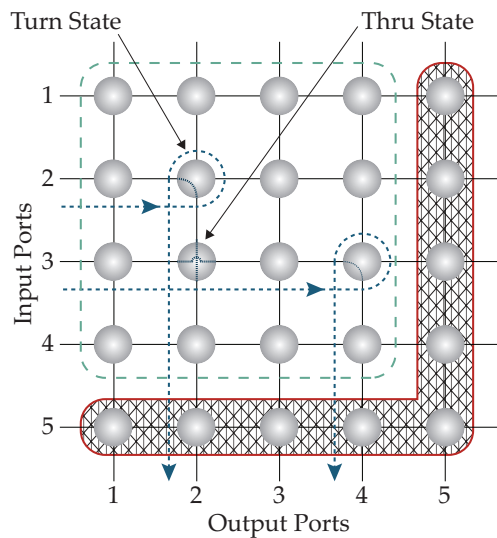


Figure 2.14: Crossbar switch matrix architecture realization using switch cells

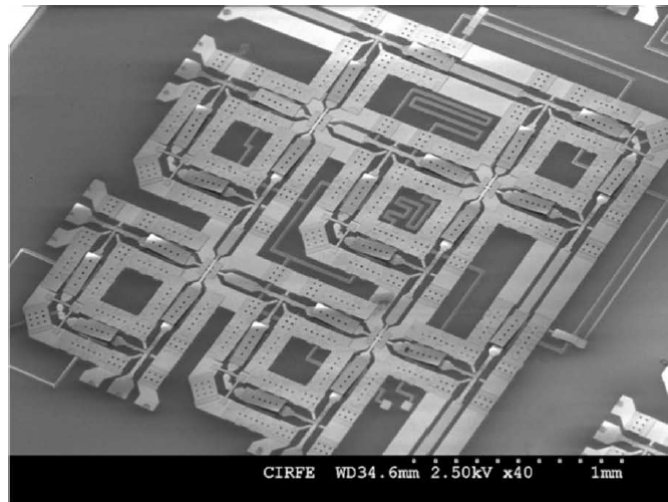


Figure 2.15: SEM image of fabricated 3×3 crossbar RF MEMS switch matrix [30]

The size of such matrices can be easily adjusted by having additional columns and rows of the switch cells.

A 4×4 crossbar switch matrix can be easily expanded to 5×5 switch matrix by adding an additional column and row as shown in Fig. 2.14. The required switching cell for the switch matrix must be able to achieve two operational states; the “Turn” and “Thru” operations. The “Turn” operation implements a 90° rotation to the input signal, while the “Thru” operation provides a crossover for two different input signals in the same cell. At the “Turn” state, connections are switched such that only two 90° ports are connected, while other two ports are left floating as shown in State I or II Fig. 2.16. At the “Thru” state, connections are established between Ports 1 and 3, and Ports 2 and 4 as shown in State III of Fig. 2.18. A compact version of 4×4 MEMS-based crossbar switch

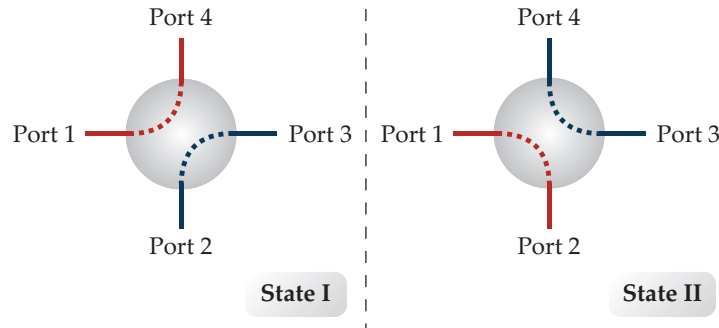


Figure 2.16: Operating Principle of a C-type switch and its two operational states. This four-port device connects Ports 1 and 4 and Ports 2 and 3 in State I and Ports 1 and 2 and Ports 3 and 4 in State II.

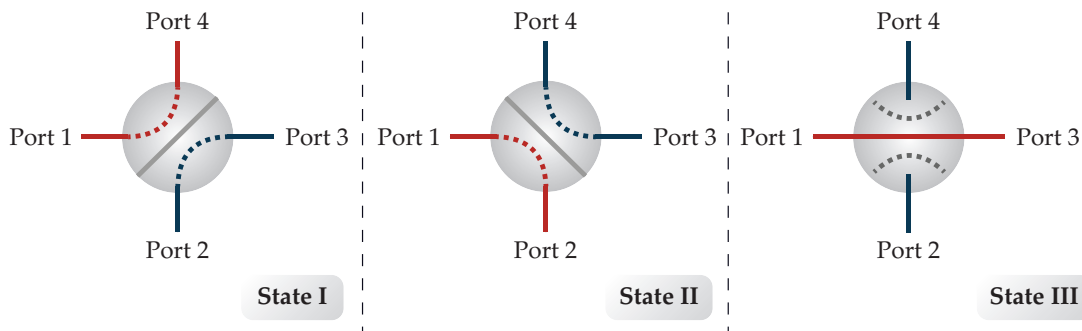


Figure 2.17: Operating principle of an R-type switch and its three different states. In State I, the signal can be routed between Ports 1 to 4 and Ports 2 to 3; in State II, the signal can be routed between Ports 1 to 2 and Ports 3 to 4; and State III connects Ports 1 and 3.

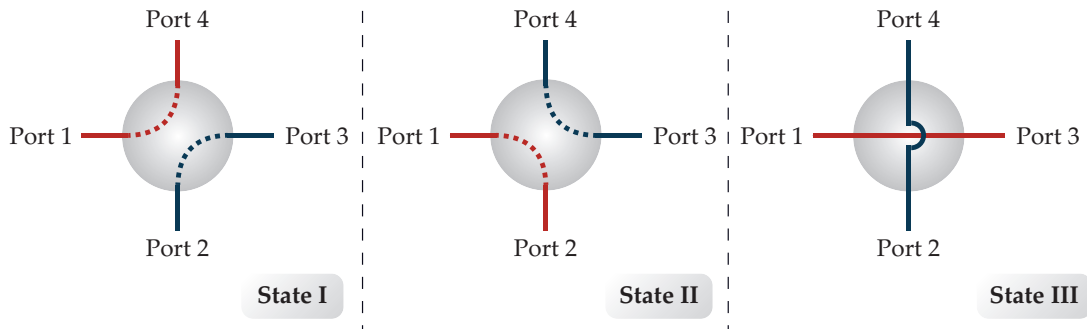


Figure 2.18: Operating principle of a T-type switch and its three different states. In State I, the signal can be routed between Ports 1 to 4 and Ports 2 to 4; in State II, the signal can be routed between Ports 1 to 2 and Ports 3 to 4; and between Ports 1 to 3 and Ports 2 to 4 in State III.

matrix is also developed at CIRFE [83].

Although there are many reports on SPST RF switches using MEMS and solid-state technology, but limited research has been conducted on multi-port structures. Possibly, this is due to the complexity of the RF design, as well as the increased number of the actuating mechanisms. Commercial switches in multi-port configurations are available that has single input and multiple outputs or dual input dual output configurations. One of the main applications of the switches is for signal routing or redundancy schemes. The complexity of an interconnect network is determined by trade offs of user needs, insertion loss, and cost. Multi-port switches including C and R switches are used as the basic building blocks of the matrix [12].

2.5.2 C and R-Type Switches

In a typical satellite payload, hundreds of switches are used to provide system redundancy and maintain full functionality. The basic building block of this switch matrix is a C-type switch as shown in Fig. 2.16. In case of failure, this is achieved by rerouting the signal to a spare amplifier. Fig. 2.19 shows an example of a 5-to-7 input redundancy switch matrix connected to a 7-to-5 output redundancy switch matrix to provide system redundancy that will allow for two amplifiers to fail without losing system functionality.

R-type switches have one additional operation state which considerably simplifies the switch matrix integration as shown in Fig. 2.17. Fig. 2.20 shows a schematic of a 5-to-7 redundancy switch matrix employing R-type switches rather than C-type switches. In normal operation, all the switch cells are in operation State III. In case of failure in an

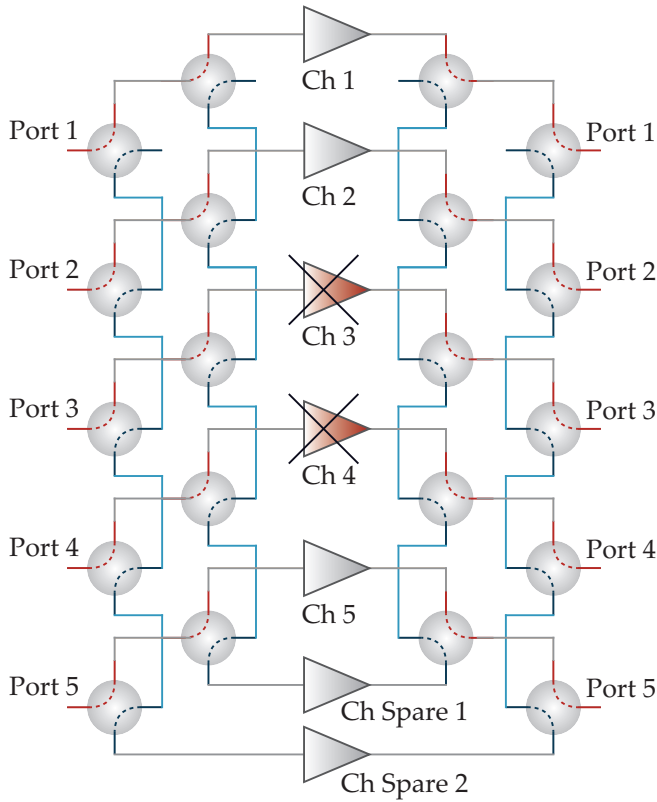


Figure 2.19: Redundancy system with five primary channels and two spare channels using C-type switches as building blocks.

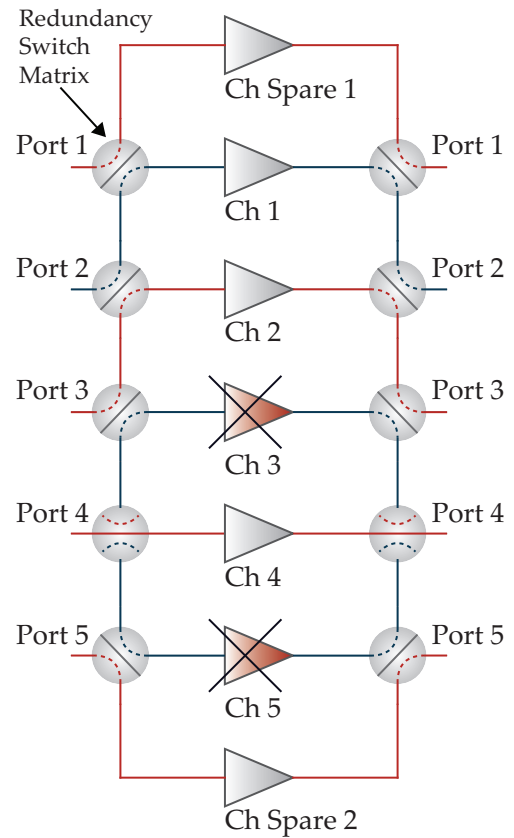


Figure 2.20: Redundancy system using R-type switches as building blocks.

amplifier, the switch matrix reroutes the signal to the spare amplifiers at Port 1 and Port 7. Fig. 2.20 illustrates the reconfigured switch matrix to reroute the signal and avoid faulty amplifiers 3 and 5. It is clear that the number of required switch elements is considerably reduced that required in the matrix consisting C-type switches only.

2.5.3 T-Type Switch

The T-switch is another type of multi-port switch that provides a high degree of flexibility in the redundancy network design as shown in Fig. 2.18. It consists of four ports and six signal paths with three operational states. Each state has two conducting paths connecting to two pairs of ports. In State I, Ports 1 and 4, and Ports 2 and 3 are connected.

In State II, Ports 1 and 2, and Ports 3 and 4 are connected. In State III, the two RF signals crossover to provide connectivity between Ports 1 and 3, and 2 and 4. The application of the T-type switch in redundancy networks is very attractive as it provides one more routing that simplifies the integration of switch matrices considerably. Authors from the University of New South Wales and the University of Waterloo [84] have presented a realization of a T-type switch using MEMS technology but can be potentially implemented using PCM technology as well.

2.5.4 Switch Matrices Scalability

In some applications in satellite payloads, very high isolation is required that cannot be satisfied with the above mentioned switch matrix topologies. In these cases, one approach to connect N input ports to N output ports is to use single-pole multi-throw (SPNT) switches and to make pairwise connections between every input and output switch, as shown in Fig. 2.21. Though the concept can theoretically be used for any size switch matrix, when used in practical applications, to achieve better RF performance, small matrices are employed as basic building blocks to create larger structures [12].

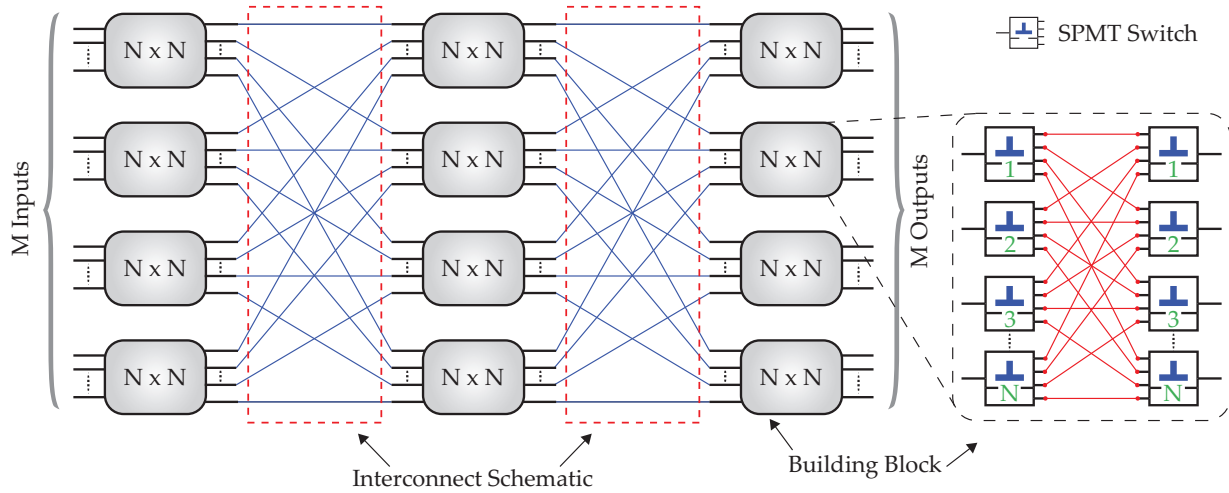


Figure 2.21: Switch matrices with pairwise connections showing several $N \times N$ matrices connected to form a larger switch matrix

Multi-port RF switches plays a crucial role in modern communication systems. C, R and T-type RF switch can be combined together as a unit cell to create $N \times N$ switch

matrices. Although RF performance degrades due to the addition of switching elements in a single path. Thus, high performance and reliable switches are required for the development towards robust and powerful communication systems.



Chapter 3

Thin-Film Characterization of Chalcogenide PCM GeTe for RF Switches

This chapter reports the characterization and optimization of PCM GeTe for RF switches investigating the materials' aspect. Surface properties of GeTe thin-films are investigated through atomic force microscopy (AFM), scanning electron microscopy (SEM) and cross-wafer resistance mapping measurements. Optimized GeTe thin-films exhibit over five orders of resistance change. Various GeTe switch design constraints are studied via cross-sectioning of the fabricated device using focused ion beam (FIB)-SEM. Current-carrying capacity and resistance of micro-heaters is extracted using electrical characterization. The RF performance of the PCM switches is optimized using diverse design parameters and characterization of PCM thin films. Methods to reduce parasitic elements in PCM switches are discussed. The RF performance of the optimized PCM based switch is simulated and measured demonstrating better than 0.4 dB of insertion loss and a return loss better than 20 dB from DC to 67 GHz.

The phase transformation in GeTe switches is achieved by localized embedded micro-heaters for thermally switching the materials' state in a melt-quench process. The embedded micro-heater circuit, on the other hand introduces capacitance that affects the RF performance. Further, the resistivity of PCMs is affected heavily by the thin-film deposition method and conditions. Thus, optimization of micro-fabrication process parameters is essential to enhance the RF performance of the switch.

Parts of this chapter are published in [85, 86]

Initial prototypes of RF PCM switches in series and shunt configuration are presented in [87] and a brief description of the fabrication process with an outline of the issues associated with the design and fabrication of GeTe thin film RF switches is discussed in [85]. In this chapter, GeTe thin-films are characterized thoroughly to maximize the resistance ratio between amorphous and crystalline state. Surface properties of GeTe thin-films are studied and characterized through high-resolution atomic force microscopy (AFM), scanning electron microscopy (SEM) and cross-wafer resistance mapping measurements. GeTe films are optimized, yielding films that demonstrate over five orders of resistance change. Focused ion-beam (FIB) SEM is used to investigate the design and micro-fabrication constraints by studying the cross-section of the fabricated device. Electrical characterization of micro-heaters is carried out to investigate the resistance and current-carrying capacity of the heaters.

3.1 Phase Transition in Chalcogenide Materials

The PCM-based RF switches take advantage of the GeTe material that exhibits a transition between crystalline (ON) and amorphous state (OFF) that is attained by heating the PCM above its melting temperature (T_m), and followed by quenching the material, which solidifies the atoms in the amorphous state as shown in Fig. 2.1. Switching from crystalline to amorphous state can be achieved by applying short high voltage (\sim ns) pulse via the embedded micro-heater. Switching the PCM from amorphous to crystalline state is achieved by heating the material beyond its recrystallization temperature (T_c), at which the growth of crystalline grains and nucleation is enabled. Electrical pulse of ($\sim\mu$ s) duration switches the state of the PCM from amorphous to crystalline [23]. High voltage pulses of 18 V are used to amorphize the material and low voltage pulses of 8 V are used to crystalize the PCM. Pulse amplitude scales with the micro-fabrication process parameters of thin-film resistor (TFR) material. The voltage required to change the GeTe states can be down scaled by reducing the resistivity of the micro-heater, either through changing the design dimensions or thickness of the thin-film.

3.2 Characterization of Phase Change Material

Optimization of GeTe thin films is a crucial step in the development of high performance RF switches with low ON-state loss and high OFF-state isolation. Performance of the PCM switch depends on the GeTe film quality. Poor quality films exhibit lower resistance

ratio between crystalline and amorphous state than the films deposited using optimized deposition conditions mentioned in the following sections. Various factors including but not limited to deposition type, base pressure, chamber pressure, material purity, deposition power, DC/RF sputtering, inert gas flow rate, and deposition temperature can affect the film quality from resistance ratio to surface morphology.

3.2.1 Deposition Conditions

GeTe thin films are deposited using dc magnetron sputtering using an ultra high purity Ge[50%]:Te[50%] target. Deposition parameters are given in Table 3.1. Deposition pressure is varied from 2 mTorr to 10 mTorr, and the deposition temperature is varied from 25 °C to 200 °C. While samples 'A', 'B', 'C' and 'D' are deposited with varying argon flow rate, the flow rate is fixed to 20 sccm for the rest of the samples. For the films deposited at elevated temperatures, deposition power, time, and pressure is kept consistent. Deposition time is not mentioned as it depends on the target size, power, pressure and argon flow rate. Deposition time is different for all the mentioned films and uniform film thickness of 150 nm is used for comparison.

Table 3.1: Deposition Parameters for GeTe Thin-Films

Sample ID	Power (W)	Pressure (mTorr)	Temperature (°C)	Argon (sccm)
A	30	3	25	27
B	60	5	25	40
C	30	8	25	27
D	30	10	25	50
E	60	3	25	20
F	60	3	100	20
G	60	3	150	20
H	60	3	200	20
I	30	2	25	20
J	30	3	25	20
K	30	5	25	20
L	30	10	25	20

3.2.2 Study of Surface Topography

GeTe thin-films are characterized to get optimal film quality that demonstrate higher resistance ratio between crystalline and amorphous states. The primary issues with GeTe films are cracks and voids formation after annealing as discussed in the previous section. To avoid such problems, films deposited at various deposition conditions are studied by investigating the surface topography using high resolution AFM, SEM, and cross-wafer resistance mapping measurements.

Initial study of GeTe thin-films included four samples ('A', 'B', 'C' and 'D') of 150 nm which are dc sputtered on 2.5 in \times 2.5 in, 635 μ m thick Al₂O₃ substrate. 3D AFM scan of sample 'B' in amorphous state is shown in Fig. 3.1 (a) and the crystalline state of the film is shown in Fig. 3.1 (b). The average roughness is almost identical in both amorphous and crystalline states except the larger particle size. The AFM scan area for samples 'A' to 'D' is 3 μ m \times 3 μ m.

Surface roughness of alumina substrate and scratches from the substrate polishing affects the film morphology making it challenging to study the grain size. Surface defects of alumina wafers are prominent in the AFM scans of GeTe films as shown in Fig. 3.2 (a-f). Sample 'D' in Fig. 3.2 (f) shows GeTe film after annealing that exhibits only two orders of resistance change and Fig. 3.2 (e) shows Sample 'D', as-deposited film. 3D surface topography of crystalline and amorphous GeTe film on Sample 'B' is shown in Fig. 3.1. Samples 'A', 'B', and 'D' are shown in Fig. 3.1. Left side micrographs are of amorphous films and right side are of crystalline films. Films are annealed for 30 min at 220 $^{\circ}$ C to get a crystalline state of the material.

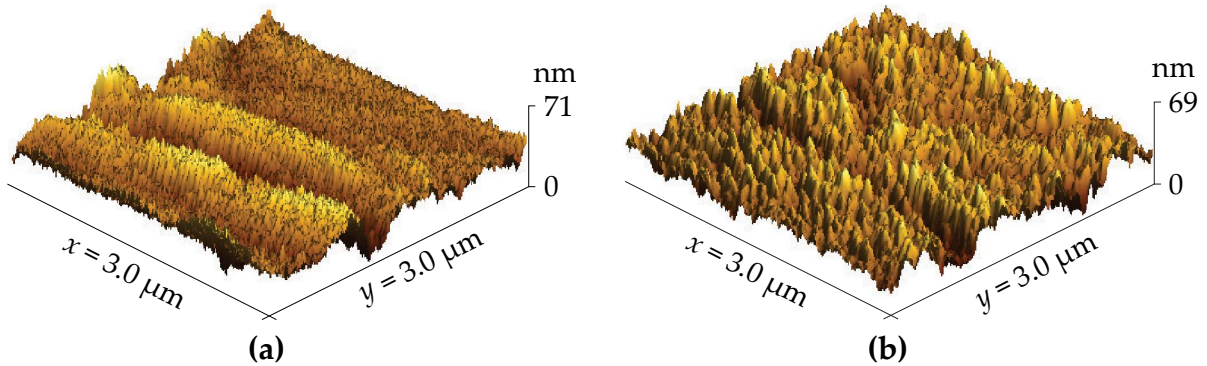


Figure 3.1: 3D surface scan of GeTe film in (a) amorphous state (Sample 'B'), and (b) crystalline state (Sample 'B'). Scan area is 3 μ m \times 3 μ m.

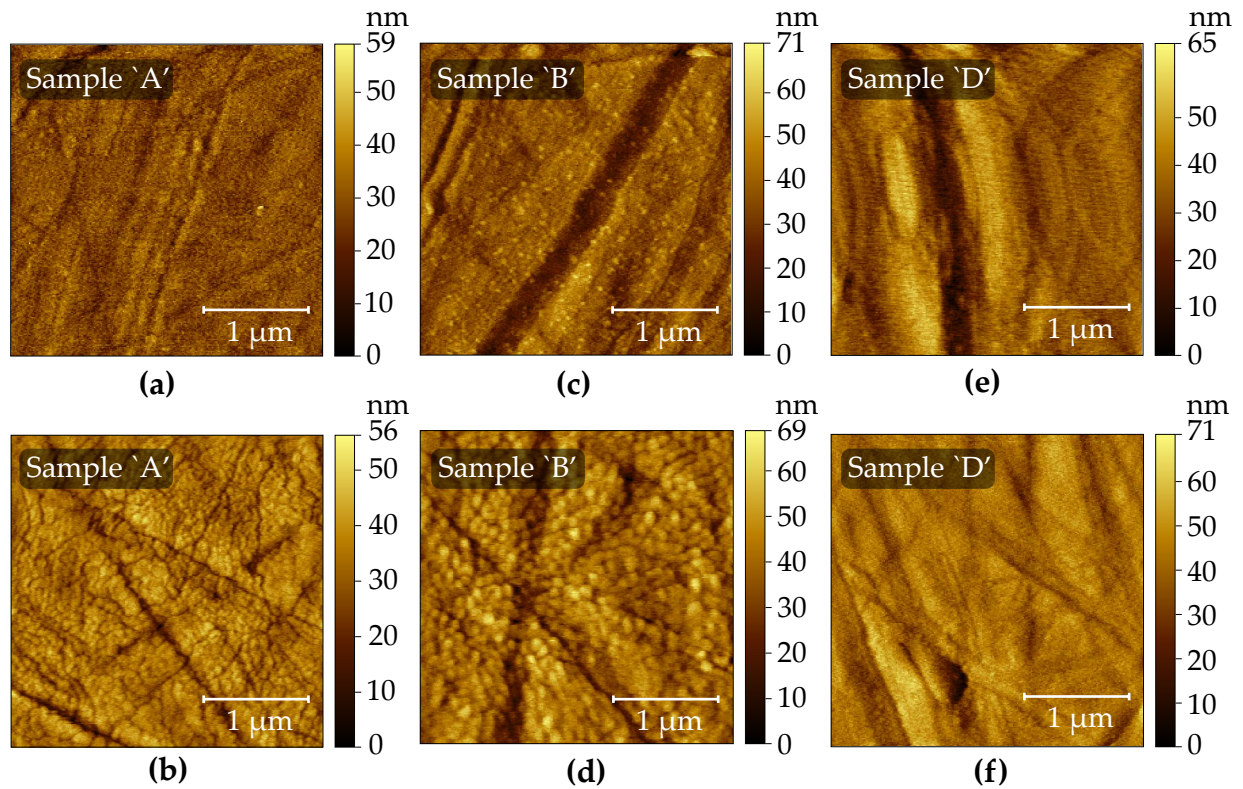


Figure 3.2: AFM scan of GeTe thin film deposited on Al_2O_3 substrate. (a) Sample 'A' amorphous, (b) Sample 'A' crystalline, (c) Sample 'B' amorphous, (d) Sample 'B' crystalline, (e) Sample 'D' amorphous, and (f) Sample 'D' annealed with only two orders of resistance change. Streaks are from substrate with average roughness of 25 nm.

Amorphous films are smoother than crystalline films as shown in Fig. 3.2. The AFM scan shown in Fig. 3.2 (a) is of sample 'A' and the image shown in Fig. 3.2 (c) is of sample 'B'. Sample 'B' is deposited at 60 W deposition power and 5 mTorr deposition pressure with higher argon flow of 40 sccm. Although the films are of same thickness, crystalline films as shown in Fig. 3.2 (b) and (d) show higher roughness.

Surface profile is extracted from AFM scans as shown in Fig. 3.3. Film roughness, texture and waviness is extracted from surface profile. Larger particles and higher roughness is prominent in crystalline films as shown in surface profile. Surface profile shown in Fig. 3.3 is measured from sample 'B' of size $3 \mu\text{m} \times 3 \mu\text{m}$.

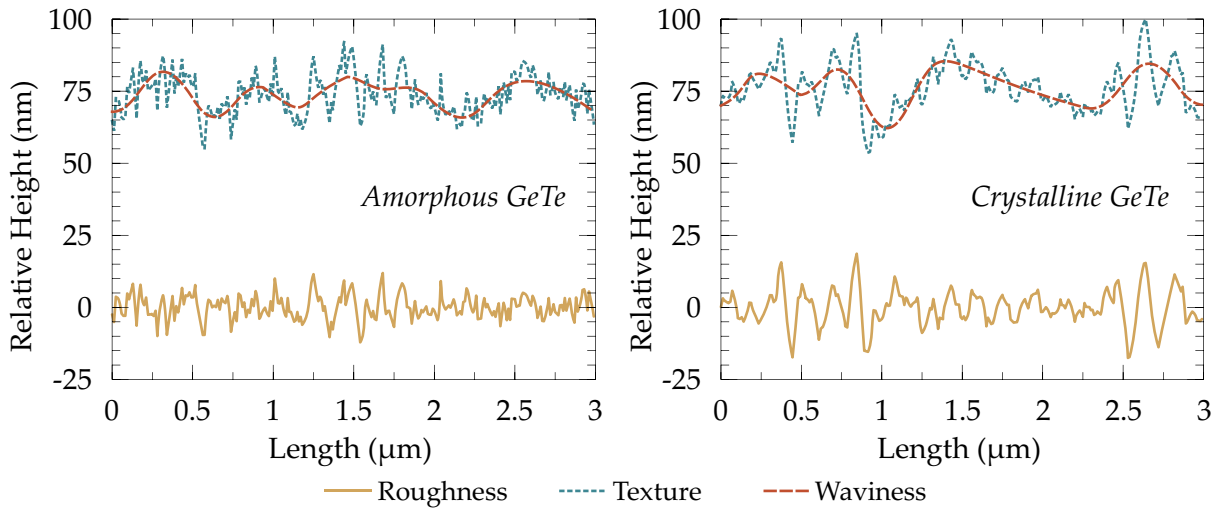


Figure 3.3: Surface line profile of 3 μm GeTe sample including roughness, texture and waviness of the film in crystalline and amorphous state.

3.2.2.1 Effect on Deposition Temperature

Commercial high-resolution AFM is used to evaluate the surface topography and film roughness on glass substrate due to its negligible surface roughness. GeTe samples 'E', 'F', 'G', and 'H' are deposited at elevated temperatures to study the effect of deposition temperature on GeTe films. In these samples, sputter deposition power is kept at a constant value of 60 W, a deposition pressure of 3 mTorr, and an argon flow of 20 sccm were used while varying the temperature from 25 °C to 200 °C. These samples are also annealed for 30 min at 220 °C after the deposition.

Films deposited at room temperature show distinct large grain size in annealed GeTe films (crystalline state) and rather smooth surface profile in the as-deposited amorphous state. Voids and cracks formation are more prominent in crystalline films as shown in Fig. 3.4 (b). Amorphous or as-deposited films at different temperatures show uniform roughness as shown in Fig. 3.4 (a), (c), (e), and (g) while crystalline films show different surface topographies when deposited at elevated temperatures. Fig. 3.4 (d) shows the crystalline state of film deposited at 100 °C.

Fewer cracks are observed in the films deposited at elevated temperatures compared to the ones deposited at room temperature. However, elevated temperature deposition of GeTe films show high roughness. Films deposited at 150 °C, as shown in Fig. 3.4 (f) are almost free from cracks and voids, but roughness is higher than that of sample 'E'

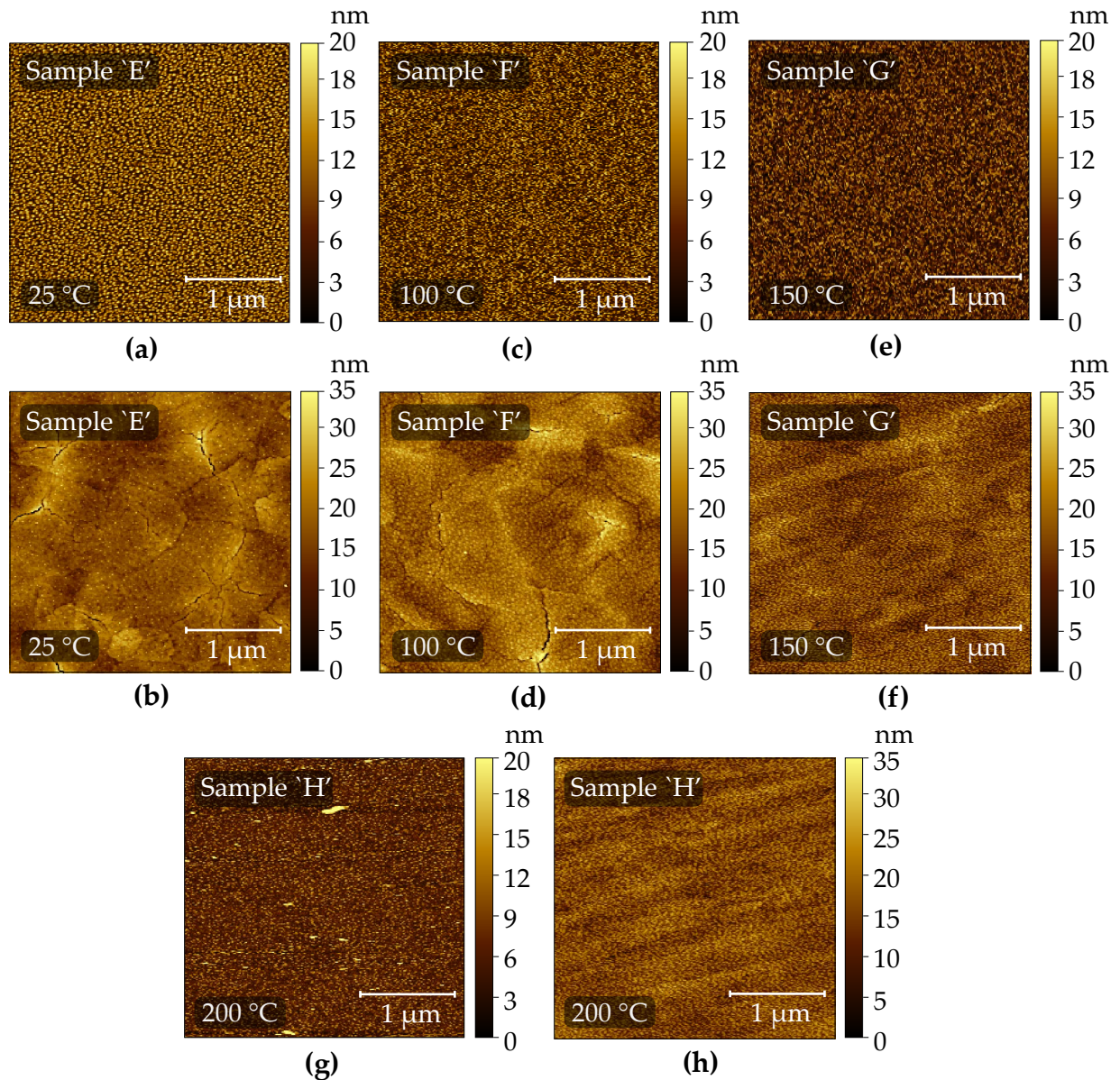


Figure 3.4: AFM scan of GeTe thin film deposited on glass substrate. (a) Sample 'E' amorphous, (b) Sample 'E' crystalline deposited at room temperature, (c) Sample 'F' amorphous, (d) Sample 'F' crystalline deposited at 100 °C, (e) Sample 'G' amorphous, (f) Sample 'G' crystalline deposited at 150 °C, (g) Sample 'H' amorphous, and (h) Sample 'H' crystalline deposited at 200 °C. Change in grain boundaries is prominent in films deposited at room and elevated temperatures.

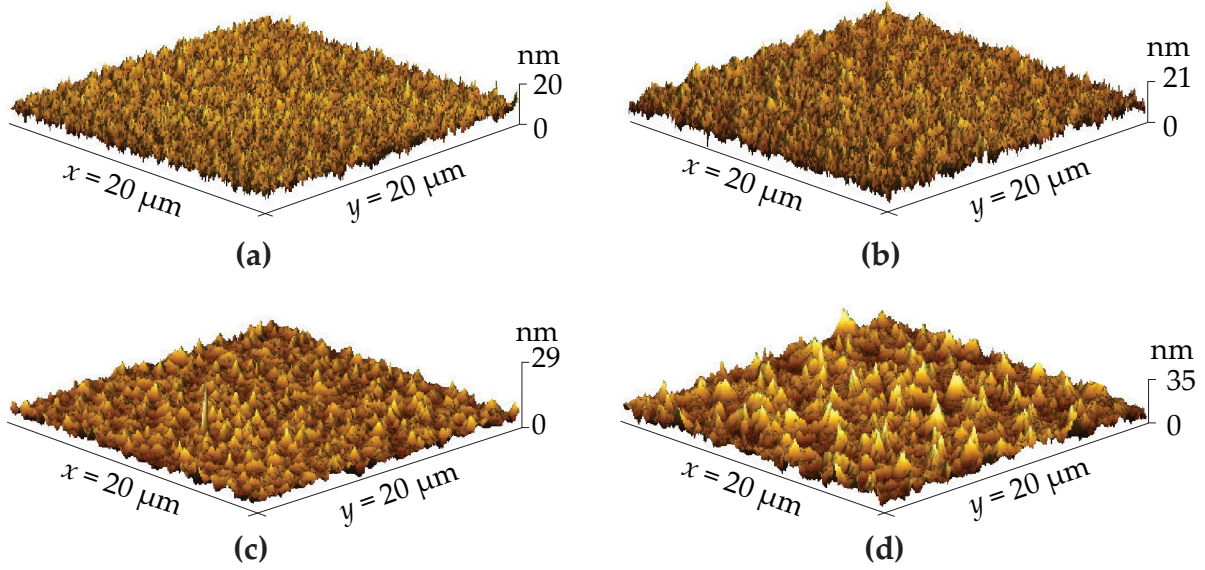


Figure 3.5: 3D surface scan of GeTe films in crystalline states deposited at (a). 25 °C (Sample E), (b). 100 °C (Sample F), (c). 150 °C (Sample G), and (d). 200 °C (Sample H). Scan area for the samples is $20\ \mu\text{m} \times 20\ \mu\text{m}$.

and ‘F’. Crystalline films deposited at 200 °C as shown in Fig. 3.4 (h) do not show any prominent sign of cracks or voids, but are not usable for PCM switches. High roughness of PCM thin-films is not favorable for achieving narrow PCM channel in series SPST switches.

Scan area has been extended from $3\ \mu\text{m} \times 3\ \mu\text{m}$ range to $20\ \mu\text{m} \times 20\ \mu\text{m}$ since surface roughness and larger grains becomes more prominent in large scan area. 3D surface scans of the same samples are shown in Fig. 3.5 (a) for sample ‘E’, (b) for sample ‘F’, (c) for sample ‘G’ and (d) for sample ‘H’.

3.2.2.2 Roughness Estimation Using Grain Mapping

To evaluate the grain mapping, an AFM scan of sample ‘H’ is used, as it shows larger roughness peaks. Grain mapping of crystalline films is shown in Fig. 3.6. 3D surface scan shows the overlap of grain mapping plot in Fig. 3.6 (a). Top view of the scan is shown in Fig. 3.6 (b). Grain mapping plot is set to highlight average peak diameter of equal or larger than $1\ \mu\text{m}$ grain size. Scan area is $20\ \mu\text{m} \times 20\ \mu\text{m}$. Cross-section of the plot is shown in Fig. 3.6 (c). Within the section of $5\ \mu\text{m}$ scan line, two peaks can be seen

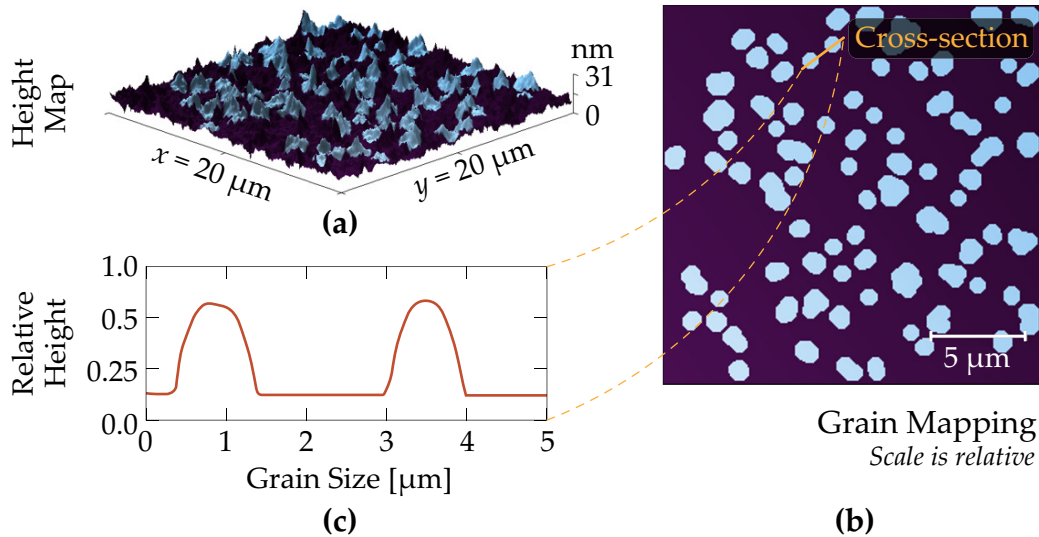


Figure 3.6: Grain mapping of GeTe film in crystalline state deposited at 200 °C. (a). 3D surface scan of the film with grain mapping mask, (b). Surface scan of GeTe crystalline film with grain mapping mask revealing grains larger than $0.8 \mu\text{m}$. (c). Inset showing profile scan of two grains from (b) surface plot cross-section line. Grain height is relative in all cases.

of relative height 0.5 and of diameter $1 \mu\text{m}$.

Grain mapping allows an in-depth evaluation of the films. Films deposited at elevated temperatures are free from voids and cracks, but micron-size roughness are not usable with the average PCM length of $1 \mu\text{m}$ or less. Films deposited at $150 \text{ }^\circ\text{C}$ show adequate roughness with average peak diameter of 200 nm to 400 nm.

3.2.2.3 Effect on Deposition Pressure

The change in deposition pressure also affects the surface roughness in crystalline GeTe thin films. SEM is used to study the films deposited at elevated deposition pressure. Fig. 3.7 (a) shows the amorphous film deposited at 3 mTorr and crystalline state of the film is shown in (b). Amorphous films show uniform roughness as depicted in the inset of Fig. 3.7 (a) in a 3x zoomed view. Crystalline film shows small voids at several locations. Films deposited at 10 mTorr affect the roughness of crystalline films shown in Fig. 3.7 (d). The film becomes free from voids or cracks but are extremely rough. Deposition pressure between 2 mTorr to 4 mTorr can provide adequate quality of GeTe thin films, which can be further optimized by changing deposition temperature.

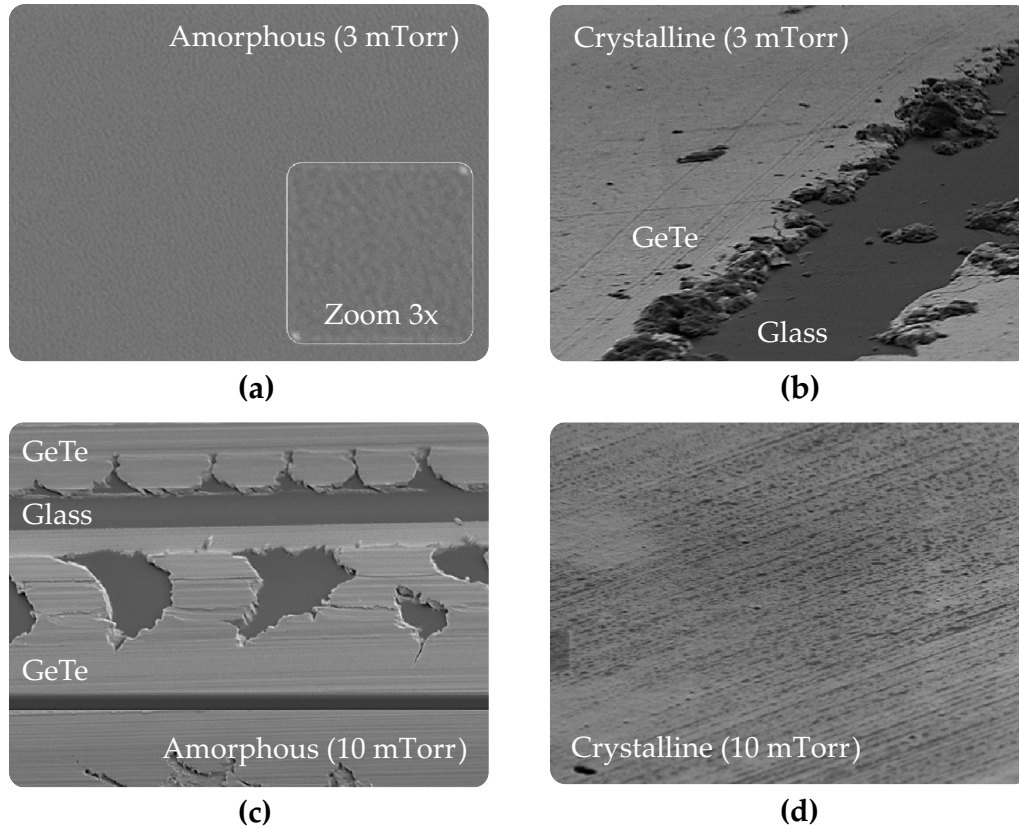


Figure 3.7: SEM micrographs of the GeTe films deposited at elevated pressure results in change of film roughness. (a) Amorphous state of GeTe deposited at at 3 mTorr, (b) Crystalline state of GeTe deposited at 3 mTorr, (c) GeTe in amorphous state deposited at 10 mTorr), and (d) GeTe in crystalline state deposited at 10 mTorr).

3.2.2.4 Resistance Mapping Across Wafer

The sheet resistance distribution across the 2.5 in \times 2.5 in Al_2O_3 wafer in crystalline state is evaluated using commercial automated 4PP (four-point probe) as shown in Fig. 3.8. The sheet resistance in amorphous state is beyond the maximum measurement range of automated 4PP. Therefore, it is evaluated using a manual 4PP and the measurements are recorded at different locations across the wafers. Contour plots of samples 'A', 'B', and 'C' show lowest sheet resistance of $32 \Omega/\square$, $17 \Omega/\square$, and $16 \Omega/\square$ near to the mid section of the wafer with slight deviations around the edges and corners. The variations are due to sputter deposition conditions.

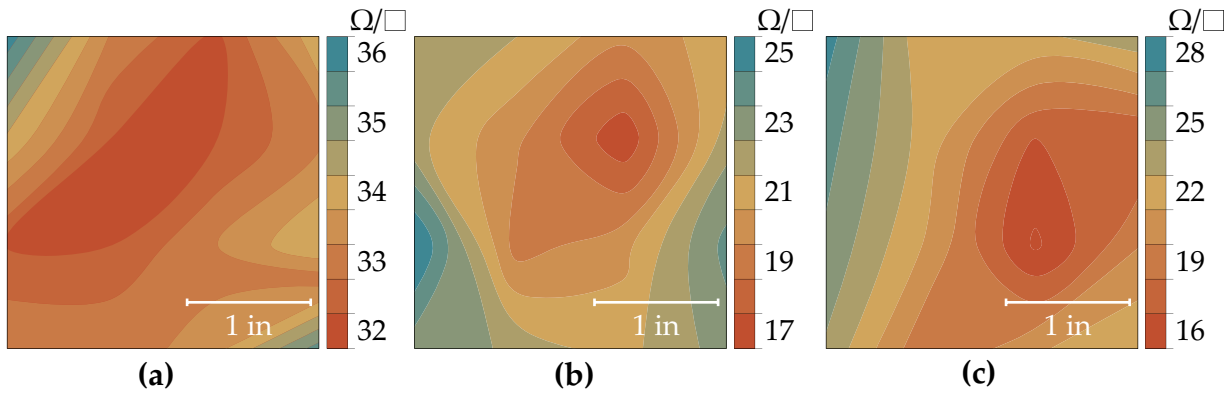


Figure 3.8: Sheet resistance measurement across wafer using four-point probe method. (a) Sample 'A', (b) Sample 'B', and (c) Sample 'C' shows the resistance distribution in crystalline state of annealed 150 nm GeTe thin-films.

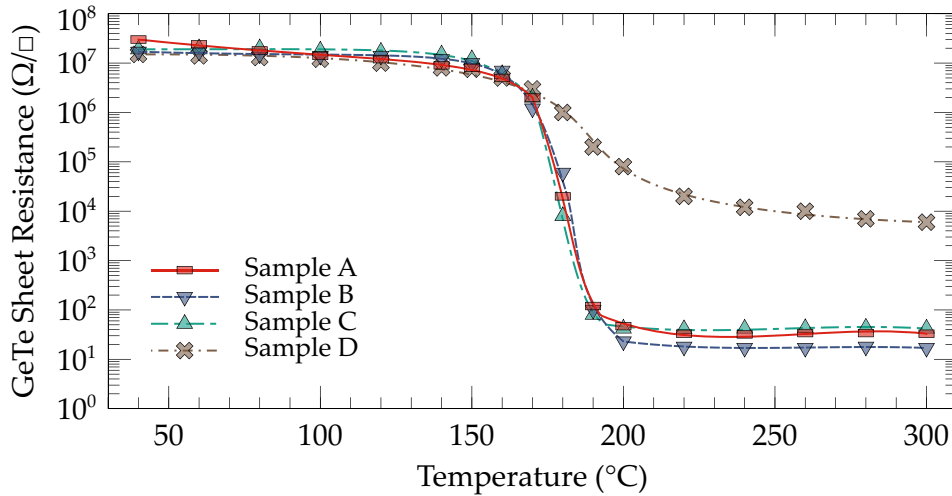


Figure 3.9: Sheet resistance change in GeTe thin-films from amorphous to crystalline state. Films are deposited using variation in process parameters. State change occurs at 180 $^{\circ}\text{C}$ to 200 $^{\circ}\text{C}$. Sample D shows only two order of resistance change while other samples exhibit more than five orders of resistance change.

3.2.2.5 PCM Resistance Change

Resistivity of GeTe is indispensable to get an optimal RF performance. Initial samples 'A', 'B', and 'C' show over five orders of resistance change after annealing. The resistivity

of Sample 'D' did not go below $k\Omega$ range, thus making it not suitable for RF applications. GeTe shows amorphous to crystalline phase change from 170°C to 190°C . Sheet resistance of the GeTe samples is measured at discrete values of annealing temperature. The change in resistance with respect to annealing temperature is shown in Fig. 3.9. The minimum attainable sheet resistance value depends on the deposition conditions as described earlier.

3.3 Micro-Heaters for Actuation

Micro-heaters provide thermal pulses to phase change material to change the state from crystalline to amorphous and vice-versa. The material properties of such embedded micro-heaters directly impact the operation of PCM switches. Micro-heaters of thin-film resistor (TFR) can be made using numerous materials, but in case of embedding micro-heater for the application of PCM switches, the heaters should be able to heat the PCM higher than its melting temperature 725°C . Tungsten is a perfect candidate for employing it as TFR for heating applications. Tungsten has the melting point of 3400°C , thus can provide reliable thermal actuation pulses to PCM. Maximum power required to change the state of PCM from crystalline to amorphous depends on the material property. Specific resistance of the heater can be achieved by changing the thickness or width of the heater. However, changing the width of the micro-heater reduces isolation by inducing parasitic capacitance to the RF signal path. Thick micro-heaters require subsequent sputtered or evaporated thin-films to be thicker than the micro-heater thickness to get proper step coverage. Resistivity of tungsten can be optimized by deposition process control.

3.3.1 Residual Stresses in Tungsten

Sputtered tungsten thin-films deposited at room temperature introduce telephone cord or spring coil delamination as shown in Fig. 3.10. Thin-films in compression tend to show such stresses. Such delamination is a multiscale phenomenon, as it can be induced by compressive stresses and with the presence of moisture at substrate/film interface which significantly lowers the adhesion of thin films. Stresses are more prominent in tungsten films deposited at room temperature. Moreover, the tungsten thin-films show high resistivity than the films deposited at elevated temperatures. Tungsten thin-films are also optimized to get lowest possible resistivity which can be achieved by depositing films at higher than 800°C .

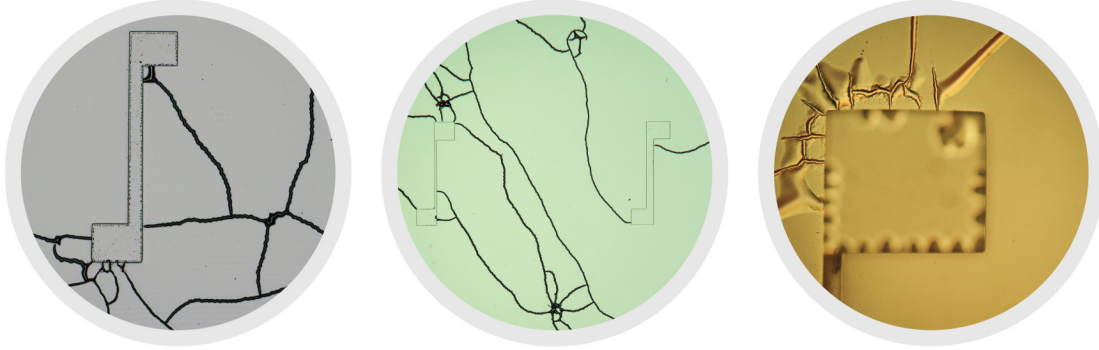


Figure 3.10: Spring coil stresses formation in tungsten thin films deposited at room temperature

Table 3.2: Evaluation of embedded micro-heater's resistance for heater length, $l_h = 20 \mu\text{m}$ and voltage applied = 5 V

Heater Width w_h (μm)	Current Measured (mA)	Resistance Extracted (Ω)	Sheet Resistance (Ω/\square)
0.9	83.34	60	2.7
1.0	104.16	48	2.4
1.1	119.56	41.8	2.3
1.2	120.01	41.6	2.5
1.3	135.41	36.9	2.4
1.5	144.23	34.6	2.6
2.0	161.29	31	3.1
3.0	234.37	21.3	3.2

3.3.2 Electrical Characterization

The resistance of micro-heaters is extracted using dc electrical measurements. Various micro-heaters are developed with width of the heater varying from $0.9 \mu\text{m}$ to $3 \mu\text{m}$. DC 5 V is applied across the micro-heater. The length of the heater is kept constant in our measurements. The measured current, resistance and calculated sheet resistance is given in Table. 3.2 highlighting the resistance change with the change in heater width. Tungsten micro-heaters used for electrical extraction are deposited at 850°C using dc sputtering. Lower resistivity of tungsten is preferred to reduce the actuation voltage requirement.

3.4 RF PCM Development Constraints

In the early stage of the proposed micro-fabrication process, various challenges related to PCM came into picture which paved the way to further investigate and to mitigate issues such as voids and cracks formation in PCM memories, which have been also reported in [88]. Such constraints limit the development of PCM technology which are discussed in the following sections.

3.4.1 Voids / Cracks Formation in GeTe

PCM switches that are not passivated show voids and cracks in GeTe material after annealing as shown in Fig. 3.11. An optical micrograph of the RF PCM switch junction is shown in the inset of Fig. 3.11, displaying the material degradation in PCM junction. Voids and cracks at micron scale appear right after annealing the GeTe. The material also

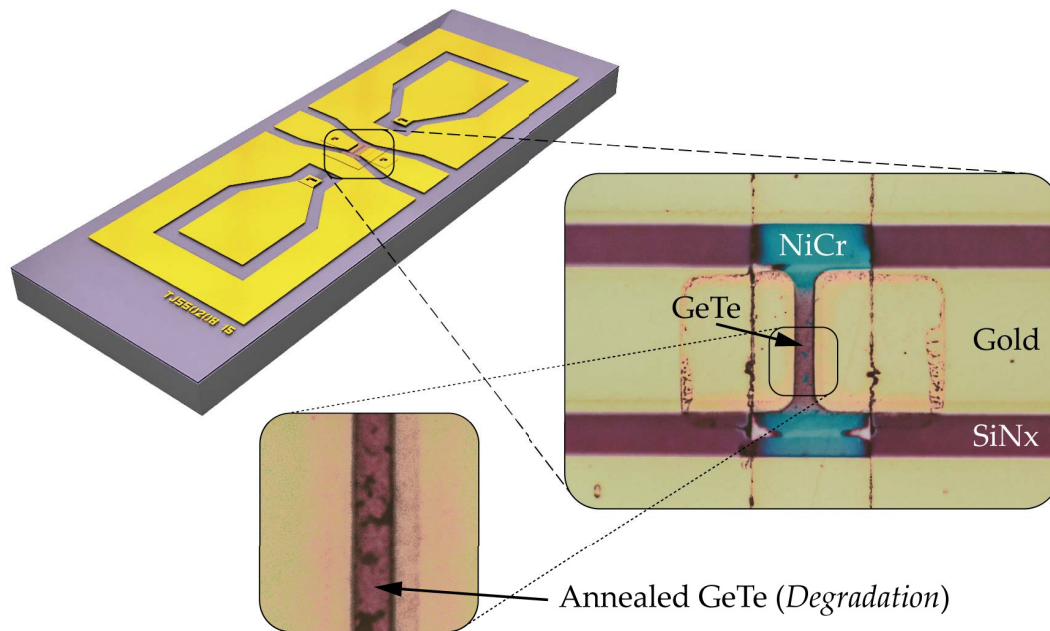


Figure 3.11: PCM switch showing voids and cracks formation in GeTe region. Inset shows the optical micrograph of switch junction after annealing. A close-up view of the GeTe region is shown highlighting the issues with crystalline GeTe films.

exhibits poor insertion loss due to the reduction in thickness. Passivation is required to avoid such problem in RF PCM-based devices.

3.4.2 Melting

Another common problem with PCM based devices is melting of GeTe after actuation. Switches fabricated using the fabrication process described in Fig. 4.2 did not have passivation layer. An optical micrograph of the switch in amorphous state is shown in Fig. 3.12 (a) and the damaged PCM switch with the application of few actuation pulses is shown in Fig. 3.12 (b). All PCM switches must be melted and quenched to achieve the highly disordered/quenched amorphous OFF-state. GeTe melts if high actuation power is supplied to the PCM during the heating pulse that elongates the quenching process. Examining the optical micrograph shown in Fig. 3.12, it is unclear if the micro-heater was damaged along with GeTe or is it the melting of the PCM. The choice of substrate and the barrier layer impacts the heat distribution to the PCM material for maintaining thermal balance.

However, it is clear from the cross-section of the switch as shown in Fig. 3.13, the heater is intact while GeTe is completely melted in the PCM channel region. FIB-SEM is used to create a small cavity along the cut-direction A–A' as shown in Fig. 3.13. FIB-SEM

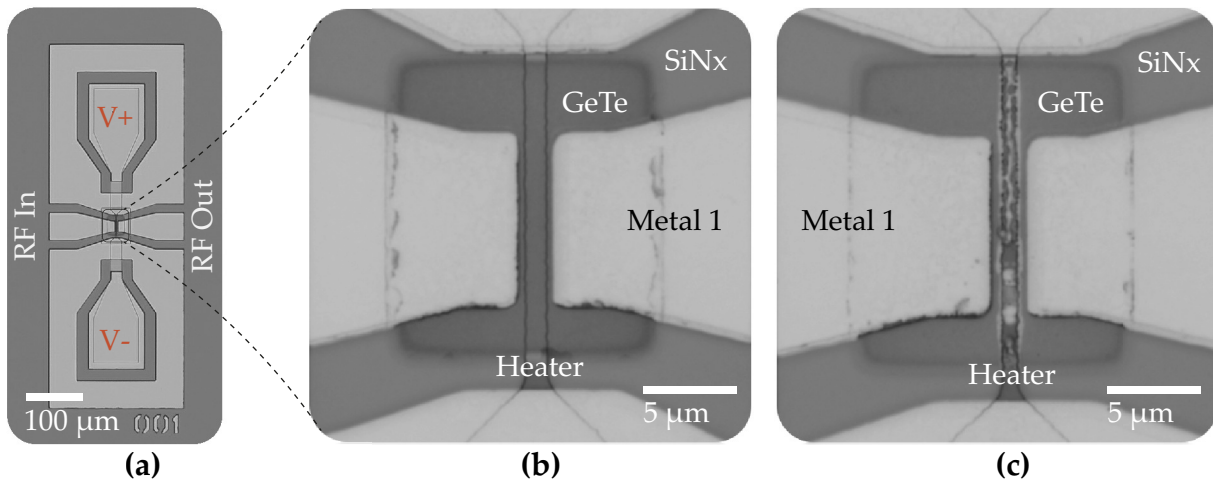


Figure 3.12: GeTe melting after few actuation cycles: (a) PCM switch when voltage is not applied yet, (b) Melting of GeTe after few voltage pulses applied. This switch was fabricated using four-layer process without any passivation layer on top.

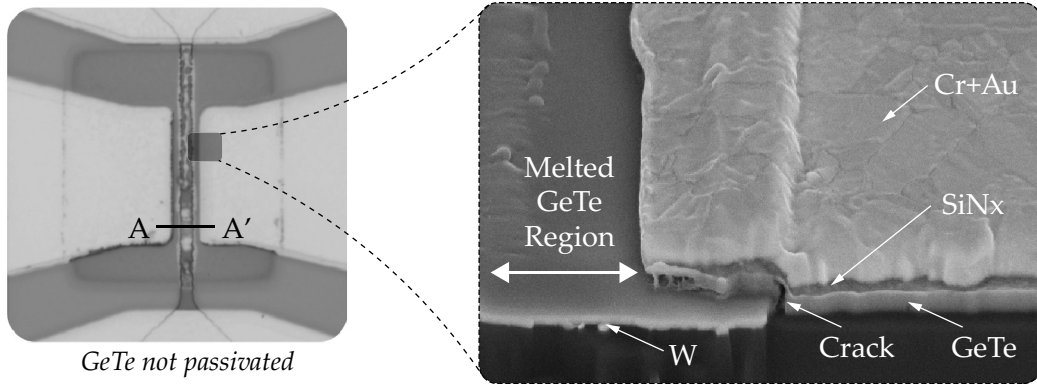


Figure 3.13: Optical micrograph of PCM switch junction highlighting GeTe melting region, and FIB-SEM showing the cross-section of the melted region. Cut-direction A–A’. Crack in GeTe layer is highlighted in FIB-SEM micrograph.

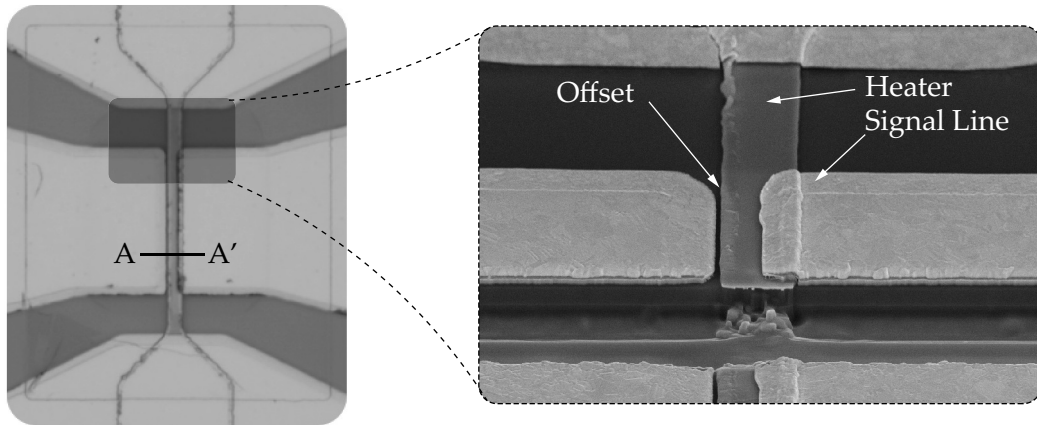


Figure 3.14: Optical lithography constraints in the development of PCM switches; optical micrograph of PCM SPST switch junction and FIB-SEM showing the cross-section of the switch where the offset in just nanometer scale can lead to non-working switches.

is shown for the switch with heater width (w_h) dimension larger than the PCM length (l_s). A crack can be seen in the SEM micrograph under the RF signal line. This highlights the requirement of having a heater with w_h larger than l_s . If w_h is less than l_s , after actuation, the cracks along the heater edge can potentially make the switches completely unusable. On the other hand, the use of a heater with wider width adds additional parasitic capacitance to the RF signal line, which is further discussed in section 4.2.

3.4.3 Optical Lithography

Optical UV lithography using SUSS MJB4 mask aligner for patterning has been employed to fabricate the RF PCM switches using the four-layer micro-fabrication process shown in Fig. 4.2. Optical UV lithography has a limit of $1\ \mu\text{m}$ to $1.5\ \mu\text{m}$ minimum feature size and requires manual alignment of the subsequent layers. Optical UV lithography hinders the yield as although the minimum width of the PCM length is $1\ \mu\text{m}$ and the heater width (w_h) is ranging from $1\ \mu\text{m}$ to $3\ \mu\text{m}$. Due to the thick glass mask used in optical UV lithography, it is extremely hard to align the heater layer with RF electrodes, as in between these two layers, there are two more layers including PCM and barrier layer. Although, we have included manual offset of heaters in our designs to mitigate such issues, it still affects the yield.

Fig. 3.14 shows the optical micrograph of RF-PCM switch, which did not actuate after applying voltage pulses. Inspection under optical microscope does not reveal any sign of micro-fabrication issues. However, a cross-section of the switch as shown in Fig. 3.14 along the cut-line A–A' using FIB-SEM exposes the offset on a sub-micron scale, which is due to the alignment error at lithography step. Electron-Beam lithography can solve such alignment problems, but requires higher operational cost and time to write on wafer. In our optimized switches, PCM switching junction is divided in two different masks, where larger patterns are exposed using mask-less UV lithography and features smaller or equal to $1\ \mu\text{m}$ are patterned using electron-beam lithography to get perfect alignment. Electron-beam lithography requires conductive substrate, which cannot be used for RF devices. Thus, a layer of conductive polymer is spin-coated before lithography.

Chapter 4

Development of mmWave PCM GeTe-Based RF Switches

This chapter reports the design, operation, fabrication and testing of PCM GeTe-based RF switches for mmWave applications. Utilizing the insights from material characterization, various design parameters of the switches and their impact on the RF performance are investigated. The RF performance of the PCM switches is optimized using diverse design parameters. Three generations of in-house developed micro-fabrication processes are reported for monolithically integrating RF circuits with PCM switches. Methods to reduce parasitic elements in PCM switches are discussed. The phase transformation in GeTe switches is achieved by localized embedded micro-heaters for thermally switching the materials' state in a melt-quench process. The embedded micro-heater circuit, on the other hand introduces capacitance that affects the RF performance.

Initial prototypes of RF PCM switches in series and shunt configurations are presented in [87] and a brief description of the fabrication process with an outline of the issues associated with the development of GeTe thin film RF switches is discussed in [85]. Various parasitic elements in PCM switches are discussed and methods to minimize the parasitics are detailed. Effects of various switch design parameters on the RF performance are studied through parametric EM simulations, and are discussed in depth. RF switches are fully characterized and tested for its high power handling capability, third-order intercept (TOI) through two-tone testing setup. Maximum current carrying capacity and PCM's non-volatility or resistance stability are experimentally investigated. Improved RF PCM switches are cycled for more than 1 million times demonstrating com-

Parts of this chapter are published in [85–87]

petitive reliability with the various other switch technologies. PCM switches developed are compared with the current state-of-the-art demonstrating a clear improvement in various aspects of the performance of the switch. PCM RF switches demonstrates measured RF performance over DC to 67 GHz for mmWave application. The RF PCM SPST switches reported in this chapter hold tremendous potential to highly miniaturize and monolithically/heterogeneously integrate a vast variety of mmWave RF components.

4.1 Design, Operation and Fabrication

4.1.1 Principle of Operation

Fig. 4.1 shows the 3D view of RF-PCM inline SPST switch in series configuration with four terminals, two CPW ports allow RF signal transmission and two bias pads supply DC actuation pulses for micro-heaters. The change in material's resistance from amorphous to crystalline state, through the application of short thermal pulses, allows or blocks the RF signal from one port to another. The inset of Fig. 4.1 shows the switching region with GeTe thin film present on embedded micro-heater with SiN_x as a barrier layer between heater and PCM. The GeTe thin films are characterized to achieve optimum performance of RF-PCM switches as discussed in earlier sections.

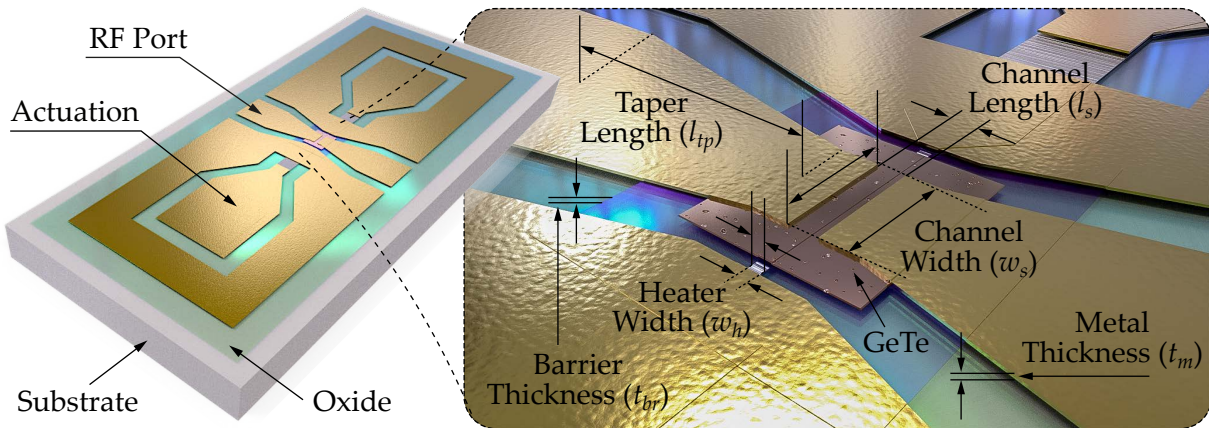


Figure 4.1: 3D view of PCM-based RF SPST series switch with two metal layers for RF signal flow. Inset shows the close-up view of PCM switching unit highlighting PCM GeTe and embedded micro-heater. Passivation layer between two metal layers is not shown. Close-up view of PCM junction geometry highlights various design parameters for parametric study in FEM simulation.

4.1.2 Microfabrication Process (Gen 1)

Initial RF-PCM switches were developed utilizing four-layer micro-fabrication process (Gen 1) as shown in Fig. 4.2. The switches were fabricated on a 2.5 in \times 2.5 in Al_2O_3 substrate with $\epsilon_r = 9.8$. Wafers are cleaned using standard RCA1 process followed by a) deposition of silicon dioxide (SiO_2) layer using plasma enhanced chemical vapor deposition (PECVD) and DC magnetron sputtering of micro-heaters (M0) utilizing two different materials: tungsten and Ni/Chrome, followed by b) patterning micro-heaters (M0) using reactive ion etching (RIE), c) deposition of silicon nitride (SiN_x) thin barrier layer (V0) using PECVD to get conformal coverage, d) dry etching of SiN_x vias (V0) using RIE. e) deposition of GeTe (PC) thin layer using DC magnetron sputtering and, f) patterning of GeTe through lift-off technique. GeTe is annealed for 30 min at 220 $^\circ\text{C}$ in an argon rich rapid thermal annealing system. g) electron beam evaporation of gold (Au) with chrome (Cr) as a seed layer for RF signal flow (M1) succeeded by h) patterning Au/Cr (M1) using lift-off technique. i) PECVD of silicon oxide (SiO_2) as passivation layer (PV) and patterning using RIE. Devices are tested with and without passivation to see the effect of passivation on GeTe melting.

Optical micrograph of the fabricated RF PCM-based single-pole single-throw (SPST) switches in series and shunt configuration are shown in Fig. 4.3. A series SPST switch is presented in Fig. 4.3 (a), a shunt SPST switch is shown in Fig. 4.3 (b). The cut-away de-

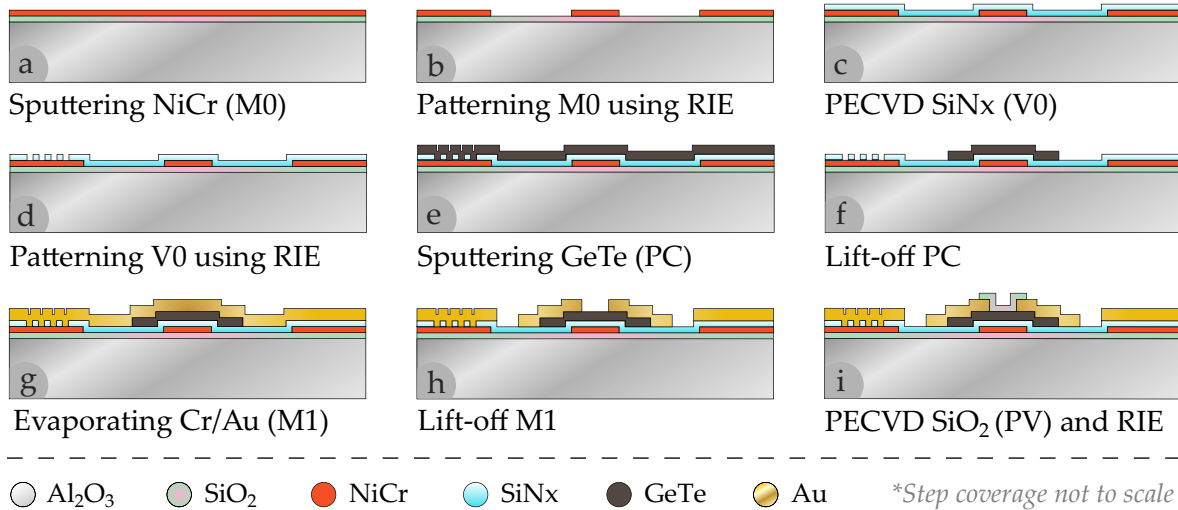


Figure 4.2: Cross-section of RF-PCM fabrication process flow using four-layers having one metal layer for RF signal routing.

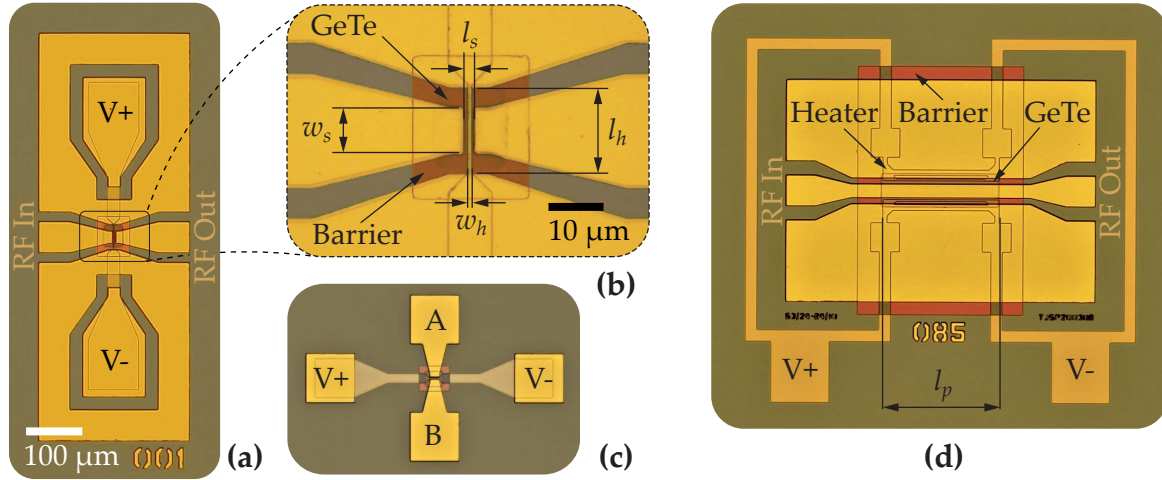


Figure 4.3: Optical micrograph of RF-PCM SPST switches (Gen 1): (a) Series configuration, (b) Shunt configuration, (c) Close-up view of switching region in series switch, and (d) 4-Port RF-PCM junction.

tailed view of the PCM switching region is depicted in Fig. 4.3 (c) and a 4-port RF-PCM junction demonstrated in Fig. 4.3 (d) is used to characterize the electrical properties and reliability testing of GeTe thin films. The RF switch in series configuration is designed with micro-heaters of width, $w_h = 3 \mu\text{m}$, length, $l_h = 35 \mu\text{m}$, PCM length, $l_s = 3 \mu\text{m}$ and RF signal line width, $w_s = 20 \mu\text{m}$. Fig. 4.3 (c) shows the close-up of series switch with $l_s = 5 \mu\text{m}$. The shunt switch has two independent heaters under the RF ground that overlaps with CPW gaps (g). The GeTe thin film width is fixed, which is greater than $(w_s + 2 \times g)$, but the length, l_p is varied to optimize the RF performance. Functional switches require heaters underneath a large patch of PCM, introducing parasitic capacitance, which must be taken into consideration in the RF design as described in section 4.2.

4.1.3 Parametric Study on Design Optimization

An optimal RF performance can only be achieved through accurate design and careful characterization of the micro-fabrication process. Parametric studies are carried out on PCM SPST switch model as shown in and inset of Fig. 4.1 to optimize the RF performance using EM simulations in ANSYS Electronics Desktop (Previously HFSS). The switch is designed with conformal coverage of the materials to represent actual fabricated device. Following design parameters are chosen for the optimization:

- PCM Channel Width, (w_s)
- PCM Channel Length, (l_s)
- Heater Width, (w_h)
- Taper Length, (l_{tp})
- Barrier Thickness, (t_{br})
- Metal Thickness, (t_m)

The PCM channel width (w_s) is varied from 5 μm to 15 μm with a step of 5 μm , and PCM channel length (l_s) is varied from 0.4 μm to 2 μm with a step of 0.2 μm . Heater width (w_h) is varied from 1 μm to 3 μm with a step of 0.5 μm . Taper length (l_{tp}) is varied from 30 μm to 100 μm with a step of 10 μm while barrier thickness (t_{br}) and metal thickness (t_m) is varied from 40 nm to 200 nm with a step of 20 nm and 0.4 μm to 0.8 μm with a step of 0.2 μm respectively. Thickness of PCM (t_{pcm}) is kept constant at 135 nm as it acts like a resistance in the signal line. However, the resistivity of the PCM thin-film depends on the film quality. In EM simulations, the resistivity of the materials is matched with the measured experimental values of thin-films. Resistivity of the deposited thin-films is measured using automated cross-wafer four-point probe (4PP).

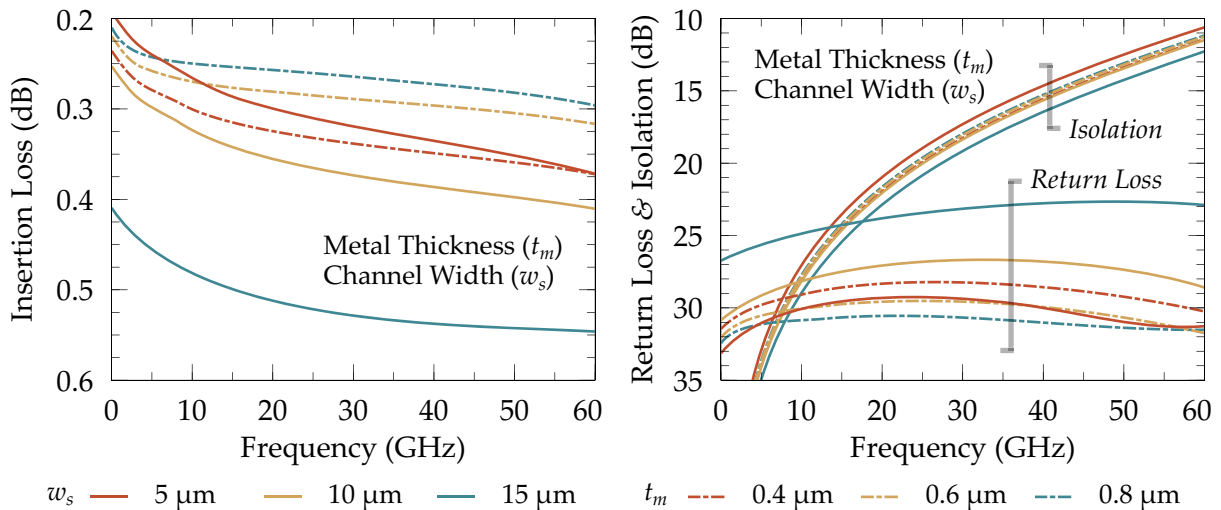


Figure 4.4: Parametric RF performance EM simulation of PCM SPST switch with variation of metal thickness and channel width

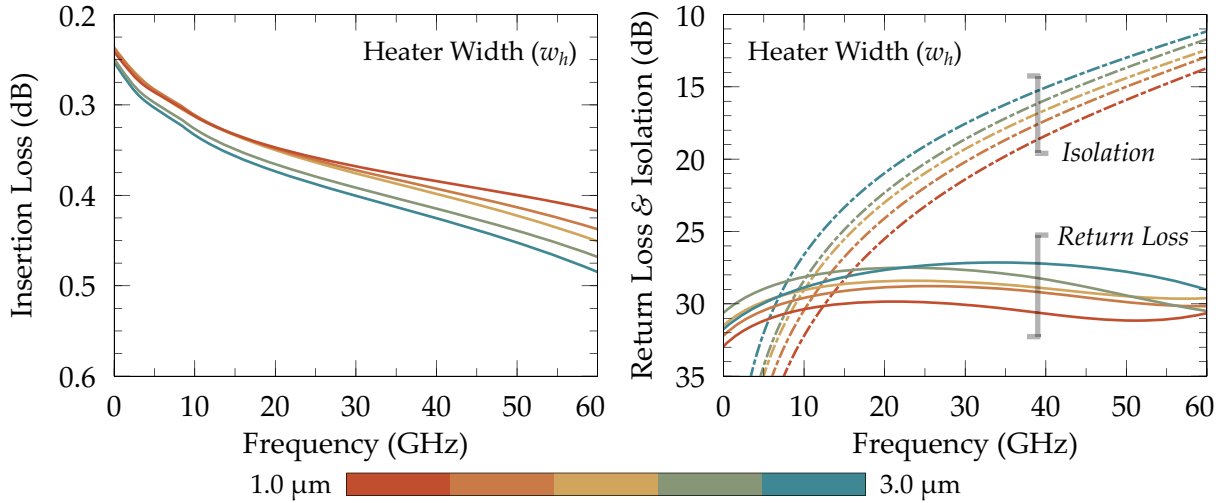


Figure 4.5: Parametric RF performance EM simulation of PCM SPST switch with variation of heater width.

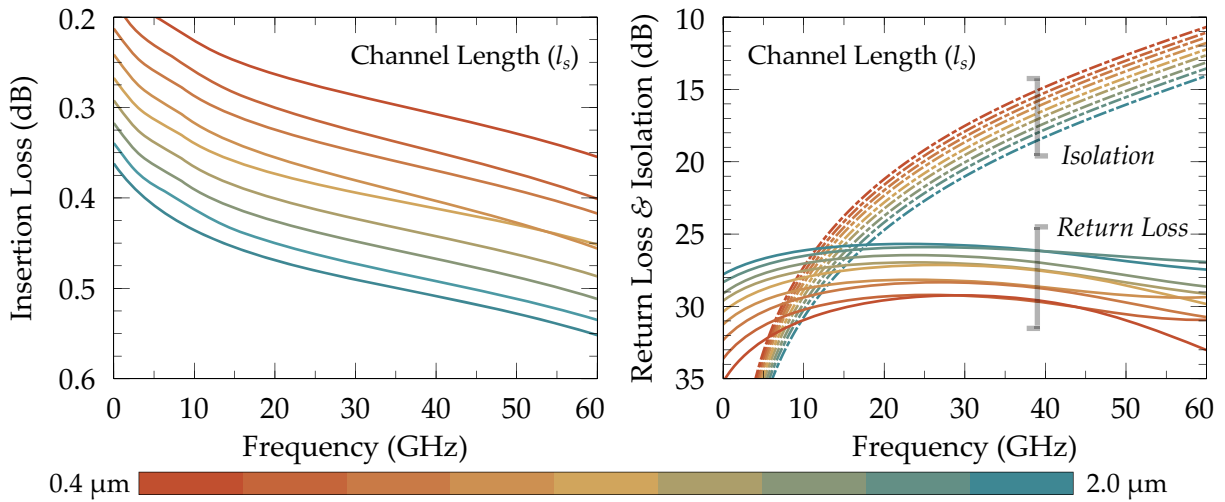


Figure 4.6: Parametric RF performance EM simulation of PCM SPST switch with variation of channel length.

For optimal RF performance, PCM switches are simulated using the designed parameters mentioned above. The RF-PCM series switches are simulated over DC–60 GHz. Fig. 4.4 shows the simulated RF performance of SPST switch with varying metal thickness (t_m) and channel width (w_s). Change in the RF performance with change in heater

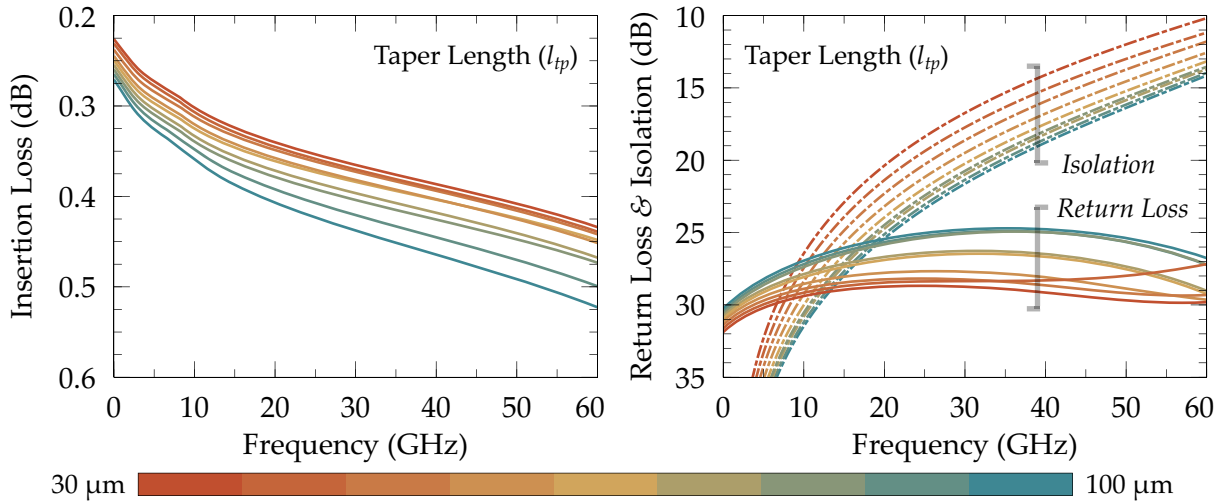


Figure 4.7: Parametric RF performance EM simulation of PCM SPST switch with variation of taper length.

width (w_h), channel length (l_s), taper length (l_{tp}), and barrier thickness (t_{br}) is shown in Fig. 4.5, 4.6, 4.7, and 4.8 respectively. Certain design parameter values are carefully chosen except the ones which are parameterized. The default values are $w_s = 10 \mu\text{m}$, $l_s = 1 \mu\text{m}$, $w_h = 2 \mu\text{m}$, $l_{tp} = 50 \mu\text{m}$, $t_{br} = 50 \text{nm}$, $t_m = 0.35 \mu\text{m}$, and $t_{pcm} = 135 \text{nm}$.

Design parameters including w_s , t_m , and l_s reflect high impact on the ON-state RF performance of the switch, while l_{tp} , t_{br} , and w_h moderately affect the ON-state performance. On the other hand, w_s , w_h , and l_{tp} affect the OFF-state performance. While t_m , l_s , and t_{br} show minor effect on the OFF-state performance.

The use of thicker metal for RF signal flow improves the insertion loss without sacrificing isolation, but getting a narrow PCM channel with the thicker metal is a challenge. A metal thickness, $t_m = 0.4 \mu\text{m}$, exhibits an insertion loss less than 0.35 dB and isolation better than 17 dB at 30 GHz. Varying the channel width from $5 \mu\text{m}$ to $15 \mu\text{m}$ increases the insertion loss by 0.23 dB while improving the isolation by only 2 dB. The heater width (l_h) moderately affects the insertion loss, a narrow heater can provide over 5 dB improvement of isolation while sacrificing only 0.05 dB of insertion loss. The channel length (l_s) should be kept narrower than heater width (w_h), thus it needs to be scaled with the selected heater width. Varying l_s from $0.4 \mu\text{m}$ to $2 \mu\text{m}$ downgrades the performance by adding 0.25 dB of insertion loss with an improvement of 4 dB in isolation. The taper length (l_{tp}) needs to be selected carefully, as there is a trade-off between insertion loss and isolation. Varying l_{tp} from $30 \mu\text{m}$ to $100 \mu\text{m}$ provides improvement of more than

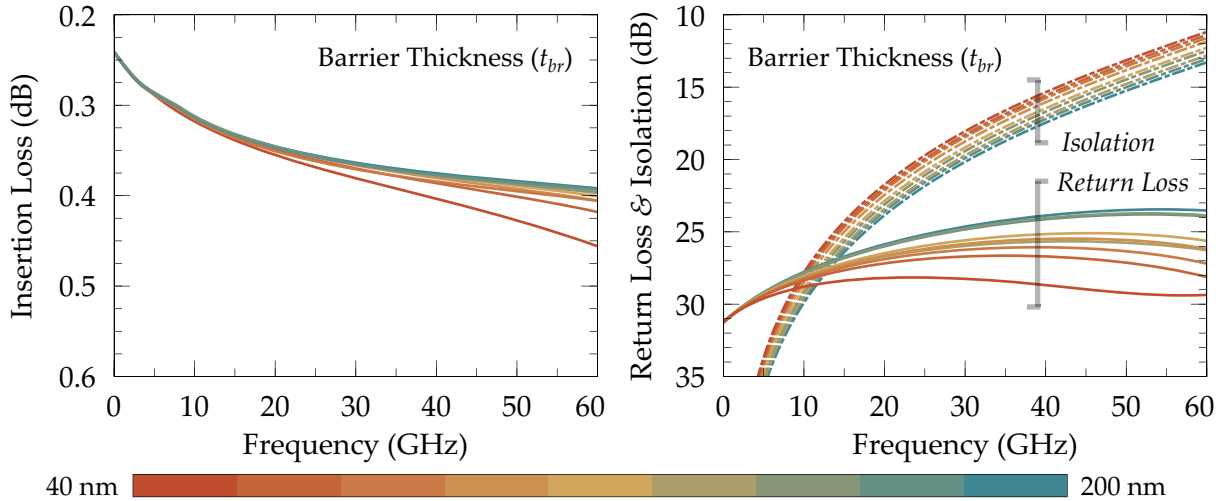


Figure 4.8: Parametric RF performance EM simulation of PCM SPST switch with variation of barrier thickness.

6 dB in isolation while adding 0.1 dB of insertion loss. The return loss is better than 23 dB in all cases from DC to 60 GHz.

The barrier thickness (t_{br}) does not affect the ON-state RF performance adversely; however, a thick barrier layer (>200 nm) helps in getting higher isolation in OFF-state. Thick barrier layer affects the principle of operation of the device by limiting the thermal conduction from the micro-heater to the PCM. On the other hand, thick barrier layer requires higher power to change the state of the material. A thin barrier layer (<50 nm) improves the thermal conduction by isolating the micro-heater and PCM, but it adds significant parasitic capacitance to the RF signal flow that needs to be addressed by careful choice of design parameters.

4.1.4 Microfabrication Process (Gen 2)

Based on the results from characterization, an optimized fabrication process has been developed to improve the RF performance of PCM switches. Gen 2 micro-fabrication process that is developed for the 2nd generation of PCM devices includes two metal layers that can help in integrating RF circuits. The fabrication process flow is shown in Fig. 4.9. The process starts with a RCA1 cleaning of single crystal sapphire wafer (C-plane orientation) having dielectric loss tangent of 1×10^{-4} and 400 μm thickness. The

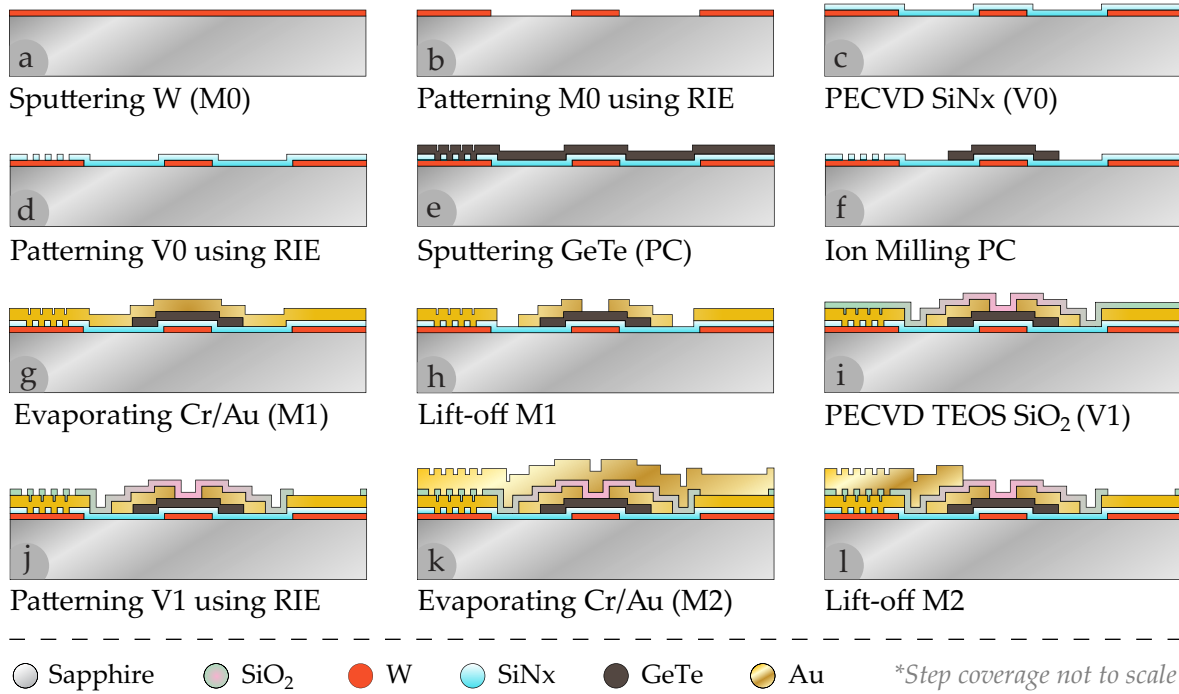


Figure 4.9: Cross-section of Gen 2 RF-PCM fabrication process flow using six-layers having two metal layer for RF signal routing.

process includes six layers with three metal layers (M0, M1 and M2), one PCM layer and two dielectric layers (V0 and V1). Two metal layers are used for RF signal routing and one layer is used for the micro-heaters. a) 70 nm tungsten (W) is sputtered as M0 at elevated temperature of 850 °C to get low resistivity and stress-free thin film for micro-heaters that is b) patterned using RIE. c) 40 nm SiNx layer deposited using PECVD and, d) patterned using RIE to act as a barrier layer (V0) between micro-heaters and PCM in order to get conformal coverage. e) 135 nm GeTe thin film is sputtered using Ge [50]:Te [50] target (PCM) and, f) patterned using ion milling. g) evaporation of 300 nm of Au that serves as M1 with 30 nm of Cr as a seed layer. h) M1 is patterned using lift-off technique. i) 300 nm SiO₂ layer is deposited using low temperature PECVD and, j) patterned using RIE that serves as a passivation layer for PCM (V1). k) evaporation of 350 nm Au layer (M2) with 30 nm Cr layer as a seed layer. l) M2 is patterned using lift-off technique with a bi-layer resist.

Optical micrograph of the RF PCM GeTe-based SPST switch fabricated using Gen 2 micro-fabrication process is shown in Fig. 4.10(a). Based on the fabrication issues dis-

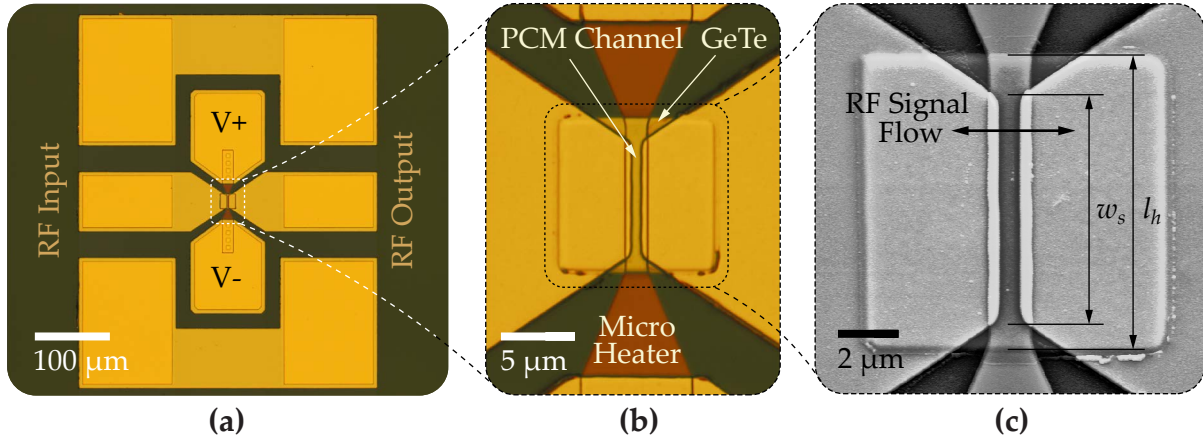


Figure 4.10: Fabricated RF PCM SPST switch (Gen 2): (a) Optical micrograph, (b) inset shows close up view of the switch junction, and (c) SEM micrograph of the PCM region.

cussed in chapter 3, optical lithography is not feasible for narrow PCM channel. To get the RF electrodes perfectly aligned on top of micro-heater, 100 kV electron-beam lithography is used to create PCM channels which is complemented with UV lithography through maskless writer to expose larger features. A zoomed-in view of the fabricated PCM switch junction is shown in Fig. 4.10(b). A SEM micrograph of the switch junction is depicted in Fig. 4.10(c) highlighting RF signal flow direction, length of the micro-heater (l_h) and width of PCM channel (w_s). Crumbles on the edges of the PCM GeTe are of photoresist which got excess ion energy from ion-milling and was harder to remove. The PCM switch is fully passivated and only RF pads and bias pads are etched for measurements.

4.1.5 Improvements in Bias Networks

RF SPST switches do not require any bias network, as micro-heater is directly connected to gold metal layer. To develop multi-port complex RF components, two metal layers are required for RF signal flow. Devices like switch matrices where long bias lines routing is required, a resistive metal layer like tungsten pose challenges in controlling RC time constant and delivering desired actuation pulse to the micro-heaters. Gen 3 process incorporates a high conductivity Ag bias split lines to minimize RC time constant and any resistive losses from the bias lines. Most of the devices from here onwards are developed using Gen 3 micro-fabrication process that is optimized for the development of monolithically integrated multi-port RF PCM components.

Gen 2 microfabrication process is also incorporates the use of high resistivity silicon (HRSi) substrates opposed to sapphire. Single-crystal sapphire wafer limits the dicing of individual dies from the wafer due to the hardness of the material. Silicon offers faster processing of dicing individual dies and also the blade channel width required is smaller compared to that required for sapphire.

Initial samples were developed using tungsten bias lines, but due to the lossy nature of the material, thin and long bias lines add significant resistance from the bias pads to the micro-heaters for PCM switches, which in turn will increase time constant of the bias network. For example, if the sheet resistance of the tungsten thin film is $2 \Omega/\square$, a micro-heater of width (w_h) = $1.5 \mu\text{m}$ and length (l_h) = $20 \mu\text{m}$ will act as a 27Ω resistor. If the longest bias line in the circuit is $100 \mu\text{m}$ in length and $5 \mu\text{m}$ in width (not including bends), it acts as a 40Ω resistor, which is significant compared to the resistance of the micro-heater. Thus, it is viable to use an additional metal layer with high conductivity to mitigate this issue.

Silver (Ag) has higher conductivity than other metals commonly used in micro-fabrication, but it must be passivated, since it gets oxidized in a short time. In Gen 3 micro-fabrication process, Silver is used as a supplementary layer to complement tungsten micro-heaters. Thin oxidized layer developed on 'Ag' is removed before depositing subsequent dielectric layer. Moreover, instead of using a small patch to create a barrier layer between micro-heater and PCM, negative tone of the mask is used and vias are etched to create contact between bias lines and gold metal layer. None of the micro-fabrication process steps exceeded 150°C except the barrier layer, which is deposited at 330°C . To get clean edges, bi-layer resist is preferred for lift-off, but certain photo resist solvents attack GeTe layer. Thus a bi-layer resist is only used for second RF metal layer patterning as GeTe is passivated at this step. The resist removal after every patterning step is done using a combination of acetone and plasma ashing. First gold metal layer layer is evaporated due to the use of a negative tone single resist, while second gold layer is sputtered to get a high deposition rate as bi-layer resist can be used at this processing step.

4.1.6 Microfabrication Process (Gen 3)

The fabrication process flow is shown in Fig. 4.11. The microfabrication process starts with a RCA-1 and Piranha cleaning of high resistivity Si wafer ($>20 \text{ k}\Omega \cdot \text{cm}$) and $500 \mu\text{m}$ thickness. The process includes eight layers with four metal layers (M0, M1, M2, and M3), one PCM layer and three dielectric layers (D0, V0, and V1). D0 is the substrate

oxide for thermal isolation. M2 and M3 are used for RF signal routing and M0 layer is used for the micro-heaters while M1 is used for biasing networks that can be used for some RF components. a) 50 nm tungsten (W) is sputtered (M0) at elevated temperature of 850 °C deposited on a thin dielectric insulator oxide layer that is b) patterned using RIE. c) 70 nm silver (Ag) is sputtered (M1) and d) patterned using RIE, followed by e) deposition of 100 nm AlN layer using RF sputtering and, f) patterned using RIE to act as a barrier layer (V0) between micro-heaters and PCM. g) 130 nm GeTe thin film is sputtered using Ge [50]:Te [50] target (PC) and, h) patterned using ion milling. i) evaporation of 350 nm of Au that serves as M2 with 30 nm of Ti as a seed layer. j) M2 is patterned using lift-off technique. k) 200 nm SiO₂ layer is deposited using low temperature PECVD and, l) patterned using RIE that serves as a passivation layer for PCM (V1). m) sputtering

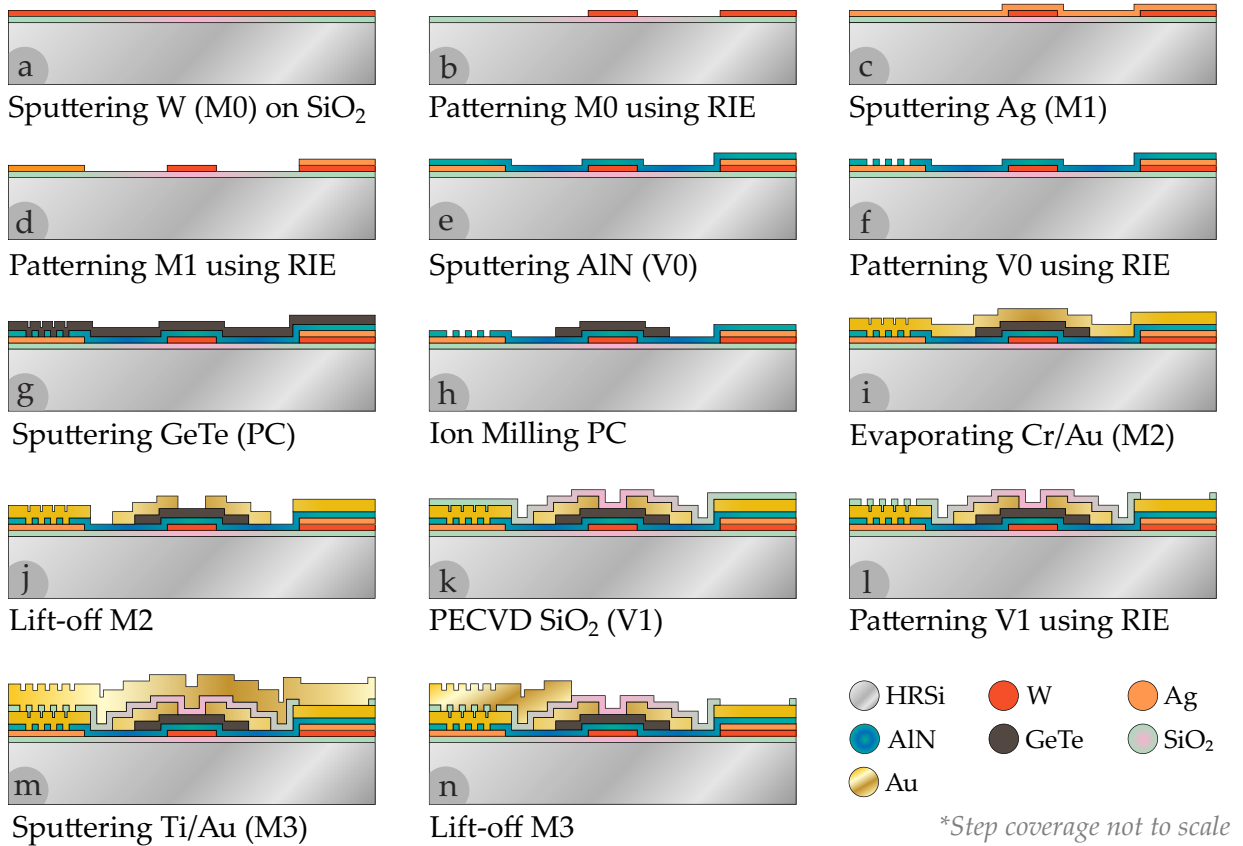


Figure 4.11: Cross-section of Gen 3 RF-PCM fabrication process flow using seven-layers having two metal layer for RF signal routing and two metal layers for bias routing.

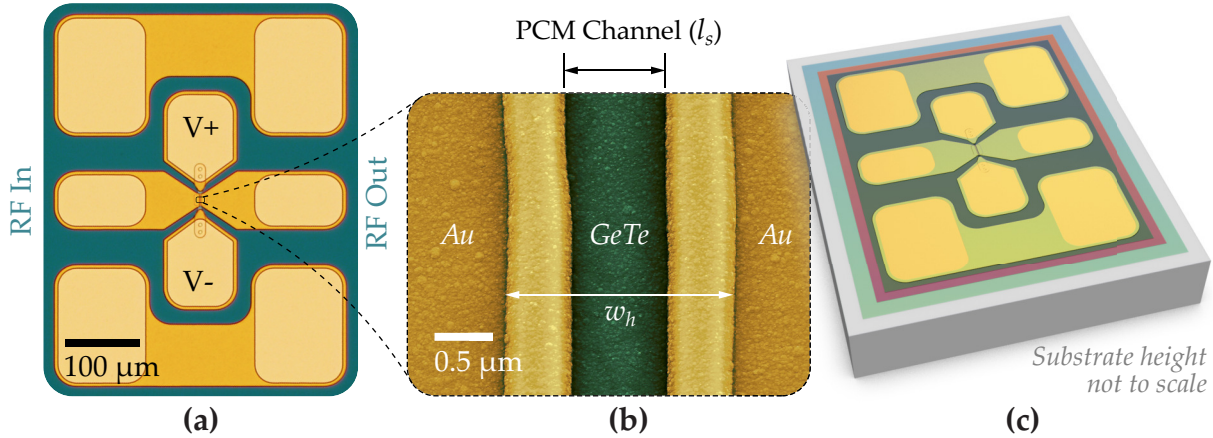


Figure 4.12: Fabricated RF PCM SPST switch (Gen 3): (a) Optical micrograph, (b) False coloured SEM micrograph of the PCM channel, and (c) 3D rendered view of the PCM SPST (Gen 3) switch.

of 450 nm Au layer (M3) with 40 nm Ti layer as a seed layer. n) M2 is patterned using lift-off technique.

Optical micrograph of RF PCM SPST switch fabricated using Gen 3 process is shown in Fig. 4.12(a) highlighting RF signal input and output ports and bias ports for actuation signal. The device is fully passivated and can be used for heterogeneous integration via flip-chip or by wire-bonding. A false coloured SEM image shows the closeup view of the narrow PCM channel (l_s) and width of the micro-heater (w_h) in Fig. 4.12(b). RF electrodes overlap the micro-heater to avoid switch failure due to cracks formation in GeTe near to the edges of micro-heater as shown in Fig. 3.13. Fig. 4.12(c) depicts a 3D rendered view of the switch. Optical micrograph shown in Fig 4.12(a) shows the natural colors of three different stacked dielectric layers. The overall switch area of the fabricated switch is $400 \mu\text{m} \times 500 \mu\text{m}$.

The RF PCM SPST switch fabricated using Gen 3 process demonstrate better isolation due to the use of AlN layer as a barrier layer between micro-heater and PCM GeTe. Wafer yield is improved by reducing resistance variation of the thin-films across the wafer which guarantees specified bias pulses for the certain switch dimensions across the wafer. The developed switches not only compete with the state-of-the-art but also outperform in certain aspects. Various parameters of the switch including switch cycle testing, RF performance measurements, two-tone linearity, high-power handling, current carrying capacity, self-actuation, and reliability (lifetime cycles) have been experi-

Gen 3 microfabrication processing steps are procedures are detailed in appendix A

mentally measured and reported in next sections.

4.1.6.1 Summary of Microfabrication Processes

Microfabrication processes are summarized in Table 4.1. Gen 1 process is sufficient to develop SPST RF switches. Gen 2 process is the improved version with the addition of an additional metal layer for signal routing and utilizing tungsten for micro-heaters. Thicker metal layer for RF signal flow are used in Gen 3 micro-fabrication process to reduce the overall RF loss. Dielectric layer materials and thickness are carefully chosen after characterizing the proper thermal balance near the PCM switch junction to achieve reliable switching operation. Gen 3 process is complex due to the split bias metal layer and split e-beam and UV lithography layer for PCM channels, but it is more suitable for complex RF components which are detailed in next chapters.

Table 4.1: Summary of microfabrication processes

Layer	Material	Gen 1	Gen 2	Gen 3
0	Substrate	Alumina 635 μm	Sapphire 400 μm	HRSi 500 μm
1	Insulator	SiO ₂ 100 nm	NA	SiO ₂ 60 nm
2	Micro-heaters	NiCr/W 100 nm	W 70 nm	W 70 nm
3	Bias Lines	NA	NA	Ag 70 nm
4	Barrier	SiNx 40 nm	SiNx 40 nm	AlN 100 nm
5	PCM	GeTe 150 nm	GeTe 135 nm	GeTe 130 nm
6	RF Metal 1	Au 350 nm	Au 330 nm	Au 380 nm
7	Passivation	SiO ₂ 40 nm	SiO ₂ 300 nm	SiO ₂ 200 nm
8	RF Metal 2	NA	Au 380 nm	Au 490 nm

4.2 Parasitic Capacitance in RF-PCM Switches

Due to the thin dielectric layer (used as a barrier layer between PCM and micro-heater) and the metal layers in micro-fabrication process, many parasitic capacitances arise that can degrade the RF signal performance. Various parasitic capacitances that are formed from different metal layers are shown in the cross-section of RF-PCM switch in Fig. 4.13. Parasitic capacitances can be minimized either by design changes or by optimizing the fabrication process, but cannot be removed completely.

The capacitance in OFF-state (C_{off}) impacts the overall performance of the switch. C_{off} consists of all the unwanted parasitic capacitances generated between different metal layers, and C_{off} of a switch should be as low as possible. PCM GeTe acts as a conductive layer in crystalline state, thus the micro-heater underneath the barrier layer acts as the capacitor (C_{pcm}) degrading the ON-state transmission. However, the impedance mismatch created by C_{pcm} can be compensated by changing the width of the signal line or length of the PCM junction (w_s). The most prominent capacitance is between RF metal electrodes and the micro-heater (C_{hm1}). Isolation of the switch can be improved by reducing the metal overlap on the micro-heater. This is limited by the lithography equipment and resist development time. OFF-state isolation can be improved as C_{pcm} and C_{hm1} scales with the change in barrier layer thickness. It is required to keep the barrier layer as thin as possible for appropriate heat transfer from the micro-heater to the PCM, but on the other hand thin dielectric effectively increases the parasitic capacitance. A thicker layer limits the sufficient heat flow to the PCM GeTe affecting melt-quench switching. In Gen 3 micro-fabrication process, a thermally conductive AlN layer is used as a barrier layer, which does not hinder heat migration.

If two metal layers are used for the RF signal routing, the capacitance between RF metal 1 and RF metal 2, (C_{mmpad}) also affects the RF performance. This can be tackled by increasing effective via array size. Vias generally add inductance, thus multiple vias openings are preferred to reduce via inductance and RF loss. In the PCM switch topology discussed in this thesis has an extremely narrow channel between two metal electrodes. The capacitance between two metal RF electrodes is denoted as C_{cont} affects the OFF-state isolation. A thin passivation layer is required to avoid degradation of GeTe, which increases C_{cont} between two metal electrodes. This capacitance scales with PCM channel length (l_s) and channel width (w_s). The interconnects introduce parasitic capacitance (C_{mm}) in case where two metal layers are used for RF routing and only be-

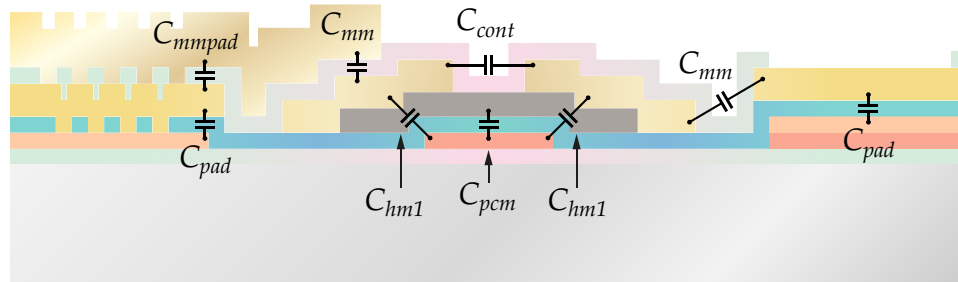


Figure 4.13: Various parasitic capacitances couple through thin-films degrading device performance

comes prominent is there is an excessive overlap of two metal layers. Contact pads also induce capacitance (C_{pad}) when interconnects are used. Certain parasitic capacitances can be reduced drastically by effective design and while some are dependant on the micro-fabrication process.

4.3 Lumped Model of the RF PCM Switch

A lumped model (circuit model) of the RF PCM SPST switch is developed which generates a close match to EM simulated and measured RF performance of an SPST switch is shown in Fig. 4.14. The model consists of four-ports, port 1 and port 2 are the RF input and output ports, while port 3 and 4 are control or bias ports. The port configuration matches with the fabricated SPST switches as shown in Fig. 4.12. A voltage pulse is applied between port 3 and 4. The switch consist of its fundamental components, resistance of the PCM GeTe in crystalline state (R_{on}), resistance in amorphous state (R_{off}), and OFF-state capacitance (C_{off}). PCM is a solid state technology and the switching action is dependent on the resistance of the two states of PCM. Circuit model of the RF PCM switch in ON-state and OFF-state remains identical with the only change in the resistance between R_{on} and R_{off} . Micro-heater's resistance is denoted as (R_h).

Various parasitic elements of the SPST switch are also shown in Fig. 4.14. Inductance of the PCM junction (L_{junc}), contact resistance between PCM GeTe and RF electrodes on the both sides of the junction is denoted as R_{cont} . CPW transmission line is shown as T_{lin} , while the capacitance between micro-heater and RF electrodes around the PCM junction is shown C_{hm1} . Pad capacitance (C_{pad}) and pad resistance (R_{pad}) are prominent in micro-heater between port 3 and 4 of the lumped model.

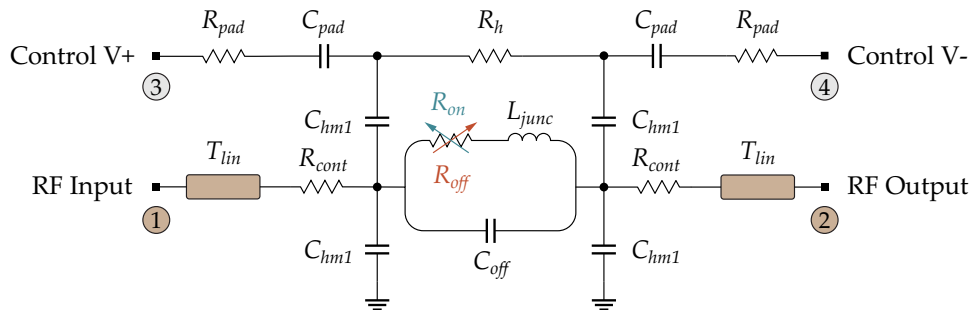


Figure 4.14: Lumped model of the RF PCM SPST switch showing switching element along with various parasitic circuit elements.

4.4 RF PCM Switch Measurements

4.4.1 Switch Actuation Testing

Switch actuation cycles are measured on-wafer as shown in Fig. 4.15. Multiple four-port PCM switch junctions are designed with variations in design parameters discussed in section 4.1.3. A four-port PCM switch junction is shown in Fig. 4.15. RF PCM switches and four-port PCM switch junctions share similar design parameters. Larger DC pads

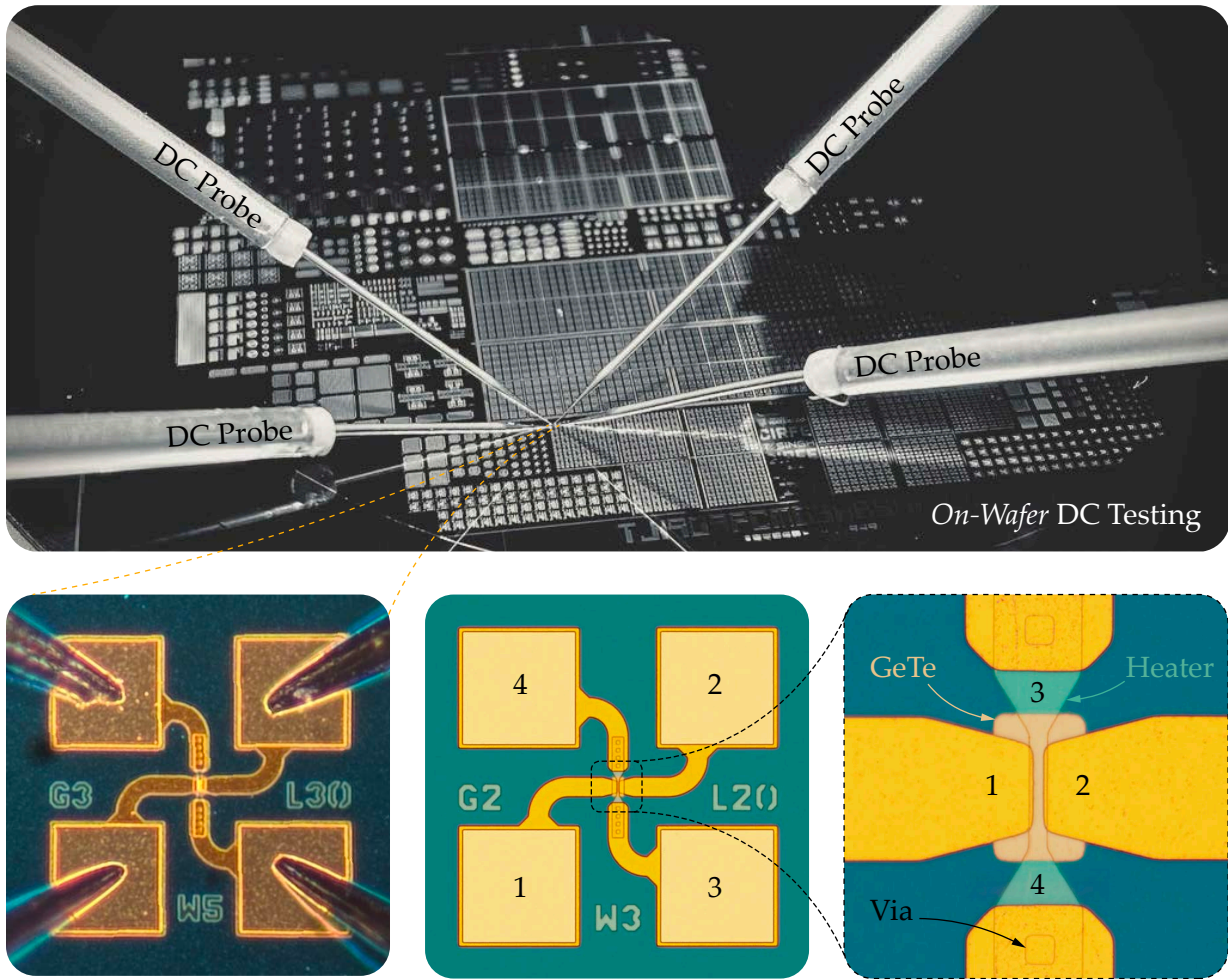


Figure 4.15: On-wafer DC testing of a four-port PCM switch junction. Optical micrographs highlighting DC probe pads and PCM junction.

in four-port junctions makes it easy to probe the devices. Port 1 and 2 have the PCM in series with the metal electrodes, while port 3 and 4 has an embedded micro-heater to provide melt-quench sequence to the PCM. An inset in Fig. 4.15 shows the close-up of the PCM junction.

PCM switches are cycled by providing two different pulses conditions (amorphous pulse and crystalline pulse) to the micro-heater terminal 3 and 4 and the resistance change is recorded from terminal 1 and 2. For accurately capturing the resistance change, two source measure units are used, one between terminal 1 and 2, while the other unit is used between micro-heater terminal 3 and 4. Micro-heater's resistance change due to pulsing thus it is important to translate the micro-heater resistance to the pulse generator for effectively delivering the bias signal to load impedance (micro-heater's resistance in this case).

4.4.1.1 Bias Signature

An optimal biasing signature for the Gen 3 PCM switches is shown in Fig. 4.16. A single pulse of 12 V amplitude and 200 ns is supplied to the micro-heater for latching the device from crystalline state (low resistance) to amorphous state (high resistance), while a pulse of 7.8 V amplitude and 1.2 μ s provides reversible resistive switching by latching the switch in crystalline state from amorphous state. PCM switches demonstrate more than four orders of resistance change which shows potential for RF switching applications as discussed in the following chapters.

Initial switching cycle characterization was carried out by manually supplying individual pulses from two independent pulse generators. However, the test setup is automated for reliability testing as discussed in section 4.4.8

4.4.2 RF Performance Measurements

Multiple variations of RF-PCM switches were fabricated based on the initial fabrication process described in Fig. 4.2. Optimized RF switches are developed using the enhanced fabrication process as shown in Fig. 4.11. The series switch includes variations of l_h ranging from 20 μ m to 40 μ m, w_h from 1.5 μ m to 4 μ m, w_s from 10 μ m to 30 μ m, and l_s from 1.5 μ m to 5 μ m as shown in Fig. 4.3 (b). The shunt switch configuration includes variation of l_p ranging from 100 μ m to 500 μ m and various heater designs as shown in Fig. 4.3 (d). The 4-port RF-PCM junctions are designed extract the equivalent lumped parameters for characterization of various PCM properties including resistance change

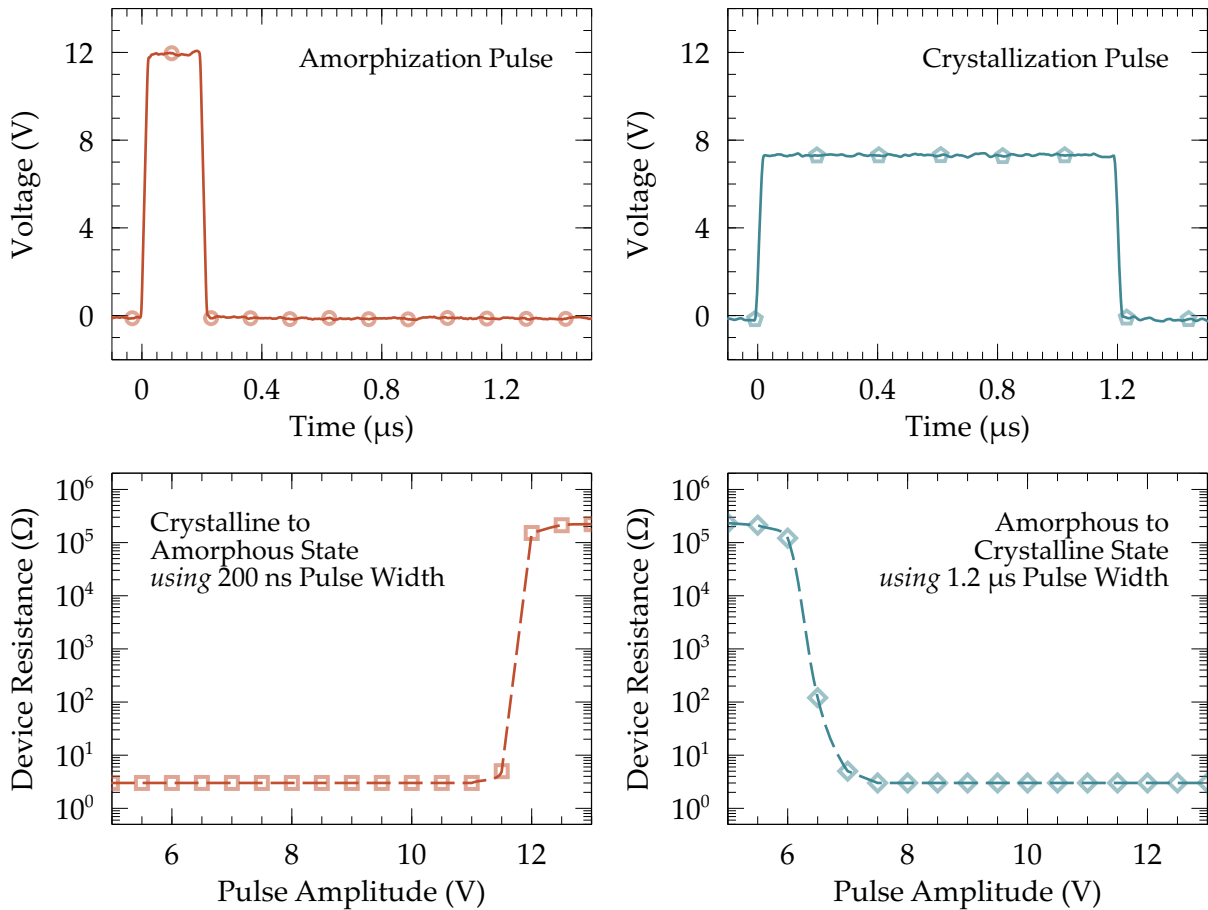


Figure 4.16: (Top) Bias signature applied to cycle the RF PCM SPST switches between amorphous and crystalline states. (Bottom) Measured PCM device resistance with change in applied pulse amplitude.

behavior, capacitive loading of the heater, heating performance using different dielectrics etc. In spite of various heater designs, shunt switches were not able to fully change the PCM state. Due to the large area of PCM, heating the PCM requires high power to actuate the shunt switch. Limited micro-heater power handling could not change the PCM state from crystalline to amorphous. Thus, the RF performance of shunt switches is studied from annealed and crystalline state of the PCM material at chip level. The shunt switch design is being currently optimized to circumvent this issue. The series switches are actuated using DC pulse of width 200 ns and 1.2 μs applied between $V+$ and $V-$ pads to switch between crystalline and amorphous state of GeTe.

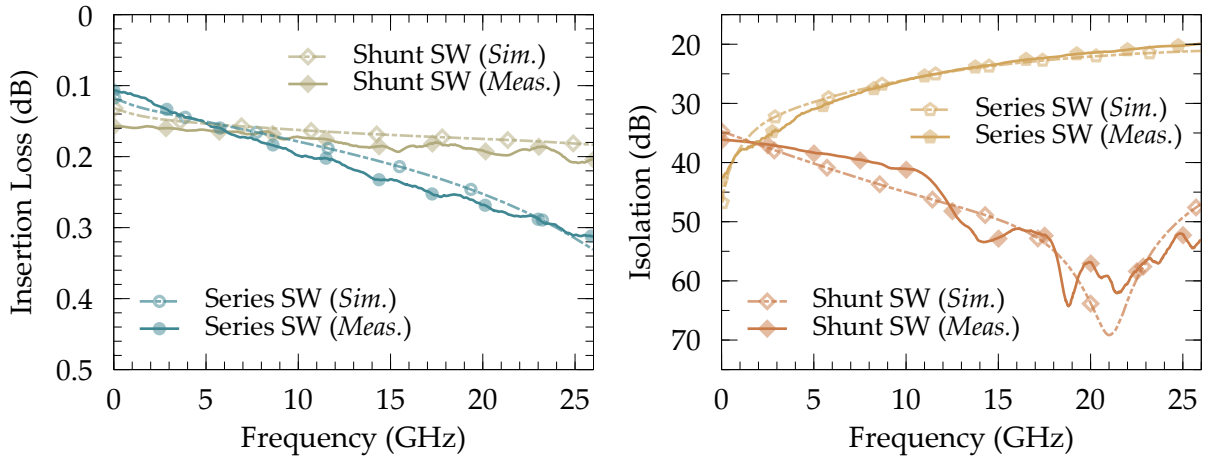


Figure 4.17: Measured and simulated RF performance of RF-PCM SPST series and shunt switches with $l_h = 35 \mu\text{m}$, $w_h = 2 \mu\text{m}$, $l_s = 2 \mu\text{m}$ and $w_s = 20 \mu\text{m}$.

The RF performance of PCM based SPST switches in series and shunt configuration are simulated and measured from DC to 26.5 GHz as shown in Fig. 4.17. The series switch configuration demonstrates an insertion loss lower than 0.3 dB, and an isolation greater than 20 dB, while the shunt switch configuration shows low insertion loss of less than 0.2 dB, and an isolation better than 36 dB. EM simulations are carried out by using ANSYS HFSS that agree well with the measurement results with slight deviations that are attributed to fabrication process parameter variations. Resistivity of GeTe is measured using four-point probe to define the actuation state of PCM in EM simulations. It should be mentioned that the micro-heaters used in the shunt switch presented were not able to switch the material's resistivity due to the large size of PCM material and wide micro-heater. Higher voltage further damaged the PCM material. Optimal design of micro-heaters for shunt switches will be studied in future work. Moreover, the shunt switch configuration can still be realized using two series switches connected between RF signal and ground path gap.

Following the analysis presented, the RF-PCM switches are optimized for millimeter-wave application. Electron beam lithography is used to get narrow PCM length (l_s). An optical micrograph of the SPST series switch is shown in Fig. 4.10, which is fabricated using the fabrication process illustrated in Fig. 4.9. The switch shown in Fig. 4.10 is developed with the dimensions: $l_s = 0.8 \mu\text{m}$, $w_s = 10 \mu\text{m}$, $l_h = 20 \mu\text{m}$, and $w_h = 1.2 \mu\text{m}$. The RF performance of the optimized switch is measured and simulated from DC to 67 GHz as shown in Fig. 4.18. The SPST switch exhibits an insertion loss of better than

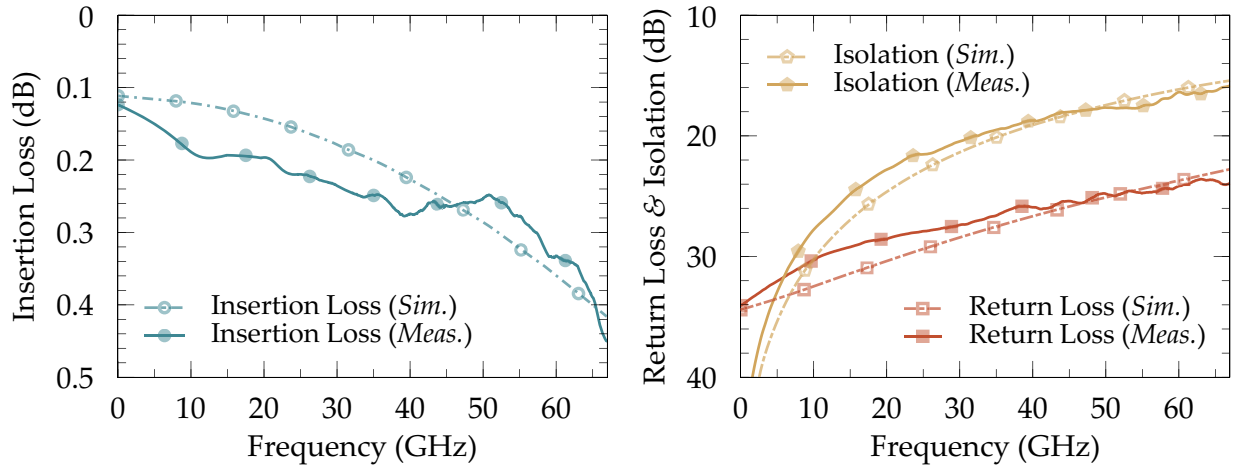


Figure 4.18: Measured and simulated RF performance of optimized RF-PCM SPST series switch for millimeter-wave applications.

0.3 dB up to 40 GHz, and better than 0.4 dB up to 67 GHz. The isolation is better than 20 dB from DC to 30 GHz and better than 15 dB up to 67 GHz. The return loss is better than 22 dB from DC to 67 GHz.

The embedded micro-heaters are responsible for parasitic capacitance coupling to RF signal line due to the thin barrier between heater and PCM. Scaling down l_s and w_h reduces the capacitance coupling but limits the isolation in OFF-state. Design parameters need to be carefully selected to enhance the RF performance without sacrificing reliability. A R_{off}/R_{on} ratio of 3.9×10^4 and 5.6×10^4 has been achieved using series and shunt switch respectively, while improved switches exhibit 4.35×10^4 . The effect of design parameters on R_{off}/R_{on} is shown in Table 4.2. Barrier between heater and GeTe needs to be

Table 4.2: Measured RF Performance of RF-PCM Switches with Variations in Design Parameters

w_s	l_s	w_h	l_h	R_{on}	R_{off}/R_{on} Ratio
10 μm	3 μm	2 μm	20 μm	4.9 Ω	1.2×10^4
15 μm	3 μm	3 μm	25 μm	3.7 Ω	1.6×10^4
15 μm	2 μm	3 μm	30 μm	2.4 Ω	2.9×10^4
20 μm	2 μm	2 μm	35 μm	1.8 Ω	3.9×10^4
20 μm	3 μm	3 μm	35 μm	2.3 Ω	2.6×10^4
10 μm	1.2 μm	0.8 μm	20 μm	1.61 Ω	4.35×10^4

of appropriate thickness for efficient thermal energy transport, as it also introduces capacitance to the RF line. A relatively higher R_{off}/R_{on} ratio of 4.35×10^4 has been achieved with the optimized fabrication process and by choosing optimal design parameters.

4.4.3 DC Current Carrying Capacity of PCM Switches

The RF PCM switches can be tested by applying bias signal to the control pads and measuring the S-parameters as detailed in the previous section. However, PCM switches can also be used for DC or low frequency applications. RF measurements require proper calibration of the PNA. RF GSG probes and cables for mmWave frequencies are expensive and fragile. Four-port junctions which have the same design parameters as RF switches except for the 50Ω ports. A quick way to accurately measure the resistance change is by using an SMU. The study of DC current carrying capacity is important to understand behavior of PCM GeTe with respect to the injected current in the switches. Device performance relies heavily on design parameters and microfabrication process.

Amorphous and crystalline pulse amplitude and width required to change the PCM state is shown in Fig. 4.16. However, a 100 mV constant DC voltage is sourced to ports 1 and 2 to read the current state of the material. A continuous reading with respect to time allows fully characterize the bias signature. The wafer is annealed to crystalline the PCM GeTe and set all the switches across wafer in ON-state. Amorphous pulse is applied to different PCM junction geometries to turn OFF the switches.

PCM GeTe acts as a resistor which change its resistance as a function of temperature. Applying DC voltage directly to the switch terminals 1 and 2 heats the resistive material due to Joule heating. DC current carrying capacity can be translated to its power handling capability in ON and OFF-state as high RF power generates heat. Self-actuation in the PCM switches can be studied by sourcing DC voltage sweep and measuring the current flow. When DC voltage is sourced in the amorphous state of the switch, PCM junctions with narrow channel dimensions (incl. width and length) heats up above its crystalline temperature leading to change the resistance from amorphous to crystalline. If the DC voltage is sourced in the crystalline state of the switch, PCM junctions with narrow channel dimensions degrade faster which eventually damages the switch catastrophically.

DC voltage is swept from 100 mV to 10 V which is sourced between port 1 and 2 while measuring the current flow between these terminals. The compliance current is set to 1 mA to not damage the devices and to use the same devices for ON-state IV measurements. IV characteristics of four different PCM switches are recorded as shown in

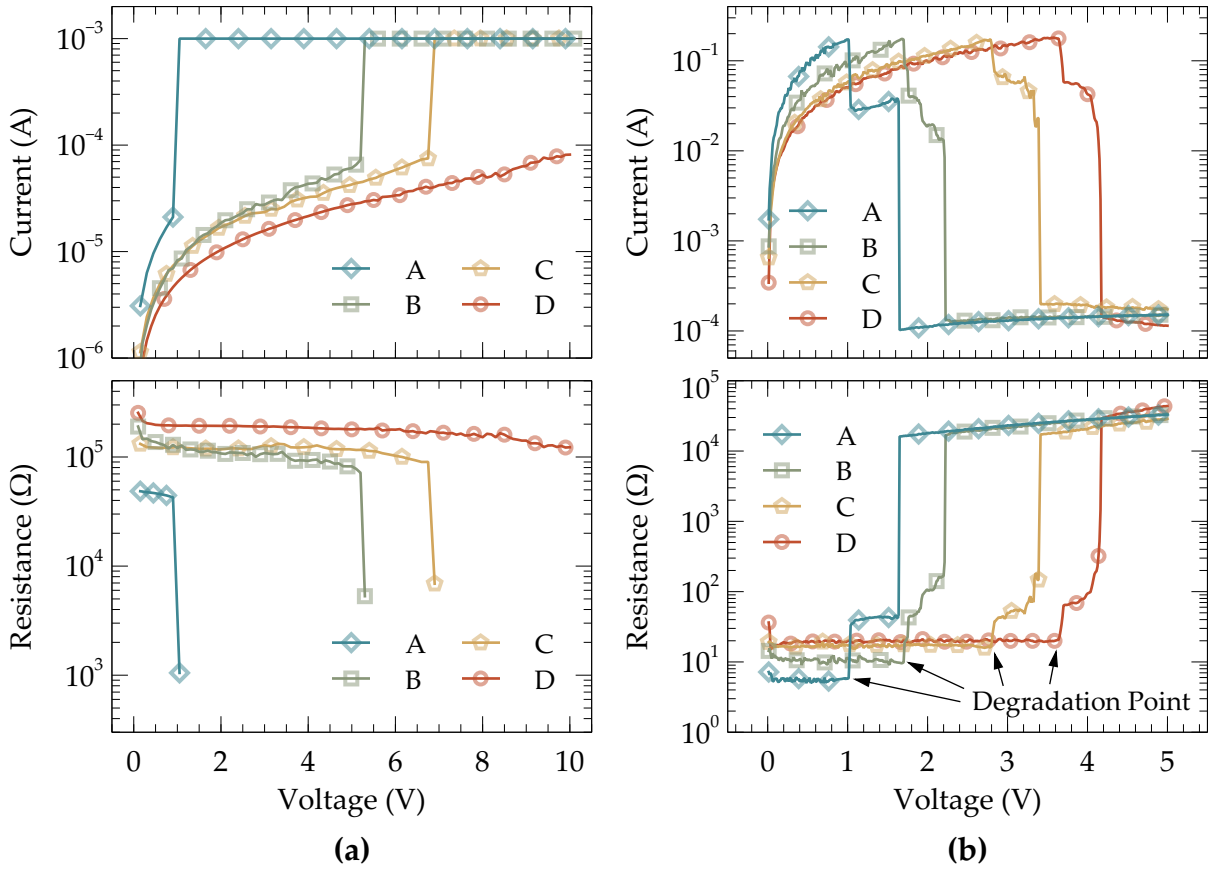


Figure 4.19: Measured self actuation and current carrying capacity of four different RF PCM SPST switch geometries: (Top left) Measured IV characteristics highlighting self-actuation, (Bottom left) Resistance change with change in DC voltage, (Top right) Maximum current carrying capacity in ON-state, and (Bottom right) Switch failure with change in DC voltage.

Fig. 4.19. IV characteristics and resistance change with increasing DC voltage reported in Fig. 4.19(a) shows switch ‘A’ which has the channel length smaller than other three devices actuates (resistance drops). Switch ‘A’ hits compliance current at 1 V, while device ‘B’ and ‘C’ actuates at 5.2 V and 6.7 V respectively. Switch ‘D’ did not actuate even at constant 10 V thus can handle more current than other three devices, but on the other hand, device ‘D’ shows poor RF insertion loss due to relatively high crystalline state resistance.

Maximum current carrying capacity of the PCM switches ‘A’ to ‘D’ is studied in ON-state by actuating the switches using crystalline pulse and sourcing DC voltage sweep

from 100 mV to 5 V. Compliance current is set to 1 A to capture material degradation or damage pattern. Fig. 4.19(b) shows the IV characteristics and corresponding resistance change with increasing DC voltage. Switch 'A' shows material degradation at 1 V, while switch 'B', 'C' and 'D' show degradation point at 1.7 V, 2.8 V and 3.6 V respectively. Depending on the device geometry, a specified voltage is sufficient to melt the material. All the switches can handle constant current between 180 mA to 200 mA without any damage to the switch. The switches are fully reversible till the degradation point and reversible with resistance degradation between 200 mA to 30 mA. PCM switches 'A' to 'D' are catastrophically damaged with constant 1.6 V, 2.2 V, 3.4 V and 4.2 V respectively.

From Fig. 4.19, current carrying capacity can be related to RF power handling, as for certain switch dimensions, input power at which the failure occurs generates same amount of heat at the junction as DC voltage generates more than 200 mA current to damage the devices. Similarly OFF-state self-actuation using DC voltage can also be related to self-actuation through RF power as detailed in the next section.

4.4.4 RF Power Handling and Self Actuation

In some applications where there is a clear need to channel high-power signals, for such applications the limited switching speeds (typically in ms) of electromechanical switch may prove adequate for many systems that can handle hundreds of watts CW power levels with trade-offs of size and weight. While RF-MEMS offer extremely compact size switches with switching speeds (in μ s) and excellent RF performance, there is always a question of reliability and hermetic packaging. Power handling capability of RF-MEMS switches is limited in terms of hot-switching, cold-switching, average power and peak power.

Unfortunately, there are very limited choices available till date for high performance mmWave switches. From the performance standpoint, PCM based RF switches show promising RF results but limitations include low power-handling capability than RF-MEMS switches. One important parameter in the case of PCM-RF switches that is not rigorously investigated is the power-handling capabilities for these switches. Investigating the limitation factors in PCM switches not only helps in the development of better devices but also helps to avoid catastrophic failure of the switch or instruments.

RF power handling capability of PCM switches is experimentally investigated for two different device geometries. Self-actuation using RF power in PCM switches is also investigated in this section. Power handling capacity of two different devices 'A' and 'B' are measured. Device 'A' has 3 times narrow PCM channel dimensions than device 'B'.

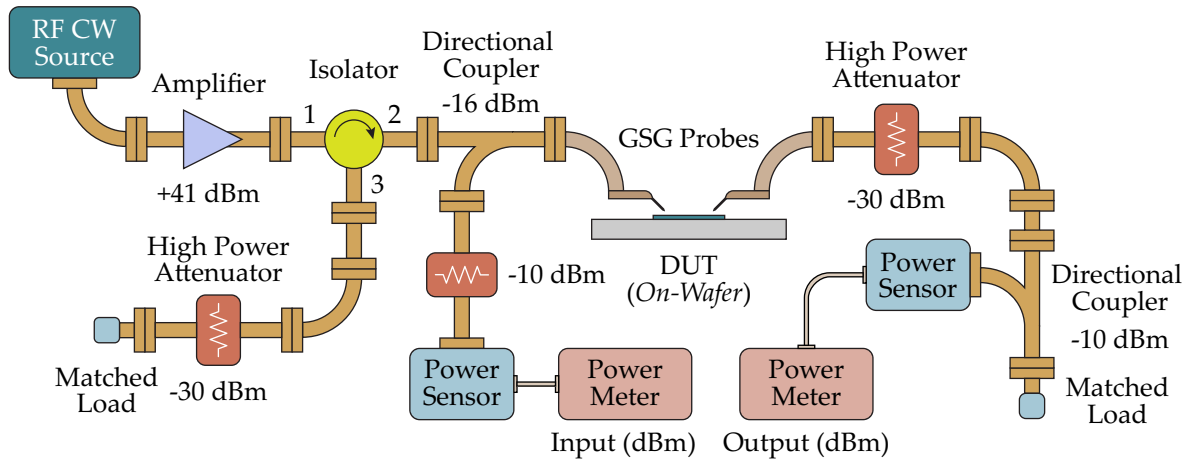


Figure 4.20: Block diagram of on-wafer high RF power handling setup for PCM switches.

The block diagram of on-wafer high RF power handling setup is shown in Fig. 4.20 and the photograph of the power handling measurements testbench is shown in Fig. 4.21. The setup consists of an RF CW source/generator which is connected to a fixed 41 dBm RF amplifier. The output of the amplifier is connected to an isolator's port 1. The port 3 of the isolator is connected to a -30 dBm fixed high power attenuator which is terminated with a $50\ \Omega$ matched termination. Isolator protects the amplifier's input by routing any signal mismatch reflected from port 2 to isolated port 3. Port 2 of the isolator is connected to a high power directional coupler with -16 dBm of coupling at coupled port. USB based power sensors are used in the test setup. The maximum input RF power available at coupled port of an input directional coupler is -25 dBm, which is 5 dBm higher than maximum input rating of the power sensor. A -10 dBm low power attenuator is connected to limit the signal flowing to power sensor. Power meter is used to read input power from power sensor. Signal from the output of directional coupler is fed to input CPW GSG probe which is connected to the RF input of the SPST switch (on-wafer measurements). An output CPW GSG probe is connected to the output port of the switch (DUT). DUT is mounted on the two-port probe station. RF signal is attenuated by -30 dBm using a fixed high power attenuator. Output of the attenuator has a theoretical maximum signal level of -11 dBm is fed to a -10 dBm directional coupler. The output of the directional coupler is terminated with a matched load. The coupled port of the output directional coupler is connected to a USB power sensor to read output power at DUT. Power meter displays the RF power at the output. Data logger is used in the setup due to the USB functionality of the both input and output power meters.

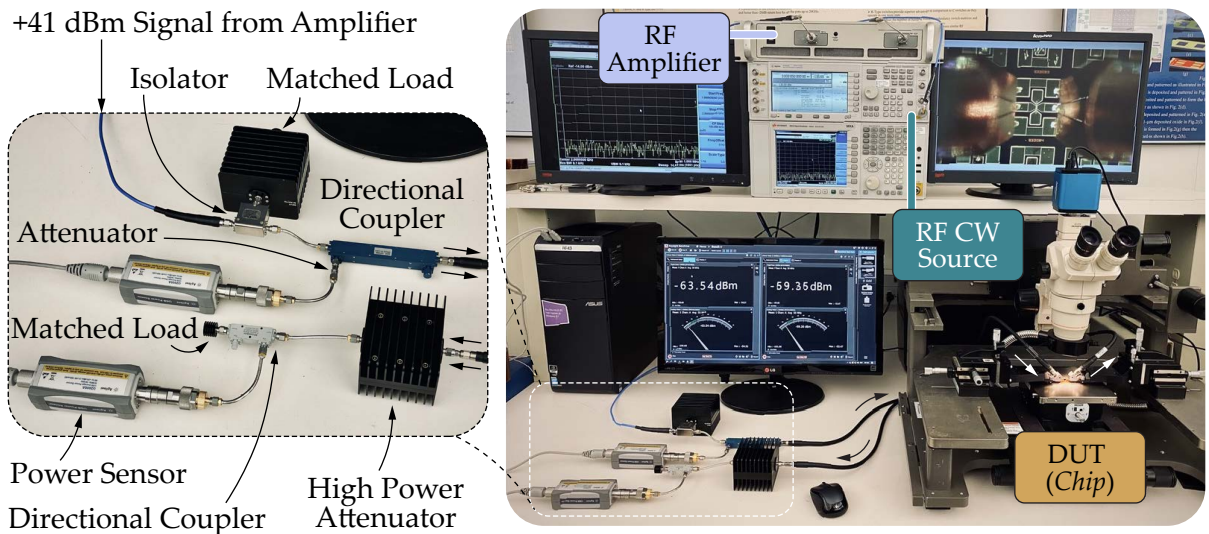


Figure 4.21: Photograph of on-wafer high RF power handling measurements testbench. Inset shows various RF components and RF signal flow direction.

It is important to measure S-parameters of all the components or cables used in this setup to properly calibrate the setup. RF transmission loss of GSG probes, cables, connectors, and attenuators are taken into consideration when offsetting the input and output power sensors' reading. Power source and sensors are also calibrated at all different power levels to get readings at desired RF levels such that input power sensor reads the power at DUT input and output power sensor reads power at the output of the DUT.

4.4.4.1 RF Power Handling Measurements

CW RF input power is increased from 0 dBm to 40 dBm and output power is recorded simultaneously for the devices in ON-state. Input power sweep step size is reduced to capture failure point precisely. Device 'A' is functional with 35.5 dBm (3.5 W) of CW power. Each data point is recorded after 2 minutes of power level change to make sure the device can handle the injected input power. Device 'A' fails catastrophically within few seconds when the input power is increased to 36 dBm (4 W). Device 'B' on the other hand which has 2 times longer PCM channel length than device 'A' did not show any degradation or failure even at 40 dBm (10 W) of CW RF power limited by the test setup. Measured RF power handling capacity of two different devices is shown in Fig. 4.22.

List of test equipment used are listen in Appendix B

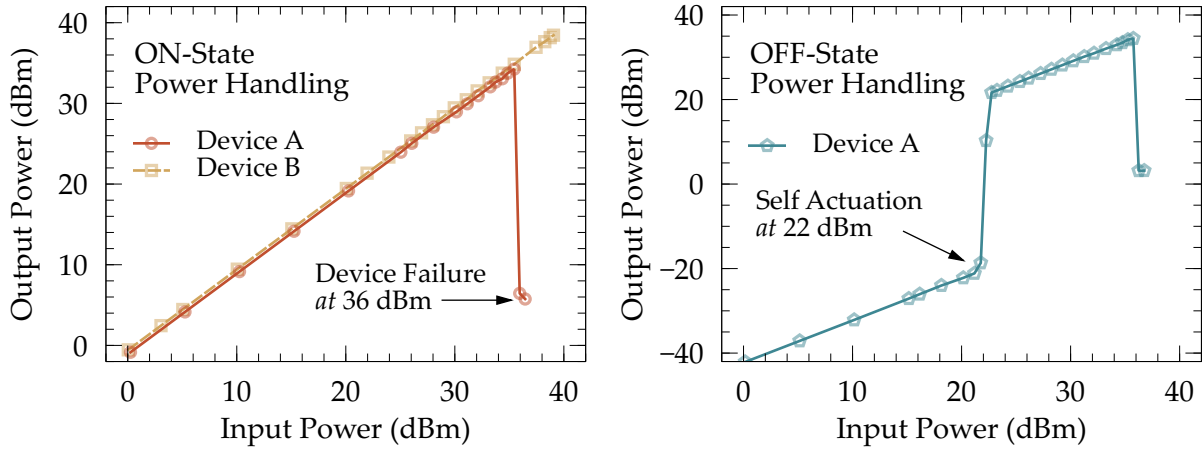


Figure 4.22: RF power handling measurements of two different RF PCM SPST switches in ON-state and OFF-state.

4.4.4.2 Self-Actuation using RF Power

Self-actuation phenomena in RF PCM switches is not reported till date. It is clear from current carrying capacity of PCM switches shown in Fig. 4.19(a) that when the switch is in OFF-state, it can get actuated when current is passed through the device with the applied voltage. Switches actuate at different voltage/current levels depending on the junction design parameters. Similarly as shown in Fig. 4.22, 22 dBm CW power generates heat in the PCM GeTe region beyond its crystalline threshold temperature leading to switch the state from OFF to ON. Self-actuated switch did not show any signs of damage and is fully functional till 35.5 dBm of CW input RF power. Till 35.5 dBm, same switch can be cycled between OFF and ON-state with applying amorphous and crystalline pulses as detailed in Fig. 4.16.

4.4.5 Linearity and Intermodulation Distortion Measurements

4.4.5.1 Harmonic Distortion

As most of the RF devices, switches exhibit a degree of non-linearity, thus if switches are stimulated at a single frequency f_0 by a signal, spurious output signals will be generated at the harmonic frequencies/tones $2f_0, 3f_0 \dots Nf_0$, where N th harmonic is the the N th

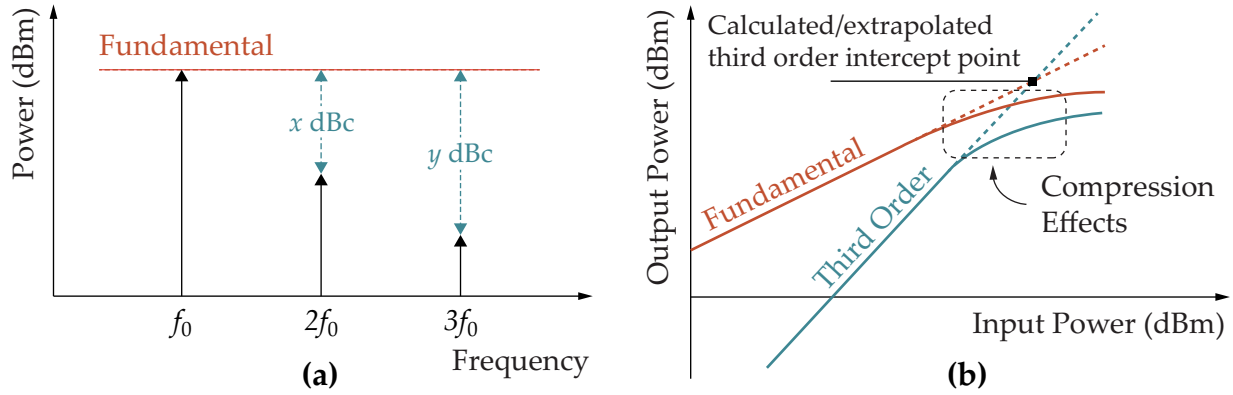


Figure 4.23: (a) Harmonics of a fundamental tone. (b) Realistic representation of third order intercept point calculation.

order product. These harmonics are usually measured in dBc (dB below the fundamental output signal) as shown in Fig. 4.23(a).

4.4.6 Intermodulation Distortion

When the non-linearity of a system or a device with two or more input frequencies cause undesired outputs at other frequencies, it gives rise to intermodulation distortion. Investigating intermodulation distortion is important as it causes the signals in one channel to interfere with adjacent channels. Reducing the intermodulation distortion has become more critical as the spectrum becomes more crammed and channels are more tightly spaced.

The spurious products are mathematically related to the fundamental input signals. It is thus a common practice to limit the analysis to two fundamental frequencies, f_1 and f_2 . These frequencies/tones are usually separated by a very small offset frequency Δf , the output frequencies of the two-tone intermodulation products are given as:

$$nf_1 \pm mf_2, \quad n, m = 0, 1, 2, 3, \dots$$

The order of the distortion product is the sum of $n + m$. So, the third order intermodulation products of the two signals, f_1 and f_2 , would be

$$2f_1 - f_2, 2f_2 - f_1, 2f_1 + f_2, \text{ and } 2f_2 + f_1$$

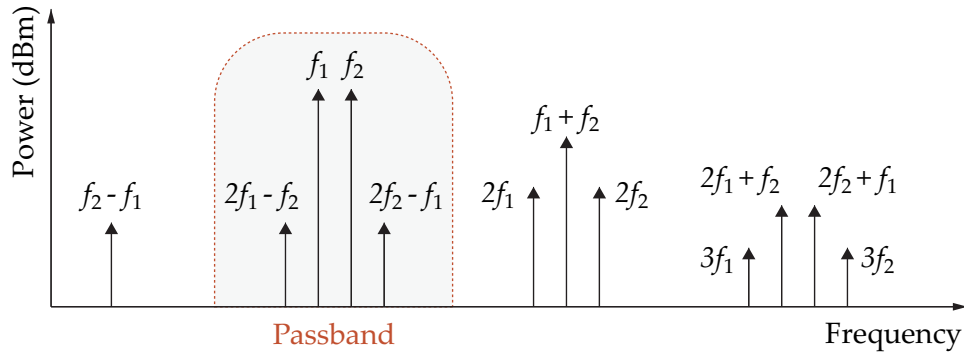


Figure 4.24: Second and third order intermodulation products with two fundamental tones.

The third order intermodulation products of two fundamental tones are shown in Fig. 4.24. All the non-linear distortion products might affect broadband systems. However, unlike harmonic and second order distortion products, third order intermodulation distortion products (IM3) are always too close to the fundamental signals to be easily filtered as shown in Fig. 4.24. Usually in communication systems, when strong signals from more than one transmitter are present at the input of the receiver, unwanted products will be generated affecting the receiver performance.

Higher order intermodulation products increase in power way faster (in dBm, a logarithmic function) than the fundamental as shown in Fig. 4.23(b). The intermodulation signal increase in power three times faster than the carrier signal. The relationship is valid for other harmonics or intermodulation products as well. Similarly, the second harmonic and the second order intermodulation products' power increase two folds faster than the fundamental.

Manufacturers typically measure the third order intercept point (IP3) or third-order intermodulation (TOI) distortion point as a performance parameter of their RF device. Higher IP3 point is considered better as an RF device with higher IP3 does not generate spurious as fast as the device with relatively lower IP3 point. Input and output power level where fundamental tone and third order product intersect are denoted as IIP3 and OIP3 respectively. IP3 is an extrapolated point where fundamental and third order product intersect. TOI can also be computed directly from the output spectrum of the measured device using

$$IP3 = P_{out} + 0.5 \times \Delta P$$

where, P_{out} is the output power (dBm) of the fundamental tone and ΔP is the difference

of fundamental tone output power and third order product power.

The block diagram of on-wafer two-tone linearity or intermodulation distortion measurements setup is shown in Fig. 4.25. Two RF CW sources generate two tones (f_1 and f_2) at desired separation ($BW = f_2 - f_1$). Power of two tones are combined using a

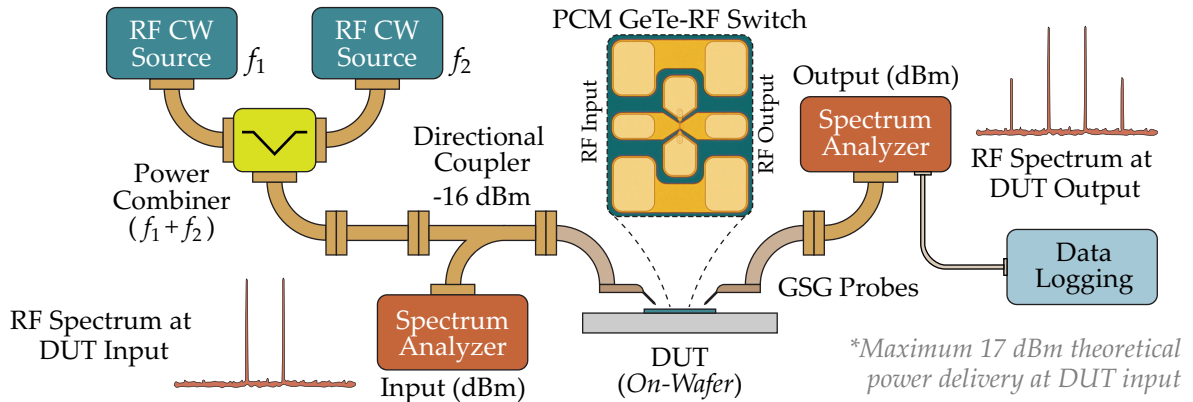


Figure 4.25: Block diagram of on-wafer linearity or intermodulation distortion measurement setup for PCM switches.

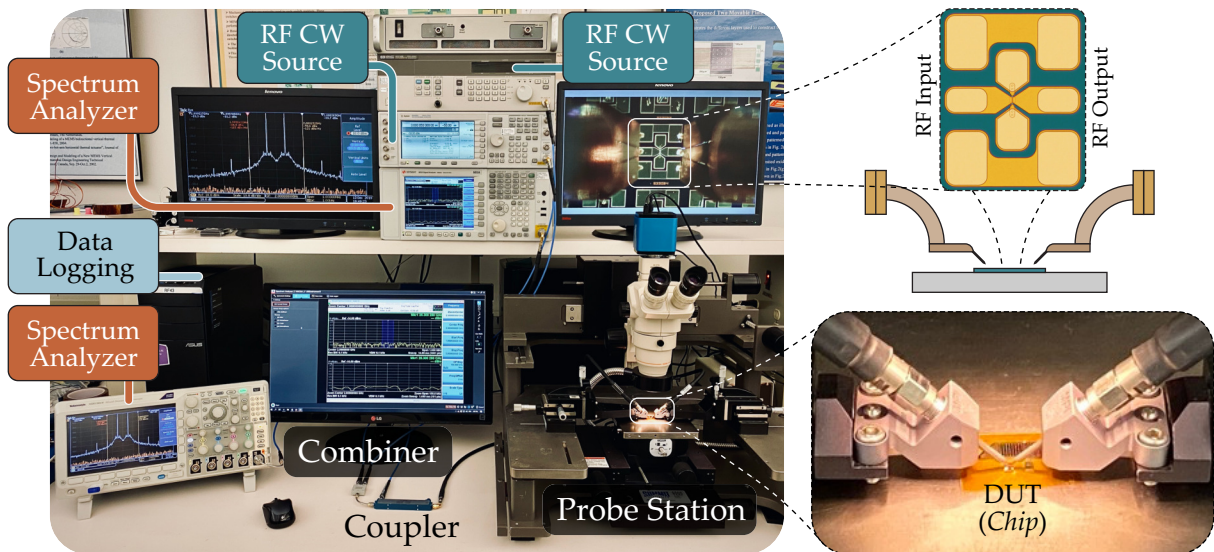


Figure 4.26: Photograph of on-wafer two-tone linearity / intermodulation distortion measurement test-bench. Inset shows CPW GSG probes landed on a DUT.

power combiner which outputs to a directional coupler. A spectrum analyzer is connected to the coupled port of the directional coupler to monitor the input power level of two fundamental tones. Input side spectrum analyzer is helpful to monitor if RF CW sources are generating any intermodulation products. Input levels are offset to respective output levels by subtracting any loss from the connected components or cables. The RF input and output port of the DUT is connected to two CPW GSG probes (mounted on the wafer probe station). Output of the directional coupler is connected to DUT input and a spectrum analyzer is connected to the output port of the DUT (RF PCM SPST switch in this case) to measure the output spectrum. Ignoring the loss of the components and cables, a theoretical maximum of 17 dBm power can be delivered at DUT input port assuming both of the sources can output 20 dBm. Photograph of the test setup is shown in Fig. 4.26. Inset of the Fig. 4.26 shows two CPW GSG probes landed on the PCM SPST switch. The output spectrum of the device is logged at different input power levels of both fundamental tones.

Measured IP3 or TOI of RF PCM SPST switch is shown in Fig. 4.27. Input power levels of two fundamental tones are swept from -10 dBm to 10 dBm with a step size of 1 dBm. Two tones are separated by 100 kHz with a centre frequency, $f_0 = 2$ GHz. Dynamic range of the spectrum analyzer is improved by using in-built attenuation levels. Averaged output spectrum with 1 MHz span when the DUT is stimulated with two 10 dBm tones is

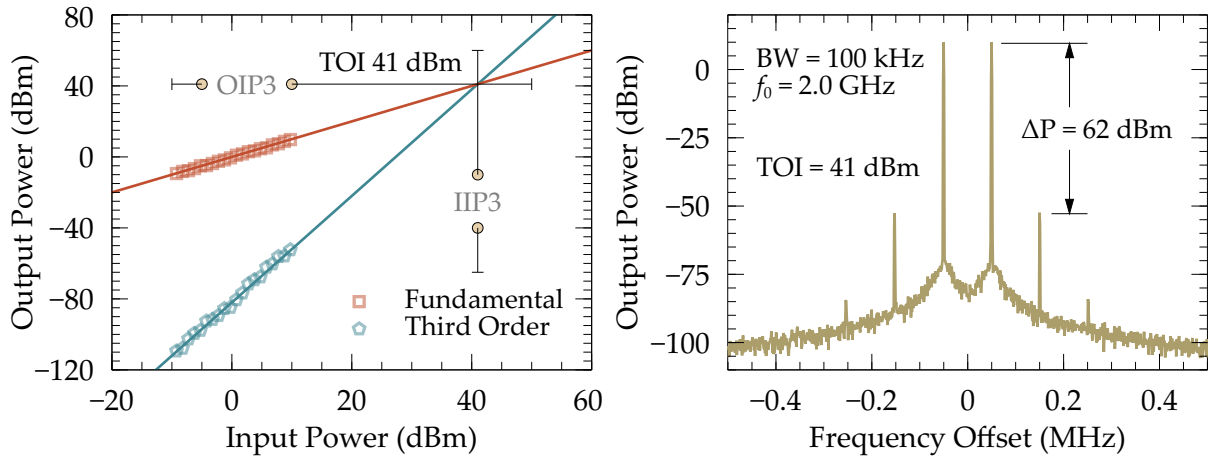


Figure 4.27: Intermodulation distortion measurements of RF PCM SPST switches. (Left) Fundamental and third-order intermodulation products measured and extrapolated third-order intercept point, (Right) Output spectrum observed with 10 dBm power of two fundamental tones with third and fifth order products visible.

Table 4.3: Third order intercept point measurements of RF PCM switch at varying centre frequency and tone separation.

Centre Frequency (f_0)	Tone Separation ($BW = f_2 - f_1$)	Measured IP3 / TOI
2 GHz	100 kHz	41 dBm
2 GHz	500 kHz	42 dBm
2 GHz	1 MHz	45 dBm
3 GHz	100 kHz	42 dBm
3 GHz	500 kHz	42 dBm
3 GHz	1 MHz	44 dBm
4 GHz	100 kHz	41 dBm
4 GHz	500 kHz	42 dBm
4 GHz	1 MHz	42 dBm

Note: Best and Worst case scenarios are highlighted.

shown in Fig. 4.27. Extrapolated intercept point and calculated from the output spectrum reports 41 dBm of IP3. Third order and fifth order products visible in the output spectrum at the expected frequencies. IP3 of the switch is also measured at $f_0 = 2$ GHz, 3 GHz and 4 GHz with tone separations 100 kHz, 500 kHz and 1 MHz that is summarized in Table 4.3. RF PCM switches exhibit a minimum IP3 of 41 dBm.

4.4.7 Switching Speed Analysis

Switching or transition speed of an RF switch is crucial for many applications and fast switching speed is always desired. Semiconductor switches provide switching speed in nanosecond regime, while MEMS switches (depends on the topology) provide switching speed in microsecond range. Mechanical or coaxial switches are the slowest with switching speed in millisecond region. PCM based RF switches require nanosecond pulse to switch from crystalline state to amorphous state while microsecond pulse to switch back from amorphous to crystalline state. Switching speed for the RF SPST switch is experimentally evaluated. The experimental setup employed to measure the switching speed of the PCM GeTe-based RF switch is shown in Fig. 4.28. The setup consists of a pulse generator to provide amorphous (t_{off}) pulse and crystalline (t_{on}) pulse to the switch at terminal 3 and 4. RF CW signal is generated from the source which passes

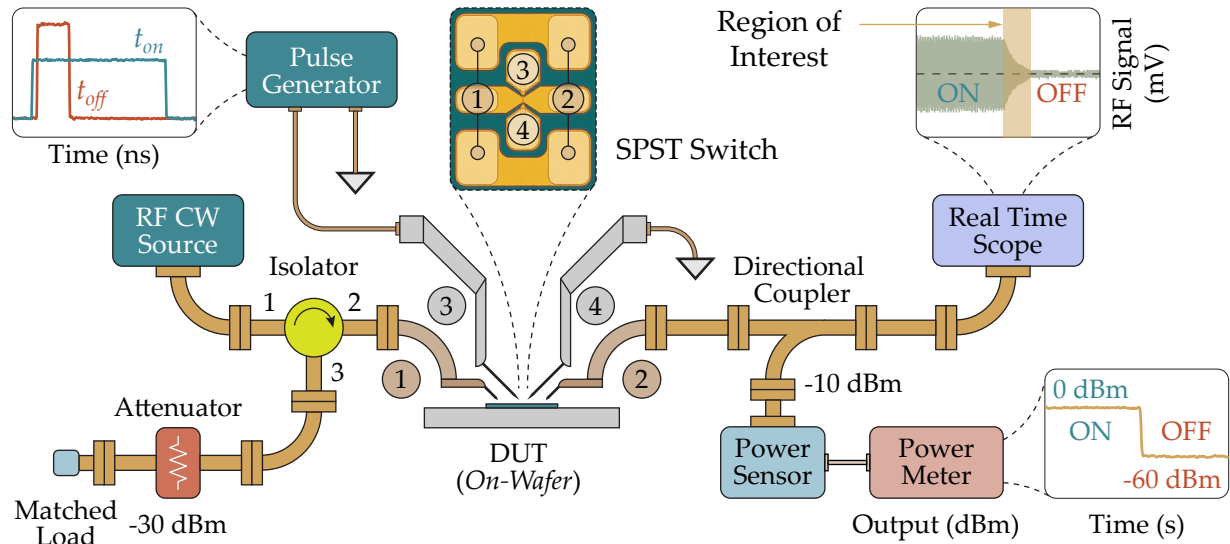


Figure 4.28: Experimental setup for measuring the switching speed of an PCM based RF switch.

through an isolator between port 1 and 2. Port 2 of the isolator is connected to the RF input port of the switch (Terminal 1). Port 3 of the isolator is connected to an attenuator followed by a matched load. RF signal gets passed or blocked by the switch depending on the actuation pulse provided. To analyze the switching speed, usually diode-based detectors are frequently used due to their dynamic range. A high speed power sensor is utilized in this setup which is based on diode stacks in place of single diode to improve the measurement accuracy. A high speed power sensor with nanosecond rise/fall time detection detects the RF signal change with respect to time. A power meter reads the power from the sensor. In this case, a USB based power sensor is used, thus RF power flow is read via software. The switching speed is also verified by using a high speed real time oscilloscope. RF signal (on voltage scale) is captured by the scope to get insights into switching or transition speed of the device.

The measured switching speed of the switch with the application of amorphous or crystalline pulse is shown in Fig. 4.4.7. Depending on the applied pulse, the RF signal captured by the scope shows switch ON or OFF with the change in the level of RF power. Sourcing a 200 ns pulse of 12 V amplitude changes the switch state to amorphous and the switch turns OFF completely within 275 ns. A longer pulse of 1.2 μ s width and 7.8 V changes the switch state to ON within 1.1 μ s which translates the slowest switching speed of the device. Transition speeds captured by the scope are verified by the power sensor readings which are sampled for the entire duration.

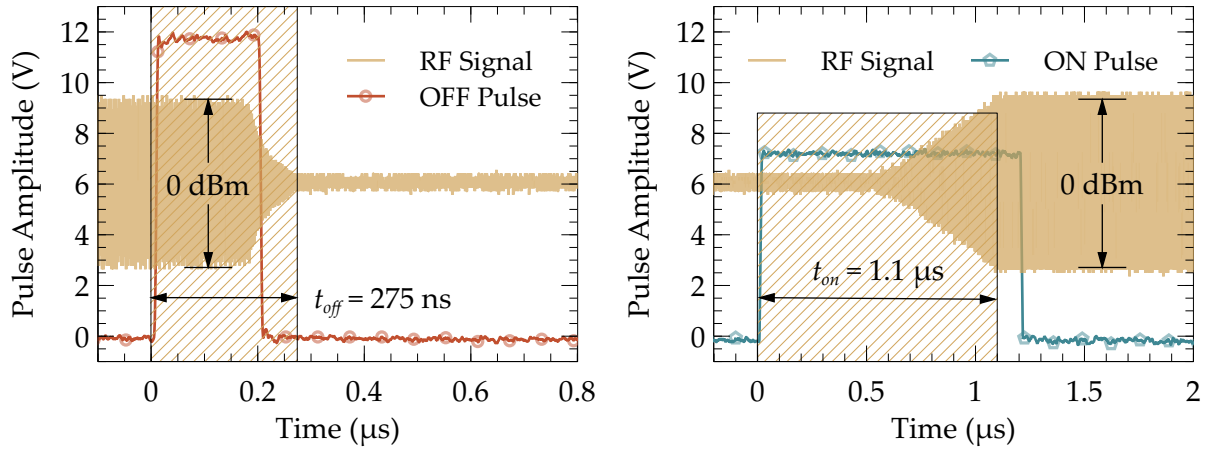


Figure 4.29: Measured switching/transition speed of an RF PCM-based SPST switch. Actuation signal applied to the switch is also shown.

4.4.8 Device Lifetime Cycles and Reliability Testing

Reliability of a device is one of the utmost important parameter depending on its use case scenario. Most of the reconfigurable RF systems utilize switches to achieve reconfigurability. Many sectors including aerospace and automotive industry require highly reliable devices. Reliability of the RF PCM switches is not very well studied till date. An automated test setup is configured to test the RF PCM switching actuation cycles. PCM GeTe based RF switches provide latching functionality, thus non-volatility of the switches has also been studied.

The block diagram of a reconfigurable switch cycle testing and RF performance measurement setup is shown in Fig. 4.30. Initial samples are tested by manual triggering of actuation pulses using four DC probes. To test the switches for hundreds of thousands of cycles, an automated test setup is configured. PCM switches can be cycled through a high frequency custom pulse pattern from a single arbitrary pulse generator, but to make sure the resistance change stays stable for a duration of time, very low frequency pulses are triggered by automatically switching test equipments as demonstrated in Fig. 4.30. The test setup also allows measuring PCM switch resistance, RF parameters, and micro-heater resistance without changing the probe positions.

The RF PCM SPST switch developed using Gen 3 microfabrication process is shown in Fig. 4.30. SEM micrograph of the PCM GeTe junction is highlighted. Corresponding equivalent simplified switch model in both ON and OFF-state is also shown in Fig. 4.30.

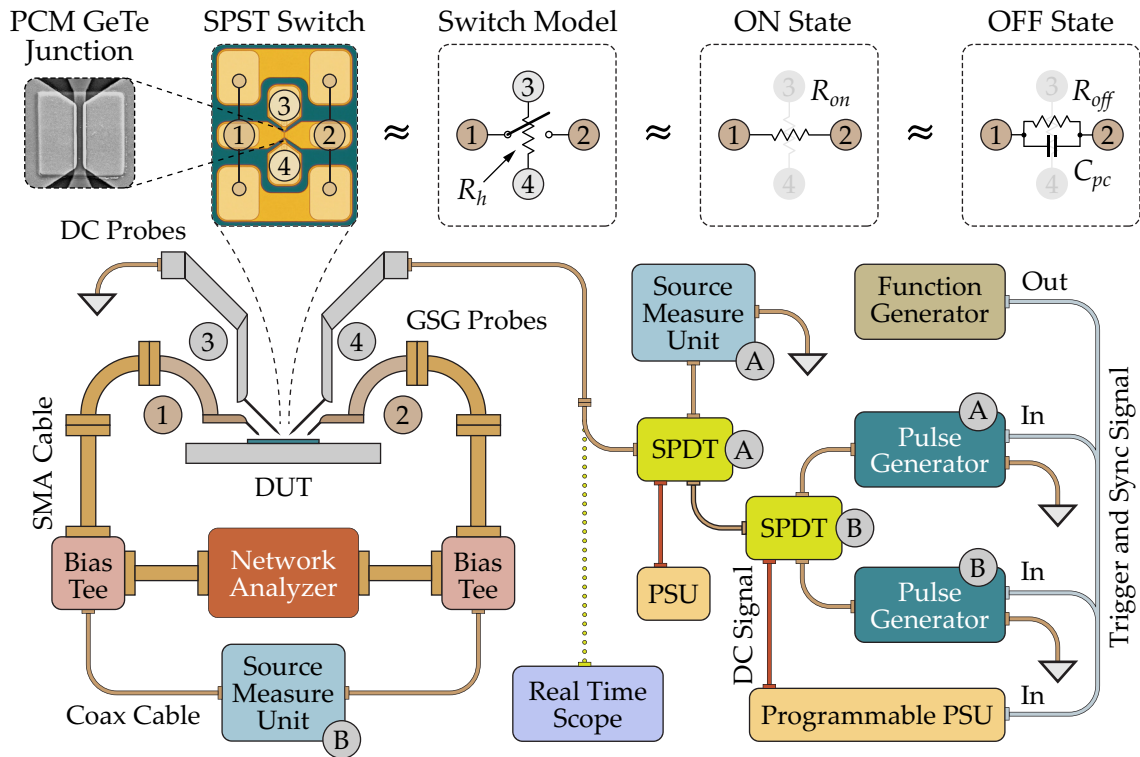


Figure 4.30: Block diagram of reconfigurable switch cycle testing setup and RF measurements setup. Inset shows RF PCM SPST switch and PCM GeTe junction. Top level circuit model model of the SPST switch in ON-state and OFF-state is highlighted.

The test setup consists of a probe station with two CPW GSG probes to measure RF performance and also to source/measure voltage/current. Two source measure units (A and B) are used in the setup. Two ports of SMU-B are connected to bias tees for decoupling DC signal from RF. CPW GSG probes are connected to port 1 and 2 of the DUT and S-parameters are monitored using a 67 GHz performance network analyzer (PNA). SMU-B connects to port 1 and 2 as well. Two DC probes are connected to port 3 and 4 of the DUT to supply actuation pulses to micro-heater and also to source/measure voltage/current. DC probes are connected to the common port of a high performance military grade electromechanical coaxial RF SPDT latching switch (SPDT-A). Output channel 1 of the SPDT switch is connected to SMU-A while channel 2 is connected to another similarly performing RF SPDT switch (SPDT-B). SPDT-B is a failsafe switch while SPDT-A is a latching switch. A failsafe switch is incorporated to ease in reconfigurability. A pulse generator (PG-A) is connected to channel 1 of SPDT-B and another similar

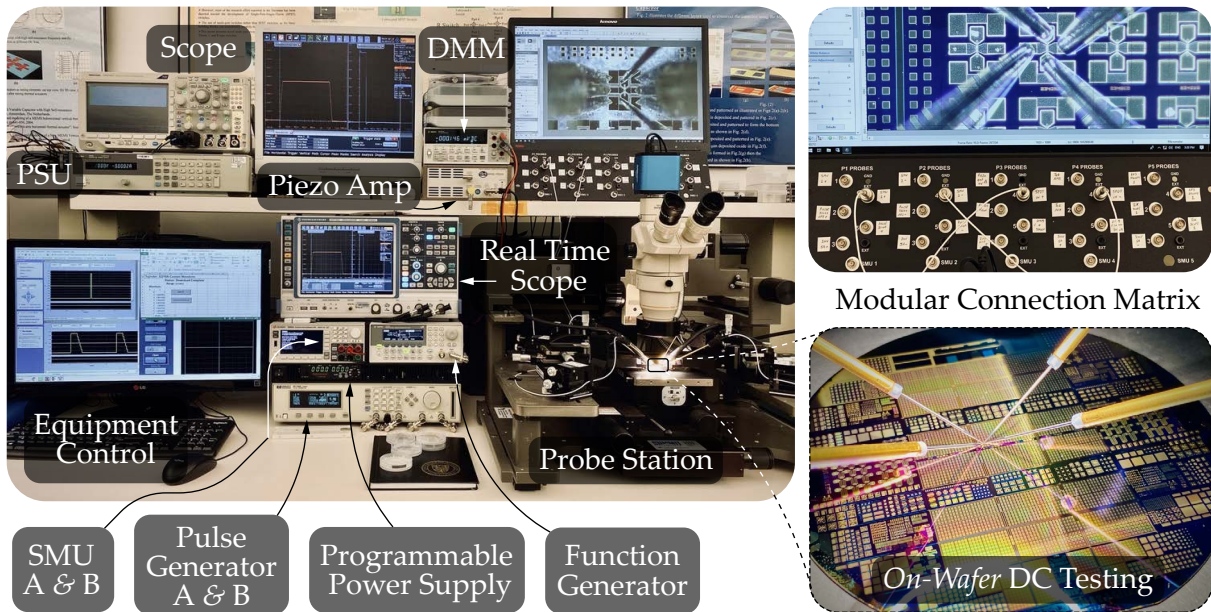
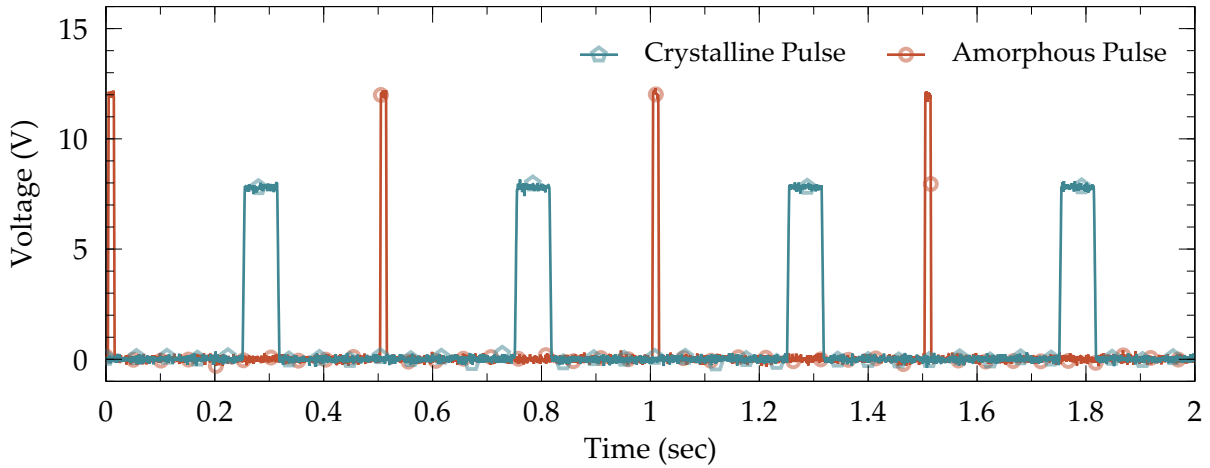


Figure 4.31: Photograph of an automated on-wafer DC switch cycle testing setup. Inset shows an in-house assembled modular connection matrix to connect DC probes to any equipment. Zoomed-in view highlights the fabricated RF-PCM Si wafer probed with four DC probes.

pulse generator (PG-B) is connected to channel 2 of SPDT-B. An arbitrary function generator’s output is connected to trigger-in functionality of both the pulse generators. A programmable power supply provides actuation to SPDT-B, which is controlled by the same trigger signal through the function generator. A real time oscilloscope is connected with a weak link to check the pulse shape at the end of the DC probe to offset any pulse amplitude or width deterioration.

Reliability test setup photograph is shown in Fig. 4.31. A modular connection matrix is built and all the input and outputs test port connections are routed to the connection matrix as shown in the inset of Fig. 4.31. A photo of the fabricated wafer using Gen 3 process with four DC probes is also shown in the inset of Fig. 4.31. Two channel SMU and a pulse generator are used to independently control SMU-A, SMU-B, PG-A and PG-B. CPW GSG probes and DC probes landed on the device can be seen on the microscope monitor beside DMM in Fig. 4.31.

Most of pulse generators require more than 0.1% duty cycle at minimum. Thus with the smallest pulse width of 200 ns, pulse pattern at 5 kHz train is the limit. To test the switches at low speed and to make sure the state is stable, independent pulse generators



**Pulse width is scaled by the factor of (5×10^4) for illustration purposes*

Figure 4.32: Pulse pattern at the DUT input for switch cycles reliability testing. Crystalline and amorphous pulses are scaled for illustration purposes. Crystalline and amorphous pulse patterns are generated from two independent pulses generators and synced to trigger at 4 Hz frequency.

PG-A and PG-B provide amorphous pulses and crystalline pulses respectively. Both pulse generators are set to output a single pulse such that the cycle testing frequency can be controlled by trigger-in signal from the function generator. SMU-B source a constant 100 mV to the DUT while measuring change in current. Measured current from SMU-B is logged at a speed of test frequency with a delay of few milliseconds to make sure the device gets in stable state before recording a data point. Pulse generators PG-A and PG-B are connected to the DC probes 3 and 4 at the test setup frequency set by function generator. Impedance of the micro-heater is stabilized and matched with the output load impedance of the pulse generators by cycling the device manually before starting the automated setup. However, the PCM switch resistance is recorded from first cycle onwards. Triggered sync signal from function generator triggers both amorphous and crystalline pulses at the same time while triggering the output of programmable PSU. A failsafe SPDT connects PG-A or PG-B depending on whether programmable PSU outputs the actuation signal or not. Utilizing this method, amorphous and crystalline pulses are generated in a pattern as shown in Fig. 4.32. Pulse width is scaled by the factor of (5×10^4) for illustration purposes only. However the test setup frequency is set to 250 ms. SPDT switches toggle the connected equipment at a minimum speed of 10 ms.

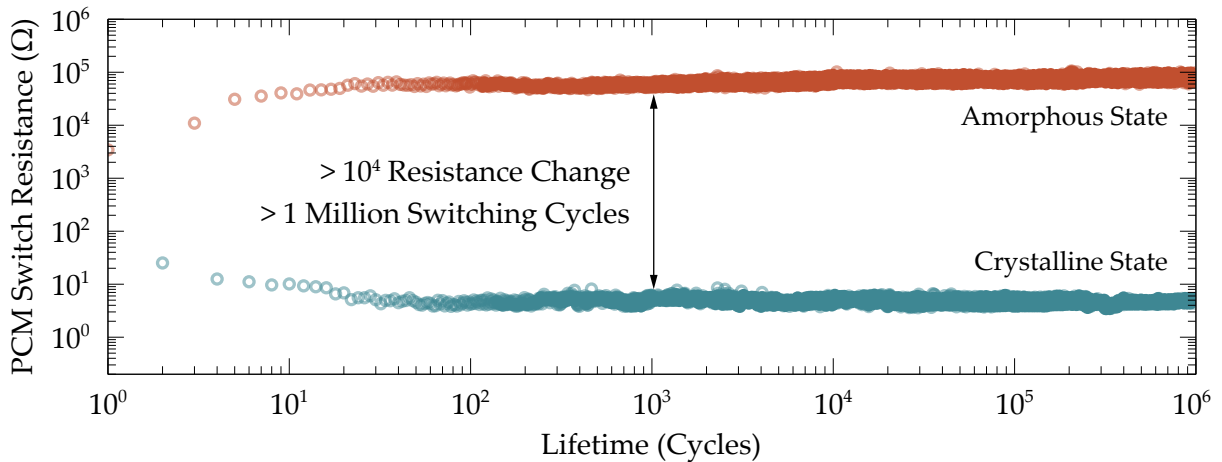


Figure 4.33: RF PCM switch lifetime switching cycles measurement demonstrating 1 million cycles tested with more than four orders of resistance change.

4.4.8.1 Reliability: Device Switching Cycles

The fabricated RF PCM SPST switches demonstrate more than 1 million actuation cycles experimentally without showing any sign of performance degradation or failure. At 250 ms test frequency, testing 1 million cycles took close to 70 hrs. The device was fully functional at the termination of cycle testing. The test setup is limited by test-bench availability and the lifetime of SPDT switches used. Two SPDT switches utilized in the testing are highly reliable and high performance electromechanical RF switches but have standard lifetime of 1 million cycles only. Reliability test was terminated to perform other performance parameter tests on PCM devices. Device lifetime cycles measurement showing over 1 million reliable cycles can be seen in Fig. 4.33.

4.4.8.2 Reliability: State Stability

In this section, reliability of the RF PCM switches is tested for its state stability over time. Latching or non-volatility of the PCM GeTe switches is tested in both ON and OFF-states over a period of 28 hrs. Resistance of the device is recorded by SMU at a rate of 1 Hz. Device resistance change over time is shown in Fig. 4.34. The deviation seen at the middle of the the ON-state resistance is due to the movement of DC probes. Micro movements in DC probes are also due to ground vibrations as the probe station used is not set on a vibration compensation table.

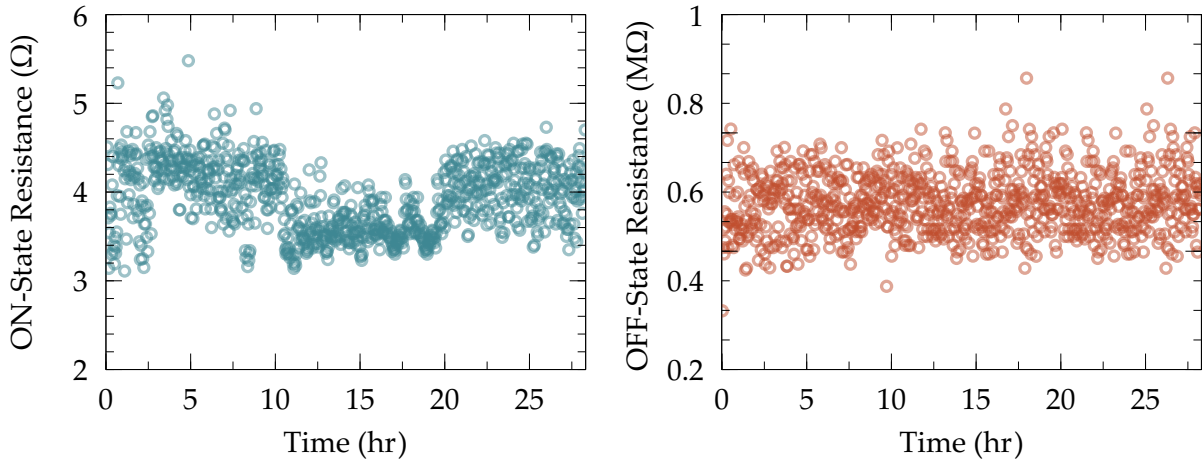


Figure 4.34: Non-volatility or resistance stability measurements over a course of more than 28 hours in ON-state and OFF-state.

4.5 Comparison with State-of-the-Art

It is important to compare the developed technology with the state-of-the-art competition. Most of the commercial switches are available in the form of multi-port configurations. To keep up with the technological advancement, RF PCM GeTe SP3T switches are compared with the commercially available state-of-the-art RF switches developed using several other technologies. The measured S-parameters of the devices used for comparison are taken directly from the manufacturer. PCM GeTe-based SP3T switches are compared with broadband microwave switches developed using RF-MEMS, magnetic relay, GaAs pHEMT and also with mmWave switches developed using SOI-MEMS, Silicon-CMOS, UltraCMOS SOI and GaAs MMIC. Part number of the compared devices are given in the footnotes of Table 4.4. Each of the switches used in comparison in the Table 4.4 has its own performance pros and cons over the others. It depends on the use case scenario or application to decide which performance parameter is the primary selection criteria for the switches.

RF performance of the compared devices in ON and OFF-states is shown in Fig. 4.35 and a summary of the comparison in tabular form is provided in Table 4.4. The RF PCM GeTe switch developed using Gen 3 microfabrication process outshines the competition with its exceptional and best in class insertion loss performance over DC to 67 GHz. It offers smallest die size among the competition, latching based and reasonable switching speed and close to second best power handling capability among the compared devices.

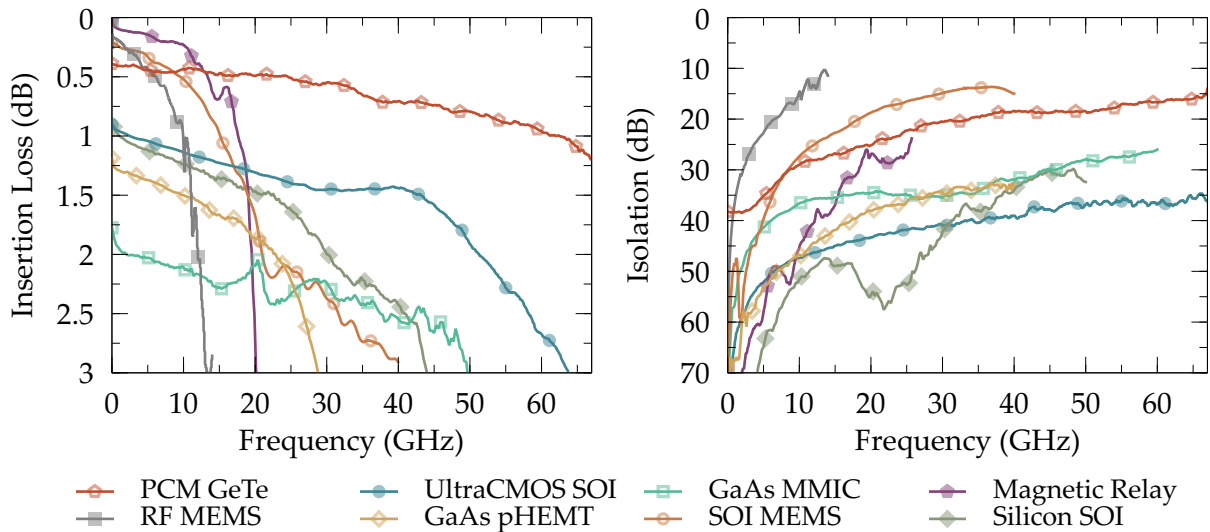


Figure 4.35: Measured insertion loss and isolation performance of current state-of-the-art technologies.

UltraCMOS SOI technology based SPDT switch demonstrates excellent isolation, reasonable insertion loss till 60 GHz, low voltage, but has $15\times$ larger chip area than PCM GeTe SP3T switch.

A commercially available and highly reliable SP4T RF-MEMS switch is compared that guarantees 1 billion switching cycles. This is the only commercially available RF MEMS-based switch with excellent reliability. Commercial RF-MEMS also demonstrate exceptional linearity performance, but only work up to 14 GHz. The compared RF-MEMS switch has power handling capability close to PCM GeTe switches but on the other side has a device size $56\times$ larger than PCM GeTe SP3T switch. Magnetic relay offers great RF performance, latching functionality and outstanding power handling capability among the competition, but works up to 18 GHz only, reliable till 3 million cycles with slowest switching time of 7 ms among the compared devices. Magnetic relay also has the biggest chip/die size, which is $260\times$ larger than PCM GeTe SP3T switches. GaAs MMIC and CMOS are top of the line switches in terms of switching time and control voltage, but lack behind on the RF performance forefront.

Out of all the RF devices compared, each switch technology is unique in some way or the other and also lack in one or more aspects. Switch technology selection choice all comes down to the applications and frequency range. The developed PCM GeTe switches push the boundaries by offering technology which leads in terms of high oper-

Table 4.4: Comparison with the commercially available state-of-the-art RF switches

Technology	Device	Frequency Range (GHz)	Chip/Die Size (mm)	Control Voltage (V)	Switching Time 10–90%
PCM GeTe ^a	SP3T	DC–67	0.6 × 0.6	12 V [†]	1.2 μs
UltraCMOS SOI ^b	SP2T	DC–60	2.5 × 2.2	±3 V	12 ns
GaAs MMIC ^c	SP2T	DC–50	0.98 × 0.75	–5 V	11 ns
Silicon SOI ^d	SP4T	DC–44	3 × 3	±3.3 V	50 ns
SOI RF-MEMS ^e	SPST	DC–40	1.2 × 0.9	8 V	2 ms
GaAs pHEMT ^f	SP2T	DC–20	1.3 × 0.85	–7 V	10 ns
Magnetic Relay ^g	SP2T	DC–18	11 × 8.5	12 V [†]	7 ms
RF-MEMS ^h	SP4T	DC–14	5 × 4	3.6 V	75 μs

Technology	Insertion Loss (dB) at f_{\max}	Isolation (dB) at f_{\max}	Power Handling (dBm)	Linearity IIP3 (dBm)	Lifetime Cycles (Count)
PCM GeTe ^a	1.2	16	35.5	41	>1 M
UltraCMOS SOI ^b	2.8	36	27	48	—
GaAs MMIC ^c	3.0	30	27	40	—
Silicon SOI ^d	3.0	31	27	50	—
SOI RF-MEMS ^e	2.8	14	—	—	—
GaAs pHEMT ^f	1.7	39	25	41	—
Magnetic Relay ^g	1.1	31	44.7 ⁱ	—	3 M
RF-MEMS ^h	3.0	10	36	69	1 B

^a This work, developed *in-house* at the University of Waterloo, Part No. PC3S3T80.

^b pSemi (Previously Peregrine Semiconductors), Part No. PE42525

^c Analog Devices, Inc., Part No. HMC986A

^d Analog Devices, Inc., Part No. ADRF5046

^e Developed *in-house*, Part No. SM1CHV48

^f Analog Devices, Inc., Part No. HMC347B

^g Teledyne Relays, Part No. GRF121

f_{\max} = maximum operation frequency

^h Analog Devices, Inc., Part No. ADGM1304

ⁱ Power handling data is shown of RF100/RF103 device from Teledyne Relays.

[†] Latching operation, thus no steady state power consumption.

* Best, Reasonable and Worst performance parameters are highlighted.

ational frequency, broadband, insertion loss and die size. PCM GeTe technology carries the potential for next generation wireless systems. RF PCM switches discussed in this chapter are monolithically integrated to develop a vast library of RF components as detailed in next chapters.



Chapter 5

Investigation on Transient Heat Distribution in PCM Switches

PCM RF switches operate on melt-quench principle which happens in sub-microsecond regime. PCM GeTe requires more than 725°C melting temperature for few hundred nanoseconds followed by quenching to change the crystal structure of the material to amorphous state. PCM GeTe needs around 450°C to recrystallize from amorphous state. Utilization of embedded micro-heaters to accurately deliver high speed and high temperature heat pulses is unique to chalcogenide material based devices. This chapter reports the design, investigation, and development of ultra high speed embedded micro-heaters for PCM GeTe-based RF switches. Finite element modeling can predict thermal performance close to the real world results, but relies on material thermal constants which are provided by the user. A slight deviation in such constants lead to misleading results. Transient thermal performance of the micro-heaters are experimentally measured using thermoreflectance based transient thermal imaging technique with nanosecond spatial resolution. Heat distribution is investigated to optimize the micro-heaters and RF switches. FEM models are reverse engineered to match with experimental results to accurately predict cross-section thermal performance of RF PCM switches.

High temperature in miniaturized chips is of interest to the development of multi port switches and scaling switch matrices. Thermal actuation crosstalk being the daunting concern for PCM GeTe technology designers, RF PCM switches despite of the requirement of sub-microsecond high temperatures do not show any sign of thermal actuation crosstalk. Thermal crosstalk is studied using FEM and also experimentally proven. Transient thermal imaging also allows investigation of the heat distribution in the thermal cross-section. Some PCM SPST switches are intentionally supplied with more than the

rated actuation voltage to push the thermal limits and get the safe limits for placing PCM switches for complex monolithically integrated systems.

5.1 Thermoreflectance Based Transient Thermal Imaging

Thermoreflectance imaging technique is based on the change in surface reflectivity as a function of material's temperature. The physical mechanism of thermoreflectance with a pump-probe laser source for measuring the thermal properties of a material have temperature dependence of a material's refractive index [89]. The refractive index is temperature dependent due to the distance between atoms, thus with change in temperature, the bandgap of a material varies on a microscopic view resulting in a slight change in material's reflectivity [90, 91].

The relation between the change in material temperature and the change in reflectivity can be computed as a linear approximation when the temperature variation is not large. The amount of the reflectivity changes with the change in temperature, and is called thermoreflectance coefficient C_{th} . Thermoreflectance coefficient is a property of the reflective surface for the incident light wave. C_{th} can be expressed as

$$C_{th}\Delta T = \frac{\Delta R(\lambda)}{R(\lambda)} = \left(\frac{1}{R(\lambda)} \frac{\delta R}{\delta T} \right) \Delta T$$

where, $R(\lambda)$ is the reflection intensity, T is the temperature. C_{th} is the property of a material that is only a function of the illumination wavelength, λ , for a homogeneous surface of a homogeneous material.

The thermoreflectance coefficient, C_{th} is dependent heavily on wavelength which is non-zero for most of the materials over majority of the visible wavelength range. C_{th} need to be calibrated properly to get accurate thermal measurements. A stable calibrated C_{th} when used in conjunction with the hardware setup shown in Fig. 5.1 allows transient thermal measurements with nanosecond spatial resolution [89–92].

5.1.1 Experimental Setup

The thermal imaging experimental setup used for measuring the transient heat distribution in PCM-based RF switches is shown in Fig. 5.1. NT220B high resolution thermal imaging system from Microsanj [90, 93] is used for this experiment. Chip level

calibration tool, piezo-controller to auto calibrate the vibrations at nanometer scale with post-processing spectral analysis modules are used to fully characterize the thermal performance of the PCM based RF switches. Thermal crosstalk is also investigated with the same experimental setup. A scientific grade Si CCD camera is used with $20\times$ objective to get the field of view on the PCM junction. The RF switch (DUT) is mounted on a 3-axis piezo-enabled stage that provide nanometer level vibration compensation. Thermoreflectance technique requires highly sensitive vibration compensation to accurately measure the temperature drift from the captured pixels, the experimental setup is fixed on an actively tuned damped vibration compensation optical table. The sample is held by back-side vacuum suction on the flexure stage mounted on a probe-station. DC probes provide the device excitation pulse (amorphous or crystalline pulse), while a high speed LED driver drives a light source. Due to the dependence of C_{th} on wavelength of the light source, an optimum LED illumination wavelength is chosen that is dependent on the stack of materials on DUT being imaged. An optical bandpass filter, matched with the wavelength of source eliminate background noise from ambient light is used to improve the signal-to-noise ratio. The LED source is pulsed to provide short

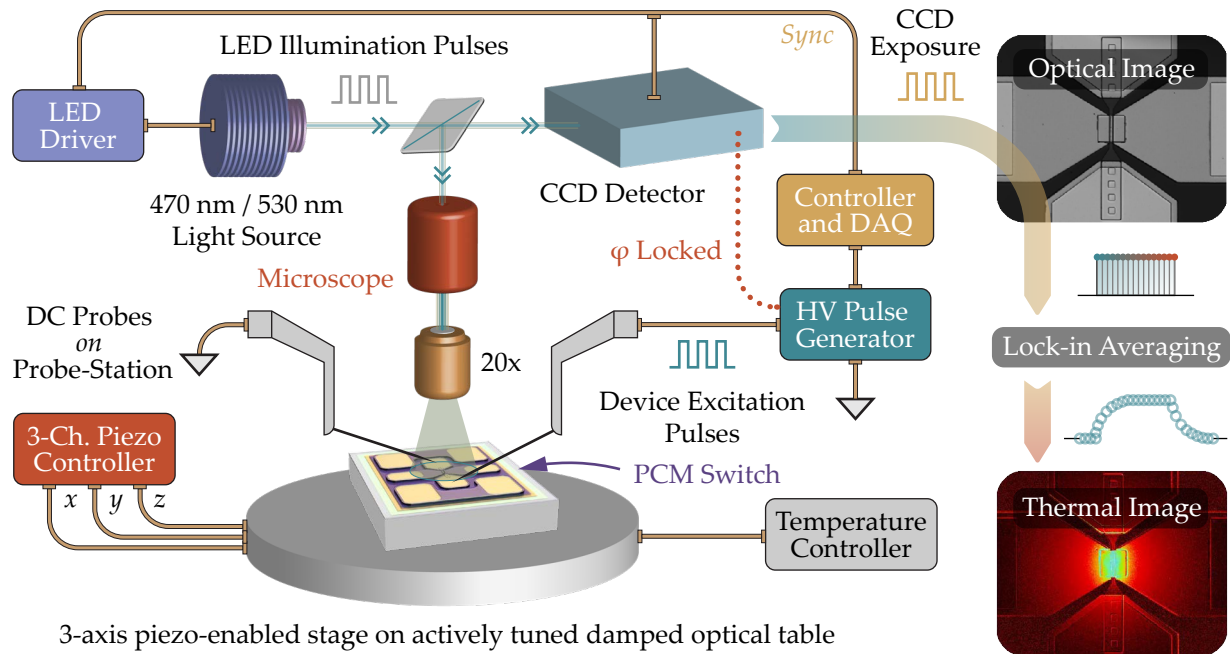


Figure 5.1: Thermoreflectance transient thermal imaging of PCM GeTe-based RF switches highlighting the technique to generate thermal images using lock-in averaged pulses.

sampling pulses of light.

To measure the time dependent temperature response of the switch, precise synchronization of the device actuation pulses, LED pulses and the CCD exposure is required (lock-in signals) which is performed at the system’s timebase electronics. A time series of thermal images can be captured by shifting the delay continuously. Reflection intensity is measured at both the off and on portions of the device actuation cycle, and the difference is taken.

Thermoreflectance technique captures thermal images directly in the time domain with time resolution as low as 100 ns which is required to capture thermal response of the PCM switches. Transient temperature measurements and thermal images are generated synchronization of time averaged device excitation pulses, LED pulses and CCD exposure as shown in Fig. 5.2. Time-resolved imaging data is collected by pulsing the device excitation pulses (actuation pulses) along with LED illumination pulses at a controllable time delay [90, 91]. Fig 5.2 highlights the collection of $t = 0$ data point. Inter-locking transient imaging method allows acquiring the temperature data points by shifting the timing delay each cycle to achieve a time resolution. Time resolution is limited by the equipment’s capability of pulsing the LED probe light as tightly as possible. To generate a transient thermoreflectance image, a reference CCD exposed image with LED illumina-

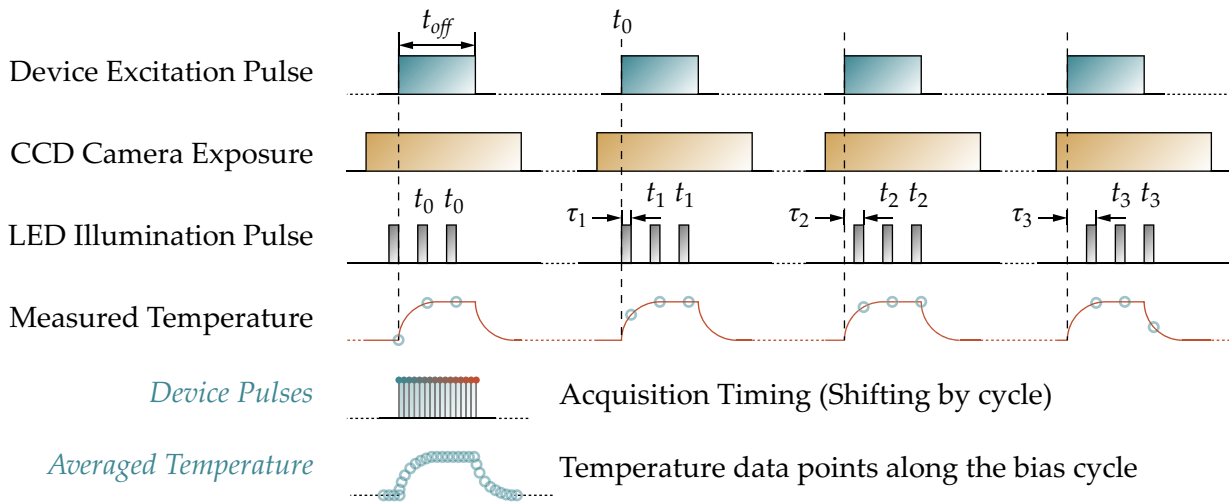


Figure 5.2: Timing diagram of time-resolved imaging data acquisition by pulsing the device excitation and LED illumination pulses at a controllable relative time delay. Timing diagram highlights the acquisition of $t = 0$ data point. Temperature data points are acquired by shifting the timing delay.

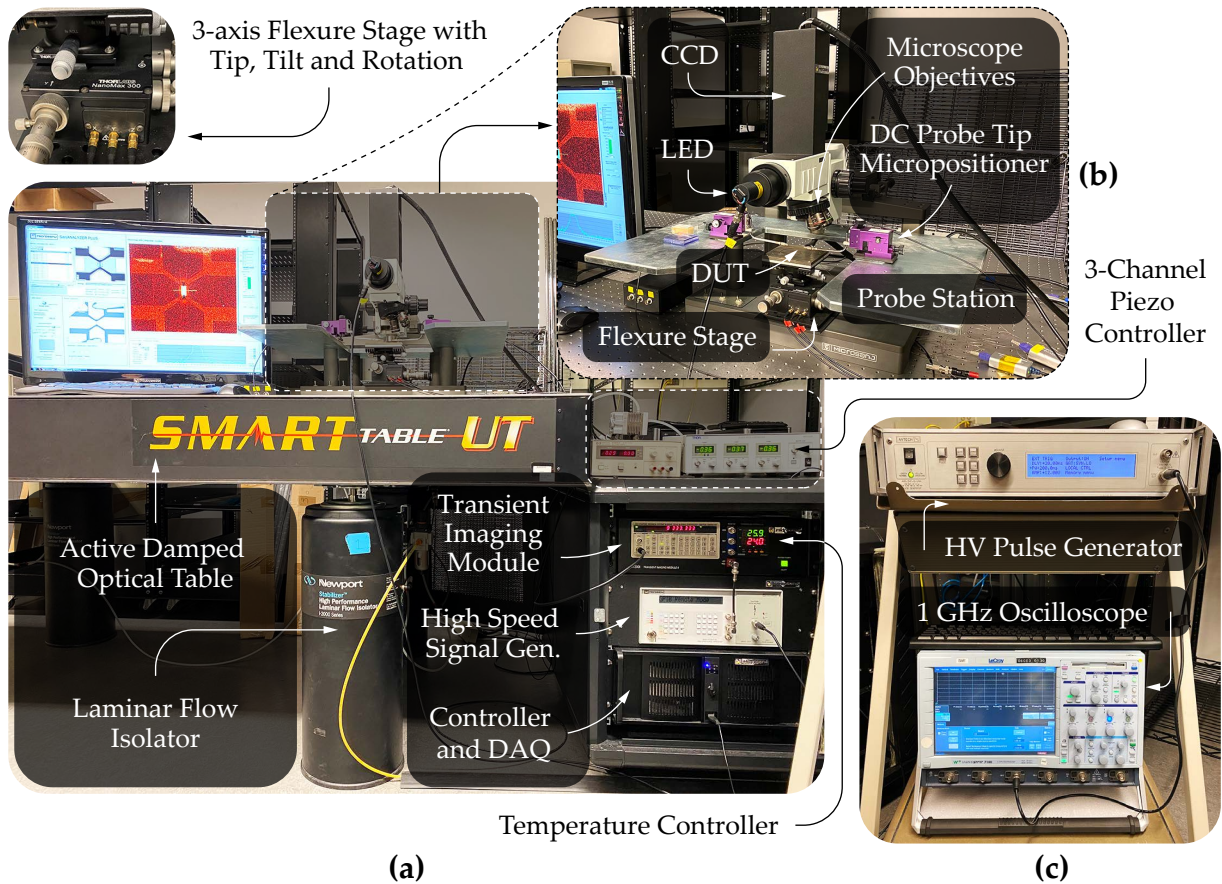


Figure 5.3: Photograph of: (a) thermoreflectance based transient thermal imaging experimental setup, (b) close-up view of probe-station and flexure stage, and (c) pulse generator and oscilloscope.

nation pulse delay $t = 0$ is collected, followed by $t > 0$ CCD image. A subpixel image registration algorithm is applied to a subset of the CCD images to align the $t > 0$ to the reference followed by subtracting the registered $t > 0$ images from the $t = 0$ reference. In-depth detail on the acquisition procedure is given by Microsanj LLC [90, 92–94]. Repeated and averaged measurements are taken to ensure accuracy of the data. Thermal measurements test setup photograph is shown in Fig. 5.3 (a) by highlighting equipment and components depicted in Fig. 5.1. Fig. 5.3 (b) shows the close-up view of the probe-station, and Fig. 5.3 (c) depicts the photograph of HV pulse generator and oscilloscope. Transient imaging module shown in Fig. 5.3 (a) has an in-built pulse generator, but due to the restriction on amplitude, a custom pulse generator is used to provide excitation

pulses.

5.2 High Speed Refractory Micro-Heaters

The melt-quench sequence to change the material’s resistance state can be achieved by either directly heating the PCM GeTe material without using any localized and isolated micro-heater or by providing the required temperature through an embedded micro-heater. RF signal should be isolated from DC signals. For some applications, SPST switches can take advantage of external decoupling of DC from RF, but in most of the cases it is not a practical implementation approach. Bias signal should be isolated when multi-port complex RF devices are designed. Micro-heaters are developed for PCM GeTe switches that can provide the adequate temperatures required for melt-quench sequence. Primarily the thin-film resistive micro-heaters should be designed with a material that can withstand more than 1000 °C repeated actuation cycles. Nichrome, tungsten or molybdenum are potential candidates with high melting point.

The RF PCM GeTe switches have critical design parameters that radically affect the RF performance. Micro-heaters add significant capacitive coupling in the RF signal line as discussed in chapter 4. RF electrodes need to cover the width of the heater to avoid

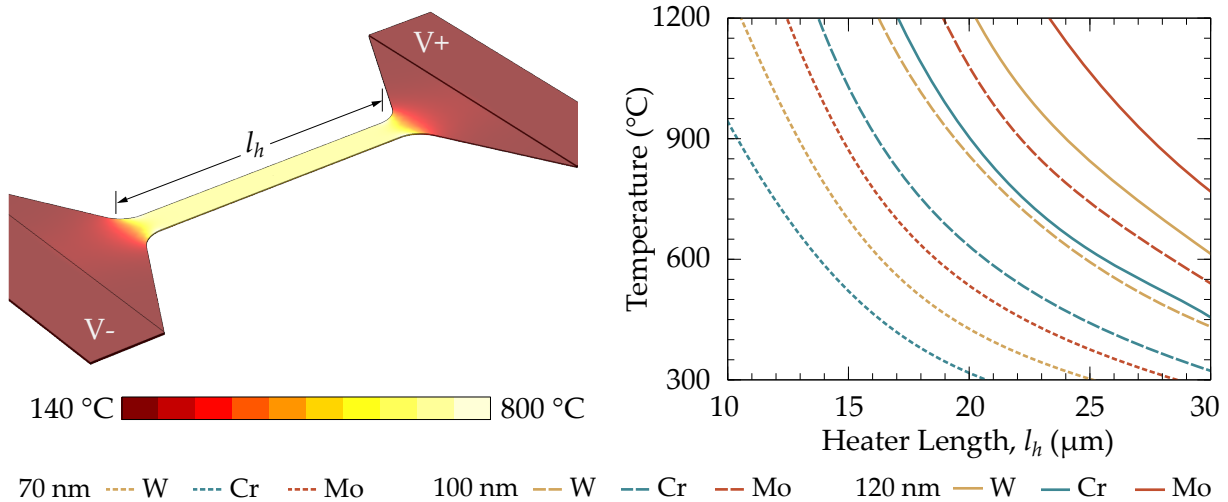


Figure 5.4: (Left) FEM simulations of micro-heater highlighting actuation terminals and heated region of the heater. (Right) Change in temperature with various heater lengths for different materials and thickness.

edge cracks in the PCM as discussed in section 3.12. Thermal performance of the high speed micro-heaters depends largely on the design dimensions, length of the heater (l_h) and width of the heater (w_h) as well as on the thickness of thin-film and material used for the heaters. Initial RF PCM switches were designed using NiCr micro-heaters, but during material characterization, tungsten micro-heaters were developed in subsequent microfabrication processes. Tungsten being the refractory metal is resistant to heat and wear. Tungsten also has the highest melting point $>3400^\circ\text{C}$ and the highest boiling point $>5900^\circ\text{C}$ of all the elements discovered which makes this material perfect for providing thermal actuation pulses.

Sputtered tungsten films show spring-coil stresses in a couple of initial samples as discussed in section 3.10. Optimized deposition conditions allow forming stress free sputtered tungsten thin-films for Gen 2 and Gen 3 microfabrication processes. It is well known that material properties of thin-films are far off from the bulk properties and they depend heavily on the deposition conditions and the source of deposition. FEM modeling can accurately predict the thermal performance, but it requires thermal properties and heat coefficients of the material stack, which needs to be measured to get reasonable thermal performance prediction. Experimental transient thermal imaging is used to investigate the accurate temperature profile for the development of reliable RF PCM switches.

5.3 Transient Thermal Imaging of Micro-Heaters

Thermoreflectance transient thermal imaging technique is used to experimentally analyze the heat distribution across the fabricated micro-heaters. Thermal performance is analyzed using light source wavelength 530 nm. A CCD micrograph of the heater probes at both the positive and negative end is shown in Fig. 5.5. Transient thermal images are captured at every 25 ns intervals. Thermal images are shown for the same applied pulse width 200 ns and two different pulse amplitudes 8 V, 12 V. Later, a wider 500 ns pulse is applied with 15 V amplitude to the same heater. Pulse amplitude 12 V generates 763°C which is sufficient to melt the material. Temperature drops quickly to less than 200°C within 50 ns at the end of 200 ns pulse as shown in Fig. 5.5. Under-powered pulse with 8 V amplitude generates only 482°C temperature, while an over-powered wider pulse of 15 V generates high temperature leading to heater breakage as shown in Fig. 5.9. Burnt and cooldown phase of the damaged heater is captured at 50 ns intervals after the damage as shown in Fig. 5.5.

Thermoreflectance technique requires careful calibration of C_{th} coefficient and after

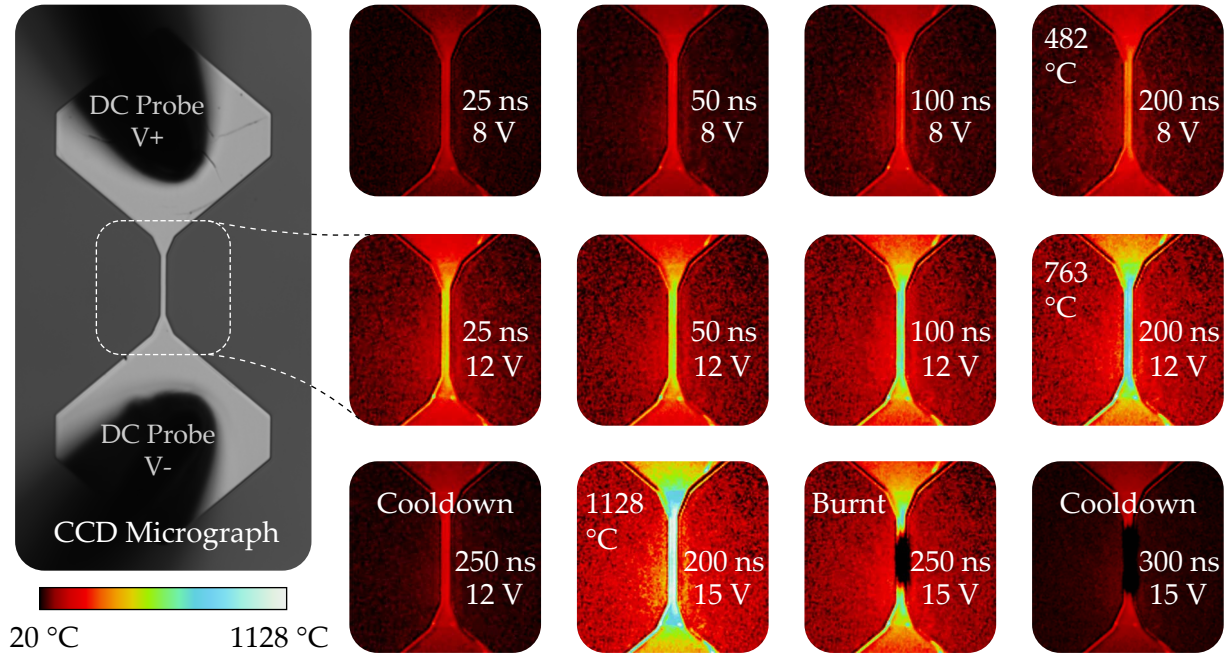


Figure 5.5: Transient thermal imaging of fabricated tungsten micro-heaters on sapphire substrate. (Left) CCD micrograph and DC probes, (Right) Heat distribution in micro-heater at different time intervals with the application of 200 ns pulse width and change in pulse amplitude. 12 V, 200 ns pulse shows sufficient temperature to melt the PCM GeTe, while 15 V, 500 ns pulse damages the heater.

calibration, if the material thickness or stack has not been altered in any way, same C_{th} coefficient can be used for repeated measurements between wafers. Infrared thermal imaging is not a suitable technique to evaluate high speed thermal performance as required for PCM switches. Thermoreflectance provides nanosecond spatial resolution which is perfect to evaluate the thermal performance of the micro-heaters. Experimental results are mapped with multi-physics FEM models to get accurate simulation results and to speed up further designs and analysis of full 3D PCM switch.

Heat-distribution across the width and length of the micro-heaters is evaluated as shown in Fig. 5.6. The micro-heaters when stimulated using 12 V, 200 ns pulse, can generate more than 750 °C. Temperature drops near the edges across the width of the heater (w_h) as plotted across the cross-section A-A' while equally distributed across the length of the heater (l_h) as shown across the cross-section B-B' in Fig. 5.6(a) and 5.6(b) respectively. This clearly shows that the width of the heater should be wider than the PCM

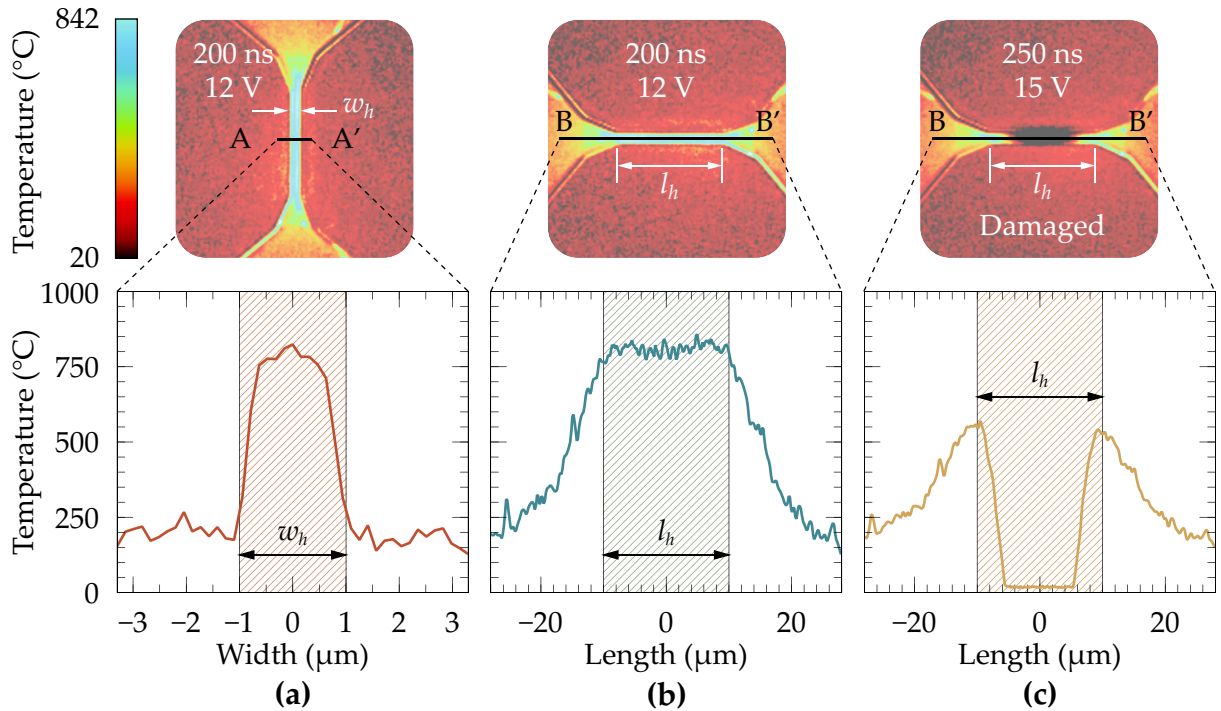


Figure 5.6: Heat distribution across micro-heater surface: (a) Cross-section profile across the width of the heater using amorphous pulse, (b) Cross-section profile across the length of the heater using amorphous pulse, and (c) Cross-section profile across the length of the heater captured at 250 ns with the stimulus of 15 V, 200 ns pulse.

channel length (l_s). Excessive voltage provided to the heater leads to damage from the middle as shown across the cross-section B–B’ in Fig. 5.6(c). Thermal cross-section profiles are captured right before the cooldown stage, while the damaged heater profile is captured 50 ns after the breakage when supplied with 200 ns 15 V pulse. The breakage occurs somewhere between 225 ns to 250 ns regime, which can not be captured as it is out of the spatial resolution limits of the equipment.

A single layer tungsten micro-heaters of certain length, width and thickness fabricated on the sapphire wafer provides expected thermal performance, but for the heaters to be used in PCM switches, it requires careful calibration and analysis of heat distribution due to the use of multiple thin-film layers. Full 3D model transient simulation is carried out on the PCM switch as discussed in the subsequent sections.

5.4 Transient Thermal 3D Multiphysics Modeling of PCM Switches

A 3D FEM multiphysics model is developed to optimize the thermal balance and heat flow in the RF PCM switches. Quenching is extremely important in PCM GeTe switches, thus thermal performance of the chosen dielectrics should push the heat into the PCM and helps sink the heat out as quickly as possible. Thinner thermally conductive dielectric layer like silicon nitride (SiN_x) between micro-heater and PCM GeTe can adequately transfer heat to the PCM, but generates parasitic capacitance. Slightly thicker dielectric material can reduce the capacitance but does not source/sink adequate heat to the PCM. A more robust thermally conductive dielectric material alumina nitride (AlN) is an excellent choice. Reasonably thick AlN can source heat to the PCM without generating significant capacitance. Most of the material properties are extracted experimentally to get thermal coefficients that are used in FEM modeling for improving the accuracy of the simulations.

Transient heat distribution in PCM GeTe switches is studied using 3D multiphysics modeling as shown in Fig. 5.7. Photograph of a fabricated PCM SPST switch die/chip developed using Gen 3 microfabrication process on a tip of a finger is shown in Fig. 5.7(a). A quarter 3D FEM model is studied due to its symmetrical nature. Symmetry planes and a quarter 3D model used for transient thermal simulations is shown in Fig. 5.7(b) and Fig. 5.7(c) respectively. An optical micrograph of the PCM SPST switch is shown in Fig. 5.7(d). An amorphous pulse of 12 V amplitude, 200 ns width is used as a stimulus to the FEM model. A delay of $t=20$ ns is added to capture any mid rise time transients. Heat distribution at $t=195$ ns is shown in a 2D cross-section of the material stack depicted in Fig. 5.7(f). An inset in Fig. 5.7(g) shows a close-up view of the PCM junction spliced across the symmetry planes representing the 3D rendered view to visualize different thin-film materials.

Melt-quench sequence at the PCM switch junction is captured after every 5 ns intervals. Fig. 5.7(h) shows heat distribution in PCM switch at various time intervals. At $t=195$ ns, maximum temperature is sourced to the PCM following the quench stage, where the temperature sinks towards to top of the switch. Thermals in the PCM junction are balanced by using appropriate thermally insulator or conductive dielectric layers. Appropriate thickness of substrate insulator and barrier layer helps directing the heat flow towards the PCM rather than sinking all the heat into substrate or not sinking any heat at all. Dielectric layer deposition methods and properties dictate the reliability of PCM switches. PCM switches are passivated using oxide layer to avoid any material

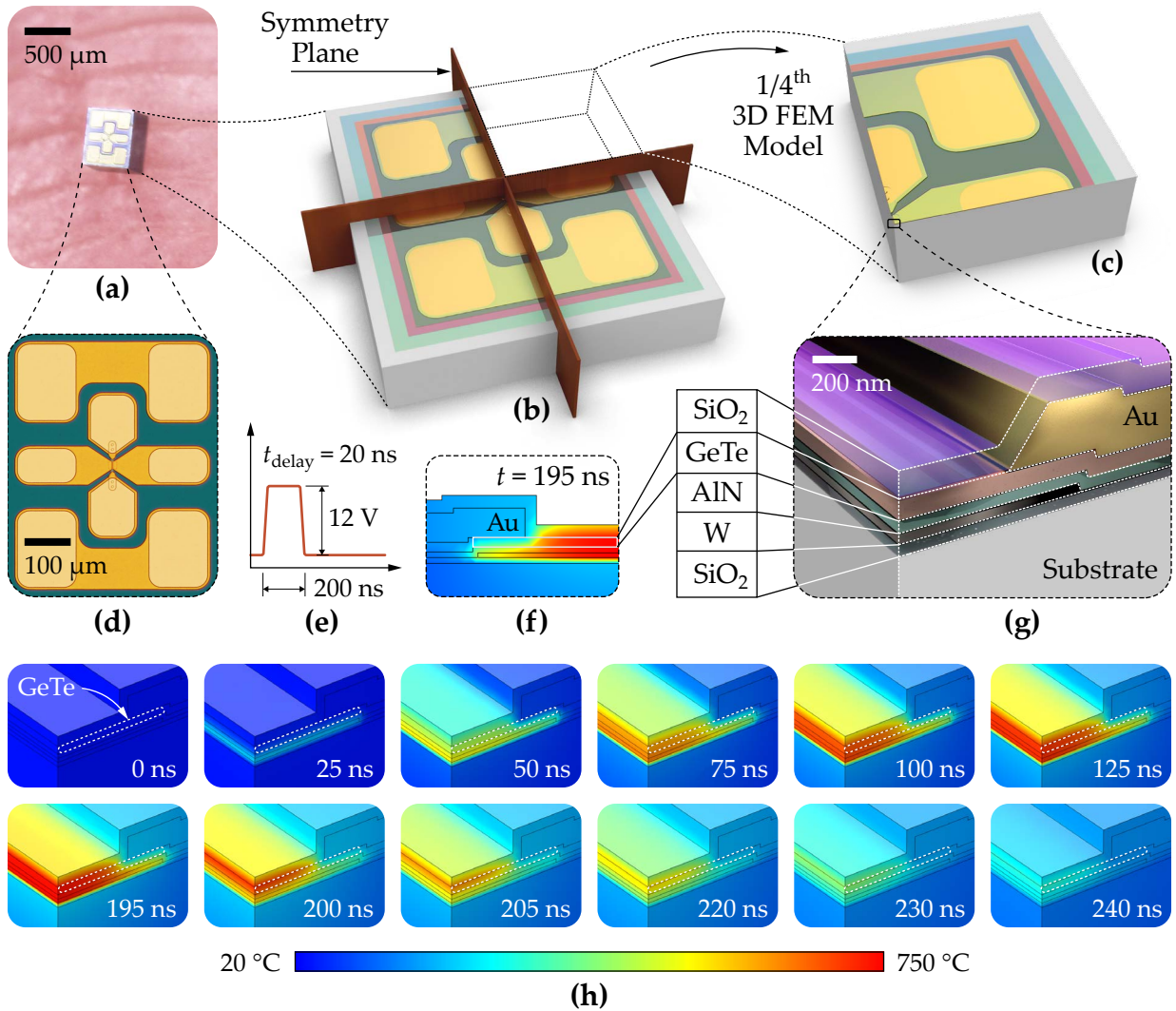


Figure 5.7: Transient heat distribution using FEM modeling of RF PCM SPST switch: (a) Photograph of a fabricated RF PCM SPST switch die/chip on tip of a finger, (b) 3D rendered model of the RF PCM SPST switch with two symmetry planes, (c) Quarter symmetrical 3D model for FEM modeling the heat distribution in the PCM junction. (d) Optical micrograph of the RF PCM SPST switch fabricated using Gen 3 microfabrication process, (e) Amorphous pulse shape applied for FEM transient analysis, (f) 2D cross-section of the quarter model showing heat distribution at $t=195$ ns, (g) 3D rendered model highlighting thin-film stacks equivalent of Gen 3 microfabrication process, and (h) Transient heat distribution in 3D FEM model of the PCM switch at different time intervals with the application of a single amorphous pulse. Temperature starts rising after $t=20$ ns delay and reached its maximum value at $t=195$ ns before quenching.

degradation due to melt-quench sequence.

Change in temperature distribution over time is plotted for both amorphous and crystalline phase change case with the application of appropriate pulse. Heat distribution in the material stack across the z -axis and x -axis of the FEM model is also studied as shown in Fig. 5.8. A quarter 3D model of the RF PCM switch is shown with 3D coordinates and materials. Temperature change is monitored at the mid point on the surface of PCM and micro-heater for the amorphous pulse (12 V, 200 ns pulse) and crystalline pulse (8 V, 1.2 μ s pulse) case as depicted in Fig. 5.8. Amorphous pulse generates more than 750 °C temperature at the mid section of the PCM junction. Temperature reached to the surface of the PCM GeTe with a slight delay of 20 ns due to the use of sandwiched barrier layer in between. During the fall time of the applied pulse, temperature drops instantly to less than 400 °C right after 20 ns of amorphous pulse width. Quenching in PCM switches is important to make sure the material does not recrystallize at the end of amorphous pulse. If the heat does not sink efficiently and quickly, switching the PCM from crystalline to amorphous would require high pulse power, which ultimately does not offer reliable operation. This phenomenon has been observed in some of the initial prototype switches, in which the switch actuated for only few cycles and catastrophically damaged thereafter due to the retention of heat at the PCM junction.

Applying the crystalline pulse stabilizes the required temperature for recrystallization of PCM GeTe. The pulse conditions mentioned provide reliable reversible switching operation. Heat distribution across the vertical cross-section A–A' and B–B' is shown in Fig. 5.8. A–A' and B–B' cross-sections are 1.2 μ m apart. A–A' cross-section is across z -axis ($x=0$ μ m, $y=0$ μ m, $z=-100$ μ m to 400 μ m), while the cross-section B–B' is plotted 1.2 μ m apart across z -axis ($x=1.2$ μ m, $y=0$ μ m, $z=-100$ μ m to 400 μ m). Corresponding temperature at the cross-sections are shown in Fig. 5.8 for amorphous pulse and crystalline pulse cases. There is close to 250 °C temperature difference in micro-heater between A–A' and B–B'. At $t=195$ ns, there is negligible temperature gradient from micro-heater to PCM surface temperature across A–A'. However, there is a large temperature gradient in PCM GeTe across B–B' which is mainly caused by gold metal electrode on top of PCM. Slightly thicker metal layer is deposited to minimized RF losses, but it acts as a heat sink and takes out most of the heat from the PCM leads to a large gradient across the thickness of PCM. Similar temperature gradient can be seen in crystalline case, where metal electrode on top of PCM acts as a heat sink dropping the temperature across the thickness of PCM GeTe. Substrate region, heater thickness and PCM thickness is highlighted in cross-section plots as shown in Fig. 5.8 to clarify thickness of all the materials.

Apart from the metal electrodes acting as heat sink to generate temperature gradient, micro-heaters also do not provide sufficient heat near the edges across the width.

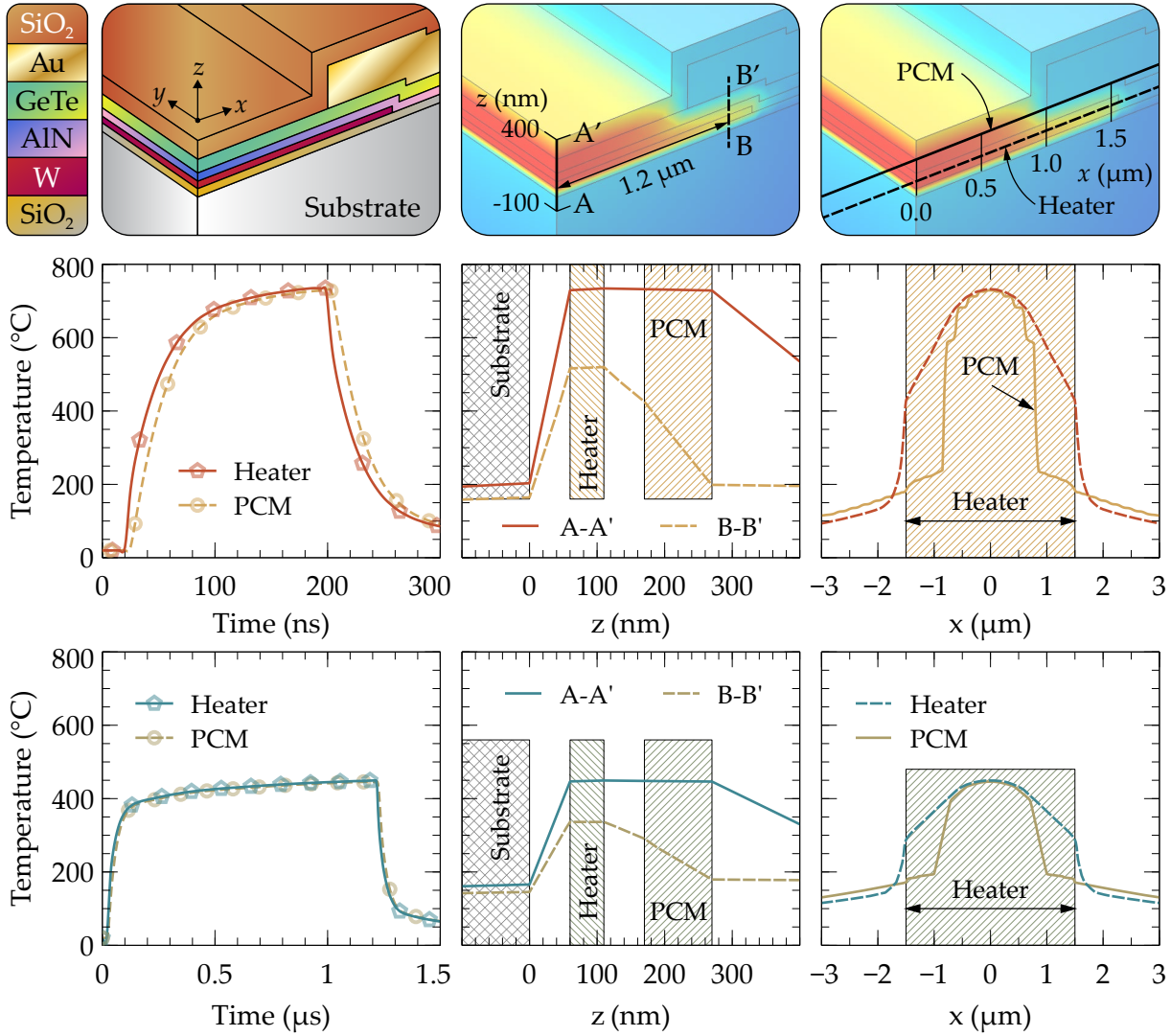


Figure 5.8: (Top left) Quarter 3D model of the RF PCM SPST switch highlighting the 3D space coordinates, (Top mid) Cross-sections of vertical profiles along z-axis, A–A’ is at the centre of the model while B–B’ is at 1.2 μm apart under the RF electrodes, (Top right) Horizontal cross-sections along x-axis, solid line for PCM GeTe and dashed line for micro-heater. Change in temperature over time on the surface of PCM GeTe and micro-heater is plotted using amorphous pulse and crystalline pulse. Corresponding plots show temperature across z-axis and x-axis of the FEM model cross-sections. z-axis and x-axis cross-sections are plotted at $t=195$ ns with amorphous pulse stimulus, and at $t=1.2$ μs with crystalline pulse application. Temperature drops significantly at B–B’ as a slightly thicker gold metal layer acts as a heat sink.

Temperature drops across the width of micro-heaters as shown the x -axis cross-sections in Fig. 5.8. Temperature distribution is studied over the surface of PCM and across the width of micro-heater across x -axis ($x = -3 \mu\text{m}$ to $3 \mu\text{m}$, $y = 0 \mu\text{m}$, $z = 0.1 \mu\text{m}$ across micro-heater and $z = 0.26 \mu\text{m}$ across PCM surface). Temperature drops across the width of the micro-heater can also be seen in the experimental measurements as shown in Fig. 5.6(a). Sudden temperature drops in the PCM cross-section is due to metal electrode, which starts exactly from $x = -1 \mu\text{m}$ towards negative side and $x = 1 \mu\text{m}$ towards the positive side of the model. Heater width (w_h) is highlighted using cross-hatch in Fig. 5.8.

5.5 Experimental Investigation of Thermal Crosstalk

Heat distribution studied using FEM model is experimentally validated using transient thermal imaging. Various multi-port miniaturized monolithically integrated complex RF components require a number of switches to be integrated very close to each other. PCM technology allows very tight integration of switches due to the smaller size of switches compared to other technologies. One of the daunting concern that designers can think of is the thermal crosstalk in PCM switches. Thermal crosstalk has not been investigated for PCM technology till date. Due to such high temperature required for PCM switch actuation, a common question arises if the temperature generated to actuate a PCM switch can also actuate closely placed PCM switches!

Experimental investigation of thermal actuation crosstalk using transient thermal imaging proves no actuation crosstalk. It also provide safe limits to closely integrate PCM switches monolithically. Thermorefectance coefficient C_{th} is calibrated and tested on known standards to make sure the reliability of the calibration. Transient thermal imaging of the fabricated RF PCM switch for investigating thermal crosstalk is shown in Fig. 5.9. A CCD micrograph at $20\times$ objective is shown in Fig. 5.9(a) highlighting landed DC probes on micro-heater terminals to provide actuation pulse and also showing RF input and output ports. PCM junction is marked as region of interest. Fig. 5.9(b) shows the heat distribution in a thermal image when single over-powered 15 V , $2 \mu\text{s}$ pulse is applied across micro-heater terminals.

Thermal images of the PCM switch junction are captured at different time intervals while applying a 12 V , 200 ns pulse with 5 ns rise/fall time. Melt sequence completes at $t = 200 \text{ ns}$ followed by quench and cool-down sequence from at $t = 200 \text{ ns}$ onwards. A CCD micrograph merged with temperature at $t = 200 \text{ ns}$ is also shown in Fig. 5.9(c). Thermal images are captured at 20 ns time internals. A melt sequence is observed till $t = 200 \text{ ns}$. By $t = 350 \text{ ns}$, the switch has already completed cool-down phase and the temperature at

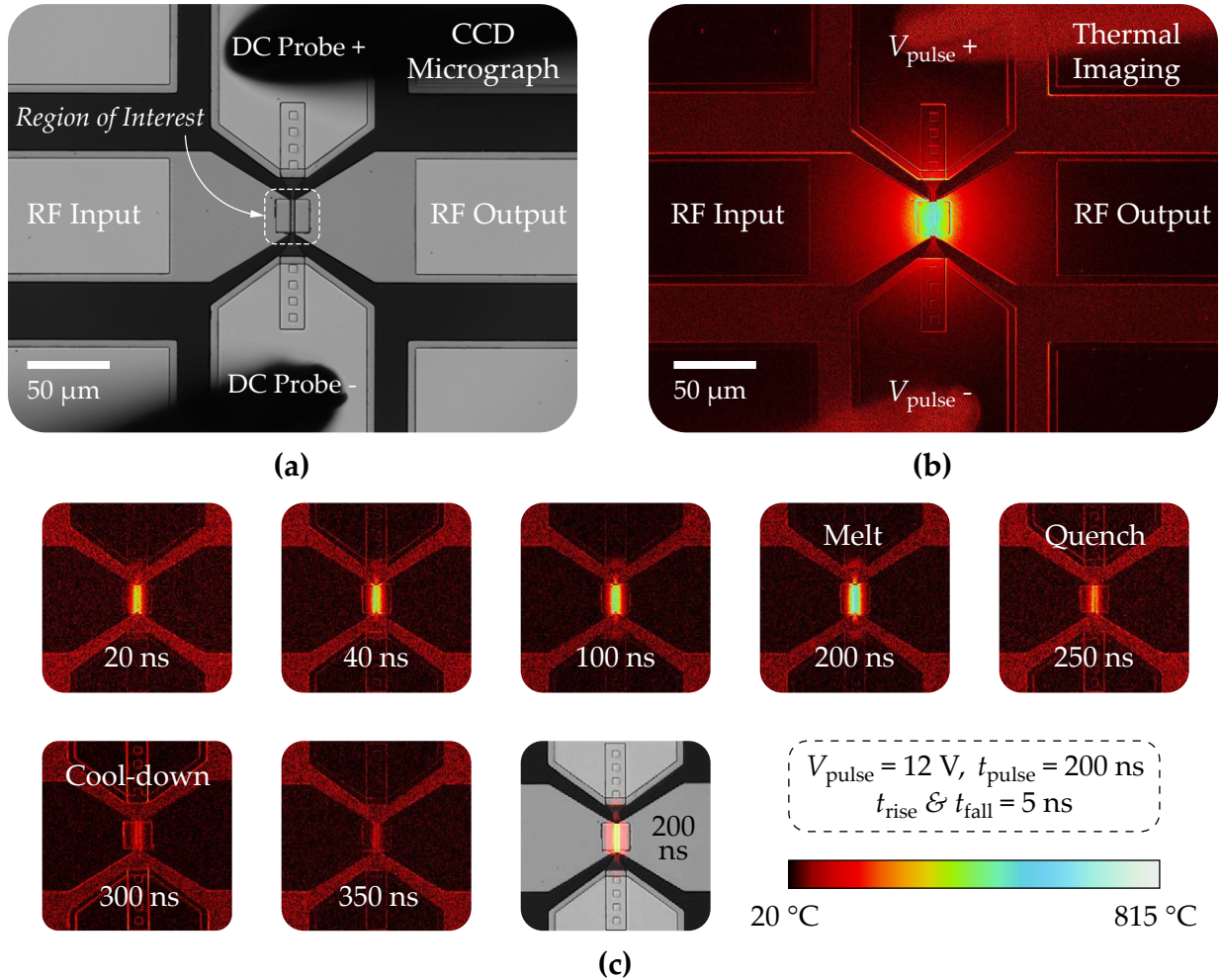


Figure 5.9: Transient thermal imaging of RF PCM SPST switch for investigating thermal crosstalk: (a) CCD micrograph showing the region of interest, DC probes and RF ports, (b). Thermal image of the switch captured at $t=200$ ns on the application of a 15 V, 2 μ s pulse. (c) Thermal images of the switch captured at different time intervals with the stimulus of pulse conditions mentioned above the temperature scale. Melt sequence completes at $t=200$ ns followed by quench and cool-down sequence from at $t=200$ ns onwards. A CCD micrograph merged with temperature at $t=200$ ns is also shown.

the junction drops below 50 °C. A CCD micrograph is merged with thermal image at $t=200$ ns for better readability in Fig. 5.9(c).

3D plots of transient thermal imaging measurements of the RF PCM switch at differ-

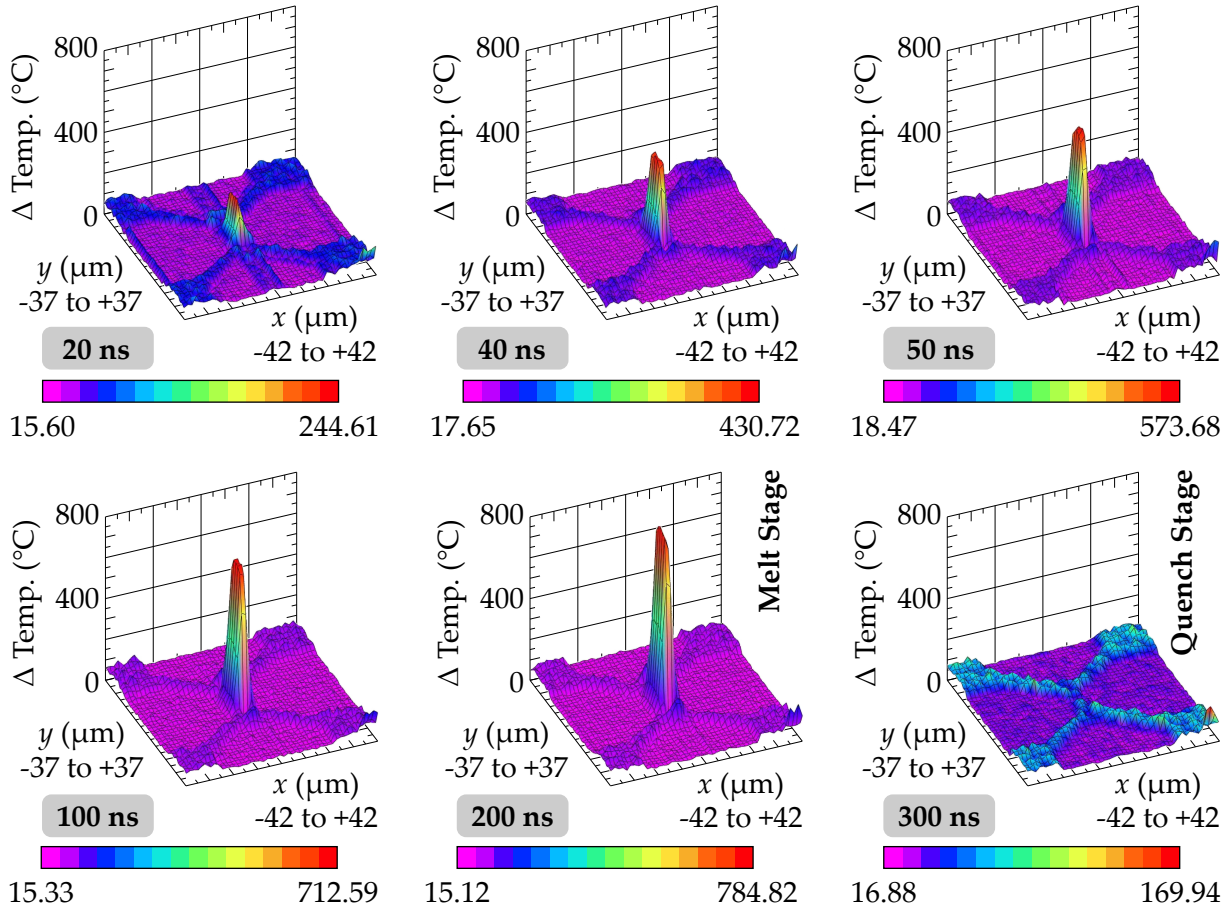


Figure 5.10: Experimental 3D transient thermal imaging measurements of the RF PCM SPST switch at different time intervals showing melt-quench action with the application of a single 12 V, 200 ns pulse. Maximum temperature is recorded at $t=200$ ns, followed by a quick cool-down phase shown at $t=300$ ns. Temperature scale is different for each image.

ent time intervals showing melt-quench sequence with the application of a single amorphous pulse is shown in Fig. 5.10. Maximum temperature is observed at $t=200$ ns followed by cool-down phase. It should be noted that the temperature scale is different for each plot. The 3D plots shown in Fig. 5.10 represent the same thermal measurements given in Fig. 5.9.

To investigate the thermal cross-section in PCM switches, heat profiles are measured across 300 μm A–A' cross-section of the RF PCM switch as shown in Fig. 5.11. T_c is the recrystallization temperature and T_a is amorphization temperature. With a crystalline

actuation pulse (8 V, 1.2 μ s), heat distribution across the A–A' cross-section is measured at $t=1.2 \mu$ s. No thermal crosstalk or any hot-spots are observed across 300 μ m length. Temperature rises past T_c within 7 μ m length and is less than 200 $^{\circ}$ C within 14 μ m around the junction. Metal electrodes sink the temperature, thus heat is extremely localized and confined within 15 μ m junction surface area as shown in Fig. 5.11(a). Amorphous pulse (12 V, 200 ns) is applied across micro-heater terminal and across A–A' cross-section, no thermal hot-spots or crosstalk is observed. Across 300 μ m, temperature above T_a is confined to 5 μ m junction area and is below 200 $^{\circ}$ C within 16 μ m region. With the amorphous and crystalline pulses, temperature is localized to 20 μ m area of the PCM junction and is below safe limits of 50 $^{\circ}$ C as shown in Fig. 5.11(b).

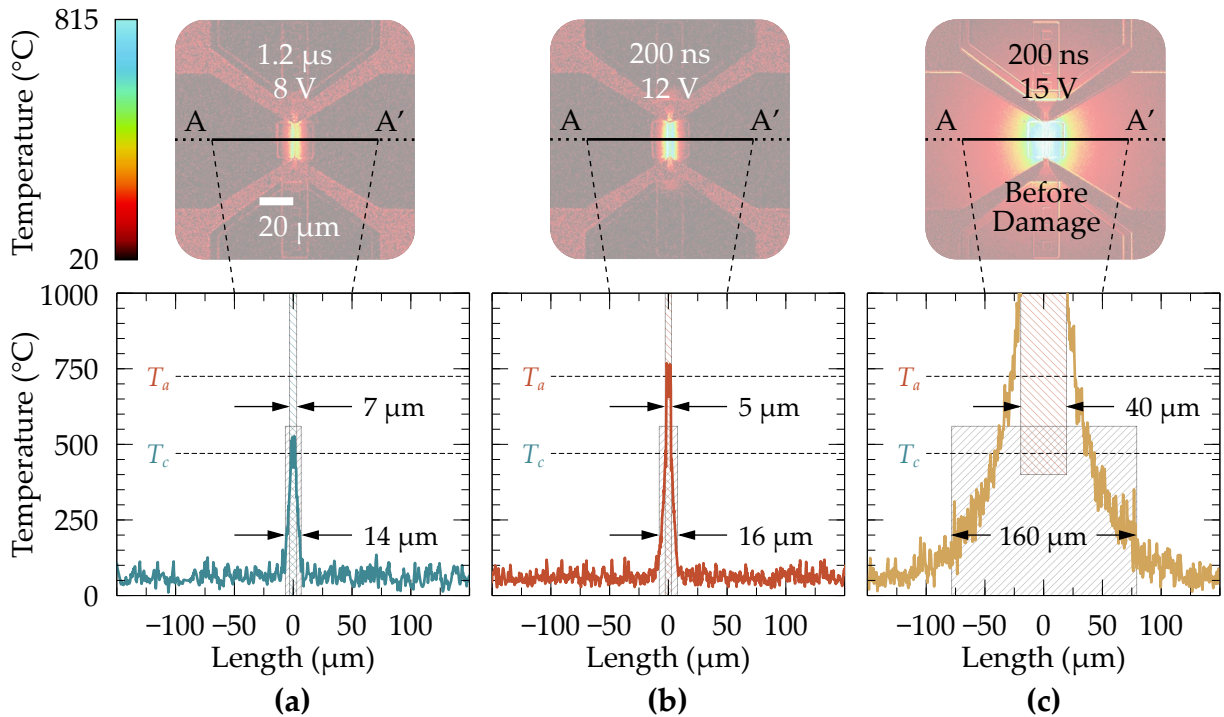


Figure 5.11: Heat distribution across 300 μ m A–A' cross-section of the RF PCM switch to study thermal crosstalk: (a) A crystalline pulse of amplitude 8 V and 1.2 μ s width generates sufficient heat (T_c) to crystalline the PCM switch. (b) An amorphous pulse of amplitude 12 V and 200 ns width generates temperature (T_a) to melt the PCM GeTe. No thermal crosstalk is seen in (a) and (b). (c) A 15 V amplitude and 2 μ s wide pulse is supplied to the heater which is beyond its rated actuation limits. Thermal image is captured just before the switch breakdown showing crosstalk across 80 μ m width.

It is interesting to study the thermal crosstalk and safe integration limits if by any means a high-power pulse (either high amplitude or wider pulse) is accidentally supplied to the switch. A voltage pulse of 15 V amplitude and 2 μs width which is beyond the rated specifications, is applied which leads to catastrophic non-reversible damage to the PCM switch. Thermal image is captured at $t=200$ ns right before the start of degradation of the switch. Excessive heat is generated which completely melts the PCM for a long duration and ultimately damaging the micro-heater as shown in Fig. 5.11(c). Heat profile is plotted across A–A' cross-section over 300 μm length showing 40 μm region with >1000 $^{\circ}\text{C}$ temperature, 50 μm region with temperature beyond T_a limit, 90 μm area with temperature above T_c and 160 μm region with temperature above 200 $^{\circ}\text{C}$. Temperature drops below 50 $^{\circ}\text{C}$ beyond 250 μm area. This clearly shows that if accidentally a high power pulse is supplied to one of the many PCM switches integrated closely, it turns into amorphous stage within 50 μm limits, changes to crystalline state within 90 μm periphery with signs of signal leakage due to slight change in resistance within 160 μm region.

For the rated bias signature, RF PCM switches can be integrated as close as a distance of 20 μm . If miniaturization is not the primary design criteria, switches should be placed at least 200 μm apart as ultimate safe limits.

5.6 Post Pulsing Failure Investigation

Thermal crosstalk in PCM switches becomes prominent only if more than rated bias signature is supplied to the switches. With a stimulus of a 15 V, 2 μs wide pulse with 10 ns rise and fall time, temperatures close to the melting point of refractory tungsten is observed damaging PCM junction and the heater as shown in Fig. 5.12. A 3D plot of measured surface heat distribution across PCM switch junction is shown in Fig. 5.12(a). Thermal images shown in Fig. 5.12(b) are captured at 50 ns intervals. Switch degradation can be seen at the middle part of the junction at $t=250$ ns. At $t=250$ ns it is not clear whether the degradation occurs only in PCM or both PCM and micro-heater. Although a 2 μs wide pulse is applied, if only the PCM GeTe has melted, then heat distribution should propagate till the end of the pulse width, instead, starting at $t=300$ ns in Fig. 5.12(b), the damage becomes prominent that the micro-heater failed which led to a sharp drop in temperature. Metal electrodes acts as a heat sink that speed up the cool-down phase. Starting at $t=400$ ns, the temperature across PCM junction drops below 500 $^{\circ}\text{C}$ equivalent to the temperature scale shown in Fig. 5.12(b). The RF PCM switch is catastrophically damaged when more than rated bias signature is provided.

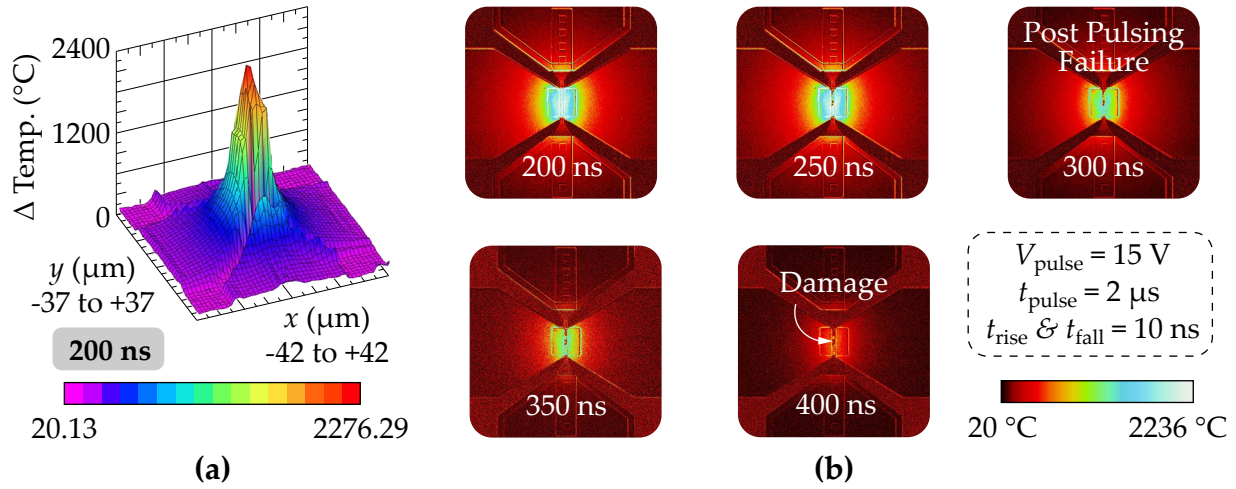


Figure 5.12: Experimental post pulsing failure investigation in RF PCM switches if excessive power is delivered to the via beyond specified pulse characteristics. (a) 3D plot showing heat distribution across PCM junction region with the maximum temperature of greater than 2000 $^\circ\text{C}$ before damage. (b) Thermal images of PCM switch at different time intervals. Damage starts within few nanoseconds right after applying 15 V, 2 μs wide pulse.

5.6.1 Thermal Balance in PCM Switches

Initial prototype PCM switches exhibited similar failures, which motivated this study to investigate this thermal analysis experimentally. After fabrication, depending on the material thickness, properties and deposition conditions, it is extremely important to carefully characterize the PCM switches. It is utmost important to thermally balance the PCM switch junction such that the heat flow sources desired T_a or T_c temperatures and properly sinks the heat at quenching. Failure to meet any one of the stated conditions lead to either no resistance change or switch failure. The margin between benchmarking successful switch cycling falls between following condition of heat flow:

- Ideal condition (proper sourcing and proper sinking)
- No resistance change (under sourcing or over sinking)
- No resistance change (proper sourcing and under sinking)
- Switch failure (over sourcing and under sinking)

Actuation cycling of PCM devices requires careful characterization to manage the heat flow until a proper bias condition is found. An established bias signature works only for the characterized PCM junction dimensions including PCM channel length (l_s), PCM channel width (w_s), micro-heater length (l_h) and micro-heater width (w_h). Apart from design parameters, micro-fabrication process, layer thickness and choice of materials affect the thermal balance. Deviation in across wafer resistivity of micro-heater layer, leads to change in bias condition which requires re-characterization.



Chapter 6

Multi-Port RF PCM Switches and Switch Matrices

Multi-Port switches are an integral part of any reconfigurable RF system. Switch configurations like single-pole double-throw (SPDT) and single-pole triple-throw (SP3T) are the most commonly used ones in various applications. Single-pole N -throw (SPNT), where $N = 2, 3, 4, \dots$ provides the flexibility to easily route the RF signal at input port to one of the available output ports. Conventionally, the overall size of any SPNT switch scales with an increasing number of output ports, but as demonstrated in the previous chapters, PCM based RF switches carries tremendous potential to miniaturize and monolithically integrate switches for the development of multi-port devices.

While, SPNT switches offer reconfigurability through routing the RF input signal to any available output port, switch matrices on the other hand provides the flexibility to route RF signals between multiple inputs and multiple output ports. Majority of the RF switch matrices are used in test equipment, communication systems, and satellite communication. Traditionally available switch matrices are built using discrete electronic components increasing the overall size and weight of the switch matrix. RF-MEMS based switch matrices were developed in past decade, which offer RF performance up to 40 GHz. Till date, MEMS-based switch matrices are not commercially available due to their reliability and packaging challenges. Miniaturized PCM-based mmWave switch matrices can offer tremendous size reduction while offering excellent RF performance.

This chapter details the various PCM based RF SPNT switch configurations developed in-house. Various mmWave switch matrices are monolithically integrated, which

Parts of this chapter are published in [95–97]

outperforms current state-of-the-art competitive RF technologies in terms of frequency range of operation to overall device size.

6.1 Multi-Port Switches

6.1.1 SP2T and SP3T Switches

The RF PCM SPST switches discussed in chapter 4 outperform the state-of-the-art RF switches in terms of broadband operation frequency, highly miniaturized chip/die size, low insertion loss, low control voltage requirement, latching operation, better power handling capability, and reasonable linearity and switching time. Based on the RF switch aspects, compact multi-port RF PCM-based SP2T and SP3T switches are developed.

Multi-port switches share the same junction dimensions as of SPST switches developed using Gen 3 microfabrication process. Layout of SP2T and SP3T switches are shown in Fig. 6.1(a) and (b) respectively. Any RF device with more than two RF ports in CPW configuration require RF grounds interconnected. M3 layer in Gen 3 microfabrication process is utilized to connect RF grounds. The dielectric constant and thick-

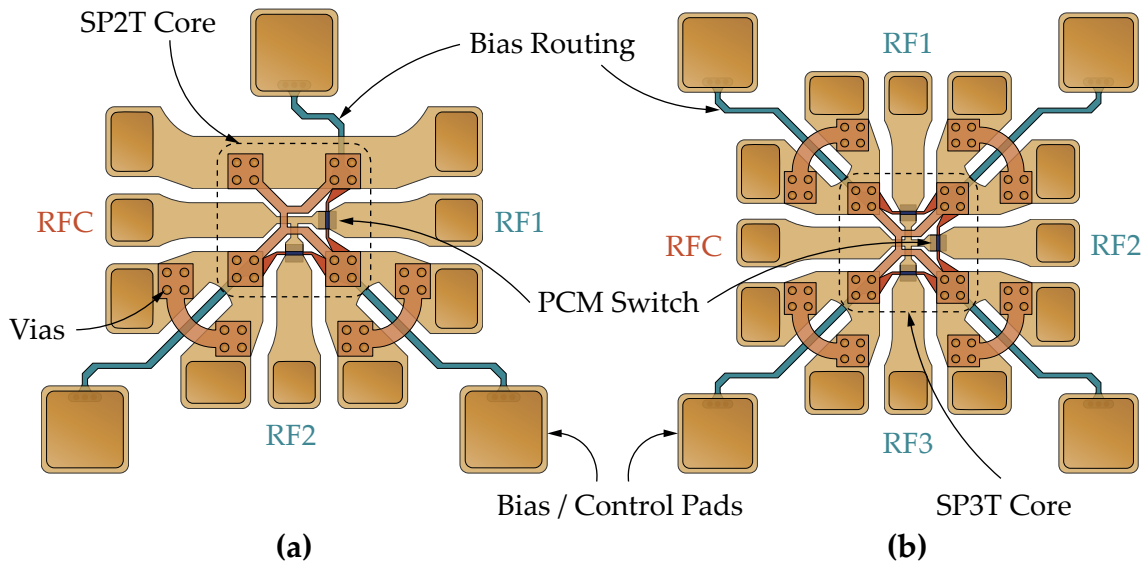


Figure 6.1: Device layouts of RF PCM multi-port switches: (a) SP2T switch, (b) SP3T switch. Device geometries highlight core area of the switch, bias routing, and control pads.

ness between M2 and M3 generates large parasitic capacitance, which creates impedance mismatch to the $50\ \Omega$ RF signal line. SP2T and SP3T core share similar ground connections and the RF signal path underneath is optimized to maintain the characteristic impedance. Optimizing the impedance and loss of the overlapping metal layer is utmost important especially for the mmWave devices, as the parasitic capacitance can block the signal flow if not taken care of in the design phase. Optical micrograph of the fabricated SP2T and SP3T switches are shown in Fig. 6.2(a) and in Fig. 6.2(b) respectively.

6.1.1.1 Routing Functionality

The RF PCM SP2T has three ports namely RFC, RF1 and RF2. RFC is a common input RF port while RF1 and RF2 are the two output RF ports. SP2T utilizes two PCM switches. CTRL1, CTRL2 and GND are the control signals. Providing actuation pulse (amorphous/crystalline) between CTRL1 and GND actuates the switch between RFC and RF1 while providing a pulse between CTRL2 and GND routes the signal between RFC and RF2. Due to the compact dimensions of RF PCM switches, these switches are placed as close to the T-junction to minimize any reflected RF signals from the non-connected port.

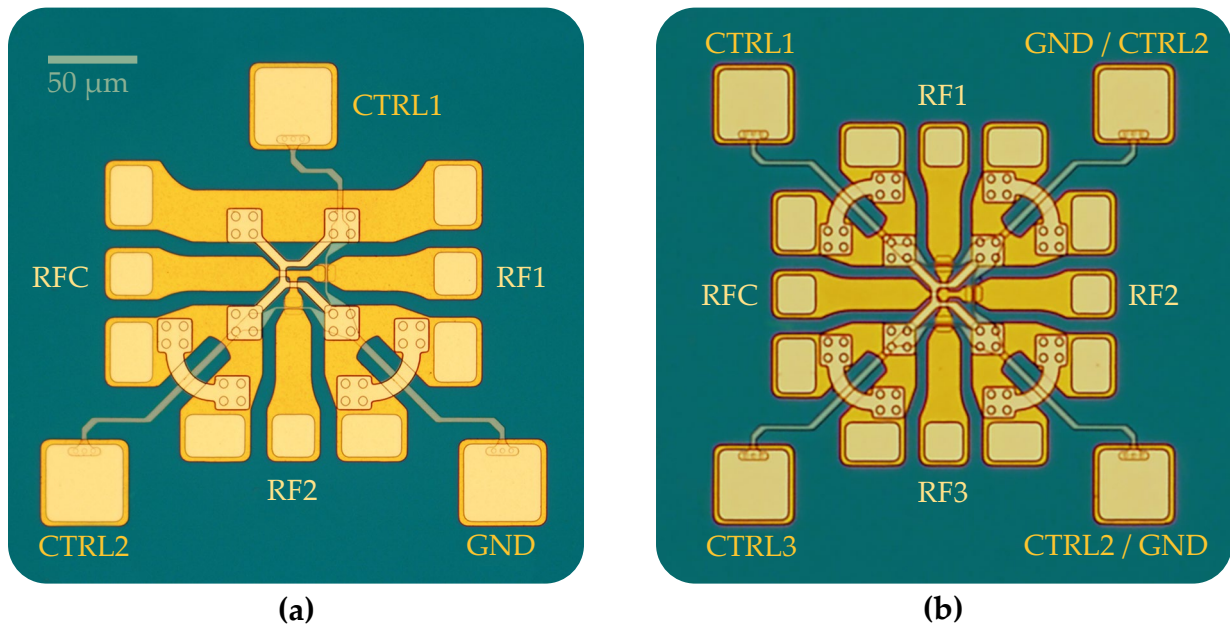


Figure 6.2: Optical micrographs of RF PCM GeTe-based multi-port switches in (a) SP2T configuration, (b) SP3T configuration.

Similarly, the PCM SP3T switch works exactly as SP2T switch with an added functionality of an additional RF3 output port. PCM switches are latching (non-volatile) switches that does not require constant control signal connection, which allows sharing the control/bias pads. To minimize the number of control pads, the SP3T switch is designed with only four control pads namely CTRL1, CTRL3, and two shared pads GND/CTRL2 and CTRL2/GND. To route the signal between RFC and RF1, pulse should be applied at CTRL1 and GND/CTRL2 (acts as a GND terminal). To actuate the signal between RFC and RF2, actuation signal need to be applied at GND/CTRL2 and CTRL2/GND, while the signal should be provided at CTRL3 and CTRL2/GND (acts as a GND) if routing the RF signal between RFC and RF3. A dummy pad NC in SP16T switch is not connected.

6.1.1.2 RF Port Size and Device Core Area

The RF PCM switch junction (PCM SPST switch core) utilized in SPST switches are of $20\ \mu\text{m} \times 20\ \mu\text{m}$ in size while the overall periphery of the switch is $500\ \mu\text{m} \times 400\ \mu\text{m}$. The additional area is occupied by the required RF ports and bias pads. RF CPW port size can be designed for the required GSG probe pitch size. Various manufacturers provide GSG probes with pitch size varying from $50\ \mu\text{m}$ to $250\ \mu\text{m}$, thus the overall device size depends largely on the desired probe pitch size. To report the realistic device size, the core area is highlighted, which can be monolithically integrated in any circuit. The overall device size is also reported including all the RF ports and bias pads (that depends on the probe pitch). If the core is smaller in size than the port size, it not only increase the overall device size, but also introduce additional RF signal transmission loss due to length and tapering of the RF signal path. The RF SPST switch is designed to accommodate GSG probe pitch range $100\ \mu\text{m}$ to $250\ \mu\text{m}$ thus increasing the overall device size.

6.1.1.3 SP3T Switch v2

An optical micrograph of the RF PCM based SP3T switch with larger port size is shown in Fig. 6.3. The switch functionality and performance is identical to the SP3T switch shown in Fig. 6.1(b) and in Fig. 6.2(b) with the only different of RF port size, which can accommodate larger probe pitch ($150\ \mu\text{m}$). The SP3T core is shown in an inset of Fig. 6.3 with dimensions $76\ \mu\text{m} \times 76\ \mu\text{m}$, which is highly miniaturized and can be monolithically integrated into any RF device. The overall device area of SP2T and SP3T switch shown in Fig. 6.2(a) and (b) is less than $300\ \mu\text{m} \times 300\ \mu\text{m}$, while the overall device periphery of the SP3T switch shown in Fig. 6.3 is $600\ \mu\text{m} \times 600\ \mu\text{m}$.

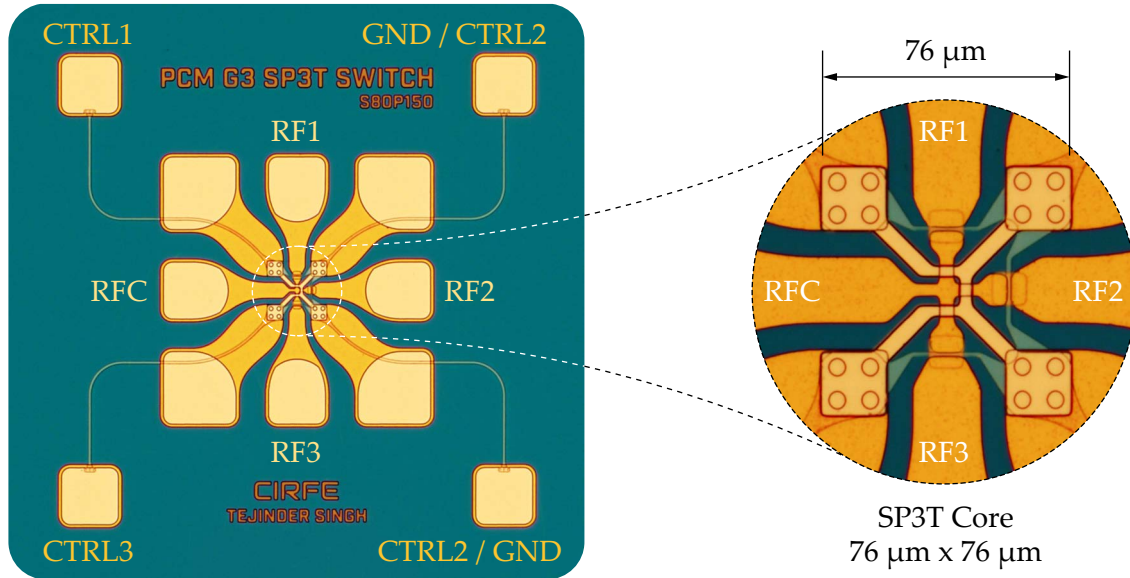


Figure 6.3: Optical micrograph of PCM GeTe-based RF SP3T switch. Inset shows an optical micrograph of the SP3T core with dimensions.

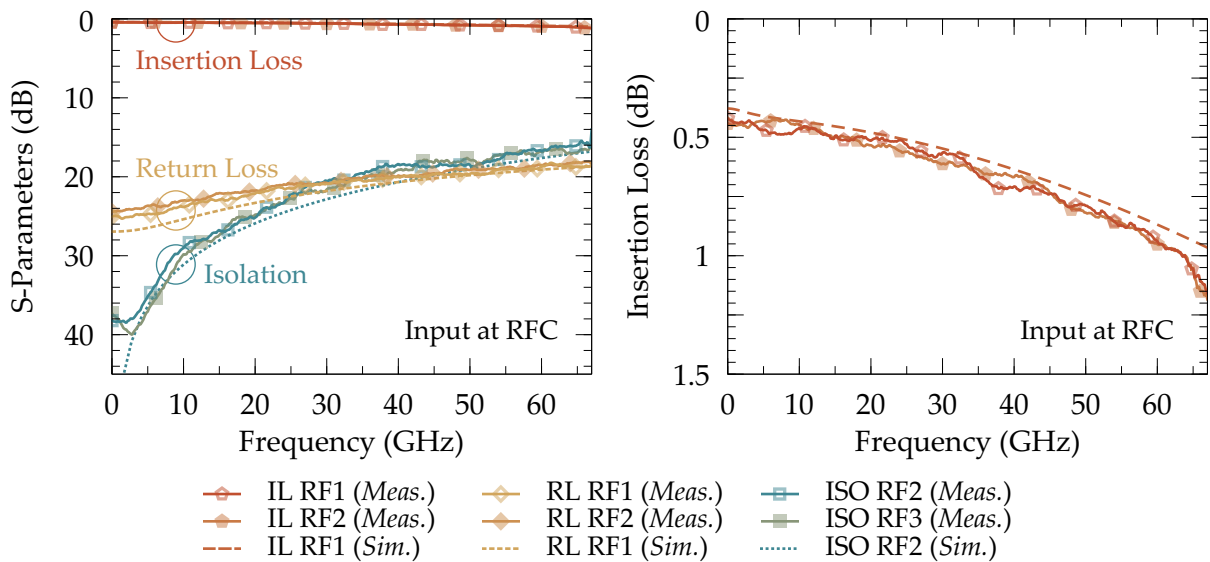


Figure 6.4: Measured and simulated RF performance of RF PCM SP3T switch. RF performance of SP2T switch (*not shown*) is identical to SP3T switch due to its identical core design.

The EM simulated and measured RF performance of the SP3T switch is depicted in Fig. 6.4. Due to the similar and symmetrical device core, only the RF performance of SP3T switch is shown. The SP2T switch has an identical RF performance. The SP3T switch exhibits lower than 1.2 dB insertion loss while better than 16 dB isolation. Return loss is better than 18 dB over the frequency range. Measurements match closely with the EM simulations as all the material parameters required for EM simulations are taken by measuring various test structures. The switch reported have better than 41 dBm IIP3 and can handle 3.5 W CW power (not including self-actuating concerns, which can be improved by modifying the PCM switch junction dimensions).

6.1.2 SP8T and SP16T Switches

Developing higher order multi-port switches (SPNT with $N > 8$) pose tremendous challenge in terms of meeting the RF performance and device size goals. A unique design approach is applied in designing SP8T and SP16T switches. Most of the higher order multi-port switches are designed using cascading SP2T, SP3T or SP4T switches, but cascading the switches impact RF performance. The cascading approach limits the number of outputs in case of a switch failure (open circuit). Unlike RF-MEMS or mechanical switches, which can either fail in open (membrane damage) or short circuit (micro-welding/stiction) state, PCM switches are very unlikely to show short circuit failure. PCM GeTe will melt providing open circuit in the RF signal path.

To get identical RF performance to available ports, a circular shaped SP8T and SP16T switches are designed and developed based on kaleidoscopic design approach. The

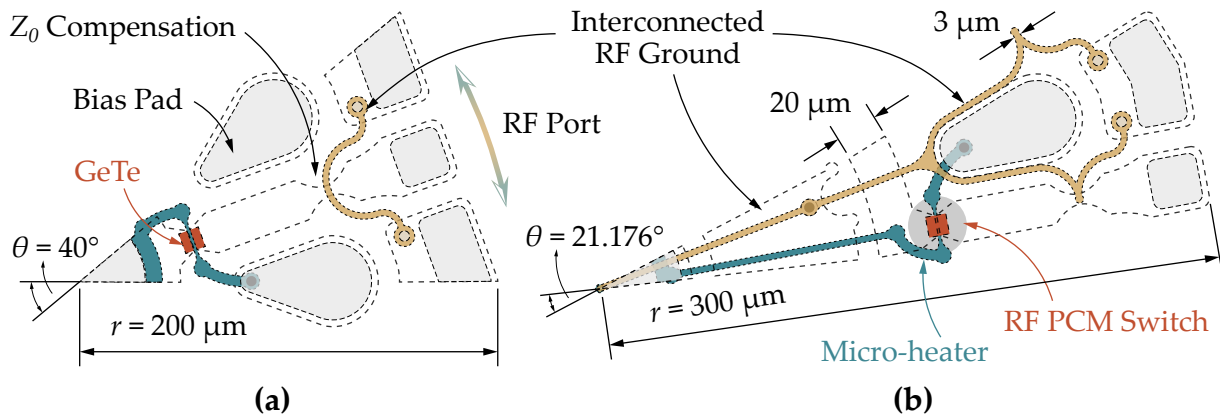


Figure 6.5: Unit-cells for (a) SP8T switch and (b) SP16T switch.

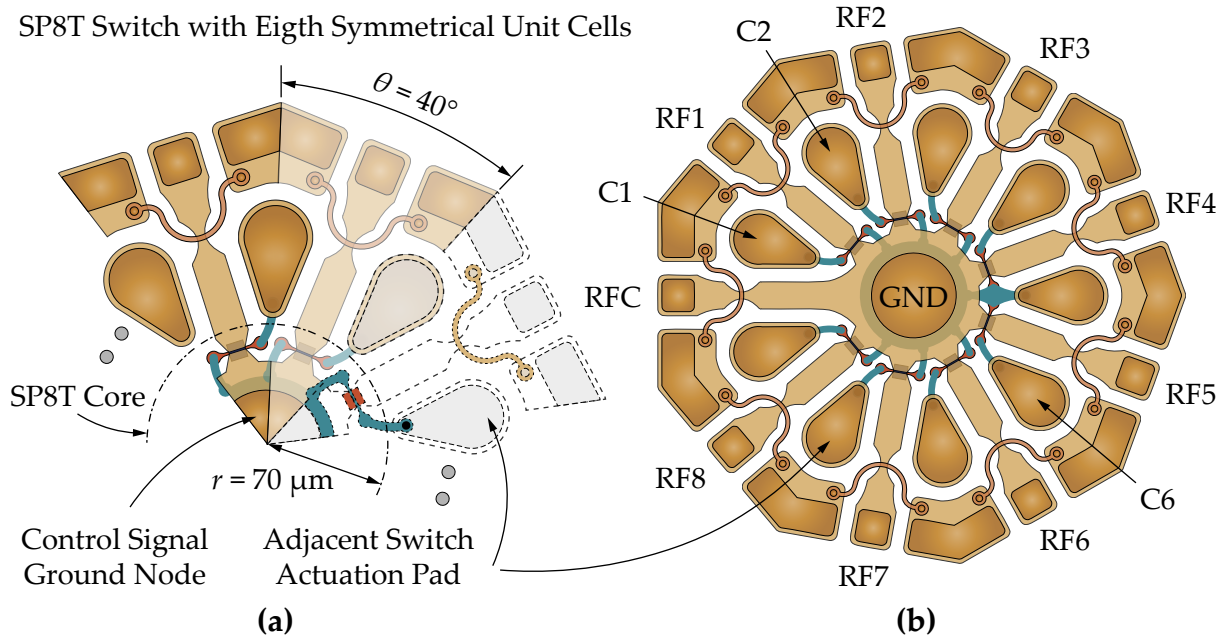


Figure 6.6: RF PCM SP8T Switch: (a) Arrangement of unit-cells, (b) Chip layout of the switch.

SP8T and SP16T switches are extremely compact in terms of size. Unit cells are designed and pivoted around the central point. All of the output ports have a PCM switch in series to allow or block the signal through that port, while the input RF port does not have any switch. The unit cells for SP8T and SP16T switches are shown in Fig. 6.5(a) and (b) respectively. The SP8T switch is developed utilizing 8 identical and 1 input side unit-cells with a rotation angle $\theta=40^\circ$. Interconnected RF grounds are designed using top metal layer (M3) in Gen 3 microfabrication process. Bias connections to micro-heaters share a common ground node and a control pad integrated adjacent to the PCM switch path. Impedance mismatch throughout the circuit is optimized for any parasitic couplings.

The RF PCM SP16T switch is designed using the similar design approach, but rather the switches are spaced out to accommodate 16 RF routes as shown in an unit-cell in Fig. 6.5(b). The unit-cell for SP16T are arranged in a circular fashion around the mid point with rotation angle $\theta=21.176^\circ$. Except for the input side unit-cell, which does not have any switching element, all the remaining 16 unit-cells are identical.

Unit-cells arrangement in SP8T switch and the switch core is shown in Fig. 6.6(a). Chip layout of the SP8T switch is depicted in Fig. 6.6(b). The SP8T switch is extremely compact utilizing chip area of 0.126 mm^2 while the SP8T core with radius $r=70 \mu\text{m}$ con-

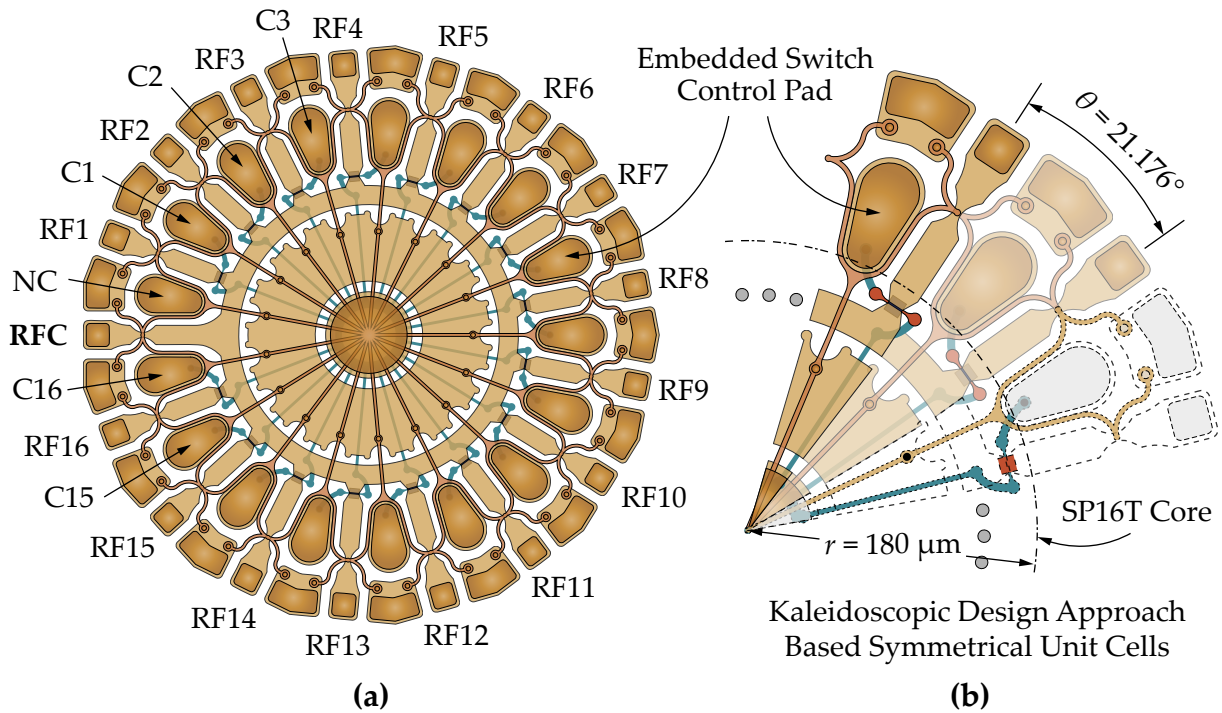


Figure 6.7: (a) Chip layout of the RF PCM SP16T switch, (b) Symmetrical unit-cells arrangement.

sumes only 0.0154 mm^2 area. The SP16T switch layout is shown in Fig. 6.7 and the unit-cells arrangement is shown in Fig. 6.7(b). The SP16T core has area 0.1 mm^2 while the whole SP16T switch has chip area under 0.3 mm^2 .

The RF input is applied at common RF port RFC which can be routed to any one of the RF output ports (RF1 to RF8) in case of SP8T switch. The SP16T switch has an input port RFC and 16 output ports RF1 to RF16. The RF PCM switch at the desired routing port is actuated by applying the amorphous/crystalline pulse between control pad (C1 to C8 in case of SP8T and C1 to C16 in case of SP16T switch) and common GND terminal.

Two different versions of both SP8T and SP16T switches are developed for two different probe pitch dimensions. Optical micrographs of two different SP8T switches are shown in Fig. 6.8(a) and (b). The switch shown in Fig. 6.8(a) is designed with the control pads inside the switch periphery to reduce the overall device footprints. While this approach is excellent for flip chip bonding but not preferred for wire-bonding chip mounting approach. Thus a version with control pads outside of the chip periphery is developed, which can be integrated using both the chip mounting approaches. The switch shown in Fig. 6.8(b) can accommodate pitch probe from $80 \mu\text{m}$ to $150 \mu\text{m}$. The chip area

of the compact SP8T switch is 0.126 mm^2 including RF ports and bias pads while for the larger version of SP8T, the chip area is 0.5 mm^2 excluding the control pads and 0.92 mm^2 with the control pads. Control/Bias lines are routed underneath the signal lines to minimize any impact of metal in between RF signal gaps. Control/Bias lines are electrically isolated with the use of a dielectric layer between control lines and RF metal. Inset of Fig. 6.8 shows a close-up view of PCM switches with junctions fully etched and overlapping micro-heaters. Such precise microfabrication layer alignment is achieved with two step lithography approach (EBL and UV direct writing) with layer offset characterization.

Optical micrograph of the SP16T switch with control pads embedded within the device area is shown in Fig. 6.9(a). Zoomed-in view of a SP16T switch section and one of the 16 PCM GeTe-based RF switch monolithically integrated in the switch is shown

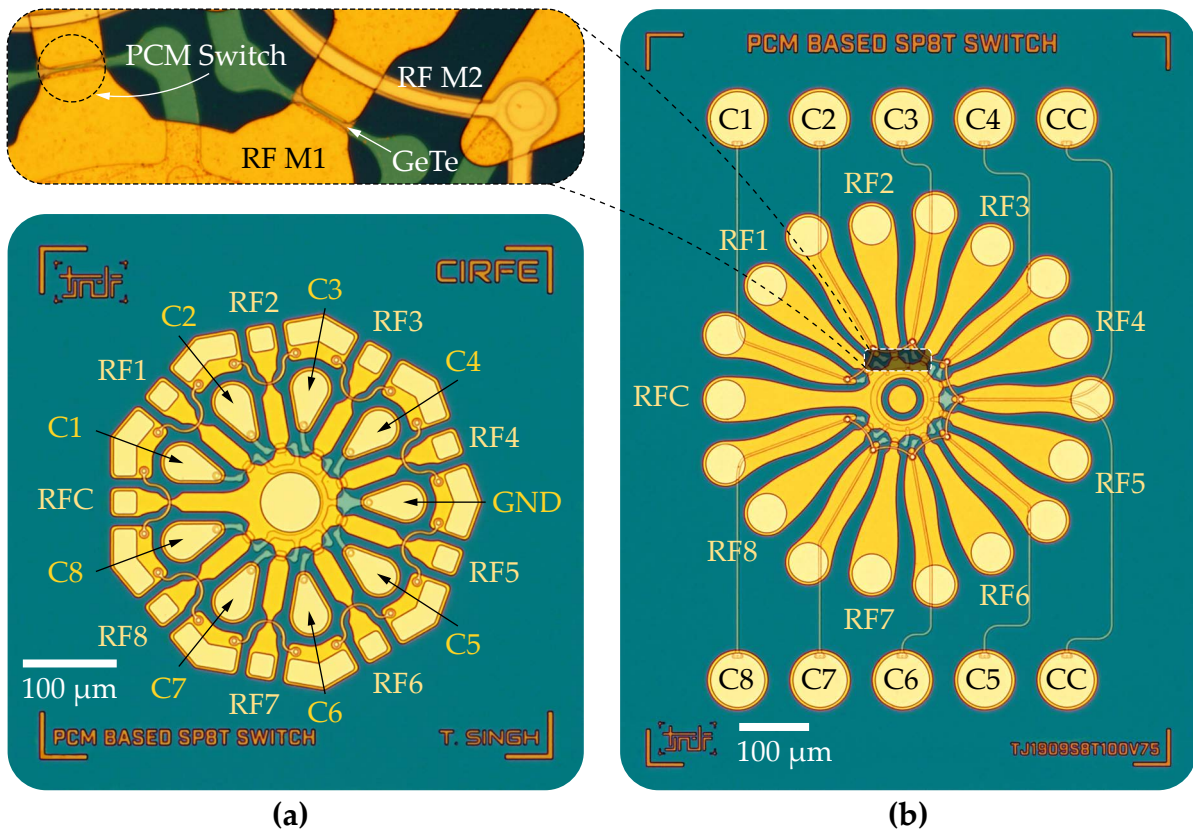


Figure 6.8: Optical micrographs of the fabricated SP8T switches. (a) Compact SP8T with integrated control pads, (b) SP8T switch with control pads outside the chip periphery.

in Fig. 6.9(b) and (c) respectively. From the heterogeneous integration reason point-of-view, the switch can be fully integrated to any technology with flip-chip bonding approach. The SP16T switch consumes less than 0.3 mm^2 area of the floorplan. A version of the SP16T switch to accommodate large probe pitch is developed with control pads outside of the chip area as shown in Fig. 6.10. Increasing the RF port pad size for larger probe pitch leads to drastic increase in the area of the chip. Although the SP16T core area is still the same for both switches, but the overall area of the chip is increased from 0.3 mm^2 to 1.4 mm^2 (0.8 mm^2 excluding the control pads). Due to the increase in RF signal path length at each port, RF transmission performance impacts.

Due to the symmetrical nature of the design, the RF performance is measured between ports $\text{RFC}-\text{RF}2$ and between the ports at opposite ends $\text{RFC}-\text{RF}4$ in case of SP8T. The isolation is measured between port $\text{RFC}-\text{RF}3$, and also between $\text{RFC}-\text{RF}5$ when the

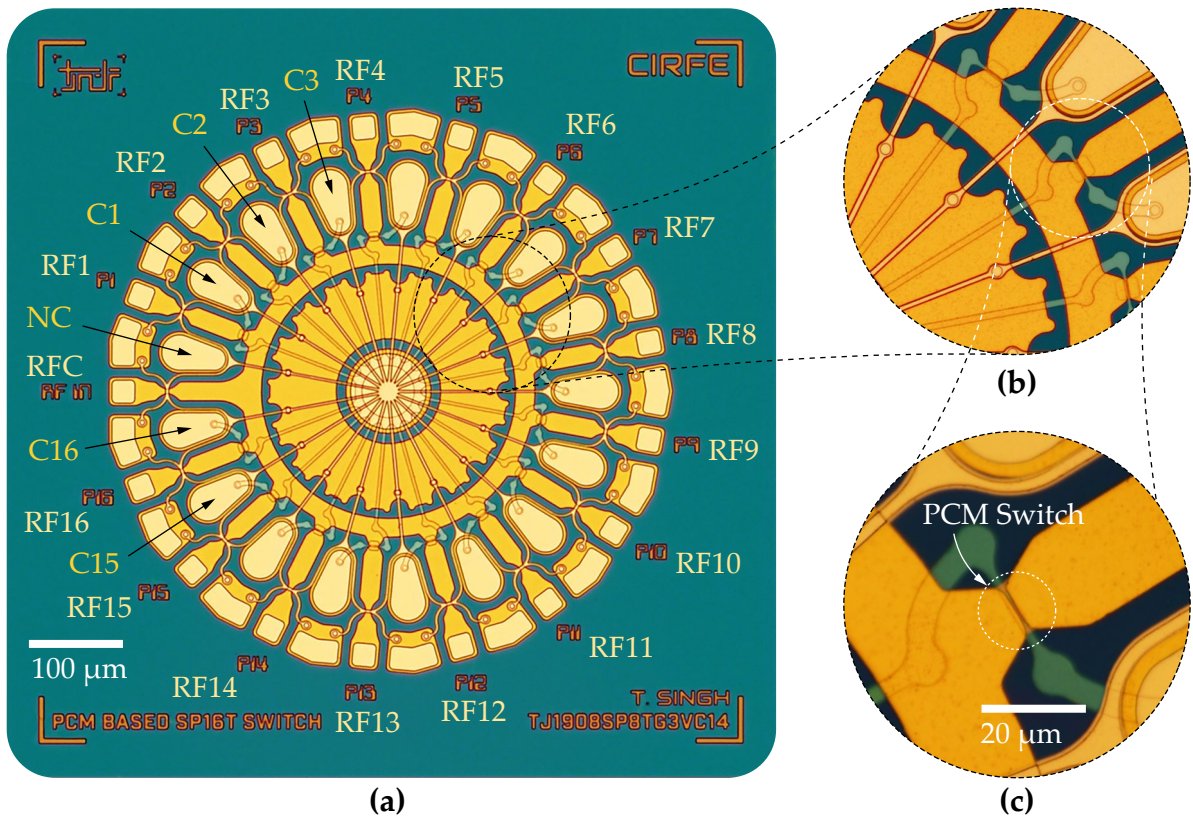


Figure 6.9: (a) Optical micrograph of the RF PCM SP16T switch, (b) zoomed-in view a section of SP16T switch, and (c) zoomed-in view of the RF PCM switches utilized in SP16T switch.

RF signal is connected between RF_C – RF_4 . In case of SP16T, the performance is also measured between ports RF_C – RF_2 , and between the opposite end ports RF_C – RF_8 . Due to the design symmetry, the RF performance is identical. To measure the devices on an on-wafer two-port RF probe station, on-chip port extensions are added and rotated to align at 180° angle (not shown in optical micrographs). Any RF loss from port extension measurements are deembedded. The EM simulated and measured RF performance of the SP8T and SP16T switches is shown in Fig. 6.11 and in Fig. 6.12 respectively.

The RF performance of the SP8T switch is measured over DC to 40 GHz while the SP16T switch is measured over DC to 15 GHz as due to a slight overdevelopment of the

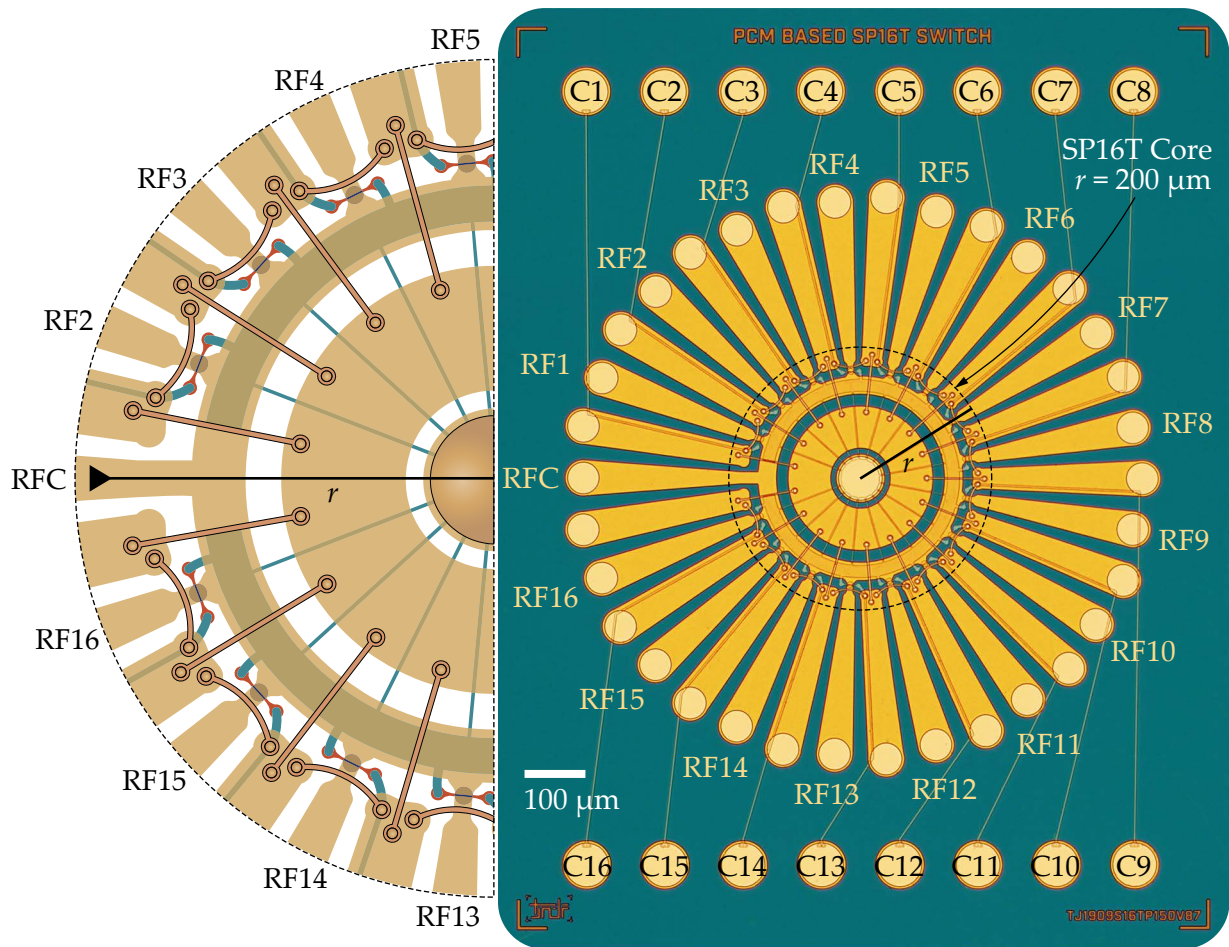


Figure 6.10: Chip layout and optical micrograph of the RF PCM GeTe-based SP16T switch.

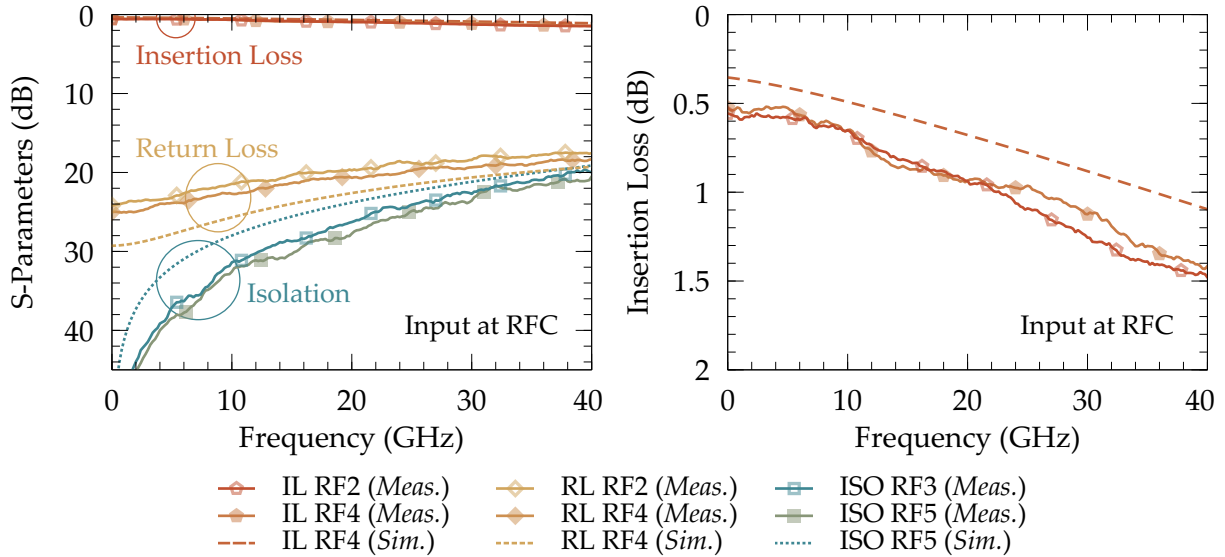


Figure 6.11: Measured and simulated RF performance of RF PCM SP8T switch. Due to the symmetrical nature of design, RF performance is shown for two different ports RF2 and RF4 while input is connected at RFC port.

RF metal layer during lithography step in microfabrication of a wafer portion containing SP8T and SP16T switches, the PCM junction lengths became few nanometer wider than expected. Increase in PCM lengths leads to improvement in isolation but on the other hand slight degradation in insertion loss at higher frequencies. The SP8T switch exhibits measured insertion loss better than 1.5 dB and isolation higher than 20 dB from DC to 40 GHz while the EM simulations shows insertion loss less than 1.1 dB and isolation better than 20 dB. Measured return loss is better than 18 dB and simulated return loss is higher than 20 dB over DC to 40 GHz.

The SP16T demonstrate measured insertion loss lower than 1.7 dB, isolation better than 26 dB and return loss higher than 12 dB. The EM simulated response show insertion loss less than 1.1 dB, isolation higher than 24 dB and return loss better than 17 dB over the frequency range DC to 15 GHz. The RF performance of the SP16T switch is limited in terms of frequency range due to the larger core radius ($3\times$ larger than the SP8T core) as well as CPW transition lengths to accommodate larger probe pitch. Insertion loss increases abruptly beyond 16 GHz. The bias lines routed underneath the larger version of SP16T switch creates capacitance resulting in degraded performance. The RF performance described is of the larger versions of SP8T and SP16T switches.

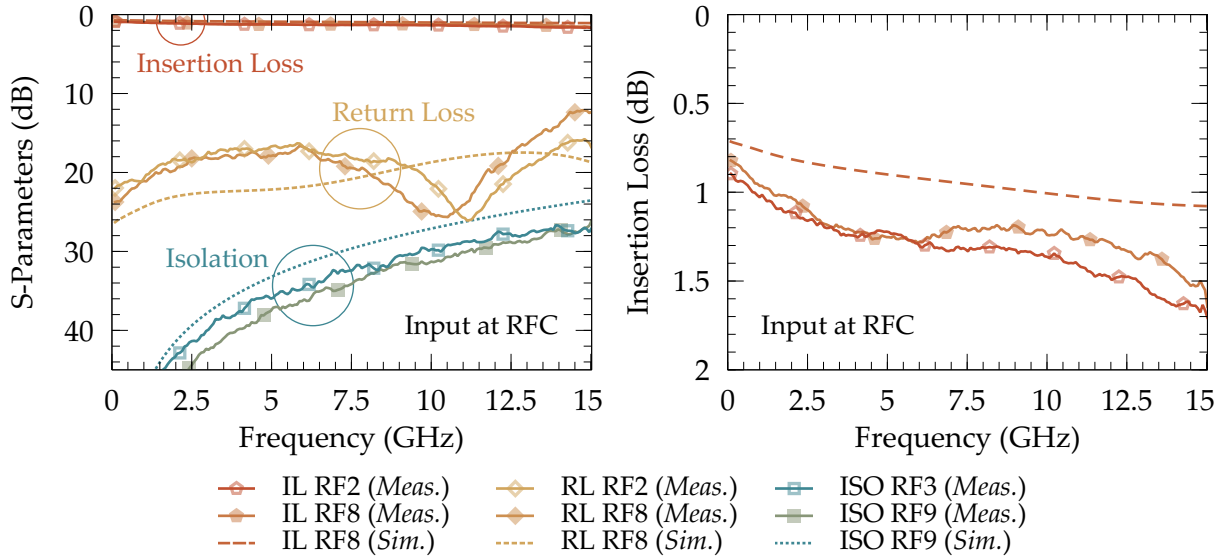


Figure 6.12: Measured and simulated RF performance of RF PCM SP16T switch. RF performance is shown for two different ports RF2 and RF8 while input is connected at RFC port.

6.2 RF PCM Switch Matrices

Switch matrices has some niche use case scenarios in test equipment and communication systems for reconfigurability. SPNT switches and switch matrices are used for signal routing, but SPNT switches lack full reconfigurability as these switches only allow routing signal applied at one common to port to any available desired output port. Switch matrices on the other hand offer signal routing between any two ports and depending on the intended functionality, some switch matrices can route multi inputs to any output port. Switch matrices pose tremendous challenges in terms of design and optimizing the RF performance. Apart from few standard switch matrix configurations like crossbar switch matrix or T-type switch, majority of the switch matrices do not offer one-size-fits-all functionality. Switch matrices are rather fully custom designed to meet certain specifications for intended applications. Some applications might need full reconfigurability with minimum chip size with reasonable RF performance, while some are required to be used for system redundancy to route signal in case of a device failure. In this chapter, various switch matrix configurations are presented ranging from a scalable 2×2 scalable switch matrix for device selector application, a monolithically integrated miniaturized T-type switch, 4×6 redundancy switch matrix to 4×4 crossbar switch matrices for mmWave applications. A full custom 16×16 crossbar matrix is also

developed for low frequency applications.

6.2.1 2x2 Scalable Switch Matrix

A PCM GeTe-based four-port scalable miniaturized switch unit-cell is developed to have only two states of a T-type switch. The four-port scalable switch unit-cell itself provides the functionality of a 2x2 switch matrix functionality. The objective of this switch unit-cell is to minimize the number of SPST switches that the RF signal passes through in each case. The device offers scalability to $m \times n$ switch matrix by stacking the unit-cells in a certain order. The RF performance of the unit-cell is measured over DC to 26 GHz demonstrating excellent RF performance between all possible signal paths.

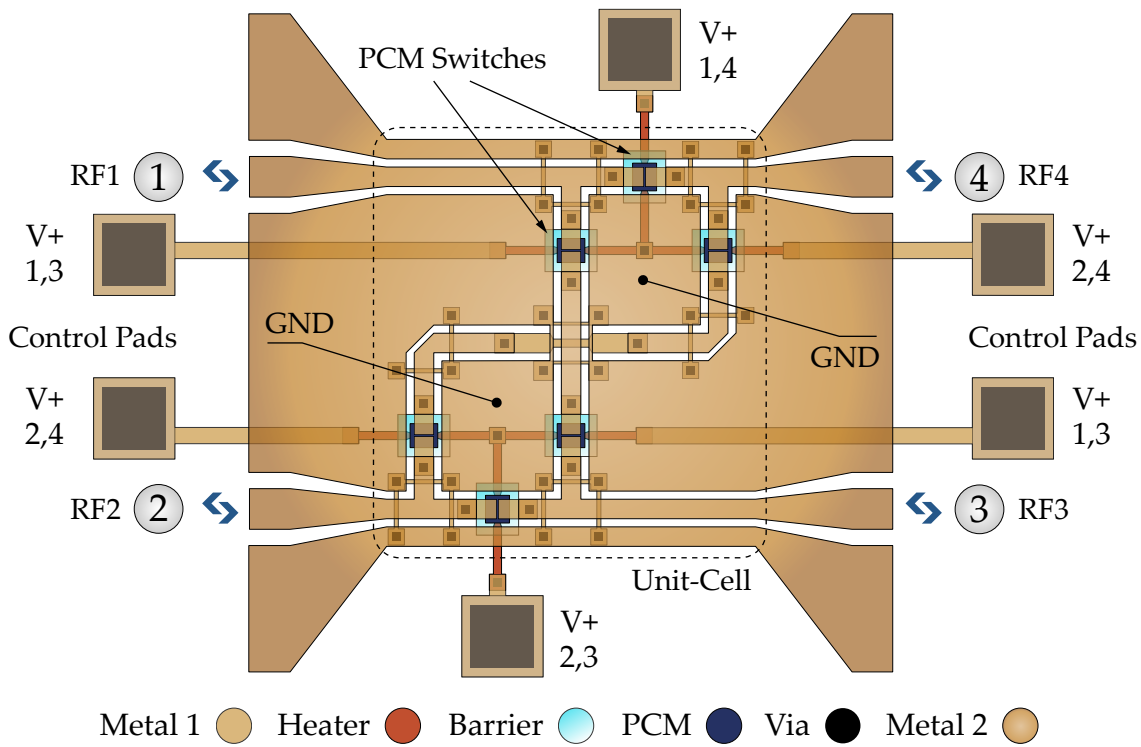


Figure 6.13: Chip/Die layout of the miniaturized scalable RF PCM-based four-port switch unit-cell highlighting various layers and RF ports.

6.2.1.1 Design and Operation Principle

The chip layout of the miniaturized switch unit-cell is shown in Fig. 6.13. The device is developed using Gen 2 microfabrication process discussed in section 4.1.4. Control signals to the respective PCM switches is provided by the bias pads. RF ground is shared with DC ground as GND signal. There are four RF signal paths to route the signal between them. The switch unit-cell has two operational states and four RF signal routes as shown in Fig. 6.14. The switch unit-cell is designed with 6 RF PCM SPST switches (A, B, C, D, E, and F) monolithically integrated with individual control pads for providing actuation pulse signals. The switches can be actuated by respective control pads as given in Table 6.1. The switch unit-cell is optimized to have compact device footprints and to have a minimum of one or a maximum of two RF PCM SPST switches in signal path to minimize the insertion loss. The RF signal paths are fabricated utilizing M2 layer of the Gen 2 microfabrication process. The signal connects to M1 layer close to the PCM switches. This allows minimizing the RF loss by utilizing a thin M1 layer to precisely control PCM junction dimensions, while the signal lines can be made of a slightly thicker M2 layer. M2 layer can also be electroplated to further improve the RF performance.

In state-I, ports RF1–RF4 (Route I_1) and ports RF2–RF3 (Route I_2) are connected while in state-II, ports RF1–RF3 (Route I_3) and ports RF2–RF4 (Route I_4) are connected. The unit-cell thus allows routing the signal available at input side ports to any output side ports. Unconnected signal paths can also be used to take advantage of the available capacity of the device. Simultaneous signal routing is one of the neat features some switch matrices. While the chip layout is not symmetrical, the RF performance remains closely identical in both combinations.

The overall device size is $1\text{ mm} \times 0.8\text{ mm}$ including CPW ports and control pads. The core of the switch excluding the bias pads is just under $0.75\text{ mm} \times 0.8\text{ mm}$. The Gen 2

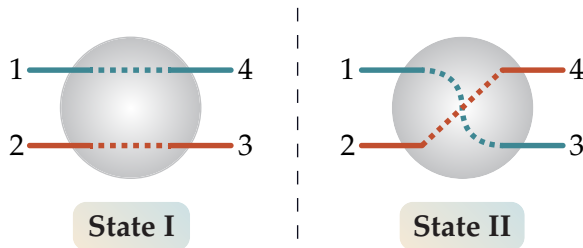


Figure 6.14: Two operational states of switch unit-cell with an option to extend the functionality of an additional state.

Route	Connection	Switches	Control
I_1	RF1 \leftrightarrow RF4	A	V+ 1,4
I_2	RF2 \leftrightarrow RF3	F	V+ 2,3
I_3	RF1 \leftrightarrow RF3	B, E	V+ 1,3
I_4	RF2 \leftrightarrow RF4	D, C	V+ 2,4

Table 6.1: Operational states of the RF PCM-based four-port switch unit-cell with relevant switches and control signals

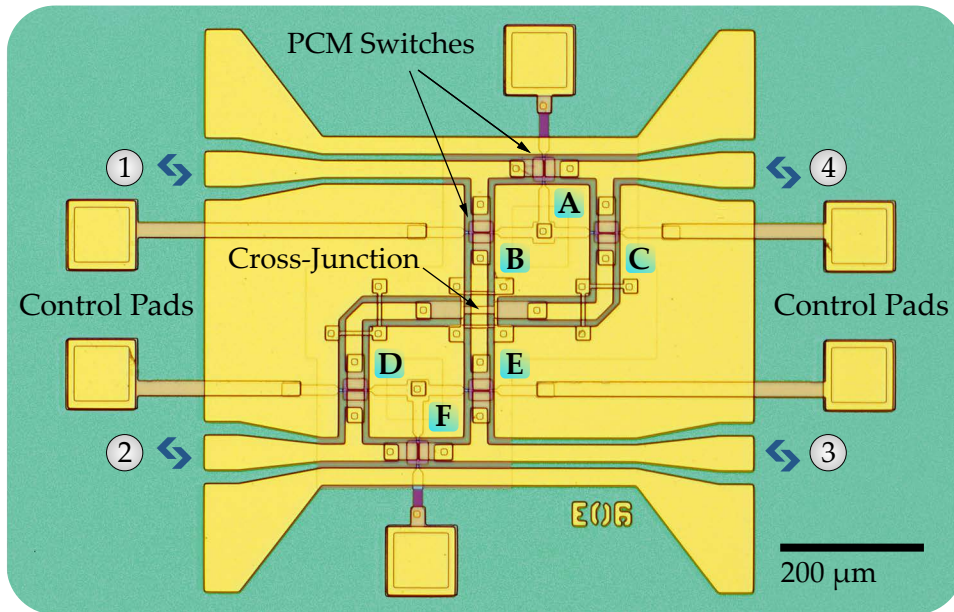


Figure 6.15: Optical micrograph of 2×2 switch matrix unit-cell fabricated using Gen 2 micro-fabrication process.

microfabrication process utilized in developing the switch unit-cell allows monolithically integrating planar RF circuits like filters, resonators and lumped components to get reconfigurability, thus making this design approach an attractive choice in terms of overall device size and performance. The optical micrograph of the fabricated scalable switch unit-cell is shown in Fig. 6.15.

6.2.1.2 RF Performance Measurement

The RF PCM GeTe-based four-port switch unit-cell is simulated to optimize the RF performance. Apart from the RF SPST switches used in the unit-cell for signal switching, the cross-over junction plays a crucial role on the RF performance of the switch unit-cell. The cross-over junction induces capacitance due to a thin dielectric between two metal layers M1 and M2. The junction is optimized using EM simulator and the RF performance of the cross-over junction including cross-coupling is shown in Fig. 6.16(a). The cross-over junction provides return loss better than 26 dB and cross-coupling better than 30 dB when all four ports are connected. Insertion loss is lower than 0.15 dB.

The OFF-state isolation of the switch is measured between various ports in all possible

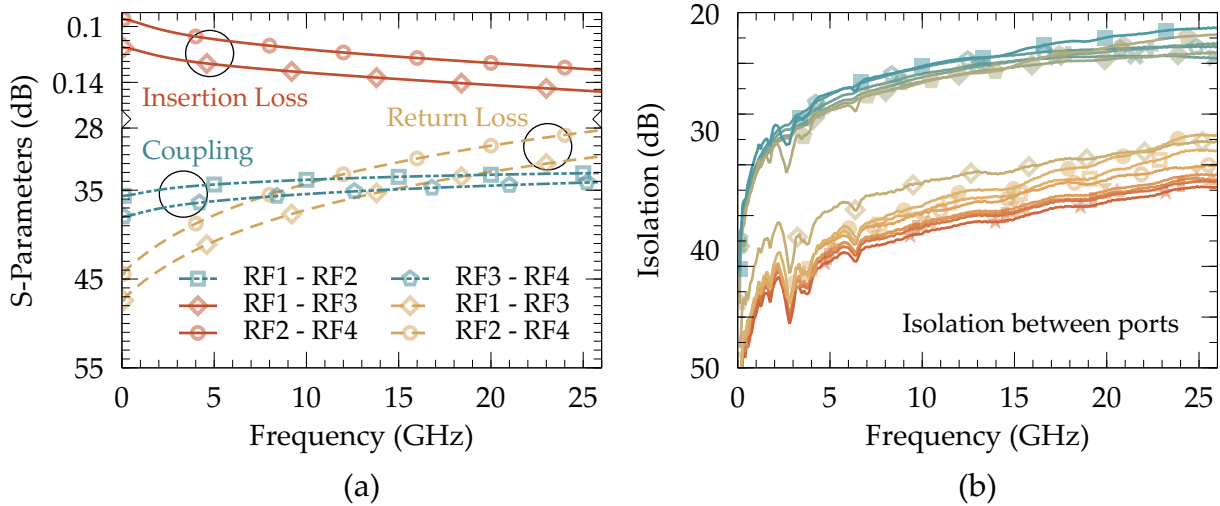


Figure 6.16: (a) Simulated RF performance of the cross-junction with RF signal flowing between port RF1 to RF3 and RF2 to RF4, (b) Measured OFF-state isolation between various ports of PCM-based four-port switch unit-cell from DC to 26 GHz in all possible combinations.

combinations depicted in Fig. 6.16(b). Isolation is higher than 20 dB in any possible RF signal path that is in OFF-state. Certain RF signal paths, which are completely isolated such as when signal is passing between RF1 and RF4, while the isolation is measured between RF1 and RF3 (route I_1 of State-I, when only switch A is activated, and all other switches are in OFF-state) or RF2 and RF4 ports demonstrate higher isolation than some combinations. Isolation measured between RF2 and RF3 or RF1 and RF3 is better than 30 dB. Higher isolation is possible to achieve by including two switches per path, which is required in case the device implementation is scaled to a higher number of ports.

Measured RF performance of the switch unit-cell in ON-state is shown in Fig. 6.16(b) and 6.17. The return loss is better than 18 dB in all possible combinations. Insertion loss is lower than 0.75 dB in State-I and less than 1.4 dB in State-II from DC to 26 GHz. Measured RF performance of the RF PCM SPST switch utilized in the unit-cell is also shown for reference in Fig. 6.17. In State-II, the insertion loss is higher than that of State-I due to the utilization of two switches per path along with cross-over junction and two 90° CPW discontinuities.

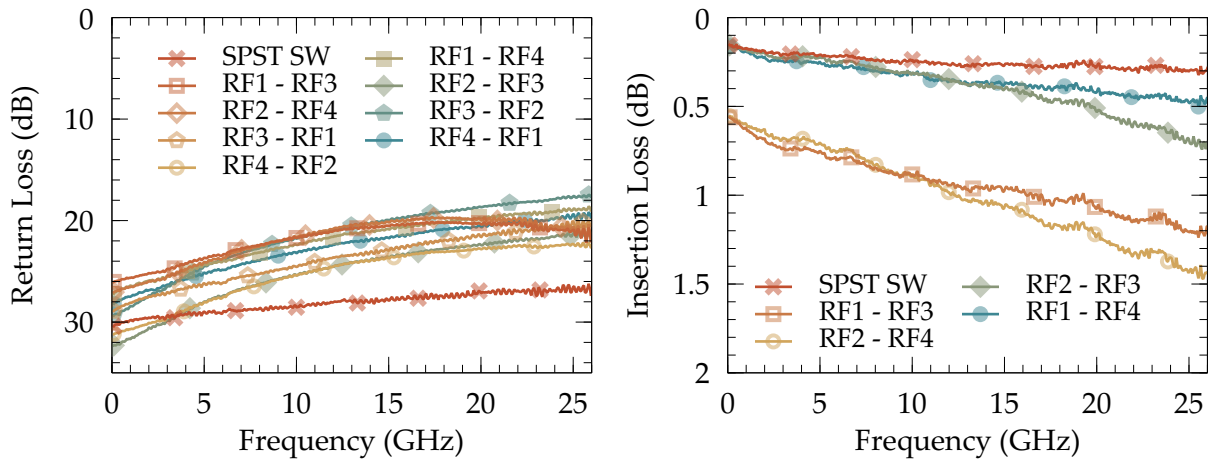


Figure 6.17: Measured ON-state RF performance of PCM GeTe-based four-port switch unit-cell over DC to 26 GHz in all possible combinations.

6.2.1.3 RF Device Selector Application

The switch unit-cell shown in Fig. 6.13 is implemented using four RF PCM SPST switches in the cross-connection State-II, which in turn helps to improve the operating bandwidth for the switch unit-cell. Excellent RF performance over a wideband DC to 26 GHz is achieved. The same functionality can be obtained with the use of only two switches in the State-II. This in turn reduces the operating frequency range of the switch cell, which may be reasonable enough for many applications. Fig. 6.18 illustrates the schematic of the wide-band and narrow-band implementation of the unit-cell.

To illustrate the benefits of using such switch unit-cell, consider the application of having a switchable device (dual band-reject filter) which only requires the use of a

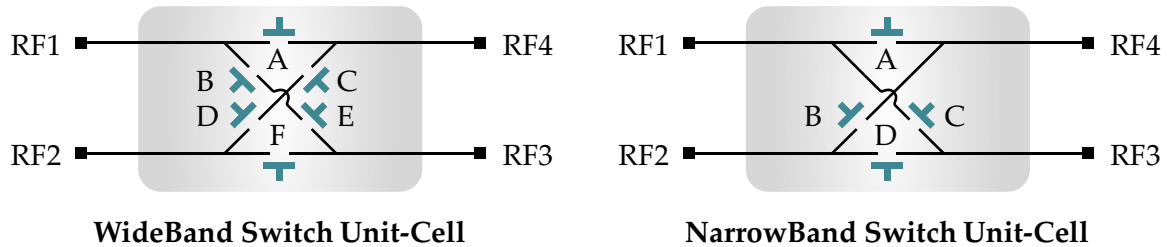


Figure 6.18: Number of switches in the four-port switch unit-cell for narrowband and wideband application.

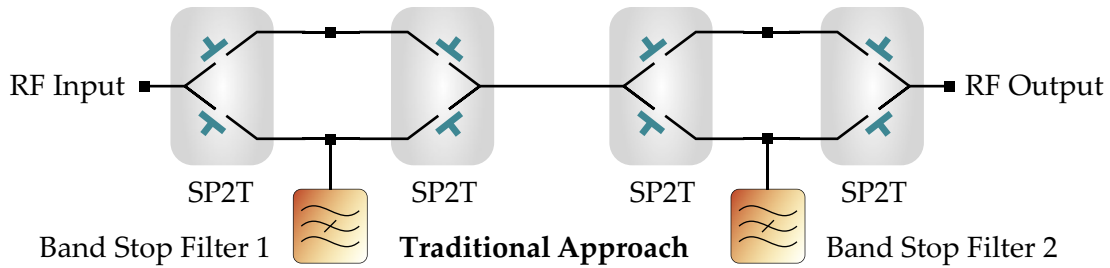


Figure 6.19: Traditional approach to device selector reconfigurability by using back to back cascaded multi-port switches. Adding an additional bit requires cascading two more SPDT switches.

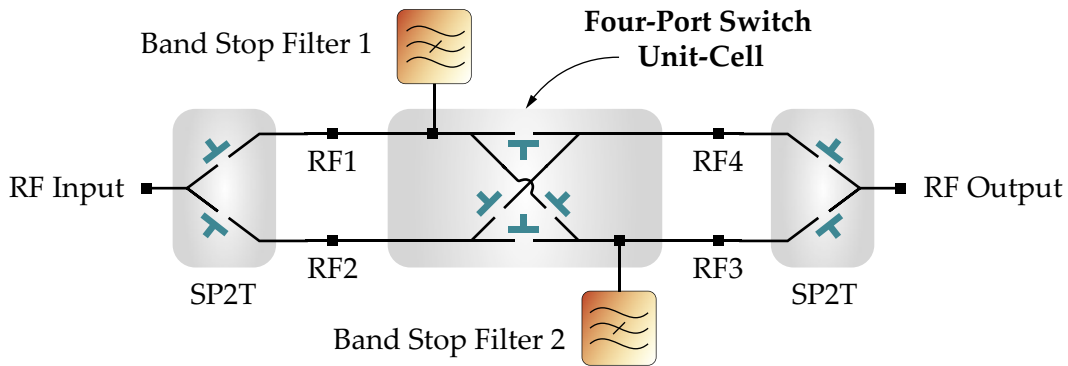


Figure 6.20: Switch unit-cell in a switchable band reject filter application to reject either an individual frequency or rejecting both the frequencies offered by band stop filters. The RF signal can be routed without rejecting any frequency band at all.

narrow-band switch unit-cell. Fig. 6.19 shows a traditional approach to achieve a switchable dual-band filter using four SP2T switches connected back to back with two transmission lines in which the RF signal can pass/bypass two band-stop filters connected in cascade yielding four possible states (rejection at f_1 only, f_2 only, $f_1 + f_2$, or no rejection). The disadvantage of this approach is that the RF signal has to pass through four SP2T switches (four SPST switches, assuming SP2T switches have one switch per path) in each state. Alternatively, the same functionality can be achieved using the developed switch unit-cell as shown in Fig. 6.15.

Using the narrow-band implementation approach, the RF band-stop filters can be connected to I_1 and I_2 paths as shown in Fig. 6.20. Frequencies f_1 , f_2 , or $f_1 + f_2$ can be rejected from the RF signal by actuating respective switches in desired signal path as given in Table 6.2, or the signal be be routed from input to output without rejecting any

Table 6.2: Switches require to reject appropriate frequency band

Frequency Band Reject	Switches			
	A	B	C	D
None	OFF	ON	OFF	OFF
f_1	ON	OFF	OFF	OFF
f_2	OFF	OFF	OFF	ON
$f_1 + f_2$	OFF	OFF	ON	OFF

frequency. The advantage of such approach is to reduce the overall device size and improve the RF performance by limiting the number of switches per path. The advantages become even more pronounced when dealing with switchable multi-band reject filters with a large number of channels.

6.2.1.4 Scalability to Higher Order Matrices

The miniaturized PCM GeTe-based unit-cell offers scalability to higher order matrices through cascading the unit-cells and adding intermediate connections as demonstrated in Fig. 6.21. A unit-cell has only 6 SPST switches in case of wideband operation. A 4×4 switch matrix can be constructed by 6 unit-cells and a 8×8 switch matrix require 20 unit-cells. In comparison with popular crossbar switch matrix topology, RF signal de-

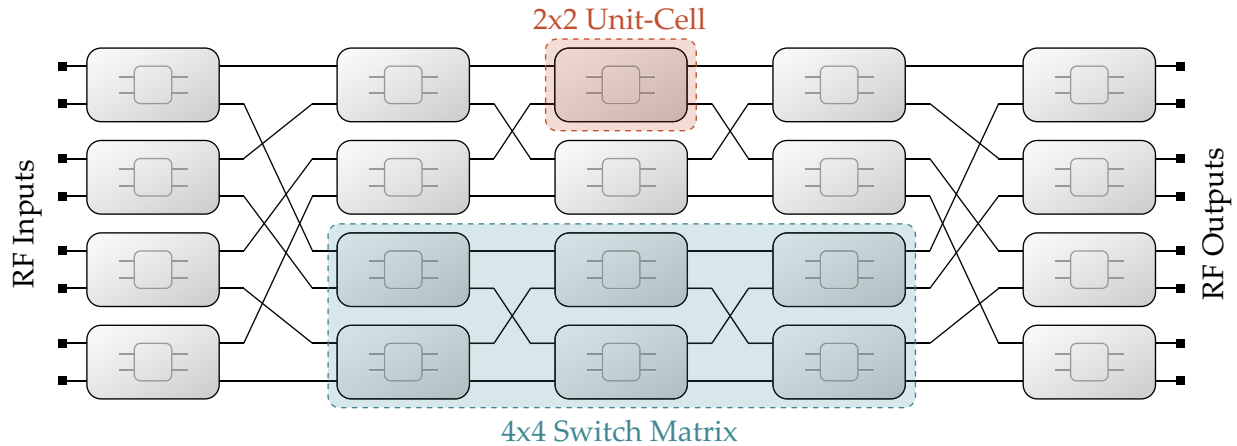


Figure 6.21: Scalability to higher order switch matrices utilizing 2×2 unit-cells.

grades in the longest path. 8×8 crossbar switch matrix require at least 15 cascaded SPST switches while only 10 switches (5 switches in case of narrowband operation) are required in the worst case scenario using the topology shown in Fig. 6.21. Higher order switch matrices developed utilizing unit-cells reduces the number of SPST switches requires as the order of the matrix increases. A 8×8 matrix provides 33% reduction in number of required switching elements compared to a common crossbar topology.

6.2.2 Reconfigurable Band Rejection Utilizing 2×2 Switch Matrix

Based on the implementation approach of the scalable 2×2 switch matrix shown in Fig. 6.20, a miniaturized monolithically integrated reconfigurable band reject filter circuit is developed utilizing four-port switch unit-cell to selectively reject RF response between input and output port at two different frequencies. Two SP2T switches are con-

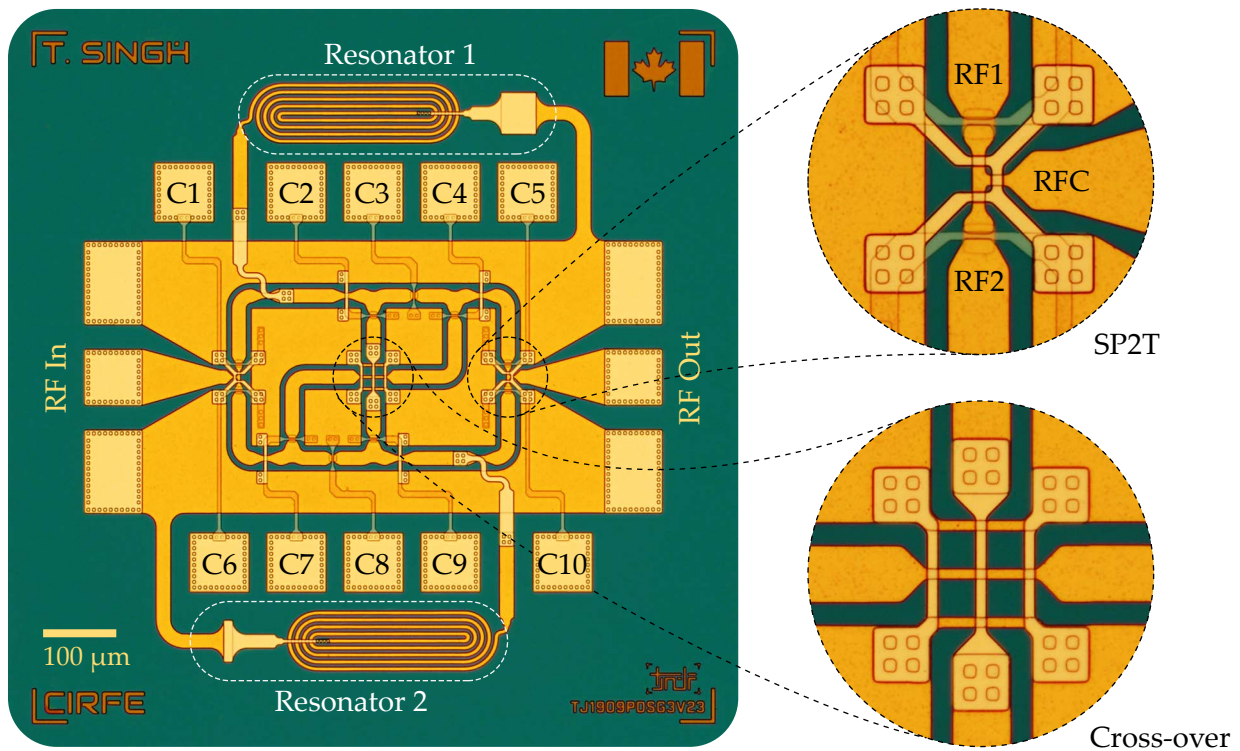


Figure 6.22: Optical micrograph of a PCM GeTe-based reconfigurable band reject filter utilizing four-port switch unit-cell.

nected back-to-back and as a proof of concept, two resonators provide frequency band rejection at two different frequencies.

Optical micrograph of the fully integrated circuit is shown in Fig. 6.22. Inset shows close-up view of a miniature PCM GeTe-based SP2T switch and an RF optimized cross-over junction, which allows simultaneous RF signal flow while providing reasonable isolation between two signals. The unit-cell utilized in this circuit is developed for wide-band approach. The four-port unit-cell has four control pads to actuate any one of the 6 available switches for routing the signal. The integrated circuit shown in Fig. 6.22 has 10 control signal pads due to the added SP2T switches. The truth table of the device is given in Table 6.3. RF and DC ground is common.

The PCM-based SP2T switches integrated in the circuits are of $76 \mu\text{m} \times 76 \mu\text{m}$. The cross-over shown in an inset of Fig. 6.22 also measures $76 \mu\text{m} \times 76 \mu\text{m}$. The band rejection circuit is developed utilizing Gen 3 microfabrication process. RF paths are optimized for improved RF performance than the unit-cell shown in Fig. 6.13. Micro-heaters bias lines are replaced with a conductive metal layer to improve the RC time constant of the switches.

The resonators connected in shunt with RF signal paths provide band rejection at $f_1 = 2.6 \text{ GHz}$ and $f_2 = 5.8 \text{ GHz}$. RF signal can be routed through the available four states of the circuits. State 1 rejects f_1 and routes the RF signal through 3 SPST switches and State 2 provides signal rejection at f_2 while keeping identical performance to State 1. State 3 includes rejection at $f_1 + f_2$. To achieve this functionality, the RF signal routes through resonator 1 followed by an SPST switch, cross-over junction and a second SPST switch before adding the response of resonator 2 to the signal path. In case of state 3, an additional switch and cross-over junction reduces the return loss at f_2 band. State 4 bypasses both resonators and routes signal from RF input to output without rejecting any frequency band. The resistance of the inductors is reduced by adding M1 layer in parallel to M2.

Table 6.3: Truth table of integrated reconfigurable band rejection circuit

Device State	Frequency Band Reject	Actuation Pulse to be applied at									
		C1	C2	C3	C4	C5	C6	C7	C8	C9	C10
State 1	f_1	1	0	1	0	1	0	0	0	0	0
State 2	f_2	0	0	0	0	0	1	0	1	0	1
State 3	$f_1 + f_2$	1	1	0	0	0	0	0	0	1	1
State 4	None	0	0	0	1	1	1	1	0	0	0

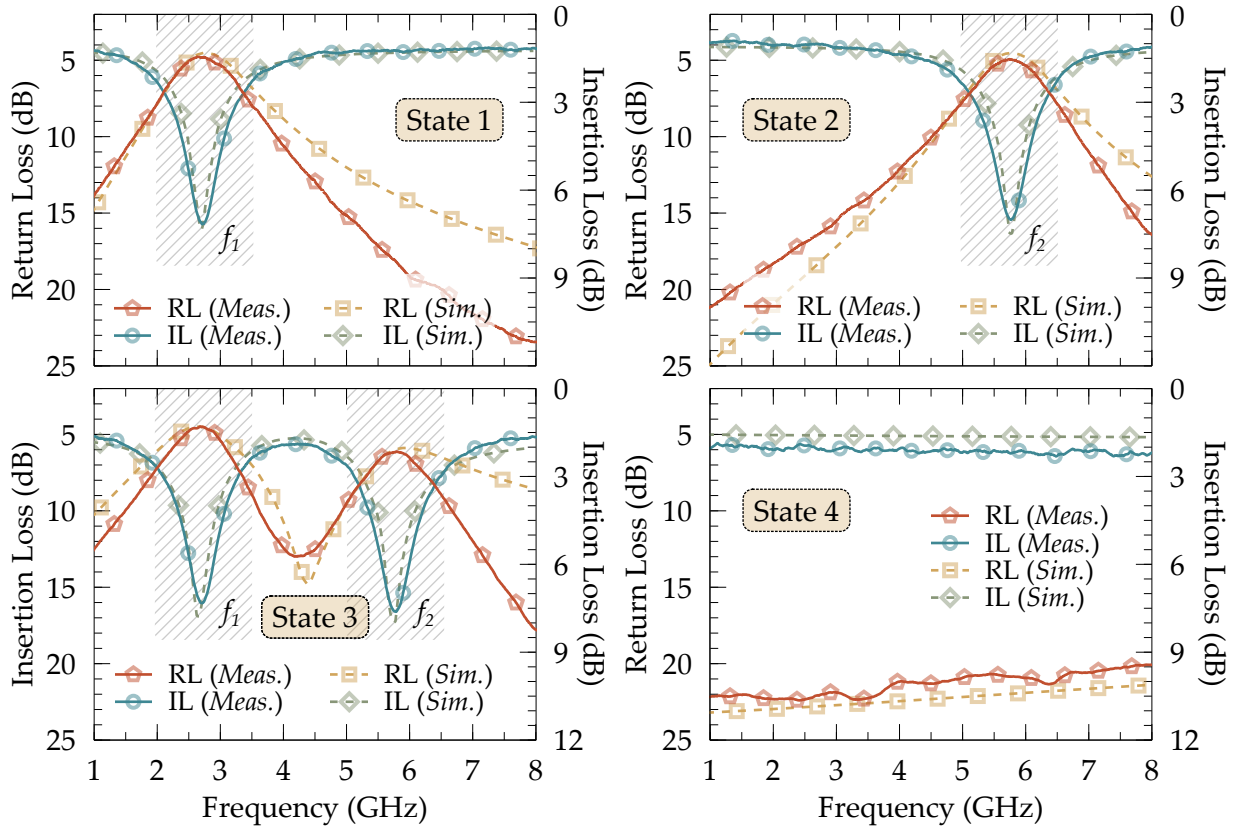


Figure 6.23: Measured and simulated RF response of fully integrated PCM-based reconfigurable band rejection circuit.

The measured and simulated RF performance of the band rejection circuit is shown in Fig. 6.23. Measured results match closely with the EM simulated RF response. Return loss at f_2 is higher than that is seen at f_1 in state 3 response. Due to the thin metal layer, on-chip lumped elements do not offer high quality factor. Low- Q of the resonators contribute to the inherent loss of resonator and the sharpness of the of stop band. In state 4 when the RF signal routes to output port bypassing both resonators, shows less than 2.2 dB insertion loss and better than 19 dB return loss over 7 GHz bandwidth.

A 2-bit device selection shown in Fig. 6.22 proves the potential of a 2×2 scalable switch unit-cell to utilize in any switchable RF device. Resonators can be replaced by higher order filters, antennas, delay lines, resistor networks to name a few. The ease in scalability of the unit-cell allows developing a 4-bit device selector with only 6 unit-cells and 8-bit device selector with 20 unit-cells as shown in Fig. 6.21.

6.2.3 Miniaturized DC–67 GHz T-type Switch Unit-Cell

The unit-cell presented in previous section provides signal routing with two operational states. The limitation of the four-port unit-cell shown in Fig. 6.13 is the unavailability of signal routing from RF1 to RF2 and from RF3 to RF4. A T-type switch addresses this routing limitation. T-type switch is a four-port RF device, which performs signal routing from any two input ports to the remaining two output ports. The T-type switch has four ports with six signal paths and three operational states providing higher degree of flexibility for redundancy networks. A monolithic PCM based compact T-type RF switch is developed for mmWave switch matrix applications.

6.2.3.1 Device Design and Operation

The T-type switch offers three operational states for signal routing as shown in Fig. 6.24. A miniaturized PCM GeTe-based T-type switch is developed with 12 PCM SPST switch arranged in a way to have 6 possible RF paths for signal routing. Any two ports can be connected by biasing the respective PCM switches in signal path. The T-type switch design is optimized to have very small device periphery and to have only 2 SPST switches in any given signal path to minimize RF loading, hence expanding the frequency range of operation.

The presented T-type switch is shown in Fig. 6.25 with overall device periphery under $0.55 \text{ mm} \times 0.55 \text{ mm}$ including CPW RF ports and biasing pads for measurements, while the core area of the T-type switch is highly miniaturized to only $0.23 \text{ mm} \times 0.23 \text{ mm}$.

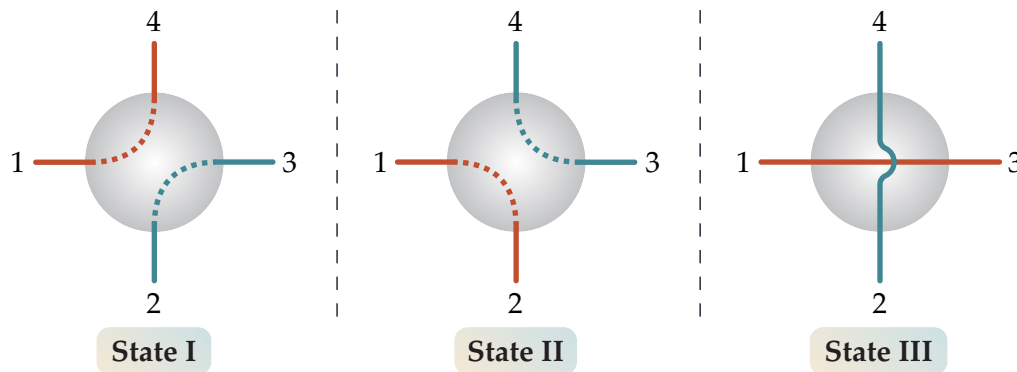


Figure 6.24: Three different operational states of a T-type RF switch. RF performance of the state I and II is identical due to the design symmetry.

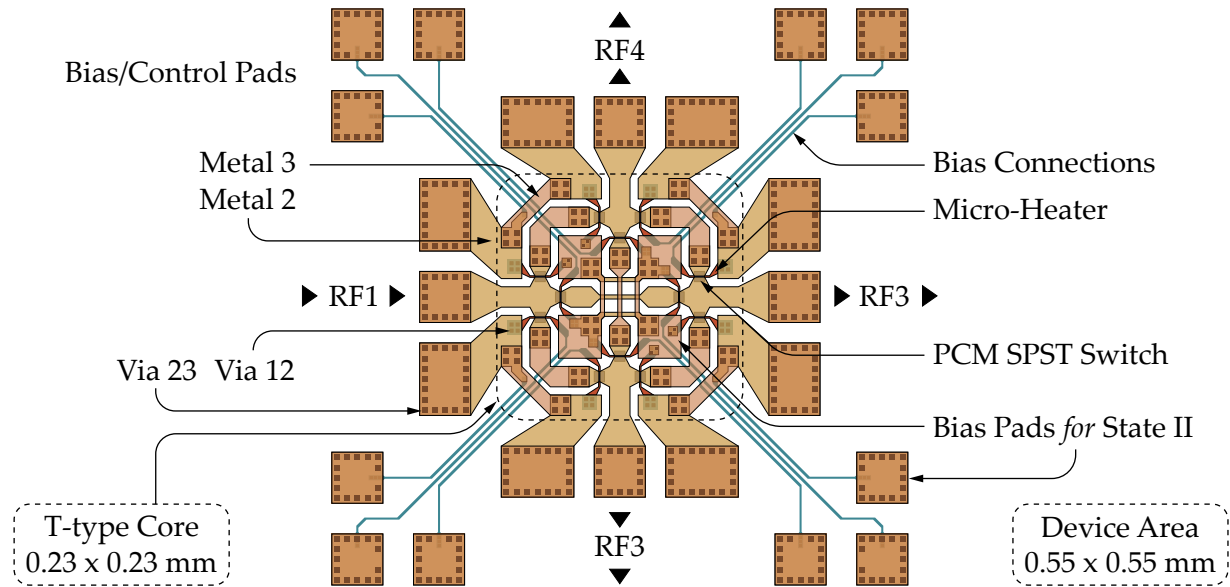


Figure 6.25: Chip layout of the monolithically integrated compact RF PCM-based T-type switch.

Three PCM SPST switches are arranged in a way to minimize any RF reflections from additional signal line lengths. The RF crossover is optimized to reduce RF coupling between two signal paths. A common bias pad for state II is designed targeting the reduction of overall device area. The SPST switches for state II are biased in a way to allow their simultaneous actuation.

In state I, ports RF1–RF4 and ports RF2–RF3 are connected while in state II, ports RF1–RF2 and ports RF3–RF4 are connected. Due to the symmetrical design of the T-type switch, the RF performance remains the same in state I and II. State III connects ports RF1–RF3 and ports RF2–RF4. Previously reported Gen 2 microfabrication process based PCM T-type switch [96] had tungsten (W) based micro-heaters and bias lines for providing thermal actuation pulses. The bulk resistivity of the micro-heaters was optimized in the microfabrication process reported in [96] to minimize the resistance of the long bias lines, but using a lossy metal for long bias lines still adds additional resistance increasing the time constant. A better alternative is to add a conductive path for long bias lines. An improved version of the T-type switch is developed using Gen 3 microfabrication process on sapphire substrate. The reported tungsten micro-heaters have higher resistivity than the bias lines. A highly conductive metal ‘Ag’ is used as a bias split layer. In the switch shown in Fig. 6.25, via openings are etched around contact pads to minimize any pad inductance.

The optical micrograph of the reported T-type switch is shown in Fig. 6.26, highlighting the overall device size. The 90-degree bends and the RF cross-over junction are optimized for wide band operation. The T-type switch is developed using twelve RF-PCM SPST switches with dimensions: length of PCM channel (l_s) = 0.6 μm , width of PCM channel (w_s) = 8 μm , length of micro-heater (l_h) = 10 μm , and width of micro-heater (w_h) = 1.5 μm . Generally, the minimum feature size achievable by UV lithography is limited to 1 μm thus, 100 kV electron-beam lithography has been used in the fabrication process, which provides resolution as small as few nanometers. As we have previously reported [86], developing precise switch junctions and fabrication layers alignment is crucial for PCM switches, which is not achievable using contact-based UV lithography. Use of electron-beam lithography made it possible to attain the desired alignment which is crucial in case of multi-port devices, thus improving the yield. RF-PCM switches utilized in T-type switch are shown in Fig. 6.26. Fig. 6.26 (b) shows the 3D rendered view of the PCM switch (passivation layer is not rendered to highlight the switch junction

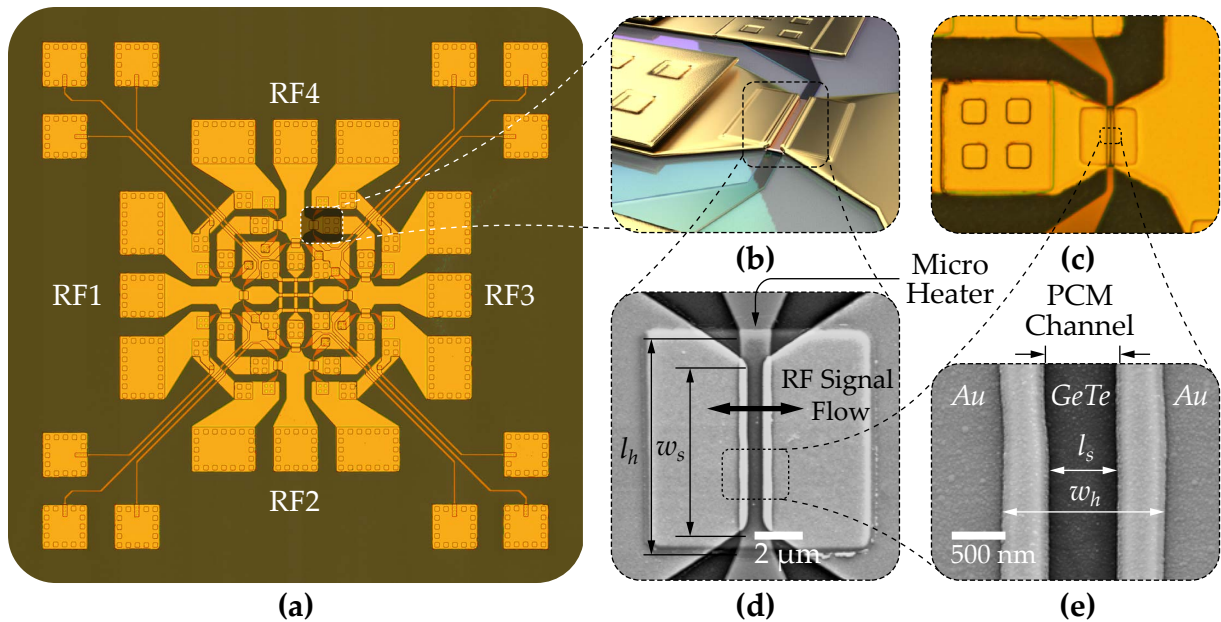


Figure 6.26: RF PCM-based T-type switch: (a) Optical micrograph of the fabricated T-type switch developed on sapphire substrate, (b) 3D rendered view of a single RF-PCM SPST switch, (c) Optical micrograph of RF-PCM SPST switch (d) SEM micrograph of SPST switch junction highlighting the RF signal flow path, and (e) SEM micrograph of a close-up view of PCM channel highlighting perfect micro-fabrication alignment of the Au contacts over micro-heater.

for better understanding). The shaded portion in Fig. 6.26 (a) is expanded into an optical micrograph in Fig. 6.26 (c) displaying the RF-PCM SPST switch. The SEM micrograph in Fig. 6.26 (d) shows the PCM SPST switch junction highlighting the RF signal flow direction and, a close-up view of PCM channel is revealed in the SEM micrograph shown in Fig. 6.26 (e). Fig. 6.26 (d) and (e) highlight perfect alignment of layers in the micro-fabrication process. SPST switch dimensions are shown in Fig. 6.26 (d) and (e) respectively.

6.2.3.2 Thermal Crosstalk

Due to the dense integration of the PCM-based T-type switch, thermal crosstalk need to be addressed. Thermal crosstalk in closely packed RF SPST switches is investigated experimentally using non-invasive thermorefectance based transient thermal imaging technique, which allows investigating the heat distribution and hot-spots at sub-micron spatial resolution with nano-second transient response as reported in chapter 5. Based on the experimental thermal crosstalk measurements, the multi-port T-type switch consists of 12 PCM SPST switches arranged in a close proximity to reduce the overall device footprints and also designed at a safer distance from one another to avoid any potential switch damage that might occur from providing from more than rated bias signals. Latching nature of GeTe material allows integrating multiple switches in a close proximity to develop highly miniaturized multi-port switches and switch matrices. Based on the thermal imaging, the PCM SPST switches are designed at least 40 μm apart in the switch matrix and T-type unit cell.

6.2.3.3 Performance Optimization of CPW Discontinuities

The T-type switch is a complex microwave system thus designing and optimizing the RF performance especially for millimeter wave applications is a challenge. Apart from PCM SPST switches, the T-type switch shown in Fig. 6.25 consists of 90-degree bends, four port RF cross-over to simultaneously route RF signal without inducing any coupling, bias lines to provide control signals, interconnects to connect metal layers and routing micro-heaters. Dielectric layer between PCM and micro-heaters (M0) is extremely thin, thus routing induces capacitance to RF signal line. To avoid capacitive coupling, M2 layer is utilized for signal routing. 90-degree bends are optimized for having 2, 3 or 4 bias lines crossing without interfering with the RF signal.

The RF cross-over junction is the most critical component in T-type switch design. The cross-over is designed and optimized to get near ideal RF matching while maintain-

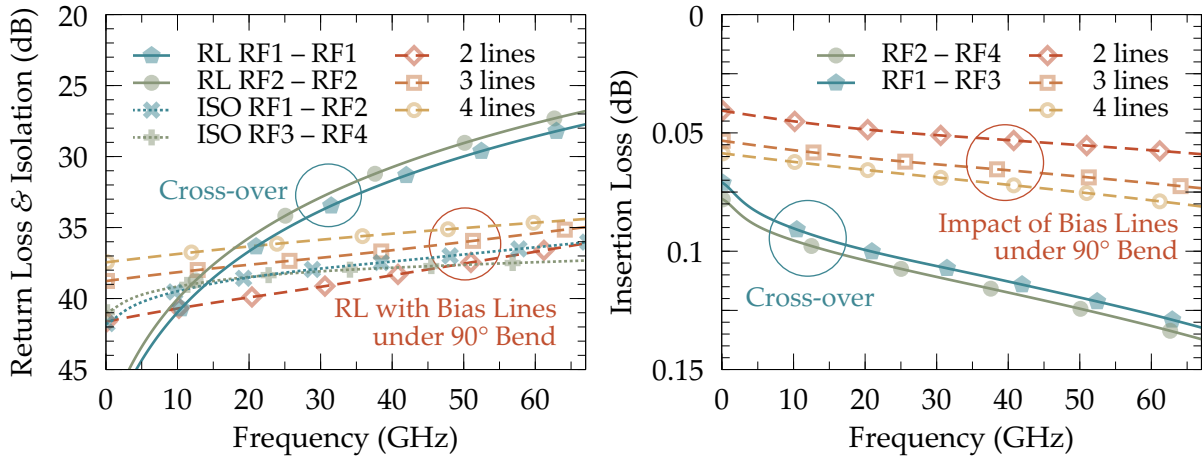


Figure 6.27: EM simulations of the return loss, isolation and insertion loss of cross-over junction and the impact of conductive bias lines routed under 90° CPW bends.

ing reasonable RF signal loss. The cross-over junction has functionality to allow two RF signal paths from ports RF2–RF4 and ports RF1–RF3 simultaneously. The dielectric between two metal layers create a large capacitance between two signal lines whose effects are pronounced at millimeter-wave frequencies. The design of the junction is carefully chosen to provide decent RF performance from DC to 67 GHz frequency range. This design also eliminates the need of having air bridges, as the RF ground planes are connected through ‘M3’ layer.

CPW discontinuities including 90° bends and cross-over junction are optimized for wideband operation. Fig. 6.27 shows the EM simulation of the return loss, isolation and insertion loss of the RF cross-over junction and 90° bend with number of bias lines routed underneath. The RF crossover is simulated as a four-port network connecting ports RF1–RF3 and ports RF2–RF4. Return loss is better than 26 dB while isolation between ports is better than 37 dB from DC to 67 GHz. Insertion loss is better than 0.14 dB throughout the frequency range. The 90° bends are simulated and optimized for the case of 2, 3, and 4 conductive bias line crossing, providing return loss better than 34 dB and insertion loss less than 0.08 dB.

6.2.3.4 RF Performance Measurement

Fig. 6.28 reports the simulated and measured RF performance of the developed T-type switch from DC to 67 GHz. Similar RF performance is observed in state I and state II

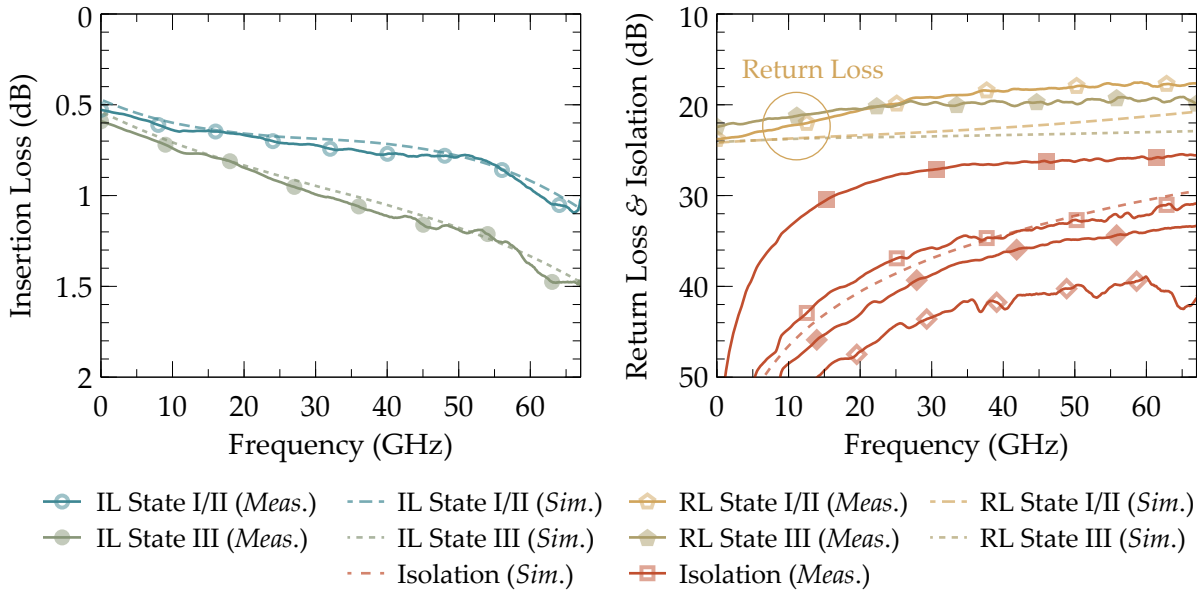


Figure 6.28: Measured and simulated RF performance of RF PCM-based T-type switch over DC to 67 GHz. Multiple isolation measurements represent the RF performance from different states and combinations.

due to the design symmetry. In both of these states, the device exhibits remarkable RF performance with insertion loss lower than 1 dB and return loss better than 17 dB from DC to 67 GHz. State III also exhibits similar RF performance to state I and II with the exception of insertion loss, which is slightly higher in this case. The measured results for state III demonstrate a return loss better than 18 dB, insertion loss less than 1.6 dB from DC to 67 GHz and loss less than 1 dB over DC to 30 GHz. Isolation between the remaining unconnected ports is more than 26 dB in all states. While the PCM SPST switches have poor isolation due to the narrow channel in signal path, the miniaturized T-type switch has 2 SPST switches per path, offering better isolation up to 67 GHz.

6.2.4 Monolithically Integrated DC–60 GHz 4×6 Redundancy Switch Matrix

In a typical satellite payload system, hundreds of RF switches are used in the form of switch matrices to provide system redundancy for maintaining full functionality by rerouting the signal to spare receivers in case of any malfunction of one of the receivers.

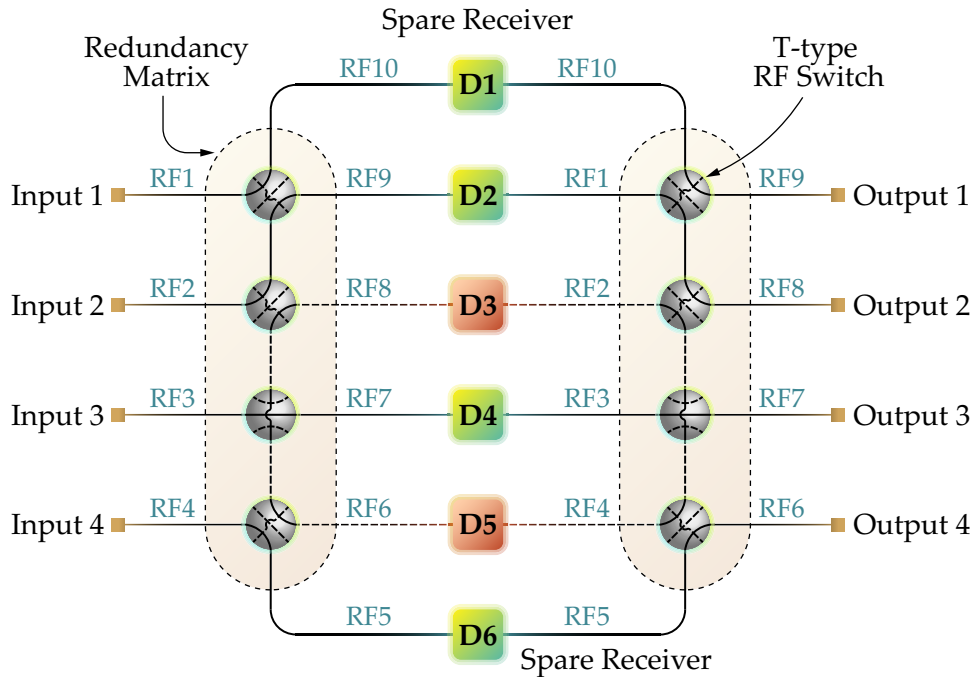


Figure 6.29: A 4×6 redundancy system utilizing two switch matrices using six receivers with two of these receivers are used as spare. This figure illustrates the signal routing functionality of the switch matrices in case of failure of two receivers ‘D3’ and ‘D5’.

The 4×6 redundancy switch matrix presented in this section allows continuous system operation even if any two of the receivers fail. The redundancy matrix, up to a certain extent, also covers for any SPST switch failure in a signal path. For example, if a switch between ports RF1–RF9 fails, signal can be routed through ports RF1–RF10 and if the receiver connected to port RF9 fails, the same path from port RF1–RF10 can be used to maintain full system functionality. The configuration of the redundancy switch matrix is shown in Fig. 6.29, and the layout of the presented 4×6 redundancy switch matrix is shown in Fig. 6.30. The redundancy matrix is based on T-type switch shown in Fig. 6.25 as a basic building block. The overall size of the redundancy switch matrix is $0.88 \text{ mm} \times 1.1 \text{ mm}$ including CPW ports and bias pads. Bias pads can be routed towards the side for ease of wire-bonding. The device measures $0.4 \text{ mm} \times 1.1 \text{ mm}$ without the bias pads. Ports RF1 to RF4 serve as RF input ports and ports RF5 to RF10 act as RF output ports.

The redundancy switch matrix offers the functionality of routing signal from any input port to any output port. In general, input is routed to output ports as per state

III of the T-type switch. Ports RF1–RF9, RF2–RF8, RF3–RF7, and from RF4–RF6 follow state III operation, which has only two SPST switches per path and a crossover junction. In case of a malfunction of any connected receiver, signal can be routed as per state I and II, with ports RF1–RF10, RF2–RF9, RF3–RF8, RF4–RF7 connected as per state I and ports RF1–RF8, RF2–RF7, RF3–RF6, and RF4–RF5 connected as per state II. State I and II have four switches per path, due to the cascaded T-type switches and two 90° bends per path with an exception of ports RF1–RF10 of state I and RF4–RF5 of state II,

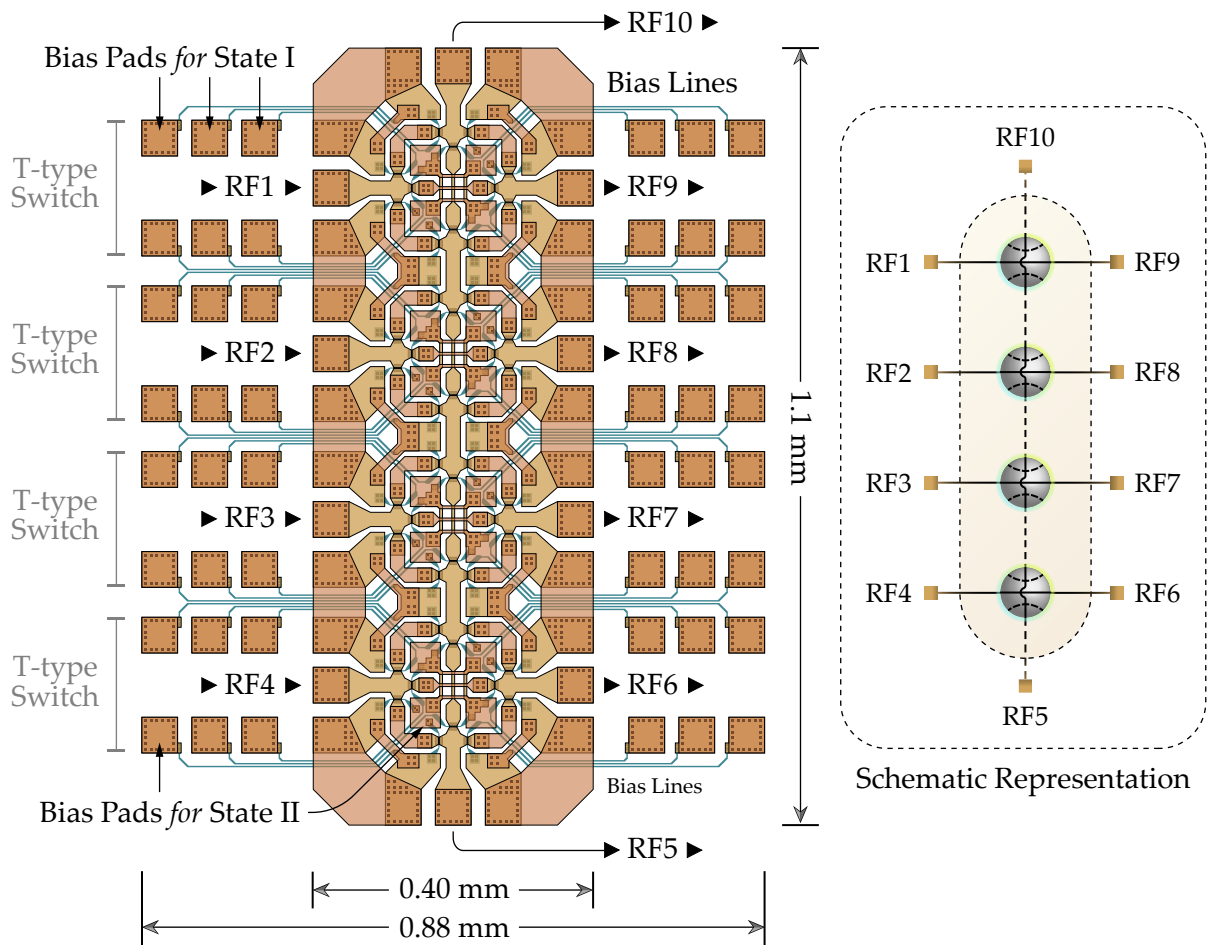


Figure 6.30: Layout of the miniaturized monolithically integrated PCM GeTe-based 4 × 6 redundancy switch matrix developed using cascaded T-type switching unit-cells. Schematic representation shows symbols of four T-type switches arranged in order to develop a 10 port switch matrix.

that have only two switches per path, and only one 90° bend in the signal path. At any given time, for redundancy applications, the maximum number of switches from input to output does not exceed more than four.

Fig. 6.29 illustrates the use of T-type switches in redundancy switch matrices. In case a receiver becomes non-functional (e.g. 'D3' or 'D5'), the switches can be reconfigured to route the input signal through spare devices 'D1' or 'D6'. It should also be noted that while C-type or R-type switches can be employed to realize similar functionality of the redundancy switch matrix shown in Fig. 6.29, the number of required C-type switches to achieve the same redundancy will be significantly higher. On the other hand, R-type switches lack simultaneous signal routing in state III. Thus, the T-type switches are the perfect candidate offering the desired signal routing functionality keeping the number of components to a minimum.

The redundancy switch matrix is designed by cascading four T-type switches reported in the previous section. Cascading the T-type switches makes it challenging to route the biasing circuit. Bias network is routed in a way to achieve equal RC time con-

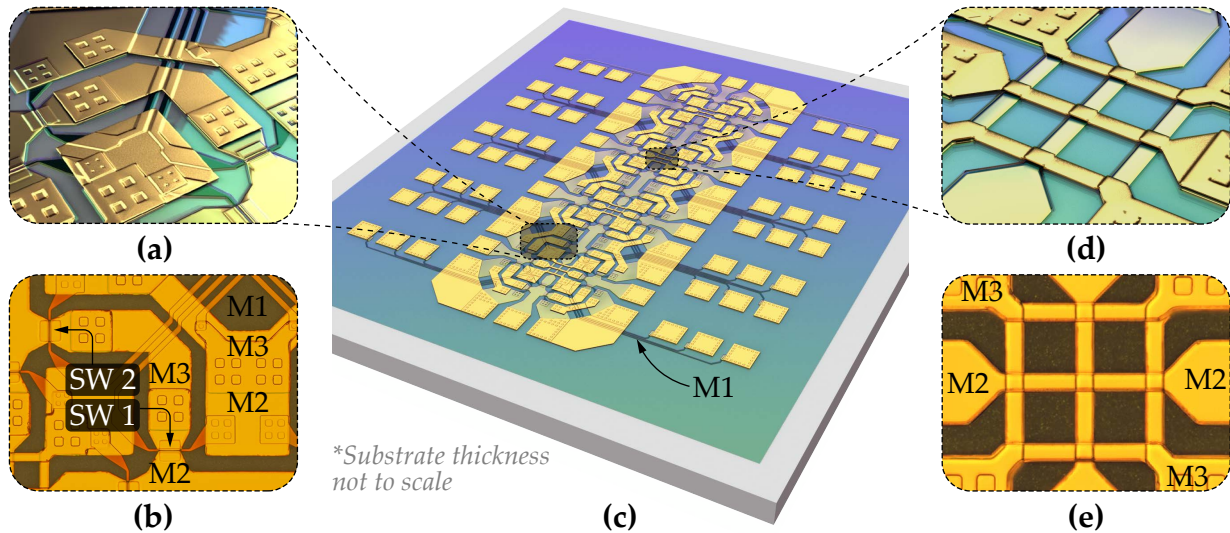


Figure 6.31: 3D rendered view of redundancy switch matrix: (a) 3D rendered view of a four-port RF crossover, (b) Optical micrograph of the RF crossover, (c) 3D rendered view of redundancy matrix highlighting bias split layer, (d) 3D rendered view of 90° bend with two PCM SPST switches, and (e) Optical micrograph of the 90° bend highlighting M2 to M3 vias, two PCM switches at the both ends and two bias lines crossing underneath. Optical micrographs shown are from the microfabrication process based on sapphire substrate.

stant for switches required per state. Conductive bias lines induce parasitic capacitance to the RF signal lines, thus, RF signal that is crossing over bias network is routed through M3 layer. 3D rendered view of the redundancy switch matrix is shown in Fig. 6.31 (c) that highlights two sub-components of a T-type switch: 90° bend and RF cross-over junction. Fig. 6.31 (a) shows the crossover junction that allows simultaneous RF signal flow and fulfils the functionality of state III. The optical micrograph of the crossover junction is shown in Fig. 6.31 (b). Two PCM SPST switches are implemented at the extreme ends of 90° bend and close to input/output ports of the T-type switch to minimize the RF loading. 3D rendered view of 90° bend is shown in Fig. 6.31 (d) and an optical micrograph of

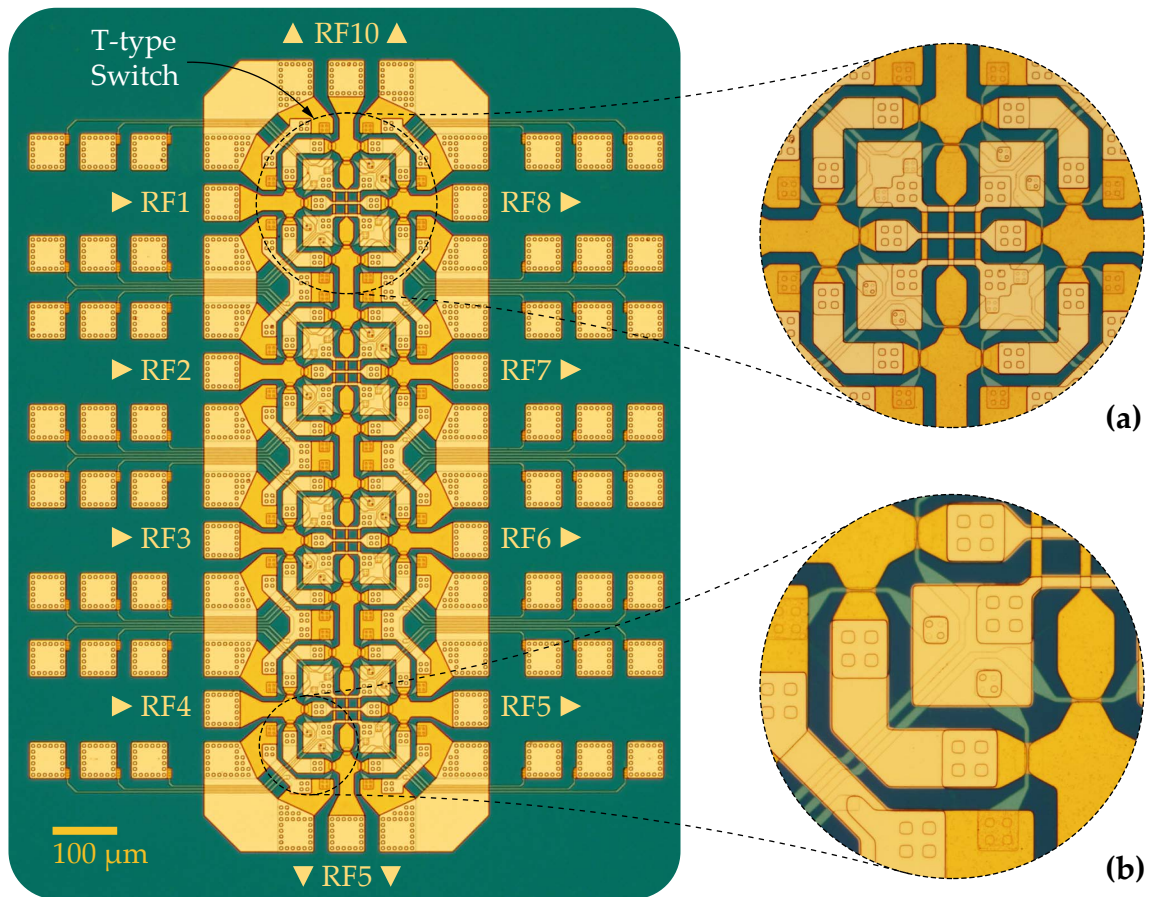


Figure 6.32: Optical micrograph of the PCM-based monolithically integrated redundancy switch matrix using cascaded T-type switching unit cells. Insets (a) and (b) highlights the T-type switching unit-cell and 90° bend with 2 bias lines routed underneath.

the 90° bend, highlighting two PCM SPST switches at both ends on the bend, bias lines crossing and M2 to M3 vias are shown in Fig. 6.31 (e). Optical micrographs shown are from the microfabrication process based on sapphire substrate. Common control signal connection to a pair of switches only works in case of GeTe as a PCM material, due to its latching nature. Metal insulator transition (MIT) materials such as vanadium oxide (VO₂), that require constant control voltage, cannot utilize the similar biasing network approach. Latching nature of PCM switches allow sharing of ground pads for common actuation nodes.

The optical micrograph of the fabricated PCM-based redundancy switch matrix using Gen 3 microfabrication process is shown in Fig. 6.32. The switch matrix is designed by cascading T-type switching unit cells; thus, it exhibits RF performance at par with T-type switch's performance. Biasing network routing in the core area of the T-type switching unit cell is similar to that is shown in Fig. 6.25. Thus, biasing network does not induce any additional parasitic capacitance to the RF signal paths. Due to the cascaded structures, the RF performance between ports RF1–RF9, RF2–RF8, RF3–RF7, and RF4–RF6 is similar to that of state III of the T-type switch as there are only two SPST switches between these ports. Ports RF1–RF10 and RF4–RF5 also encounter two RF SPST switches offering the RF performance similar to the state I and II of the T-type switch. The RF performance is identical between ports RF2–RF9, RF3–RF8, RF4–RF7, RF1–RF8, RF2–RF7, and RF3–RF6, as these paths have four SPST switches, with the theoretical performance equivalent to that of two cascades T-type switches in state I or in state II.

6.2.4.1 RF Performance Measurement

The RF performance of the integrated redundancy matrix is simulated and measured from DC to 60 GHz. Due to the symmetrical nature of the structure and cascaded T-type switching unit blocks, the RF performance is simulated and measured between ports RF4–RF5, RF4–RF6, and RF4–RF7. These three combinations reflect similar RF performance between other possible routing ports as described. The measured and simulated insertion loss, return loss and isolation of the redundancy switch matrix is shown in Fig. 6.33. The loss between ports RF4–RF5 and RF1–RF10 is less than 1.5 dB from DC to 60 GHz and lower than 1 dB over DC to 40 GHz, while the loss between port RF4–RF6, RF3–RF7, RF2–RF8 and RF1–RF9 is less than 2.2 dB from DC to 60 GHz and less than 1.5 dB from DC to 40 GHz. Although there are only two switches between these ports, additional loss is induced by the cross-over junction. Cascaded T-type switches show higher loss than other paths due to the four SPST switches between ports RF4–RF7, RF3–RF6, RF2–RF9, RF1–RF8, RF2–RF7, and RF3–RF6. Because of the large size

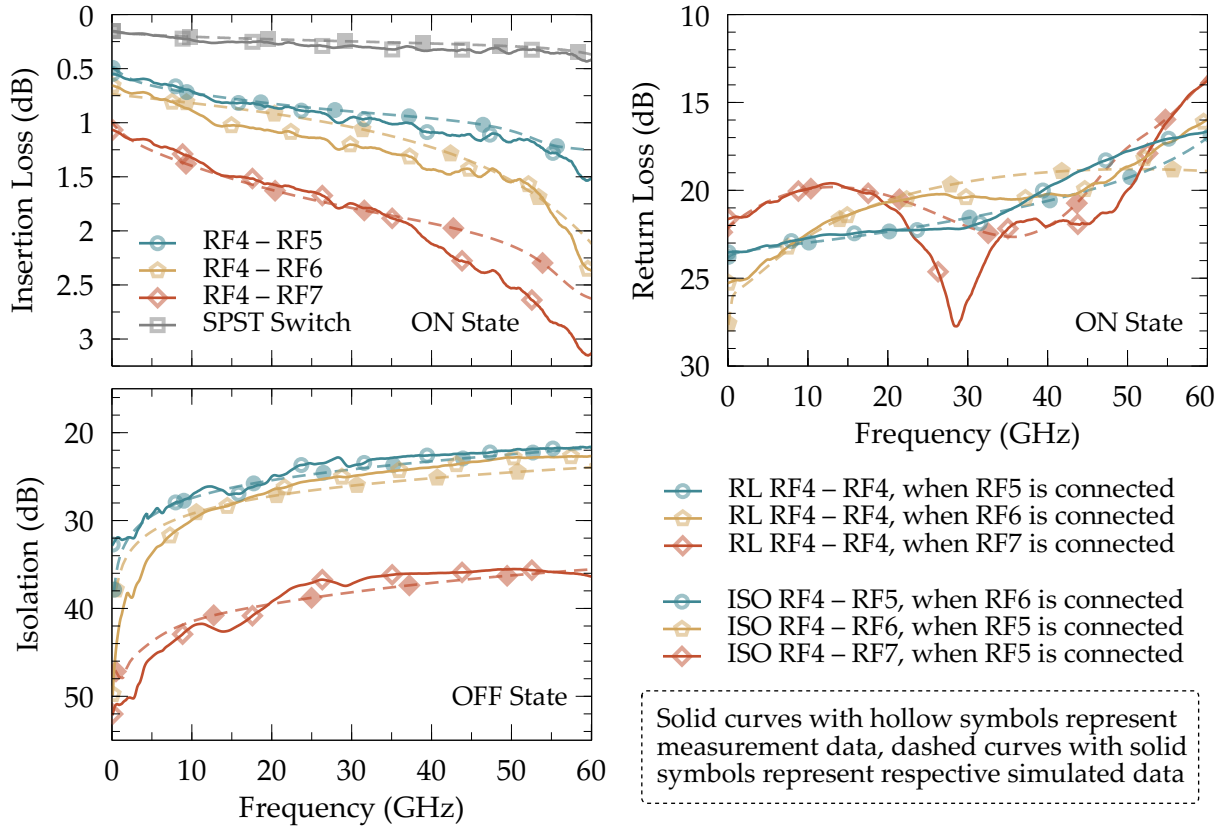


Figure 6.33: Measured and simulated RF response of monolithically integrated PCM-based redundancy switch matrix over DC to 60 GHz.

of the structure, resonance near 64 GHz was observed in simulation as well as in measurement. Therefore, the results in Fig. 6.33 are only shown up to 60 GHz. Return loss is better than 20 dB from DC to 40 GHz when port RF4-RF7, RF4-RF6 and RF4-RF5 are connected respectively, and greater than 16 dB from DC to 60 GHz when port RF4-RF6 and RF4-RF5 are connected. Return loss drops to 14 dB at 60 GHz for signal routing between port RF4-RF7.

Isolation is measured and simulated between non-connected ports. When port RF4-RF5 are connected, isolation is measured between port RF4-RF6, RF4-RF7, RF3-RF5 and RF5-RF6. With port RF4-RF6 connected, isolation is measured between ports RF4-RF5, RF4-RF7, RF5-RF6 and RF3-RF7. Isolation is also measured between ports RF4-RF8, RF4-RF6, RF4-RF5, RF3-RF7 and RF5-RF7 when ports RF4-RF7 are connected. Isolation is better than 21 dB in all the cases from DC to 60 GHz. Insertion loss can be

improved by minimizing the PCM channel width (w_s), with the trade-off of drop-in isolation. Additionally, shunt PCM switches can be utilized in conjunction with series SPST switches to achieve better isolation. On the other hand, adding shunt switch would complicate the structure further.

The reliability of the switch matrix can be estimated based on the lifespan of the SPST switch elements used to construct this matrix. The complex 4×6 redundancy switch matrix is comprehensively tested to verify its numerous states. Gen 3 microfabrication based process reported reliable RF switches, which translates the reliability of the fully integrated switch matrix.

6.2.5 Ultra Compact RF mmWave 4×4 Crossbar Switch Matrix

Ultra compact multiport switch matrices are possible using monolithically integrating PCM GeTe-based switches in crossbar configurations. A common approach towards switch matrices is to integrate several SPNT switching unit-cells along with $m \times n$ interconnection network. A 4×4 switch matrix using SP4T MEMS switches and LTCC based interconnect network is reported in [98]. The interconnect network although demonstrates reasonable RF performance up to 20 GHz, but the fully integrated system limits the operational bandwidth to 7 GHz only. A monolithically integrated 3×3 network is reported in [99] utilizing front and back side processing of the wafer. Microfabrication on both sides of the wafer has certain disadvantages such as large overall size, capacitive coupling between transitions, which limits the operational bandwidth with limited microfabrication process yields. The implementation of SPNT switches becomes challenging as N increases.

A crossbar architecture switch matrix based on MEMS was reported to provide the expansion of the system to a large number of RF input and output ports [84] with added benefit of monolithically integrated interconnect networks. The MEMS-based 3×3 network is limited to operational frequencies lower than 20 GHz. Another MEMS-based 4×4 switch matrix approach was reported in [30], which utilizes T-type switch with SP2T switches in a L-shaped topology to minimize insertion loss and phase variation. Recently, a MEMS-based compact monolithically integrated 4×4 crossbar switch matrix is demonstrated with scalable design [83, 100]. Despite of the excellent RF performance of the MEMS-based crossbar switch matrices, contact based MEMS switches utilized in most of the reported switch matrices are not latching type, which require constant DC power to hold the switching state. Due to the continuous requirement of multiple DC connections to the switches, MEMS-based switch matrices require high resistive

bias network to reduce DC coupling effects, which significantly increase the switching time close to sub millisecond range. Packaging and reliability concerns make RF-MEMS switch matrices less attractive options from implementation standpoint.

The PCM GeTe-based technology offers the flexibility to reduce the overall device area by dense integration of switching unit-cells. Latching functionality does not require constant DC power and the developed PCM switches offer switching speed faster than $1 \mu\text{s}$. Switch unit-cells are developed with two operational states. In this section, an ultra compact 4×4 crossbar switch matrix is presented. Switch matrix architecture is developed by arranging unit-cells and SP2T switches in a way to provide $m \times n$ input output routing with scalability provision to higher order switch matrices.

6.2.5.1 Scalable Crossbar Switch Matrix Architecture

The scalable crossbar switch matrix architecture shown in Fig. 6.34 consists of an array of switch unit-cells ($SU_{x,y}$) and SP2T switches ($SD_{x,y}$) connected in a grid pattern to

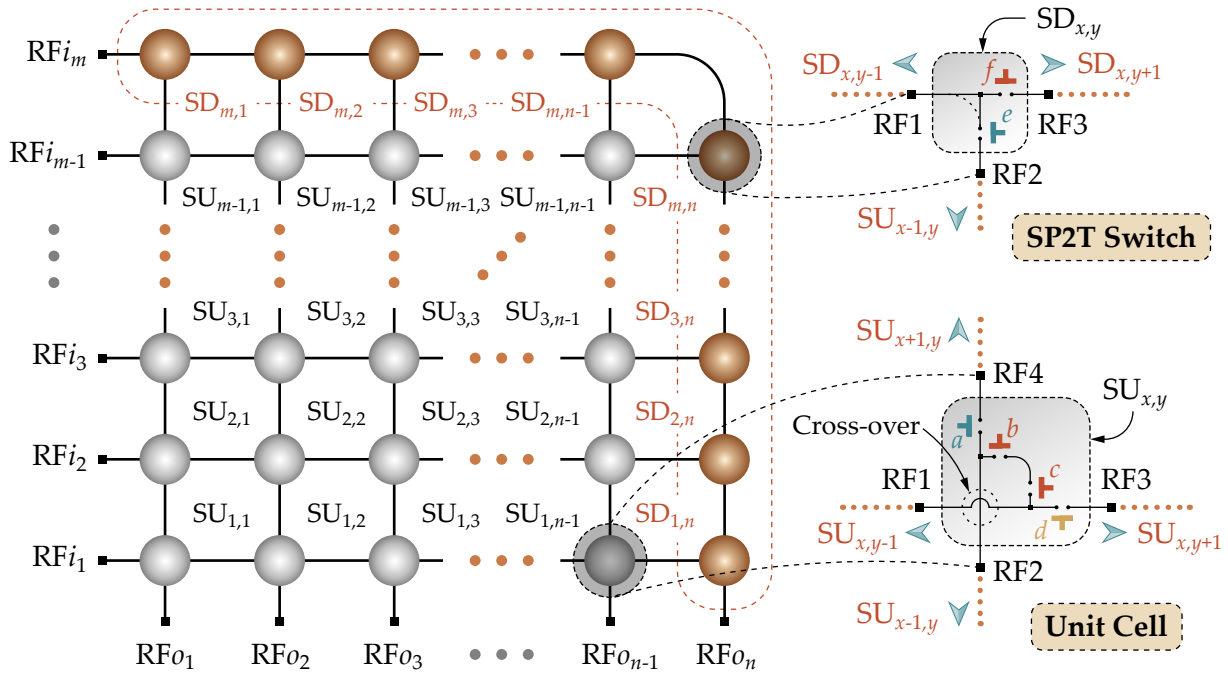


Figure 6.34: Scalable $m \times n$ crossbar switch matrix architecture utilizing switch unit-cells and SP2T switches arranged in a grid pattern to achieve signal routing.

achieve signal routing. RF signal at any m input ($RF_{i_1}, RF_{i_2}, \dots, RF_{i_{m-1}}, RF_{i_m}$) can be routed to any available n output port ($RF_{o_1}, RF_{o_2}, \dots, RF_{o_{n-1}}, RF_{o_n}$). Cross-over paths designed in switch unit-cells offer signal routing between two overlapping RF paths. With the switch architecture shown in Fig. 6.34, a $m \times n$ crossbar switch matrix requires a total of $(mn - 1)$ total cells, with $((m - 1) \times (n - 1))$ switch unit-cells and $((m - 1) + (n - 1))$ SP2T switches.

6.2.5.2 Crossbar Switch Matrix Unit-Cell

To attain the routing functionality of RF signal at any input port to output port, unit-cells ($SU_{x,y}$) are designed to provide two operational states: ‘turn state’ and ‘thru state’ as shown in Fig. 6.35. 3D crossbar architecture is extensively used in digital memories where each cell stores 1 bit information. Crossbar unit-cells with two operational states are typically implemented using three switches as shown in Fig. 6.35. For memories or low-frequency applications, a single turn-state switch is sufficient to connect input/output ports. For high-frequency applications it is required to isolate signal paths as close to the junction as possible to avoid degrading RF performance.

The PCM GeTe-based crossbar switch unit-cell is designed using four SPST switches monolithically integrated to satisfy the two operational state requirement. SP2T switch cell has two SPST switches as shown in Fig 6.36.

Switch configurations of the unit-cell is shown in Fig. 6.37. Unit-cell has four ports (RF_1, RF_2, RF_3 and RF_4), three RF paths (one ‘turn’ path RF_1 – RF_2 and two ‘thru’ paths RF_1 – RF_3 , and RF_2 – RF_4). Two ‘thru’ paths can be connected simultaneously due to the

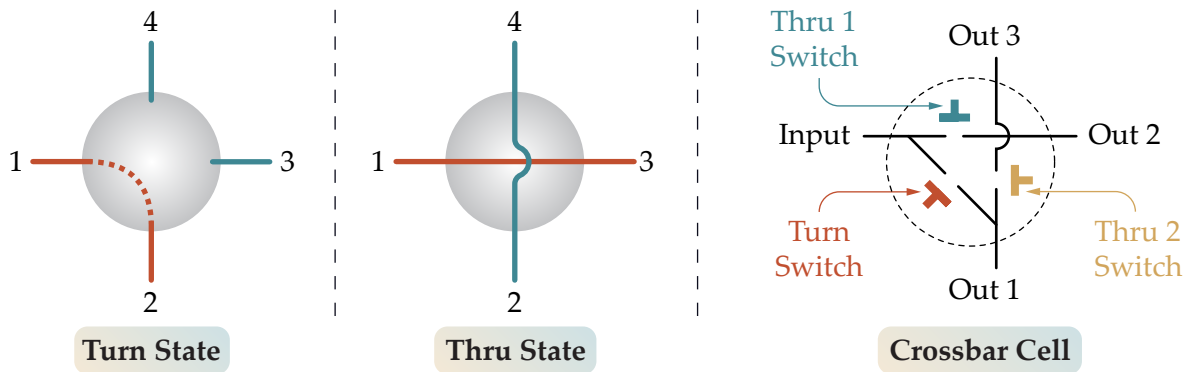


Figure 6.35: Crossbar switch unit-cell operation states and a typical unit-cell configuration with three switches.

cross-over junction. Two PCM SPST series switches (b and c for RF1–RF2) are required to route signal in ‘turn’ state and only one PCM SPST series switch is required for signal routing in ‘thru’ state (a for RF2–RF4 and d for RF1–RF3). Switches b and c are controlled using a single control pad by adjusting the pulse amplitude. 3D rendered views of a four-port PCM GeTe-based switch unit-cell with four SPST switches, and one SP2T switch cell with two SPST switches is shown in Fig. 6.36. The SP2T cells and crossbar cells are arranged in a way such that, for a SP2T switch cell ($SD_{x,y}$), RF3 of $SD_{x,y}$ is connected to the next cell’s $SD_{x,y+1}$ ’s RF1 port, while RF2 port of the $SD_{x,y}$ is connected to RF4 of the switch unit cell ($SU_{x,y}$). Crossbar switch unit cells are also arranged in the similar manner.

The chip layout and the optical micrograph of the switch unit-cell implemented to demonstrate ‘turn’ state is shown in Fig. 6.38. RF signal is routed from input to output

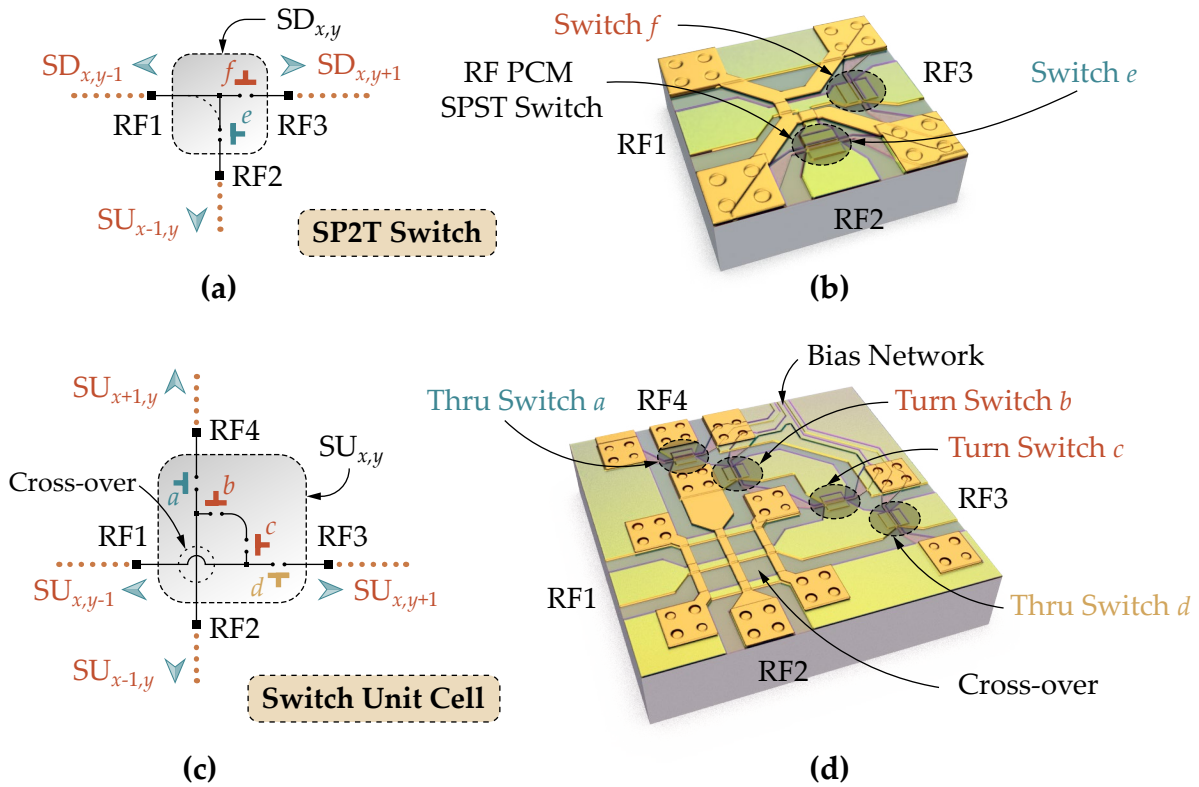


Figure 6.36: Switch unit cells: (a) Schematic of a SP2T switch cell, (b) 3D rendered view of the SP2T switch cell with two SPST switches, (c) schematic and (d) 3D view of the crossbar switch unit-cell with four SPST switches used in crossbar architecture.

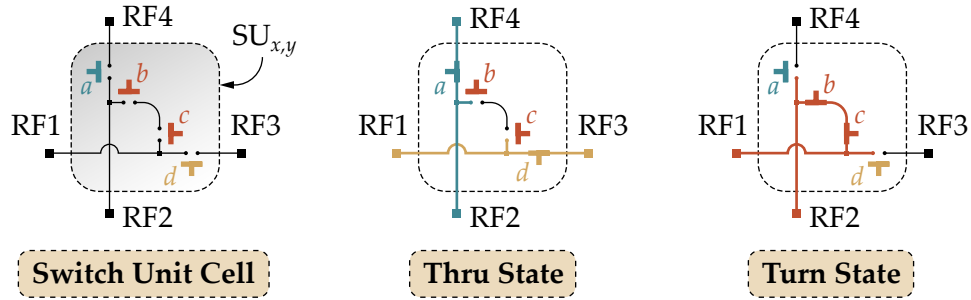


Figure 6.37: Crossbar switch unit-cell highlighting four SPST switches and signal paths in ‘thru’ and ‘turn’ states.

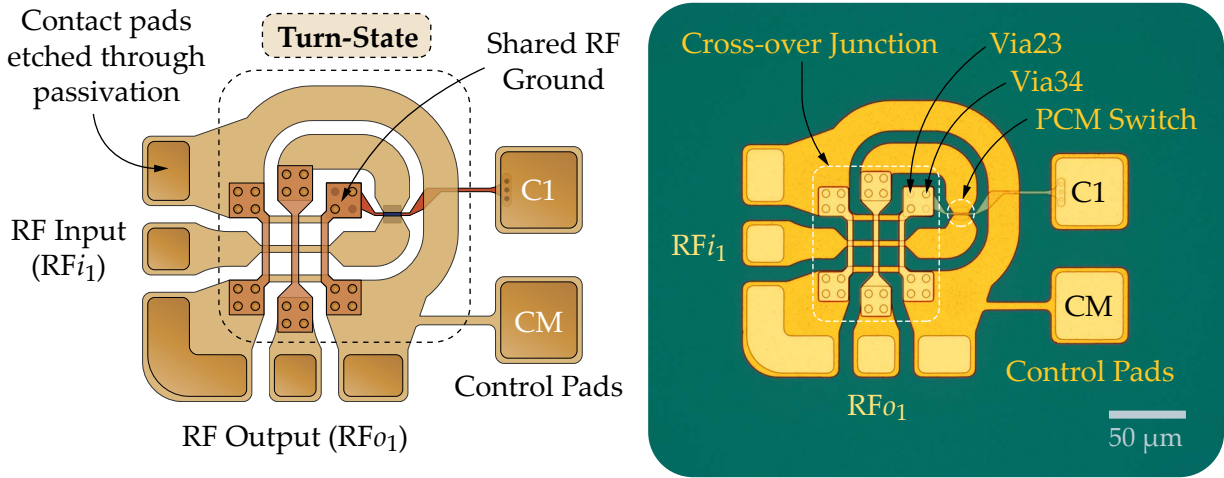


Figure 6.38: Chip layout and optical micrograph of a ‘turn’ state implementation using unit-cell.

through a PCM SPST switch and designed beside a cross-over junction to implement a 90° turn. Actuation pulse of 12 V amplitude and 200 ns width is applied between ‘C1’ and ‘CM’ pads to turn OFF the switch, and a pulse of 7.8 V amplitude and 1.2 μs width turn ON the switch. RF PCM SPST switch design dimensions and performance is identical to the one reported in chapter 4.

6.2.5.3 2×2 Crossbar Switch Matrix

A PCM-based 2 × 2 switch matrix is implemented in crossbar architecture. For $m = 2$ and $n = 2$ switch matrix, only one switch unit-cell ($SU_{1,1}$) and two SP2T switch cells ($SD_{1,2}$ and $SD_{2,1}$) are required as shown in the chip layout in Fig. 6.39. 2-bit function-

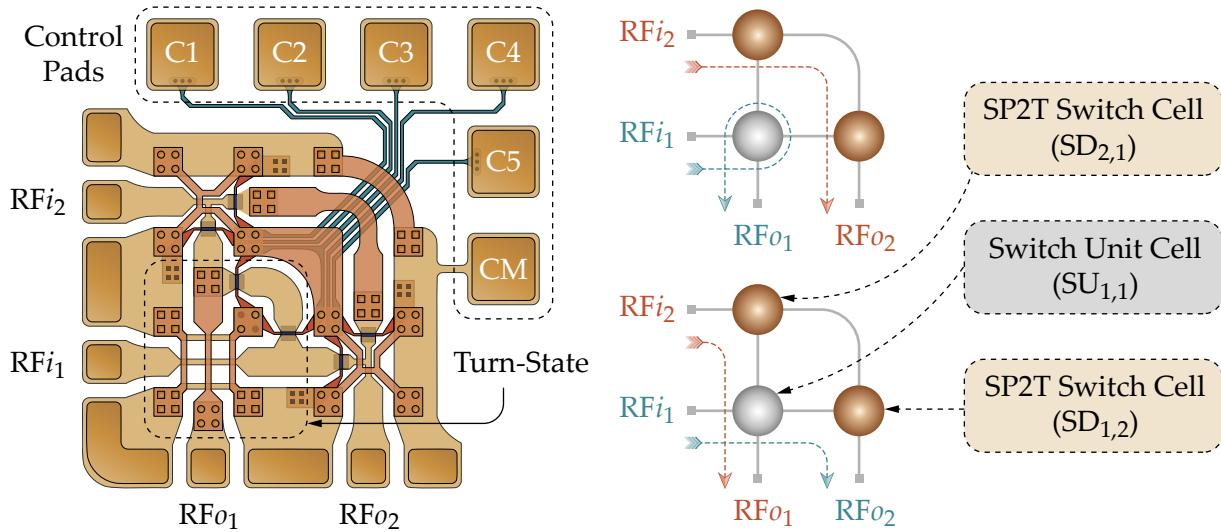


Figure 6.39: Layout of 2×2 crossbar switch matrix. All signal routing combinations are highlighted to demonstrate fully reconfigurable 2-bit operation of the circuit.

ality of the 2×2 configuration is also depicted in Fig. 6.39. Signal routing and control signal requirement for the 2×2 matrix is shown in Table 6.4. 90° bend between two SP2T switches is implemented on the top metal layer of Gen 3 microfabrication process. Capacitive coupling from the bias network routed underneath is minimized by optimizing the CPW discontinuity. Programming a minimum one SPST switch or a maximum two SPST switches is enough to fully route the RF signal between any available input and output ports as per the Table 6.4. Two SPST switches in SP2T switch are wired individually with their respective control pads, while a turn state between RF_{i1} – RF_{o1} has two switches, which are tied to a single control connection. Actuation pulse amplitude degrades at the split node, thus $1.5x$ actuation pulse amplitude is required at control

Table 6.4: Truth table of 2-bit crossbar switch matrix

Route	Signal Path	Number of Switches	Control Pads	Actuation Pulse Amplitude Multiplier
1	RF_{i1} – RF_{o2}	1	C4, CM	$1 \times$
2	RF_{i2} – RF_{o1}	1	C1, CM	$1 \times$
3	RF_{i1} – RF_{o1}	2	C3, CM	$1.5 \times$
4	RF_{i2} – RF_{o2}	2	C2, C5, CM	$1 \times$

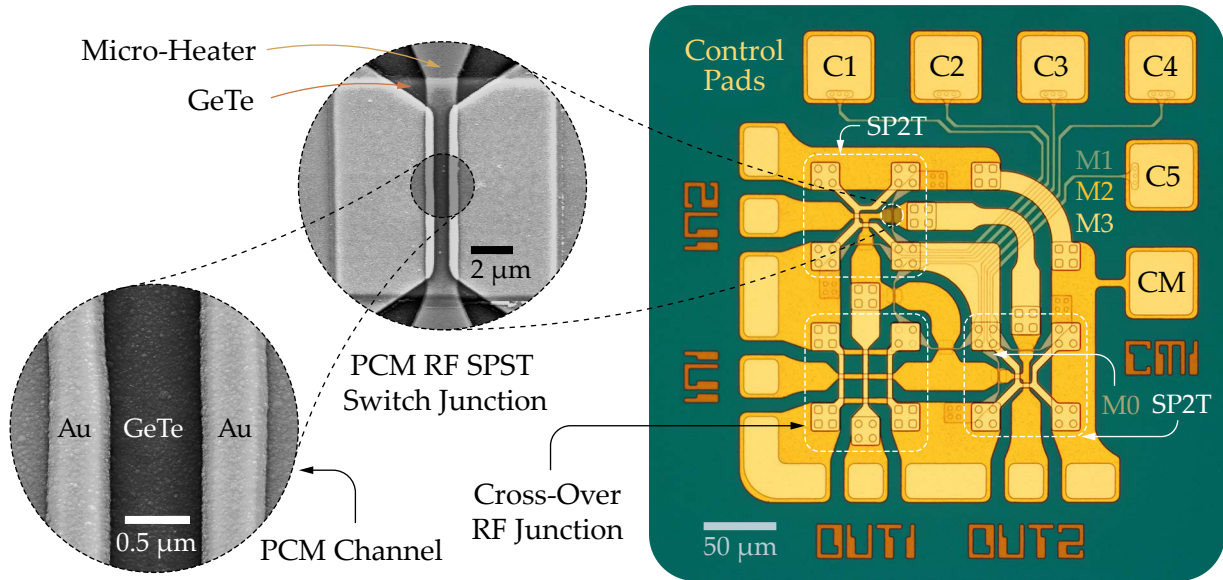


Figure 6.40: Optical micrograph of 2×2 crossbar switch matrix. Insets show SEM micrographs of PCM SPST switch and PCM junction at two different magnification levels.

pad 'C3' to actuate both switches at the same time. This approach reduces the number of control pads in switch matrices with large number of input/output ports.

Optical micrograph of the fabricated 2×2 crossbar RF switch matrix is shown in Fig. 6.40. Various metal layers are highlighted in the optical micrograph. Insets show SEM micrographs of the PCM SPST switch junction at two different magnification levels. Port names shown in the optical micrograph are patterned using V0 layer of the Gen 3 process.

For a pulse generator in which the load impedance is configurable and the micro-heater's resistance is communicated to the pulse generator, the delivered pulse amplitude is equal to the amplitude reported by the pulse generator (50Ω source impedance and unmatched load impedance, which is an arbitrary micro-heater resistance). Wiring two switches in a shunt configuration, the total resistance of both the micro-heaters gets half, thus the resistance need to be translated to the pulse generator for accurate delivery of control signals. If the pulse generator does not allow changing the load impedance but to choose from either a 50Ω or high impedance load (typical for most of the signal generators), the actual pulse amplitude (V_p) delivered to the micro-heater can be computed as:

$$V_{p1} = \frac{2R_h \cdot V_s}{R_l + R_h} \tag{6.1}$$

where, R_h is the resistance of the micro-heater, V_{p1} is the actual voltage pulse delivered to one SPST switch, R_l is the load impedance of the pulse generator, and V_s is the pulse amplitude reported by the pulse generator. Typically, R_l is 50Ω . When two switches are connected in shunt configuration with a single control pad, voltage (V_p) can be calculated as:

$$V_{p2} = \frac{2R_h \cdot V_{source}}{2R_l + R_h} \tag{6.2}$$

where, V_{p2} is the actual voltage pulse delivered to two shunt wired SPST switches using a single control pad. If the load impedance of the pulse generator (R_l) is set to micro-heater's resistance (R_h), then V_{p2} can be scaled up as $V_{p2} = 1.5 \times V_{p1}$.

6.2.5.4 4×4 Crossbar Switch Matrix

Strategic signal routing feasibility (RF and bias network) allows scaling the switch matrices to higher order utilizing switch unit-cells. Similar to 2×2 crossbar switch matrix

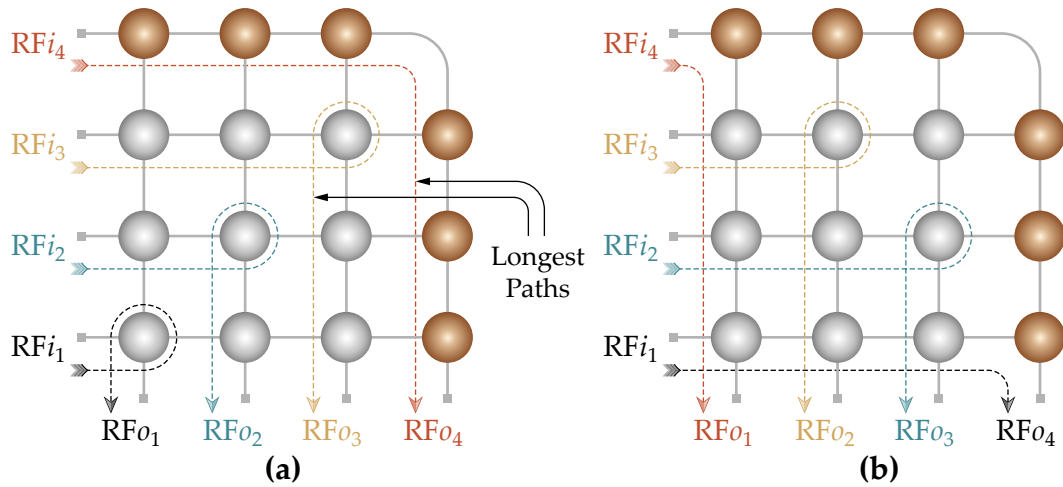


Figure 6.41: Signal routing paths of a 4×4 crossbar switch matrix highlighting longest paths, which have maximum number of switches in the signal path.

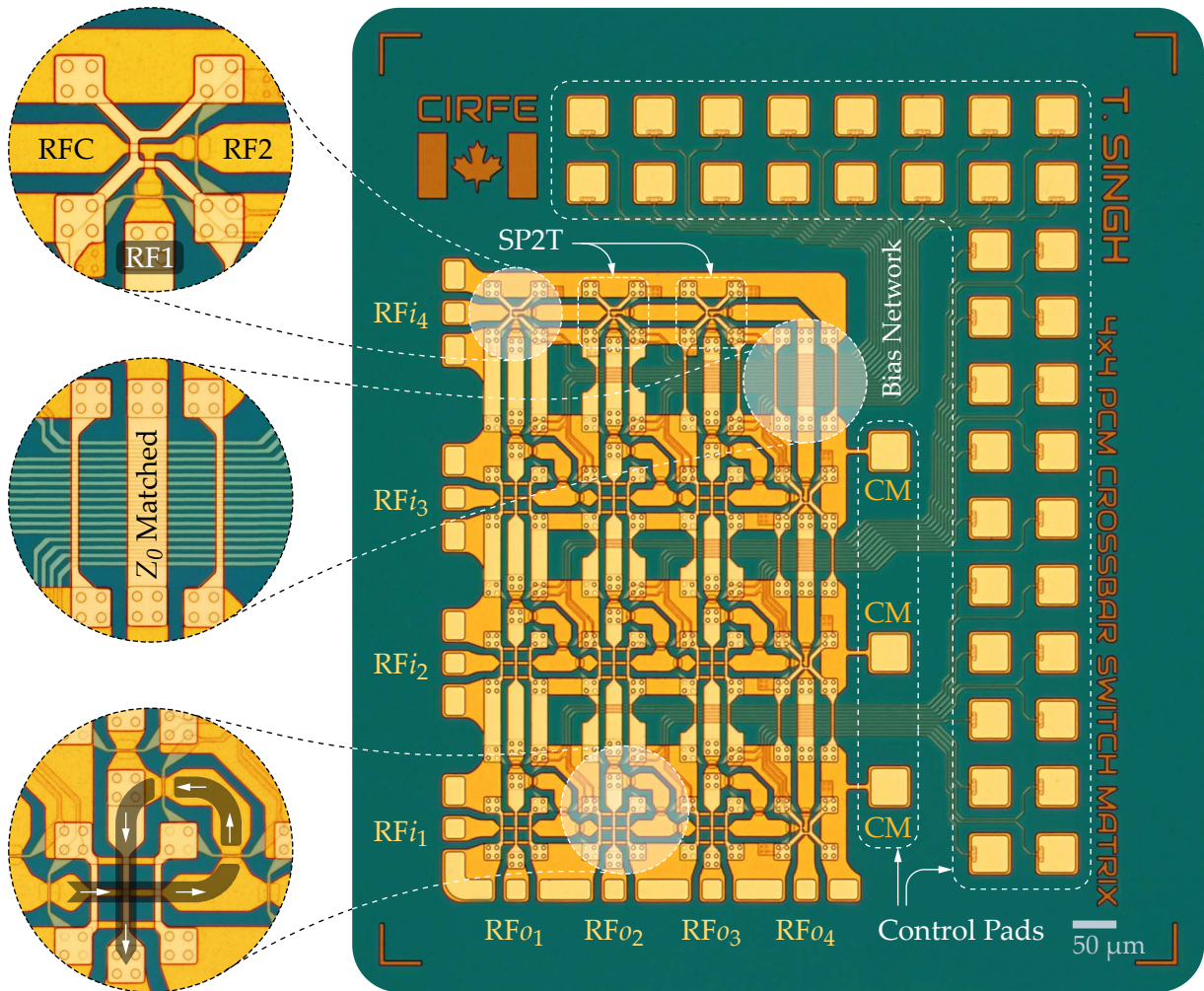


Figure 6.42: Optical micrograph of the PCM GeTe-based 4×4 switch matrix. Inset shows magnified optical micrographs of SP2T switch elements, impedance matching and capacitance compensation of bias network, and a unit-cell implemented in switch matrix highlighting turn state.

shown in Fig. 6.40, A PCM-based 4×4 crossbar switch matrix is developed. The switch matrix is scaled as per the architecture shown in Fig. 6.21. 4×4 switch matrix consists of nine $(m - 1 \times n - 1)$ switch unit-cells ($SU_{x,y}$) arranged in a 3×3 matrix ($SU_{1,1}, SU_{1,2}, \dots, SU_{3,2}, SU_{3,3}$) and six $(m - 1 + n - 1)$ SP2T switches ($SD_{4,1}, SD_{4,2}, \dots, SD_{1,4}$) integrated around unit-cells. SP2T switches in a 4×4 crossbar configuration accommodate signal routing from RF_i to any available output port and/or from any available input

port to RF_4 output port.

Signal routing paths of a 4×4 crossbar switch matrix highlighting longest paths with maximum number of switches is shown in Fig. 6.41. The presented crossbar switch matrix exhibits a minimum insertion loss in a shortest path RF_{i_1} – RF_{o_1} with two SPST switch elements only. Longest paths have maximum of six SPST switches in signal path.

The 4×4 crossbar switch matrix is designed with 48 PCM SPST switches distributed within switch unit-cells and SP2T cells. 36 control pads in addition to ‘CM’ (ground) pads provides actuation signal to program the respective latching PCM switches to route the RF signal between any RF input port to any available RF output port. Turn-signal in switch unit-cell have two switches per path wired to single control pad as described in previous sections. All the ports can be cross-connected to utilize the switch matrix full bandwidth.

Optical micrograph of the PCM GeTe-based 4×4 switch matrix is shown in Fig. 6.42. Inset shows magnified optical micrographs of SP2T switch elements, impedance matching and capacitance compensation of bias network, and a unit-cell implemented in the crossbar switch matrix highlighting turn state. The crossbar switch matrix is highly miniaturized with overall device size of $0.5 \text{ mm} \times 0.75 \text{ mm}$ including RF input and output ports and excluding control pads. With the control pads arrangement depicted in Fig. 6.42, the device periphery is $0.96 \text{ mm} \times 0.77 \text{ mm}$. This is the smallest crossbar switch matrix ever reported for mmWave applications.

6.2.5.5 RF Performance Evaluation of Crossbar Switch Matrices

The RF performance of the presented crossbar switch matrices is simulated in EM packages including Ansys Electronics Desktop (Previously Ansys HFSS), and verified using Sonnet EM Professional Suite over DC to 40 GHz. Measured and simulated performance of an unit-cell ($SU_{x,y}$) in ‘Turn’ state is shown in Fig. 6.43. Measured and simulated insertion loss of a series PCM GeTe-based SPST switch is shown for comparison. A 1×1 unit-cell, implemented for ‘Turn’ state operation consists of a single PCM SPST switch as shown in Fig. 6.38. The RF performance of the unit-cell in ‘Turn’ state degrades due to the crossover junction and CPW discontinuities in the RF signal path. The insertion loss is more prominent at higher frequencies as shown in Fig. 6.43. The measured RF performance reports less than 0.8 dB insertion loss over DC to 40 GHz. At low frequencies, thin metal films contribute to the losses. The measured return loss is better than 21 dB and isolation higher than 26 dB over the entire bandwidth. The unit-cells utilized in higher order matrices consist of two SPST switches in turn-state to achieve better RF

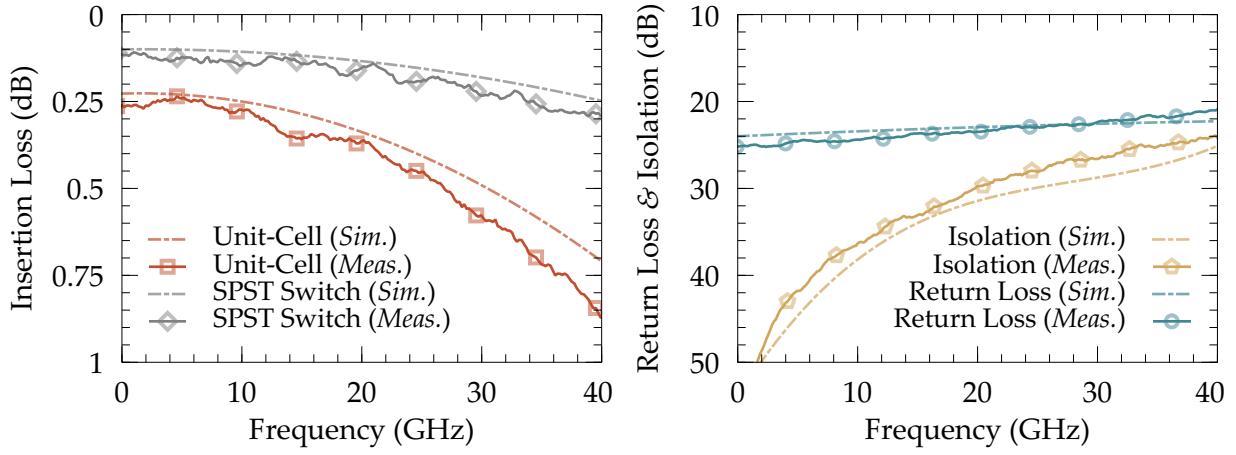


Figure 6.43: Measured and simulated RF performance of an unit-cell for crossbar switch matrix implementation. Insertion loss of a PCM GeTe-based SPST switch is shown for comparison.

matching in ON-state and high isolation in OFF-state. RF performance of 2×2 and 4×4 crossbar switch matrices is simulated and measured over DC to 40 GHz.

The RF performance of a 2×2 crossbar switch matrix shown in Fig. 6.44 follows route configuration as depicted in Table 6.4. The measured insertion loss is less than 1.1 dB in route 1 and 2 while the loss is lower than 1.3 dB and 1.4 dB in routes 3 and 4 respectively as shown in Fig. 6.44. Route 4 is the worst case scenario in a 2×2 switch

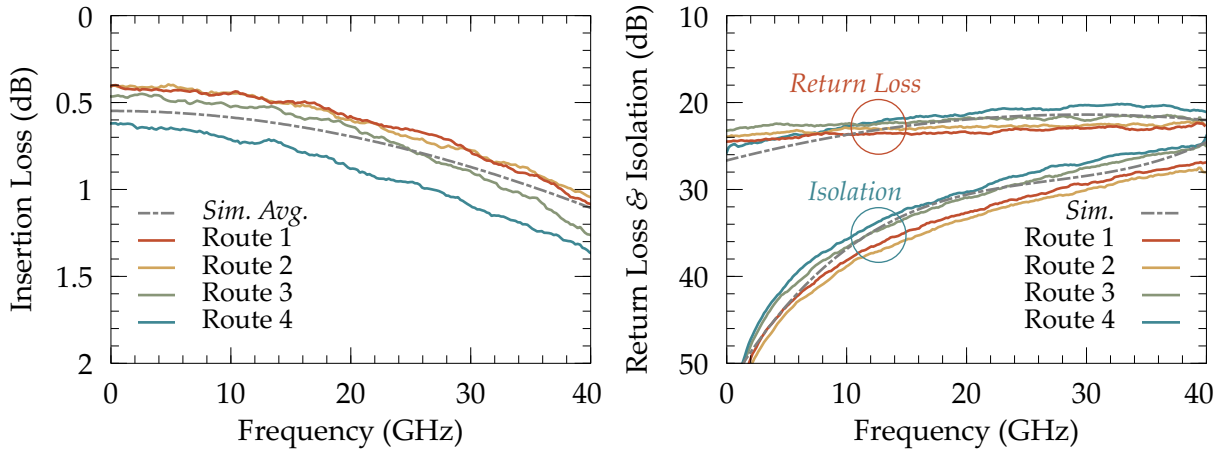


Figure 6.44: Measured RF performance of a 2×2 crossbar switch matrix over DC to 40 GHz in all possible routes. Simulation average is shown.

matrix, as the signal passes through two SPDT switches and 90° with conductive lines crossing underneath, which contribute to higher loss than other routes. Simulated and measured return loss is better than 20 dB and isolation is higher than 24 dB in all possible routing scenarios. Only the simulation average is shown in Fig. 6.44.

The PCM based 4×4 crossbar switch matrix as shown in Fig. 6.42 provides 4-bit routing functionality between input and output ports. Due to the use of unit-cells to achieve scalability, the RF performance remains similar between certain routes. The RF performance is measured between 7 unique routes to get minimum and maximum performance limits of the 4×4 crossbar switch matrix. The RF signal passes through a number of PCM GeTe-based SPST switches between input and output ports depending on the route chosen, thus the RF performance varies depending on the number of switches per signal route and type of signal discontinuities in the path. Table 6.5 summarizes path configuration and number of switches in signal path. RF performance is simulated and measured for the routes specified in Table 6.5. Route 1 exhibits the best RF performance as the signal travels through least number of switches and discontinuities. The measured RF performance of route 1 shows insertion loss lower than 1.2 dB over the entire 40 GHz bandwidth.

Route 1–7 are carefully chosen to depict the RF performance of the crossbar switch in best, worst and in-between cases. In best case scenario (Route 1), the signal passes through two PCM SPST switches, one 90° bend and one RF crossover junction. While, in the worst case (Route 7), the signal is routed between RF_{i4} – RF_{o4} ports, which consists of 6 SPDT switches, one 90° bend and three bias bridges with more than 16 conductive bias wires crossing underneath bias bridges. Despite of all the signal degradation elements in the RF path, the switch matrix is designed to exhibit less than 4.2 dB insertion loss in

Table 6.5: Path configuration of 4×4 crossbar switch matrix.

Route	Signal Path	No. of Switches	No. of Crossovers	Signal Discontinuities	Performance Remarks
1	RF_{i1} – RF_{o1}	2	1	1 Bend	Best Case
2	RF_{i1} – RF_{o4}	3	3	1 SPDT Junction	Good
3	RF_{i2} – RF_{o2}	4	3	1 Bend, 1 Bias Bridges	Good
4	RF_{i4} – RF_{o1}	4	3	3 Metal Bridges	Reasonable
5	RF_{i2} – RF_{o3}	5	4	1 Bend, 1 Bias Bridge	Worse
6	RF_{i3} – RF_{o2}	5	4	1 Bend, 2 Bias Bridges	Worse
7	RF_{i4} – RF_{o4}	6	0	6 SPDT, 3 Bias Bridges	Worst Case

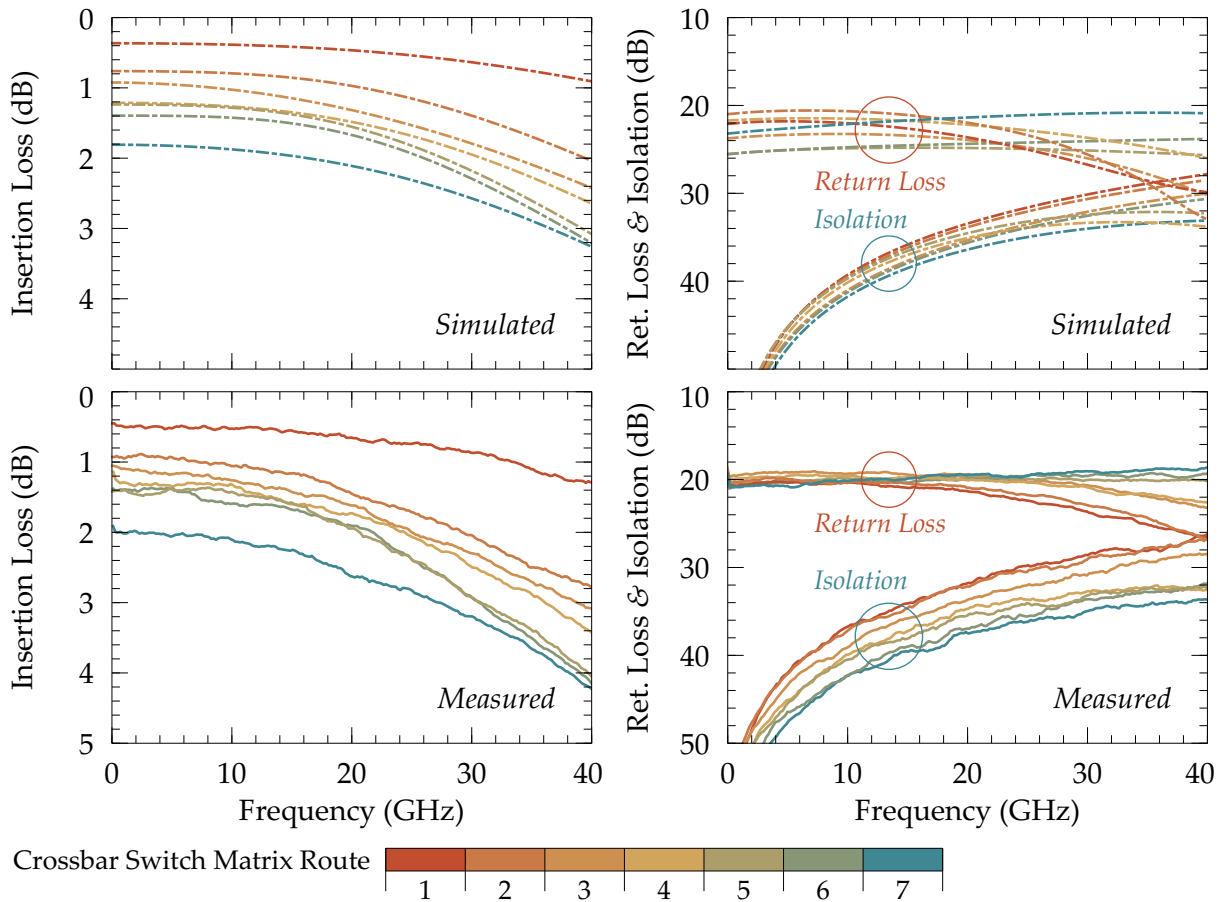


Figure 6.45: Measured and simulated RF performance of a PCM GeTe-based 4×4 switch matrix over DC to 40 GHz. RF performance is shown for 7 possible routes, with route 7 exhibiting the worst case scenario.

worst case. Most of the signal routing combinations show performance with loss less than 4 dB, measured return loss is better than 18 dB and isolation higher than 26 dB over DC to 40 dB. EM simulated performance shows a close match with the measured results with worst case loss lower than 3.2 dB, return loss better than 20 dB and isolation higher than 26 dB. The difference between measured and simulation insertion loss is due to the cumulative nature of reversible binary switch loss.

For the first time ever, the PCM-based RF crossbar switch matrix is demonstrated, which is first of its class capable of providing excellent RF performance on top of latching functionality, no steady state power consumption, reliable operation with high speed

reconfigurability in an extremely compact package, which makes the presented crossbar switch matrix highly attractive choice compared to current state-of-the-art.

6.2.6 PCM-based Scalable Latching Crossbar Switch Matrices for Low Frequency Applications

Miniaturized higher order monolithically integrated scalable crossbar switch matrices are developed for low frequency applications. RF switch matrices require careful signal routing and accurate impedance balancing throughout the RF signal path while taking care of any capacitive, inductive and/or resistive loading effects. Multi-port RF switch matrices are highly complex circuits in terms of meeting design specs and performance criterion. There are tremendous applications, which do not require routing high frequency signals. Based on the crossbar switch matrix discussed in previous sections, scalable higher order crossbar switch matrices are designed for low frequency applications. Similar to RF crossbar switch matrices, low frequency (LF) crossbar switch matrices are designed based on cascading switch unit-cells in 2D matrix form. Two distinct switch unit-cell ($UC_{x,y}$) designs (ver1 and ver2) are investigated as shown in the layouts in Fig. 6.46 (a) and (b).

Switch unit-cells ($UC_{x,y}$) are cascaded in both x and y direction to create a $m \times n$ switch matrix. Desired signals are routed through a single PCM switch element connected in a ‘Turn’ state. Signals are routed between $UC_{x-1,y}$ and $UC_{x,y-1}$ path by actuating the PCM switch through the control network $Uct_{x,y}$. Actuating the PCM switch in ON-state allows the signal flow from $UC_{x-1,y}$ to $UC_{x,y-1}$. When the switch is in OFF-state, signal flow follows ‘Thru’ path between $UC_{x-1,y}$ to $UC_{x+1,y}$ and $UC_{x,y+1}$ to $UC_{x,y-1}$. Switch routing functionality is similar between ver1 and ver2 of unit-cells.

Optical micrographs of the ver1 and ver2 switch unit-cells are shown in Fig. 6.46 (c) and (d). In LF crossbar switch matrices, M1 layer of the Gen 3 microfabrication process is not used, as M2 and M3 serves both signal paths along with control paths.

6.2.6.1 LF 4×12 Crossbar Switch Matrix

A 4×12 crossbar switch matrix is developed having 4 input ports ($i1, i2 \dots i4$) and 12 output ports ($o1, o2, \dots o12$) as shown in the chip layout of the switch matrix in Fig. 6.47. Two sets of control pads ($1, 2, \dots 12$ and $a, b, \dots d$) allow programming the desired PCM switch to route signal between any input port to any available output port. Applying

actuation pulse between control pads $a-1$ routes the signal at $i1$ port to $o1$ port, $c-6$ routes the signal from $i3$ to $o6$ port. 4×12 switch matrix is designed with 48 ver1 switch unit-cells and each unit-cell has only one PCM switch. Control pads provide 48 combinations to address all the available PCM switches. A 4×12 switch matrix demonstrates the easy scaling possibility of unit-cells into $m \times n$ order switch matrices.

Fabricated 4×12 crossbar switch matrix is shown in Fig. 6.48. The switch matrix is highly miniaturized with device area measuring under 0.9 mm^2 including all the input/output ports and control pads. Utilizing a single PCM switch is not a concern for low frequency applications, but does not work for high frequency applications, due to signal reflections and standing waves on unmatched signal lines.

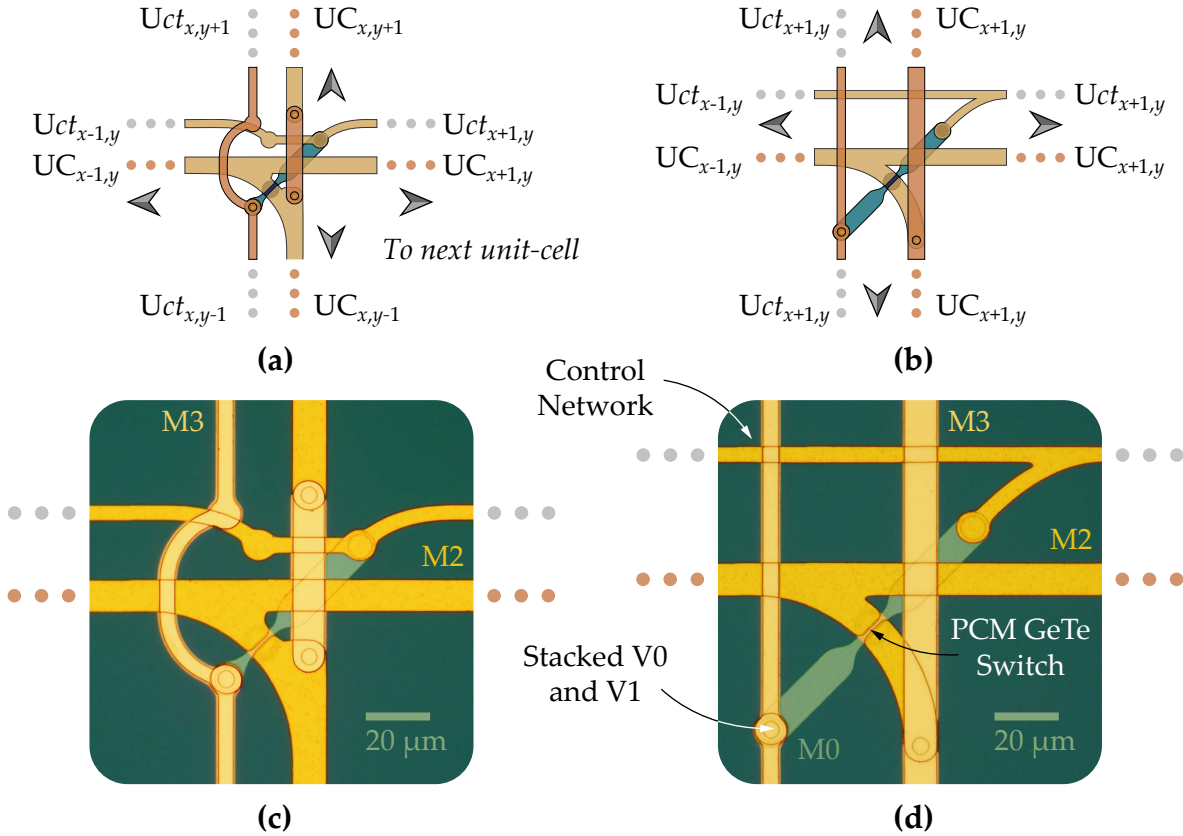


Figure 6.46: PCM GeTe-based unit-cells for low frequency crossbar switch matrices: (a) Layout of ver1 unit-cell, (b) layout of ver2 unit-cell, (c) optical micrograph of ver1 unit-cell, and (d) optical micrograph of ver2 unit-cell.

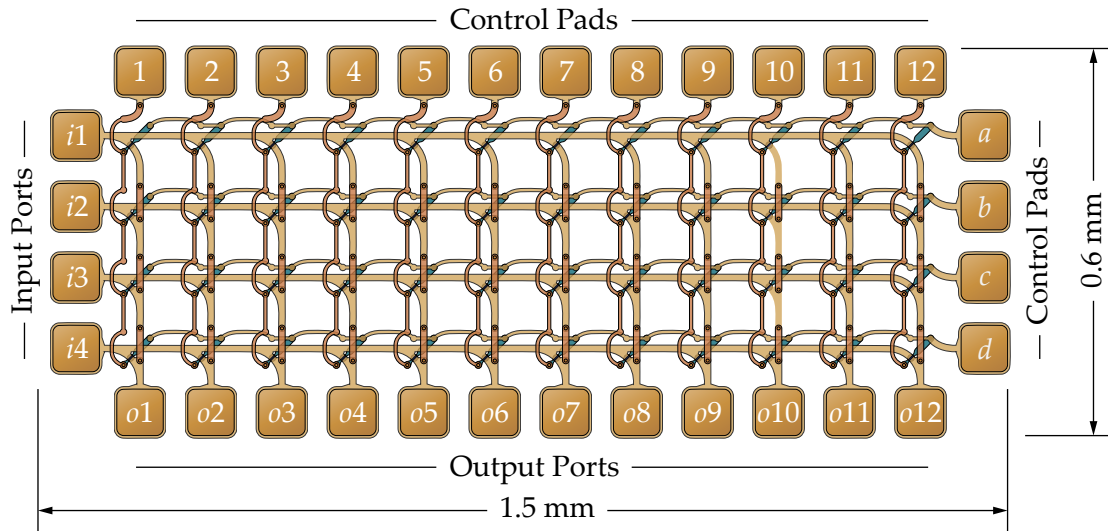


Figure 6.47: Layout of a 4×12 DC crossbar switch matrix. Only one PCM GeTe-based switch is used per unit-cell.

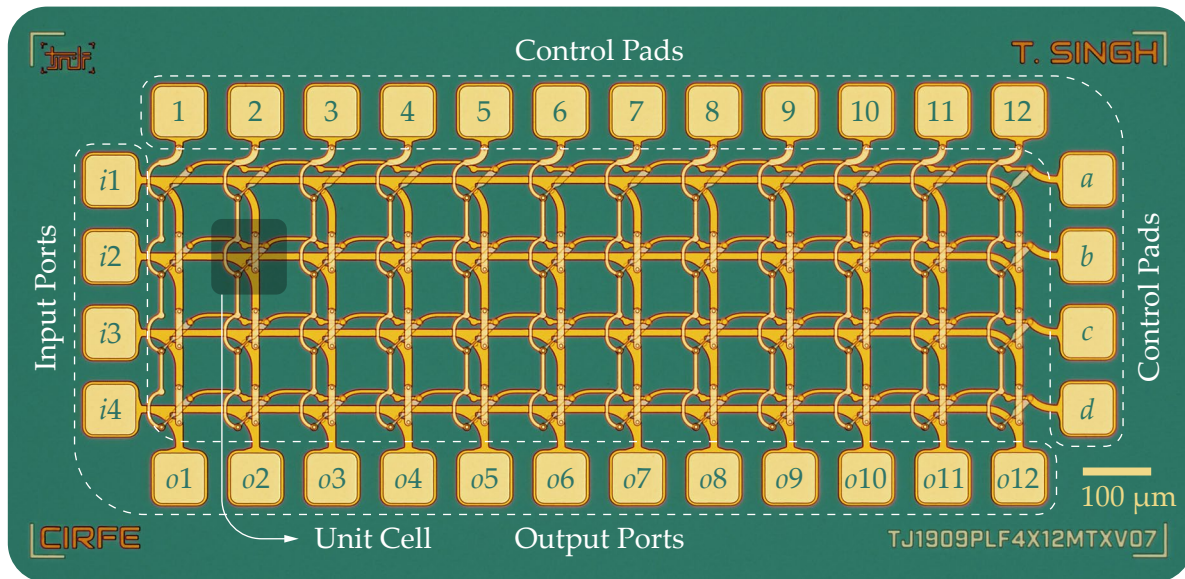


Figure 6.48: Optical micrograph of a 4×12 DC crossbar switch matrix developed using ver1 switch unit-cells.

6.2.6.2 LF 16×16 Crossbar Switch Matrix

For the first time, an ultra compact higher order 16×16 crossbar switch matrix is developed with complete device size under $2 \text{ mm} \times 2 \text{ mm}$ as shown in the optical micrograph in Fig. 6.49. 16×16 switch matrix utilizes 256 ver2 switch unit-cells cascaded in 2D matrix form. Similar to 4×12 matrix architecture, 16×16 switch matrix has 16 input ports ($i1, i1, \dots, i16$) and 16 output ports ($o1, o2, \dots, o16$). Control pads (1, 2, \dots , 16 and a, b, \dots, p) allows programming the PCM switches for signal routing between input

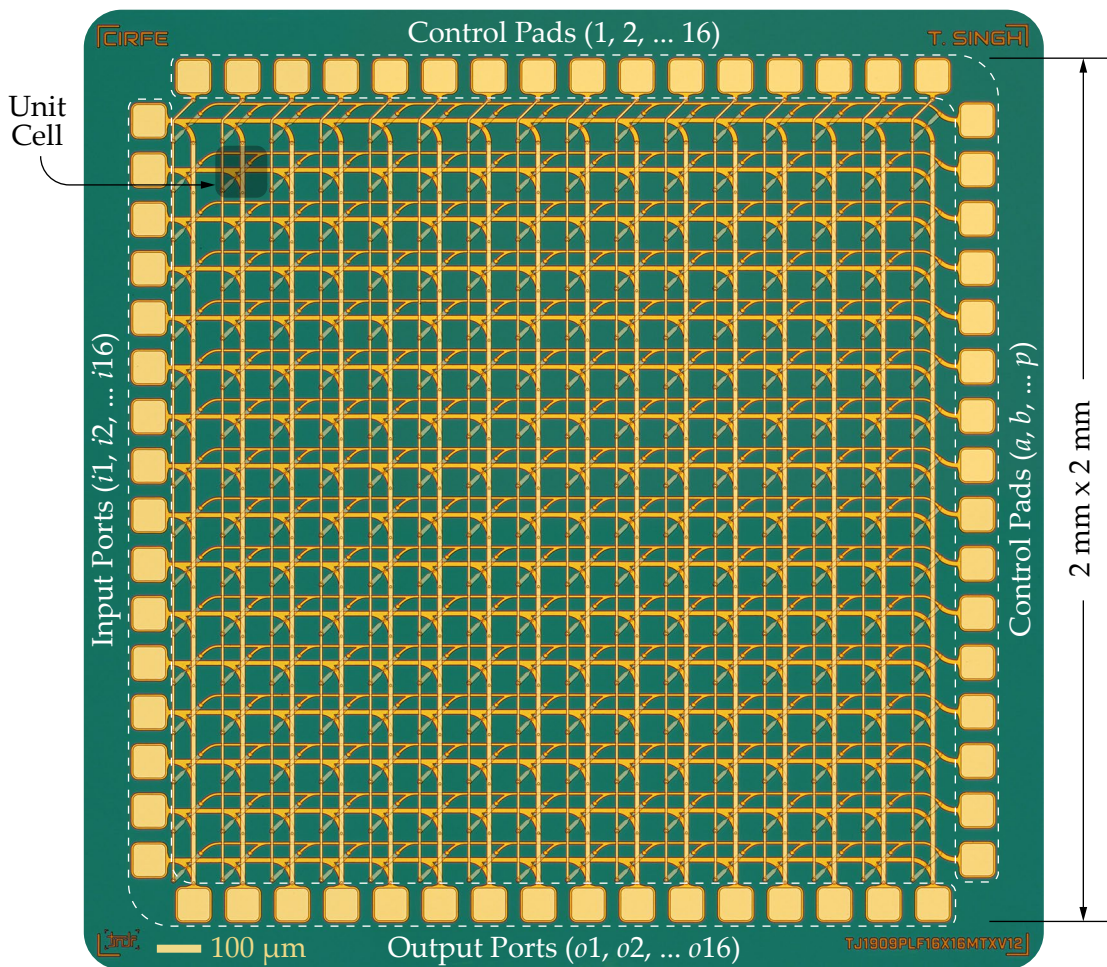


Figure 6.49: Optical micrograph of 16×16 crossbar switch matrix for DC or low frequency applications. 16×16 crossbar matrix use 64 PCM switches in 256 ver2 switch unit-cells.

and output ports. RF devices are typically benchmarked based on their RF performance measured using S-parameters, the only performance measure for crossbar switch matrices is to measure the resistance between signal paths from input to output. Each PCM switch provides $1.2\ \Omega$ to $1.8\ \Omega$ series resistance in signal path. Depending on the thickness of metal layers, the resistance of the lines can be ignored for calculations, as the device size is very compact. 16×16 matrix has the shortest and least resistive path between $i1-o1$ with only 1 switch in path and the longest and worst resistive path between $i16-o16$ with 31 switches in signal path. For an $m \times n$ switch matrix, number of switches between input m and output n are $(m + n - 1)$. A 4×4 crossbar switch matrix has the worst case scenario resistive loss of $10\ \Omega$ (average $1.5\ \Omega$ switch resistance), and the loss scales with higher order matrices, such as a 8×8 switch matrix has worst case loss of $22\ \Omega$ and 16×16 matrix having a maximum loss of $46\ \Omega$. Various LF crossbar switch matrix configurations are developed such as 1×1 , 2×2 , 3×3 , 4×4 , 4×8 , 4×12 , 8×8 and 16×16 . Due to the similar core design of such LF matrices, only 4×12 and 16×16

Table 6.6: Summary of multi-port switches and switch matrices presented

Device	Operation Range	Number of Switches	Device Size
SP2T Switch	DC – 67 GHz	2	$0.26\ \text{mm} \times 0.26\ \text{mm}$
SP3T Switch	DC – 67 GHz	3	$0.30\ \text{mm} \times 0.30\ \text{mm}$
SP2T / SP3T Core	DC – 67 GHz	2/3	$0.08\ \text{mm} \times 0.08\ \text{mm}$
SP8T Switch	DC – 40 GHz	8	$0.40\ \text{mm} \times 0.40\ \text{mm}$
SP8T Core	DC – 40 GHz	8	$0.07\ \text{mm} \times 0.07\ \text{mm}$
SP16T Switch	DC – 15 GHz	16	$0.60\ \text{mm} \times 0.60\ \text{mm}$
2×2 Switch Matrix	DC – 26 GHz	6	$1.00\ \text{mm} \times 0.80\ \text{mm}$
Reconfigurable Band Rejector	1 GHz to 8 GHz	10	$0.83\ \text{mm} \times 0.83\ \text{mm}$
T-type Switch	DC – 67 GHz	12	$0.55\ \text{mm} \times 0.55\ \text{mm}$
4×6 Redundancy Matrix	DC – 60 GHz	48	$1.10\ \text{mm} \times 0.88\ \text{mm}$
Crossbar Matrix Unit-Cell	DC – 40 GHz	4	$0.12\ \text{mm} \times 0.12\ \text{mm}$
2×2 Crossbar Switch Matrix	DC – 40 GHz	6	$0.32\ \text{mm} \times 0.32\ \text{mm}$
4×4 Crossbar Switch Matrix	DC – 40 GHz	45	$0.77\ \text{mm} \times 0.96\ \text{mm}$
LF Crossbar Matrix Unit-Cell	LF	1	$0.11\ \text{mm} \times 0.11\ \text{mm}$
4×12 Crossbar Switch Matrix	LF	48	$1.50\ \text{mm} \times 0.60\ \text{mm}$
16×16 Crossbar Switch Matrix	LF	256	$2.00\ \text{mm} \times 2.00\ \text{mm}$

switch matrix configurations are reported in this chapter.

6.3 Summary of Devices

Various RF PCM GeTe-based multi-port switches and switch matrices are reported with operational frequencies ranging from DC to mmWave range. Except SP2T switch, all the other devices reported in this chapter are the first demonstration of PCM GeTe-based devices for RF applications. Table 6.6 summarizes all the devices presented in this chapter.

Chapter 7

Reconfigurable PCM-Based Passive RF Components

This section reports the first demonstrations of various reconfigurable PCM-based passive RF components integrated monolithically. A 6-bit latching switched capacitor bank is developed utilizing on-chip MIM capacitors with high tuning range in a highly miniaturized package. MIM capacitor design optimization is discussed to improve the self resonance frequency (SFR) of the on-chip MIM capacitors. An improved version of 6-bit switched capacitor bank is demonstrated with more than 40% improvement in SFR than non-optimized version. An 8-bit rotary switched capacitor bank is designed for tuning reconfigurable circuits requiring inductive tuning behavior at mmWave frequencies. The rotary design of the capacitor bank allows minimizing tuning variations.

Variable attenuators are used in many applications to adjust the signal levels in various RF circuits such as full duplex wireless systems, radar systems, vector modulators to name a few. A 4-bit PCM-based latching variable attenuator is developed that exhibits measured attenuation up to 37 dB at 28 GHz with 8 GHz bandwidth. Variable attenuators are developed using linear broadband mmWave on-chip resistors. A mmWave scalable variable attenuator is also demonstrated using T-type unit-cells.

Phase shifters are crucial components for electronic beam steering in phased-array systems. A monolithically integrated loss compensated 3-bit switched 30 GHz true-time-delay phase shifter is developed for mmWave phase arrays. The phase shifter is developed using SP3T switches connected back-to-back. A low-loss and loss-compensated

Parts of this chapter are published in [101–103]

phase shifter is also developed utilizing SP8T switches to reduce the number of cascaded signal paths. Both phase shifters exhibit minimum loss variation in comparison to the current state-of-the-art. A 3-bit reflective type phase shifter using mmWave inductor bank is also reported for the first time.

Finally, utilizing 4-bit capacitor banks, a PCM-based reconfigurable impedance tuner is reported as a proof of concept. 4-bit capacitor banks are highly miniaturized and fully integrated in the ground planes of the impedance tuner. This vast library of passive RF components demonstrate the potential of PCM technology for mmWave applications.

7.1 PCM-Based Capacitor Bank

Reconfigurable RF devices such as impedance matching networks, tunable filters, and various front-end modules require switched capacitor banks as a key component to provide tunability [104, 105]. MEMS based capacitive switches used in capacitor banks require high operational voltage and suffer from reliability concerns due to dielectric charging effects, microwelding and stiction issues [106].

The emerging RF switches based on PCM technology offer one order higher figure of merit (FoM) than its semiconductor counterparts including GaN, GaAs, CMOS and InP, which translates to higher isolation and lower insertion loss of a switching circuit [80]. PCM technology also offers latching functionality due to the non-volatile property of the GeTe material [85, 86]. Commercially available RF-MEMS based switched capacitors [107, 108], and recently reported switched capacitor banks [109–112] based on RF-MEMS technology operate at lower frequencies with a limited tuning range and are larger in size. More recently a 4-bit CMOS-MEMS based switched capacitor bank was published demonstrating a tuning range only from 0.15 pF to 1.2 pF [113]. A PCM based 4-bit capacitor bank was reported [114], but it has a very coarse and limited capacitance tuning ratio of 10:1.

7.1.1 Reconfigurable Latching 6-Bit Digital Switched Capacitor Bank

A highly miniaturized reconfigurable PCM GeTe-based 64-state switched capacitor bank is presented, demonstrating high capacitance tuning ratio 58:1. It provides a linear capacitance range from 0.14 pF to 8 pF over 2 GHz to 7 GHz. The developed capacitor bank is designed to have an extremely small footprint compared to other capacitor banks [109, 110, 113, 114]. The reported fabrication process offers the flexibility to

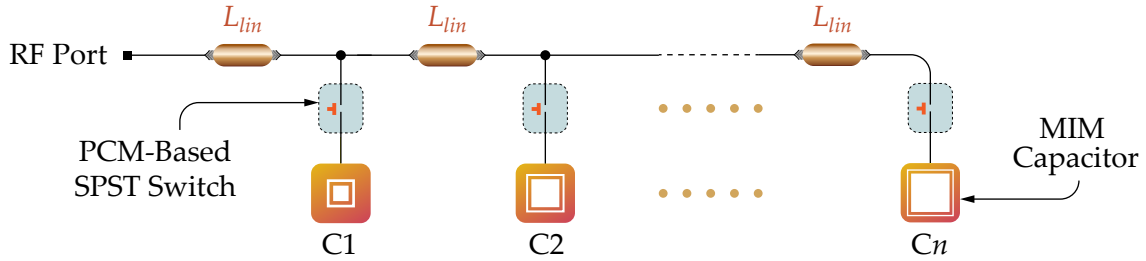


Figure 7.1: Schematic of n -bit digital switched capacitor bank utilizing MIM capacitors.

monolithically integrate various planar RF devices [95]. The switched capacitor bank is fabricated using Gen 3 microfabrication process that includes conductive bias network to improve the switching speed and also utilizes a thermally conductive dielectric layer to reduce the switch actuation voltage. To the best of our knowledge, this is the first implementation of such large capacitance ratio PCM-based capacitor bank in a highly compact package.

7.1.1.1 Operation Principle of Switched Capacitor Bank

A miniature latching 6-bit digital capacitor bank is designed and fabricated that incorporates six PCM GeTe-based SPST RF-PCM series switches. Due to the nature of GeTe as PCM material, this device offers latching functionality thus eliminating the requirement of constant DC power consumption. Switched capacitor bank functionality is achieved using PCM SPST switches which load or unload a metal-insulator-metal (MIM) capacitor connected at the output of SPST switch as shown in Fig. 7.1. The device area is under $0.5 \text{ mm} \times 0.5 \text{ mm}$ including CPW RF port having $150 \mu\text{m}$ probe pitch and seven control pads, each measuring $100 \mu\text{m} \times 100 \mu\text{m}$ for providing bias/actuation signal to the six individual SPST switches as shown in the chip layout in Fig. 7.2. RF ground is shared with DC ground through V0. The core of the device measures only $0.2 \text{ mm} \times 0.28 \text{ mm}$ for integration, making this device extremely compact in size compared to recently published capacitor banks [109–114]. Bias lines provide control signal to micro-heaters for the actuation of PCM switches. Details of the PCM RF SPST switch are described in chapter 4.

MIM capacitors are connected in series with the PCM switches. A simplified lumped circuit model of the capacitor bank is shown in Fig. 7.3. The PCM switches are represented as reversible binary resistive switches providing resistance between ON-state (R_{on}) and OFF-state (R_{off}). The PCM switches utilize thin-film refractory micro-heaters

to provide thermal actuation pulses which also introduce capacitance in the OFF-state (C_{off}). The value of C_{off} depends on the width of micro-heater (w_h), length of PCM channel (l_s), length of micro-heater (l_h), width of PCM channel (w_s), thickness of barrier layer (V_0) and choice of barrier layer. L_{lin} is the effective inductance of the trans-

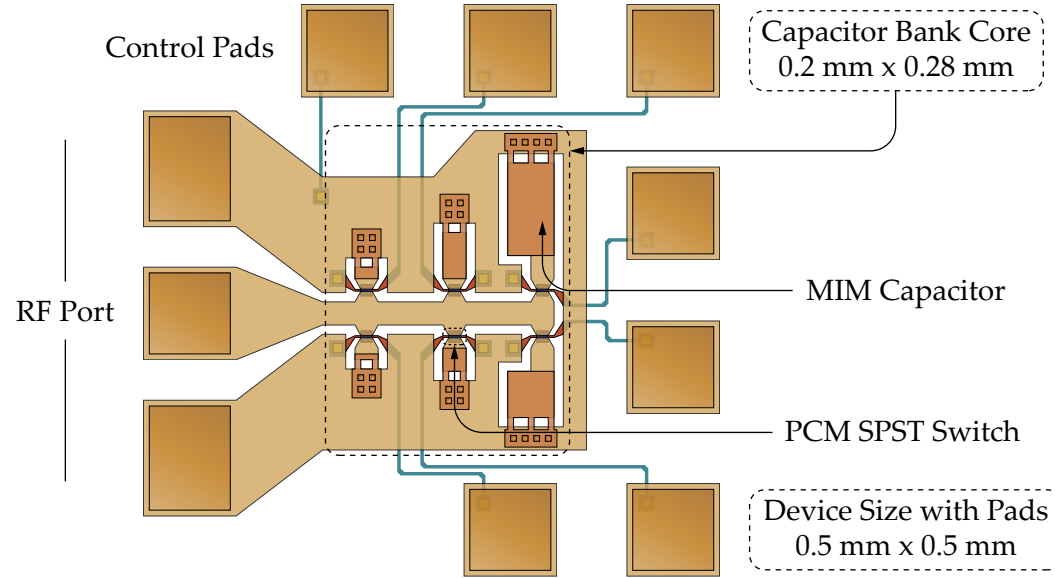


Figure 7.2: Chip layout of a monolithically integrated PCM GeTe-based 6-bit switched capacitor bank highlighting various layers and control pads.

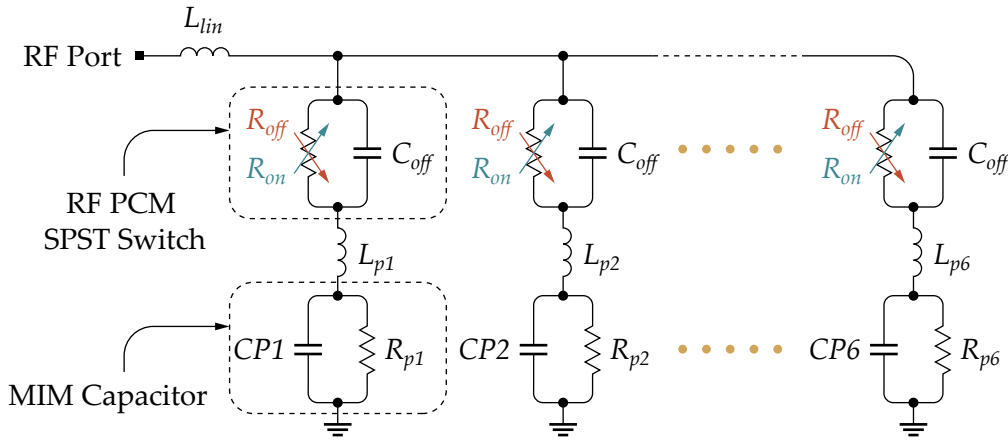


Figure 7.3: Simplified lumped model of the PCM-based 6-bit capacitor bank. PCM switches are represented as reversible binary resistive switches for tuning elements.

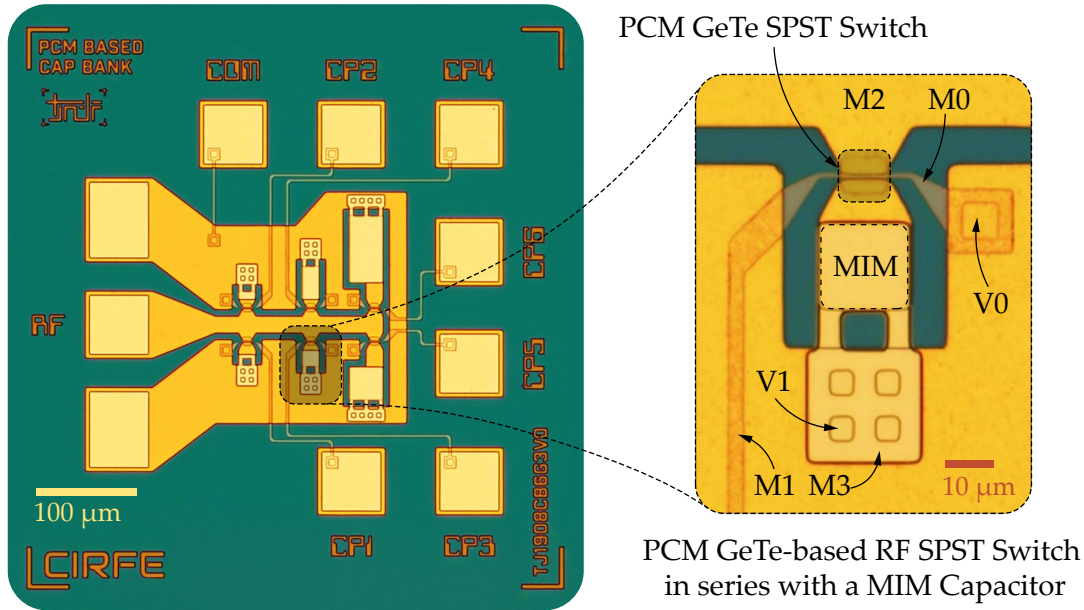


Figure 7.4: Optical micrograph of the fabricated 6-bit latching PCM-based digital switched capacitor bank. Inset shows optical micrograph of a MIM capacitor in series with PCM switch.

mission line connecting all six PCM switches, while $L_{p1}, L_{p1}, \dots, L_{p6}$ are parasitic inductances between PCM switches and MIM capacitors ($CP1, CP2, \dots, CP6$). The resistors $R_{p1}, R_{p1}, \dots, R_{p6}$ are associated with respective MIM capacitor losses.

In state ‘1’, when all the switches are in OFF-state, this device has a capacitance of $C_p = 0.14$ pF due to the combined C_{off} in series with MIM capacitor, length of RF line shared between PCM switches and various associated parasitics. States ‘2’ to ‘64’ are various combinations of MIM capacitors. State ‘2’ is when PCM switch is actuated to ON-state introducing $CP1$ while state ‘64’ is when all six PCM switches are actuated to the ON-state combining capacitance of all the MIM capacitors.

The device presented is developed using Gen 3 microfabrication process as shown in Fig. 4.11. Metal layers (M2 and M3) are used for RF signal routing, while M0 is used as a thin-film resistor for providing actuation signal to individual PCM switches and M1 is a highly conductive metal layer used for routing control connections to the switches, reducing any resistive effects. Thermally conductive barrier layer is used to reduce the voltage requirements of the switch.

The capacitor values can be scaled by either changing the dielectric material of the (V0) layer or by changing its thickness. The capacitor bank is optimized to reduce the

inductive effect by keeping a consistent spacing between the PCM switches. This compact capacitor bank provides capacitance tuning ratio up to 58:1 with no self-resonance up to 7 GHz providing measured capacitance range from 0.14 pF to 8 pF.

7.1.1.2 Performance Measurements

Optical micrograph of the fabricated PCM-based capacitor bank is shown in Fig. 7.4. Control pads (CP1, CP2 \dots CP6) are used to actuate respective MIM capacitors. COM port is the common DC port for ground connection. Insets in Fig. 7.4 highlight a MIM capacitor in series with RF SPST switch.

Measured and simulated RF performance of PCM SPST switches used in capacitor bank is depicted in Fig. 4.18. The switch demonstrates a loss lower than 0.2 dB and isolation better than 30 dB over 2 GHz to 7 GHz. The PCM switches are actuated to the OFF-state by a pulse of 200 ns width and 12 V amplitude, and to the ON-pulse by a pulse of 1.2 μ s width and 7.8 V between ‘COM’ port and respective ‘CP1, CP2 \dots CP6’ ports.

Measured and simulated results are shown in Fig. 7.5. EM simulations are carried out using Ansys HFSS which are in close agreement with measured results. Out of 64

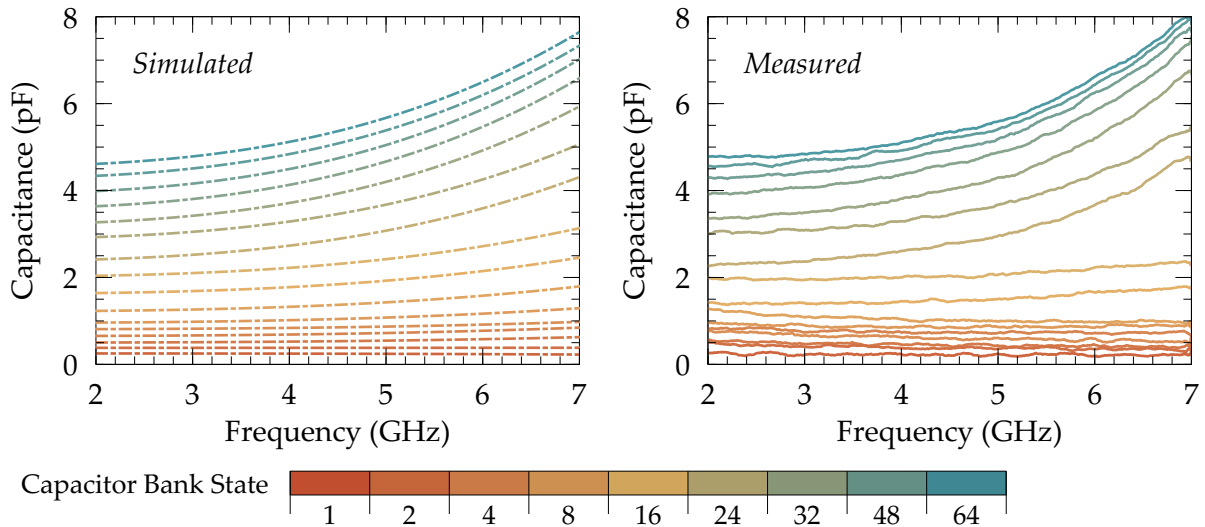


Figure 7.5: Measured and simulated results of 6-bit PCM-based switched capacitor bank showing linear variation from 0.14 pF to 8 pF capacitance. 9 different states are shown out of a total of 64 states. Self-resonance is beyond 8 GHz when all the capacitors are switched to ON state (corresponds to state 64).

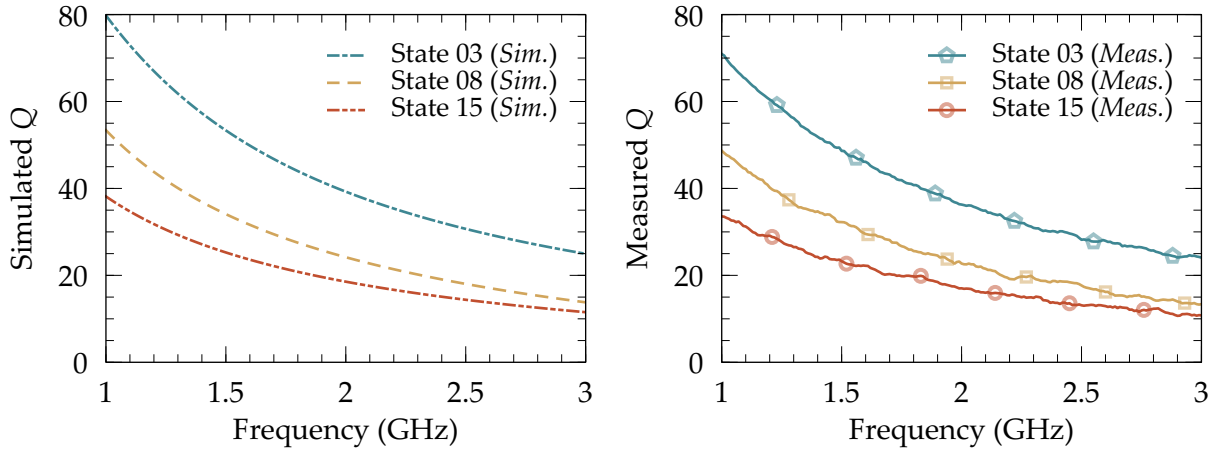


Figure 7.6: Measured and simulated Q -factor of capacitor bank in various states.

states, only few states are measured highlighting extended capacitance range. 9 different states are chosen to demonstrate the capacitance tuning range from 0.14 pF to 8 pF. The smallest capacitor $CP1$ have 0.25 pF capacitance instead of 0.125 pF. The difference is attributed to the added parasitic C_p from shared CPW line and from V1 vias, making a 0.14 pF the smallest capacitance when all the switches are OFF. Measured and simulated Q -factor of the capacitor bank for states 3, 8 and 15 is shown in Fig. 7.6. The Q can be improved by increasing the thickness of the gold layers M2 and M3 through electroplating and by optimizing the thickness of the dielectric layers of the MIM capacitors and their plate sizes.

7.1.2 Self Resonance Frequency Improvement

Self resonance frequency (SFR) of a capacitor decides the maximum operating frequency. Generally, SFR drops with increasing capacitance value. As shown in Fig. 7.5, the SFR is between 8 GHz to 9 GHz range, which limits the higher states of capacitor band operation till 7 GHz. Capacitors can be made by various techniques but for on-chip MIM capacitors, an easy tweak of inductance shows improvement in SRF along with Q -factor. After numerous design iterations to improve the SRF, a simple technique for CPW based MIM capacitors is proposed to cover the ground plane and connecting ground plane around overlapping capacitance area with vias. It shows improved SRF and Q . Four MIM capacitors are fabricated namely C1, C2, C3 and C4 as shown in Fig. 7.7. C1 and C3 are MIM capacitors with overlapping area $50\ \mu\text{m} \times 50\ \mu\text{m}$ and C2 and C4 with overlapping area

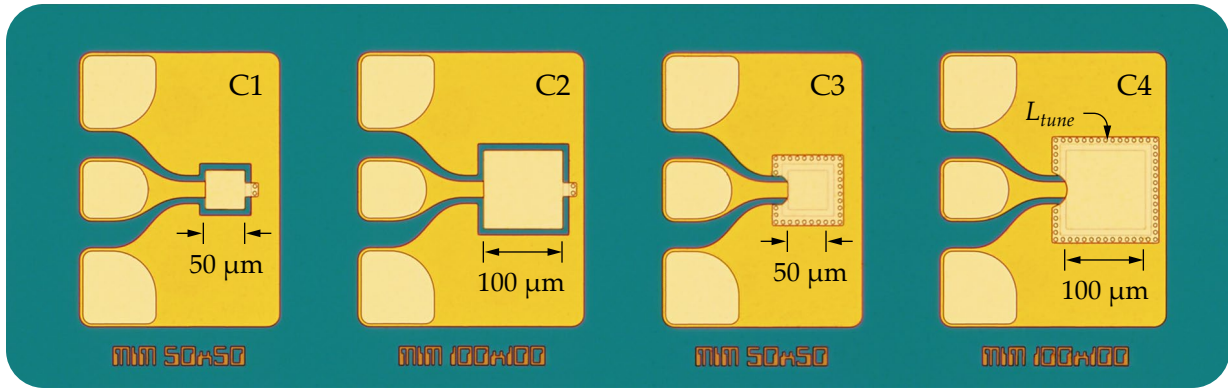


Figure 7.7: Optical micrograph of four MIM capacitors. C1 and C3 have similar capacitance overlapping area, and C2 and C4 has similar capacitance area. C3 and C4 capacitors show improvement in SRF and Q-factor.

100 μm × 100 μm. C1 and C2 are commonly used MIM capacitor geometries, while C3 and C4 are MIM capacitors with shielded ground plane connected using array of vias.

Capacitance and Q-factor is measured over frequency as shown in Fig. 7.8. MIM capacitors C1 and C3 shows capacitance of 1.75 pF and C2 and C4 shows 5.8 pF capacitance at 1 GHz. C1 has SRF at 16.1 GHz and Q of 10.5 while C2 has SRF at 6.8 GHz and Q of 7.3. Capacitors with shielded ground plane have better SRF and Q. Capacitor C3 has identical capacitance as that of C1, but higher SRF at 21 GHz and Q of 12.6. Similarly,

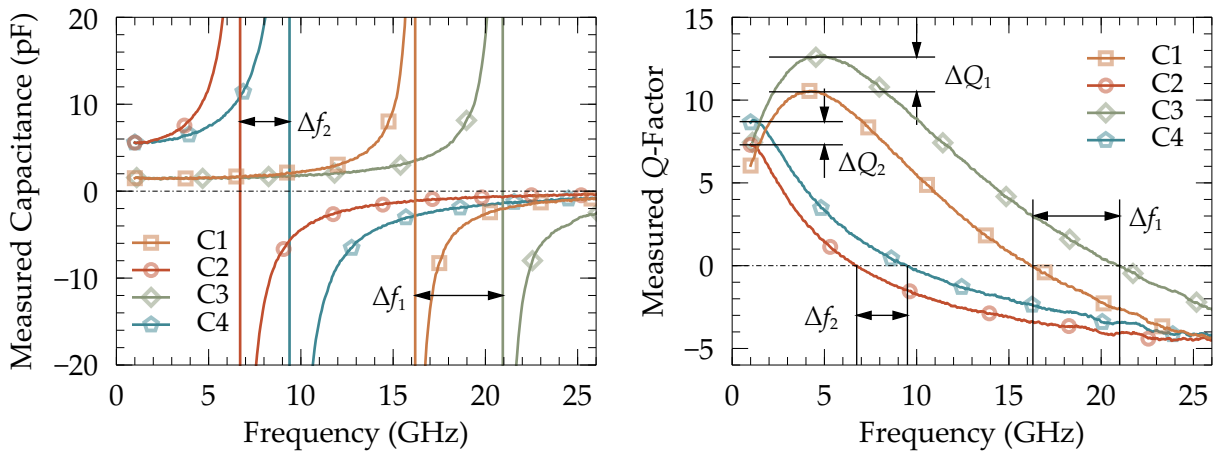


Figure 7.8: Measured capacitance and Q-factor for MIM capacitors C1, C2, C3 and C4.

C4 has identical capacitance as that of C2, but better SRF at 9.5 GHz and Q of 8.7. Δf_1 and Δf_2 shown in Fig. 7.8 represent the difference between low SRF and improved SRF between two identical value capacitors. Similarly, ΔQ_1 and ΔQ_2 represents the difference in Q between low SRF and improved SRF capacitors. C3 shows 30% improvement in SRF and 22% better Q compared to an identical value capacitor C1. C4 exhibits 40% improved SRF and 19% higher Q compared to an identical value capacitor C2.

Based on MIM capacitors with improved SRF and Q , a 6-bit PCM based capacitor bank is developed. The operation and functionality of the capacitor bank is identical to that of described in previous sections with only difference is MIM capacitor designs. Optical micrograph of the improved capacitor bank is shown in Fig. 7.9. Fig. 7.9(a) and (b) show the change in capacitor design, while Fig. 7.9(c) and (d) highlights SEM micrographs of PCM GeTe based switch junctions. Measured capacitance values of this capacitor bank is identical to that shown in Fig. 7.5 with SRF pushed higher than 10 GHz

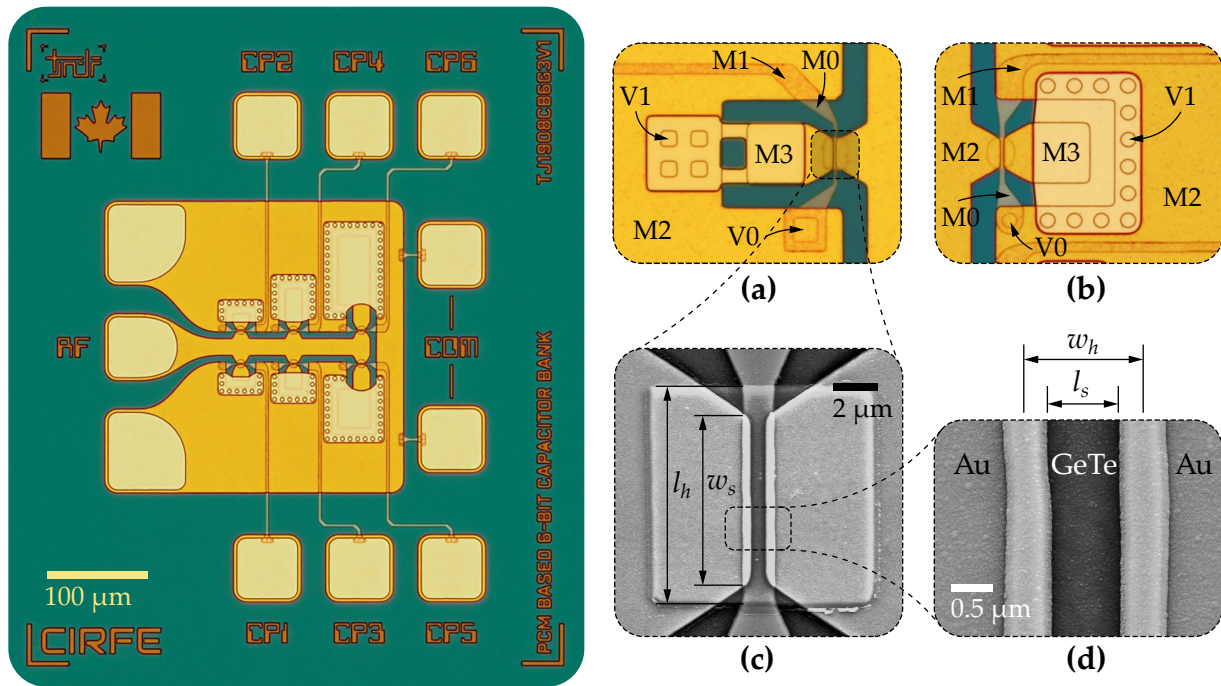


Figure 7.9: Optical micrograph of the 6-bit latching digital switched capacitor bank with high self resonance frequency: (a). Optical micrograph of a standard MIM capacitor implementation, (b) Optical micrograph of a high self resonance MIM capacitor, (c) SEM micrograph of a PCM SPST switch, and (d) SEM micrograph of the PCM junction.

thus making this capacitor bank operational till 10 GHz. A simple design modification provides 42% improvement in operation frequency.

7.1.3 Monolithically Integrated 8-Bit Rotary Switched Capacitor Bank

A compact reconfigurable PCM GeTe-based 256-state rotary switched capacitor bank is presented, demonstrating an inductive behavior with tuning ratio 8.2:1. It provides a 2-bit capacitance range from 110 fF to 360 fF and 6-bit inductive behavior from 38 pH to 310 pH over 4 GHz bandwidth at 28 GHz center frequency. The developed hybrid capacitor/inductor bank is designed to have an extremely small footprint. The rotary switch core allows symmetrical RF performance to the input of the series capacitors, thus reducing performance variation between states. To the best of our knowledge, this is the first implementation of hybrid PCM-based capacitor/inductor bank in a highly miniaturized package.

7.1.3.1 Operation Principle of 8-Bit Switched Capacitor Bank

A miniature latching 8-bit hybrid capacitor/inductor bank is designed and fabricated that incorporates eight PCM GeTe-based SPST RF-PCM series switches. Due to the nature of GeTe as PCM material, this device offers latching functionality thus eliminating the requirement of constant DC power consumption. Switched capacitor bank functionality is achieved using PCM SPST switches which load or unload high value MIM capacitors connected at the output of SPST switch as shown in Fig. 7.10. The device area is under $0.5 \text{ mm} \times 0.5 \text{ mm}$ including CPW RF port having $150 \text{ }\mu\text{m}$ probe pitch and nine control pads, each measuring $100 \text{ }\mu\text{m} \times 100 \text{ }\mu\text{m}$ for providing bias/actuation signal to the

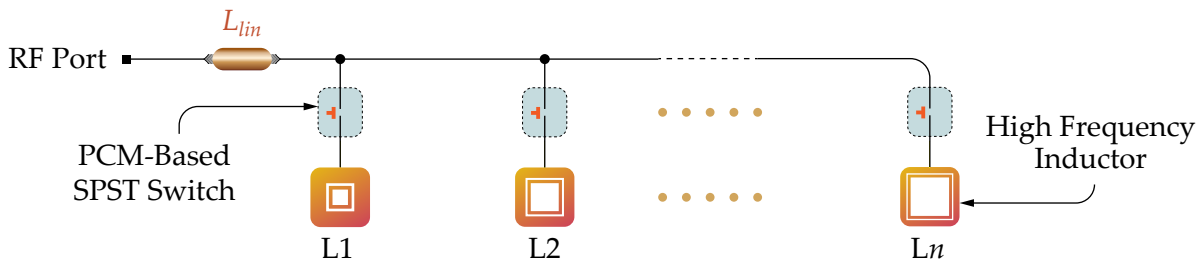


Figure 7.10: Schematic of an n -bit hybrid capacitor/inductor bank. High value MIM capacitors act as inductors at high frequency. SPST switches load or unloads the desired elements to the RF signal path.

six individual SPST switches as shown in the chip layout in Fig. 7.2. RF ground is shared with DC ground through V0. The core of the device measures only $0.3 \text{ mm} \times 0.27 \text{ mm}$ for integration, making this device extremely compact in size. Bias lines provide control signal to micro-heaters for the actuation of PCM switches. Details of the PCM RF SPST switch are described in chapter 4.

High value MIM capacitors are connected in series with the PCM switches. The simplified lumped circuit model of the hybrid capacitor/inductor bank is similar to that of capacitor bank shown in Fig. 7.3. Due to the circular design symmetry, the presented device does not have large parasitic capacitance in OFF-state. Two capacitors are designed with value 50 fF and 200 fF. In state '1', when all the switches are in OFF-state, this device has a capacitance of $C_p = 60 \text{ fF}$ only.

Both of the capacitors have SRF beyond 50 GHz which is far off from the operational bandwidth. Rest of the MIM capacitors are designed with SRF lower than operational bandwidth such that the operational bandwidth region remains free from resonance when multiple capacitors are actuated. High value capacitors act as inductors after the

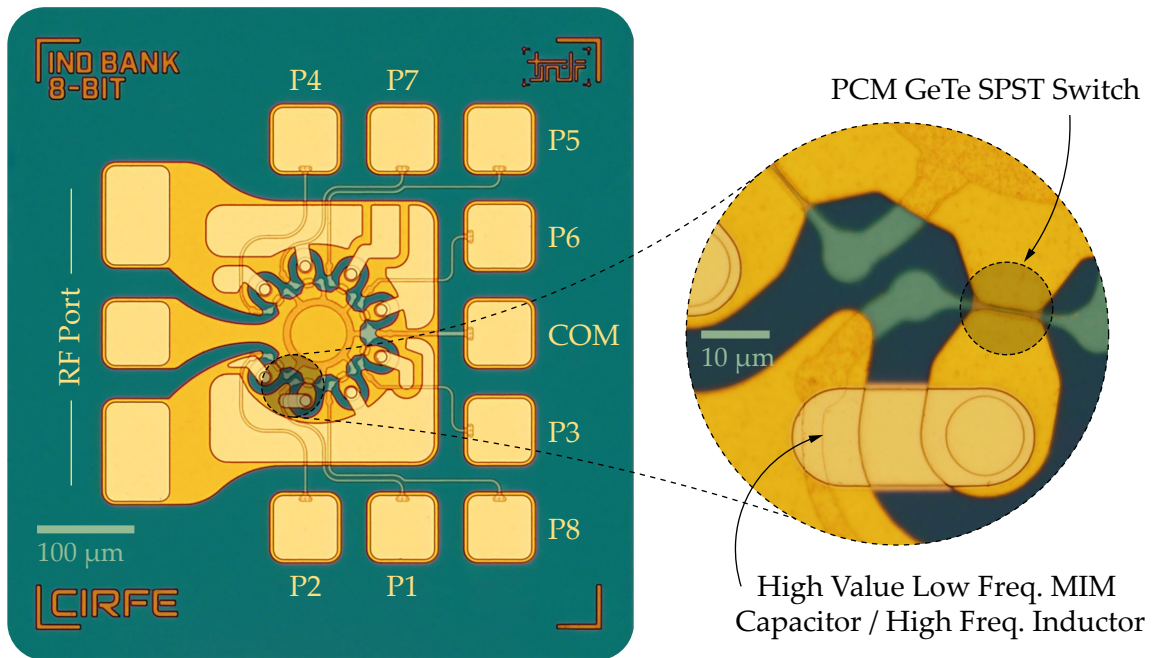


Figure 7.11: Optical micrograph of a highly miniaturized PCM-based hybrid capacitor/inductor bank. Inset shows PCM GeTe SPST switch and a high value low frequency MIM capacitor which acts as an inductor at high frequency.

SRF. Combining all the eight elements, this device provides 2-bit capacitive operation and 6-bit inductive operation over 4 GHz bandwidth at 28 GHz center frequency.

This design is highly adaptable to adjust capacitor values by easily modifying the insulator layer between two electrodes of capacitors. This approach keeps the design compact as designing traditional inductors at high frequency is very challenging due to unwanted parasitics. SRF of individual capacitors is precisely tuned by changing the overlapping area between signal and ground plane as discussed in previous section. This compact device provides 110 fF to 360 fF capacitance and 38 pH to 310 pH inductance at 28 GHz with 4 GHz bandwidth.

7.1.3.2 Simulation and Measurement

The optical micrograph of the hybrid capacitor/inductor bank is shown in Fig. 7.11. Inset in Fig. 7.11 shows SPST switch connected in series with a high value low frequency capacitor which acts as an inductor at high frequency. Simulated and measured inductance is shown in Fig. 7.12. 14 states out of a total of 256 are simulated and measured. Measured capacitance is not shown due to the 2-bit operation. The primary focus of this hybrid capacitor/inductor bank is on inductors, thus simulated and measured inductor values are depicted in Fig. 7.12.

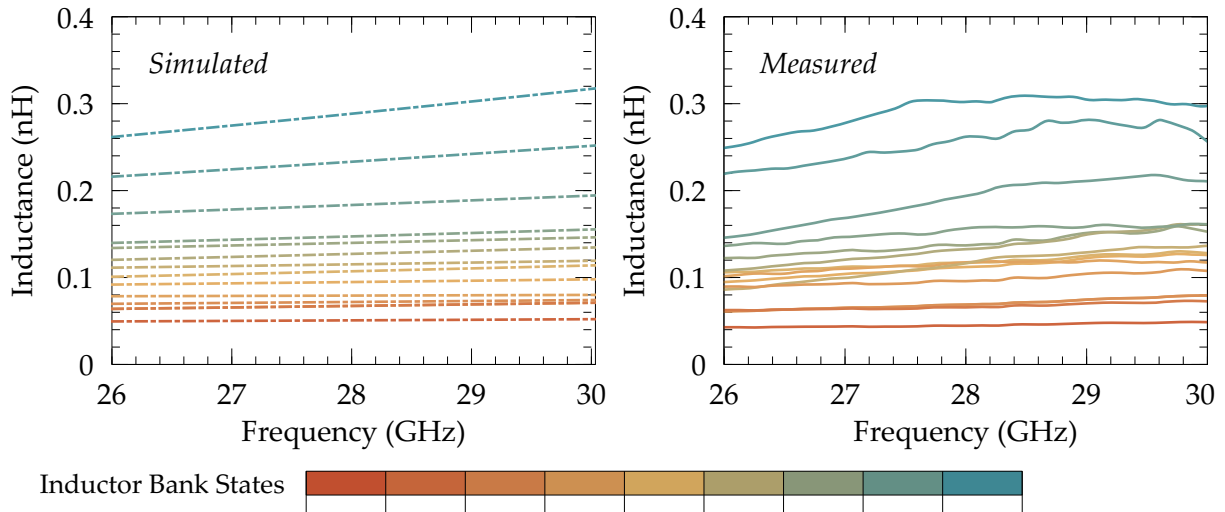


Figure 7.12: Simulated and measured inductance over 26 GHz to 30 GHz. Response of 14 states are shown out of a total of 256 possible states.

This hybrid capacitor/inductor bank has many use case scenarios. One of the most interesting use of this device is in reflective type phase shifters which is discussed in section 7.3.3.

7.2 PCM-Based Latching mmWave Variable Attenuators

Variable attenuators are commonly used for adjusting signal levels in various RF circuits such as full duplex wireless systems, radar systems, automatic gain control amplifiers, vector modulators to name a few [115]. Miniaturized attenuators with high linearity and precision are highly in demand particularly for mmWave applications [116]. Ka-band especially at 28 GHz have tremendous applications for 5G wireless communication systems especially beamforming networks [117].

Variable attenuators are commonly realized using semiconductor elements such as p-i-n diodes, as these diodes behave as current-controlled resistors at high frequencies [118]. However, their inherent limited power handling, low linearity and high power consumption degrades their performance, limiting their use for mmWave systems. MEMS-based devices provide excellent RF performance, linearity and power handling [11, 104, 105, 119], but MEMS usually suffer from reliability concerns such as contact degradation, dielectric charging, beam warping, and micro-welding problems [11, 120]. Novel materials such as metal insulator transition (MIT) vanadium oxide (VO₂) and graphene based variable attenuators have been reported which require constant supply of DC power [121, 122]. Recently reported PCM GeTe-based RF devices provide exceptional RF performance for mmWave applications [85–87, 123–127]. Latching nature of GeTe material allows the development of integrated RF devices with zero static DC power consumption [95–97]. Two scalable variable attenuator implementations are developed with each having its own pros and cons.

7.2.1 Reconfigurable 28 GHz 4-bit Latching Variable Attenuator

A novel miniaturized monolithically integrated mmWave reconfigurable PCM GeTe-based 4-bit latching variable attenuator for 5G application is developed. The variable attenuator is designed using PCM SPDT switches monolithically integrated with four passive bridged-T resistor network based fixed attenuators to provide wide attenuation range. The PCM switching units are latching type thus consume no static DC power.

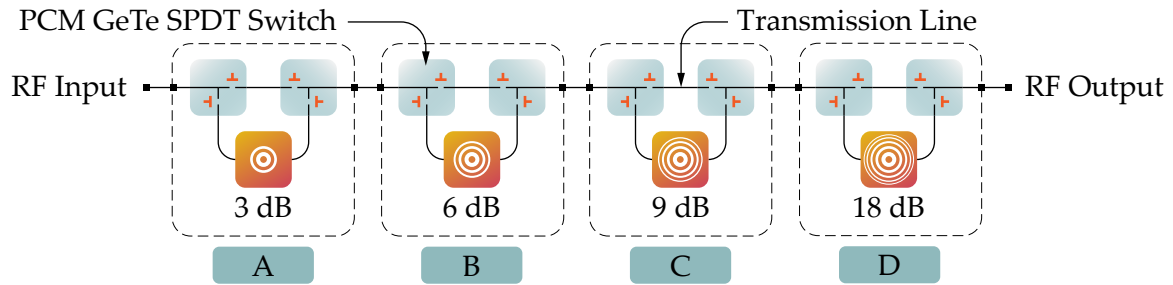


Figure 7.13: Schematic of a reconfigurable 4-bit attenuator consisting of SPDT switches and four attenuator bits (A–D).

The integrated planar resistors are fabricated precisely on-wafer to get wide-band operation at desired 8 GHz frequency band. The presented device is highly miniaturized with device area under 0.52 mm^2 . At the centre frequency of 28 GHz, the measured attenuation level varies from 4.7 dB to 37 dB with 16 discrete linear steps. The attenuator can be reconfigured at a tuning speed of less than $1.2 \mu\text{s}$. This is the first demonstration of a PCM-based reconfigurable attenuator for mmWave applications.

7.2.1.1 Description and Operation of Variable Attenuator

The monolithically integrated PCM-based 4-bit attenuator is designed by utilizing SPDT switches to route the RF signal through a section of transmission line or through an attenuator section (bit). Four attenuator bits (A–D) are cascaded to form a 4-bit device as shown in Fig. 7.13. SPDT switches are highly miniaturized utilizing two series PCM-

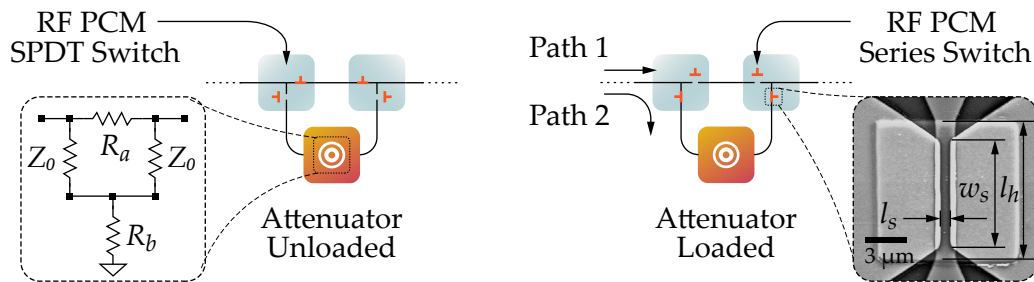


Figure 7.14: Operation principle of attenuator bit loading and unloading: Actuating two SPST switches in Path 1 deselects the attenuator bit, while actuating two SPST switches in Path 2 selects the attenuator bit. Attenuator bits (A–D) developed using passive bridged-T resistor network topology sections with different values of R_a and R_b .

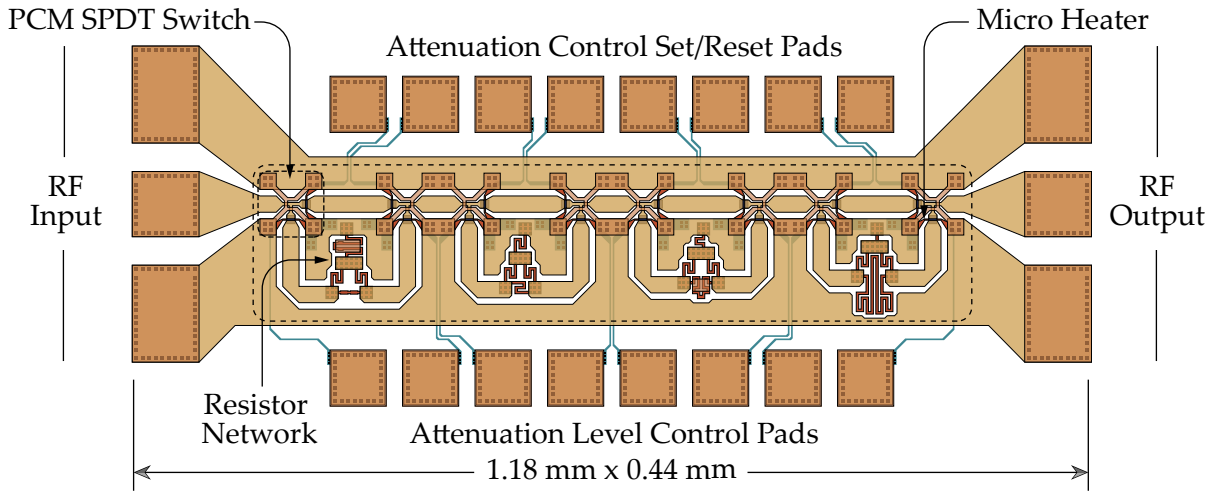


Figure 7.15: Layout of the PCM-based 4-bit attenuator. PCM SPDT switches are used to select desired attenuation level by loading/unloading a combination of attenuator section(s).

Table 7.1: Resistor values for attenuation bits

Resistor	3 dB	6 dB	9 dB	18 dB
R_a	20.6 Ω	50 Ω	91 Ω	347 Ω
R_b	121 Ω	50 Ω	27.5 Ω	7.2 Ω

based SPST switches to route the signal between path 1 or 2 as shown in Fig. 7.14. Detailed description of SPDT switches is reported in chapter 6. Individual attenuator bits are designed using high frequency wide-band integrated passive bridged-T resistor networks to provide discrete attenuation levels. Bits (A–D) provides attenuation level of 3 dB, 6 dB, 9 dB and 18 dB respectively. Combining four bits provides 16 discrete attenuation levels.

Bridged-T resistor networks are chosen over standard ‘T’ or ‘ π ’ topology as an additional resistive element. It enables the resistor network to provide desired attenuation without changing the characteristic impedance of the signal line, as the signal appears to bridge across ‘T’ network. Four resistor elements are required to form individual attenuator bits. For 50 Ω impedance, R_a and R_b values are chosen to get desired attenuation levels as given in Table 7.1. Larger resistor values show inductive behavior at high frequencies, thus capacitive compensation is included to cancel out the inductive component for resistor values greater than 100 Ω .

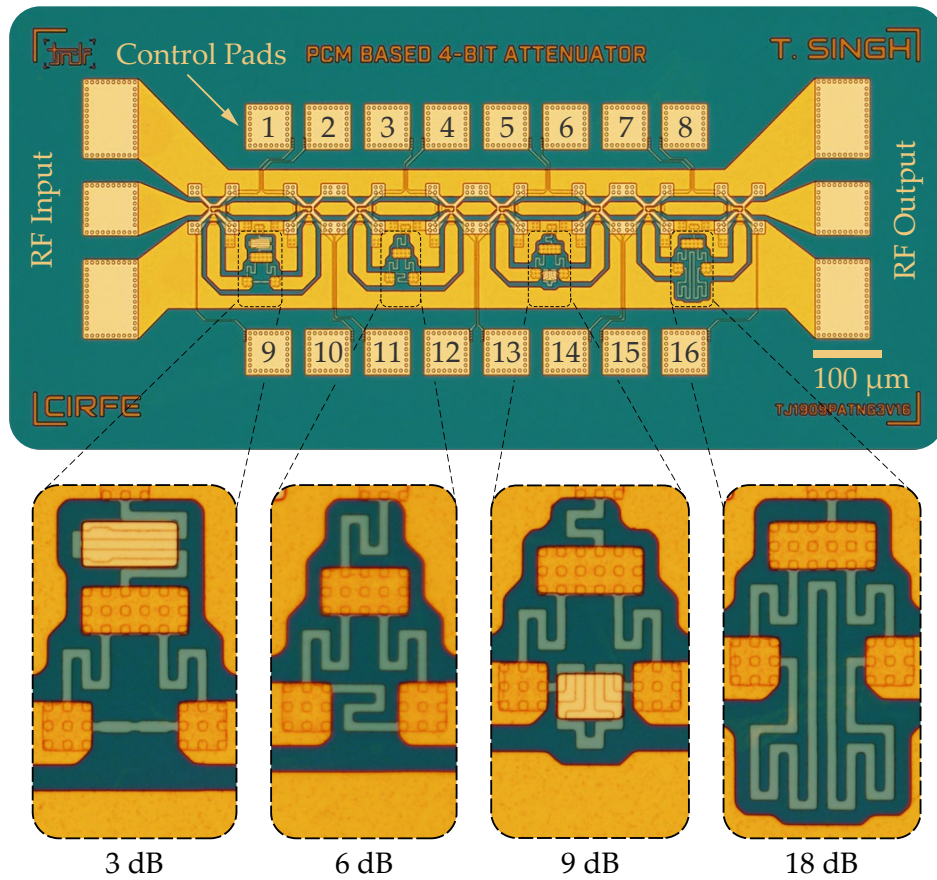


Figure 7.16: Optical micrograph of the monolithically integrated PCM-based 4-bit variable attenuator. Control pads 1–16 are used to tune the attenuation levels. Four passive bridged-T attenuator sections are shown in zoomed-in view.

Layout of the fully integrated device is shown in Fig. 7.15. The overall device footprints are under $1.18 \text{ mm} \times 0.44 \text{ mm}$ including RF input/output ports and bias pads. Attenuation control set/reset pads actuate the switches in path 1, while attenuation level control pads actuate the switches in path 2. Desired attenuation level can be achieved by loading the transmission line with any combination of fixed attenuators (A-D). Actuating all the eight SPST switches in path 1 resets the device to its lowest attenuation level. The attenuation levels are selected by applying a $1.2 \mu\text{s}$ pulse to turn ON the switching element, while a 200 ns pulse turns the switch OFF. On-chip micro resistors are designed to get precise resistance. Developing planar resistors using lossy material is viable option to minimize resistor area. Gen 3 microfabrication process includes micro-heater layer of

tungsten (W). When a conductive metal layer is utilized for biasing, sheet resistance of tungsten can be tuned to achieve desired resistivity to develop precise resistor values.

7.2.1.2 Simulation and Measurement Data

An optical micrograph of the fabricated reconfigurable PCM-based 4-bit attenuator is shown in Fig. 7.16, highlighting the overall device size, control pads and individual passive bridged-T attenuators. Embedded high frequency wide-band resistors are optimized for the desired 8 GHz frequency band. Eight SPDT switches are monolithically integrated to load/unload desired passive bridged-T resistor network which provides

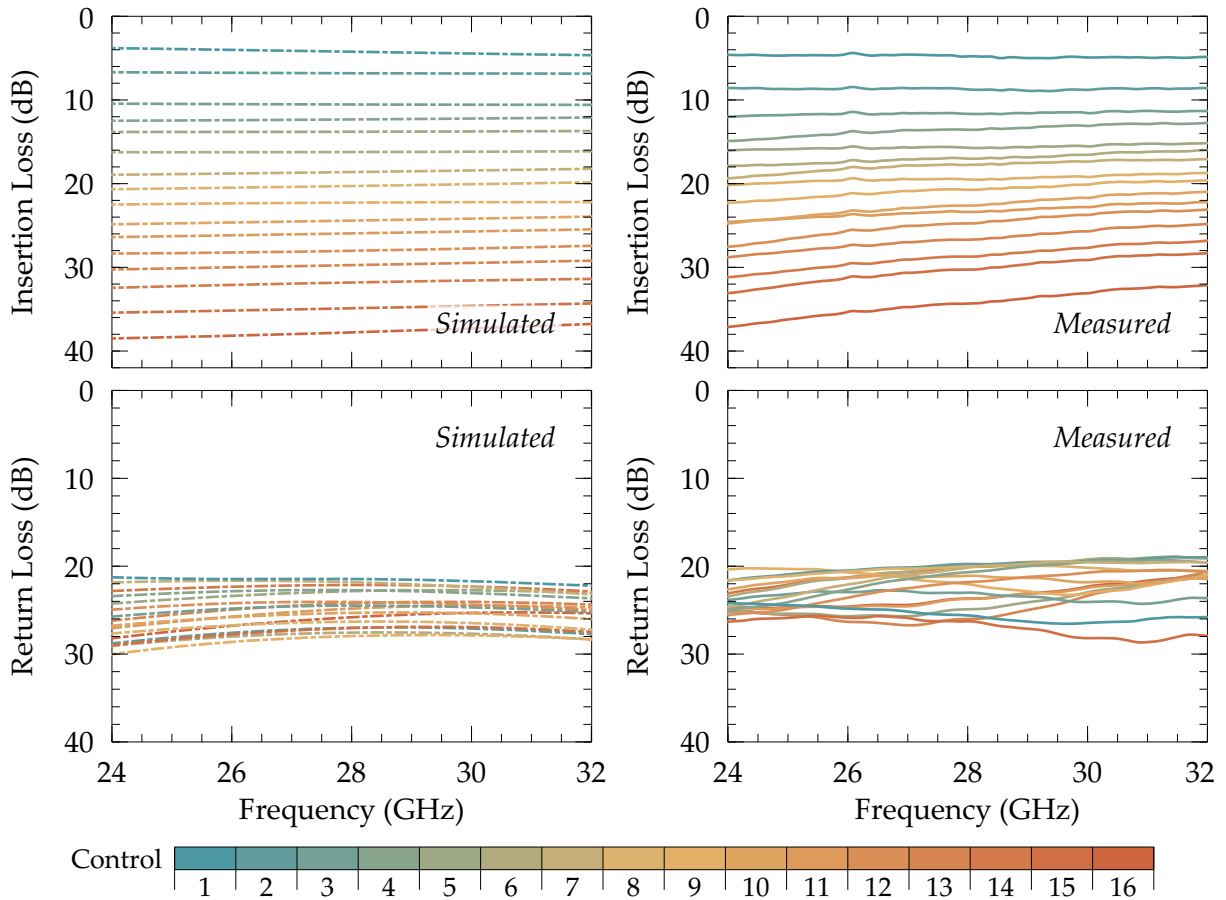


Figure 7.17: Measured and simulated insertion loss and return loss of the PCM-based 4-bit variable attenuator over 24–32 GHz band. Response of all 16 states (4-bit) is shown.

certain attenuation in the RF path. Resistor networks are simulated in Sonnet EM suite while the fully integrated device is EM simulated in Ansys HFSS. PCM-based SPST series switches demonstrate less than 0.28 dB loss and better than 28 dB return loss in ON-state while exhibit higher than 21 dB of isolation in OFF-state from 24 GHz to 32 GHz as shown in Fig. 4.18.

Measured and simulated RF response of the PCM-based 4-bit variable attenuator is shown in Fig. 7.17 from 24 GHz to 32 GHz. The response of all 16 states (4-bit) is demonstrated in Fig. 7.17. EM simulated response shows minimum attenuation of 3.6 dB and maximum attenuation of 38 dB at 28 GHz. All measurements were done on wafer at room temperature. Measured RF response exhibits minimum attenuation of 4.7 dB and maximum attenuation of 37 dB at the centre frequency. Simulated and measured return loss is better than 20 dB over the bandwidth. Attenuator bits (A–D) are designed to provide fixed attenuation relative to reset state (all attenuators bits unloaded). The variable attenuator can be reconfigured with a switching time less than 1.2 μ s. The reliability of the switches was experimentally validated for more than 1 million cycles.

7.2.1.3 Broadband On-Chip Resistors

It is challenging to get precise values of integrated resistors, which are fabricated on-wafer using resistivity measurement of the thin-film layer with more than 120 points. Sheet resistance data including wafer orientation is fed to a custom script to map the

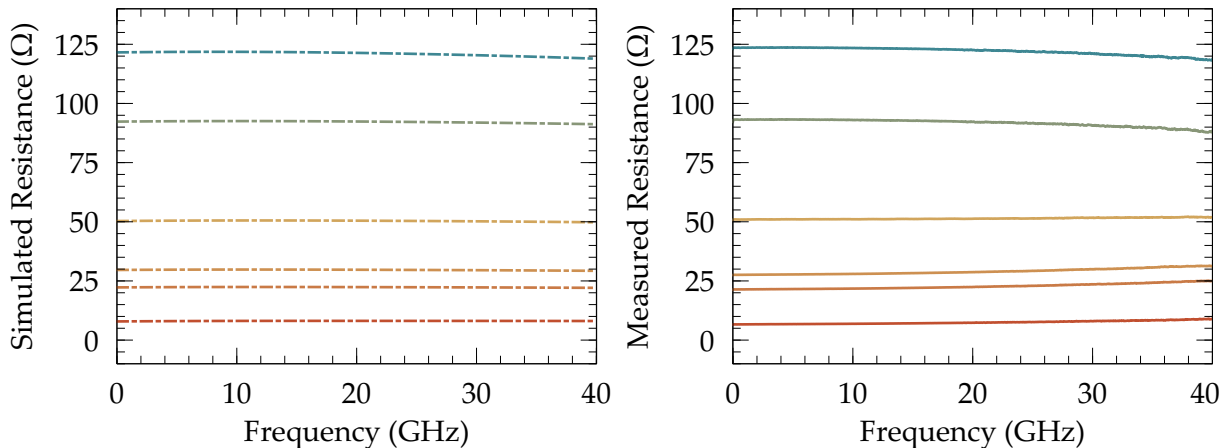


Figure 7.18: Measured broadband on-chip resistors over DC to 40 GHz.

Table 7.2: Variation in measured resistor values over bandwidth

Resistor	at 10 MHz	at 40 GHz	Avg. $R\Omega$	$\pm\Delta R\Omega$
7 Ω	7.10 Ω	9.5 Ω	8.3 Ω	1.18 Ω
21 Ω	21.3 Ω	25.0 Ω	23.2 Ω	1.84 Ω
27 Ω	27.5 Ω	31.3 Ω	29.4 Ω	1.90 Ω
50 Ω	50.5 Ω	53.4 Ω	51.9 Ω	1.45 Ω
90 Ω	91.2 Ω	87.3 Ω	89.3 Ω	1.95 Ω
120 Ω	121.1 Ω	116.6 Ω	118.8 Ω	2.25 Ω

measured sheet resistance of the thin-film to resistor designs. Measured on-chip fabricated resistors exhibit relatively flat response over DC to 40 GHz as shown in Fig. 7.18. Six individual resistors are measured and the deviation over frequency range is given in Table 7.2. As mentioned earlier, due to the lossy material used to design resistors, long meander lines introduces inductance at high frequencies for which a capacitive element is used to precisely bring back the resistor value from roll-off.

Measured resistors exhibit only an average of $\pm 1.7 \Omega$ resistance variation over DC to 40 GHz frequency band. Similar resistors are measured from different location of wafer with mean deviation of less than 3.8% across wafer. These on-chip resistors are suitable for designing matched terminations in multi-port devices as well as to design precise resistor networks as used in variable attenuator circuits.

7.2.2 Scalable PCM-Based Variable Attenuator Using T-type Switch

A PCM based scalable variable attenuator is developed utilizing T-type unit-cells. The scalable attenuator is based on the redundancy switch matrix discussed in section 6.2.4. Scalability of n^2 is achieved utilizing bridged-T resistor networks on both sides of the switch matrix with signal routing functionality. SPNT switches are monolithically integrated at the input and output side. A n^2 with $n = 3$ scalable variable attenuator is developed utilizing two T-type unit-cells, four bridge-T resistor networks and two SP3T switches as shown in Fig. 7.19. Actuating one of the switches in SP3T allows RF signal to either bypass attenuators passing through the switch matrix to the output terminal, or introducing an individual or a set of attenuators in the signal path.

Utilizing switch matrix approach for developing switchable/reconfigurable components is preferred over traditional approach of cascading back-to-back SPDT switches

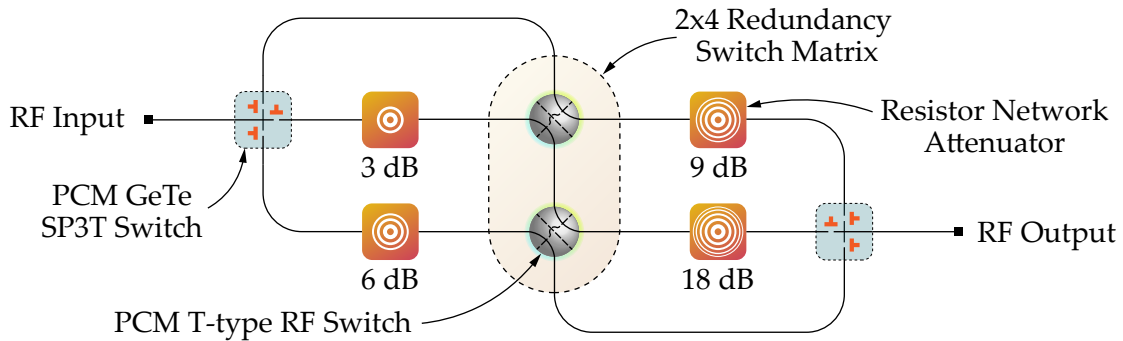


Figure 7.19: Schematic of a reconfigurable and scalable variable attenuator consisting of T-type unit cells in 2×4 configuration, PCM SP3T switches and resistor networks.

for two discrete reasons: this approach provides signal routing with less number of switches per unique control element combinations. The attenuator shown in Fig. 7.16 either passes or bypasses an attenuator bit in the signal line with the use of SPDT switches.

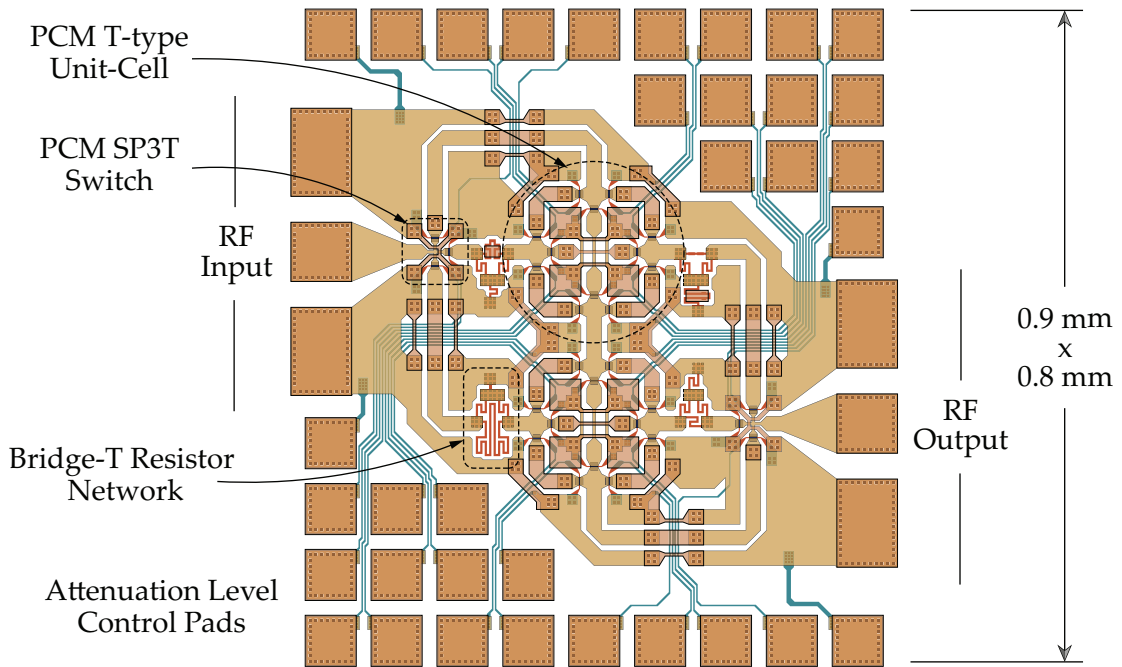


Figure 7.20: Layout of scalable PCM-based variable attenuator utilizing T-type unit-cells and multi-port RF switches.

Table 7.3: Comparison of 2^n and n^2 variable attenuators

Order n	No. of States		Unique States		No. of Switches	
	2^n	n^2	2^n	n^2	2^n	n^2
1	2	2	2	2	2	3
2	4	4	4	4	4	4
3	8	9	7	9	6	4 – 6
4	16	16	13	16	8	4 – 8
5	32	25	23	25	10	4 – 10

From design point-of-view, the approach to reconfigurability is simple, but the length of the signal path increases with number of bits. With each added bit to the signal line, 2^n scalability is achieved and the RF signal need to pass through a total of $2 \times n$ switching elements. A single point switch failure in a signal chain could make the device susceptible to latch in a non-desirable state. Scalable attenuator with T-type unit-cells mitigate these concerns due to flexible routing mechanism. Except design and routing, for n^2 scalable attenuator, switches between 4 and $2 \times n$ are required for reconfiguration. SPNT switches also scale well with $N = n$. For n^2 variable attenuator, $n - 1$ T-type unit-cells are required. Scalable n^2 attenuator also provides more unique states than the previously discussed variable attenuator. 2^n device has redundant states as shown in Table 7.3. With the increasing order of n , 2^n variable attenuator becomes more practical and appealing as it utilizes resources efficiently, but in the case of n^2 attenuator, redundant states increase which makes number of unique states lower. In case of a switch failure, 2^n variable attenuator provides flexibility in routing the signal through any other path.

Layout of the compact PCM-based scalable monolithically integrated variable attenuator is shown in Fig. 7.20 highlighting various RF components, attenuation level control pads and overall device size. The scalable attenuator has overall device size under $0.9 \text{ mm} \times 0.8 \text{ mm}$ including control pads and RF ports. Passive bridged-T resistor networks are arranged in a way such that either an individual network or a combination of networks can be selected by latching PCM RF switches in the desired RF signal path. Line impedance is maintained for capacitance variation generated from bias network.

7.2.2.1 RF Performance Simulation and Measurement

The variable attenuator is fabricated using Gen 3 microfabrication process. Optical micrograph of the variable attenuator is shown in Fig. 7.21. Fig. 7.21(a) highlights the

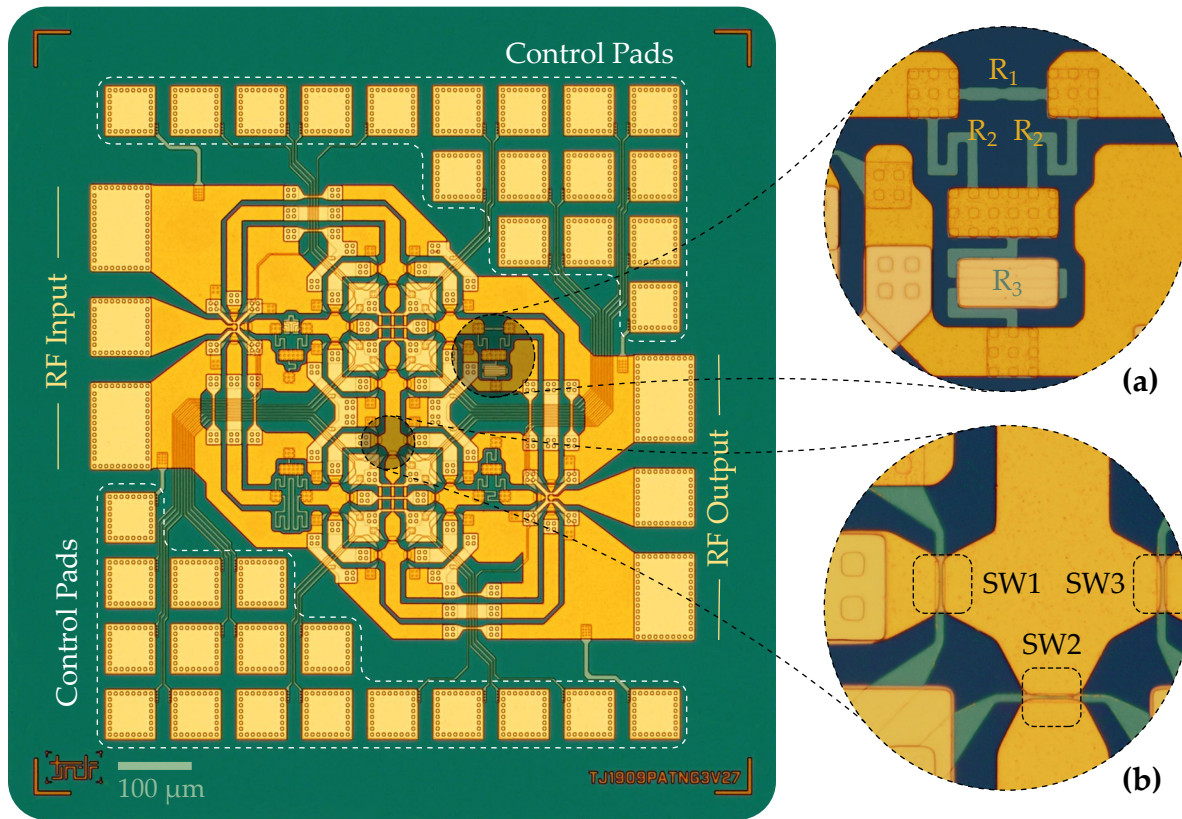


Figure 7.21: Optical micrograph of the monolithically integrated PCM-based variable attenuator. (a). Passive bridged-T resistor network for attenuation level, (b). Zoomed-in view of three-way junction in a T-type unit-cell.

bridged-T resistor network in which resistor R_3 shows capacitive compensation element and Fig. 7.21(b) shows a junction in T-type unit-cell. PCM-based SP3T switches integrated in variable attenuator demonstrate less than 0.5 dB loss and better than 21 dB return loss in ON-state while exhibiting higher than 20 dB isolation in OFF-state over 8 GHz operational bandwidth at centre frequency 30 GHz.

Measured and simulated RF response of the PCM-based scalable variable attenuator is shown in Fig. 7.22 from 26 GHz to 34 GHz. The RF response of all 9 states is demonstrated in Fig. 7.22. EM simulated response shows minimum attenuation of 3.1 dB and a maximum attenuation of 27 dB in 3 dB increments. The EM simulated return loss of better than 18 dB in all possible states. Measured response shows minimum attenuation of 3.9 dB and maximum attenuation of 28 dB at centre frequency 30 GHz. The deviation in

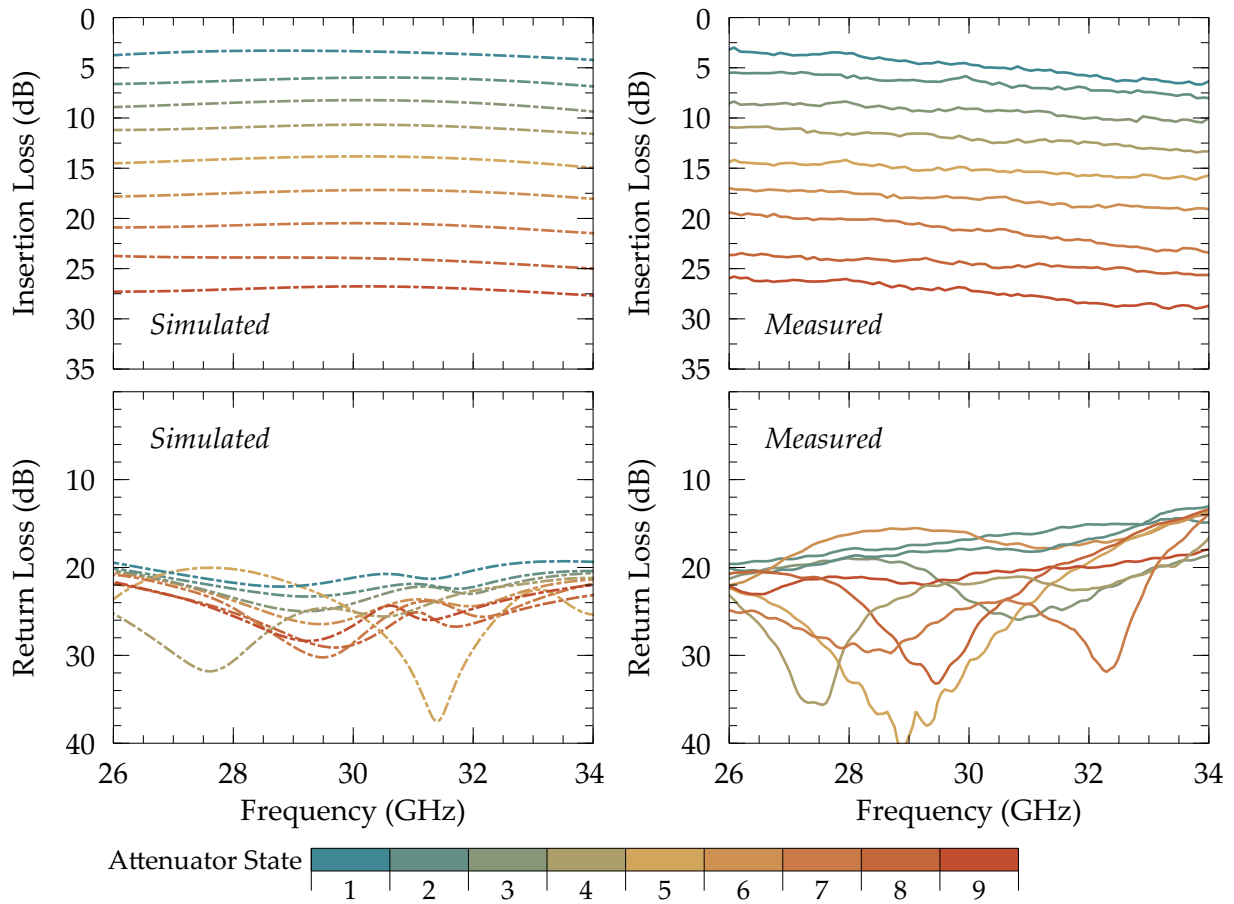


Figure 7.22: Measured and simulated attenuation and return loss of the PCM-based scalable variable attenuator over 26 GHz to 34 GHz. Response of all 9 states is shown.

measured response is due to the variation in number of switches and switch response. During microfabrication, PCM junction channel size variation leads to slight offset of RF response from the benchmarked performance. Overall, the measured response is in close agreement with the simulated data. Measured return loss is better than 13 dB in all possible combinations.

The scalable attenuator provides flexibility in terms of offering unique combinations, requiring less number of switches in certain states. It also maintains certain degree of redundancy if one or more switches fail. The disadvantage of such topology is complex design, high degree of signal routing (which can be automated), less number of states per unit chip area.

7.3 PCM-Based mmWave Phase Shifters

Phase shifters are crucial components for electronic beam steering in phased-array systems. Phase shifters are widely used to change the excitation phase of an individual antenna element in phased-array antennas. mmWave phased array antennas provide the capability of real-time beam steering with high efficiency in a miniaturized package for applications including but not limited to high-speed 5G cellular communication, automotive radar and satellite communication. A large variation in the insertion loss of the phase shifter as the state varies, can adversely affect the phased-array gain. Ideally, phase shifters should provide a constant low insertion loss and precise phase shift tuning over a wide bandwidth.

Phase shifters are commonly realized using semiconductor technologies based on CMOS, GaAs, SiGe and SOI. While mmWave semiconductor-based phase shifters offer ease of low cost integration with other front-end modules, they suffer from high insertion loss with large variation, low linearity and low power handling capability [128–130]. RF-MEMS based phase shifters provide better RF performance [131–133], but due to mechanically moving thin membranes, contact based MEMS devices do not offer latching functionality. In addition they are larger in size, and suffer from reliability concerns [131, 133]. Many of these reliability issues have been resolved over the years, yet as of today, RF MEMS have been implemented in a very limited applications and only at low frequencies.

Emerging RF switch technology based on PCM GeTe provides exceptional RF performance for mmWave applications [86]. Latching nature of GeTe material allows the development of compact integrated mmWave circuits with zero static DC power consumption [95–97]. Three different phase shifter topologies are investigated including true-time-delay phase shifters and reflective type phase shifter.

7.3.1 Loss Compensated Wideband 3-bit Switched 30 GHz True-Time-Delay Phase Shifter

This section reports the first implementation of a 3-bit mmWave switched true-time-delay (TTD) phase shifter based on PCM GeTe. The phase shifter is designed using four monolithically integrated PCM SP3T switches to route the signal through delay lines. The insertion loss variation between various states is minimized by integrating two fixed PCM GeTe elements maintained in the crystalline state, along with optimized width of the delay lines. The PCM switching cells are latching type, thus consume no

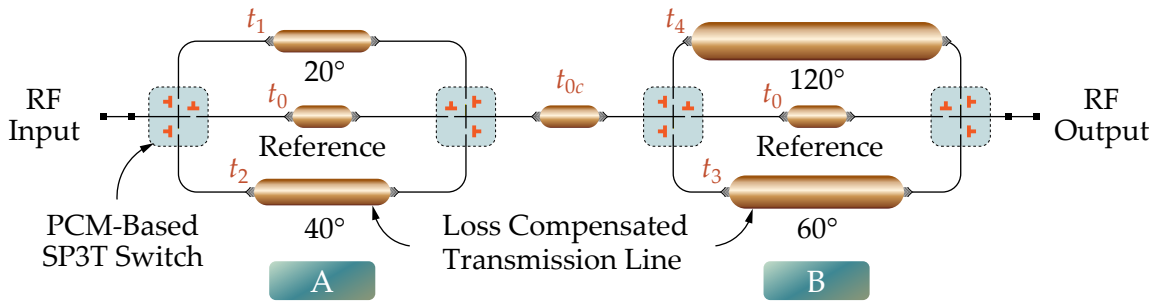


Figure 7.23: Schematic of a loss compensated 3-bit switched TTD phase shifter consisting SP3T switches and delay lines (t_0 to t_4) cascaded in two stages.

static DC power. The SP3T switches are connected back-to-back in two stages to provide 3-bit phase shift with 20° precision.

The phase shifter is designed to operate over a 8 GHz wide frequency band with a center frequency of 30 GHz. The presented phase shifter is highly miniaturized with overall device area of 0.42 mm^2 . The phase shifter exhibits a measured average loss of 4.3 dB with a variation of only $\pm 0.3 \text{ dB}$ and a return loss better than 20 dB. It provides 180° linear phase shift with a figure-of-merit of $42^\circ / \text{dB}$. The phase shifter exhibits less than 15 ps delay with 2 ps precision per state, which is lowest compared to currently available state-of-the-art MEMS-based phase shifters.

A novel monolithically integrated loss-compensated compact PCM GeTe-based 3-bit switched TTD phase shifter for mmWave applications at 30 GHz with 8 GHz bandwidth is developed. The integrated device is fabricated in-house on a high resistivity silicon wafer using seven-layer Gen 3 microfabrication process. SP3T switches integrated in this

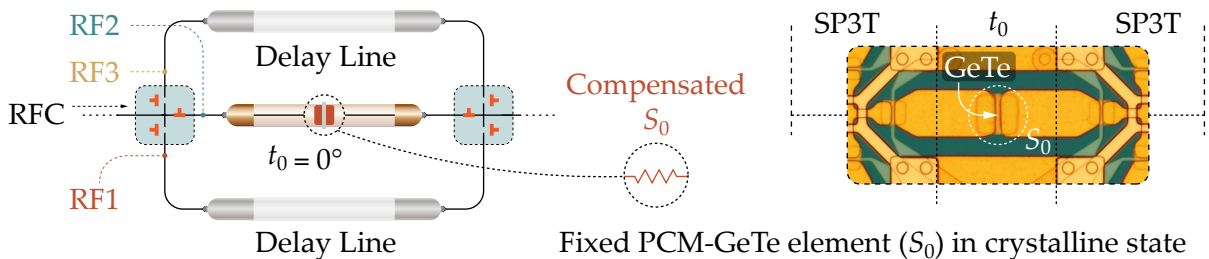


Figure 7.24: Loss compensation in t_0 sections using fixed PCM-GeTe element (S_0) in each stage. Both PCM elements S_0 elements are latched in crystalline state and does not require any switching. Addition of S_0 minimize insertion loss variation between phase shifter states.

device demonstrate exceptional RF performance over the entire bandwidth. Phase shift is controlled by selectively routing the RF signal through delay lines and four cascaded PCM-based SP3T switches.

Delay line dimensions are optimized along with fixed integrated GeTe elements designed to provide a particular insertion loss to minimize loss variation. This the first ever reported PCM-based wideband phase shifter for mmWave applications in a highly compact package with low average loss, minimum loss variation, low group delay variation along with precise phase shift tuning.

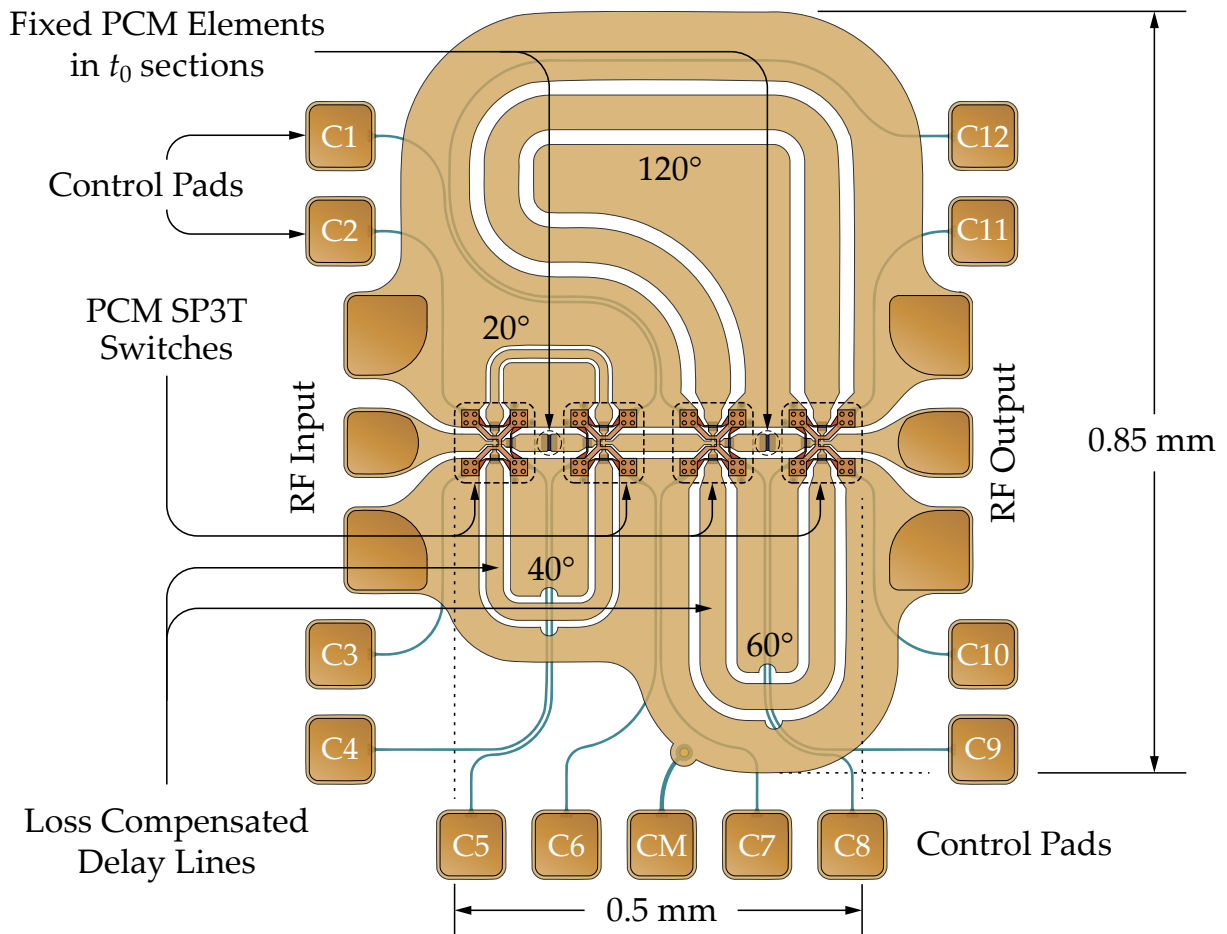


Figure 7.25: Chip layout of the loss compensated PCM-based 3-bit switched TTD phase shifter. PCM SP3T switches are used to select desired phase shift level by loading/unloading a combination of delay line section(s) in the RF path.

7.3.1.1 Operation Principle of TTD Phase Shifter

The monolithically integrated PCM-based 3-bit switched TTD phase shifter is designed by utilizing four SP3T switches to route the RF signal through a combination of delay/transmission line sections. Four delay line sections (t_1-t_4) are cascaded in two stages A and B to form a 3-bit device in reference to a delay line (t_0) as shown in Fig. 7.23. Integrated PCM-based SP3T switches utilize series SPST switches in an extremely compact area for routing the signal between three available paths in Fig. 7.24. Delay lines provide phase shift as $t_0 = 0^\circ$ (Reference), $t_1 = 20^\circ$, $t_2 = 40^\circ$, $t_3 = 60^\circ$ and $t_4 = 120^\circ$. A short line

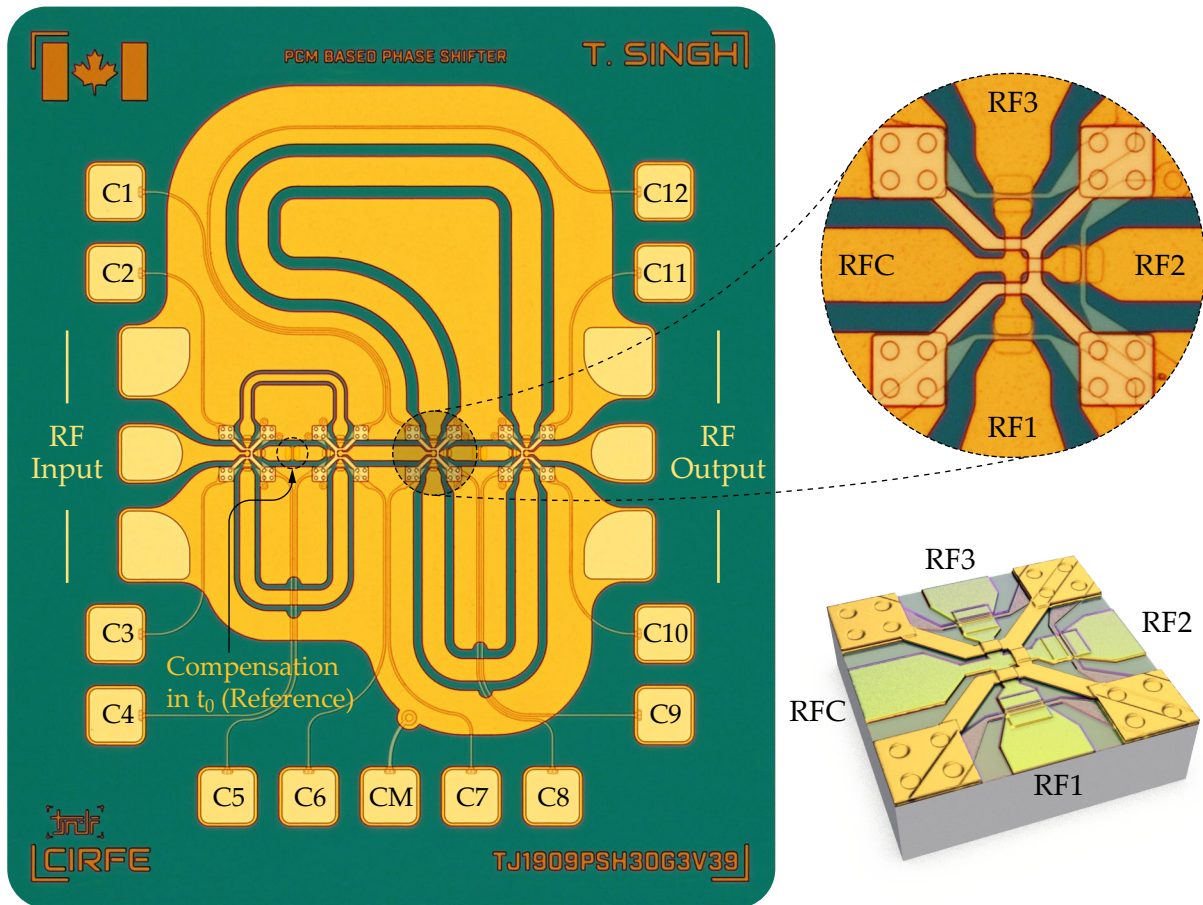


Figure 7.26: Optical micrograph of the monolithically integrated PCM-based 3-bit mmWave switched TTD phase shifter. Inset shows an optical micrograph of the zoomed-in view of a PCM-based SP3T switch. 3D rendered view of PCM SP3T switch core is highlighted.

segment (t_{0c}) connects two phase shifter stages (A and B). With a proper selection of the SP3T switching states, the phase shifter would exhibit 20° phase precision in 9 discrete states. Individual delay line sections are designed and optimized to minimize the insertion loss by varying the width of the lines. A large CPW signal line width is selected for longer delay lines while smaller CPW signal line widths are chosen for shorter delay lines to minimize variation of the insertion loss. Width of the delay line t_4 is larger than subsequent delay lines to match the insertion loss with the lowest bit t_1 .

RF signal passes through t_{0c} in all possible states. In addition to t_{0c} , in state 1, the signal passes through two t_0 sections, while the signal routes through $t_1 + t_0$, $t_2 + t_0$, $t_0 + t_3$, or $t_0 + t_4$ in state 2, 3, 4 and 7 respectively, utilizing one delay line segment in conjunction with t_0 . In state 5, 6, 8 and 9, the signal passes through two delay line segments $t_1 + t_3$, $t_2 + t_3$, $t_1 + t_4$ or $t_2 + t_4$ bypassing both t_0 segments respectively. To compensate for the high insertion loss exhibited in states when a combination of two delay line segments are selected, two fixed PCM GeTe elements (S_0) that are designed without micro-heater, are monolithically integrated in two t_0 sections to minimize the insertion loss deviation and to match the loss in state 1, 2, 3, 4, and 7 with the remaining states as highlighted in schematic and in optical micrograph depicted in Fig. 7.24. PCM elements (S_0) are kept in crystalline state to compensate for the loss in lower order states of the phase shifter. PCM-based technology provides flexibility to highly miniaturize the integrated device.

Layout of the fully integrated device is shown in Fig. 7.25. The overall device core area

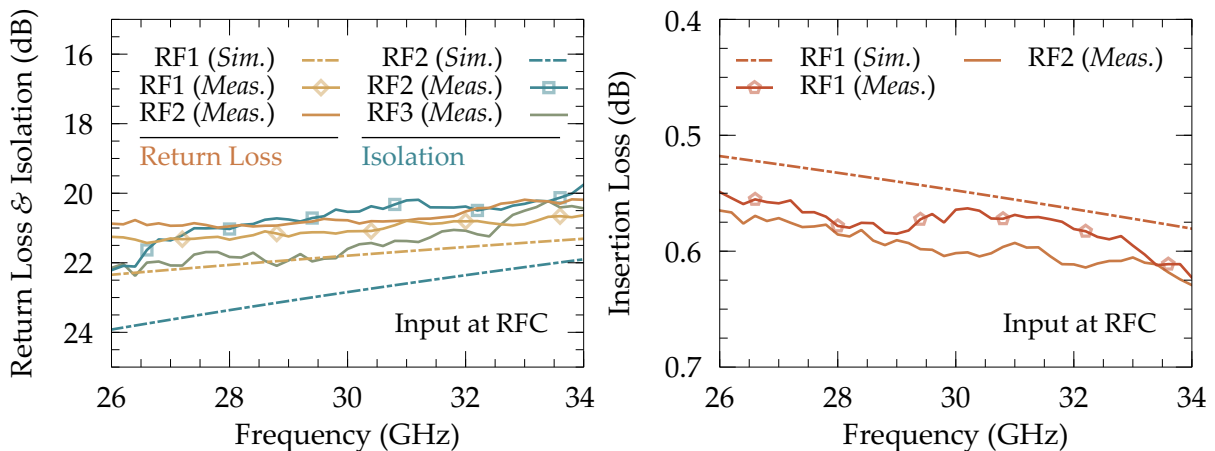


Figure 7.27: Measured and simulated RF performance of PCM-based SP3T switches over 8 GHz bandwidth. Due to the design symmetry, RF performance between RFC and three output ports is identical as shown for two states.

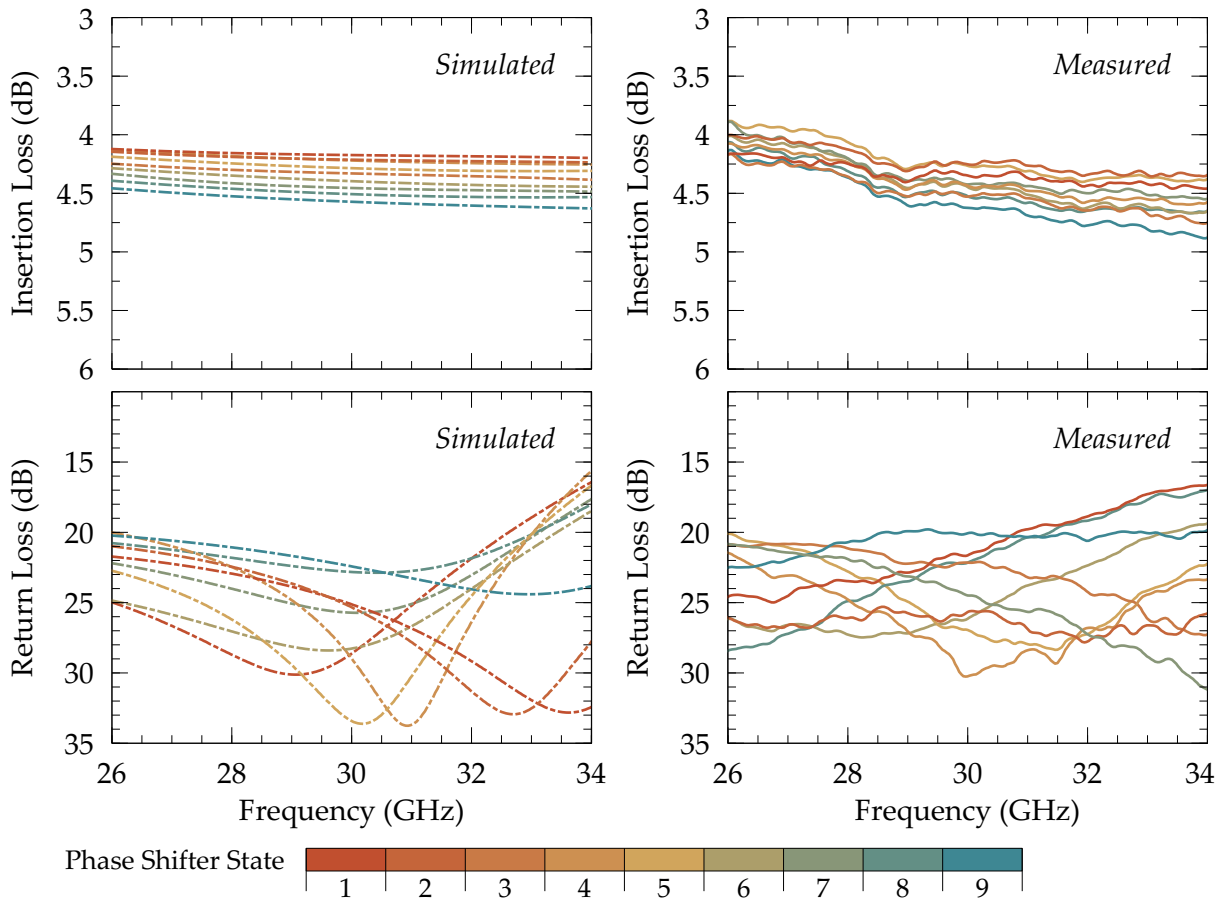


Figure 7.28: Measured and simulated RF performance of the PCM-based 3-bit switched TTD phase shifter over 26–34 GHz band. Response of all 9 states is shown. Insertion loss variation is minimized by choosing optimum delay line widths for higher states.

is under 0.42 mm^2 making it a highly miniature phase shifter. The PCM SP3T switch has one common input port ‘RFC’ and three output ports ‘RF1, RF2 and RF3’ as shown in Fig. 7.24. Desired phase shift level is achieved by routing the RF signal through delay lines and actuating the cascaded PCM-based switches with the application of OFF or ON pulse. The control pulse is provided between respective control pads and a common bias pad ‘CM’. PCM switches are reversible binary resistive switches which are actuated by applying an OFF pulse of 200 ns width and 12 V amplitude and an ON pulse of 1.2 μs width and 7.8 V amplitude.

7.3.1.2 RF Performance Measurement

An optical micrograph of the fabricated PCM-based 3-bit switched TTD phase shifter is shown in Fig. 7.26, highlighting the overall device size, control pads and delay lines and loss compensation fixed PCM elements. Inset of Fig. 7.26 shows the optical micrograph of the close-up view of monolithically integrated PCM SP3T switches. 3D rendered SP3T switch is also shown in Fig. 7.26. Control pads provide the desired phase shift by reconfiguring the respective PCM switches in desired phase shift path. Four RF PCM GeTe-based SP3T switches (12 RF SPST switch elements) along with two fixed PCM GeTe elements S_0 in t_0 sections (these elements are always in the ON-state to compensate loss)

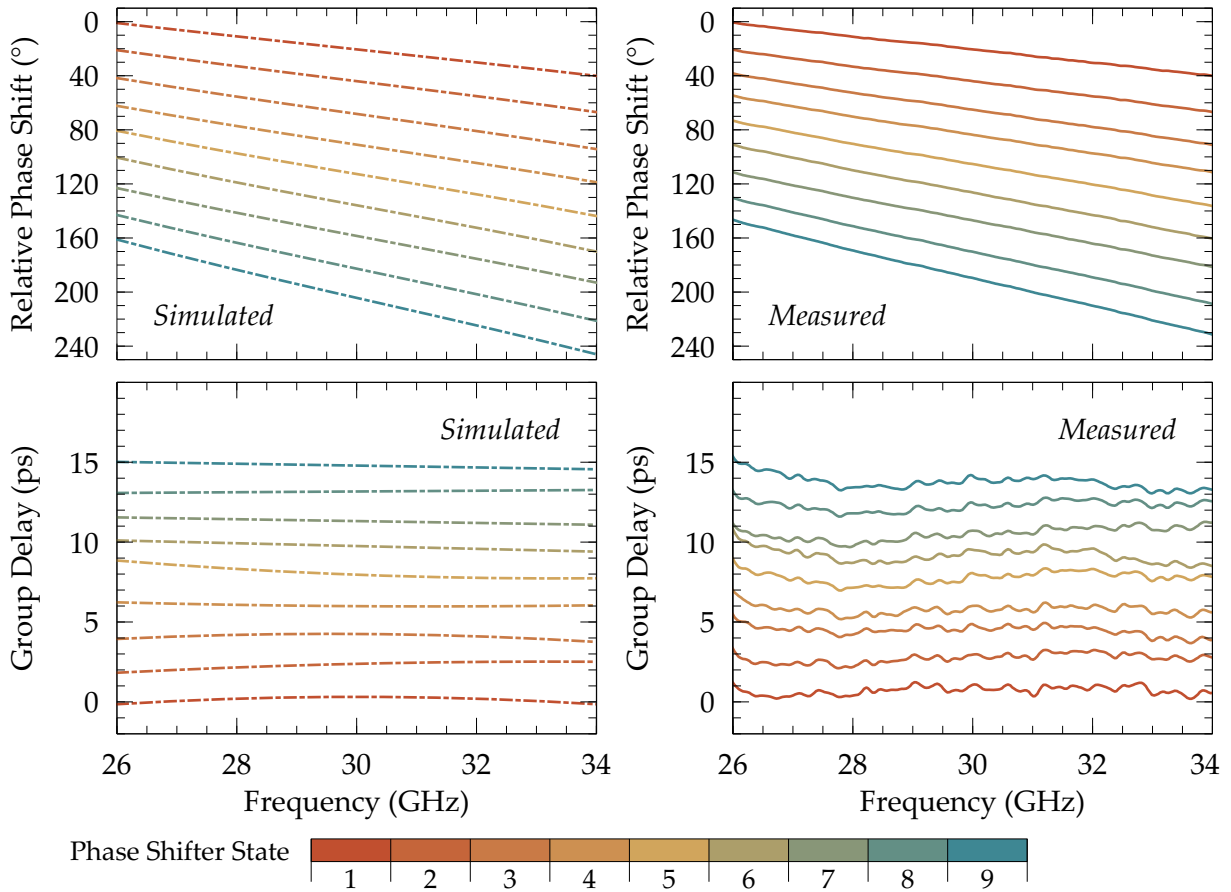


Figure 7.29: Measured and simulated phase shift and group delay of the PCM-based 3-bit TTD phase shifter over 26–34 GHz band. Response of all possible states is shown.

are monolithically integrated to form the phase shifter as shown in Fig. 7.26. Fig. 7.27 shows the measured RF performance of the SP3T demonstrating a return loss better than 21 dB, isolation higher than 20 dB and insertion loss lower than 0.6 dB over the 8 GHz operational bandwidth. RF ground is connected using cross-connect junctions over SP3T switches which are optimized to remove any capacitive effect from the M3 bridges by adding inductive element to the signal line.

Table 7.4: Comparison of the mmWave PCM GeTe-based phase shifter with state-of-the-art

Reference	Device Technology	Frequency (GHz) [†]	No. of States	Device Area	Phase Shift at 30 GHz
This Work	PCM-GeTe	26–34	9	0.43 mm ²	160°
[134]	Liquid Crystal	20–40	2	540 mm ²	60°
[133]	RF MEMS	27–33	16	20 mm ²	290°
[129]	65 nm CMOS	20–30	64	0.18 mm ²	360°
[132]	RF MEMS	10–35	8	14.3 mm ²	360°
[128]	0.25 μm SiGe	10–50	64	0.22 mm ²	80°
[131]	RF MEMS	DC–40	4	200 mm ²	200°
[130]	0.18 μm SiGe	28–40	16	0.18 mm ²	320°

Reference	Insertion Loss Max.	δ Loss Variation	Return Loss Min.	Tuning Elements	Latching (Yes/No)
This Work	4.9 dB	±0.3 dB	16.5 dB	12	Yes
[134]	9.5 dB	±2.5 dB	6 dB	Liquid	No
[133]	6.2 dB	±2.0 dB	8 dB	13	No
[129]	13.5 dB	±1.3 dB	13.3 dB	24	No
[132]	4.2 dB	±1.8 dB	3 dB	14	No
[128]	18 dB	±2.0 dB	12 dB	25*	No
[131]	2.0 dB	±0.6 dB	12 dB	21	No
[130]	21 dB	±5.5 dB	8.2 dB	9*	No

[†] RF performance reported is for 4 GHz to 8 GHz bandwidth (depending on the maximum operating frequency of a device) at 30 GHz center frequency.

* Tuning elements in [128] and [130] are estimated based on the described circuit configurations. Number of tuning elements are ranked depending on the number of states of the phase shifter. Best, Reasonable and Worst performance parameters are highlighted.

The RF performance of the phase shifter is simulated in Ansys Electronics Desktop (Previously Ansys HFSS) and Sonnet EM Professional Suite. Measured results are in close agreement with the EM simulated results as shown in Fig. 7.28. The phase shifter exhibits return loss better than 20 dB at 30 GHz and better than 16 dB over the 8 GHz bandwidth. Measured average insertion loss is 4.3 dB with a loss variation remarkably reduced to only ± 0.3 dB over the entire bandwidth.

Measured and simulated relative phase shift is depicted in Fig. 7.29 reporting highly linear 180° phase shift with 20° step precision over the operational bandwidth with figure-of-merit (FoM) of 42°/dB. The presented phase shifter exhibits less than 15 ps of measured group delay in 2 ps per state precision as shown in Fig. 7.29. The demonstrated group delay is lowest compared to current state-of-the-art.

7.3.2 Low Loss 3-bit Switched True-Time-Delay 30 GHz Phase Shifter Using PCM SP8T Switches

This section reports a low-loss 3-bit mmWave switched TTD phase shifter based on PCM GeTe. The phase shifter is designed using two monolithically integrated PCM GeTe-based SP8T switches to route the RF signal through delay lines. The insertion loss variation between various phase shifter states is minimized by utilizing optimized width of the delay lines. The phase shifter reported in section 7.3.1 use two stages 'A' and 'B', thus the RF signal passes through four switches. Although, two fixed PCM GeTe elements are used in reference ' t_0 ' delay line to compensate for the loss, but it is always preferred to reduce the number of switches which mainly add loss to the signal path. The PCM SP8T switches are connected back-to-back beside 8 delay lines to provide 3-bit phase shift with 20° precision. Similar to the phase shifter reported in section 7.3.1, this phase shifter is also designed to operate over a 8 GHz bandwidth with a center frequency of 30 GHz. The miniaturized phase shifter is developed with overall device area of 1.74 mm². The phase shifter reported in this section exhibits a measured average loss of 3.8 dB with a variation of only ± 0.2 dB and return loss better than 17 dB at 30 GHz. It provides 180° linear phase shift with a figure-of-merit of 47°/dB. The phase shifter exhibits less than 20 ps delay with 2.5 ps precision per state.

The reported TTD phase shifter is designed utilizing rotary PCM-GeTe based SP8T switch to maintain the RF performance from various switch paths in all possible operating states. The phase shifter is developed using Gen 3 microfabrication process. Details on design and operation of SP8T switches integrated in this phase shifter are provided in section 6.1.2. The operation principle is similar to the one reported in Fig. 7.23 with

the exception that this phase shifter is designed to have 3-bit operation using a single stage with two SP8T switches rather than four cascaded SP3T switches. Phase shift is controlled by selectively routing the RF signal through delay lines and two PCM-based SP8T switches. Delay line dimensions are optimized to minimize the loss variation. Due to the use of a single stage of delay lines, loss compensation using fixed GeTe elements are not required in this design.

The TTD phase shifter has eight delay lines ($t_1 - t_8$) which are controlled by actuating respective switches aligned in SP8T configuration. The optical micrograph of the monolithically integrated PCM-based 3-bit TTD phase shifter is shown in Fig. 7.30. SP8T core and zoomed-in view of one of the PCM SPST switch in SP8T configuration is high-

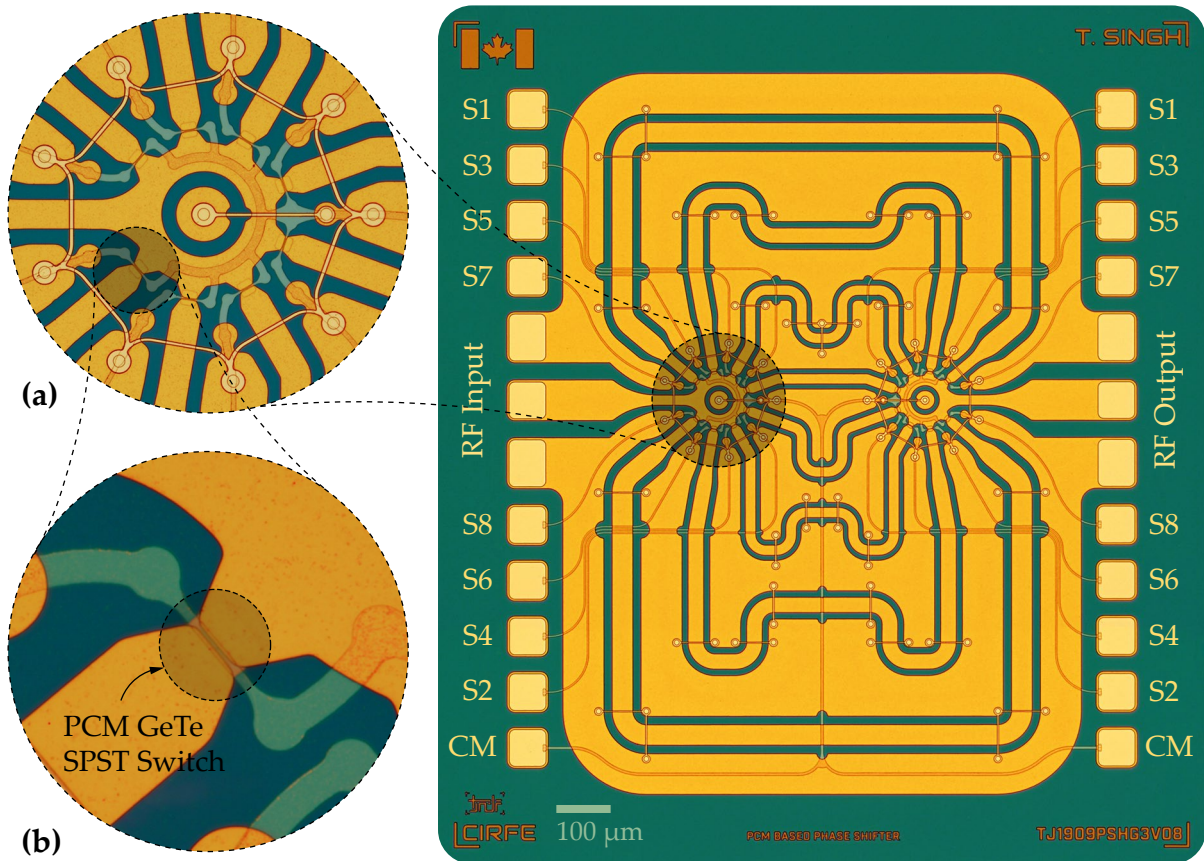


Figure 7.30: Optical micrograph of the monolithically integrated PCM-based 3-bit mmWave switched TTD phase shifter using SP8T switches. (a). Optical micrograph of SP8T switch core, (b). Zoomed-in view of an individual PCM GeTe SPST switch used in SP8T switches.

lighted in Fig. 7.30(a) and (b) respectively. With a proper selection of the SP8T route, the phase shifter would exhibit 20° phase precision in 8 discrete states. The delay line widths are wider for longer delay lines to compensate for the loss.

7.3.2.1 RF Performance Measurement

The optical micrograph shown in Fig. 7.30 highlights SP8T switches, delay lines and control pads to actuate respective phase shifter state. ‘COM’ pads are the common ground nodes for actuation signals. EM simulated and measured RF response of SP8T switches for the 8 GHz operational bandwidth is shown in Fig. 7.31. At center frequency 30 GHz, the insertion loss of the switches is less than 1.2 dB and return loss is better than 20 dB, while the isolation is higher than 23 dB.

The fully integrated phase shifter shows an average 3.5 dB of insertion loss with ±0.2 dB loss variation and return loss better than 23 dB at center frequency 30 GHz. The measured average insertion loss is 3.8 dB with loss variation of ±0.2 dB. The measured return loss is better than 17 dB at 30 GHz. Over the entire 8 GHz operational bandwidth, the simulated return loss is better than 18 dB and measured return loss is higher than 14 dB, while the average insertion loss is 4 dB. The simulated and measured phase shift and group delay is shown in Fig. 7.29. EM simulation and measurement of the phase shifter demonstrate a relative linear phase shift of 180 deg at 30 GHz with 22.5° precision.

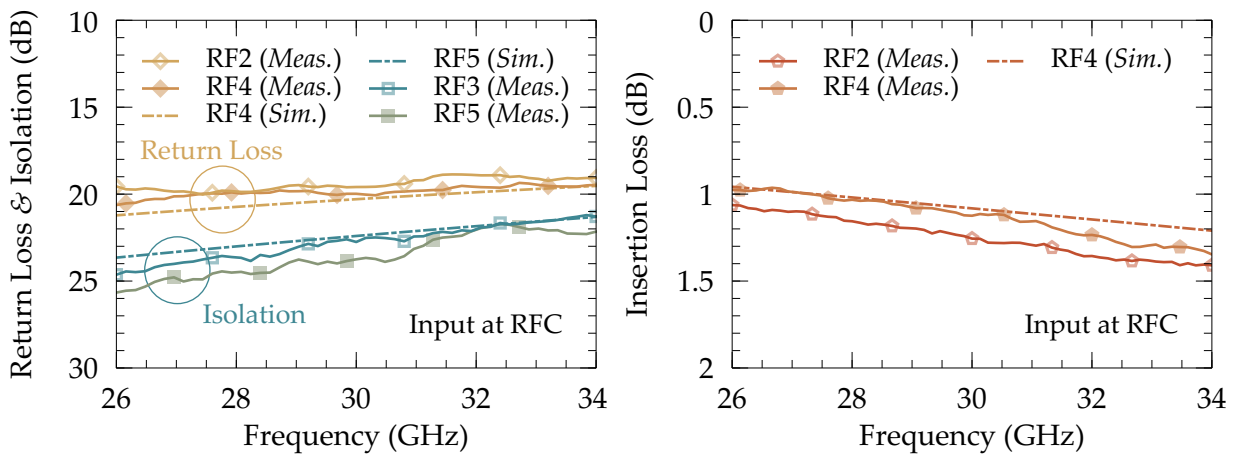


Figure 7.31: Measured and simulated RF response of SP8T switch over 26–34 GHz band. RFC is the common input port. Due to the symmetrical design, response of two states RF2 and RF4 is shown in ON-state and the OFF-state response of two different states RF3 and RF5 is shown.

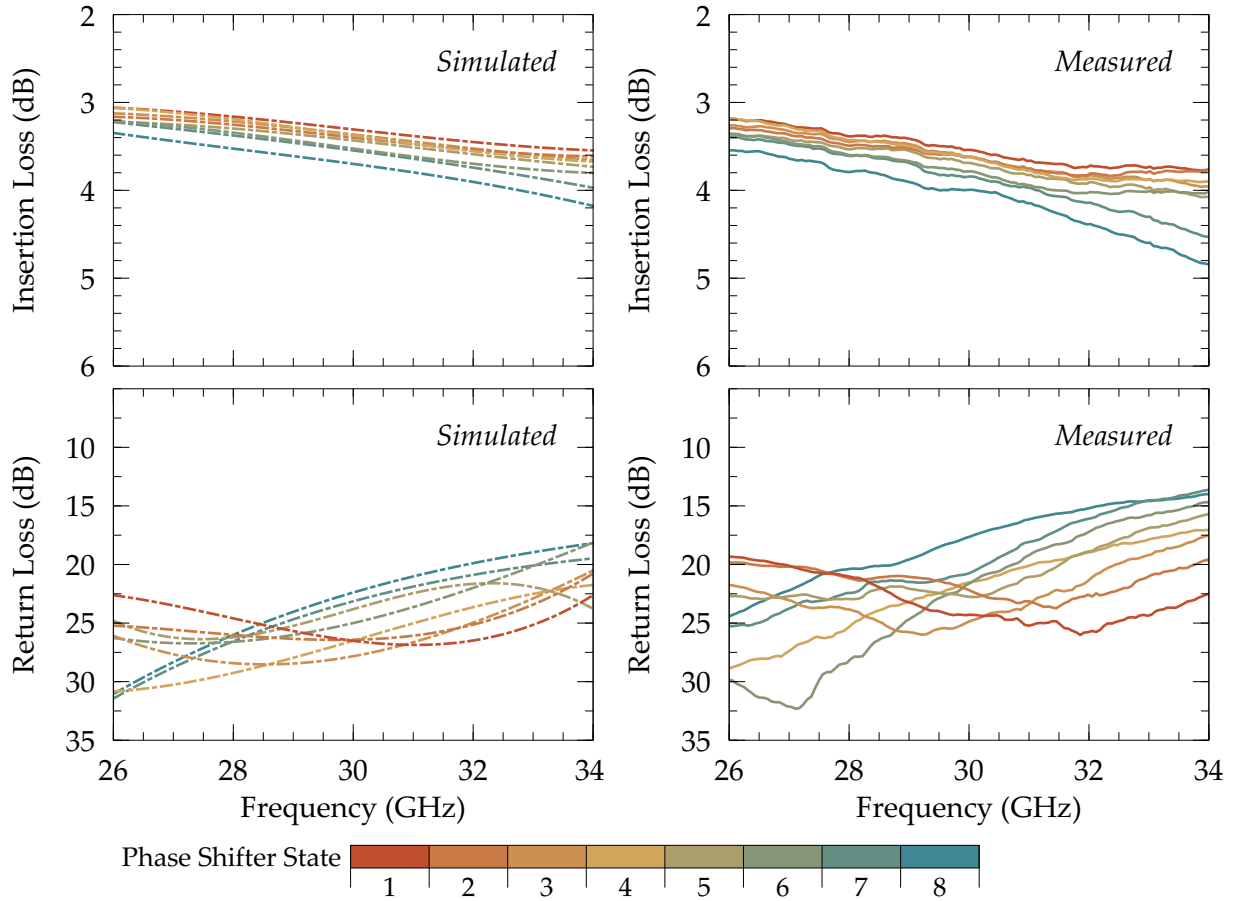


Figure 7.32: Measured and simulated insertion loss and return loss of the PCM-based 3-bit TTD phase shifter over 26–34 GHz band. Response of all 8 possible states is shown.

Simulated relative group delay shows maximum of 17 ps delay in linear 2.1 ps steps. The phase shifter demonstrates measured maximum group delay of 20 ps with 2.5 ps linear step precision per state as shown in Fig. 7.33.

Measured and simulated relative phase shift depicted in Fig. 7.33 shows a linear phase shift with figure-of-merit (FoM) of $47^\circ/\text{dB}$. The presented phase shifter shows $12\times$ better FoM at the expense of slightly larger device area and 5 ps higher group delay. Both the presented TTD phase shifters demonstrate exceptional RF performance compared to state-of-the-art.

The advantage of the PCM technology with monolithic integration of circuit elements

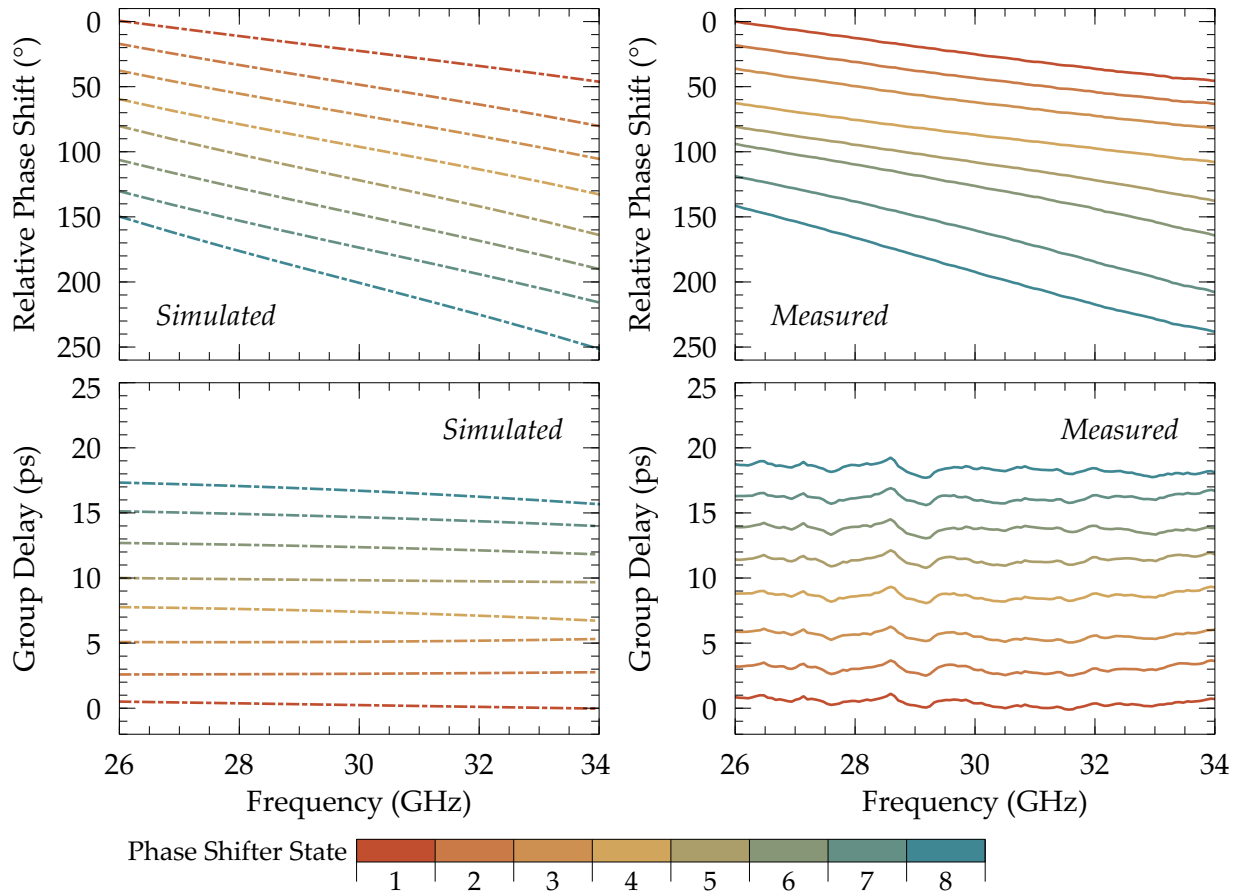


Figure 7.33: Measured and simulated phase shift and group delay of the PCM-based 3-bit TTD phase shifter over 26–34 GHz band. Response of all possible states is shown.

is that the device size is highly reduced with a clear benefit in minimizing insertion loss variation. All measurements were carried out on-wafer at room temperature. The reliability of the RF PCM GeTe series switches was experimentally validated for more than 1 million cycles. The PCM GeTe-based phase shifter is compared with the current state-of-the-art and the presented device provides better RF performance and exhibits minimum loss variation with lesser number of tuning elements required than the other phase shifters reported in literature as shown in Table 7.4. As per our knowledge, there is no latching type phase shifters available for mmWave in such a miniaturized packages.

Apart from switched-type/TTD based phase shifters, an interesting approach to develop phase shifter is to integrate tunable reflective loads with a quadrature coupler.

Depending on the choice and implementation of reflective loads, reflective type phase shifter offers precise phase shift with broad tuning range. A mmWave reflective type phase shifter is discussed in next section.

7.3.3 Monolithically Integrated 28 GHz PCM-Based Reflective Type Latching Phase Shifter

Reflective-type phase shifters (RTPS) are suitable candidates for realizing monolithically integrated phased array systems due to their smaller size and high phase resolution compared to switched-type or TTD phase shifters. Recently, several CMOS-based implementations of RTPS at mmWave frequencies are reported [135–137]. The most common designs of RTPS utilize microstrip-based 3 dB Lange/broadside/hybrid coupler with two LC reflection loads [138, 139]. The output phase shift of RTPS is controlled by the reflection coefficient of the loads. A highly compact phase shifter implementation based on GaAs MESFET is reported in [140].

The major challenge in the design of phase shifter is to achieve low insertion loss, large phase shift range, linear phase shift deviation over a desired frequency band, and low loss variation simultaneously. The phase shifting range can be improved by cascading two RTPS designs, but this method leads to high insertion loss [136]. Therefore, it is utmost challenging to develop RTPS with a large phase shift range, low insertion loss.

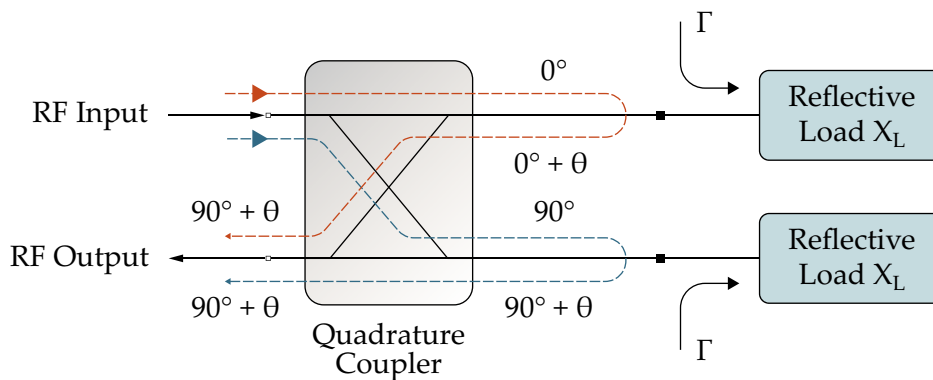


Figure 7.34: Schematic of the single-ended RTPS consisting of a quadrature hybrid coupler terminated with two identical reflective loads. The desired phase shift in the output RF signal is added by the hybrid coupler and the reflective loads. Γ is the reflection coefficient and X_L is the tunable reactance of each reflective load.

In this section, a PCM-based monolithically integrated RTPS is developed using Gen 3 microfabrication process. The RTPS phase shifter is developed utilizing two identical hybrid capacitor/inductor banks integrated with a 28 GHz quadrature coupler as tunable reflective loads. The demonstrated phase shifter exhibits measured 280° phase shift over 26 GHz to 30 GHz in 256 steps precision. Various reflective load topologies are discussed with respect to achievable phase shift range.

7.3.3.1 Phase Shifter Design and Operation Principle

The schematic of the PCM-based RTPS is shown in Fig. 7.34. The output phase shift is controlled by simultaneously tuning reflective loads. The PCM-based RTPS is designed using hybrid capacitor/inductor bank, which provides reactive load tuning simultaneously providing change in phase shift between input and output port.

The design of RTPS presented in this section comprises of a 90° (quadrature) hybrid coupler terminated by two identical reflection loads as shown in the schematic in Fig. 7.34. When two identical reflective loads are attached at the through port 2 and the coupled port 3 of a quadrature hybrid, the RF signal at input port will be transmitted to output port with phase shift determined by the phase of the reflective load.

If Z_0 is the characteristic impedance of the quadrature coupler and X_L is the reactance of the reflective load, then if assuming the reflective loads and hybrid coupler lossless, the phase shift between input and output port will vary with the load reactance X_L [112]. If X_{Lmin} and X_{Lmax} are the minimum and maximum reactance values of the tunable load, respectively, then the total phase shift range θ_{range} achieved can be described as:

$$\begin{aligned}\theta_{range} &= -2 \left| \tan^{-1} \left(\frac{X_{Lmax}}{Z_0} \right) - \left(\frac{X_{Lmin}}{Z_0} \right) \right| \\ &= \angle \Gamma_{Lmax} - \angle \Gamma_{Lmin}\end{aligned}\quad (7.1)$$

where $\angle \Gamma_{Lmax}$ and $\angle \Gamma_{Lmin}$ are the maximum and minimum values of the phase of reflection coefficient.

7.3.3.2 Reflective Loads

The design of reflective-type phase shifters is primarily focused on the optimization of reflective loads by using inductive and capacitive elements in various configurations.

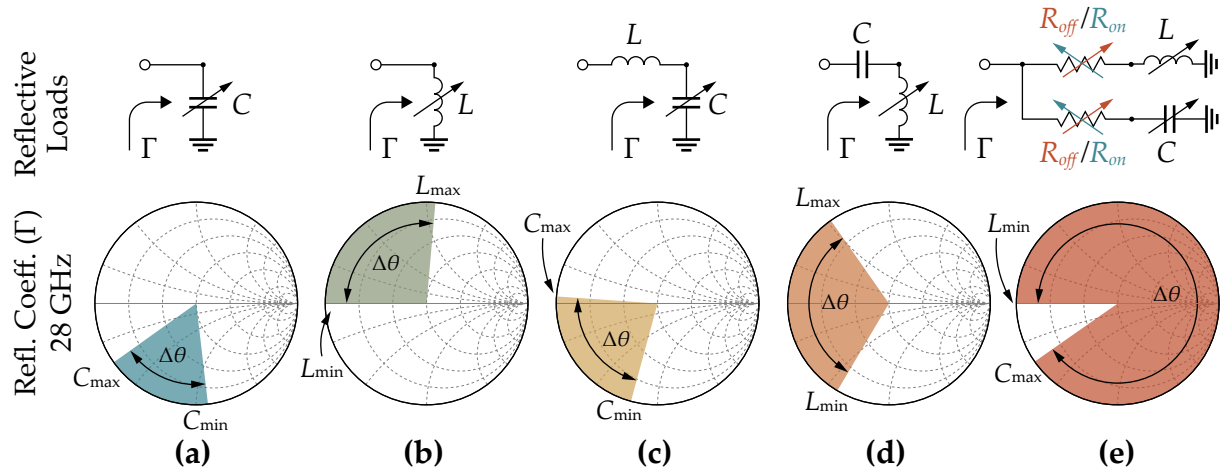


Figure 7.35: Comparison of the simulated load impedance range and phase shift range for different reflective load topologies (a) single variable capacitive load, (b) single variable inductive load, (c) fixed inductor and variable capacitor connected in series, (d) fixed capacitor and variable inductor connected in series, and (e) switchable variable capacitor and variable inductor connected in parallel as the proposed load configuration.

Several reflective load topologies have been reported in the literature [137]. The load impedance tuning range and the phase shift range provided by some common reflective load configurations along with the proposed load topology are shown in Fig. 7.35.

The basic reflective load topology shown in Fig. 7.35(a) has a single capacitive load. Its load impedance tuning range at 28 GHz as shown on the Smith chart is very limited. This leads to small phase shift range (61.15°) as described by the Eq. 7.1. A single tunable inductor also has a limited range as shown in Fig. 7.35(b). A series inductor can extend

Table 7.5: Summary of various reflective loads for RTPS

Load Topology	Phase Shift, θ at $f_0 = 28$ GHz	$\delta\theta$ ($^\circ$)
a	61.15°	$\pm 2.4^\circ$
b	94.97°	$\pm 4.1^\circ$
c	78.79°	$\pm 5.5^\circ$
d	114.38°	$\pm 10.7^\circ$
e	324.95°	$\pm 2.4^\circ$

the phase shift range as shown in Fig. 7.35(c) but still the range is limited. Although, these topologies provide larger load impedance coverage for the same capacitance range, the phase shift range is still very limited. On the other hand, the reflective loads given in Fig. 7.35(d) can provide better phase shift range, but do not yield a constant phase change ($\delta\theta$) over 26 GHz to 30 GHz. The phase shift range obtained at 28 GHz by proposed configuration shown in Fig. 7.35(e) is 325° with low $\delta\theta$.

Linearity of the phase shift change over the bandwidth of interest is critical for any phase shifter. It is desirable to attain a constant phase shift ($\delta\theta$) over the operating frequency band. It is noted that the proposed configuration shown in Fig. 7.35(e) offers the lowest variation in phase shift ($\delta\theta$) over the frequency range 26 GHz to 30 GHz. Table 7.5 gives the phase change and the delta in phase over bandwidth for the reflective loads shown in Fig. 7.35.

While using two switchable tuning elements extend the phase shift range more than 320° , it also provides low $\delta\theta$. The variable capacitance and inductor range for the simulation of phase shift range is the same that is achieved by a hybrid capacitor/inductor bank. For fixed elements, a median value of the lumped component is chosen. For variable lumped elements, $C_{\min}=110$ fF, $C_{\max}=360$ fF, $L_{\min}=38$ pH, and $L_{\max}=310$ pH are used, while for the fixed element values, $C_{\text{fixed}}=200$ fF and $L_{\text{fixed}}=100$ pH are chosen. R_{on} and R_{off} values depend on the resistance of the PCM switches. ON-state resistance drops due to the parallel connection of multiple switches. The PCM-based hybrid capacitor/inductor bank described in section 7.1.3, is an ideal choice to use in RTPS.

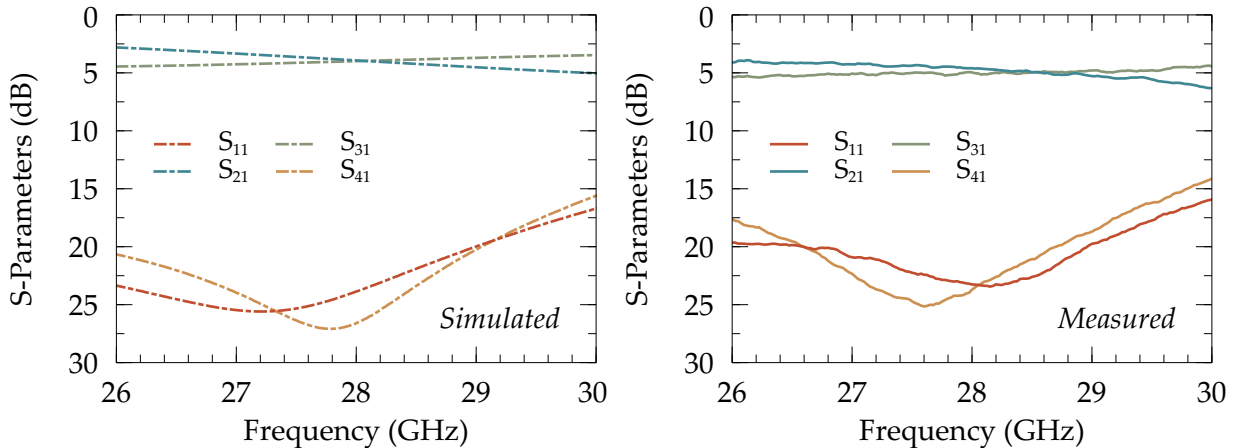


Figure 7.36: Measured and simulated S-parameters of the quadrature hybrid coupler from 26 GHz to 30 GHz.

7.3.3.3 28 GHz Hybrid Coupler

An efficient technique to design a mmWave hybrid coupler is to connect two loosely coupled CPW couplers in tandem configuration to form a tight coupler [141, 142]. For instance, two 8.3 dB CPW couplers can be combined to achieve a 3 dB tandem coupler. This topology however requires two metal layers, which is favorable for Gen 3 microfabrication process. Top metal layer used for connecting the signal lines at crossovers and the ground planes generate a broadside-coupling effect, hence the simulated length for maximum coupling at 28 GHz is smaller than $\lambda/4$. Simulated results show that the hybrid coupler provides an average transmission of 4.2 dB between the through and coupled ports over the frequency range 26 GHz to 30 GHz exhibiting an insertion loss of 1.2 dB as shown in Fig. 7.36. The return loss at the input and the isolation ports is below 25 dB at the centre frequency and better than 16 dB for the entire bandwidth.

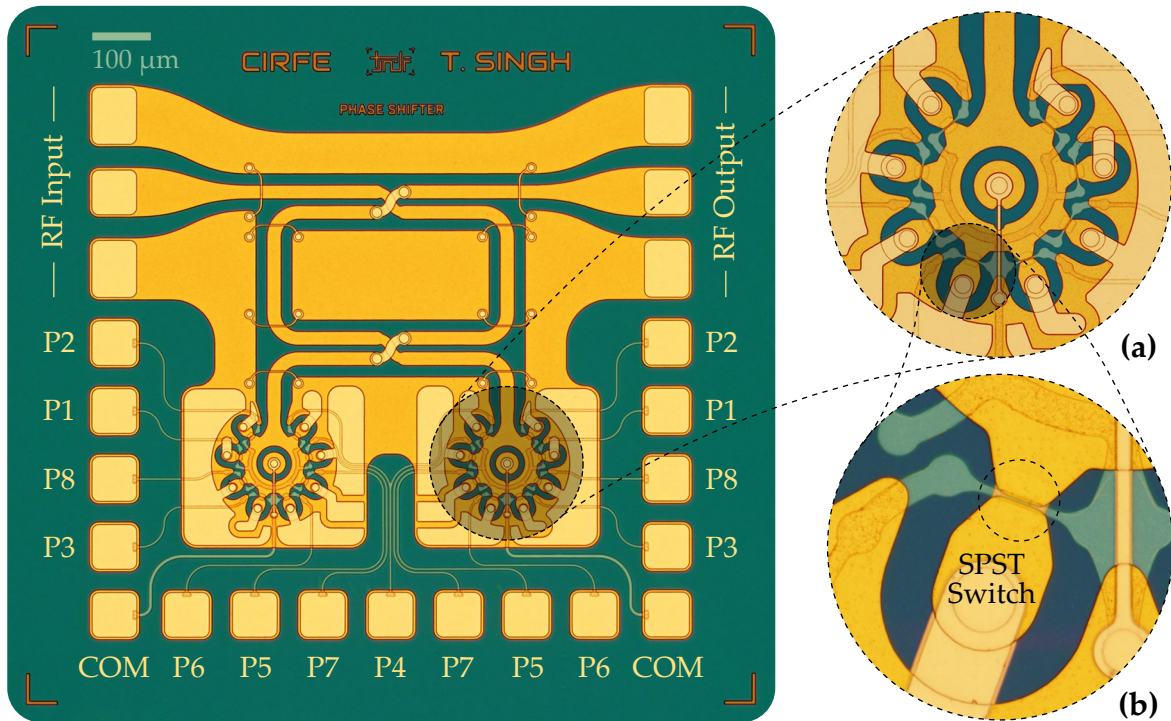


Figure 7.37: Optical micrograph of the compact PCM-based mmWave reflective type phase shifter highlighting control pads and reflective loads. (a). Optical micrograph of the mmWave hybrid capacitor/inductor bank, (b). Zoomed-in view of PCM SPST switch in series with tunable component.

The S-parameters of the fabricated quadrature hybrid coupler were measured as shown in Fig. 7.36. The measurement of the four-port characteristics in a two-port network analyzer system can be done by alternatively terminating two ports of the coupler with on-chip matched $50\ \Omega$ resistors and measuring the S-parameters between the two remaining ports. The measured results are displayed in Fig. 7.36 alongside the simulated results and a very good match was observed over the 26 GHz to 30 GHz range. A measured transmission of 5 dB was obtained at 28 GHz. The measured return loss and isolation are better than 15 dB within the frequency band.

7.3.3.4 RF Performance Measurement

The optical micrograph of the in-house fabricated PCM-based mmWave RTPS is shown in Fig. 7.37. Optical micrograph of the hybrid capacitor/inductor bank is shown in Fig. 7.37(a) and PCM SPST switch in series with tunable element is shown in Fig. 7.37(b). The phase shifter has overall device area of $1\ \text{mm}^2 \times 0.9\ \text{mm}^2$ including CPW ports and control pads while the device core footprint is under $0.7\ \text{mm}^2 \times 0.7\ \text{mm}^2$. Due to the use of hybrid coupler, RTPS usually have narrower bandwidth than TTD phase shifters. The developed phase shifter has 4 GHz operating bandwidth, which is half the bandwidth offered by two TTD phase shifters discussed in previous sections. RF performance of

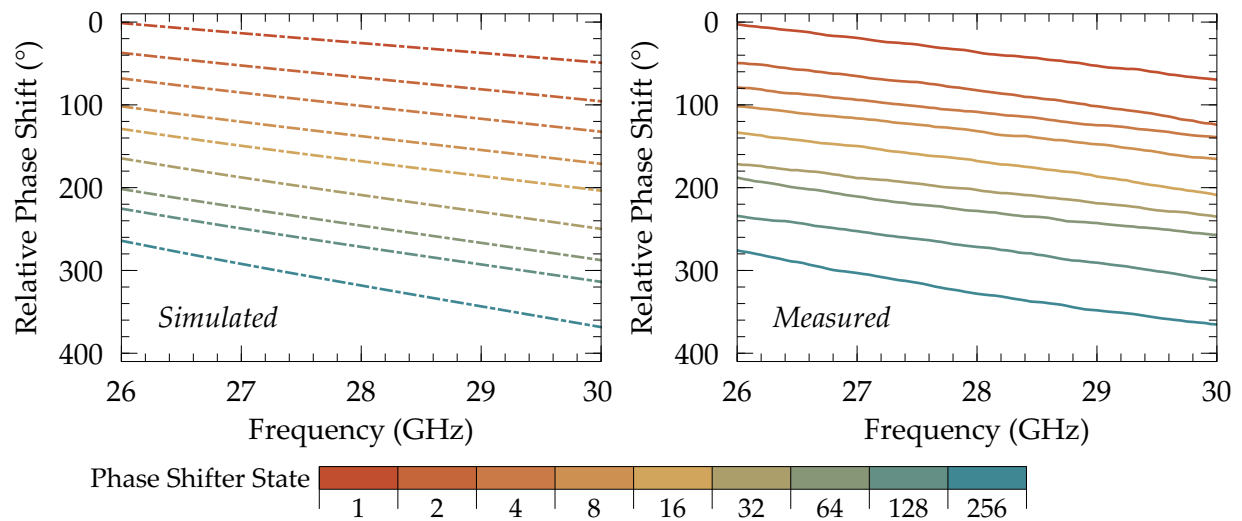


Figure 7.38: Measured and simulated phase shift of the PCM-based reflective type phase shifter over 26–34 GHz band. Response of 9 states out of 256 possible states is shown.

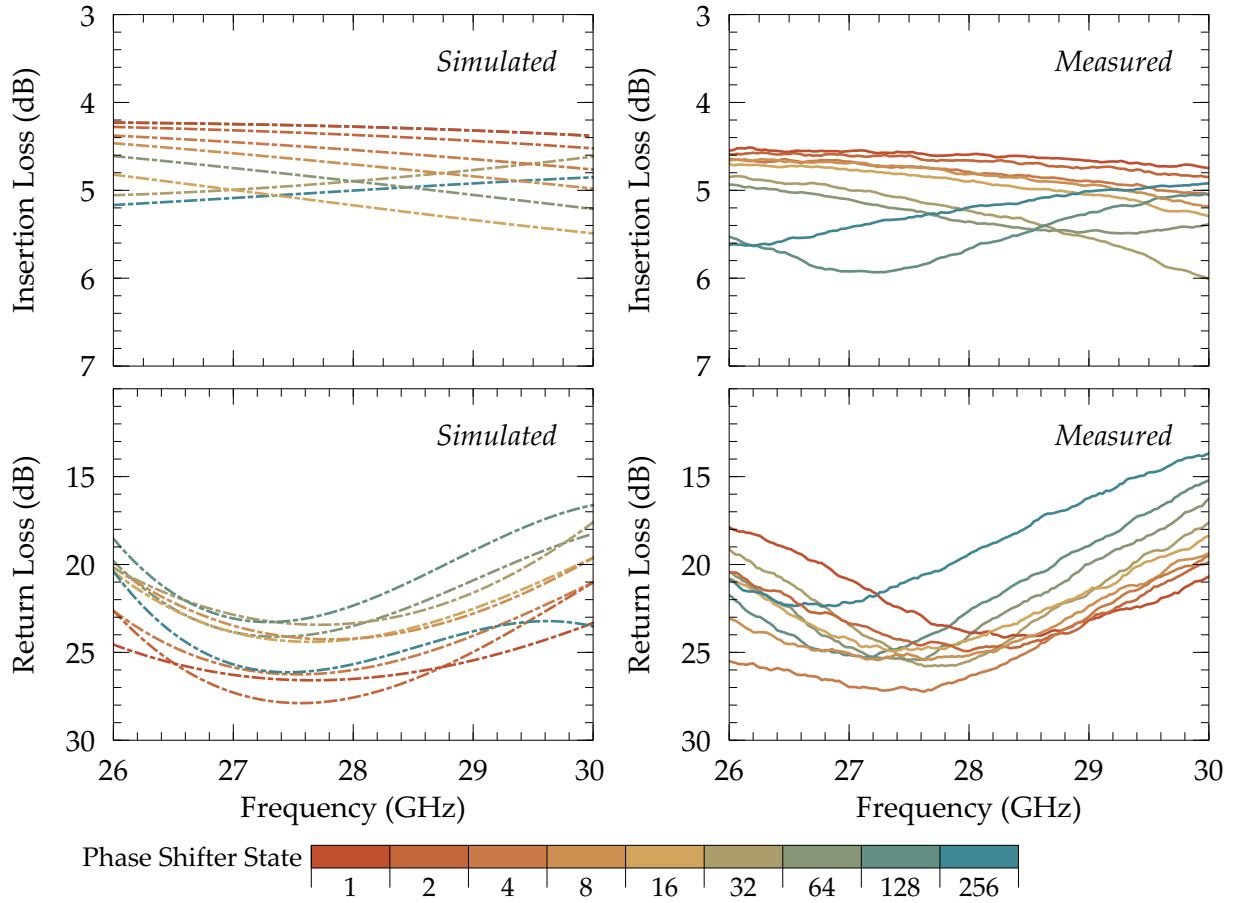


Figure 7.39: Measured and simulated RF response of reflective type phase shifter over 26 GHz to 30 GHz. RF response of 9 different states are shown out of a total of 256 states.

the RTPS is simulated and measured over 26 GHz to 30 GHz. Measured and simulated phase shift of the RTPS is shown in Fig. 7.38. The RTPS exhibits more than 300° simulated relative phase shift and better than 290° measured relative phase shift.

RF response of 9 states are shown out of a total of 256 states in Fig. 7.39. The average simulated insertion loss of the RTPS is 4.8 dB with loss variation ± 0.7 dB. The simulated return loss is better than 22 dB at center frequency and higher than 17 dB over the operating bandwidth. The measured average insertion loss of the RTPS is 5.25 dB with loss variation of ± 0.75 dB. The measured return loss is better than 18 dB at 28 GHz and higher than 14 dB over the operational bandwidth. The RTPS demonstrates measured FoM of $55^\circ/\text{dB}$ which surpasses TTD phase shifter.

7.3.3.5 Comparison of mmWave Phase Shifters

Both TTD and RTPS have their own advantages and disadvantages. RTPS provides better phase shift range if a reflective loads with large tuning range are used. TTD based phase shifters have low loss and can be made with loss-compensation technique as discussed in the previous sections. RTPS has higher loss variation than the previously described TTD phase shifters. RTPS also have narrow operating bandwidth which is due to the use of hybrid coupler. The RTPS discussed in previous section has half the operating bandwidth than its TTD phase shifter counterparts. TTD phase shifters offer more linear loss. It depends on the use case scenario if higher phase shift range is required or low loss is mandatory for the application. Looking at a single performance parameter, RTPS has better FoM than TTD based phase shifters.

7.4 Reconfigurable PCM-Based Impedance Matching Network

Reconfigurable impedance matching networks or simply impedance tuners are currently employed in a wide range of commercial communication wireless devices and have an important role in realizing intelligent multi-band RF-front ends. Impedance tuners compensate for the antenna impedance variations that arise within an RF-front end due to switching of frequency band of operation. Such systems are useful not only in enabling more than one frequency band of operation but can also adapt dynamically with variations in temperature, output power levels and process deviations. They ensure optimum power transfer and highest system efficiency [143, 144]. In this section, a reconfigurable PCM-based impedance matching network is demonstrated.

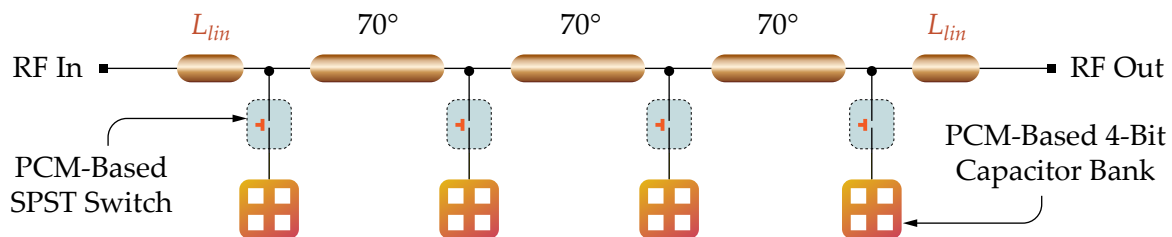


Figure 7.40: Schematic of reconfigurable impedance matching network using PCM-based 4-bit switched capacitor banks and 70° sections.

7.4.0.1 Operation Principle of Impedance Tuner

A monolithically integrated design of impedance tuner is reported with 4-bit PCM-based capacitor banks fully integrated in the ground planes of the transmission line. The integrated capacitor banks do not consume any additional chip area. The capacitor banks are integrated on the both sides of the transmission line to achieve high capacitance tuning range. The switched capacitor bank can be tuned to certain capacitance range with the application of actuation pulse. Varying the capacitance between the signal line and PCM MIM capacitors results in impedance tuning. As several combinations of capacitances can be achieved by controlling switched capacitor bank states, a large number of impedance points will be generated and a better coverage can be achieved compared to the case where a limited number of fixed capacitors are used. The impedance matching network presented in this section is a current work-in-progress proof of concept and demonstrate potential application of PCM based devices. PCM based components provide versatile use in tremendous RF applications.

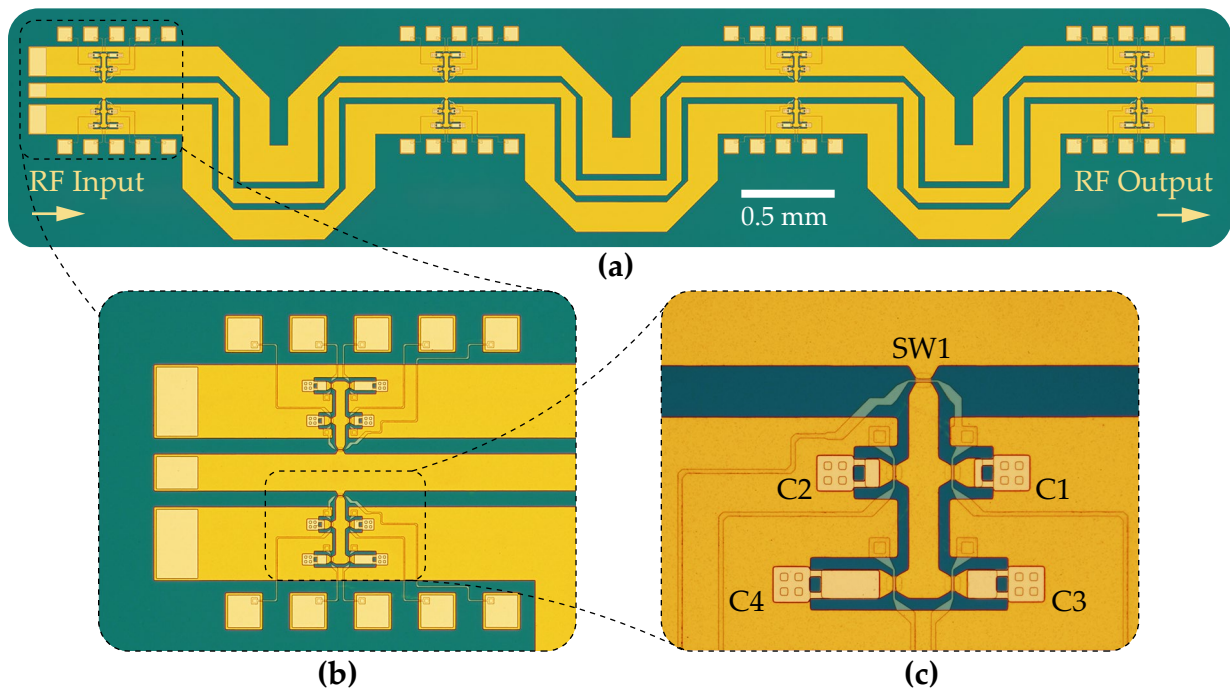


Figure 7.41: Optical micrograph: (a) Monolithically integrated PCM-based reconfigurable impedance matching network, (b). 4-bit PCM-based capacitor bank, (c). Zoomed-in view of 4-bit capacitor bank.

Fig. 7.40 illustrates the schematic of the impedance tuner. It consists of three 70° CPW transmission line sections and four PCM-based switched capacitor bank units. Each capacitor bank unit is sub-divided into two 4-bit capacitor banks one on each side of the transmission line. The simulated capacitor banks are designed to provide capacitance tuning range 0.2 pF to 1.2 pF in 16 discrete states. The optical micrograph of the fabricated PCM-based impedance tuner is shown in Fig. 7.41 highlighting integrated capacitor banks and close-up view of individual capacitors. PCM SPST switches are connected to fully unload the capacitor banks to prevent any parasitic capacitive or inductive loading from capacitor bank. The overall device area of the impedance tuner is under 6.2 mm × 1.2 mm.

7.4.0.2 RF Performance Simulation and Impedance Coverage

The RF performance is simulated using a circuit model and Ansys HFSS for EM verification. The EM simulated RF response is shown in Fig. 7.42. When all the capacitors are unloaded C_{min} , the impedance tuner shows 6 dB of insertion loss with better than 20 dB of return loss. However, at maximum capacitor loading C_{max} , the impedance tuner shows insertion loss of 8 dB with return loss higher than 9 dB. High losses are expected due to less thickness of metal and length of the transmission line. The circuit model

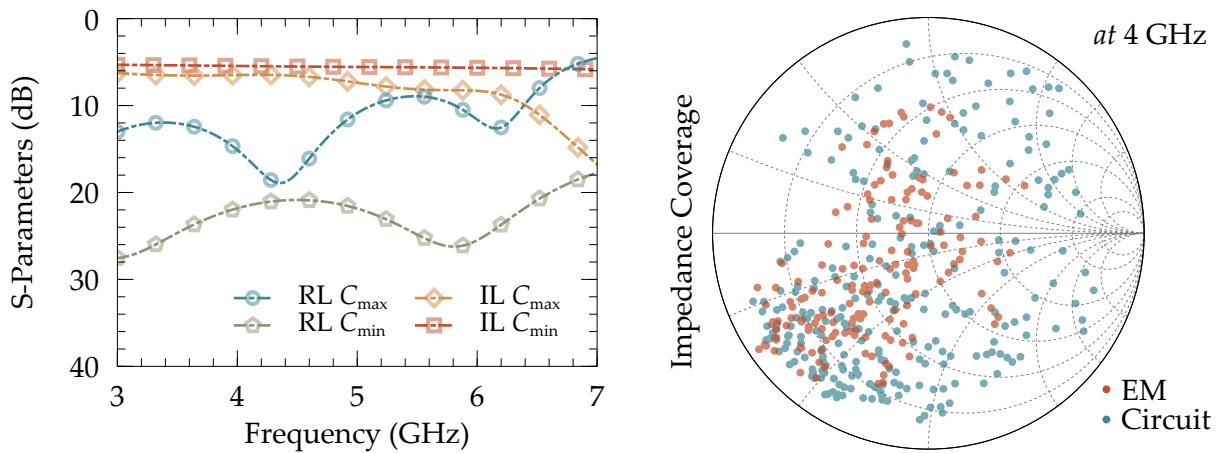


Figure 7.42: Simulated S-parameters and impedance coverage of reconfigurable impedance matching network. Impedance coverage is simulated for circuit model with ideal transmission lines and EM model with transmission lines loss considered. RF response is EM simulated for minimum and maximum capacitance case.

shows better impedance coverage on smith chart at 4 GHz, but when metal loss is added in EM simulations, the coverage is reduced, which is expected. One possible solution to reduce the losses is to electroplate the transmission line, but at the time of writing the unavailability of electroplating station hindered further development of this device. After this improvement in the loss, this device holds the potential to outperform many other currently available state-of-the-art technologies.

7.5 Summary of PCM based RF Components

In this chapter, various RF PCM GeTe-based RF components are reported with operational frequencies ranging mainly in mmWave range. All the devices reported in this chapter are the first demonstration of PCM GeTe-based components for RF applications. Table 7.6 summarizes all the devices presented in this chapter.

Table 7.6: Summary of PCM-based RF components

Device	Operation Range	Device Size
6-Bit Capacitor Bank	1 GHz to 7 GHz	0.5 mm × 0.5 mm
High SRF 6-Bit Capacitor Bank	1 GHz to 10 GHz	0.6 mm × 0.30 mm
Rotary 8-Bit Capacitor Bank	26 GHz to 30 GHz	0.5 mm × 0.5 mm
On-Chip Broadband Micro Resistors	DC – 40 GHz	25 μm to 15 μm
4-Bit Variable Attenuator	24 GHz to 32 GHz	1.2 mm × 0.5 mm
Scalable Variable Attenuator	26 GHz to 34 GHz	0.9 mm × 0.8 mm
3-Bit TTD Phase Shifter with SP3T	26 GHz to 34 GHz	1.0 mm × 0.8 mm
3-Bit TTD Phase Shifter with SP8T	26 GHz to 34 GHz	1.2 mm × 1.4 mm
8-Bit Reflective Type Phase Shifter	26 GHz to 30 GHz	1.0 mm × 0.9 mm
Switched Impedance Tuner	3 GHz to 7 GHz	6.2 mm × 1.2 mm

Chapter 8

Study of PCM RF Switches at Cryogenic Temperature

This chapter examines the DC and RF performance of PCM GeTe-based RF switches as a function of temperature. Resistance change behavior of PCM GeTe is investigated from 77 K to 335 K. The PCM GeTe shows metallic behavior in crystalline state which exhibits consistent low resistivity over a wide temperature range, while in amorphous state resistance increases more than six-orders of magnitude as a function of decreasing temperature from 300 K to 77 K. At cryogenic temperatures, sub-T Ω device resistance is achieved with exceptionally high amorphous to crystalline state resistance ratio. IV characteristics and RF performance are investigated over wide temperature range. RF performance of PCM switches with and without micro-heater are examined. Devices are pulsed to achieve stable high resistance ratio at 77 K.

Intermediate resistance states (between amorphous and crystalline states) in PCM GeTe-based devices are observed during device pulsing at cryogenic temperatures. Stability or non-volatility of PCM GeTe in various intermediate resistance states are examined. Similar behavior is also observed at room temperature in chalcogenide PCM GeTe. With proper excitation pulse conditions, reversible non-volatile resistance states are confirmed at room temperature. This phenomenon can be used in improving device reliability to precisely tune PCM resistance to achieve extremely high RF resistance ratio for future RF devices at cryogenic temperature.

High resistance ratio, stable crystalline state resistance and intermediate resistance states in PCM GeTe will pave the way for the development of high performance DC/RF devices for space applications.

8.1 Temperature Dependant Performance Improvement

The motivation behind examining the DC and RF performance of the developed PCM GeTe-based RF switches to investigate high resistance of chalcogenide PCM GeTe at cryogenic temperatures. PCM GeTe-based switches are not well studied at low temperatures till date. To investigate the temperature dependency on DC or RF performance of the PCM switches, the performance of the devices are studied over a wide temperature range varying from 77 K to 335 K (-196°C to 62°C). Test setup similar to the one used for device cycle testing is used to carry out DC IV characteristics and RF measurements simultaneously as shown in Fig. 8.1.

The PCM GeTe switches are studied in a Lakeshore CPX-VF cryogenic probe station which has built-in multiple radiation shields for better low temperature performance measurements. The probe station allows RF and DC (CV or IV) measurements from $<3\text{ K}$ to 294 K (-270°C to 21°C) at greater than 1×10^{-6} Torr vacuum pressure. Large 2.5 in cryo stage on active vibration damped table allows performing in-situ RF calibration along with DUT measurements. Typically liquid helium (LHe) is used to achieve lower than 3 K temperature, but as the measurements are taken for more than 2 consecutive days at different temperatures, limited supply and short span of LHe tank restricted

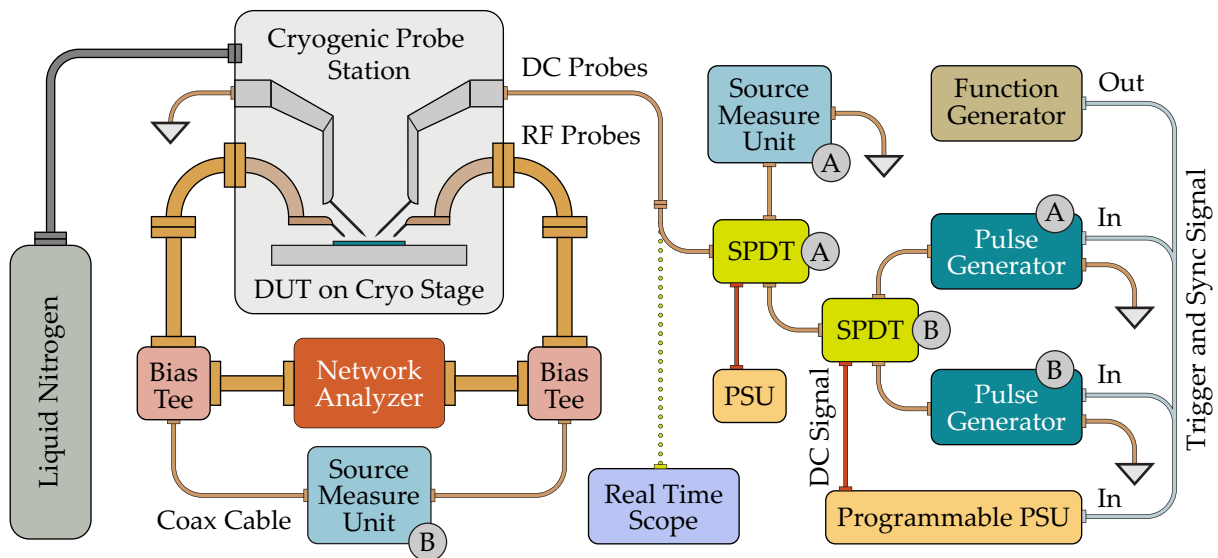


Figure 8.1: Block diagram of reconfigurable switch DC and and RF measurements test setup at cryogenic temperature.

the use of LHe for measurements. Instead, liquid nitrogen (LN) is used as a cryogenic fluid. The objective of the measurements is to investigate high resistive behavior at low temperatures, thus usage of LN allowed reaching at minimum 77 K temperature. Slow consumption of LN for the measurements allows precise control over the temperature to extract data at various temperature stages.

Resistivity in both crystalline and amorphous stage of the GeTe over a wide temperature range is investigated. PCM GeTe-based SPST switches are pulsed multiple times to get stable resistance ratio. The test setup consists of a cryogenic probe station with two CPW GSG probes to measure RF performance and also to source/measure voltage/current. Two SMUs (A and B) are used in the setup. Two ports of an SMU-B are connected to bias tees for decoupling DC signal from RF. Cryogenic probe station allows two DC probes and two RF probes for measurements. Thus, as shown in the block diagram in Fig. 8.1, network analyzer is connected with SMU-B to source read voltage constantly and measure RF performance at the same time using GSG RF probes. CPW GSG probes are connected to port 1 and 2 of the DUT and S-parameters are monitored over DC to 40 GHz. SMU-B connects to port 1 and 2 as well. Two DC probes are connected to port 3 and 4 of the DUT to supply actuation pulses to micro-heater and also to source/measure voltage/current. DC probes are connected to the common port of a high performance military grade electromechanical coaxial RF SPDT latching switch (SPDT-A). An output channel 1 of the SPDT switch is connected to an SMU-A while channel 2 is connected to another similar performance RF SPDT switch (SPDT-B). SPDT-B is a failsafe switch while SPDT-A is a latching switch. A failsafe switch is incorporated to ease in reconfigurability. A pulse generator (PG-A) is connected to channel 1 of SPDT-B and another similar pulse generator (PG-B) is connected to channel 2 of SPDT-B. An arbitrary function generator's output is connected to trigger-in functionality of both the pulse generators. A programmable power supply provides actuation to SPDT-B, which is controlled by the same trigger signal through the function generator. A real time oscilloscope is connected with a weak link to check the pulse shape at the end of the DC probe to offset any pulse amplitude or width deterioration.

Due to the surrounding temperature in the cryogenic chamber, bias signature to pulse the device between ON and OFF-state is different. PCM switches are characterized to achieve full melt-quench cycle by slowly increasing the source voltage and constantly measuring the current. RF calibrations are performed multiple time during testing at different temperatures to maintain the accuracy of the measured results. It is extremely important to perform RF calibration especially at cryogenic temperatures. Due to the vacuum pressure, temperature drops at a higher speed compared to temperature rise, thus most of the measurements are performed at 77 K. A relatively slow temperature in-

crease rate allow taking measurements at various temperatures. Fig. 8.2 shows the photograph of an automated on-chip cryogenic test setup. Cryo sample stage is shown in inset highlighting probes, calibration substrate and DUT chips. Fig. 8.2 in the CCD feed shows PCM GeTe-based SPST switch probed for DC and RF measurements. Keysight BenchVue is used as a data acquisition and control (DAC) to program the automated pulse testing and for recording data. The test setup also allows measuring PCM switch resistance, RF parameters, and micro-heater resistance without changing the probe positions.

Most of the commonly available pulse generators require at least more than 0.1% duty cycle. Thus with the smallest pulse width of 200 ns, pulse pattern reaches its limits at 5 kHz. To test the switches at low speed and to make sure the state is stable, independent pulse generators PG-A and PG-B provide amorphous and crystalline pulses respectively. Both pulse generators are set up to output a single pulse such that the cycle testing frequency can be controlled by trigger-in signal from the function generator. SMU-B source a constant 100 mV to the DUT while measuring change in current. Measured current from SMU-B is logged at a speed of test frequency with a delay of few milliseconds to make sure the device gets in stable state before recording a data point. Pulse generators PG-A and PG-B are connected to the DC probes to the micro-heater pads with the test

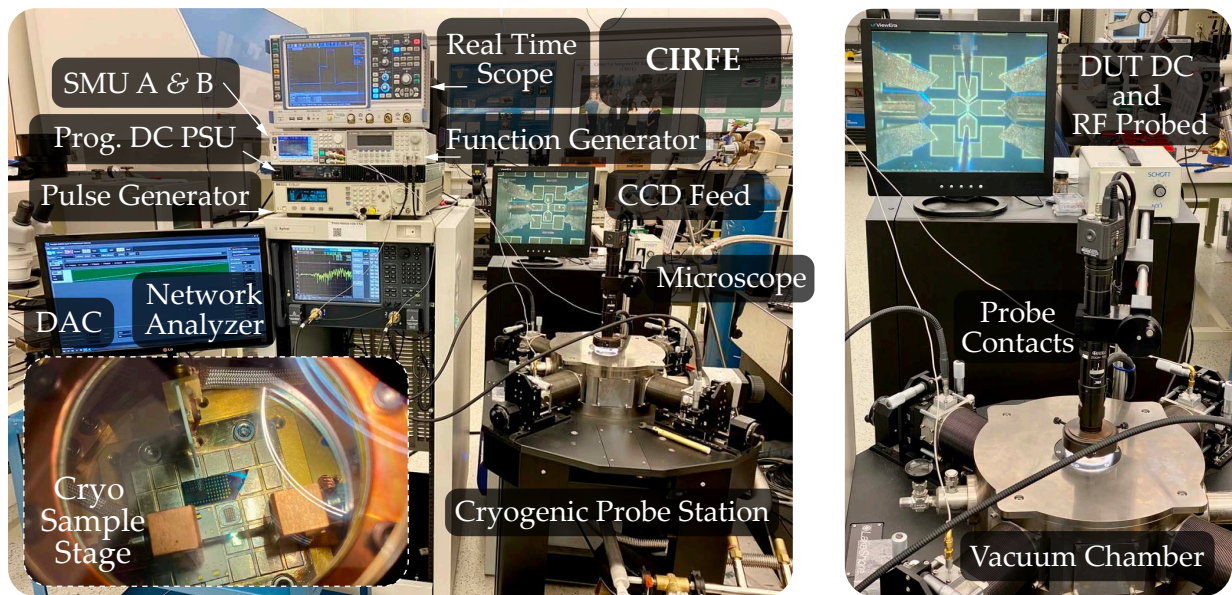


Figure 8.2: Photograph of an automated cryogenic DC and RF testing setup. Inset shows the inside of cryo sample stage.

setup frequency set by function generator. Impedance of the micro-heater is stabilized and matched with the output load impedance of the pulse generators by cycling the device manually before starting the automated setup, however the PCM switch resistance is recorded from first cycle onwards. Triggered sync signal from function generator triggers both amorphous and crystalline pulses at the same time while triggering the output of programmable PSU. A failsafe SPDT connects PG-A or PG-B depending on whether programmable PSU outputs the actuation signal or not. For pulsing, the test setup frequency is set to 250 ms. SPDT switches toggle the connected equipment at a minimum speed of 10 ms.

8.1.1 DC Measurements

8.1.1.1 IV Characteristics

IV characteristics of the PCM GeTe-based devices in amorphous state are measured as shown in Fig. 8.3. Voltage is sourced from 0.1 V to 10 V at various temperatures and the current flowing through the device is measured. Cryogenic temperatures improved the

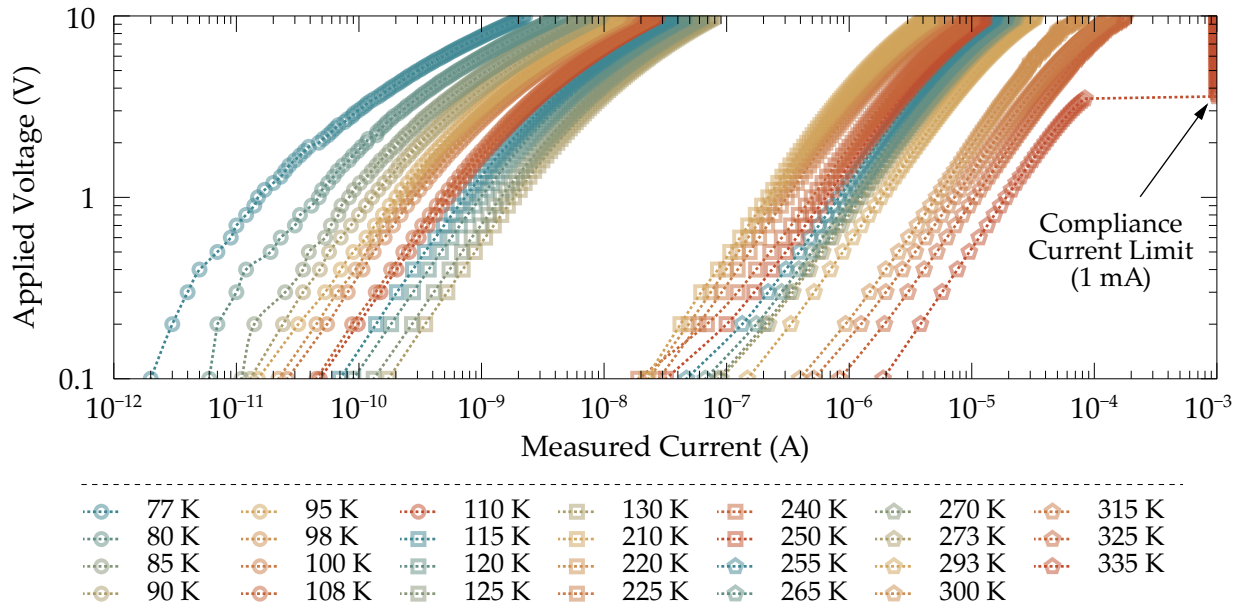


Figure 8.3: Measured IV characteristics of amorphous PCM GeTe over 77 K to 335 K. Device geometry is chosen with high current carrying capacity to allow reasonable current flow.

amorphous state resistance by more than 6 orders of magnitude. As mentioned earlier, the temperature rises from 77 K to 294 K at an extremely slow rate.

Recording data points over such a wide temperature range requires constant monitoring the cryo stage temperature and performing measurements. Data between 130 K to 210 K is not recorded due to timing constraints. Compliance current of 1 mA is set as an upper bound to avoid damaging the switch. Specific PCM junction geometries are chosen with relatively high current carrying capacity to avoid reaching compliance current at room temperature measurements. Measurements are stopped at the temperature when current hits compliance.

8.1.1.2 Sub-Teraohm Resistance

Measured resistance of the SPST switch at various temperatures is shown in Fig. 8.4. Compared to the IV characteristics and resistance of the device at room temperature, at cryogenic temperatures, more than 6 orders of resistance improvement can be seen by using operating at 77 K. The PCM GeTe shows metallic behavior in crystalline state that exhibits consistent low resistivity over a wide temperature range, while in amorphous state resistance increases more than six-orders of magnitude as a function of decreasing temperature from 300 K to 77 K. At cryogenic temperatures, sub-TΩ device resistance is achieved with exceptionally high amorphous to crystalline state resistance ratio as shown in Fig. 8.4. At low temperatures (below 100 K), resistance drops by an order of

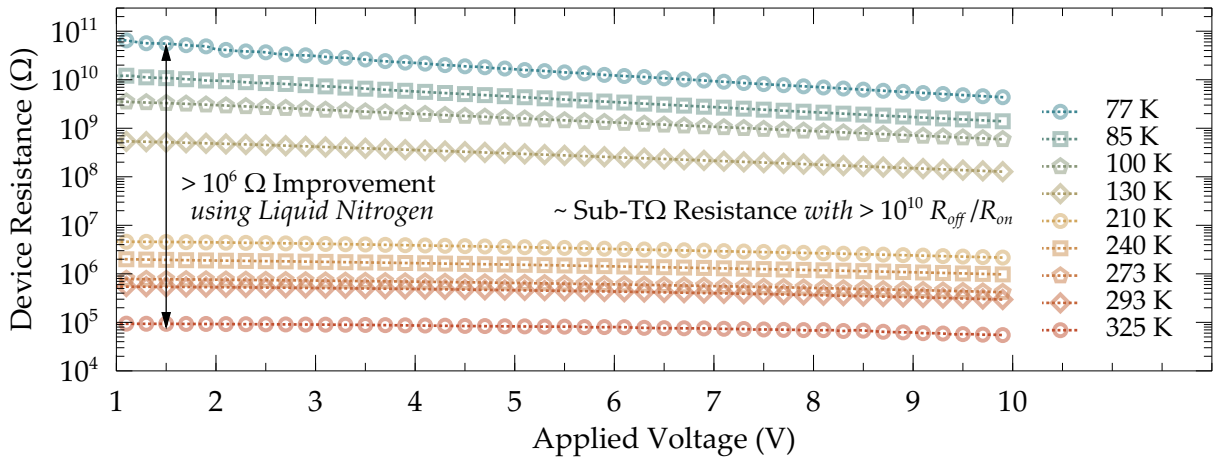


Figure 8.4: Measured OFF-state device resistance with change in applied voltage at different temperatures.

magnitude with increasing source voltage. This is due to the localized heat generation in the resistive PCM device, which results in slight increase of temperature.

8.1.1.3 High Resistance Ratio

Resistance ratio is one of the performance benchmark for PCM-based devices. Typically, phase change alloys have higher crystalline state resistance than PCM device resistance in both ON and OFF-state. In crystalline state, PCM GeTe does not show change in resistance, while in amorphous state, resistance increases linearly with the decrease in temperature. Device resistance is measured over a change in temperature. R_{on} decrease by approximately 10% with the decrease in temperature while R_{off} increases by more than 6 orders of magnitude with decrease in temperature as shown in Fig. 8.5. Resistance ratio (R_{off}/R_{on}) shows $>1 \times 10^6 \Omega$ resistance improvement from 300 K to 77 K as depicted in Fig. 8.5. $R_{off}/R_{on} >1 \times 10^{10} \Omega$ is achieved at 77 K.

In Fig. 8.5, due to the slow temperature rise in cryogenic chamber after removing cryogenic fluid, data from 130 K to 220 K is not recorded. Data could not be recorded automatically due to probe position change in the temperature, and the temperature change is not linear which makes it hard to predict current temperature in the chamber on specific time. A linear trend in resistance increase is observed with decreasing temperature as shown in Fig. 8.5. Similar linear resistance increase trend has been reported in [145]. A recent study of PCM GeTe switch at cryogenic temperature reported a sudden transition in resistance around 200 K and the resistance remains stable with the decreasing

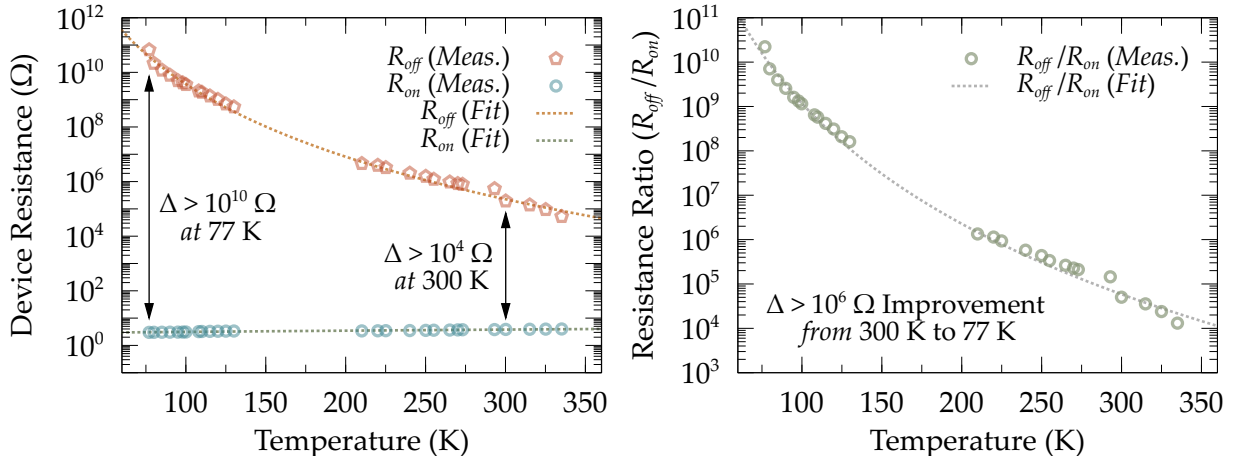


Figure 8.5: Measured and fitted PCM device resistance and ratio over temperature.

temperature [146, 147]. It is however not clear in the report about the GeTe composition. Ge rich thin film or a Te rich thin-film might show relatively different behavior. Such high resistance can be used in many applications at cryogenic temperatures.

8.1.1.4 Device Cycling at 77 K

PCM switches are cycled using an automated test setup. Device resistance is measured at each pulsed cycle. Due to the cryogenic temperature, either high voltage or longer duration pulses are required compared to the bias signature required for room temperature pulsing for adequate and reliable melt-quench sequence. Amorphous pulse of amplitude 14.8 V and width 200 ns cycles the device from low resistance state to high resistance amorphous state at 77 K, while crystalline pulse of amplitude 8.7 V and width 1.2 μ s switches the PCM from amorphous state to crystalline state. Amorphous pulse amplitude is increased by 1.24 \times while crystalline pulse amplitude is scaled by 1.12 \times at 77 K compared to that is required at 294 K.

Initial few pulses show $>1 \times 10^{10} \Omega$ resistance ratio, whereas the resistance ratio start to decrease after few cycles. This is mainly caused by localized heat generation due to continuous pulsing. After 32–35 pulses, the resistance ratio stabilized to $>1 \times 10^9 \Omega$, which is still 5 orders of magnitude higher than that of achieved at room temperature. Device resistance is measured for 100 melt-quench pulses as shown in Fig. 8.6.

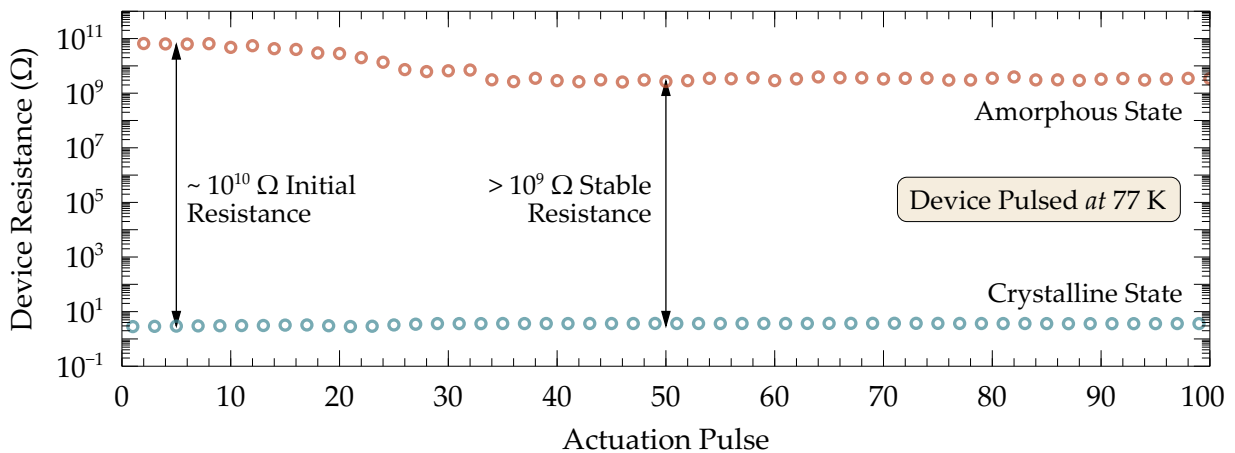


Figure 8.6: Device resistance change with number of applied pulses at 77 K. Stable high resistance ratio is achieved at cryogenic temperatures.

8.1.2 Temperature Dependency of RF Performance

While measuring the IV characteristics, RF performance is measured at the same time using CPW GSG probes at various temperatures. PCM GeTe-based SPST switches utilize thin-film refractory micro-heater that creates capacitive coupling to the RF signal line as discussed in chapter 4. Although, PCM GeTe switches exhibit exceptionally high resistance ratio at DC, the performance improvement does not necessarily translate to RF regime. The capacitance in the line caused by micro-heater (C_{hm1}) determines OFF-state isolation. Second most dominant parasitic capacitance in the RF signal line is between two electrodes (C_{cont}) as discussed in the section 4.2. For RF applications, capacitance

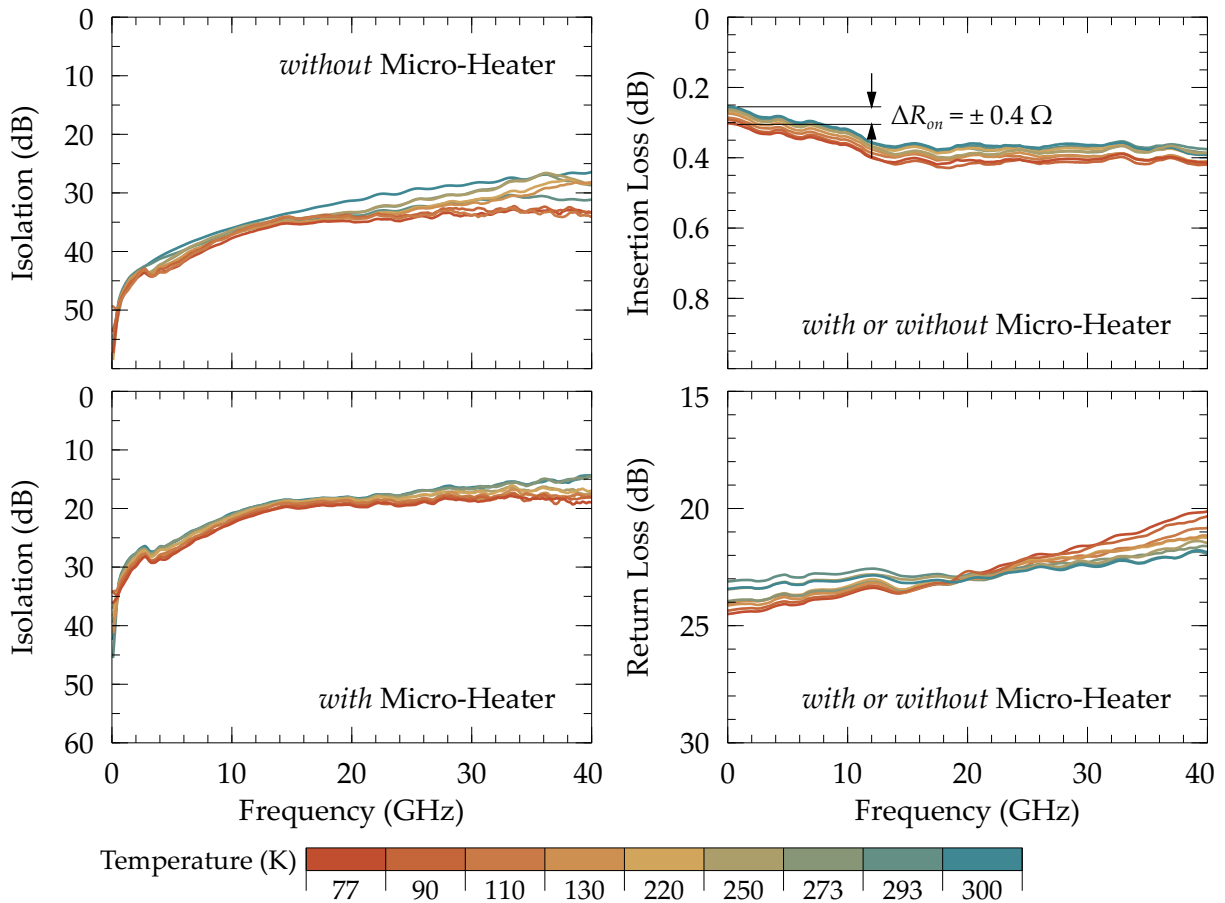


Figure 8.7: Measured RF performance of PCM GeTe-based RF switch over DC to 40 GHz from 77 K to 300 K.

in the RF line determines RF performance in conjunction with high resistance value. Increasing the resistance does not improve RF performance in PCM switches with or without micro-heater as shown in Fig. 8.7. While, there is no change in the crystalline state resistance of PCM GeTe, ON-state RF performance is identical for the switches with or without micro-heater. Embedded micro-heater limits the cut-off frequency of the RF PCM switch with limited isolation performance as shown in Fig. 8.7.

Depending on the design geometry and junction dimensions of the PCM GeTe-based RF SPST switches, the performance does not vary over a wide temperature range, which confirms the RF performance stability of the developed switches. Insertion loss improves by approximately 10% at low temperatures. No performance degradation has been observed in the measurements from 77 K to 300 K. At low temperatures, switch actuation conditions are different than that required at room temperature.

8.2 Intermediate Resistance States in PCM GeTe

Chalcogenides are fundamentally classified as binary resistive materials and the resistance of the material depends on its current phase. Amorphous and crystalline are the two states where a chalcogenide material demonstrate orders of magnitude resistance change. Depending on the device geometry and actuation method selected (direct or indirect heating), a partial melt-quench sequence latches the material in one of the two prominent states partially which leads to new observed states of resistance in between a crystalline and amorphous phase. Recent report on the formation of dendrite filaments in phase change memories show similar behavior when a dendrite connects two electrodes with overall resistance of the device lower than that of amorphous state [148]. Similar reports are published for phase change memories utilizing GST alloys which show intermediate resistance states [145, 149–152]. Most of the recently reported results highlight applications in multi-stage memory storage [153–157]. Intermediate resistance states in PCM have not been fully investigated at cryogenic temperatures so far.

8.2.1 At Cryogenic Temperature

While characterizing the actuation pulse requirements at cryogenic temperatures, intermediate resistance states in PCM GeTe have been observed. Due to the extremely cold surrounding temperature, pulse amplitude or width are optimized to transport sufficient energy to the PCM GeTe. At 77 K, PCM switches demonstrate $>1 \times 10^9 \Omega$ stable

resistance change. Amorphous pulse of 14.8 V, 200 ns width and crystalline pulse of 8.7 V, 1.2 μ s width latches the PCM GeTe between low and high resistance states. Voltage pulse amplitudes for both amorphous and crystalline pulses are provided in 100 mV increments. At certain voltage level, due to semi melt-quench sequence in the material, PCM GeTe latches in intermediate resistance state between amorphous and crystalline phase.

Non-volatile reversible intermediate resistance states in GeTe are not very well investigated. Intermediate states are investigated at cryogenic and room temperature. At 77 K, 100 mV voltage is sourced to the device to avoid self heating. Crystalline and amorphous pulses of varying amplitude are applied to the micro-heater to cycle the device. Resistance states for 22 unique pulses are investigated to confirm the behavior as shown in Fig. 8.8. Initially the device is pulsed to fully amorphous state and the first crystalline pulse is applied to switch the material into crystalline state. Second pulse of slightly lower amplitude is applied, but due to the lack of sufficient thermal transport, the device did not switch to amorphous state, rather the resistance is increased by 2.4 Ω . Similarly, a pulse similar in characteristics to pulse 2 is applied, and the resistance increases by close to two orders of magnitude. Pulse 4 raises the resistance by few ohms than the previous state. At pulse 5, the device is neither in crystalline nor in amorphous state. An amorphous pulse is then applied and the device switches fully to amorphous state, followed by a pulse with amplitude lower than the crystalline pulse. The device switches

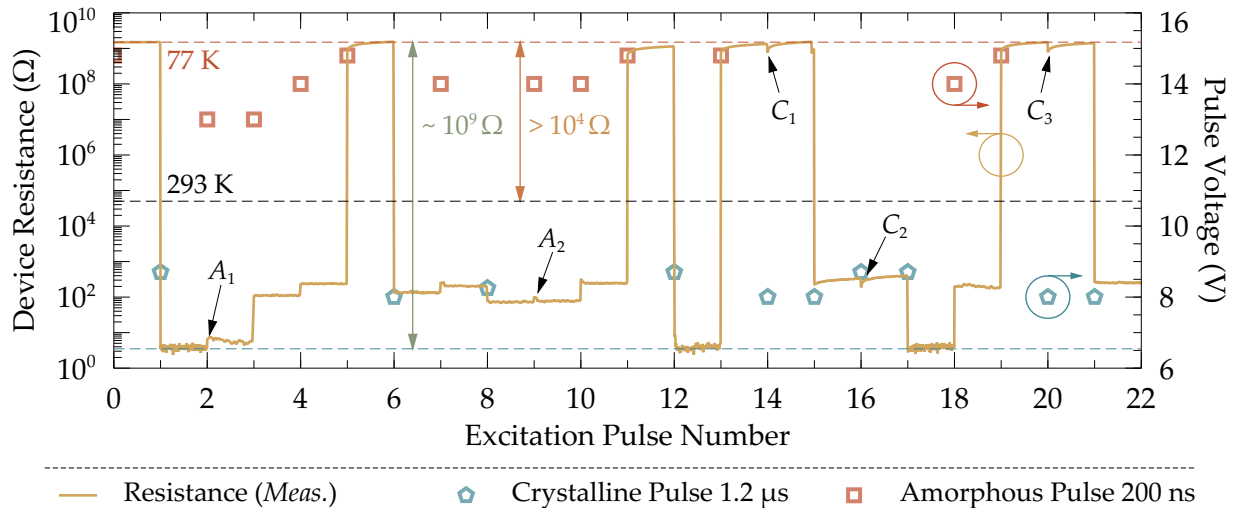


Figure 8.8: Measured reversible intermediate resistance states in PCM GeTe at 77 K with the application of crystalline and amorphous pulses of varying amplitude.

back to intermediate resistance state. Similar pulse variations are followed to confirm non-volatile reversible intermediate resistance states in PCM GeTe. Markers (A_1 and A_2) denote when a low amplitude amorphous pulse is supplied, but the device fail to fully actuate. Markers (C_1 , C_2 and C_3) show when a crystalline pulse of varying amplitude is applied, but the switch fail to fully actuate. Missed actuations or failure points are due to the surrounding temperature. At 77 K, the device require high thermal energy to achieve full or semi melt-quench sequence.

8.2.2 At Room Temperature

Testing sequence is followed for the device at room temperature (293 K) similar to that described in previous section. Reversible intermediate resistance states are observed at room temperature. During characterization of the PCM GeTe-based switch, if the amplitude margin between subsequent pulses is reduced to a point where the thermal transport does not perform full melt-quench sequence, PCM GeTe switch latches in intermediate resistance state. Intermediate resistance states occur when the PCM is not in fully amorphous or crystalline state, but rather only part of the material is in amorphous state. This is due to the lack of efficient thermal transport. Pushing energy into the PCM when to achieve a full melt-quench sequence makes the device a switch with

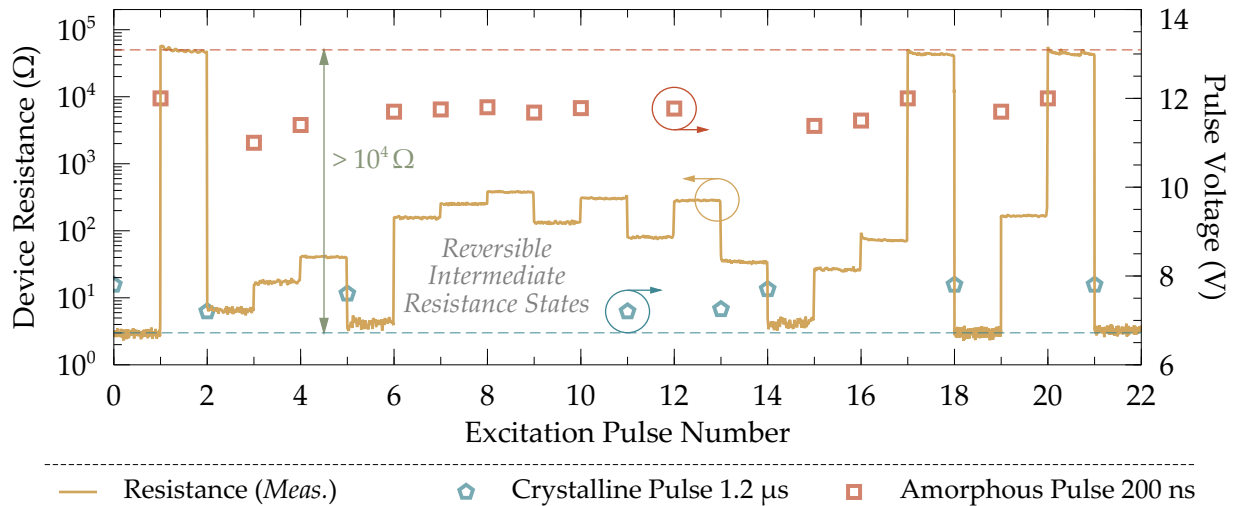


Figure 8.9: Measured reversible intermediate resistance states in PCM GeTe at 293 K with the application of crystalline and amorphous pulses of varying amplitude.

high amorphous to crystalline resistance ratio. Partial melt-quench cycle allows achieving low resistance ratio.

Measured intermediate reversible resistance states observed at room temperature with varying voltage is shown in Fig. 8.9. Initially the device is pulsed to start from a fully crystalline state. At pulse 1, the device is cycled to fully amorphous state with the application of 12 V, 200 ns pulse. Subsequent pulses of varying amplitude latches the PCM GeTe device into resistance states between amorphous and crystalline state. Resistance tuning at room temperature can be achieved from crystalline state resistance up to 400 Ω . The transition period between an upper bound of the semi melt-quench sequence (intermediate resistance up to 400 Ω) to a full melt-quench (amorphous state) is extremely hard to control. A slight increase in either voltage or pulse width increases to its full amorphous state.

As discussed above, the PCM switches require appropriate thermal transport for melt-quench sequence, which impacts the reliability of the switch. While characterizing the switches, if more than required heat is fed to the PCM either due to high voltage pulse/longer than required pulse width or a poor choice of dielectric between micro-heater and PCM. Two possible failures can occur; either high power pulse damages the refractory micro-heater or it melts the PCM due to poor thermals. The partial melt-quench phenomenon exhibits reversible resistance change that can be used in tremendous applications. Unlike at the cryogenic temperatures, missed actuations occurred due to the cold surrounding temperature, this is not prominent at room temperature. Possible applications of intermediate resistance states include but not limited to precise tuning of resistance in reconfigurable circuits, improving the reliability of the device at cryogenic temperatures by latching the device in an intermediate state and then cooling the device to improve the resistance, tunable resistors at DC to name a few.

8.2.3 Stability of Intermediate Resistance State

Non-volatility or stability of reversible resistance states are measured for an hour. At 77 K, when providing actuation pulses, localized heat generation from the micro-heater change the surrounding temperature around the device. With the low surrounding temperature, resistance start to increase and becomes stable at a specific temperature as shown in Fig. 8.10. Same device is latched into two different resistance states 1 (385 Ω) and 2 (154 Ω). Shaded portion shows when the resistance linearly increases due to the gradient in the surrounding temperature. The gradient sets to 77 K after few minutes. Apart from very small localized heating, another factor that contributed to slightly

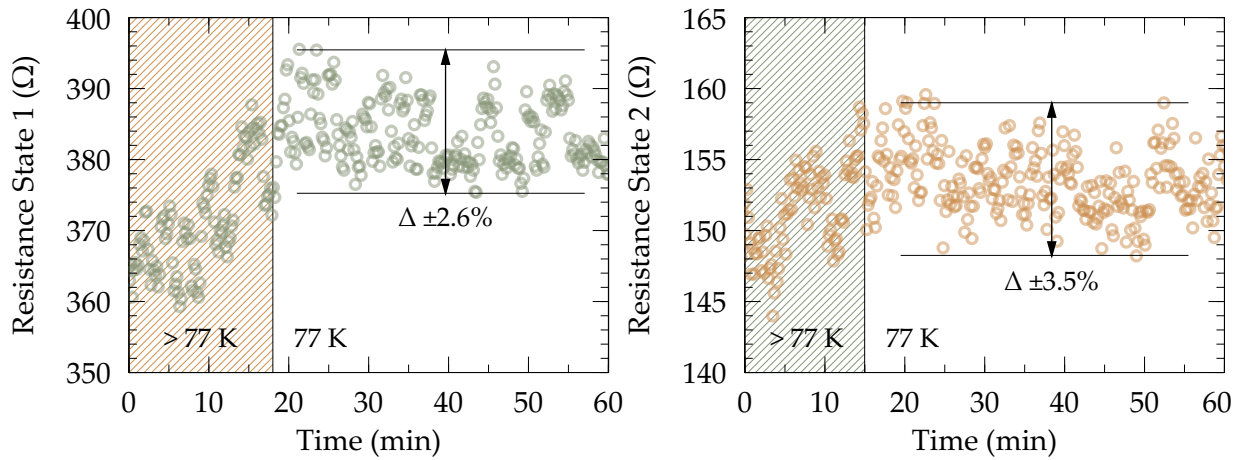


Figure 8.10: Measured stability of intermediate resistance states at 77 K over a period of 60 mins.

warmer temperature is the light source used for CCD camera to observe the chip in the chamber. During the stability test the device is cycled to latch in a specific intermediate resistance state and the lamp luminance is turned off. As per the measured IV characteristics, cryogenic temperature improves the device resistance. The device is latched at a certain resistance state, which is partially in amorphous state and partially in crystalline state, thus the resistance improvement is confined to $\pm 2.6\%$ to $\pm 3.5\%$ only. Latching nature of the PCM GeTe in intermediate resistance states is validated over the duration of 60 mins.

PCM GeTe's stability over a wide temperature range ranging from cryogenic temperature 77 K to hot temperature 335 K demonstrate stable RF performance makes this technology useful in a wide range of applications. Partial melt-quench of the material which leads to latching the switch in intermediate resistance states with reversible behavior open doors for the development of tremendous reconfigurable circuits. At cryogenic temperatures, PCM GeTe exhibits more than $1 \times 10^{10} \Omega$ resistance which is six orders of magnitude improvement than that of measured at room temperature.

Chapter 9

Conclusions and Future Directions

The main focus of this doctoral thesis is on the development of high performance and reliable mmWave PCM GeTe-based RF switches, multi-port switches, switch matrices in various configurations, experimental investigation on transient thermal behavior, and development of various monolithically integrated mmWave RF components. The major contributions of this research are summarized below.

9.1 Contributions

Development of Reliable PCM GeTe-based RF switches for mmWave applications

The primary contribution of this research is to develop high-performance and reliable PCM GeTe-based RF switches with RF performance surpassing the current state-of-the-art in terms of low-loss, extended frequency range and reduced device area. RF PCM switches reported in literature have poor RF performance at mmWave frequencies. PCM GeTe is characterized and optimized with the use of atomic force microscopy, scanning electron microscopy and other material characterization methods. Three custom microfabrication processes are developed in-house for three generation of RF switches with improvement in RF performance and reliability achieved in each subsequent microfabrication process. Various design parameters of the RF PCM switches are studied to improve the RF performance. RF PCM switches developed using Gen 3 microfabrication process

demonstrate exceptional RF performance from DC to 67 GHz. RF power handling capacity of the switches has been experimentally investigated. Linearity and intermodulation distortion, third order intercept point (IP3) of the PCM switches is measured for different set of input parameters. IV characteristics of the devices are investigated for different device geometries to study the self-actuation and current carrying capacity of the switches. Self-actuation in RF PCM switches using high RF power is observed which is related to the current carrying capacity of the switches. Various parasitic elements affecting the RF performance in switches has been reported. A lumped model of the RF switch is developed which matches the measurement data. Device switching pulse parameters are studied to determine actuation limits. An automated test-bench is configured to measure the device lifetime cycles and reliability. RF PCM switches are developed demonstrating more than 1 million switching cycles experimentally. Reliability in non-volatile device resistance is also investigated. A multi-port RF switch is compared with the current state-of-the-art highlighting the developed PCM switches surpassing the conventional switches in terms of operating frequency range, miniature die size, latching functionality, and low-loss.

Experimental investigation on transient heat distribution and thermal actuation crosstalk in GeTe RF Switches

PCM GeTe-based RF switches require high speed embedded thin-film refractory micro-heaters to provide actuation pulse signal. GeTe required more than 725 °C heat for sub nano-microsecond duration to achieve a full melt-quench sequence for reversible phase change operation. Embedded refractory ultra high speed micro-heaters are developed. Heat profile of the micro-heaters are studied using FEM modeling. For the first time ever, transient thermal performance of the micro-heaters for PCM switches are experimentally investigated using thermoreflectance based transient thermal imaging technique with nanosecond spatial resolution. Heat distribution is investigated to optimize the micro-heaters and RF switches. FEM models are reverse engineered to match with experimental results to accurately predict cross-section thermal performance of RF PCM switches. FEM models are developed to study the transient heat distribution at switch junction to optimize the microfabrication process. Due to high temperature requirements of PCM based switches, thermal crosstalk in RF switches is also experimentally investigated for the first time. Measured cross-section profiles of heat distribution provides accurate safe limits of dense integration of PCM switches in multi-port switching networks and reconfigurable RF circuits.

Development of multi-port PCM-based RF switches and monolithically integrated miniaturized switch matrices

Multi-port switches are an integral part of any reconfigurable and switchable RF system. Multi-port switch configuration SPNT provides the flexibility to route the RF signals at input port to any available output port. Various multi-port PCM GeTe-based RF switches are developed in SP2T, SP3T, SP8T and SP16T configurations. The SP2T and SP3T switches are highly miniaturized and can be easily integrated in various reconfigurable RF devices. Kaleidoscope design approach is used to reduce the overall die size of SP8T and SP16T switches. Design symmetry is incorporated in multi-port switches to keep the RF performance identical from port to port. Various RF switch matrix configurations are investigated. A scalable 2×2 switch matrix unit-cell is developed and a reconfigurable band reject circuit is fabricated by monolithically integrating multi-port switches, resonators and switch matrix unit-cell. A compact mmWave T-type switch is developed with outstanding RF performance from DC to 67 GHz. A broadband DC to 60 GHz monolithically integrated 4×6 redundancy switch matrix is developed utilizing cascaded T-type switching unit-cells. Crossbar switch matrices in 2×2 and 4×4 configurations are developed with highly compact device footprints. Crossbar switch matrices up to 16×16 ports are also developed for DC or low-frequency applications.

Demonstration of reconfigurable monolithically integrated PCM GeTe-based RF components

The RF PCM SPST and SPNT switches are incorporated into various RF components. Switchable PCM based capacitor banks are developed in 6-bit configurations, providing up to 64 capacitance states. Self resonance frequency improvement technique for on-chip integrated MIM capacitors utilized in capacitor bank is discussed. A rotary switchable 8-bit capacitor bank is developed for tunable RF components requiring inductive component tuning at mmWave frequencies. A miniaturized PCM-based 4-bit (16 states) latching variable attenuator is developed for 28 GHz band with wideband operation and high attenuation range. A scalable T-type switch based 3-bit variable attenuator topology is also fabricated to reduce number of redundant states. Broadband on-chip thin-film embedded resistors and resistor networks are developed with minimum resistance deviation across operation bandwidth. Miniature monolithically integrated switched

type phase shifters are developed for mmWave applications with SP3T and SP8T switches. A hybrid coupler is optimized for mmWave frequencies which is monolithically integrated to design PCM-based reflective type phase shifter. A reconfigurable impedance matching network is designed with integrated capacitor banks as tuning elements. This doctoral research reports the first implementation of such an extensive set of PCM-based RF components.

Characterization of PCM GeTe RF Switches at Cryogenic Temperature

RF PCM switches are characterized at cryogenic temperature. PCM switches exhibited more than 11 orders of resistance change at 77 K. Resistance in amorphous state and crystalline state of PCM switches is studied with change in temperature from 77 K to 335 K. IV characteristics and RF performance of the PCM switches is recorded over time. Improved resistance ratio between amorphous and crystalline state at 77 K is achieved with an improvement of six orders of magnitude compared to room temperature performance. Sub- $T\Omega$ resistance range at cryogenic temperature is reported. Benchmarked bias conditions for PCM switches are tested at low temperatures. RF performance is studied over a wide temperature range, showing stable RF performance due to dominant capacitive coupling. RF performance is investigated for switches with and without embedded microheaters.

Investigation of Intermediate Resistance States in PCM GeTe

Intermediate resistance states in GeTe PCM switches are observed in the temperature range 77 K to 293 K. Resistance states occur due to partial melt-quench which latches the GeTe in a resistance state in between two binary amorphous and crystalline states. Intermediate resistance states are reversible non-volatile states which are confirmed by studying the stability of the states over time with less than average $\pm 3\%$ resistance change. Intermediate resistance states allow developing reconfigurable circuits which require precise tuning of resistance in discrete steps.

9.2 Future Work

Based on the thesis contributions, it is clear that PCM GeTe-based RF switches demonstrate tremendous potential for mmWave applications. Various reconfigurable RF com-

ponents proves the potential of PCM technology for future wireless networks. Following are some of the possible future directions that can take this research step further:

Improving the RF Performance

The RF switch topology used in this research work is limited by the OFF-state performance as the embedded micro-heater adds unwanted parasitic capacitance in the RF signal line. If the micro-fabrication process allows planarization, the heater width can be reduced further to mitigate step profile in PCM GeTe. Other topology such as an array of PCM vias possibly improve the isolation.

Precise Tuning of Reconfigurable Circuits

Intermediate resistance states in PCM GeTe open door for developing reconfigurable circuits that require multi-step tuning using a single tuning element. This will further reduce the number of tuning elements (switches) and provide fine tuning range utilizing various resistance states from a single PCM switch.

Monolithically Integrated PCM GeTe-based Superconducting RF Circuits

The demonstration of stable RF performance over a wide temperature range allows operation of PCM switches at cryogenic temperatures. Thin-films limit the design of lumped components due to the resistance of the metal with limited-Q. Niobium (Nb) based multi-layer superconducting circuits provides the flexibility of developing high-Q passive components and PCM microfabrication process can be monolithically developed on top of superconducting circuits. The idea is to use the PCM switching functionality, while RF circuitry can be made using superconducting metal. This allows extreme miniaturization and allows development of high performance integrated circuits.

Heterogenous Integration Possibilities

Heterogenous integration provides quick, simple and cost effective solution to develop reconfigurable RF components. Small die size of PCM switches can be integrated either using flip-chip method or wire-bonds with various multi-layer technologies such

as CMOS, Low Temperature Co-fired Ceramic (LTCC) circuits or multi-layer PCBs. It is quite common to etch cavities in the top substrate of any multi-layer process. PCM dies can be flushed into the cavities to reduce the length of wire-bonds.

Optically Tuned Reconfigurable PCM Devices

One possibility is to optically change the PCM states between amorphous and crystalline. This will allow removing the micro-heaters for improved RF performance and optical elements such as lasers can be used to reconfigure the PCM elements. Lasers have been used to read and write the phase change memories such as CD/DVDs. Similar mechanism provides potential in developing automated reconfigurable optically tuned PCM devices and components.



Thesis List of Publications (as of April 2020)

Journal Article

- 1 **T. Singh** and R. R. Mansour, "Loss compensated PCM GeTe-based latching wideband 3-bit switched true-time-delay phase shifter for mmWave phased arrays," in *IEEE Transactions on Microwave Theory and Techniques*, pp. 1-11, Mar. 2020. (*under review*)
- 2 **T. Singh**, N. K. Khaira and R. R. Mansour, "Thermally actuated SOI RF MEMS-based fully integrated passive reflective-type analog phase shifter for mmWave applications," *IEEE Transactions on Microwave Theory and Techniques*, pp. 1-12, Feb. 2020. (*accepted*)
- 3 **T. Singh** and R. R. Mansour, "Miniaturized DC-60 GHz RF PCM GeTe-based monolithically integrated redundancy switch matrix using T-type switching unit cells," *IEEE Transactions on Microwave Theory and Techniques*, vol. 67, no. 12, pp. 5181-5190, Dec. 2019.
- 4 **T. Singh** and R. R. Mansour, "Characterization, optimization and fabrication of phase change material germanium telluride based miniaturized DC-67 GHz RF switches," *IEEE Transactions on Microwave Theory and Techniques*, vol. 67, no. 8, pp. 3237-3250, Aug. 2019.
- 5 N. K. Khaira, **T. Singh** and R. R. Mansour, "Monolithically integrated RF-MEMS based variable attenuator for millimeter-wave applications," *IEEE Transactions on Microwave Theory and Techniques*, vol. 67, no. 8, pp. 3251-3259, Aug. 2019.
- 6 **T. Singh**, A. Elhady, H. Jia, A. Mojdeh, C. Kaplan, V. Sharma, M. Basha and E. Abdel-Rahman, "Modeling of low-damping laterally actuated MEMS," *Mechatronics*, vol. 52, no. 2018, pp. 1-6, Jun. 2018.
- 7 **T. Singh** and R. R. Mansour, "Miniaturized reconfigurable 28 GHz PCM-based scalable non-volatile variation attenuators," pp. 1-10, 2020. (*under preparation, planned submission in IEEE Transactions on Microwave Theory and Techniques*)
- 8 **T. Singh** and R. R. Mansour, "Switchable high tuning ratio latching PCM GeTe-based capacitor banks with improved self resonance frequency," pp. 1-12, 2020. (*under preparation, planned submission in IEEE Transactions on Microwave Theory and Techniques*)
- 9 **T. Singh** and R. R. Mansour, "PCM GeTe-based monolithically integrated millimeter wave latching 8-bit switched reflection type phase shifter," pp. 1-9, 2020. (*under preparation, planned submission in IEEE Transactions on Microwave Theory and Techniques*)

- 10 **T. Singh** and R. R. Mansour, "Ultra-wideband monolithically integrated compact multi-port PCM GeTe-based latching mmWave RF switches up to SP16T configurations," pp. 1-10, 2020. (*under preparation, planned submission in IEEE Transactions on Microwave Theory and Techniques*)
- 11 **T. Singh** and R. R. Mansour, "Ultra-compact non-volatile PCM GeTe-based RF crossbar switch matrices," pp. 1-11, 2020. (*under preparation, planned submission in IEEE Transactions on Microwave Theory and Techniques*)
- 12 **T. Singh** and R. R. Mansour, "Extensive performance analysis of reliable RF PCM GeTe switches," pp. 1-8, 2020. (*under preparation, planned submission in IEEE Transactions on Microwave Theory and Techniques*)
- 13 **T. Singh** and R. R. Mansour, "Non-volatile reversible intermediate resistance states in chalcogenide PCM GeTe for multi-step resistance tuning," pp. 1-4, 2020. (*under preparation, planned submission in IEEE Electron Device Letters*)
- 14 **T. Singh** and R. R. Mansour, "Thermal crosstalk investigation in RF PCM GeTe-based RF switches for safe integration limits," pp. 1-4, 2020. (*under preparation, planned submission in IEEE Electron Device Letters*)
- 15 **T. Singh** and R. R. Mansour, "Experimental transient thermal imaging of high-speed refractory micro-heaters for PCM GeTe-based RF switches," pp. 1-4, 2020. (*under preparation, planned submission in IEEE Electron Device Letters*)
- 16 **T. Singh** and R. R. Mansour, "High resistance ratio behavior and stable RF performance of PCM GeTe-based switches at cryogenic temperatures," pp. 1-5, 2020. (*under preparation, planned submission in Applied Physics Letters*)

Conference Papers

- 17 **T. Singh** and R. R. Mansour, "Reconfigurable PCM GeTe-based latching 6-bit digital switched capacitor bank," in *50th European Microwave Conference (EuMC)*, Utrecht, The Netherlands, Sept 13–18, 2020. pp. 1–4 (*accepted, to be presented*).
- 18 **T. Singh** and R. R. Mansour, "Miniaturized reconfigurable 28 GHz PCM-based 4-bit latching variable attenuator for 5G mmWave applications," in *2020 IEEE MTT-S International Microwave Symposium (IMS)*, Los Angeles, CA, USA, June 20–26, 2020. pp. 1–4. (*accepted, to be presented, Shortlisted for Student Paper Competition*)

- 19 **T. Singh** and R. R. Mansour, "A miniaturized monolithic PCM based scalable four-port RF switch unit-cell," in *Proceedings of the 49th European Microwave Conference (EuMC)*, Paris, France, Sept 29 – Oct 4, 2019. pp. 180–183.
- 20 **T. Singh** and R. R. Mansour, "Monolithic PCM-based miniaturized T-type RF switch for millimeter wave redundancy switch matrix applications," in *Proceedings of the IEEE MTT-S International Microwave Symposium Digest (IMS)*, Boston, MA, USA, June 3–7, 2019. pp. 658–660. (**First Place Student Paper Competition, Best Paper Award**)
- 21 **T. Singh**, N. K. Khaira and R. R. Mansour, "Monolithically integrated reconfigurable RF MEMS based impedance tuner on SOI substrate," in *Proceedings of the IEEE MTT-S International Microwave Symposium Digest (IMS)*, Boston, MA, USA, June 3–7, 2019. pp. 790–792.
- 22 **T. Singh** and R. R. Mansour, "Characterization of phase change material germanium telluride for RF switches," in *Proceedings of the 48th European Microwave Conference (EuMC)*, Madrid, Spain, Sept 23–27, 2018. pp. 475–478. (**Student Award Winner**)
- 23 **T. Singh** and R. R. Mansour, "Modeling of frequency shift in RF-MEMS switches under residual stress gradient," in *Proceedings of the 18th IEEE International Symposium on Antenna Technology and Applied Electromagnetics (ANTEM)*, Waterloo, ON, Canada, Aug 19–22, 2018. pp. 1–3.
- 24 **T. Singh** and R. R. Mansour, "Chalcogenide phase change material GeTe based inline RF SPST series and shunt switches," in *Proceedings of the IEEE MTT-S International Microwave Workshop Series on Advanced Materials and Processes for RF and THz Applications (IMWS-AMP)*, Ann Arbor, MI, USA, July 16–18, 2018. pp. 1–3. (**Best Paper Award**)
- 25 N. K. Khaira, **T. Singh** and R. R. Mansour, "RF MEMS based 60 GHz variable attenuator," in *Proceedings of the IEEE MTT-S International Microwave Workshop Series on Advanced Materials and Processes for RF and THz Applications (IMWS-AMP)*, Ann Arbor, MI, USA, July 16–18, 2018. pp. 1–3.

Poster Presentations

- 26 **T. Singh** and R. R. Mansour, "Miniaturized mmWave chalcogenide PCM GeTe-based switch matrices for wireless and satellite communication systems," in *2019 TEXPO Graduate Student Competition and Exposition*, Montreal, QC, Canada, Oct 17–18, 2019. (**Canada Wide First Place, Recipient of Brian L. Barge Microsystems Integration Award**)

Research publications 2, 5, 6, 21, 23, and 25 are from related projects
Title and venue (journal/conference) of the manuscripts under preparation are preliminary

References

- [1] Grand View Research Inc. (2020, Feb 06) RF components market worth \$45.05 billion by 2025. San Francisco, CA, 2020. [Online]. Available: <https://www.grandviewresearch.com/press-release/global-rf-components-market>
- [2] A. Clavin, "Microwave switching networks," U.S. Patent 3,305,797, February 21, 1967.
- [3] T. S. Rappaport *et al.*, *Wireless Communications: Principles and Practice*. Prentice Hall PTR New Jersey, 1996, vol. 2.
- [4] P. Baran, "On distributed communications networks," *IEEE Transactions on Communications Systems*, vol. 12, no. 1, pp. 1–9, 1964.
- [5] M. Daneshmand and R. R. Mansour, "Redundancy RF MEMS multiport switches and switch matrices," *Journal of Microelectromechanical Systems*, vol. 16, no. 2, pp. 296–303, 2007.
- [6] F. T. Assal, C. E. Mahle, and A. Berman, "Redundant microwave configuration," U.S. Patent 4,070,637, January 24, 1978.
- [7] F. Assal, R. Gupta, K. Betaharon, A. Zaghloul, and J. Apple, "A wide-band satellite microwave switch matrix for SS/TDMA communications," *IEEE Journal on Selected Areas in Communications*, vol. 1, no. 1, pp. 223–231, 1983.
- [8] J. S. Schoenberg, J. W. Burger, J. S. Tyo, M. D. Abdalla, M. C. Skipper, and W. R. Buchwald, "Ultra-wideband source using gallium arsenide photoconductive semiconductor switches," *IEEE Transactions on Plasma Science*, vol. 25, no. 2, pp. 327–334, 1997.
- [9] P. M. Zavracky, N. E. McGruer, R. H. Morrison, and D. Potter, "Microswitches and microrelays with a view toward microwave applications," *International Journal of RF and Microwave Computer-Aided Engineering*, vol. 9, no. 4, pp. 338–347, 1999.
- [10] P. Grant, M. Denhoff, and R. Mansour, "A Comparison between RF MEMS Switches and Semiconductor Switches," in *Proceedings of International Conference on MEMS, NANO and Smart Systems (ICMENS)*. IEEE, 2004, pp. 515–521.

REFERENCES

- [11] G. M. Rebeiz, *RF MEMS: Theory, Design, and Technology*. John Wiley & Sons, 2004.
- [12] M. Daneshmand and R. Mansour, "RF MEMS satellite switch matrices," *IEEE Microwave Magazine*, vol. 12, no. 5, pp. 92–109, 2011.
- [13] O. Brand, G. K. Fedder, C. Hierold, J. G. Korvink, O. Tabata, and T. Tsuchiya, *Reliability of MEMS: Testing of Materials and Devices*. John Wiley & Sons, 2013.
- [14] T. Singh, "Design and finite element modeling of series-shunt configuration based RF MEMS switch for high isolation operation in K-Ka band," *Journal of Computational Electronics*, vol. 14, no. 1, pp. 167–179, 2015.
- [15] W. M. Van Spengen, "MEMS reliability from a failure mechanisms perspective," *Microelectronics Reliability*, vol. 43, no. 7, pp. 1049–1060, 2003.
- [16] W. M. Van Spengen, "Capacitive RF MEMS switch dielectric charging and reliability: a critical review with recommendations," *Journal of Micromechanics and Microengineering*, vol. 22, no. 7, p. 074001, 2012.
- [17] S. Raoux and M. E. Wuttig, *Phase Change Materials: Science and Applications*. Springer Science & Business Media, 2010.
- [18] M. Wuttig and N. Yamada, "Phase-change materials for rewriteable data storage," *Nature Materials*, vol. 6, no. 11, pp. 824–832, 2007.
- [19] M. Wuttig, "Phase-change materials: Towards a universal memory?" *Nature Materials*, vol. 4, no. 4, pp. 265–266, 2005.
- [20] M. Nardone, M. Simon, I. Karpov, and V. Karpov, "Electrical conduction in chalcogenide glasses of phase change memory," *Journal of Applied Physics*, vol. 112, no. 7, p. 071101, 2012.
- [21] P. Ramani and J. D. Porter, "Phase change memory," U.S. Patent 7,729,163, June 1, 2010.
- [22] S. R. Ovshinsky, "Reversible electrical switching phenomena in disordered structures," *Physical Review Letters*, vol. 21, no. 20, pp. 1450–1453, 1968.
- [23] N. El-Hinnawy, P. Borodulin, B. Wagner, M. R. King, J. S. Mason, E. B. Jones, S. McLaughlin, V. Veliadis, M. Snook, M. E. Sherwin *et al.*, "A four-terminal, inline, chalcogenide phase-change rf switch using an independent resistive heater for thermal actuation," *IEEE Electron Device Letters*, vol. 34, no. 10, pp. 1313–1315, 2013.
- [24] M. Wang, Y. Shim, and M. Rais-Zadeh, "A low-loss directly heated two-port rf phase change switch," *IEEE Electron Device Letters*, vol. 35, no. 4, pp. 491–493, 2014.

REFERENCES

- [25] Y. Shim and M. Rais-Zadeh, "Non-linearity analysis of rf ohmic switches based on phase change materials," *IEEE Electron Device Letters*, vol. 35, no. 3, pp. 405–407, 2014.
- [26] Y. Shim, G. Hummel, and M. Rais-Zadeh, "RF switches using phase change materials," in *IEEE 26th International Conference on Micro Electro Mechanical Systems (MEMS)*. IEEE, 2013, pp. 237–240.
- [27] N. Ciocchini, M. Laudato, M. Boniardi, E. Varesi, P. Fantini, A. Lacaita, and D. Ielmini, "Bipolar switching in chalcogenide phase change memory," *Scientific Reports*, vol. 6, 2016.
- [28] M. Daneshmand and R. R. Mansour, "Multi-port monolithic RF MEMS switches and switch matrices," U.S. Patent 7,778,506, August 17, 2010.
- [29] C. Pavageau, "RF MEMS crosspoint switch and crosspoint switch matrix comprising RF MEMS crosspoint switches," U.S. Patent 9,048,523, June 2, 2015.
- [30] K. Y. Chan, M. Daneshmand, R. R. Mansour, and R. Ramer, "Scalable RF MEMS Switch Matrices: Methodology and Design," *IEEE Transactions on Microwave Theory and Techniques*, vol. 57, no. 6, pp. 1612–1621, 2009.
- [31] A. T. Waterman, "On the positive ionization from certain hot salts, together with some observations on the electrical properties of molybdenite at high temperatures," *Philosophical Magazine and Journal of Science*, vol. 33, no. 195, pp. 225–247, 1917.
- [32] A. T. Waterman, "The electrical conductivity of molybdenite," *Physical Review*, vol. 21, no. 5, p. 540, 1923.
- [33] A. D. Pearson, W. R. Northover, J. F. Dewald, and W. F. Peck Jr., "Chemical, physical, and electrical properties of some unusual inorganic glasses," *Advances in Glass Technology*, pp. 357–365, 1962.
- [34] R. Neale, D. Nelson, and G. E. Moore, "Nonvolatile and reprogrammable, the read-mostly memory is here," *Electronics*, vol. 43, no. 20, pp. 56–60, 1970.
- [35] L. Chua, "Memristor-the missing circuit element," *IEEE Transactions on Circuit Theory*, vol. 18, no. 5, pp. 507–519, 1971.
- [36] R. Shanks and C. Davis, "A 1024-bit nonvolatile 15ns bipolar read-write memory," in *Digest of Technical Papers 1978 IEEE International Solid-State Circuits Conference*, vol. 21. IEEE, 1978, pp. 112–113.
- [37] E. K. Chua, "Development of phase change switches with low resistance in the "ON" state," PhD Thesis, Carnegie Mellon University, 2011.

REFERENCES

- [38] T. Matsunaga, N. Yamada, and Y. Kubota, "Structures of stable and metastable $\text{Ge}_2\text{Sb}_2\text{Te}_5$, an intermetallic compound in $\text{GeTe-Sb}_2\text{Te}_3$ pseudobinary systems," *Acta Crystallographica Section B: Structural Science*, vol. 60, no. 6, pp. 685–691, 2004.
- [39] N. N. Greenwood and A. Earnshaw, *Chemistry of the Elements*. Oxford Press, 1984.
- [40] J. B. Goodenough, "The two components of the crystallographic transition in VO_2 ," *Journal of Solid State Chemistry*, vol. 3, no. 4, pp. 490–500, 1971.
- [41] Y. Li, S. Ji, Y. Gao, H. Luo, and M. Kanehira, "Core-shell VO_2 TiO_2 nanorods that combine thermochromic and photocatalytic properties for application as energy-saving smart coatings," *Scientific Reports*, vol. 3, p. 1370, 2013.
- [42] B. Hu, Y. Ding, W. Chen, D. Kulkarni, Y. Shen, V. V. Tsukruk, and Z. L. Wang, "External-strain induced insulating phase transition in VO_2 nanobeam and its application as flexible strain sensor," *Advanced Materials*, vol. 22, no. 45, pp. 5134–5139, 2010.
- [43] M. Gurvitch, S. Luryi, A. Polyakov, and A. Shabalov, "Nonhysteretic behavior inside the hysteresis loop of VO_2 and its possible application in infrared imaging," *Journal of Applied Physics*, vol. 106, no. 10, p. 104504, 2009.
- [44] M.-J. Lee, Y. Park, D.-S. Suh, E.-H. Lee, S. Seo, D.-C. Kim, R. Jung, B.-S. Kang, S.-E. Ahn, C. B. Lee *et al.*, "Two series oxide resistors applicable to high speed and high density non-volatile memory," *Advanced Materials*, vol. 19, no. 22, pp. 3919–3923, 2007.
- [45] F. Dumas-Bouchiat, C. Champeaux, A. Catherinot, A. Crunteanu, and P. Blondy, "RF-microwave switches based on reversible semiconductor-metal transition of VO_2 thin films synthesized by pulsed-laser deposition," *Applied Physics Letters*, vol. 91, no. 22, p. 223505, 2007.
- [46] G. Chugunov, "Reactive RF sputtering of VO_2 ," MAsc Thesis, University of Waterloo, 2016.
- [47] A. Lebedev, I. Sluchinskaya, V. Demin, and I. Munro, "Influence of Se, Pb and Mn impurities on the ferroelectric phase transition in GeTe studied by EXAFS," *Phase Transitions*, vol. 60, no. 2, pp. 67–77, 1997.
- [48] E. I. Givargizov, A. Melnikova, and D. W. Wester, *Growth of crystals*. Springer, 1986.
- [49] G. Pawley, W. Cochran, R. Cowley, and G. Dolling, "Diatomic ferroelectrics," *Physical Review Letters*, vol. 17, no. 14, p. 753, 1966.
- [50] R. Hein, J. Gibson, R. Mazelsky, R. Miller, and J. Hulm, "Superconductivity in germanium telluride," *Physical Review Letters*, vol. 12, no. 12, p. 320, 1964.

REFERENCES

- [51] S. Bahl and K. Chopra, "Amorphous versus crystalline GeTe films. III. electrical properties and band structure," *Journal of Applied Physics*, vol. 41, no. 5, pp. 2196–2212, 1970.
- [52] A. Pirovano, A. L. Lacaita, A. Benvenuti, F. Pellizzer, and R. Bez, "Electronic switching in phase-change memories," *IEEE Transactions on Electron Devices*, vol. 51, no. 3, pp. 452–459, 2004.
- [53] D. Adler, M. Shur, M. Silver, and S. Ovshinsky, "Threshold switching in chalcogenide-glass thin films," *Journal of Applied Physics*, vol. 51, no. 6, pp. 3289–3309, 1980.
- [54] D. Ielmini and Y. Zhang, "Analytical model for subthreshold conduction and threshold switching in chalcogenide-based memory devices," *Journal of Applied Physics*, vol. 102, no. 5, p. 054517, 2007.
- [55] D. Emin, "Current-driven threshold switching of a small polaron semiconductor to a metastable conductor," *Physical Review B*, vol. 74, no. 3, p. 035206, 2006.
- [56] V. Karpov, Y. Kryukov, S. Savransky, and I. Karpov, "Nucleation switching in phase change memory," *Applied physics letters*, vol. 90, no. 12, p. 123504, 2007.
- [57] K. Nishiuchi, N. Yamada, N. Akahira, M. Takenaga, and R. Akutagawa, "Laser diode beam exposure instrument for rapid quenching of thin-film materials," *Review of Scientific Instruments*, vol. 63, no. 6, pp. 3425–3430, 1992.
- [58] C. Peng, L. Cheng, and M. Mansuripur, "Experimental and theoretical investigations of laser-induced crystallization and amorphization in phase-change optical recording media," *Journal of Applied Physics*, vol. 82, no. 9, pp. 4183–4191, 1997.
- [59] D. Baker, M. Paesler, G. Lucovsky, S. Agarwal, and P. Taylor, "Application of bond constraint theory to the switchable optical memory material $\text{Ge}_2\text{Sb}_2\text{Te}_5$," *Physical Review Letters*, vol. 96, no. 25, p. 255501, 2006.
- [60] A. Kolobov, M. Krbal, P. Fons, J. Tominaga, and T. Uruga, "Distortion-triggered loss of long-range order in solids with bonding energy hierarchy," *Nature Chemistry*, vol. 3, no. 4, pp. 311–316, 2011.
- [61] A. V. Kolobov, P. Fons, A. I. Frenkel, A. L. Ankudinov, J. Tominaga, and T. Uruga, "Understanding the phase-change mechanism of rewritable optical media," *Nature Materials*, vol. 3, no. 10, pp. 703–708, 2004.
- [62] Sivers Lab Sweden. (2020, Feb 06) Waveguide microwave switches. [Online]. Available: <https://www.siversima.com/>

REFERENCES

- [63] M. Daneshmand, "Multi-Port RF MEMS Switches and Switch Matrices," PhD Thesis, University of Waterloo, 2006.
- [64] Dow-Key Microwave Corp. (2020, Feb 06) Coaxial RF and Microwave Switches. [Online]. Available: <https://www.dowkey.com/>
- [65] S. M. Sze and K. K. Ng, *Physics of semiconductor devices*. John Wiley & sons, 2006.
- [66] G. M. Rebeiz and J. B. Muldavin, "RF MEMS switches and switch circuits," *IEEE Microwave magazine*, vol. 2, no. 4, pp. 59–71, 2001.
- [67] General Electric (GE) Global Research. (2020, Feb 06) GE MEMS switch technology demonstrates performance which could meet demands for next-generation "True 4G" mobile devices. General Electric (GE). [Online]. Available: <http://www.geglobalresearch.com/news/press-releases/ge-mems-switch-technology-demonstrates-performance-meet-demands-next-generation-true-4g-mobile-devices>
- [68] G. M. Rebeiz, C. D. Patel, S. K. Han, C. H. Ko, and K. M. J. Ho, "The search for a reliable MEMS switch," *IEEE Microwave Magazine*, vol. 14, no. 1, pp. 57–67, Jan 2013.
- [69] M. Wang and M. Rais-zadeh, "Need a change? try GeTe: A reconfigurable filter using germanium telluride phase change rf switches," *IEEE Microwave Magazine*, vol. 17, no. 12, pp. 70–79, 2016.
- [70] N. El-Hinnawy, P. Borodulin, B. P. Wagner, M. R. King, E. B. Jones, R. S. Howell, M. J. Lee, and R. M. Young, "Low-loss latching microwave switch using thermally pulsed non-volatile chalcogenide phase change materials," *Applied Physics Letters*, vol. 105, no. 1, p. 013501, 2014.
- [71] J.-S. Moon, H.-C. Seo, D. Le, H. Fung, A. Schmitz, T. Oh, S. Kim, K.-a. Son, B. Yang, and H. R. L. Laboratories, "10.6 THz figure-of-merit phase-change RF switches with embedded micro-heater," in *15th IEEE Topical Meeting on Silicon Monolithic Integrated Circuits in RF Systems (SiRF)*. San Diego, CA: IEEE, 2015, pp. 73–75.
- [72] E. K. Chua, L. P. Shi, R. Zhao, K. G. Lim, T. C. Chong, T. E. Schlesinger, and J. A. Bain, "Low resistance, high dynamic range reconfigurable phase change switch for radio frequency applications," *Applied Physics Letters*, vol. 97, no. 18, pp. 95–98, 2010.
- [73] M. Field, C. Hillman, P. Stupar, J. Hacker, Z. Griffith, and K.-J. Lee, "Vanadium dioxide phase change switches," in *Proceedings of the SPIE Open Architecture/Open Business Model Net-Centric Systems and Defense Transformation*, vol. 9479, no. 947908, Baltimore, MD, 2015, pp. 1–8.

REFERENCES

- [74] M. Wang and M. Rais-zadeh, "Directly heated four-terminal phase change switches," in *Proceedings of the IEEE MTT-S International Microwave Symposium Digest (IMS)*, Tampa, FL, 2014, pp. 1–4.
- [75] M. Wang and M. Rais-Zadeh, "Development and evaluation of germanium telluride phase change material based ohmic switches for RF applications," *Journal of Micromechanics and Microengineering*, vol. 27, no. 1, p. 013001, 2017.
- [76] N. El-Hinnawy, P. Borodulin, E. B. Jones, B. P. Wagner, M. R. King, S. John, J. Bain, J. Paramesh, T. E. Schlesinger, R. S. Howell *et al.*, "12.5 THz Fco GeTe inline phase-change switch technology for reconfigurable RF and switching applications," in *IEEE Compound Semiconductor Integrated Circuit Symposium (CSICS)*. La Jolla, CA: IEEE, 2014, pp. 1–3.
- [77] J.-S. Moon, "Method to make RF-PCM switches and circuits with phase-change materials," Patent 8,900,930, December 2, 2014.
- [78] J.-S. Moon, H.-C. Seo, D. Le, H. Fung, A. Schmitz, T. Oh, S. Kim, K.-A. Son, D. Zehnder, and B. Yang, "11 THz figure-of-merit phase-change RF switches for reconfigurable wireless front-ends," in *Proceedings of the IEEE MTT-S International Microwave Symposium Digest (IMS)*. IEEE, 2015, pp. 1–4.
- [79] J.-S. Moon, H.-C. Seo, and D. Le, "High linearity 1-ohm rf switches with phase-change materials," in *Silicon Monolithic Integrated Circuits in Rf Systems (SiRF), 2014 IEEE 14th Topical Meeting on*. IEEE, 2014, pp. 7–9.
- [80] P. Borodulin, N. El-Hinnawy, C. R. Padilla, A. Ezis, M. R. King, D. R. Johnson, D. T. Nichols, and R. M. Young, "Recent advances in fabrication and characterization of GeTe-based phase-change RF switches and MMICs," in *Proceedings of the IEEE MTT-S International Microwave Symposium Digest (IMS)*. Honolulu, HI, USA: IEEE, June 04–09 2017, pp. 285–288.
- [81] J.-s. Moon, H.-c. Seo, K.-a. Son, K. Lee, D. Zehnder, and H. Tai, "5 THz figure-of-merit reliable phase-change RF switches for millimeter-wave applications," in *Proceedings of the IEEE MTT-S International Microwave Symposium Digest (IMS)*. Philadelphia, PA, USA: IEEE, June 10–15 2018, pp. 836–838.
- [82] H. Madan, H.-T. Zhang, M. Jerry, D. Mukherjee, N. Alem, and S. Datta, "26.5 Terahertz Electrically Triggered RF Switch on Epitaxial VO₂-on-Sapphire (VOS) Wafer," in *IEEE International Electron Devices Meeting (IEDM)*, Washington, DC, 2015, pp. 9.3.1–9.3.4.
- [83] A. Fomani and R. R. Mansour, "Monolithically integrated multiport RF MEMS switch matrices," *IEEE Transactions on Microwave Theory and Techniques*, vol. 57, no. 12, pp. 3434–3441, 2009.

REFERENCES

- [84] K. Y. Chan, M. Daneshmand, A. A. Fomani, R. R. Mansour, and R. Ramer, "Monolithic MEMS T-type Switch for Redundancy Switch Matrix Applications," in *Proceedings of the 38th European Microwave Conference (EuMC)*. IEEE, 2008, pp. 1513–1516.
- [85] T. Singh and R. R. Mansour, "Characterization of phase change material germanium telluride for RF switches," in *Proceedings of the 48th European Microwave Conference (EuMC)*. Madrid, Spain: IEEE, Sep 23–27 2018, pp. 475–478.
- [86] T. Singh and R. R. Mansour, "Characterization, optimization, and fabrication of phase change material germanium telluride based miniaturized DC–67 GHz RF switches," *IEEE Transactions on Microwave Theory and Techniques*, vol. 67, no. 8, pp. 3237–3250, Aug. 2019.
- [87] T. Singh and R. R. Mansour, "Chalcogenide Phase Change Material GeTe based Inline RF SPST Series and Shunt Switches," in *Proceedings of the IEEE MTT-S International Microwave Workshop Series on Adv. Mater. and Processes for RF and THz Appl. (IMWS-AMP)*. Ann Arbor, MI, USA: IEEE, July 16–18 2018, pp. 1–3.
- [88] S. Meister, D. T. Schoen, M. A. Topinka, A. M. Minor, and Y. Cui, "Void Formation Induced Electrical Switching in Phase-Change Nanowires," *Nano Letters*, vol. 8, no. 12, pp. 4562–4567, 2008.
- [89] K. Yazawa, J. A. L. Gil, K. Maze, D. Kendig, and A. Shakouri, "Optical pump-probe thermoreflectance imaging for anisotropic heat diffusion," in *Proceedings of the 17th IEEE Intersociety Conference on Thermal and Thermomechanical Phenomena in Electronic Systems (ITherm)*. San Diego, CA, USA: IEEE, May 29 – Jun 1 2018, pp. 59–66.
- [90] D. Kendig, G. Hohensee, E. Pek, W. Kuang, K. Yazawa, and A. Shakouri, "Accurate Thermoreflectance Imaging of Nano-Features Using Thermal Decay," in *Proceedings of the 16th IEEE Intersociety Conference on Thermal and Thermomechanical Phenomena in Electronic Systems (ITherm)*. Orlando, FL, USA: IEEE, May 30 – Jun 02 2017, pp. 23–29.
- [91] A. Ziabari, P. Torres, B. Vermeersch, Y. Xuan, X. Cartoixà, A. Torelló, J.-H. Bahk, Y. R. Koh, M. Parsa, D. Y. Peide *et al.*, "Full-field thermal imaging of quasiballistic crosstalk reduction in nanoscale devices," *Nature Communications*, vol. 9, no. 1, pp. 1–7, 2018.
- [92] A. Ziabari, P. Torres, B. Vermeersch, Y. Xuan, X. Cartoixà, A. Torelló, J.-H. Bahk, Y. R. Koh, M. Parsa, D. Y. Peide *et al.*, "Full-Field Thermal Imaging of Quasiballistic Crosstalk Reduction in Nanoscale Devices," *Nature Communications*, vol. 9, no. 1, pp. 1–7, 2018.
- [93] Microsanj LLC. NanoTherm Series: NT220B Nanosecond Transient Thermal Imaging Systems. Santa Clara, CA, 2019. [Online]. Available: <https://www.microsanj.com/>

REFERENCES

- [94] K. Yazawa, D. Kendig, and A. Shakouri, "Time-Resolved Thermoreflectance Imaging for Thermal Testing and Analysis," in *Proceedings of the 39th International Symposium for Testing and Failure Analysis (ISTFA)*. San Jose, CA, USA: ASM International, Nov 3–7 2013, pp. 194–202.
- [95] T. Singh and R. R. Mansour, "A miniaturized monolithic PCM based scalable four-port RF switch unit-cell," in *Proceedings of the 49th European Microwave Conference (EuMC)*. Paris, France: IEEE, Sep 29 – Oct 4 2019, pp. 180–183.
- [96] T. Singh and R. R. Mansour, "Monolithic PCM based miniaturized T-type RF switch for millimeter wave redundancy switch matrix applications," in *Proceedings of the IEEE MTT-S International Microwave Symposium Digest (IMS)*. Boston, MA, USA: IEEE, June 3–7 2019, pp. 658–660.
- [97] T. Singh and R. R. Mansour, "Miniaturized DC–60 GHz RF PCM GeTe-based monolithically integrated redundancy switch matrix using T-Type switching unit cells," *IEEE Transactions on Microwave Theory and Techniques*, vol. 67, no. 12, pp. 5181–5190, Dec. 2019.
- [98] B. Yassini, S. Choi, A. Zybura, M. Yu, R. E. Mihailovich, and J. F. DeNatale, "A Novel MEMS LTCC Switch Matrix," in *Proceedings of the IEEE MTT-S International Microwave Symposium Digest (IMS)*, vol. 2. Fort Worth, TX, USA: IEEE, Jun 6–11 2004, pp. 721–724.
- [99] M. Daneshmand and R. R. Mansour, "Monolithic RF MEMS Switch Matrix Integration," in *Proceedings of the IEEE MTT-S International Microwave Symposium Digest (IMS)*. San Francisco, CA, USA: IEEE, Jun 11–16 2006, pp. 140–143.
- [100] A. A. Fomani and R. R. Mansour, "Miniature RF MEMS Switch Matrices," in *Proceedings of the IEEE MTT-S International Microwave Symposium Digest (IMS)*. Boston, MA, USA: IEEE, Jun 7–12 2009, pp. 1221–1224.
- [101] T. Singh and R. R. Mansour, "Miniaturized reconfigurable 28 GHz PCM-based 4-bit latching variable attenuator for 5G mmWave applications," in *Proceedings of the IEEE MTT-S International Microwave Symposium Digest (IMS)*. Los Angeles, CA, USA: IEEE, June 21–26 2020 (*accepted, to be presented*), pp. 1–4.
- [102] T. Singh and R. R. Mansour, "Reconfigurable PCM GeTe-based latching 6-bit digital switched capacitor bank," in *Proceedings of the 50th European Microwave Conference (EuMC)*. Utrecht, The Netherlands: IEEE, Sep 13–18 2020 (*accepted, to be presented*), pp. 1–4.
- [103] T. Singh and R. R. Mansour, "Loss compensated PCM GeTe-based latching wideband 3-bit switched True-Time-Delay phase shifter for mmWave phased arrays," *IEEE Transactions on Microwave Theory and Techniques*, vol. –, no. –, pp. 1–11, 2020 (*under review*).

REFERENCES

- [104] T. Singh, N. K. Khaira, and R. R. Mansour, "Monolithically integrated reconfigurable RF MEMS based impedance tuner on SOI substrate," in *Proceedings of the IEEE MTT-S International Microwave Symposium Digest (IMS)*. Boston, MA, USA: IEEE, Jun 2–7 2019, pp. 790–792.
- [105] N. K. Khaira, T. Singh, and R. R. Mansour, "Monolithically integrated RF MEMS-based variable attenuator for millimeter-wave applications," *IEEE Transactions on Microwave Theory and Techniques*, vol. 67, no. 8, pp. 3251–3259, Aug. 2019.
- [106] J. Luo, M. Lin, Y. Q. Fu, L. Wang, A. Flewitt, S. Spearing, N. Fleck, and W. Milne, "MEMS based digital variable capacitors with a high-k dielectric insulator," *Sensors and Actuators A: Physical*, vol. 132, no. 1, pp. 139–146, 2006.
- [107] WiSpry. (2020, Feb 13) Tunable digital capacitor arrays. [Online]. Available: <https://www.wispry.com/>
- [108] Cavendish Kinetics Inc. (Now Qorvo). (2020, Feb 13) RF MEMS SmarTuners. [Online]. Available: <https://www.cavendish-kinetics.com/>
- [109] R. G. Pesel, S. S. Attar, and R. R. Mansour, "MEMS-based capacitor banks for impedance matching networks," in *Proceedings of the 45th European Microwave Conference (EuMC)*, Paris, France, Sep 6–11 2015, pp. 1018–1021.
- [110] K. Nadaud, F. Roubeau, A. Pothier, P. Blondy, L.-Y. Zhang, and R. Stefanini, "High Q zero level packaged RF-MEMS switched capacitor arrays," in *Proceedings of the 11th European Microwave Integr. Circuits Conference (EuMIC)*. London, UK: IEEE, Oct 3–7 2016, pp. 448–451.
- [111] R. Stefanini, C. Guines, F. Barrière, E. Lemoine, and P. Blondy, "High power handling low-voltage RF MEMS switched capacitors," in *Proceedings of the 7th European Microwave Integr. Circuit Conference (EuMIC)*. Amsterdam, The Netherlands: IEEE, Oct 28 – Nov 2 2012, pp. 449–452.
- [112] I. Reines, B. Pillans, and G. M. Rebeiz, "Performance of temperature-stable RF MEMS switched capacitors under high RF power conditions," in *Proceedings of the IEEE MTT-S International Microwave Symposium Digest (IMS)*. Anaheim, CA, USA: IEEE, May 23–28 2010, pp. 292–295.
- [113] A. A. Aziz and R. R. Mansour, "Design, fabrication and characterization of compact 4-bit RF MEMS capacitor bank in standard CMOS 0.35 μm process," in *Proceedings of the IEEE MTT-S International Microwave Symposium Digest (IMS)*. Honolulu, HI, USA: IEEE, Jun 4–9 2017, pp. 572–574.

REFERENCES

- [114] J. Jiang and R. R. Mansour, "Design, fabrication and characterization of a PCM-based 4-bit capacitor bank," in *Proceedings of the IEEE MTT-S International Microwave Symposium Digest (IMS)*, Philadelphia, PA, USA, Jun 10–15 2018, pp. 736–738.
- [115] Y.-Y. Huang, W. Woo, Y. Yoon, and C.-H. Lee, "Highly linear RF CMOS variable attenuators with adaptive body biasing," *IEEE Journal of Solid-State Circuits*, vol. 46, no. 5, pp. 1023–1033, 2011.
- [116] H. Dogan, R. G. Meyer, and A. M. Niknejad, "Analysis and Design of RF CMOS Attenuators," *IEEE Journal of Solid-State Circuits*, vol. 43, no. 10, pp. 2269–2283, 2008.
- [117] J. Park, D. Baek, and J.-G. Kim, "A 28 GHz 8-channel Fully Differential Beamforming IC in 65nm CMOS process," in *Proceedings of the 49th European Microwave Conference (EuMC)*. Paris, France: IEEE, Sept 28 – Oct 4 2019, pp. 476–479.
- [118] K.-O. Sun, M. K. Choi, and D. van der Weide, "A PIN Diode Controlled Variable Attenuator Using a 0-dB Branch-Line Coupler," *IEEE Microwave and Wireless Component Letters*, vol. 15, no. 6, pp. 440–442, 2005.
- [119] T. Singh, A. Elhady, H. Jia, A. Mojdeh, C. Kaplan, V. Sharma, M. Basha, and E. Abdel-Rahman, "Modeling of Low-Damping Laterally Actuated Electrostatic MEMS," *Mechanics*, vol. 52, pp. 1–6, 2018.
- [120] A. Raeesi, H. Al-Saedi, A. Palizban, A. Taeb, W. M. Abdel-Wahab, S. Gigoyan, and S. Safavi-Naeini, "Low-Cost Planar RF MEMS-Based Attenuator," in *Proceedings of the IEEE MTT-S International Microwave Symposium Digest (IMS)*. Boston, MA, USA: IEEE, June 3–7 2019, pp. 869–872.
- [121] J. Givernaud, A. Crunteanu, J.-C. Orlianges, A. Pothier, C. Champeaux, A. Catherinot, and P. Blondy, "Microwave Power Limiting Devices Based on the Semiconductor–Metal Transition in Vanadium–Dioxide Thin Films," *IEEE Transactions on Microwave Theory and Techniques*, vol. 58, no. 9, pp. 2352–2361, 2010.
- [122] L. Pierantoni, D. Mencarelli, M. Bozzi, R. Moro, and S. Bellucci, "Graphene-Based Electronically Tuneable Microstrip Attenuator," *Nanomaterials and Nanotechnology*, vol. 4, p. 18, 2014.
- [123] N. El-Hinnawy, P. Borodulin, E. B. Jones, B. P. Wagner, M. R. King, J. S. Mason, J. Bain, J. Paramesh, T. Schlesinger, R. S. Howell *et al.*, "12.5 THz F_{co} GeTe inline phase-change switch technology for reconfigurable RF and switching applications," in *Proceedings of the IEEE Compound Semicond. Integr. Circuit Symposium (CSICS)*. La Jolla, CA, USA: IEEE, Oct. 19–22 2014, pp. 1–3.

REFERENCES

- [124] M. Wang and M. Rais-Zadeh, "Directly heated four-terminal phase change switches," in *Proceedings of the IEEE MTT-S International Microwave Symposium Digest (IMS)*. Tampa, FL, USA: IEEE, June 1–6 2014, pp. 1–4.
- [125] N. El-Hinnawy, P. Borodulin, M. Torpey, F. Kuss, A. Ezis, J. Paramesh, J. Bain, T. Schlesinger, R. Howell, M. Lee *et al.*, "Reconfigurable inline phase-change switches for broadband applications," in *Proceedings of the IEEE MTT-S International Microwave Symposium Digest (IMS)*. Phoenix, AZ, USA: IEEE, May 17–22 2015, pp. 1–4.
- [126] A. Crunteanu, A. Mennai, C. Guines, D. Passerieux, and P. Blondy, "Out-of-plane and inline RF switches based on Ge₂Sb₂Te₅ phase-change material," in *Proceedings of the IEEE MTT-S International Microwave Symposium Digest (IMS)*. Tampa, FL, USA: IEEE, June 1–6 2014, pp. 1–4.
- [127] J.-s. Moon, H.-c. Seo, K.-a. Son, K. Lee, D. Zehnder, H. Tai, and D. Le, "Phase-change RF switches with robust switching cycle endurance," in *Proceedings of the IEEE Radio and Wireless Symposium (RWS)*. Anaheim, CA, USA: IEEE, Jan. 15–18 2018, pp. 231–233.
- [128] Q. Ma, D. Leenaerts, and R. Mahmoudi, "A 10-50 GHz True-Time-Delay Phase Shifter with Max 3.9% delay Variation," in *Proceedings of the IEEE Radio Frequency Integrated Circuits Symposium (RFIC)*. Tampa, FL, USA: IEEE, June 1–3 2014, pp. 83–86.
- [129] W. Lee and S. Hong, "Ka-Band Inductor-Shared SP_nT DP_nT Switches and Their Applications to TTD Phase Shifter," *IEEE Transactions on Microwave Theory and Techniques*, vol. 67, no. 7, pp. 2546–2554, 2019.
- [130] B.-W. Min and G. M. Rebeiz, "Single-Ended and Differential Ka-band BiCMOS Phased Array Front-Ends," *IEEE Journal of Solid-State Circuits*, vol. 43, no. 10, pp. 2239–2250, 2008.
- [131] J. S. Hayden and G. M. Rebeiz, "Very Low-Loss Distributed X-band and Ka-band MEMS Phase Shifters Using Metal-Air-Metal Capacitors," *IEEE Transactions on Microwave Theory and Techniques*, vol. 51, no. 1, pp. 309–314, 2003.
- [132] Y. Liu, A. Borgioli, A. S. Nagra, and R. A. York, "K-band 3-bit Low-Loss Distributed MEMS Phase Shifter," *IEEE Microwave and Guided Wave Letters*, vol. 10, no. 10, pp. 415–417, 2000.
- [133] B. Pillans, L. Coryell, A. Malczewski, C. Moody, F. Morris, and A. Brown, "Advances in RF MEMS Phase Shifters from 15 GHz to 35 GHz," in *Proceedings of the IEEE MTT-S International Microwave Symposium Digest (IMS)*. Montreal, QC, Canada: IEEE, June 17–22 2012, pp. 1–3.
- [134] M. Jost, S. Strunck, A. Heunisch, A. Wiens, A. Prasetiadi, C. Weickhmann, B. Schulz, M. Quibeldey, O. Karabey, T. Rabe *et al.*, "Continuously Tuneable Liquid Crystal Based

REFERENCES

- Stripline Phase Shifter Realised in LTCC Technology," in *Proceedings of the 45th European Microwave Conference (EuMC)*. Paris, France: IEEE, Sept 7–10 2015, pp. 1260–1263.
- [135] B. Biglarbegan, M.-R. Nezhad-Ahmadi, M. Fakharzadeh, and S. Safavi-Naeini, "A wide-band 90° continuous phase shifter for 60 GHz phased array transceiver in 90 nm CMOS technology," in *Proceedings of the 39th European Microwave Conference (EuMC)*. Rome, Italy: IEEE, Sep 28 – Oct 02 2009, pp. 479–482.
- [136] M. Tabesh, A. Arbabian, and A. Niknejad, "60 GHz low-loss compact phase shifters using a transformer-based hybrid in 65nm CMOS," in *Proceedings of the IEEE Custom International Circuits Conference (CICC)*. San Jose, CA, USA: IEEE, Sep 19–21 2011, pp. 1–4.
- [137] T.-W. Li and H. Wang, "A millimeter-wave fully integrated passive reflection-type phase shifter with transformer-based multi-resonance loads for 360° phase shifting," *IEEE Transactions on Circuits and Systems I: Regular Papers*, vol. 65, no. 4, pp. 1406–1419, 2017.
- [138] W.-T. Li, Y.-H. Kuo, Y.-M. Wu, J.-H. Cheng, T.-W. Huang, and J.-H. Tsai, "An X-band full-360° reflection type phase shifter with low insertion loss," in *Proceedings of the 42nd European Microwave Conference (EuMC)*. IEEE, Oct 29 – Nov 01 2012, pp. 754–757.
- [139] T. Huang, L. Jeevananthan, S. Ituah, G. Chen, M.-R. Nezhad-Ahmadi, and S. Safavi-Naeini, "A miniaturized 0.13- μm BiCMOS reflective-type phase shifter for K-Band phased arrays," in *Proceedings of the IEEE International Symposium on Circuits and Systems (ISCAS)*. Sapporo, Japan: IEEE, May 26–29 2019, pp. 1–5.
- [140] F. Ellinger, R. Vogt, and W. Bachtold, "Compact reflective-type phase-shifter MMIC for C-band using a lumped-element coupler," *IEEE Transactions on Microwave Theory and Techniques*, vol. 49, no. 5, pp. 913–917, 2001.
- [141] T.-Y. Chang, C.-L. Liao, and C. H. Chen, "Novel uniplanar tandem couplers," in *Proceedings of the 32nd European Microwave Conference (EuMC)*, Sep 23–26, pp. 1–4.
- [142] J.-H. Cho, H.-Y. Hwang, and S.-W. Yun, "A design of wideband 3-dB coupler with N-section microstrip tandem structure," *IEEE Microwave Wireless Compon. Lett.*, vol. 15, no. 2, pp. 113–115, 2005.
- [143] A. Tombak, "A ferroelectric-capacitor-based tunable matching network for quad-band cellular power amplifiers," *IEEE Transactions on Microwave Theory and Techniques*, vol. 55, no. 2, pp. 370–375, 2007.
- [144] C. Sanchez-Perez, J. De Mingo, P. Garcia-Ducar, and P. L. Carro, "Performance improvement of mobile DVB-H terminals using a reconfigurable impedance tuning network," *IEEE Transactions on Consumer Electronics*, vol. 55, no. 4, pp. 1875–1882, 2009.

REFERENCES

- [145] P. Nukala, "Crystal-amorphous transformation via defect templating in phase-change materials," Ph.D. dissertation, University of Pennsylvania, Philadelphia, PA, USA, 2015. [Online]. Available: <https://repository.upenn.edu/edissertations/1108>
- [146] J. G. Champlain, L. B. Ruppalt, A. C. Guyette, N. El-Hinnawy, P. Borodulin, E. Jones, R. M. Young, and D. Nichols, "Examination of the temperature dependent electronic behavior of GeTe for switching applications," *Journal of Applied Physics*, vol. 119, no. 24, p. 244501, 2016.
- [147] P. Borodulin, N. El-Hinnawy, A. Graninger, M. King, C. Padilla, L. Upton, R. Hinkey, T. Schlesinger, A. Pesetski, M. Sherwin *et al.*, "Operation of a latching, low-loss, wideband microwave phase-change switch below 1 K," *Journal of Low Temperature Physics*, vol. 194, no. 3-4, pp. 273–284, 2019.
- [148] Y. Yin, H. Sone, and S. Hosaka, "A chalcogenide-based device with potential for multi-state storage," *Microelectronics Journal*, vol. 38, no. 6-7, pp. 695–699, 2007.
- [149] S.-H. Hong, H. Lee, K.-I. Kim, Y. Choi, and Y.-K. Lee, "Fabrication of multilevel switching high density phase change data recording using stacked GeTe/GeSbTe structure," *Japanese Journal of Applied Physics*, vol. 50, no. 8R, p. 081201, 2011.
- [150] P. Nukala, C.-C. Lin, R. Composto, and R. Agarwal, "Ultralow-power switching via defect engineering in germanium telluride phase-change memory devices," *Nature communications*, vol. 7, no. 1, pp. 1–8, 2016.
- [151] Y. Hu, M. Sun, S. Song, Z. Song, and J. Zhai, "Multi-step resistance memory behavior in Ge₂Sb₂Te₅/GeTe stacked chalcogenide films," *Integrated Ferroelectrics*, vol. 140, no. 1, pp. 8–15, 2012.
- [152] Z. Li, Y. Lu, M. Wang, X. Shen, X. Zhang, S. Song, and Z. Song, "Controllable multilevel resistance state of superlattice-like GaSb/Ge₂Te films for ultralong retention phase-change memory," *Journal of Non-Crystalline Solids*, vol. 481, pp. 110–115, 2018.
- [153] N. Papandreou, H. Pozidis, A. Pantazi, A. Sebastian, M. Breitwisch, C. Lam, and E. Eleftheriou, "Programming algorithms for multilevel phase-change memory," in *Proceedings of the IEEE International Symposium of Circuits and Systems (ISCAS)*. Rio de Janeiro, Brazil: IEEE, May 15–18 2011, pp. 329–332.
- [154] N. Papandreou, A. Pantazi, A. Sebastian, M. Breitwisch, C. Lam, H. Pozidis, and E. Eleftheriou, "Multilevel phase-change memory," in *2010 17th IEEE International Conference on Electronics, Circuits and Systems*. Athens, Greece: IEEE, Dec 12–15 2010, pp. 1017–1020.

REFERENCES

- [155] F. Bedeschi, R. Fackenthal, C. Resta, E. M. Donze, M. Jagasivamani, E. C. Buda, F. Pellizzer, D. W. Chow, A. Cabrini, G. M. A. Calvi *et al.*, "A bipolar-selected phase change memory featuring multi-level cell storage," *IEEE Journal of Solid-State Circuits*, vol. 44, no. 1, pp. 217–227, 2008.
- [156] T. Nirschl, J. Philipp, T. Happ, G. W. Burr, B. Rajendran, M.-H. Lee, A. Schrott, M. Yang, M. Breitwisch, C.-F. Chen *et al.*, "Write strategies for 2 and 4-bit multi-level phase-change memory," in *Proceedings of the IEEE International Electron Devices Meeting*. Washington, DC, USA: IEEE, Dec 10–12 2007, pp. 461–464.
- [157] Y.-N. Hwang, S.-o. Park, H.-S. Jeong, and G.-T. Jeong, "Multi-bit phase change memory devices," U.S. Patent 8,320,170, Nov 27, 2012.

Appendices

Appendix A

Microfabrication Process Steps

A.1 Gen 3 Microfabrication Process Flow Sequence

Step 1. Wafer preparation

⌚ 45 min

The first step to a successful microfabrication process is to have a wafer surface free from any organic matter. Ultrasonic bath and RCA1 are standard cleaning procedures. Optionally piranha cleaning can be used.

1. Ultrasonic bath ✓ ⌚ 10 min
Materials required: Pure acetone, pyrex bath containers, ultrasonic chamber, hot plate
 - (a) Individual wafers or wafer cassettes submerged into pure acetone beaker in ultrasonic bath chamber.
 - i. Set ultrasonication power ⚡ to maximum available
 - (b) Rinse wafers with acetone, isopropanol (IPA), and deionized (DI) water.
 - (c) Heat wafers on hotplate 🔥 120 °C.
2. RCA-1 cleaning ⚠ ⌚ 30 min
Materials required: Hot plate, Ammonia hydroxide (NH₄OH), hydrogen peroxide (H₂O₂), pyrex bath containers

Legend: ⚠ Warning, use with caution. ✓ Safe to use. ✗ Don't do this. ⚙ Equipment dependent.
♻ Reuse. ⚙ Equipment, ⌚ Process time, ⚙ Spin speed, ⚠ Mixture, 🔥 Temperature.

- (a) RCA-1 or SC-1 is the standard procedure for removing organic residue and films from wafers. This process oxidizes the silicon wafers and leaves a thin oxide layer, which should be removed if desired.
 - i. Set hot plate to 70°C .
 - ii. Heat a mixture of 5 parts DI water and 1 part NH_4OH on hot plate.
 - iii. Once the temperature of the solution reaches 70°C , add 1 part H_2O_2 to the mixture.
 - iv. Wait for the solution to bubble vigorously, usually 2–3 minutes.
- (b) Soak the silicon wafers in the solution for 15 min.
- (c) Transfer the wafers to a container with overflowing DI water to rinse and remove the solution.
- (d) Heat wafers on hotplate 120°C for 3 min.

Clean up For proper disposal of the RCA-1 solution, dilute with cold water, let cool for 10 min, then pour down the drain with plenty of cold water to flush.

⚠️ ♻️ Don't use the old RCA-1 solution as it loses its effectiveness in less than a day and within 30 min at 70°C .

3. O_2 plasma ashing \checkmark \ominus ⏱️ 5 min

⚙️ Yield Engineering Systems CV200RFS Oxygen Plasma Asher

- (a) Plasma cleaning or ashing can effectively remove organic material that is difficult to remove by solvent cleaning. Ashing is a dry cleaning procedure.
 - ⚡ RF power — 1 kW
 - ☁️ Pressure — 300 mTorr
 - 🔥 Temperature — 180°C
 - ⏴ O_2 flow — 50 sccm
 - ⏴ N_2 flow — 0 sccm
 - ⌚ Duration — 2 min

≡ **Remarks:** Combined all three cleaning procedures mentioned ensures near perfect substrate to start the microfabrication process. However, if the wafers are relatively clean either one of the mentioned cleaning steps is adequate enough to clean the substrate.

Step 2. Substrate oxide (D0) deposition

⌚ 8 min/wafer + 15 min

Substrate oxide can be grown thermally by wet or dry oxide growth methods. For non-silicon substrates; PECVD, ALD, or sputtering are preferred choices. PECVD growth method is used in presented microfabrication process flow.













1. Load lock pump and vent time including wafer transfer time ⌚ 7 min
 2. Clean and preconditioning (*pilot wafer*) ✓ ⊖ ⌚ 15 min
 3. Deposit 60 nm to 80 nm SiO₂ (TEOS-based) ✓ ⊖ ⌚ 1 min
 - ⚙ Oxford Instruments System 100 PECVD / FlexAL ALD Cluster System
 - 📏 Deposition rate — 16.5 Å/ sec
 - 🔥 Temperature — 330 °C
 - ⌚ Duration — 36 sec to 48 sec
 4. Uniformity check ✓ ⊖ ⌚ 5 min
 - ⚙ Woolam M-2000 Model DI Ellipsometer/Filmetrics F50 Reflectometer
- ⊞ **Remarks:** Layer thickness and optical constants are also verified using ellipsometry (⚙ Woolam M-2000 Model DI Ellipsometer) and reflectometry (⚙ Filmetrics F50 Reflectometer).

Step 3. Metal (M0) deposition

⌚ 5.5 hr/wafer

Refractory micro-heaters utilize M0 layer. Tungsten (W) micro-heaters are dc sputtered and deposited at elevated temperature to reduce thin-film resistance and resistance variance across wafer.




















1. Load lock pump and vent time including wafer transfer time ⌚ 6 min
2. Mount graphite thermally conductive flexible thin films between wafer and holder to uniformly distribute temperature which reduce resistance variance across wafer.
3. Substrate heating to 🔥 850 °C ⌚ 20 min
4. Deposit 50 nm W ✓ ⊖ ⌚ 5 min
 - ⚙ Angstrom Engineering Nexdep PVD DC/RF Sputtering System











-  RF power density — 2.96 W/cm² (60 sec) and 4.93 W/cm² (260 sec)
 -  Pressure — 1.2 mTorr
 -  Temperature — 850 °C
 -  Ar Flow — 20 sccm
 -  Duration — 320 sec
 -  Deposition rate — 15.6 Å/ sec
5. Substrate cooldown to room temperature  5 hr
 6. Measure sheet resistance across wafer    5 min
 -  Creative Design Engineering, Inc. CDE ResMap 148 4-Point Prober
 -
-  **Remarks:** High resistivity thin W films should be chosen if paired with conductive bias lines to bias network offset resistance and for adequate bias pulse delivery.

Step 4. Lithography











 30 min/wafer


Maskless UV direct write lithography with positive tone photoresist.

1. Clean surface using plasma ashing before lithography    5 min
 -  Yield Engineering Systems CV2000RFS Oxygen Plasma Asher
 -  RF power — 300 W
 -  Pressure — 300 mTorr
 -  Temperature — 60 °C
 -  O₂ flow — 50 sccm
 -  Duration — 2 min
 2. Coat substrate with positive tone S1811 photoresist   4 min
 -  Brewer Science CEE 200X Spin Coater and 1300X Vacuum Hotplate
- Materials required:** Shipley S1811 photoresist, pipette
-  Dispense photoresist — 5 ml to 7 ml
 -  Align edge bead removal (EBR) and back side rinsing (BSR) nozzles
 -  Spin speed — 500 rpm,  ramp 100 rpm/ sec for first  5 sec and at 5000 rpm,  ramp 1000 rpm/ sec for the rest  60 sec + EBR + BSR

-  Pre-bake temperature — 110 °C for ⌚ 90 sec
-  Cooldown wafer on metal chuck — ⌚ 60 sec
- 3. UV direct write layer pattern   ⌚ 10 min
 -  Heidelberg Instruments MLA150 Direct Write UV Lithography System
 -  Laser — 405 nm
 -  Dose — 100 mJ/cm²
 -  Defocus — -2
- 4. Develop the exposed photoresist  ⌚ 3 min
 -  RaynoldsTech UV Development Hood

Materials Required: Microposit MF-319 developer, pyrex bath containers

 - (a) Prepare one bath of MF-319 resist developer and second bath of DI water
 - (b) Develop the exposed wafer in MF-319 for ⌚ 45 sec to 60 sec
 - (c) Rinse the wafer in DI water bath for ⌚ 2 min
- 5. Inspect wafer under optical microscope  ⌚ 2 min
 -  Olympus MX-61A Semiconductor Microscope
- 6. Descum unwanted photoresist particles   ⌚ 5 min
 -  Yield Engineering Systems CV2000RFS Oxygen Plasma Asher
 -  RF power — 100 W
 -  Pressure — 300 mTorr
 -  Temperature — 30 °C
 -  O₂ flow — 35 sccm
 -  Duration — 2 min





 **Remarks:** This recipe guarantees 1 μm feature size and optimum timing of development time along with dose and defocus can provide less than 1 μm features.

Step 5. Metal (M0) etching

⌚ 9 min/wafer + 15 min

M0 layer is etched using reactive ion etching (RIE).




1. Load lock pump and vent time including wafer transfer time ⌚ 8 min

2. Etch 50 nm W   ⌚ 5 min
- ⚙️ Oxford Instruments Plasmalab System 100 ICP380 Etching System
 - ⚡ RF power — 20 W at 13.56 MHz
 - ⚡ ICP power — 1200 W at 2 MHz
 - ☁️ Pressure — 20 mTorr (strike and breakthrough)
 - 🔥 Temperature — 15 °C
 - ⌇ SF₆ flow — 15 sccm
 - ⌇ CHF₃ flow — 15 sccm
 - ⌇ N₂ flow — 15 sccm
 - ⬆️ Helium (He) backing — 7 Torr
 - 📊 Etch rate — 11.7 Å/ sec
 - 🕒 Etch Duration — 45 sec
3. O₂ plasma chamber cleaning after processing wafers   ⌚ 15 min
.....
- ☰ **Remarks:** This recipe provides selectivity W:Photoresist = 6.8:1

Step 6. Resist removal

🕒 12 min/wafer

Standard resist stripping includes removal of photoresist using solvents followed by plasma stripping.

1. Resist removal using solvents  ⌚ 2 min
- Materials required:** Acetone, IPA, DI water, pyrex bath containers
- (a) Rinse the wafer in acetone bath for 🕒 2 min followed by IPA and DI water rinse. Blow dry the wafer using nitrogen.
- ⚙️ RaynoldsTech Solvent Bench
2. Strip photoresist using plasma stripper   ⌚ 10 min
- ⚙️ Yield Engineering Systems CV200RFS Oxygen Plasma Asher
 - ⚡ RF power — 300 W
 - ☁️ Pressure — 300 mTorr
 - 🔥 Temperature — 30 °C
 - ⌇ O₂ flow — 50 sccm

⌚ Duration — 10 min

3. Inspect wafer under optical microscope ✓ ⌚ 2 min
 ⚙ Olympus MX-61A Semiconductor Microscope
4. Measure layer thickness using stylus profilometer ✓ ⌚ 5 min
 ⚙ Bruker DektakXT Stylus Profiler

≡ **Remarks:** Plasma stripping is optional. For dry etched wafers with plasma exposure time less than 2 min, acetone bath for longer duration clears the photoresist. However, plasma stripping ensures proper cleaning.

Step 7. Metal (M1) deposition ⌚ 25 min/wafer

For SPST switches or devices with bias network resistance less than micro-heater resistor, M0 can be used for providing bias signals. Conductive bias lines are required for devices with complex routing patterns to ensure the resistance of the bias network remains less than that of micro-heater. Sputtered silver (Ag) bias network is used in Gen 3 microfabrication process.

1. Load lock pump and vent time including wafer transfer time ⌚ 15 min
 ⚙ AJA International Inc. ATC Orion Series Twin Chamber PVD System
2. Deposit 70 nm to 100 nm Ag ✓ - ⌚ 5 min
 ⚡ RF power density — 1.97 W/cm²
 ☁ Pressure — 3 mTorr
 🌡 Temperature — 20 °C
 ⚓ Ar Flow — 27 sccm
 ⌚ Duration — 210 sec to 300 sec
 📏 Deposition rate — 3.3 Å/ sec
3. Measure sheet resistance (*if first layer, or on pilot wafer*) ✓ - ⌚ 5 min
 ⚙ Creative Design Engineering, Inc. CDE ResMap 148 4-Point Prober

≡ **Remarks:** Sputter deposition of Ag is preferred for its high speed deposition rate. Evaporation (e-beam) deposition generally has slow deposition rate and without load-lock e-beam system require very long pump down time.

Step 8. Lithography

⌚ 30 min/wafer

Repeat procedure given in **Step 4** with only exception to **Step 4.1**. Instead of ⚡ 300 W RF power, only ⚡ 100 W power is used.

Step 9. Metal (M1) etching

⌚ 9 min/wafer + 15 min

It is preferred to etch Ag using ion milling as RIE does not generally provide residue free etching and have slow etch rates. Meanwhile, due to the thin M0 layer underneath, the inconsistency in ion milling etching rates and selectivity to W did not provide repeatable results. RIE recipe is improved by using Ar/CF₄ chemistry to get residue free films with fast etch rates.

1. Load lock pump and vent time including wafer transfer time ⌚ 8 min

2. Etch 70 nm Ag ✓ - ⌚ 32 sec

⚙ Oxford Instruments Plasmalab System 100 ICP380 Etching System

⚡ Bias voltage — -180 V

⚡ ICP power — 1500 W at 13.56 MHz

☁ Pressure — 6 mTorr (strike at 20 mTorr)

🔥 Temperature — 15 °C

⚡ Ar flow — 30 sccm

⚡ CF₄ flow — 30 sccm

⬆ Helium (He) backing — 7 Torr

📏 Etch rate — 23.3 Å/ sec

⌚ Etch Duration — 32 sec

3. O₂ plasma chamber cleaning after processing wafers ✓ - ⌚ 15 min

≡ **Remarks:** This recipe provides selectivity W:Ag = 1:2

Step 10. Resist removal

⌚ 30 min/wafer

Repeat procedure given in **Step 6**. Agitate wafer in acetone bath to remove as much photoresist as possible before ashing.

Step 11. Dielectric (V12) deposition

⌚ 4.5 hr/wafer

AlN barrier layer is RF sputtered. Thin SiN_x or other thermally conductive layers can also be used. High thermal conductivity of AlN ensures adequate melt-quench sequence and better RF isolation performance.

1. Load lock pump and vent time including wafer transfer time ⌚ 6 min
2. Mount graphite thermally conductive flexible thin films between wafer and holder to uniformly distribute temperature which reduce resistance variance across wafer.
3. Substrate heating to 🔥 500 °C ⌚ 10 min
4. Deposit 100 nm AlN ✓ ⊖ ⌚ 5 min
 - ⚙️ Angstrom Engineering Nexdep PVD DC/RF Sputtering System
 - ⚡ RF power density — 6.67 W/cm²
 - ☁️ Pressure — 3 mTorr
 - 🔥 Temperature — 500 °C
 - ⏴ Ar flow — 20 sccm
 - ⏴ N₂ flow — 14 sccm
 - ⌚ Duration — 470 sec
 - 📏 Deposition rate — 2.12 Å/sec
5. Substrate cooldown to room temperature ⌚ 4 hr
6. Measure uniformity, optical constants and thickness ✓ ⊖ ⌚ 10 min




⚙️ Woolam M-2000 Model DI Ellipsometer

≡ **Remarks:** Ellipsometry requires a model that matches closely to extract material properties. Measurements are usually performed on first or second pilot/test wafers.

Step 12. Lithography

⌚ 40 min/wafer + 30 min

To enhance photoresist adhesion, dielectric layers especially Si, SiO₂, SiN_x require hexamethyl disilazane (C₃H₉Si) or simply HMDS coating prior to any lithography step. HMDS layer is coated on AlN to ensure adequate resist adhesion.















1. Monomolecular 5 Å HMDS vapor priming   ⌚ 30 min
 Yield Engineering Systems 310TA HMDS Coater and Image Reversal System


Repeat procedure given in **Step 8**. ⌚ 10 min additional for correct mask verification and subsequent layer alignment procedure on direct write system.

Step 13. Dielectric (V12) etching

⌚ 5 min/wafer + 15 min

It is preferred to etch Ag using ion milling as RIE does not generally provide residue free etching and have slow etch rates. Meanwhile, due to the thin M0 layer underneath, the inconsistency in ion milling etching rates and selectivity to W did not provide repeatable results. RIE recipe is improved by using Ar/CF₄ chemistry to get residue free films with fast etch rates.

1. Load lock pump and vent time including wafer transfer time ⌚ 4 min
2. Etch 100 nm AlN   ⌚ 14 sec
 Oxford Instruments PlasmaPro 100 Cobra³⁰⁰ ICP Etching System
 RF power — 2000 W at 13.56 MHz
 ICP power — 1200 W at 2 MHz
 Pressure — 40 mTorr
 Temperature — 15 °C
 Ar flow — 50 sccm
 CF₄ flow — 80 sccm
 Helium (He) backing — 10 Torr
 Etch rate — 71.4 Å/ sec
 Etch Duration — 14 sec
3. O₂ plasma chamber cleaning after processing wafers   ⌚ 15 min

 **Remarks:** Etch rates can be controlled using lower RF power in conjunction with lower gas flow rates.

Step 14. Resist removal

⌚ 30 min/wafer

Repeat procedure given in **Step 6**.

Step 15. GeTe (PC) deposition

⌚ 3 hr/wafer

GeTe thin films are dc sputtered at low temperature and annealed in Ar environment.

1. Load lock pump and vent time including wafer transfer time ⌚ 6 min
2. Mount graphite thermally conductive flexible thin films between wafer and holder to uniformly distribute temperature which reduce resistance variance across wafer.
3. Substrate heating to 🔥 100 °C ⌚ 10 min
4. Deposit 130 nm GeTe ✓ ⊖ ⌚ 5.5 min

⚙️ Angstrom Engineering Nexdep PVD DC/RF Sputtering System

⚡ RF power density — 3 W/cm²

☁️ Pressure — 3 mTorr

🔥 Deposition temperature — 100 °C

🔥 Annealing temperature — 200 °C

⚡ Ar flow — 20 sccm

⌚ Duration — 342 sec

📏 Deposition rate — 3.83 Å/ sec

5. Substrate annealing inside deposition chamber with Ar ⌚ 30 min
6. Substrate cooldown to room temperature ⌚ 2 hr
7. Measure sheet resistance (*if first layer, or on pilot wafer*) ✓ ⊖ ⌚ 5 min

⚙️ Creative Design Engineering, Inc. CDE ResMap 148 4-Point Prober

≡ **Remarks:** GeTe films deposited at elevated temperature and annealed in chamber provides stress-free, low resistance thin films.

Step 16. Lithography

⌚ 40 min/wafer

Repeat procedure given in **Step 8**. ⌚ 10 min additional for correct mask verification and subsequent layer alignment procedure on direct write system.

Step 17. GeTe (PC) etching

⌚ 1 hr/wafer

Ion milling is preferred to etch GeTe which can still be etched using RIE. Due to the high etch rate of Ar/CF₄ chemistry and poor selectivity with AlN or SiN_x films, ion milling recipe is optimized to control etch rates.

1. Load lock pump and vent time including wafer transfer time ⌚ 45 min
2. Etch 130 nm GeTe ✓ ⊖ ⌚ 6 sec
 - ⚙️ AJA International Inc. ATC-2035 Ion Milling System
 - ⚡ Beam voltage and current — 400 V, 190 mA
 - ⚡ Accelerating voltage and current — 75 V, 1000 mA
 - ⚡ RF forward power — 200 W
 - ☁️ Pressure — 3 mTorr
 - 🔥 Temperature — 20 °C
 - ⌇ Ar flow — 18 sccm
 - 📏 Etch rate — 5.41 Å/ sec
 - ⌚ Etch Duration — 4 min
3. Optical verification of the sample, stylus profile if required ✓ ⊖ . . . ⌚ 5 min

≡ **Remarks:** This recipe ensures no resist heating/burning which is common in ion milling if high etch power is used to improve etch rates.

Step 18. Resist removal

⌚ 30 min/wafer

Repeat procedure given in **Step 6**.




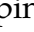

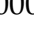
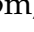





















Step 19. Lithography (Bi-layer resist)

⌚ 40 min/wafer


Maskless UV direct write lithography with bi-layer photoresist for lift-off process.

1. Repeat **Step 4.1** ⌚ 5 min
2. Coat substrate with positive tone PMGI SF7 photoresist ⚠️ ⌚ 4 min
 - ⚙️ Brewer Science CEE 200X Spin Coater and 1300X Vacuum Hotplate


Materials required: PMGI SF7 photoresist, pipette










-  Dispense photoresist — 5 ml to 7 ml
 -  Align edge bead removal (EBR) and back side rinsing (BSR) nozzles
 -  Spin speed — 500 rpm,  ramp 100 rpm/ sec for first  5 sec and at 5000 rpm,  ramp 1000 rpm/ sec for the rest  60 sec + EBR + BSR
 -  Pre-bake temperature — 140 °C for  90 sec
 -  Cooldown wafer on metal chuck —  60 sec
3. Repeat **Step 4.2**  4 min
 4. UV direct write layer align and pattern    20 min
 -  Heidelberg Instruments MLA150 Direct Write UV Lithography System
 -  Laser — 405 nm
 -  Dose — 120 mJ/cm²
 -  Defocus — 1
 5. Repeat **Step 4.4 to 4.6**  10 min
 6. E-beam lithography (EBL) for features <1 μm    5 hr
 -  JEOL JBX-6300FS 100 kV Electron Beam Lithography System
 -  EOS mode 3 — 4th Lens
 -  Dose — Depends on EBL resist and simulation
 -  Focus parameters — Vary, depends on beam current and calibration
-
-  **Remarks:** To speed up this multi lithography step, larger features can be exposed using direct write UV lithography and smaller features can be written using EBL. This requires careful choice of resists and near perfect layer alignment. EBL 100kV system guarantees <5 nm features.

Step 20. Metal (M2) deposition


 1.5 hr

Metal layer M2 is deposited using evaporation (e-beam) with chrome (Cr) seed layer. Nickel (Ni) or titanium (Ti) can also be used as a seed layer for gold (Au). Lithography step with bi-layer resist is used before depositing M2 layer for lift-off procedure.



1. Load lock pump and vent time including wafer transfer time  1 hr

2. Deposit 380 nm Cr/Au   ⌚ 30 min
 -  Intlvac Nanochrome II E-beam PVD System
 -  Beam voltage — 5 kW
 -  Base pressure — $<1 \times 10^{-6}$ Torr
 -  Cr deposition duration — 100 sec
 -  Deposition rate — 3 Å/ sec
 -  Au deposition duration — 25 min
 -  Deposition rate — 2 Å/ sec


⌘ **Remarks:** E-beam deposition is generally slower than sputtering, but for narrow PCM channels, e-beam is preferred to avoid any sidewall residue. Thin films on up to 5 wafers can be deposited simultaneously in e-beam system.


Step 21. Lift-off  1.5 hr


Lift-off time depends heavily on metal layer thickness and layer density.

1. Lift-off bi-layer resist  ⌚ 60 min
Materials required: PG remover, pyrex bath containers, hot plate
 - (a) Individual wafers or wafer cassettes submerged into PG remover.
 - i. Heat PG remover to  60 °C.
 - (b) Rinse wafers with isopropanol (IPA), and deionized (DI) water.
2. Repeat procedure given in **Step 6.2 to 6.4** ⌚ 17 min

⌘ **Remarks:** Ultrasonic acetone bath can be used if PMGI resist is not used. If PG remover deteriorates surface of GeTe, choose another NMP based remover.

Step 22. Dielectric (V23) deposition  10 min/wafer + 15 min

Repeat procedure given in **Step 2** and change deposition time to  120 sec.

Step 23. Lithography  40 min/wafer + 30 min

Repeat procedure given in **Step 12**.

Step 24. Dielectric (V23) etching

⌚ 5 min/wafer + 15 min

Repeat procedure given in **Step 13**. SiO₂ etch chemistry should be used. 📏 Etch rate — 53.7 Å/ sec

Step 25. Resist removal

⌚ 30 min/wafer

Repeat procedure given in **Step 6**.

Step 26. Lithography (Bi-layer resist)

⌚ 40 min/wafer

Repeat procedure given in **Step 19**. Skip **Step 19.6**.

Step 27. Metal (M3) deposition

⌚ 30 min/wafer

A relatively thick M3 layer is deposited using dc sputtering due to high deposition rates.

1. Load lock pump and vent time including wafer transfer time ⌚ 15 min
 ⚙ AJA International Inc. ATC Orion Series Twin Chamber PVD System
2. Deposit 490 nm Ti/Au 🟢⊖ ⌚ 9 min
 - ⚡ RF power density for Ti — 1.75 W/cm²
 - ⚡ RF power density for Au — 4.4 W/cm²
 - ☁ Pressure — 3 mTorr
 - 🔥 Temperature — 20 °C
 - ⌇ Ar Flow — 27 sccm
 - ⌚ Ti deposition duration — 150 sec
 - ⌚ Au deposition duration — 480 sec
 - 📏 Ti deposition rate — 2.7 Å/ sec
 - 📏 Au deposition rate — 9.4 Å/ sec

.....

≡ **Remarks:** At this point the devices are passivated, thus sputter deposition is preferred for M3 to improve deposition rate.

Step 27. Lift-off

⌚ 1.5 hr

Repeat procedure given in **Step 21**.



Appendix B

List of Equipment Used

B.1 Microfabrication Equipment

Physical Vapor Deposition

- AJA International Inc. ATC Orion Series Twin Chamber PVD System
- Angstrom Engineering Nexdep PVD DC/RF Sputtering System
- Intlvac Nanochrome I E-beam and Sputtering PVD System
- Intlvac Nanochrome II E-beam PVD System
- Angstrom Engineering Amod E-beam PVD System
- Leica Microsystems EM ACE600 Sputter Coater
- Allwin21 Corp. AccuThermo AW 610 Rapid Thermal Annealing System

Dry Etching

- Oxford Instruments Plasmalab System 100 ICP380 Etching System
- Oxford Instruments PlasmaPro 100 Cobra³⁰⁰ ICP Etching System
- AJA International Inc. ATC-2035 Ion Milling System
- Intlvac Nanoquest Pico Ion Milling System

- Yield Engineering Systems CV200RFS Oxygen Plasma Asher
- Trion Phantom RIE System

Chemical Vapor Deposition

- Oxford Instruments System 100 PECVD / FlexAL ALD Cluster System
- Trion PECVD System

Lithography

- JEOL JBX-6300FS 100 kV Electron Beam Lithography System
- Raith Nanofabrication RAITH150 II 30 kV Direct Write System
- Heidelberg Instruments MLA150 Direct Write UV Lithography System
- SUSS MicroTec MA6 Mask Aligner /Exposure System with Back-side Alignment
- SUSS MicroTec MJB4 Mask Aligner / Exposure System
- Yield Engineering Systems 310TA HMDS Coater and Image Reversal System
- Brewer Science CEE 200X Spin Coater and 1300X Vacuum Hotplate
- ReynoldsTech and Headway Research Hood and Spin Coaters

Characterization

- JEOL JSM-7200F Field Emission Scanning Electron Microscope
- Zeiss Auriga 40 Focused Ion Beam (FIB)-SEM
- Bruker Dimension FastScan and ICON Atomic Force Microscope
- PANalytical X'pert Pro MRD HR-X-Ray Diffractometer (XRD)
- Woolam M-2000 Model DI Ellipsometer
- Filmetrics F50 Thin Film Mapping Reflectometer
- Bruker Contour Elite I 3D Optical Metrology System
- Bruker DektakXT Stylus Profilometer
- Veeco Dektak 150 Stylus Profilometer

- TOHO Technology FLX-2320-R Thin Film Stress Mapping
- Olympus MX-61A Semiconductor Microscope
- Olympus STM-6 Measurement Microscope
- Creative Design Engineering, Inc. CDE ResMap 148 4-Point Prober

Sample Preparation and Packaging

- Logitech Chemical Delayering and Planarization System
- Disco DAD3240 Automatic Dicing Saw
- West-Bond Inc. 4546E Semi-automatic Wedge Bond Tool
- West-Bond Inc. 747677E Wire Bonding System
- QuikLaze-50 Multi-Wavelength Laser Trimming System
- Samco Inc. LFC150 Plasma Cleaner
- Tresky T-3000-FC3 Die Bonder
- JFP Microtechnic Flip Chip Bonder

B.2 RF/DC Measurement Equipment

RF Measurements

- Keysight N5127B DC–67 GHz PNA-X Network Analyzer
- Keysight N5242A DC–26.5 GHz PNA-X Network Analyzer
- Keysight N9020A MXA DC–26.5 GHz Signal Analyzer
- Keysight E4428C ESG Signal Generator (×2)
- OPHIR 5140 0.7 GHz to 3.0 GHz +41 dBm Power Amplifier
- INMET 64671 18B50W -30 dB Attenuator (×2)
- INMET TS180M 5 W Matched Load (×2)
- Krytar Model 1850 -16 dBm Directional Coupler (×2)
- RF Lambda RFLT2W2G08G 2 GHz to 8 GHz Power Combiner/Splitter

- RF Lambda RFDC2G8G10 -10 dBm Directional Coupler
- Meca Electronics C-1.950 Circulator (×2)
- SHF Communication Technologies AG SHF BT65R - HV100 Bias Tee (×2)
- Teledyne CCR-33S80-RN-1 SPDT Coaxial Latching Switch
- Transco XMSN Line SPDT Coaxial Failsafe Switch (×2)

DC Measurements

- Keysight B2902A Precision Source Measure Unit
- Keithley 4200A-SCS Semiconductor Parameter Analyzer
- Keysight B1500A Semiconductor Device Parameter Analyzer
- Keysight 33621A Arbitrary Function Generator
- Rohde and Schwartz RTO 1044 4 GHz Real Time Oscilloscope
- Tektronix MDO-3014 Mixed Signal Oscilloscope
- HP 8110A Pulse Pattern Generator
- HP 81140 High Voltage Pulse Pattern Generator
- Keysight 34470A Digital Multimeter
- Sorensen XG Series Programmable Power Supply
- HP 6632B System DC Power Supply (×3)
- Trek Model PZD700A High Voltage Amplifier / Piezo Driver
- Microsanj NT220 Nanosecond Transient Thermal Imaging System

Probes/Probe Stations

- Lakeshore CPX Cryogenic Probe Station with Vibration Isolation
- SUSS MicroTec PMC-150 Vacuum Cryoprobe
- Cascade Microtech PM5 Manual Probe Station
- Cascade Microtech Model 9000 Manual RF Probe Station
- Everbeing C-8 Probe-Station with Shielding Box
- MPI Titan 67A GSG Probes (×2)

- Cascade Microtech |Z| Series Coaxial GSG Probe (×2)
- Picoprobe M40A GSG Probes (×2)
- MPI Corp. Allstron AC-2 Calibration Standard
- TOYO Corp. ZN50R-CVT Variable Temperature Probes (×4)
- Everbeing Tungsten DC Probe Tips with Micro-Manipulators (×6)
- Junkosha 67 GHz Phase Stable RF Cables (×2)

B.3 Modeling Softwares

RF Simulations

- Ansys Electronics Desktop 2020 (Ansys HFSS)
- Sonnet EM Professional Suite v17.54
- Keysight PathWave Advanced Design System (ADS) 2020
- Keysight PathWave EM Design (EMPro) 2020
- Keysight PathWave RF Synthesis (Genesys) 2020

Circuit Simulations

- Cadence Virtuoso IC Design Suite 6.16
- Keysight PathWave Advanced Design System (ADS) 2020
- Xilinx ISE Design Suite

Multiphysics Modeling

- COMSOL Multiphysics 5.5
- Ansys Workbench 2019
- Coventorware CoventorMP and SEMulator3D
- Solidworks Professional 2020

Layout/Circuit Designs

- Cadence Virtuoso IC Design Suite 6.16
- Altium Designer 20
- Tanner EDA L-Edit
- Layout Editor and KLayout

Mathematical Solvers

- Wolfram Mathematica 12
- MathWorks Matlab R2019b

Glossary

5G is the fifth generation wireless technology for digital cellular networks that began wide deployment in 2019. As with previous standards, the covered areas are divided into regions called "cells", serviced by individual antennas. Virtually every major telecommunication service provider in the developed world is deploying antennas or intends to deploy them soon. The frequency spectrum of 5G is divided into millimeter waves, mid-band and low-band. Low-band uses a similar frequency range as the predecessor, 4G.

Active RF Components rely on an external power source to perform their functions. Some of the most commonly used active RF components are: power amplifiers, low-noise amplifiers, diodes, limiters, switches, transistors, mixers, phase-locked loops, data converters etc.

Chalcogenide a chemical compound consisting of at least one chalcogen anion and at least one more electropositive element. Although all group 16 elements of the periodic table are defined as chalcogens, the term chalcogenide is more commonly reserved for sulfides, selenides, and tellurides, rather than oxides. Many metal ores exist as chalcogenides.

Chalcogenide Phase Change Material (PCM) based on the chalcogenides are a class of solids that can be transitioned by thermal actuation between a crystalline phase, which is highly electrically conductive, and an amorphous phase, which is highly electrically insulating. In particular, germanium telluride (GeTe)-based PCMs have demonstrated a very high amorphous-to-crystalline resistance ratio and a very low crystalline-state resistance. This resistance state is non-volatile and is naturally applicable for latching RF/microwave switches.

Germanium Telluride a chemical compound of germanium and tellurium and is a component of chalcogenide glasses. It shows semi-metallic conduction and ferroelectric behavior.

Heterogeneous Integration refers to the assembly and packaging of multiple separately manufactured components onto a single chip in order to improve functionality and enhance operating characteristics.

Metal-Insulator Transition (MIT) are transitions from a metal (material with good electrical conductivity of electric charges) to an insulator (material where conductivity of charges is quickly suppressed). These transitions can be achieved by tuning various ambient parameters such as pressure or, in case of a semiconductor, doping. VO₂ shows MIT behavior at 68 °C.

Microfabrication is the process of fabricating miniature structures of micrometer scales and smaller. Historically, the earliest microfabrication processes were used for integrated circuit fabrication, also known as “semiconductor device fabrication”.

Millimeter Wave (mmWave) communication systems have attracted significant interest regarding meeting the capacity requirements of the future 5G network. Millimeter waves are electromagnetic (radio) waves typically defined to lie within the frequency range of 30 GHz to 300 GHz. The microwave band is just below the millimeter-wave band and is typically defined to cover the 3 GHz to 30 GHz range.

Monolithic Integration is a process of manufacturing a complete functional circuit or group of circuits in a single piece of substrate. Monolithic integration provides the flexibility of miniaturization, performance enhancements and packaging ready devices.

Monolithic Microwave Integrated Circuit (MMIC) is a type of integrated circuit (IC) device that operates at microwave frequencies. These devices typically perform functions such as microwave mixing, power amplification, low-noise amplification, and high-frequency switching.

Passive RF Components does not require a power source to perform their functions. Some of the most commonly used passive RF components are: capacitors, inductors, resistors, baluns, filters, attenuators, antennas, switches, phase shifters, hybrids, power dividers, power combiners, matching networks etc.

Phase Shifter is used to change the transmission phase angle of an input signal. Ideally phase shifters provide an output signal with an equal amplitude to the input signal, any loss here will be accounted to the insertion loss of the component. The input signal is shifted in phase at the output based on the configuration of the phase shifter selected.

PIN Diode a diode with a wide, undoped intrinsic semiconductor region between a p-type semiconductor and an n-type semiconductor region. The p-type and n-type regions are typically heavily doped because they are used for ohmic contacts.

RF Front End is a device or module that incorporates all the circuitry between the antenna and at least one mixing stage of a receiver and possibly the power amplifier of the transmitter. They are used in a wide variety of RF products and applications. Examples include wireless systems and FM radio systems.

RF Switch an RF switch or microwave switch is a device to route high frequency signals through transmission paths. RF and microwave switches are used extensively in microwave test systems for signal routing between instruments and devices under test (DUT).

RF Switch Matrix a system of discrete electronic components that are integrated to route RF signals between multiple inputs and multiple outputs. Popular applications requiring RF matrices are ground systems, test equipment, and communication systems.

Vanadium Oxide an inorganic compound, has a phase transition very close to room temperature (68 °C). Electrical resistivity and opacity of this material can change up several orders. Due to these properties, it has been widely used in surface coating, sensors, and imaging.

Index

- 5G, 1
- 3D modeling, 100
- Active tuning, 94
- Actuation, 43, 102
- Alignment issues, 48
- Amorphous GeTe, 36, 70, 102, 212
- Amplifiers, 1
- Antennas, 1
- Atomic force microscopy, 32, 35
- Bandgap, 92
- Bandpass, 94
- Bandwidth, 1
- Bias condition, 110, 213
- Bias lines, 138
- Bias network, 138
- Bias signature, 66, 108
- Bridged-T resistor network, 179
- Calibration, 70
- Capacitor bank, 166
- CCD, 94, 104
- Chalcogenide, 2, 10, 21, 213
 - Phase transition, 33
- Communication systems, 31
- Comparison, 87
- CPW discontinuities, 137
- Cracks formation, 45
- Cross wafer resistance mapping, 41
- Cross-section, 48, 103
- Crossbar configuration, 2, 28, 147
- Crossbar switch matrix
 - 16x16 RF configuration, 162
 - 2x2 RF configuration, 150
 - 4x12 LF configuration, 159
 - 4x4 RF configuration, 153
 - Unit-cell, 148
- Cryogenic chamber, 215
- Cryogenic device cycling, 219
- Cryogenic measurements, 212
- Cryogenic PCM RF switch, 212
- Cryogenic temperature, 218, 224
- Crystalline GeTe, 36, 70, 102, 212
- Current carrying capacity, 70
- Cycle testing, 219
- Damped vibrations, 94
- DC power handling, 70
- DC sputtering, 34, 51, 57, 61
- Delay lines, 188
- Deposition pressure, 40
- Deposition temperature, 37
- Design dimensions, 33
- Development constraints, 45

- Device cycling, 219
- Device reliability cycles, 82
- Device resistance, 218
- Distributed circuits, 18
- Dynamic range, 81

- Electrical characterization, 32, 44
- Electrical pulse, 10
- Electron beam lithography, 48
- Elements and Alloys
 - Antimony (Sb), 10
 - Antimony Telluride (SbTe), 10
 - Chrome (Cr), 51, 57, 61
 - Germanium (Ge), 10
 - Germanium Antimony Telluride ($\text{Ge}_x\text{Sb}_y\text{Te}_z$), 10
 - Germanium Telluride (GeTe), 51, 57, 61, 97, 132
 - Gold (Au), 51, 57, 61
 - Nichrome (NiCr), 51, 57, 61
 - Selenium (Se), 10
 - Silicon Dioxide (SiO_2), 51, 57, 61
 - Silicon Nitride (SiN_x), 51, 57, 61
 - Sulfur (S), 10
 - Telluride (Te), 10
 - Titanium (Ti), 51, 57, 61
 - Tungsten (W), 37, 43, 51, 57, 61, 97
 - Vanadium Oxide (VO_2), 11
 - Vanadium Pentoxide (V_2O_5), 12
 - Vanadium Sesquioxide (V_2O_3), 12
- Elements and Alloys (Alumina (Al_2O_3), 51, 57, 61
- Evaporation, 57, 61

- FEM, 97, 100
- Filter, 94
- Filters, 1
- Finite element modeling, 97, 100

- Focused ion beam SEM, 32, 47
- Four point probing, 41

- Germanium Telluride (GeTe), 10, 97, 132
 - Amorphous state, 10, 36, 70
 - Characterization, 32
 - Cryogenic, 212
 - Crystalline state, 10, 36, 70
 - Deposition conditions, 34
 - Deposition parameters, 34
 - Doped, 12
 - Electrical properties, 12
 - Ferroelectric behavior, 12
 - Grain mapping, 39
 - Material properties, 12
 - Melting, 46, 51, 57, 61
 - Optical properties, 12
 - Phases, 12
 - Physical properties, 12
 - Resistance change, 32
 - Semi-metallic conduction, 12
 - Sputtering target, 12
 - Superconductor, 12
 - Surface profile, 35
 - Surface topography, 35
 - Switching principle, 13, 15
 - Theory, 12
 - Thin film optimization, 32
 - Voids formation, 45
- Grain mapping, 39
- Grain size, 37
- GSG probes, 70

- Harmonic distortion, 75
- Heat coefficient, 97
- Heat distribution, 91, 99, 104
- Heat flow, 110

- Heat generation, 218
- High resistance, 212
- High resistance ratio, 212
- High speed micro-heaters, 96
- Hybrid integrated circuit, 17

- Impedance Tuner, 208
- Insertion loss, 18, 62
- Integrated resistors, 179
- Intermediate resistance states, 221
- Intermodulation distortion, 75
- Intermodulation products, 77
- Ion milling, 61
- Isolation, 18, 62
- IV characteristics, 71, 213

- Joule heating, 70

- Laser pulse, 10
- Latching switches, 3, 23
- LED, 94
- Lifetime cycles, 62, 82
- Lift-off technique, 61
- Linearity, 75
- Loss compensation, 188
- Low temperature measurements, 212
- Lumped components, 18
- Lumped model, 64

- Matched load, 81
- Material characterization, 47
 - Atomic force microscopy, 32
 - Focused ion beam SEM, 32
 - Grain mapping, 39
 - Resistance mapping, 32, 41
 - Scanning electron microscopy, 32
 - Surface topography, 35
- Material degradation, 46
- Material melting, 46

- Matrix
 - Switch Matrix, 3
- Measurements
 - Band reject filter, 133
 - Capacitor bank, 170
 - Crossbar switch matrices, 155
 - Cryogenic PCM, 212
 - Current carrying capacity, 70
 - Heat distribution, 102
 - Intermodulation distortion, 75
 - IV characteristics, 71
 - Lifetime cycles, 82
 - Linearity, 75
 - Low temperature, 212
 - Non-volatility, 86
 - Redundancy switch matrix, 145
 - Reliability, 82, 104
 - RF performance, 66
 - RF power handling, 72
 - RT Phase shifter, 207
 - Self actuation, 75
 - ST Phase shifter, 194, 198
 - Stability, 86
 - Switch actuation, 65
 - Switch matrix, 126
 - Switching speed, 81
 - T-type switch, 139
 - Temperature dependent, 220
 - Thermal crosstalk, 107
 - Thermal imaging, 107
 - Third order intercept, 75
 - Transient heat, 91
 - Two-tone, 79
 - Variable attenuator, 182
- Melt-quench sequence, 102, 221
- Metal Insulator Transition, 12
 - Material, 12
 - Vanadium Oxide (VO₂), 11

- Micro-heaters, 33, 43, 70, 96
 - Characterization, 44
- Microfabrication, 97
 - Alignment, 48
 - Constraints, 45
 - Deposition conditions, 34
 - Deposition pressure, 40
 - Deposition temperature, 37
 - Electron Beam Lithography, 48
 - Evaporation, 57, 61
 - Gen 1, 51
 - Gen 2, 57
 - Gen 3, 61, 132
 - Ion milling, 61
 - Lift-off, 51, 57, 61
 - Optical lithography, 48
 - Passivation, 51, 57, 61
 - PECVD, 51, 57, 61
 - Process summary, 62
 - RCA1, 51, 57, 61
 - RIE, 51, 57, 61
 - Seed layer, 51, 57, 61
 - Sputtering, 51, 57, 61
 - DC, 51, 57, 61
 - Stresses, 43
- Microwave switching, 1, 16
- Millimeter wave (mmWave), 1, 111, 134, 178, 188
 - PCM multi-port RF switches, 112
 - PCM switch matrices, 112
- Miniature RF device, 134
- MMIC, 17, 132, 179, 201
- Monolithically integrated, 132, 179, 201, 208
- Multi-port RF switches, 24, 111, 116
 - C-Type, 27
 - R-Type, 27
 - T-Type, 27
- Multi-port switches, 132
 - T-Type, 134
- Multiphysics modeling, 100
- Non-volatile, 212
- Non-volatility, 224
- Non-volatility testing, 86
- Notch filter, 132
- Optical lithography, 48
- Packaging, 111
- Parasitic capacitance, 62
- Partial melt-quench, 221
- Passive RF components, 179, 188
- Passive RF PCM components, 165
- PECVD, 51, 57, 61
- Performance improvement, 213
- Phase change alloys, 11
- Phase change material
 - Characterization, 33
- Phase change materials
 - Actuation Methods, 21
 - Advancements, 8
 - Applications, 10, 24
 - Characterization, 32
 - Development constraints, 45
 - Early attempts, 9
 - Electrical characterization, 32
 - History, 7
 - Literature, 21
 - Optical storage, 10
 - Parasitic capacitance, 62
 - Phase transition, 33
 - Principle, 9
 - Resistance change, 42
 - RF adaptability, 11
 - Surface profile, 35
 - Switches, 20

- Theory, 10
- Phase change memory, 8, 12
- Phase shifter, 188
 - Reflective type, 201
 - Switched type TTD, 188, 196
- Post pulsing, 108
- Power consumption
 - Steady-state, 23
- Pulse conditions, 70
- Pulse generator, 96, 216
- Pulsing failure, 108

- Radio frequency (RF), 1, 24
 - Components, 1, 111
 - Switches, 1
 - Continuous wave (CW), 81
 - Devices, 1
 - Linearity, 75
 - Modules, 1
 - Power handling, 72, 75
 - Switching speed, 81
- Reactive ion etching, 51, 57, 61
- Reconfigurability, 1
- Reconfigurable circuit, 188
- Reconfigurable impedance matching network, 208
- Reconfigurable PCM capacitor bank, 166
- Redundancy switch matrix, 140
- Reflective loads, 203
- Reflectivity, 92
- Refractory micro-heater, 96
- Reliability, 62, 82, 86, 104, 111, 219
- Residual stresses, 43
- Resistance change, 32, 43
- Resistance mapping, 32
- Resistance states, 222
- Resistivity, 43

- Resistor, 70
- Resonator, 132
- Return loss, 18, 62
- Reversible switching, 222
- RF calibration, 70
- RF components, 111, 208
- RF cross-over, 138
- RF device selector, 128
- RF measurements, 62, 66
- RF PCM Band reject filter, 132
- RF PCM components, 165
 - 3-bit phase shifter, 188
 - 4-bit switchable attenuator, 177
 - 6-bit capacitor bank, 166
 - Band reject filter, 132
 - Cross-over, 138
 - SP16T switch, 118
 - SP3T switch, 114
 - SP8T switch, 116
 - SPDT switch, 113, 132
 - SPST switch v2, 57
 - SPST switch v3, 61
 - Summary, 164
 - Switch matrices, 124
 - 16x16 LF Crossbar, 162
 - 2x2 scalable, 124
 - 4x12 LF Crossbar, 159
 - 4x6 Redundancy, 140
 - LF crossbar, 159
 - RF 2x2 Crossbar, 150
 - RF 4x4 Crossbar, 153
 - RF Crossbar matrix unit-cell, 148
 - T-type switch, 134
- RF PCM phase shifter, 188
- RF PCM SP16T switch, 118
- RF PCM SP3T switch, 114, 188
- RF PCM SP8T switch, 116
- RF PCM SPDT switch, 112, 132

- RF PCM SPST switch, 57, 61, 221
- RF PCM switch
 - Actuation signals, 66
 - Bias signature, 66
 - Cryogenic behavior, 212
 - Current carrying capacity, 70
 - Design, 50
 - Design optimization, 56
 - Intermodulation distortion, 75
 - IV characteristics, 71
 - Lifetime cycles, 82
 - Linearity, 75
 - Lumped model, 64
 - Measurements, 65
 - Operation, 50
 - Parametric study, 52
 - Parasitic capacitances, 63
 - Reliability, 82
 - RF measurements, 66
 - RF performance, 66
 - RF power handling, 75
 - Self actuation, 72
 - Simulations, 52
 - Stability, 86
 - Switch actuation testing, 65
 - Switching speed, 81
 - Thermal crosstalk, 107
 - Thermal imaging, 109
 - Transient heat, 91
- RF PCM switch matrices, 124
- RF PCM switchable attenuator, 177
- RF performance, 18, 97, 126, 220
 - Comparison, 22
- RF power handling, 72, 75
- RF sputtering, 34
- RF switch comparison, 87
- RF switch matrix, 111
- RF Switches
 - Comparison, 18
 - Mechanical, 2, 16
 - MEMS, 2, 81
 - Multi-port, 24, 111
 - Parasitics, 62
 - PCM, 20, 32, 49, 82, 86
 - Reliability, 19
 - Semiconductor, 1, 81
 - Solid-state (Semiconductor), 17
- RF-MEMS, 81, 111
 - Advantages, 18
 - Issues, 19
 - Switches, 18
- Routing functionality, 113
- Satellite link, 26
- Scalable crossbar architecture, 147
- Scalable switch matrix, 124
- Scanning electron microscopy, 32
- Seed layer, 51, 57, 61
- Self actuation, 72, 75
- Semiconductor technology, 25
- Simulations, 103
 - Impedance matching network, 211
- Source measure unit, 70
- Speed analysis, 81
- Spring coil stresses, 43
- Spurious, 76
- Stability, 86
- State stability, 224
- State-of-the-art, 87
- Surface profile, 35
- Surface roughness, 35, 39
- Surface topography, 35
- Switch actuation testing, 65
- Switch architectures, 1
- Switch cycle testing, 62

- Switch matrices, 24, 111, 124, 140, 147, 155, 159
 - RF-MEMS, 27
 - Semiconductor, 25
 - Waveguide, 25
- Switch matrix, 2, 24, 111, 124, 132, 134, 140, 155
 - Configurations, 26
 - Crossbar, 28
- Switching speed, 81
- T-type switch, 134
- Telecommunication industry, 1
 - Wireless technologies, 1
 - Wireless devices, 1
- Temperature, 102
- Temperature dependency, 213
- Thermal balance, 109
- Thermal cross-section, 107
- Thermal crosstalk, 108, 137
- Thermal imaging, 92, 96, 105
- Thermoreflectance, 91, 92, 96, 98
- Thin film characterization, 33
- Thin film cracks, 39
- Thin film resistor (TFR), 33
- Thin film stresses, 39
- Third order intercept, 75
- Third order intermodulation, 77
- Transient heat distribution, 100
- Transient thermal analysis, 91
- Transient thermal imaging, 96
- True-time-delay, 188
- Two-tone linearity, 79
- Unit-cell, 127, 134
- Variable attenuator, 177
- Vibration compensation, 94
- Voids formation, 45
- Waveguide technology, 25
- Wideband, 188
- Wideband resistors, 179